

Molecular Rigidification for Efficient Transition Metal Complex-Based Triplet Emitters

Inaugural Dissertation
for the attainment of the
Doctoral Degree (Dr. rer. nat.)

University of Cologne
Department of Chemistry
Institute for Inorganic and Materials Chemistry
Research Group of Prof. Dr. Axel Klein

Submitted by
Maryam Niazi (M. Sc.)

Cologne, April 2025

Referees:	Prof. Dr. Axel Klein
	Prof. Dr. Dr. (h.c.) Sanjay Mathur
Chair:	Prof. Dr. Klas Lindfors
Date of Submission:	24.02.2025
Date of Examination:	25.04.2025

Acknowledgment

I would like to express my deepest gratitude to **Prof. Dr. Axel Klein** for giving me the opportunity to pursue my doctorate. I sincerely appreciate your guidance, the exciting research topic, and the invaluable scientific and moral support throughout this journey. Working in your group has been a privilege, and I am especially grateful for your kindness, as well as that of your spouse, **Petra**.

I extend my heartfelt thanks to **Prof. Dr. Dr. (h.c.) Sanjay Mathur** for serving as my second supervisor and examiner. I always felt welcome in your group, and I truly appreciate your support and encouragement.

I am deeply thankful to the **German Academic Exchange Service** (**DAAD**) for the financial support since 2021. Being a DAAD scholar has been an honor, and I will always carry this affiliation with pride.

I would also like to acknowledge my wonderful colleagues in the **AK Klein** group, especially my lab mates in 317—**Eric Anthony Tobechukwu**, **Rose Jordan**, **Noah Sander**, and **Asia Nisar**—for making the lab a great place to work. A special thanks to the Platinum Lab, **Johannes Hohnsen** and **Joshua Friedel**, as well as the Nickel Lab, **Sascha Schäfer, Lukas Kletsch**, **Leo Payen**, and **Vladimir Kjartan Stojadinovic**, for your collaboration, support, and insightful discussions.

I am grateful to **Silke Kremer**, **Dr. Ingo Pantenburg**, and **Dr. David van Gerven** for their help in measuring my single-crystal samples. Many thanks to **Dirk Pullem** for elemental analyses, **Kathrin König** for high-field NMR measurements, and **Astrid Baum** and **Michael Neihs** for mass spectrometry.

I also appreciate the support of **Ingo Müller**, **Nihad El Ghachtoun**, and **Sylvia Rakovac** from the chemical storage department. A special acknowledgment goes to **Dr. Ivan Maisuls** from the **AK Strassert** at Universität Münster for performing photoluminescence spectroscopy.

I sincerely thank **Prof. Dr. Pablo González-Herrero** for the opportunity to visit Universidad de Murcia, where I conducted luminescence measurements and had the chance to experience life in Spain. My gratitude also extends to **EUniWell Abroad Fellowship** of the University of Cologne for financially supporting this research trip.

To my husband, **Dr. Touraj Karimpour**—words cannot express how much your love, patience, and unwavering support have meant to me. Your encouragement and belief in me made this journey possible, and I am forever grateful for having you by my side.

I would also like to thank my family, especially my beloved sister **Fateme**, for always being there for me. To my dear friends, **Niusha** and **Sumiya**, your friendship and support have been invaluable throughout this journey.

Thank you all from the bottom of my heart!

Abstract

Transition metal complexes are promising candidates for optoelectronic applications due to their ability to emit from triplet states. However, non-radiative deactivation pathways often caused by structural distortions between the ground and excited states, quench emission. In this work, we explore molecular rigidification as a strategy to enhance luminescence efficiency in cyclometalated Pt(II), Pd(II), and Ni(II) complexes by tuning second sphere interactions and steric bulk.

Square planar [M(N^C^N)Cl] (M = Pt, Pd, Ni; N^C^N = 1,3-dipyridyl-benzene) complexes with NH-functionalized ligands were synthesized to facilitate intramolecular hydrogen bonding. Structural analysis confirmed distorted square planar geometries and hydrogen bonding interactions, and DFT calculations revealed minimal reorganization between the ground and triplet excited states. While Pt(II) complexes exhibited intense phosphorescence in solution at 298 K, Pd(II) analogues remained non-emissive at 298 K, indicating that rigidification alone was insufficient to suppress non-radiative decay. In Ni(II) complexes, elongated Ni–N bonds in the excited state were observed, and emission studies confirmed structured phosphorescence. However, transient absorption spectroscopy suggested that the excited state absorptions were ligand-centered and short-lived, with potential decomposition pathways complicating the photophysical analysis.

To optimize photoluminescence, chloride coligands were replaced with phenoxide (OPh^-), strengthening hydrogen bonding (M–O···H–N), but further studies are needed to assess the impact on emission. To distinguish steric from hydrogen bonding effects, benzyl-substituted analogues of [M(N^C^N)Cl] (M = Pt, Pd, Ni), instead of NHR functionalities in the earlier complexes were synthesized. X-ray diffraction revealed steric-induced distortions, particularly in Ni(II). Pt(II) complex displayed room-temperature phosphorescence, forming emissive aggregates in polymer matrices, while Pd(II) and Ni(II) complexes were only emissive at 77 K.

Further modifications introduced electron-donating (Me) and electron-withdrawing (F or Cl) substituents on different positions of the N^C^N ligand framework, revealing π···π interactions. Pt(II) complexes exhibited highly efficient triplet emission (quantum yields up to 0.97 at 298 K), whereas Pd(II) and Ni(II) complexes showed weak luminescence at 77 K due to metal-centered deactivation.

Lastly, incorporating quinoline units into the N^C^N ligand backbone in [M(L^{Qu})Cl] (M = Pt, Pd, Ni; L^{Qu} = bis(2-pyridyl)/2-quinolyl)benzene) complexes induced minimal structural reorganization in Pt(II) but increased reorganization in Pd(II) and Ni(II) derivatives. This modification subtly red shifted absorption bands, highlighting its influence on electronic and photophysical properties.

Overall, this study demonstrates that both second sphere interactions and steric bulk influence structural rigidity and emission properties, with implications for designing next generation triplet emitters.

Table of Contents

1. Introduction 1

1.1. Properties of group 10 transition metals and their square planar d^8 complexes 1

1.2. Luminescence in Pt, Pd, and Ni complexes 2

1.2.1. What is luminescence? 2

1.2.2. The efficiency of luminescence 3

1.3. Cyclometalated Pt, Pd, and Ni complexes 5

1.3.1. Synthesis of cyclometalated Pt, Pd, and Ni complexes 10

2. Scientific Objectives 13

3. Results and Discussion 17

3.1. [M(L^{NHPh})Cl] and [M(L^{NHBn})Cl] (M = Pt or Pd) complexes 17

3.1.1. Synthesis and structure of [M(L^{NHPh})Cl] and [M(L^{NHBn})Cl] (M = Pt or Pd) 17

3.1.2. Experimental and theoretical properties of [M(L^{NHPh})Cl] and [M(L^{NHBn})Cl] (M = Pt or Pd) 19

3.2. [Ni(L^{NHPh})Cl] and [Ni(L^{NHBn})Cl] complexes 27

3.2.1. Synthesis and structure of [Ni(L^{NHPh})Cl] and [Ni(L^{NHBn})Cl] 27

3.2.2. Experimental and theoretical properties of [Ni(L^{NHPh})Cl] and [Ni(L^{NHBn})Cl] 29

3.3. [M(L^{Bn})Cl] (M = Pt, Pd, Ni) complexes 38

3.3.1. Synthesis and structure of [M(L^{Bn})Cl] (M = Pt, Pd, Ni) 38

3.3.2. Experimental and theoretical properties of [M(L^{Bn})Cl] (M = Pt, Pd, Ni) 40

3.4. [M(L^{NHPh})OPh] and [M(L^{NHBn})OPh] (M = Pt or Pd) complexes 49

3.4.1. Synthesis and structure of [M(L^{NHPh})OPh] and [M(L^{NHBn})OPh] (M = Pt or Pd) 49

3.4.2. Experimental and theoretical properties of [M(L^{NHPh})OPh] and [M(L^{NHBn})OPh] (M = Pt or Pd) 51

3.5. [M(L^{R})X] (M = Pt, Pd, Ni; R = Me, Me_2, Cl, F; X = Cl or Br) complexes 55

3.5.1. Synthesis and structure of [M(L^{R})X] (M = Pt, Pd, Ni; R = Me, Me_2, Cl, F; X = Cl or Br) 55

3.5.2. Experimental and theoretical properties of [M(L^{R})X] (M = Pt, Pd, Ni; R = Me, Me_2, Cl, F) 58

3.6. [M(L^{Qu})Cl] (M = Pt, Pd, Ni) complexes 65

3.6.1. Synthesis and structure of [M(L^{Qu})Cl] (M = Pt, Pd, Ni) 65

3.6.2. Experimental and theoretical properties of [M(L^{Qu})Cl] (M = Pt, Pd, Ni) 67

4. Conclusion and Outlook 72

5. Experimental Section 82

5.1. Materials and methods 82

5.2. Experimental procedures 85

5.2.1. Syntheses of the N^C^N ligand precursor HL^{NHPh} 85

5.2.2. Synthesis of the N^C^N ligand precursor HL^{NHBn} 86
5.2.3. Synthesis of [M(L^{NHPh})Cl] and [M(L^{NHBn})Cl] (M = Pt or Pd) complexes 87
5.2.4. Synthesis of the ligand precursor ClL^{NHPh} 89
5.2.5. Synthesis of the ligand precursor ClL^{NHBn} 90
5.2.6. Synthesis of [Ni(L^{NHPh})Cl] and [Ni(L^{NHBn})Cl] complexes 91
5.2.7. Synthesis of the ligand precursor HL^{Bn} 92
5.2.8. Synthesis of the ligand precursor ClL^{Bn} 93
5.2.9. Synthesis of the complexes [M(L^{Bn})Cl] (M = Pt or Pd) 94
5.2.10. Synthesis of [Ni(L^{Bn})Cl] complex 94
5.2.11. Synthesis of the complexes [M(L^{NHPh})NO_3] and [M(L^{NHBn})NO_3] (M = Pd or Pt) 95
5.2.12. Synthesis of the complexes [M(L^{NHPh})OPh] and [M(L^{NHBn})OPh] (M = Pt or Pd) 95
5.2.13. Synthesis of the N^C^N ligand precursors HL^{Me}, ClL^{Me}, HL^{Me2}, HL^{F}, and HL^{Cl} 97
5.2.14. Synthesis of [M(N^C^N)Cl] (M = Pt or Pd; N^C^N = L^{Me}, L^{Me2}, L^{F}, L^{Cl}) complexes 99
5.2.15. Synthesis of [Ni(N^C^N)X] (N^C^N = L^{Me}, L^{F}, L^{Cl}; X = Cl or Br) complexes 102
5.2.16. Synthesis of the N^C^N ligand precursors HL^{Qu} 103
5.2.17. Synthesis of the ligand precursor ClL^{Qu} 103
5.2.18. Synthesis of the complexes [M(L^{Qu})Cl] (M = Pt or Pd) 104
5.2.19. Synthesis of [Ni(L^{Qu})Cl] complex 105

6. References 106

7. Appendix 119

7.1. NMR spectra 119

7.2. Mass spectra 159

7.3. Single crystal XRD and calculated structural data 175

7.4. Electrochemistry and DFT-calculated frontier molecular orbitals data 206

7.5. UV-vis absorption spectra with TD-DFT-calculated electronic transitions 230

7.6. Photoluminescence data 242

7.7. Calculated coordinates of the optimized structures 265

8. Declaration regarding the dissertation 284

9. Curriculum Vitae ..... Error! Bookmark not defined.

10. Publications ..... Error! Bookmark not defined.

1. Introduction

1.1. Properties of group 10 transition metals and their square planar d^8 complexes

The transition metals nickel (Ni), palladium (Pd), and platinum (Pt) are key members of group 10 in the periodic table. Their chemistry is dominated by the +II oxidation state, which corresponds to a d^8 electron configuration. While Ni(II) forms both tetrahedral and square planar complexes as well as some octahedral geometries depending on the ligand strength, the heavier homologues Pd(II) and Pt(II) predominantly exhibit square planar coordination. This preference arises due to the thermodynamic stabilization offered by this geometry in the presence of strong-field ligands, which pushes a single antibonding orbital to high energy while stabilizing four of the occupied orbitals (Figure 1-1). Along the series from Ni to Pt, the ligand field splitting in isostructural complexes increases with the element number, further favoring square planar geometries for the heavier elements.[1]

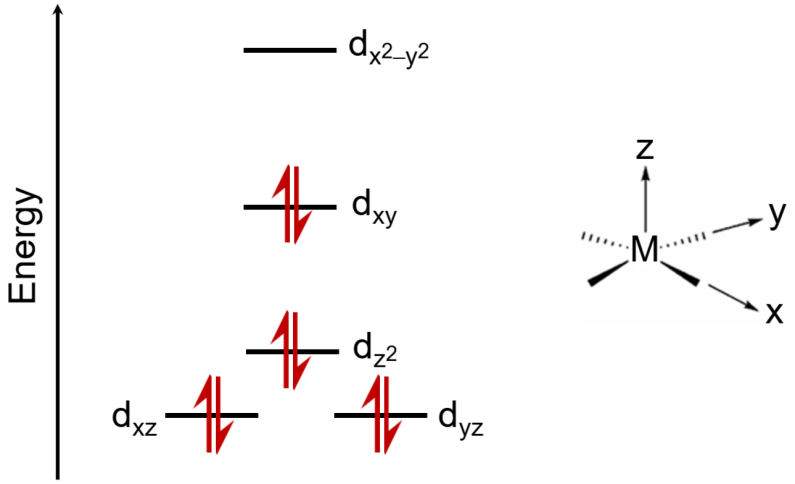


Figure 1-1. Ligand field splitting diagram for transition metal d-orbitals in a square planar complex. By convention, the z axis is oriented perpendicular to the plane of the complex, while the metal-ligand (M–L) bonds lie along the x and y axes. The exact ordering of the lower energy d-orbitals depends on the nature of the ligand, including the relative contributions of σ and π bonding. However, the $d_{x^2-y^2}$ orbital is always unequivocally the highest in energy.[1]

For Pt(II), the ligand field strength is typically sufficient to enforce a square planar geometry even with moderately strong ligands, while Ni(II) requires stronger field ligands such as cyanide (CN^-) to favour square planar over octahedral coordination.[1,2]

1.2. Luminescence in Pt, Pd, and Ni complexes

1.2.1. What is luminescence?

Luminescence describes the process in which an energetically excited state relaxes to the ground state with the emission of radiation in the form of light. In the case of photoluminescence, the excited state is generated by the absorption of photon(s), and subsequent emission may occur either via fluorescence or phosphorescence.

Fluorescence arises from the radiative decay of an excited state through a spin-allowed transition, typically from the first singlet excited state (S_1) to the singlet ground state (S_0). Higher excited singlet states (e.g., S_2) are more prone to non-radiative relaxation pathways such as internal conversion (IC) and vibrational relaxation (VR), which occur on ultrafast timescales (~10^{-12} s), thereby preventing direct emission from these states. Fluorescence, in contrast, typically occurs on the nanosecond timescale (~10^{-9} s).[3] Phosphorescence, on the other hand, originates from a spin-forbidden transition (e.g., $T_1 \rightarrow S_0$; T_1: lowest triplet excited state). The spin selection rules in organic molecules formally prohibit radiative decay from triplet states. However, in the presence of heavy elements, spin-orbit coupling (SOC) facilitates intersystem crossing (ISC), thereby enabling phosphorescence. Due to the reduced transition probability, phosphorescence typically occurs on much longer timescales, ranging from microseconds to milliseconds.[4,5] The Jablonski diagram, introduced by Alexander Jablonski in 1935, provides a visual representation of radiative and non-radiative transitions within a given molecular system (Figure 1-2).[4]

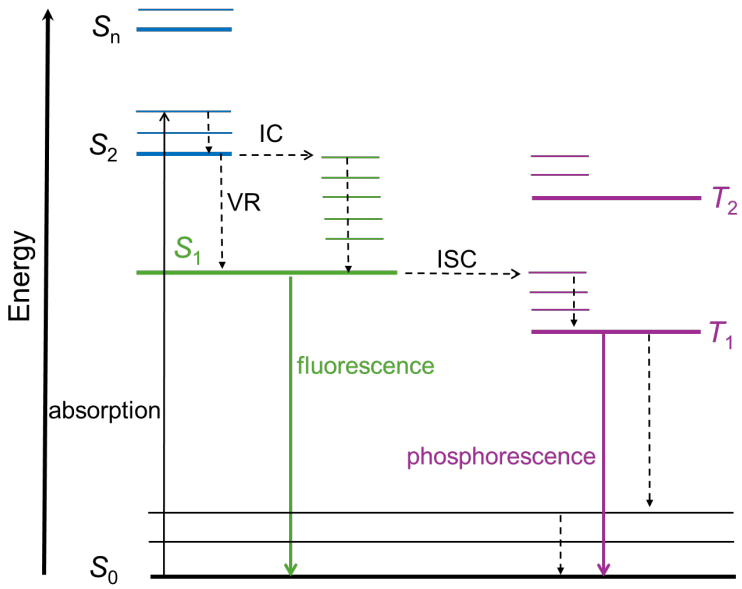


Figure 1-2. The Jablonski diagram.

1.2.2. The efficiency of luminescence

The efficiency of luminescence is quantified by the quantum yield (Φ_L), which is defined as the ratio of the numbers of photons emitted to the number of photons absorbed. This parameter, also referred to as the photoluminescence quantum yield (PLQY), can be calculated using equation 1, under the assumption that the emissive state is formed with unitary efficiency. The rates of radiative (k_r) and non-radiative (k_{nr}) decay can be defined using equations 2 and 3, respectively. The luminescence lifetime (τ) corresponds to the reciprocal of the total decay rate constant and is determined as described in equation 4.[5]

$$\Phi_L = \frac{k_r}{k_r + k_{nr}} \quad \text{(eq. 1)}$$

$$k_r = \frac{\Phi_L}{\tau} \quad \text{(eq. 2)}$$

$$k_{nr} = \frac{1-\Phi_L}{\tau} \quad \text{(eq. 3)}$$

$$\tau = \frac{1}{k_r + k_{nr}} \quad \text{(eq. 4)}$$

Optimizing the luminescence efficiency requires that the radiative rate constant k_r of the emissive state be promoted while the rate of non-radiative decay pathways k_{nr} are minimized. Efficient phosphorescence is often challenging to achieve due to the spin forbidden nature of the transition, which results in a low k_r. However, as discussed in section 1.2.1., third-row transition metals such as Re, Os, Ir, Pt, or Au, are frequently employed due to their ability to induce strong SOC (SOC scales with the fourth power of the atomic number Z (SOC $\propto Z^4$).[6] This effect significantly enhances ISC and facilitates rapid radiative decay.[2,7,8]

Equally critical for efficient phosphorescence is the suppression of k_{nr}. The presence of low-lying metal-centered (^{3}MC or d–d*) excited states often explains the non-emissive behavior of a transition metal complex. These states are characterized by potential energy minima that are markedly displaced relative to the ground state structure, thereby enabling efficient radiationless decay pathways (Figure 1-3).[1,9]

Third-row transition metal ions offer the additional advantage of higher ligand field strength compared to their first and second row congeners. This increased ligand field splitting raises the energy of the ^{3}MC states, rendering them thermally inaccessible and thereby reducing emission quenching from these states. As such, metal-to-ligand charge transfer (^{3}MLCT) or the ligand-centered (^{3}LC) states dominate the emissive properties of these complexes.[10,11]

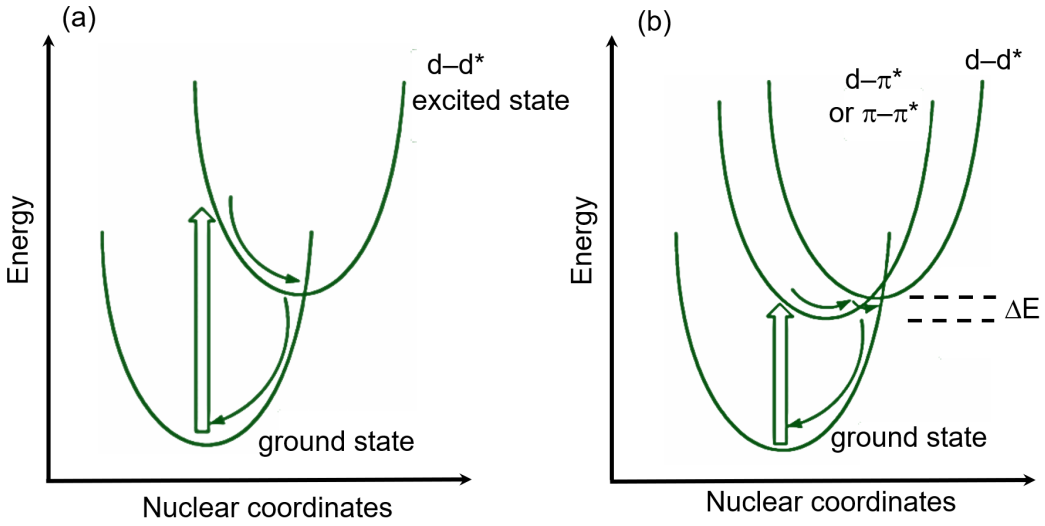


Figure 1-3. (a) Displacement of the potential energy surface for the d–d* excited state in a square planar d^8 complex, resulting from population of the $d_{x^2-y^2}$ orbital, relative to the ground state. (b) Although other excited states (e.g., d–π* or π–π*) may lie at lower energies, the d–d* excited state may be thermally accessible, facilitating non-radiative decay pathways. Thick arrows represent photon absorption; thin arrows indicate non-radiative decay.[1]

It is clear from the above discussion that, to enhance emission, it is critical to ensure that (i) the lowest excited state is not a metal-centered d–d* state but instead a ligand-centered or charge-transfer state, and (ii) the energy gap (ΔE) between the lowest excited state and the higher lying ^{3}MC state is sufficiently large to prevent thermally activated depopulation. The energy gap can be increased in two ways: either by (i) lowering the energy of the emitting state or by (ii) raising the energy of the ^{3}MC state.[12]

(i) Low energy emitting states

A well-known example is the octaethylporphyrin (OEP) derivative of Pt and Pd, referred to as [PtOEP] and [PdOEP], which emit deep into the red region with high quantum yields (λ_{max} = 641 nm, τ = 65 μs, Φ_L = 0.6 for PtOEP and λ_{max} = 660 nm, τ = 65 μs, Φ_L = 0.5 for PdOEP).[13] The rigid porphyrin framework plays a key role in stabilizing the emissive excited state (Figure 1-4).[12]

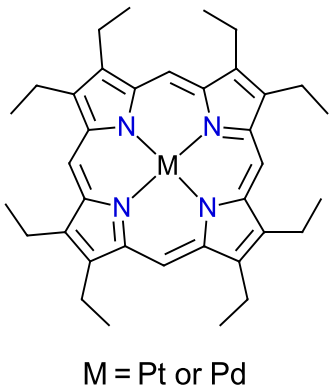


Figure 1-4. Structure of [PtOEP] and [PdOEP].[13]

Simple Pt(II) terpyridine complex, $[Pt(trpy)Cl]^+$, does not exhibit emission in fluid solution due to the high energy of its potentially emissive ^{3}MLCT state (Figure 1-5).[14] However, *McMillin* and colleagues found that introducing electron-withdrawing groups such as methylsulfonyl (SO_2Me) or cyano (CN) at the 4-position of the central pyridine ring , $[Pt(CN\text{-}T)Cl]^+$, stabilizes the ^{3}MLCT state, leading to emissive Pt(II) terpyridine complexes (Figure 1-5).[15,16] In contrast, a Pt(II) terpyridine complex featuring an electron-donating NMe_2 group at the same position, $[Pt(dma\text{-}T)Cl]^+$, displays significantly enhanced photophysical properties (τ = 1.9 μs, Φ_L = 0.11) (Figure 1-5). This improvement arises from the electron-rich NMe_2 group, which enables synergistical mixing of two charge transfer states to give a low-lying intra-ligand charge transfer (^{3}ILCT)/^{3}MLCT excited state.[14]

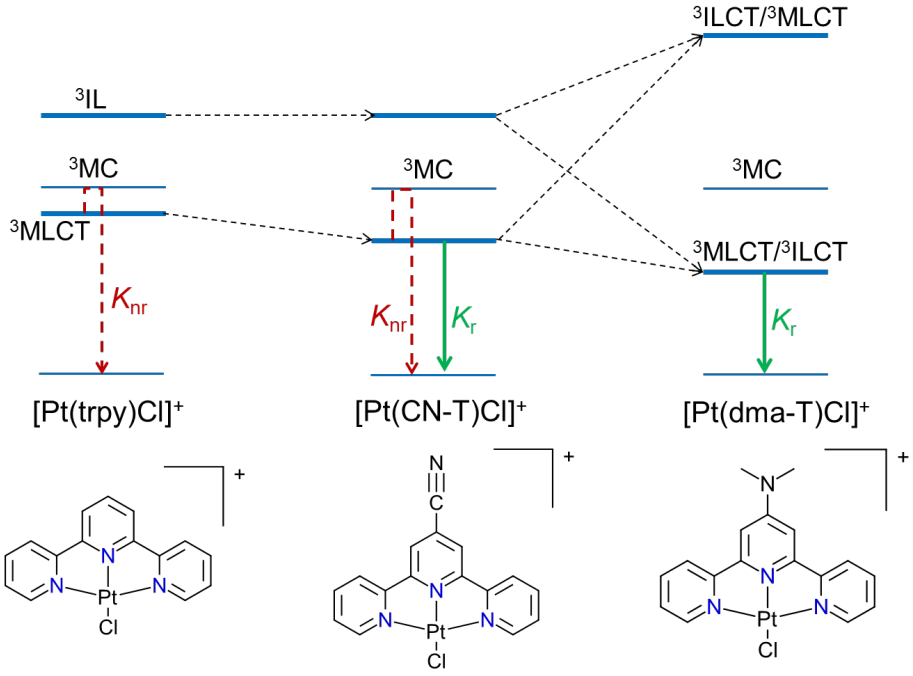


Figure 1-5. Energy state diagram of $[Pt(trpy)Cl]^+$, $[Pt(CN\text{-}T)Cl]^+$, and $[Pt(dma\text{-}T)Cl]^+$.[14]

(ii) Raising the energy of the ^{3}MC states

In order to push up ^{3}MC state to high energies to make them thermally inaccessible, strong-field ligands or coligands with good σ-donating and/or π-accepting character can be introduced.[17–21] A further strategy is to make use of cyclometalating ligands, which serve to increase the ligand filed without the need for specific coligands.[8,22–31]

1.3. Cyclometalated Pt, Pd, and Ni complexes

Cyclometalation refers to the coordination of a polydentate ligand to a metal center through a covalent metal-carbon bond, while the remaining ligand-metal interactions typically involve coordinate bonds from heteroatoms like nitrogen. As a result, cyclometalated complexes are classified as organometallic

compounds.[12] Cyclometalating ligands, particularly tridentate systems such as 1,3-di-pyridyl-benzene (Hdpb), 6-phenyl-2,2'-bipyridine (Hphbpy), and 2,6-diphenyl-pyridine (H_2dpp), have been extensively studied in this regard.[7,28,32–39] These ligands, coordinate to the metal center via a deprotonated carbon atom, a strong σ-donor, thereby significantly destabilizing the ^{3}MC excited states and effectively suppressing k_{nr}.[1,9,35,38–44] Moreover, variations in the coordination environment allow fine-tuning of the electronic properties of metal complexes (Figure 1-6) leading to a growing number of applications in optoelectronics, optical sensors, and photocatalysis.[8,24,33,43,45–57]

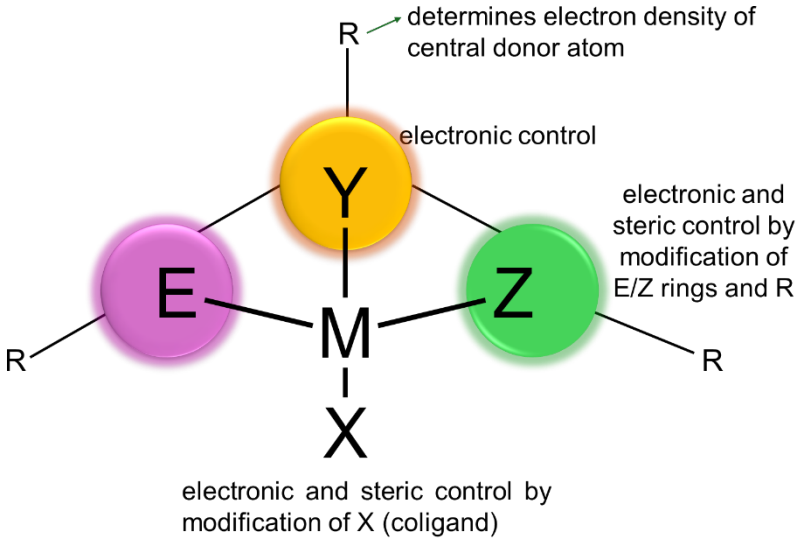


Figure 1-6. General representation of a tridentate cyclometalated complex illustrating influence of electronic and steric factors. M is metal center. E, Y, and Z rings can be chemically identical or different.

Among the group ten metals, many cyclometalated Pt(II) and a good number of Pd(II) complexes have been reported as triplet emitters.[25,28,33,41,45–49,58–64] The involved excited states are labelled either as mixed ^{3}LC/^{3}MLCT (ligand-centered/metal-to-ligand charge transfer) or as metal-perturbed ligand-centered (^{3}MP-LC) states.[29,65–69] However, there are several examples of cyclometalated Pt(II) complexes with seemingly suitable bis-cyclometalating C^N^C ligands, such as [Pt(dpp)(CO)],[70] and [Pt(dpp)(benzoisonitrile)][9,71] that are non-emissive, as well as mono-cyclometalating C^N^N ligands like [Pt(phbpy)Cl],[72] which is only weakly emissive at ambient temperature. The lack of emission from the [Pt(dpp)(L)] complexes at 298 K, despite the fact that C^N^C provides a stronger ligand field than N^N^C or N^C^N coordination modes, is due to significant structural distortions in their geometries, as the aromatic rings of the C^N^C ligand adopt a bent conformation in the T_1 excited state rather than the coplanar configuration found in the S_0 ground state, while the metal coordination geometry changes from square planar towards a tetrahedral configuration (Figure 1-7).[9,73] Such structural deformations can lead to the vibronic coupling of the T_1 and S_0 states and thus to rapid radiationless relaxation from

the T_1 state. Besides structural distortion, a smaller energy gap between the T_1 and S_0 states, and a dissociative π/d–d* character of the T_1 excited state could provide additional deactivation channels for non-radiative decays.[73] Therefore, an effective strategy to supress k_{nr} is minimizing structural distortion in the excited state with respect to the ground state.[74–77] *Yersin* and coworkers reported a series of Pt(II) complexes featuring carboranyl-functionalized C^N^C ligands, such as [Pt(L1)X] (H_2L1 = 3,6-bis(*p*-anizolyl)-2-carboranyl-pyridine; X = $S(C_2H_5)_2$, $P(C_6H_5)_3$, and $CNC(CH_3)_3$).[73] These complexes display high luminescence quantum yields, reaching up to 82% at ambient temperature, attributed to the suppression of non-radiative relaxation via a rigid molecular structure (Figure 1-7).[73]

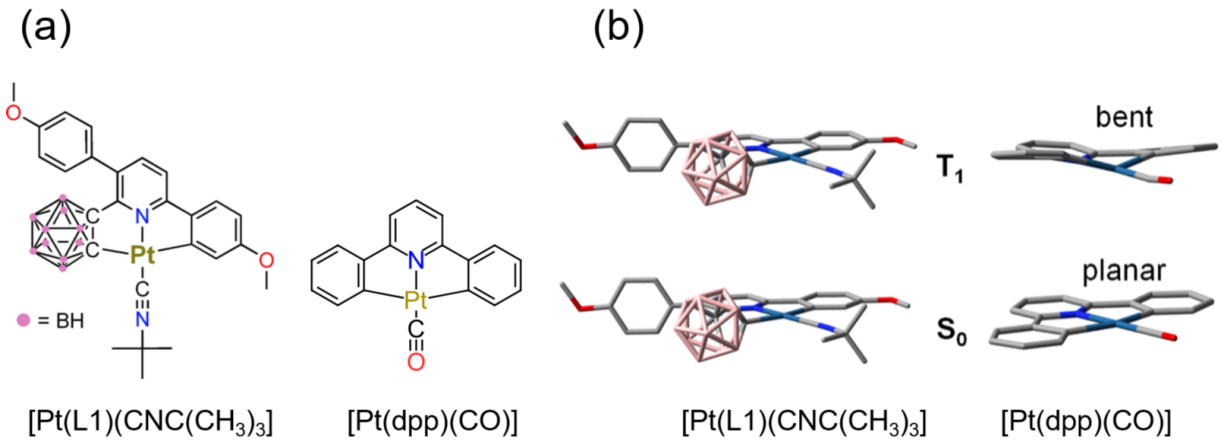


Figure 1-7. (a) Structure drawings and (b) molecular geometries of S_0 and T_1 states of [Pt(L1)(CNC(CH3)3)] and [Pt(dpp)(CO)] obtained from DFT calculations on the B3LYP/(631G*+SDD-ECP) theory level.[73] Reprinted with permission. Copyright @ 2014, American Chemical Society

Another strategy to keep k_{nr} low involves the incorporation of heavy main group elements as the fourth coligand (or ancillary ligand) in tridentate C^N^N, N^C^N or C^N^C cyclometalated complexes.[78–81] This approach not only strengthens SOC but also allows fine-tuning of the photophysical properties of square planar complexes.[78,79] *Klein* and coworkers, along with *Strassert* and colleagues, have explored this concept in cyclometalated Pt(II) complexes.[65,82,83] In particular, *Klein*'s group investigated double cyclometalated Pt(II) complexes of the type [Pt(L)($PnPh_3$)] (L = 2,6-diphenyl-pyridine (H_2dpp) or dibenzoacridine (H_2dba); Pn = pnictogen atoms P, As, or Sb) (Figure 1-8).[65] Their results demonstrated that the introduction of heavy homologues as coligands enhances phosphorescence quantum yields and radiative rates from mixed ^{3}MLCT/^{3}LC triplet states.[65] Similarly, *Breher* and *Feuerstein* reported a bis-cyclometalated Pd(II) complex featuring a diphenylpyridine-based (C^C^N) ligand and PPh_3 coligand, which exhibited solid-state emission at room temperature with Φ_L = 0.1 (Figure 1-9).[84]

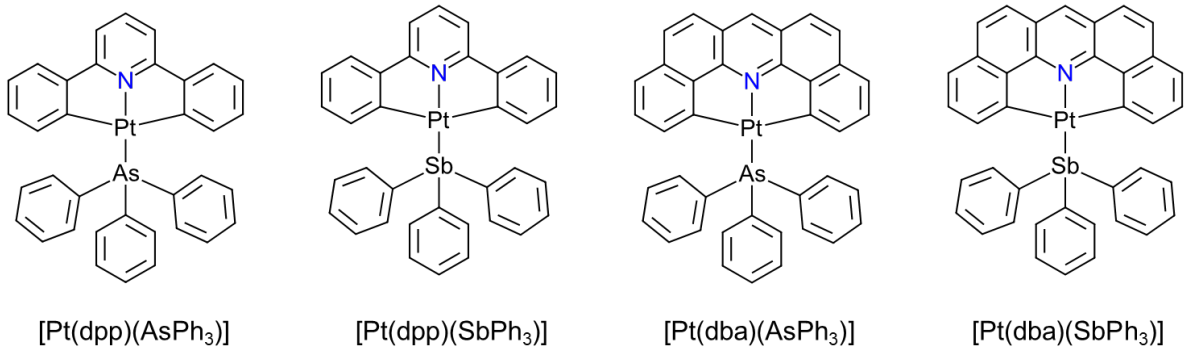


Figure 1-8. C^N^C cyclometalated Pt(II) complexes featuring heavy ancillary ligands.[65]

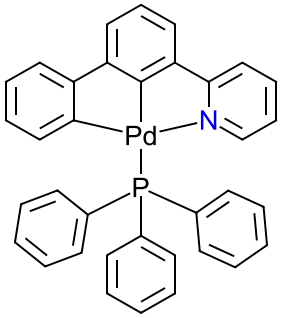


Figure 1-9. Structure of [Pd(C^C^N)PPh3] reported by *Breher* and *Feuerstein*.[84]

First row transition metal complexes, such as those of Ni(II), are often considered low-cost alternatives for Pd(II) and Pt(II). However, the photophysical properties of cyclometalated Ni(II) complexes remain largely unexplored. As a first-row metal, Ni exhibits weaker d–d ligand field splitting relative to its heavier congeners, Pd and Pt. The presence of thermally accessible ^{3}MC states in Ni(II) complexes often results in quenching of emissive excited states through thermal equilibration or energy transfer. These distorted ^{3}MC states effectively compete with emissive pathways, rendering most Ni(II) complexes non-luminescent.[25,41,74,75,85–91] In contrast, their isoelectronic d^8 Pt(II) analogues are widely studied for their rich emissive properties, and recent reports have demonstrated similar luminescence in some Pd(II) complexes.[25,28,42,45,46,58,60,69] The interplay between ligand field strength, coordination geometry, and character of the excited states remains critical for understanding and optimizing the photophysical behavior of these systems.

In 2020, *Yam* and co-workers reported the first phosphorescent cyclometalated Ni(II) complex [Ni(dpb)(carbazolate)] (Figure 1-10), which exhibited weak photoluminescence in the solid state at ambient temperature.[91] At 77 K, an emission band centered at 468 nm was observed, featuring a vibrational progression of approximately 1300 to 1400 cm^{-1}. This progression corresponded to the heteroaromatic $\nu_{(C=N)}$ and $\nu_{(C=C)}$ vibrational modes of the N^C^N ligand. The emission was accompanied by an excited state lifetime in the sub-microsecond range. Based on these observations, the emission

band was tentatively assigned to a metal-perturbed ligand-centered (^{3}LC or π–π*) excited state. The incorporation of the strong σ-donating carbazolyl ligand into the Ni(II) coordination sphere is believed to enhance the electron density at the metal center. This has the dual effect of increasing the energy of the ^{3}MC states and stabilizing the emissive state. Consequently, the likelihood of populating the emissive state is increased, particularly in low-temperature solids where the luminescence is further enhanced due to the suppression of molecular distortions in the excited states.[91]

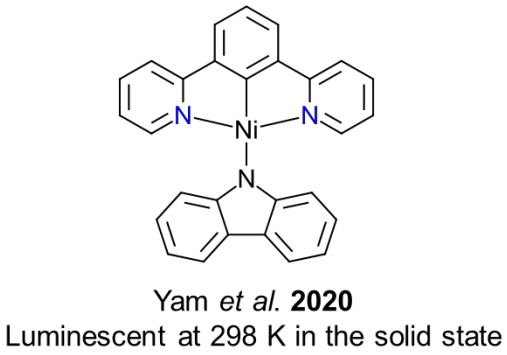


Figure 1-10. Ni(II) complex with σ-donating carbazolyl coligand as a triplet emitter.[91]

Later on *Wenger* and co-workers examined the excited-state relaxation dynamics of ^{3}MLCT states in a series of Ni(II) complexes.[75] Their investigation revealed markedly different ^{3}MLCT lifetimes of 0.5 ps for [Ni(bib)(CH_3CN)]PF_6, 17 ps for [Ni(bib)(Ln2)]PF_6 and 48 ps for [Ni(bib)(Ln1)]PF_6 (H_3bib = 1,3-bis(3′-butylimidazolyl-1′-yl)benzene; Ln1 and Ln2 = isocyanide ligands with a m-terphenyl backbone) in aerated CH_2Cl_2 at 20 °C (Figure 1-11). From these results, they concluded that the use of the tridentate H_3bib ligand (C^C^C) in combination with sterically protecting ancillary ligands provides a promising strategy to counteract the unwanted distortions in the square planar coordination geometry throughout the entire evolution of the excited state (Figure 1-11).[75]

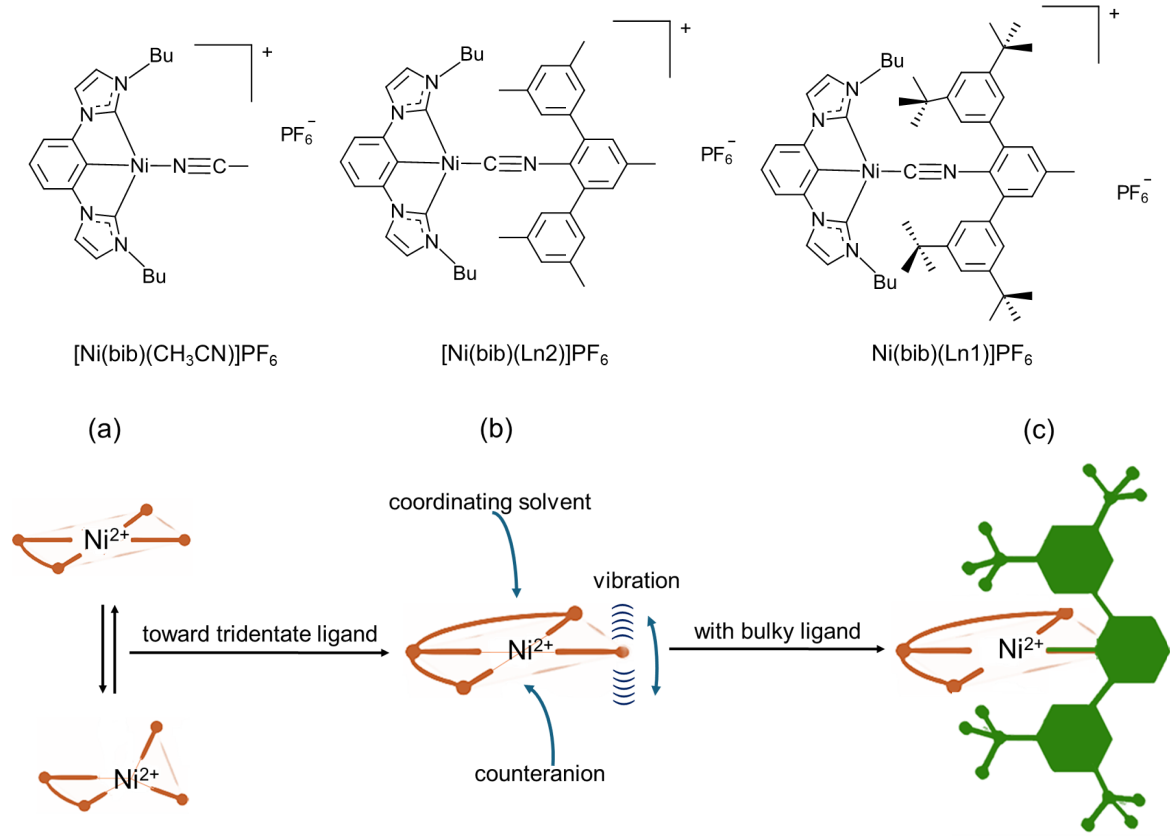


Figure 1-11. Up: Structure drawings of Ni(II) complexes explored by *Wenger et al.*,[75] **Down**: Approaches to improve the photophysical properties of square planar Ni(II) complexes (a) Typical molecular distortion in Ni(II) complexes with bidentate and two monodentate ligands, leading to undesired non-radiative excited state relaxation. (b) Potential excited state quenching processes in square planar Ni(II) complexes, including nucleophilic attack by solvent or counter-anions at the metal center, as well as molecular vibrations in complexes featuring one tridentate and monodentate ligand. (c) Optimized molecular design employed in the study for extending ^{3}MLCT excited state lifetimes. In this design, the coordination environment of Ni(II) remains four-coordinate square planar but mimic an octahedral geometry due to sterically demanding monodentate ligands effectively shielding the axial coordination sites.[75]

1.3.1. Synthesis of cyclometalated Pt, Pd, and Ni complexes

The most common method for synthesizing mono-cyclometalated Pt(II) complexes with tridentate N^C^N or C^N^N ligands involves heating the respective protoligands (protonated ligands prior to C–H metalation) with $K_2[PtCl_4]$ in glacial acetic acid (Figure 1-12).[92] This approach enables efficient C–H activation and complex formation.

Mono-cyclometalated Pd(II) complexes with tridentate C^N^N ligands are typically synthesized via C–H activation in a boiling CH_3CN/H_2O mixture.[60,93] For N^C^N, early methods involved pre-coordination of the protoligand to $Hg(OAc)_2$ forming an intermediate Hg(II) complex, which was then transmetalated with $Pd(OAc)_2$ in the presence of a lithium salt to yield the final Pd(II) complex (Figure 1-12).[94] A more direct base-assisted C–H activation method was later developed by *Klein* and colleagues, who successfully synthesized [Pd(Me$_2$dpb)Cl] from the protoligand 1,5-di(2-pyridyl)-2,4-dimethylbenzene (Me$_2$dpbH) and anhydrous $[Pd(COD)Cl_2]$ (COD = 1,5-cyclooctadiene) using KOAc and K_2CO_3 in rigorously dried aprotic solvent under strict exclusion of

light (Figure 1-12).[41] Alternatively, some Pd(II) N^C^N complexes have been synthesized via electrophilic substitution, involving heating in acetic acid (Figure 1-12).[28,95]

Early synthetic routes for mono-cyclometalated Ni(II) N^C^N complexes followed the same strategy as their Pd(II) counterparts, relying on transmetalation via an organomercury intermediate.[91] To avoid toxic mercury specie, alternative base-assisted C–H activation or C–X oxidative-addition methods have been developed, which are applicable for both N^C^N and C^N^N systems (Figure 1-12).[41,95,96] Another notable approach was introduced by *Wendt et al.*, who synthesized mono-cyclometalated Ni(II) complex using a strong base and a soluble Ni(II) precursor such as [Ni(DME)Br2] (DME = 1,2-dimethoxyethane) and seems to be applicable for N^C^N systems.[97]

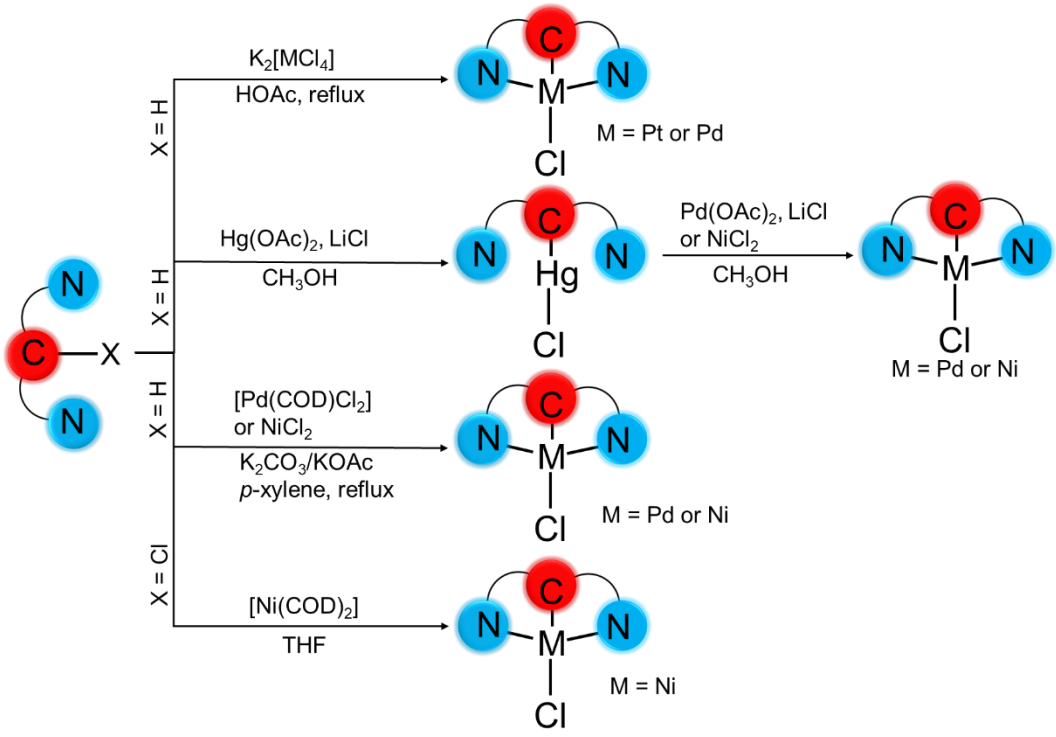


Figure 1-12. Synthesis approaches for [M(N^C^N)Cl] complexes (M = Pt, Pd, Ni).[41,91,92,94-96]

The synthesis of bis-cyclometalated Pt(II) C^N^C or C^C^N complexes typically requires a two-step approach. After an initial cyclometalation step, a second base-assisted step is carried out, often in hot dimethyl sulfoxide (DMSO) (Figure 1-13).[38,98] Unlike Pt(II) systems, the synthesis of bis-cyclometalated Pd(II) complexes under the same conditions is challenging. The dinuclear bridged intermediate formed after the first step does not readily undergo a second C–H activation. An alternative approach involves C–X instead of C–H activation, using oxidative addition with a Pd(0) precursor such as [Pd(PPh3)4] and halogenated derivatives of protoligands.[84]

While limited studies have been conducted on bis-cyclometalated Ni(II) complexes, available data suggest that a double C–X oxidative-addition strategy could be feasible synthetic route. This method mirrors the oxidative-addition approach used for Pd(II) systems, providing a promising pathway for expanding the library of bis-cyclometalated Ni(II) complexes.[84]

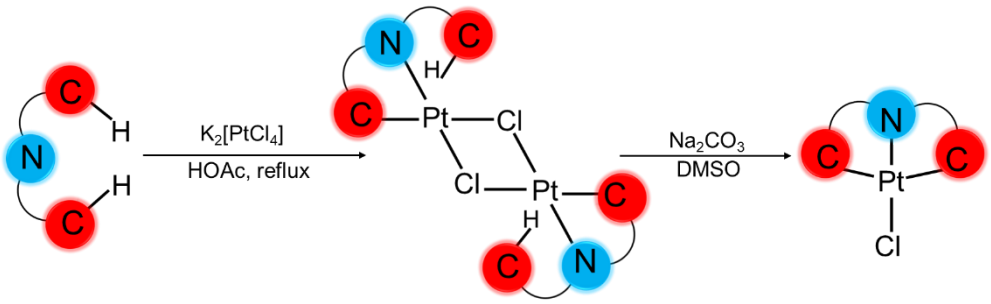


Figure 1-13. Synthesis approach for [Pt(C^N^C)Cl] complexes.[38,98]

2. Scientific Objectives

To develop efficient triplet emitters based on d^8 square planar metal complexes of Pt(II), Pd(II) and Ni(II), the key factors such as ligand field strength and coordination rigidity must be systematically integrated. A relatively new idea in this field is that the rigidity of the coordination around the metal might be enforced by non-covalent interactions in termed the second coordination sphere, potentially enhancing photoluminescence efficiently.[37,75,99]

A representative example of this design principle is the Cu(I) complexes [Cu(terpyR$_2$)Cl] (terpyR$_2$ = 6′,6′′R-2,2′;6′,2′′-terpyridine) (Figure 2-1, left). In this system, non-bulky substituents (R = OH) favor hexameric (multinuclear) structure with tetrahedral Cu(I) center, whereas bulkier NHMes substituents lead to a monomeric complex with quasi-square planar coordination. The steric bulkiness combined with the N–H···Cl hydrogen bonds provides an almost square planar surrounding for Cu(I), resulting in distinctive spectroscopic features.[100]

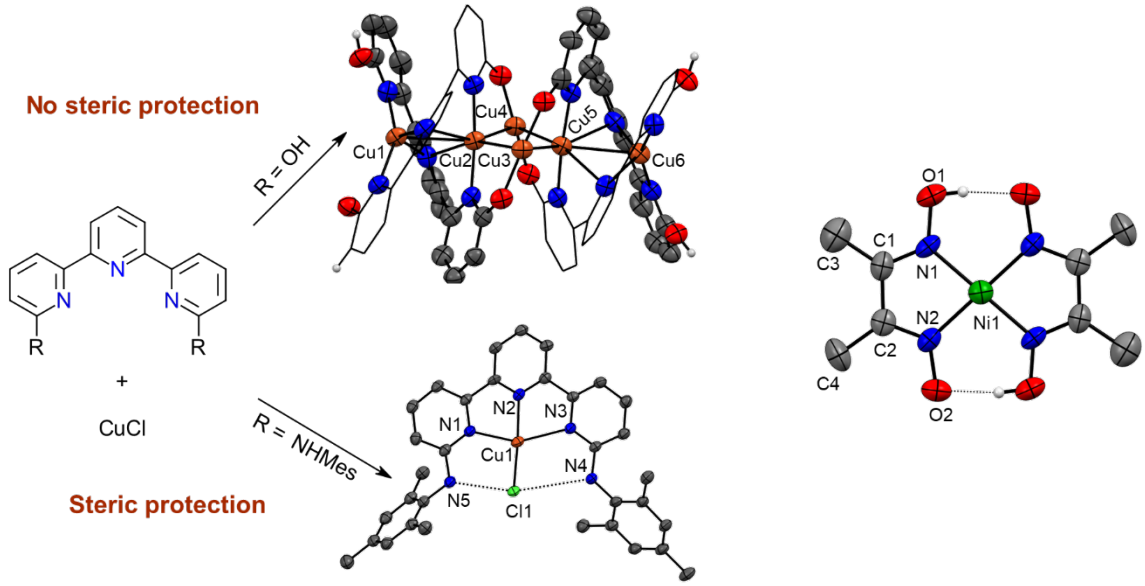


Figure 2-1. Left: Ligand design in the two Cu(I) complexes [Cu(terpyR$_2$)Cl] with terpyR$_2$ = 6′,6′′R-2,2′;6,2′′-terpyridine and R = OH or NHMes.[100] **Right:** Planar coordination and strong H bonds in [Ni(Hdmg)$_2$] (H$_2$dmg = (2*E*,3*E*)-butane-2,3-dione dioxime).[89]

Hydrogen bonding has also proven to be a critical factor in enhancing rigidity, as evidenced by the Ni(II) bis-glyoximato complex [Ni(Hdmg)$_2$] (H$_2$dmg = (2*E*,3*E*)-butane-2,3-dione dioxime) (Figure 2-1, right). This complex derives its planar structure, high stability, and low water solubility from strong intramolecular hydrogen bonds.[89] However, neither [Ni(Hdmg)$_2$] nor its Pd(II) or Pt(II) analogues exhibit luminescence due to distinct quenching mechanisms: weak ligand fields of the Hdmg$^-$ in the case of Ni(II) and pronounced metal-metal stacking for Pd(II) and Pt(II).[89,101]

An attempt to utilize H bonding in rigidifying luminescent Pt(II) complexes has been reported with the use of dianionic chelate ligands $bipz^{2-}$ and $mepz^{2-}$ (H_2bipz = 5,5′-bis(trifluoromethyl)-2H,2′H-3,3′-bipyrazole; H_2mepz = 5,5′-(1-methylethylidene)-bis(3-trifluoromethyl-1H-pyrazole) (Figure 2-2).[102] While $bipz^{2-}$ complexes demonstrated weak intramolecular H bonds (N···H–C distances ~2.32 Å), these interactions were insufficient to affect luminescence properties, as the Φ_L remained consistent across related complexes. Remarkably, despite expectations for shorter H bonds in1 $mepz^{2-}$ derivatives, the molecular structure from single crystal X-ray diffraction (XRD) revealed puckering of the non-conjugate chelate ligand, entirely avoiding N···H–C interactions.

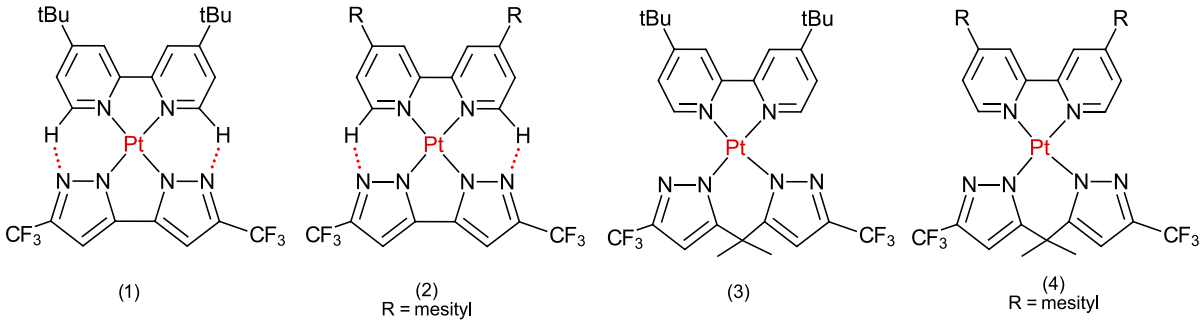


Figure 2-2. Two pairs of luminescent Pt(II) complexes.[102]

To address these limitations, this project focuses on the use of tridentate cyclometalated N^C^N ligands (N^C^N = 1,3-dipyridyl-benzene) inspired by the structural principles in Figure 2-1 (left). These ligands contain amine groups $NH(C_6H_5)$ at the two ortho-positions of the pyridyl rings (HL^{NHPh}) or $NH(C_6H_5CH_2)$ (HL^{NHBn}). The adopted ligand scaffolds will be used to synthesize cyclometalated Pt(II), Pd(II), and Ni(II) complexes to facilitate intramolecular hydrogen bonding with the Cl^- coligand (Figure 2-3), thereby promoting structural rigidity and photophysical performance.

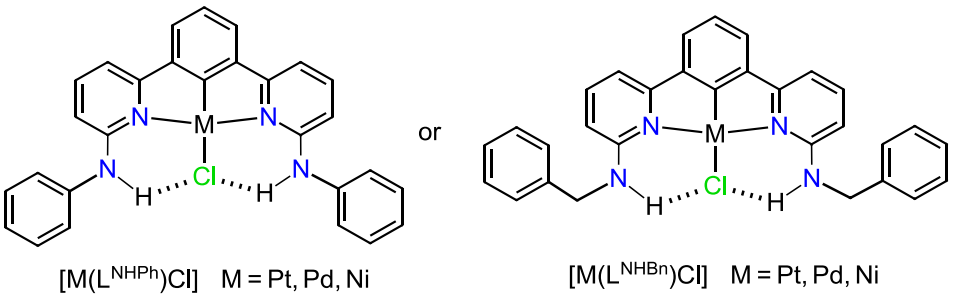
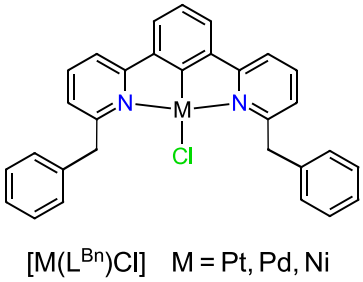


Figure 2-3. Cyclometalated complexes, designed to enhance rigidity via hydrogen bonding.

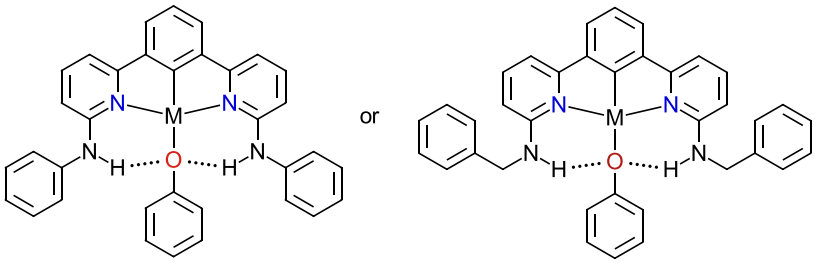
To evaluate the role of hydrogen bonding in controlling excited state distortions, analogous cyclometalated complexes [M(L^{Bn})Cl] (M = Pt, Pd, Ni) will be synthesized without N–H···Cl···N–H hydrogen bonds (Figure 2-4).



[M(L^{Bn})Cl] M = Pt, Pd, Ni

Figure 2-4. Cyclometalated complexes without hydrogen bonds.

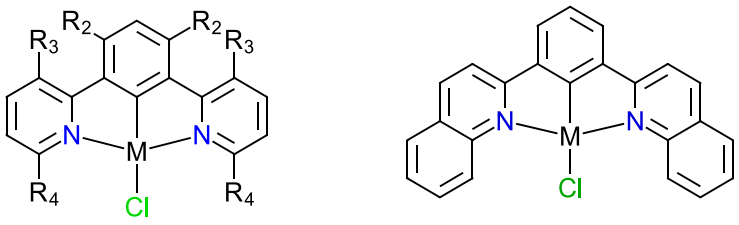
Subsequently, substitution of chloride coligand with phenoxide (OPh$^-$) in [M(L^{NHPh})Cl] and [M(L^{NHBn})Cl] complexes (M = Pd or Pt) will be performed to further strengthen hydrogen bonding within the second sphere (N–H···O···N–H) (Figure 2-5). This will help us to further explore and refine the influence of hydrogen bonding on photophysical properties.



[M(L^{NHPh})OPh], M = Pt or Pd [M(L^{NHBn})OPh], M = Pt or Pd

Figure 2-5. Cyclometalated complexes with phenoxide (OPh$^-$) coligand.

Further modifications, including the incorporation of electron-donating (Me) or electron-withdrawing (F or Cl) substituents, as well as the introduction of quinoline (Qu) units into the N^C^N ligand framework, will be explored to fine-tune both the electronic properties and structural rigidity of the complexes (Figure 2-6).



R_1 = H or Cl
R_2 = H, Me, or F
R_3 = H or Cl
R_4 = H or Me
M = Pt, Pd, Ni

[M(L^{Qu})Cl] M = Pt or Pd

Figure 2-6. Cyclometalated complexes featuring electronic modifications (left) and quinoline incorporation (right).

The synthesis of Pt(II) and Pd(II) derivatives will follow an established method involving heating the protoligands and $K_2[PtCl_4]$ or $K_2[PdCl_4]$ in glacial acetic acid.[92] Ni(II)-based cyclometalation will utilize base-assisted C–H activation method with KOAc and K_2CO_3 in *p*-xylene.[103] If necessary, chlorinated derivatives of protoligands will be employed to facilitate oxidative addition reactions of Ni(0) precursor, circumventing the use of toxic mercury-based transmetalation protocols.[91]

As part of the project, we are seeking to solve the challenging and exciting task of creating Ni-based light-emitting materials. Apart from the big aims, the project concerns the class of organometallic compounds, which has been barely studied. The synthetic efforts will be complemented by theoretical investigations using density functional theory (DFT) and detailed photophysical experiments in different media (solution, solid, rigid matrices), as well as analytical techniques such as UV-vis spectrometry and cyclic voltammetry (CV) to probe their electronic properties. Overall, this work seeks to establish a robust conceptual and experimental framework for the development of triplet emissive d^8 complexes of Ni(II), Pd(II), and Pt(II).

3. Results and Discussion

3.1. [M(L^{NHPh})Cl] and [M(L^{NHBn})Cl] (M = Pt or Pd) complexes

3.1.1. Synthesis and structure of [M(L^{NHPh})Cl] and [M(L^{NHBn})Cl] (M = Pt or Pd)

To develop transition metal complexes as efficient triplet emitters, the two ligand precursors HL^{NHPh} and HL^{NHBn} were synthesized via modification of established methods including Suzuki cross coupling reactions with 63 and 71% yield (Figure 3-1, details in the experimental section). The Pt(II) and Pd(II) complexes [M(N^C^N)Cl] were synthesized from $K_2[MCl_4]$ (M = Pt or Pd) and the ligand precursors HL^{NHPh} and HL^{NHBn} by heating in glacial acetic acid as an established method,[92] with yields ranging from 62 to 79% (Figure 3-1, for details, see experimental section). The four yellow to orange Pt(II) and Pd(II) complexes each exhibit the complete set of signals in the ^{1}H and ^{13}C NMR (nuclear magnetic resonance) spectra, as expected for C_2-symmetric square planar complexes (spectra and data in the appendix). In addition, high-resolution electrospray mass spectrometry (HR)ESI-MS and elemental (CHN) analyses confirmed their composition (spectra and data in the experimental section and the appendix).

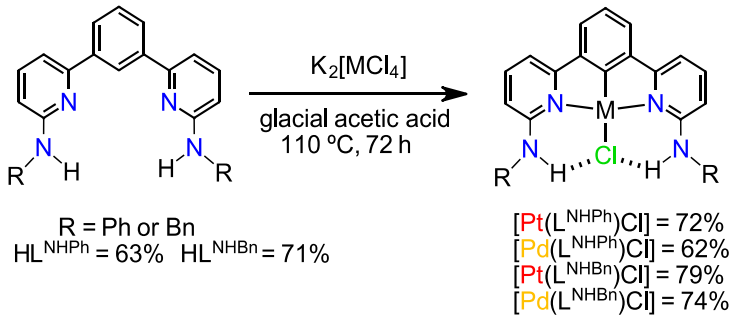


Figure 3-1. Synthesis of [M(L^{NHPh})Cl] and [M(L^{NHBn})Cl] (M = Pt or Pd) complexes.

The [M(L^{NHPh})Cl] (M = Pt or Pd) complexes crystallized isostructurally in the monoclinic space groups $P2_1/n$ or $P2_1/c$, whereas for the [M(L^{NHBn})Cl] (M = Pt or Pd) complexes, the structures were solved in the monoclinic space group $C2/c$ (Figures A106 to A109, data in Table A1, appendix). The experimental data for the Pt and Pd complexes were used to benchmark our DFT geometry optimization using TPSSh/6-31G(d)/LanL2DZ/CPCM(THF) with a very good agreement between the experimental and calculated metrics (Figure A110, Tables A2 and A3, appendix).

In all four crystal structures, head-to-tail stacking of the molecules was found (Figures A106 to A109), very similar to what has been previously reported for [M(dpb)X] or [M(phbpy)Br] derivatives (Hdpb = 1,3-diphenylbenzene; Hphbpy = 6-phenyl-2,2'-bipyridine) with M = Ni, Pd, or Pt.[36,41,59,60,64,91,95,103–105] The

metal-metal distances range from about 5 to 7 Å (beyond the sum of van der Waals radii) in the four structures; thus, no significant metallophilic M···M interactions were found. π-stacking is observable for the [M(L^{NHPh})Cl] (M = Pt or Pd) and [Pd(L^{NHBn})Cl] complexes between the pyridine units of two neighboring molecules with centroid distances ranging from 3.68 to 3.99 Å.

The pending anilines are engaged in non-symmetric M–Cl···H–N hydrogen bonds with H···Cl distances ranging from 2.23 to 2.38 Å and Cl···H–N angles ranging from 132 to 173° (Figure 3-2). They represent medium-strong hydrogen bonds.[106] DFT calculations (in solution, using the CPCM model) gave symmetric hydrogen bonds that were shorter than the experimental non-symmetric ones by about 0.13 to 0.28 Å, while the N–H···Cl angles are wider by up to 20°. We assume that DFT overestimates covalency in the M–Cl···(H–N)$_2$ moieties. This adds to the longer DFT-calculated M–C distances compared to the experimental values, to give an overall only fair agreement of calculated and experimental structures in this part of the complexes.

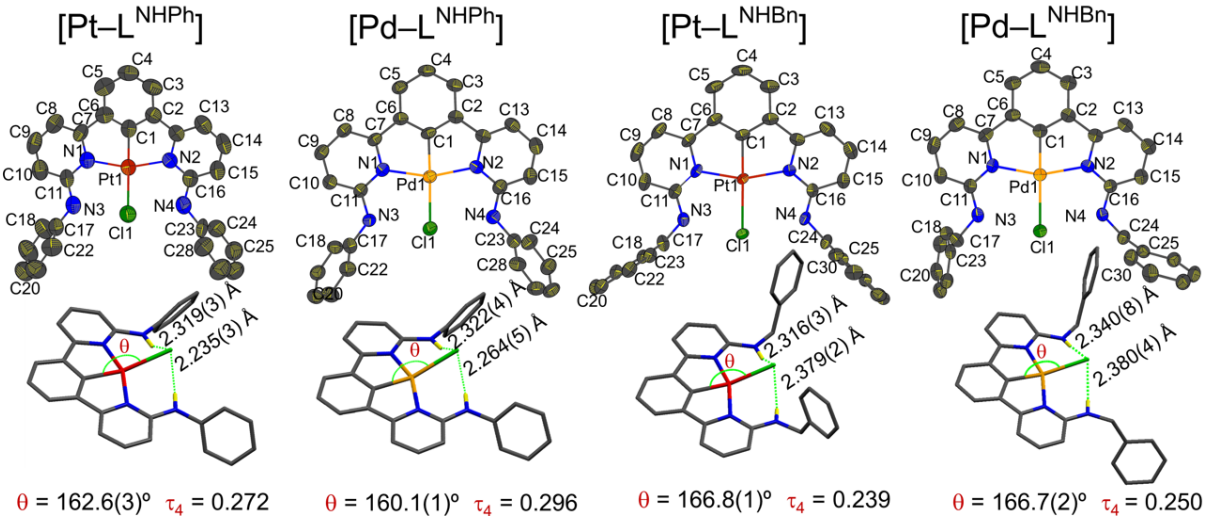


Figure 3-2. Molecular structures of the complexes from X-ray diffraction on single crystals (top, displacement ellipsoids at 50%) and their side-on views featuring the deviation τ_4 from the square-planar coordination (bottom).

The most remarkable feature is the marked distortion of the Cl^- coligand out of the N–C–N–M coordination plane (Figure 3-2), leading to τ_4 values ranging from 0.25 to 0.29 (τ_4 = 0 for perfect square planar, τ_4 = 1 for tetrahedral geometry)[100]. Generally, the τ_4 values are larger for the Pd complexes compared with the Pt derivatives by 0.024 for L^{NHPh} and 0.011 for L^{NHBn}. This is in part due to the reduced N1–M–N2 angles in the Pd complexes. DFT calculations on the hypothetical complexes [M(L^{NHPh})F] and [M(L^{NHPh})H] (M = Pt or Pd) with far smaller coligands revealed reduced τ_4 values (0.14 to 0.17), but still without complete planarity (Figures A11 and A112, Tables A4 and A5). The rigid RNH–N^C^N–NHR (R = Ph or Bn) ligand scaffold in combination with the ortho-substituents evidently restricts the space to accommodate even the smallest anionic coligand H^-. This is in line with the planar ligand arrangement in the non-substituted parent [Pt(dpb)Cl] complex and derivatives.[41,62,64,92,95] When

replacing the NHR groups by OMe substituents on the N^C^N scaffold, the DFT calculations showed increased steric bulk of the binding pocket leading to higher τ_4 values of 0.28 and 0.35 for the Pt(II)–Cl and Pd(II)–Cl complexes, respectively (Figure A113, Table A6) even though no hydrogen bonding is present. This means that the role of the hydrogen bonds for the coligand deviation is small to negligible and the steric bulk of the ortho-substituents is the main reason for the deviation from planarity.

3.1.2. Experimental and theoretical properties of [M(L^{NHPh})Cl] and [M(L^{NHBn})Cl] (M = Pt or Pd)

As discussed above, the DFT-optimized S_0 geometries of the complexes are generally in good agreement with the experimental data from crystallography with maximum deviations of 0.04 Å and 1.4° (Tables A2 and A3). However, for the Cl···H distances and the N–H···Cl angles, the deviation increased to 0.2 Å and 9°, respectively. Probably, the DFT method underestimates the ionic character of the Cl^- coligand. In the T_1 excited state, the pyridyl rings of the cyclometalated L^{NHPh} or L^{NHBn} ligands remain coplanar in the complexes (Figure 3-3). Also, the essential metrics around the metal atoms do not change significantly. Especially the M–Cl distances and C–M–Cl angles, which make up the biggest part of the distortion already found in the S_0 state, are only slightly increased in the T_1 state or even not increased at all for the [Pt(L^{NHBn})Cl] complex. Thus, through our locking ligand design approach, we were successful in reducing the conformational deviations between the S_0 and T_1 states by already distorting the S_0 ground state towards the expected geometry of the T_1 state.

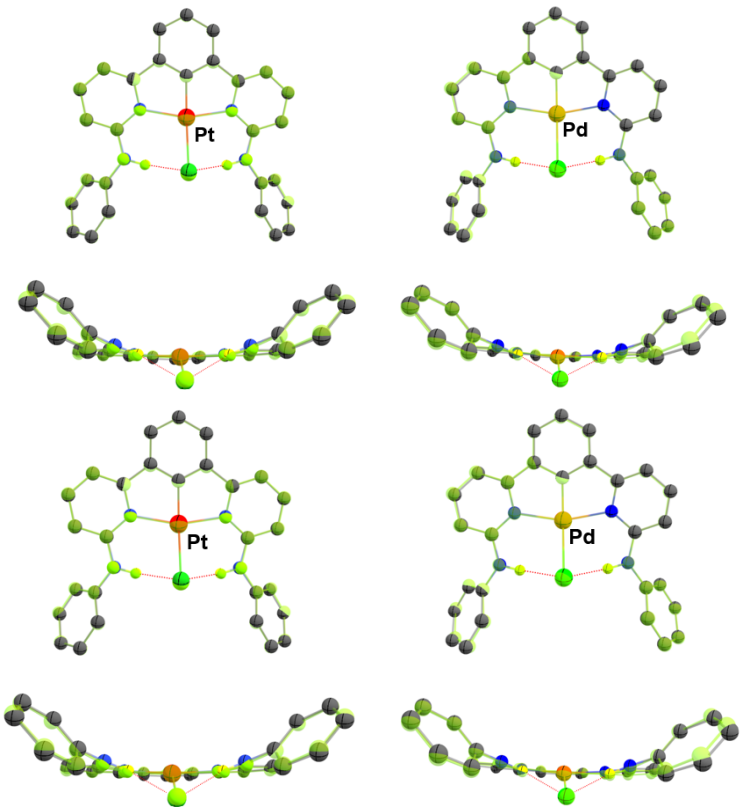


Figure 3-3. DFT-calculated geometries of [M(L^{NHPh})Cl] (up) and [M(L^{NHBn})Cl] (down) in the S_0 (black) and T_1 (green) states.

Cyclic voltammograms of all the complexes showed first reversible or partly reversible reduction waves at around –2.30 V for the L^{NHPh} species and –2.45 V for the L^{NHBn} derivatives vs. the ferrocene/ferrocenium couple (Figure 3-4; full data in Table 3-1; cyclic voltammograms are presented in Figure A138). They are usually followed by second or third irreversible reduction waves at potentials ranging from –2.50 V to –3.04 V. DFT-based single-point calculations show N^C^N ligand-centered π*-type LUMOs (lowest unoccupied molecular orbitals) with similar energies for each series of complexes at around –2.07 eV for L^{NHPh} and at –1.98 eV for L^{NHBn}.

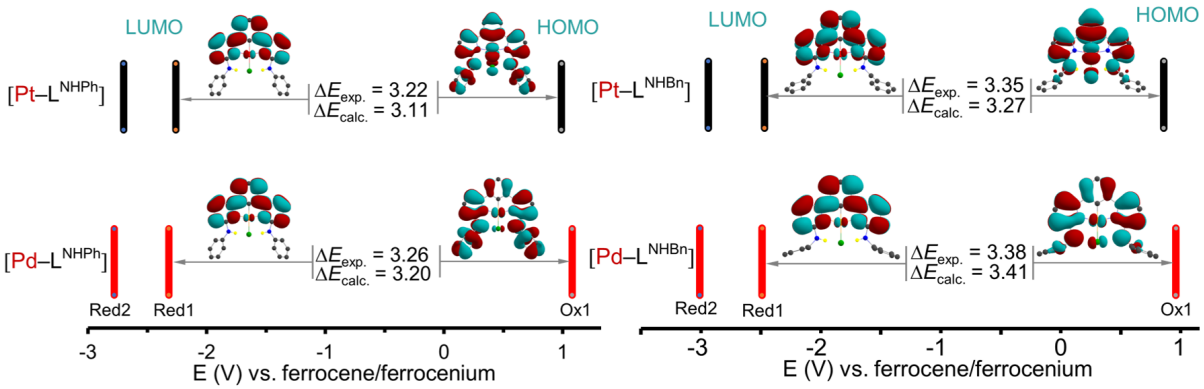


Figure 3-4. Selected experimental redox potentials (bars) and HOMO-LUMO gaps (Δ*E*exp.) from cyclic voltammetry together with DFT-calculated HOMO and LUMO compositions and HOMO-LUMO gaps (Δ*E*calc.) for the complexes. Note that for all four complexes, sets of energetically very close-lying LUMO/LUMO+1 and HOMO/HOMO-1 were found (Figures A149 and A150). The character of the HOMO-1 for the Pt complexes is very similar to the HOMO for the Pd derivatives and vice versa.

Table 3-1. Redox potentials of the complexes.[a]

complex	E_{pc} (Red3)	E_{pc} (Red2)	$E_{1/2}$ (Red1)	E_{pa} (Ox1)	ΔE (Red1–Red2)	Δ*E* (Ox1–Red1)	Solvent
[Pt(L^{NHPh})Cl]	–2.77	–2.48	–2.29	0.93	0.19	3.22	THF
[Pt(L^{NHPh})Cl]	–2.71	–2.36	–2.17	0.51	0.19	2.68	DMSO
[Pd(L^{NHPh})Cl]	–2.83	–2.56	–2.31	0.95	0.20	3.26	THF
[Pt(L^{NHBn})Cl]	–2.98	–2.64	–2.45	0.90	0.23	3.35	THF
[Pd(L^{NHBn})Cl]	–3.04	–2.70	–2.43	0.95	0.21	3.38	THF

[a] From cyclic voltammetry in 0.1 M n-Bu_4NPF_6/THF. Potentials in V vs. ferrocene/ferrocenium; accuracy of potentials: ±0.003 V. $E_{1/2}$: half-wave potential for reversible processes, E_{pc}: cathodic peak potentials for irreversible reductions, E_{pa}: anodic peak potentials for irreversible oxidations.

Essentially ligand-centered reduction processes are assumed, in line with reports on similar complexes.[41,59,64,95,103] Benzyl substitution leads to slightly lower (more negative) potentials, which might be explained by the higher contribution of benzyl groups to the unoccupied MOs (LUMO+4). The irreversible oxidation processes show slightly higher values for the Pd complexes compared with the Pt derivatives (Table 3-1). Metal (M^{II}/M^{III}) based oxidation processes are initially assumed in keeping with the easier oxidization of Pt(II) if compared with Pd(II) on previous reports.[41,59,60,95]

The DFT-calculated composition of the highest occupied molecular orbitals (HOMO) show delocalization over the entire complexes (Figure 3-4 and Figures A149 and A150, Tables A24 and A27). In contrast to the LUMO, which is localized at the N^C^N unit, the HOMO has also strong contributions from the pending NHR groups, the metals, and even the Cl^- coligand. Thus, the oxidation processes are not of pure metal (M^{II}/M^{III}) character but show a marked involvement of the cations, which is in excellent agreement with the quite invariable first oxidation and reduction potentials. The DFT-calculated HOMO-LUMO gaps increase from Pt to Pd in agreement with the order derived from the electrochemical measurements, ΔE(Ox1-Red1). Comparison with the parent/non-substituted [Pt(dpb)Cl] complex (~2.5 V)[41,64] shows markedly higher values for the herein reported [Pt(N^C^N)Cl] complexes (N^C^N = L^{NHPh}: 3.22 V and L^{NHBn}: 3.31 V) (Figure 3-4 and Table 3-1; Figures A149 and A150). A closer look reveals markedly lower oxidation potentials (E_{Ox}) for [Pt(dpb)Cl] by more than 0.5 V. This is very probably due to the amino functions stabilizing the HOMO in the [Pt(N^C^N)Cl] complexes. For Pd, only the methyl-substituted complex [Pd(Me_2dpb)Cl] is reported with a gap of 3.07 eV (E_{Ox} = 0.74 V).[41] This is markedly higher than that of the Pt derivative (3.15 eV; E_{Ox} = 0.35 V)[41] as both the difference between the Pt complex and the Pd derivative as well as the lacking stabilizing effect of the amino group in the Me_2dpb complexes are fully in line with our findings.

The UV-vis spectra of the complexes feature absorption bands in the range from 200 to 550 nm with intense maxima at around 260 nm (L^{NHBn}) and 280 nm (L^{NHPh}). These UV-bands also occur for the ligand precursors and can be assigned as transitions into excited singlet states with $^1\pi$–π^* (^{1}LC) character (Table 3-2, Figure A155). In the visible range, structured band-systems of medium intensity with maxima from 340 to 450 nm and some tailings down to 550 nm were observed (Figure 3-5, Table 3-2), which is in line with the yellow color of the compounds. By comparison with the absorption profiles reported for similar complexes, the long wavelength bands can be assigned to transitions into states with metal-perturbed LC character (^{1}MP-LC) or to mixed metal-to-ligand charge-transfer (^{1}MLCT)/ligand-centered (^{1}LC) configurations.[41,59,60,62,64,95,103,107,108] Time-dependent DFT (TD-DFT) calculated absorption spectra match quite well with the experimental results and support this assignment (Figure 3-5, Tables A42 and A43). They localize the long-wavelength $S_0 \rightarrow S_n$ transitions at around 400 nm dominated by excitation into π–π^* states, supporting the description of metal-perturbed LC excited states (^{1}MP-LC). The long-wavelength maximum of the Pt(II) complexes appear at lower energies than those of Pd(II) compounds, in line with the lower experimental and DFT-calculated HOMO-LUMO gaps. The complexes show a negative solvatochromic behavior to a very small extent (Figure A156), which is in line with the rather delocalized DFT-calculated HOMO (Figure 3-4) and the TD-DFT calculation showing dominating LC-contributions in the excited states.

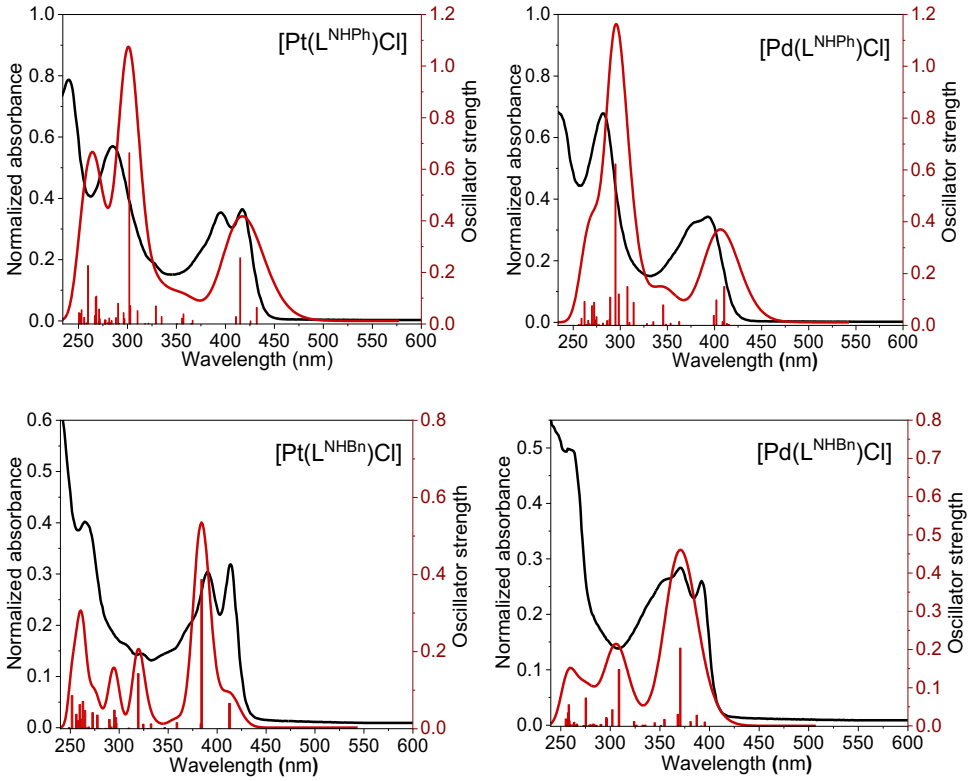


Figure 3-5. Experimental (black) UV-vis absorption spectra of the complexes in THF solution at 298 K with TD-DFT calculated transitions (calculated spectra as solid lines with sticks for individual transitions, in red).

Table 3-2. Selected UV-vis absorption maxima of the complexes.[a,b]

complex	[Pt(L^{NHPh})Cl]	[Pd(L^{NHPh})Cl]	[Pt(L^{NHBn})Cl]	[Pd(L^{NHBn})Cl]
λ_3 (ε)[b]	285 (34)	281 (41)	265 (24)	257 (30)
λ_2 (ε)[b]	396 (21)	376 (19)	390 (18)	371 (17)
λ_1 (ε)[b]	417 (22)	393 (21)	414 (19)	392 (16)

[a] Measured in THF at 298 K. [b] Absorption maxima λ in nm, and molar absorption coefficients ε in 10^3 L mol^{-1} cm^{-1}.

The introduction of the NHR substituents to the dpb ligand had only a small effect on the absorption energies of the Pt complexes. While the parent [Pt(dpb)Cl] complex shows the two maxima at 380 nm and 401 nm (with further less intense bands at 454 and 485 nm in CH_2Cl_2),[62] these bands appear only slightly red-shifted for the two [Pt(N^C^N)Cl] complexes (the second main maxima from 401 to 411 nm for [Pt-L^{NHBn}] and 414 nm for [Pt-L^{NHPh}]). However, this tiny red-shift contrasts with the markedly increased electrochemical gaps determined from cyclic voltammetry for the [Pt(N^C^N)Cl] complexes (>3 eV) compared with the parent dpb derivative (~2.5 eV). A closer look reveals, that the optical HOMO–LUMO gaps (~3 eV) are slightly smaller than the electrochemical HOMO–LUMO gaps (3.22 and 3.31 eV); normally, this is the opposite way, as electrochemistry probes the ground state. For the C^N^C coordinated Pt complexes [Pt(C^N^C)(EPh$_3$)] (E = P, Sb, or As) electrochemical HOMO-LUMO gaps were found larger than the optical gaps by even 0.5 eV.[65] As from our TD-DFT calculations we can

rule out direct singlet→triplet transitions contributing to the bands around 400 nm (Tables A42 and A43), we must assume hampered electrochemical responses to be responsible for this phenomenon.

Photoluminescence spectroscopy showed that the Pt complexes [Pt(N^C^N)Cl] (N^C^N = L^{NHPh} or L^{NHBn}) are emissive both at 298 K in argon-purged CH_2Cl_2 solution (c = 10^{-5} M), in the crystalline state and at 77 K in a frozen glassy matrix of 2MeTHF (Figures 3-6 and 3-7, Table 3-3). At 298 K, vibronically structured emission bands were observed with first maxima at 520 (L^{HNBn}) and 524 nm (L^{NHPh}), second maxima at 559 and 562 nm and shoulders at around 620 nm. At 77 K, the first emission maxima are slightly blue-shifted to 516 nm (L^{HNBn}) and 520 nm ((L^{HNPh}) and several further maxima are observed in the range 520 to 620 nm. The energy of the 0–0 transitions reaching 2.38 eV (L^{NHPh}) and 2.40 eV (L^{NHBn}) are close to the DFT-calculated ΔE (T_1-S_0) values (2.48 eV (L^{NHPh}) and 2.58 eV (L^{NHBn}). The parent [Pt(dpb)Cl] complex shows a very similar spectrum at 298 K, but the maxima at 491, 524, and 562 nm,[62] are massively blue-shifted compared with the [Pt(N^C^N)Cl] (N^C^N = L^{NHPh} or L^{NHBn}) complexes. The same is true for the behavior at 77 K, where a maximum at 486 nm is reported for the dpb complex.[64] The red-shift must be due to the substitution with the NHR groups. This is in line with the observation that this substitution causes also a red-shift for the long-wavelength absorption bands. However, the extent of this shift is far higher for the photoluminescence than for the absorption, most likely due to the different excited state character of the lowest S_n-states (predominant MLCT) if compared with the emissive T_1 (MP-LC).

For the Pd derivatives [Pd(N^C^N)Cl] (N^C^N = L^{NHPh} or L^{NHBn}), no emission was detected in liquid solutions at 298 K; however, at 77 K in a frozen glassy matrix of 2MeTHF, they showed green phosphorescence. The spectra (Figure 3-6) show one sharp emission band at 513 nm (L^{NHPh}) and 509 nm (L^{NHBn}) followed by two medium intensity shoulders at 557 and 607 nm (L^{NHPh}) or 551 and 603 nm (L^{NHBn}). This corresponds to an approximate energy of 2.41 eV (L^{NHPh}) and 2.43 eV (L^{NHBn}) for the 0–0 transitions, which agrees with the DFT-calculated ΔE (T_1-S_0) values, i.e., 2.33 eV (L^{NHPh}) and 2.39 eV (L^{NHBn}). For the complexes at 77 K, a slight blue shift of the emission spectra is observed for Pd(II) with respect to Pt(II) complexes, in line with their absorption spectra (Figure 3-6 B and C). In accordance with literature reported similar cyclometalated complexes, the luminescence originates from a metal-perturbed LC triplet state (^{3}MP-LC).[41,58,60,62,64,65]

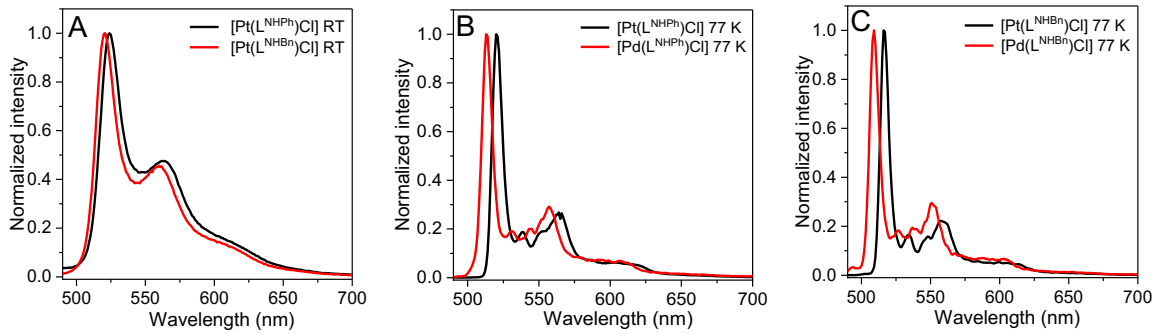


Figure 3-6. Photoluminescence emission spectra of the complexes [M(N^C^N)Cl] (M = Pt) in liquid CH_2Cl_2 solution at 298 K (A, λ_{ex} = 350 nm, c = 10^{-5} M) and [M(N^C^N)Cl] (M = Pt or Pd) in 2MeTHF at 77 K as a frozen glassy matrix (B and C, λ_{ex} = 350 nm); all solutions were optically diluted (concentration = 10^{-5} M). The Pd complexes were not emissive at 298 K. All maxima are listed in Table 3-5.

Overall, the photoluminescence spectra of the [M(N^C^N)Cl] complexes at 77 K strongly resemble those of the recently reported complexes [M(Me2dpb)Cl] (M = Pt or Pd), including the blue-shift of the Pd complex with its maximum at 468 nm compared with the Pt derivative peaking at 489 nm.[41] However, as discussed above for the parent [Pt(dpb)Cl] complex, the [M(N^C^N)Cl] derivatives emit markedly red-shifted. As for the [M(N^C^N)Cl] complexes, no emission was found for [Pd(Me2dpb)Cl] at 298 K in liquid solution.[41]

For both Pt(II) complexes at 77 K, photoluminescence quantum yields (Φ_L) of 0.63 were recorded (Table 3-3). At 298 K after purging with Ar, much lower Φ_L with values 0.17 for [Pt(L^{NHPh})Cl] and 0.22 for [Pt(L^{NHBn})Cl] were recorded, which is markedly lower than the 0.6 reported for the parent [Pt(dpb)Cl] complex.[62] At room temperature (298 K), both Pd(II) complexes are practically non-emissive and the Φ_L values are within the experimental uncertainty. However, they are weakly emissive at 77 K with Φ_L values of 0.08 for [Pd(L^{NHPh})Cl] and 0.07 for [Pd(L^{NHBn})Cl]. The photoluminescence lifetimes (τ) involving the excited triplet states of the Pt and Pd complexes under different conditions were measured (Table 3-3). In aerated solutions at 298 K, the Pt complexes show a luminescence with a lifetime of 0.364 μs (L^{NHPh}) and 0.515 μs (L^{NHBn}), which was increased to 12 μs (L^{NHPh}) and 18 μs (L^{NHBn}) upon deoxygenation. This clearly underlines the triplet character of the emission. The photoluminescence lifetimes at 77 K for the Pt complexes reached up to 30 μs (L^{NHPh}) and 33 μs (L^{NHBn}), whereas for the Pd complexes they attained up to 548 μs (L^{NHPh}) and 541 μs (L^{NHBn}) (Table 3-3). Based on the obtained Φ_L and excited-state lifetimes, we estimated the average radiative (k_r) and non-radiative (k_{nr}) rate constants (Table 3-4).

Table 3-3. Photoluminescence data of the complexes.[a]

complex	Φ_{Air}	Φ_{Argon}	$\Phi_{77\ K}$	τ_{air} / μs	τ_{Ar} / μs	$\tau_{77\ K}$ / μs	$\tau_{Crystal}$ / μs [b,c]
[Pt(L^{NHPh})Cl]	<0.01	0.17 ± 0.02	0.63 ± 0.04	0.364 ± 0.003	12.110 ± 0.008	30.90 ± 0.05	τ_{av_amp} = 5.81 ± 0.03
[Pt(L^{NHBn})Cl]	<0.01	0.22 ± 0.02	0.63 ± 0.04	0.515 ± 0.001	18.73 ± 0.02	33.31 ± 0.04	τ_{av_amp} = 0.711 ± 0.005
[Pd(L^{NHPh})Cl]	<0.01	< 0.01	0.08 ± 0.01	n.d.	n.d.	τ_{av_amp} = 548 ± 3	n.d.
[Pd(L^{NHBn})Cl]	<0.01	<0.01	0.07 ± 0.01	n.d.	n.d.	τ_{av_amp} = 541 ± 3	n.d.

[a] Photoluminescence Φ_L and lifetimes (τ) under different conditions: Liquid CH_2Cl_2 solution under air (Air) atmosphere or Ar-purged (Argon) (both c ≈ 10^{-5} M), frozen glassy matrices at 77 K (77 K) and crystalline state (Crystal). [b] For multi-exponential decays, the amplitude-weighted average lifetimes are given. [c] Measured using Phosphorescence Lifetime IMaging (PLIM). n.d. = not detected. Raw time-resolved photoluminescence decays and fitting parameters are shown in Figures A168 to A177.

Table 3-4. Radiative and non-radiative rate constants (k_r and k_{nr}) of the complexes.[a]

complex	$k_{r(Air)}$ / $10^3 s^{-1}$	$k_{nr(Air)}$ / $10^3 s^{-1}$	$k_{r(Ar)}$ / $10^3 s^{-1}$	$k_{nr(Ar)}$ / $10^3 s^{-1}$	$k_{r(77\ K)}$ / $10^3 s^{-1}$	$k_{nr(77\ K)}$ / $10^3 s^{-1}$
[Pt(L^{NHPh})Cl]	< 2.74	271 ± 3	1.4 ± 0.2	6.9 ± 0.2	2.0 ± 0.1	1.2 ± 0.1
[Pt(L^{NHBn})Cl]	< 1.94	192 ± 2	1.2 ± 0.1	4.1 ± 0.1	1.9 ± 0.1	1. 1 ± 0.1
[Pd(L^{NHPh})Cl]	--	--	--	--	0.014 ± 0.002	0.167 ± 0.003
[Pd(L^{NHBn})Cl]	--	--	--	--	0.013 ± 0.002	0.171 ± 0.002

[a] For conditions, see Table 3-3.

Table 3-5. λ_{max} of the emission spectra of complexes under different conditions.

complex	λ_{max} (DCM, RT) / nm	λ_{max} (2MeTHF, 77 K)	λ_{max} (crystal, RT)
[Pt(L^{NHPh})Cl]	524, 563, 619	52, 565, 615	527,569, 618
[Pt(L^{NHBn})Cl]	521, 560, 616	517, 558, 614	527, 600
[Pd(L^{NHPh})Cl]	n.d.	513, 557, 607	n.d.
[Pd(L^{NHBn})Cl]	n.d.	509, 551, 603	n.d.

n.d. = not detected.

Depending on the nature of the pending NHR groups, minor changes in both k_r and k_{nr} are found. When going from aerated to Ar-purged CH_2Cl_2 at 298 K, the k_{nr} values are dramatically decreased for Pt complexes, since long-lived excited states in solution are quenched through diffusion-controlled deactivation mediated by $^3O_2$.[109] At 77 K, in a frozen glassy matrix, the k_{nr} values are further decreased, since population of dissociative ^{3}MC states that are thermally accessible at ambient temperature are suppressed, whereas the k_r values remain unaffected. Also, for all the complexes, there are small differences between k_r and k_{nr} values at 77 K as they remained locked in their most stable configurations within the solidified glassy structure without solvent interaction. On the other hand, both k_r and k_{nr} values are lower for Pd complexes, owing to significantly lower SOC leading to less efficient radiative and non-radiative decay processes involving spin-forbidden transitions, if compared to the Pt complexes.

We also investigated the photoluminescence of crystalline phases for the complexes (Figure 3-7, Table 3-3). The corresponding phosphorescence spectra show an intense luminescence for the Pt(II) complexes, where the microsecond lifetime maps clearly indicate that the emission occurs from triplet states. If compared with solutions, the vibrationally resolved emission spectra in the crystalline phase

(Figure 3-7) show main peaks blue-shifted by about 10 nm for [Pt(L^{NHPh})Cl] and 28 nm for [Pt(L^{NHBn})Cl], but red-shifted by about 44 nm in the case of [Pd(L^{NHPh})Cl] and by 30 nm for [Pd(L^{NHBn})Cl].

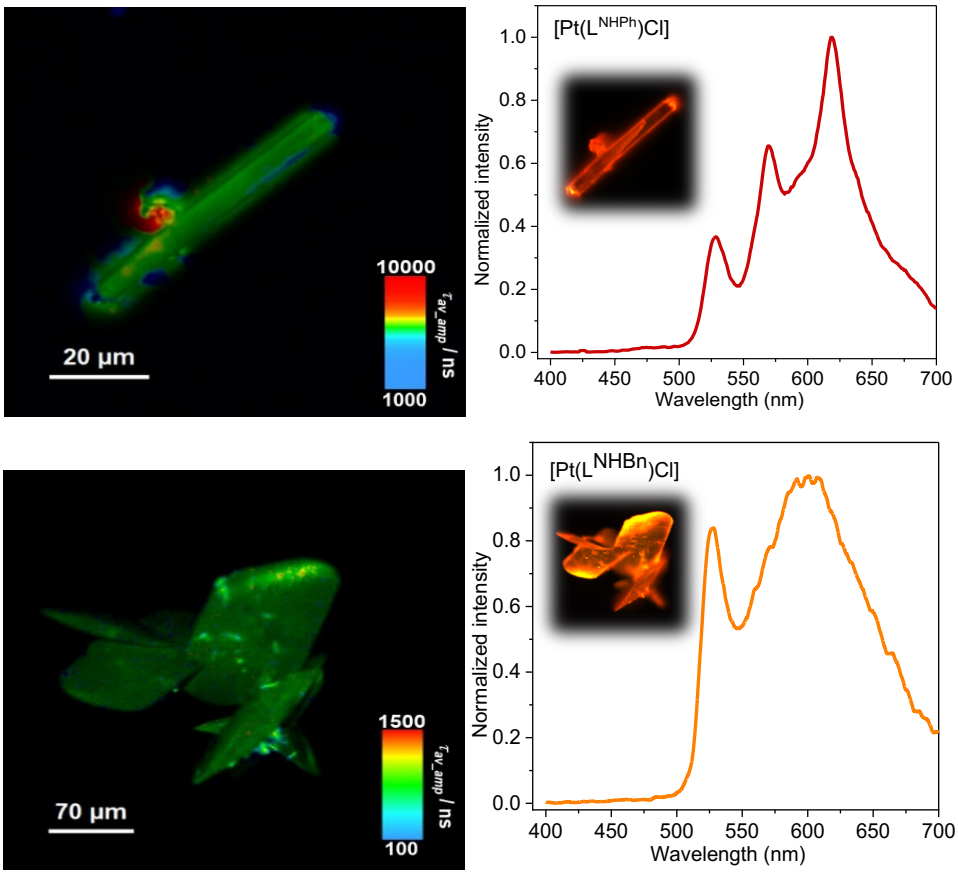


Figure 3-7. Top: Left: Lifetime map measured by PLIM of the crystalline phase of **[Pt(L^{NHPh})Cl]**. Right: Experimental photoluminescence spectra of the complex in the crystalline state at 298 K (normalized to the highest intensity), measured using a fluorometer (FT300, PicoQuant) coupled to the confocal microscope. Bottom: Left: Lifetime map measured by PLIM of the crystalline phase of **[Pt(L^{NHBn})Cl]**. Right: Experimental photoluminescence spectra of the complex in the crystalline state at 298 K (normalized to the highest intensity), measured using a fluorometer (FT300, PicoQuant, λ_{ex} = 376 nm) coupled to the confocal microscope. Luminescence micrographs of both crystals are shown as insets (λ_{ex} = 375 ± 20 nm). Raw time-resolved photoluminescence decays and fitting parameters are shown in the appendix, Figures A168 and A177.

The most relevant DFT-calculated frontier orbitals involved in the description of the excited state configurations (data in Tables A25 and A26) agree with an overall LC character. We analyzed the data in more detail, using the Theoretical Density, Orbital relaxation and Excitation analysis (TheoDORE)[110] allowing the decomposition of the excited triplet state (T_1) into contributions from MLCT, ligand-to-metal-charge-transfer (LMCT), LC, ligand'-to-ligand-charge-transfer (L'LCT), and metal-centered (MC) configurations, according to the partitioning defined in Figure 3-8. L'LCT is defined as a configuration involving different parts of the tridentate ligand, particularly NHR and N^C^N, while LC represents excitations within the same part. This analysis reveals that the excited states of the Pt complexes have a higher MLCT character in the T_1 state (with 7.9% [Pt-L^{NHPh}] and 10.7% [Pt-L^{NHBn}]), compared to the Pd derivatives (with 2.8% [Pd-L^{NHPh}] and 4.1% [Pd-L^{NHBn}]). In addition, the complexes with benzyl groups

show a lower L'LCT character (19 to 22%) than their phenyl-containing counterparts (29 to 37%), while the LC character is superior for the benzyl complexes (64 to 69%) compared with the phenyl derivatives (56 to 57%). This supports the overall characterization of the triplet excited states as metal-perturbed LC triplet states (^{3}MP-LC).

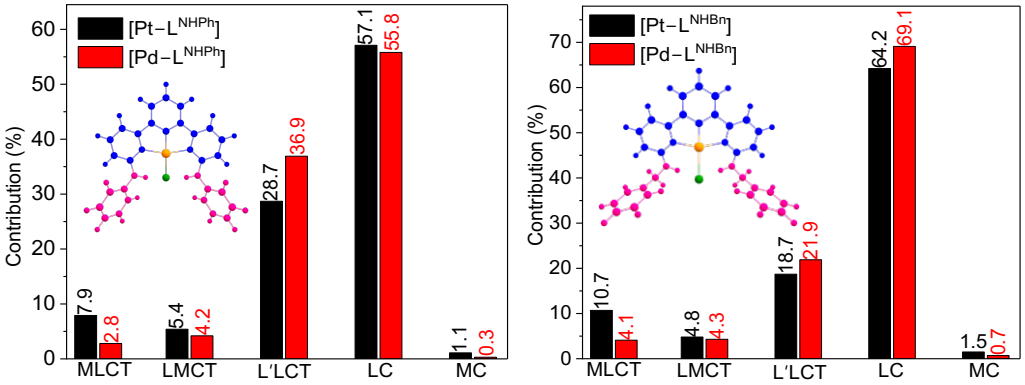


Figure 3-8. Decomposition of the T_1 state for the four calculated complexes into contributions originating from MLCT, LMCT, LC, L'LCT, or MC configurations as determined with the TheoDORE package,[110] together with the partitioning of the [M(L^{NHPh})Cl] (left) and [M(L^{NHBn})Cl] (right) complexes for the numerical analysis. L'LCT denotes ligand-centered configurations involving different parts of the tridentate ligand.

3.2. [Ni(L^{NHPh})Cl] and [Ni(L^{NHBn})Cl] complexes

3.2.1. Synthesis and structure of [Ni(L^{NHPh})Cl] and [Ni(L^{NHBn})Cl]

To replace precious transition metals like Pt by abundant base metals such as Ni towards efficient triplet emitters, the two ligand precursors ClL^{NHPh}, and ClL^{NHBn} were synthesized through optimization of established methods, including Suzuki cross-coupling reactions, with yield of 65% (details in the experimental section). The two Ni(II) complexes were obtained from an oxidative addition reaction of [Ni(COD)$_2$] (COD = 1,5- cyclooctadiene) with the chlorinated ligand precursors ClL^{NHPh}, ClL^{NHBn} in 60 and 67% yields, respectively, by modifying an established procedure.[96] The complexes were obtained as orange microcrystalline powders and were analyzed using ^{1}H NMR spectroscopy, HR-ESI mass spectrometry, and elemental (CHN) analysis (spectra and data in the experimental section and the appendix). The two complexes are insoluble in non-polar solvents but are soluble in polar solvents, though they must be handled under the exclusion of air and moisture (Figures A21 and A157, appendix).

Single crystals of the Ni(II) complexes were grown by layering saturated solutions in Ar-purged, de-aerated CH_2Cl_2 with *n*-pentane under argon flow. The complexes crystallize isostructurally, in the monoclinic space group $P2_1/n$ (Figures A114 to A116, data in Tables A7 to A9, appendix), similarly to [Ni(dpb)X][103] with X = Cl, Br, and I. Geometry optimization using density DFT at the

TPSSh/6-31G(d)/LanL2DZ level (Table A8), provides a very good agreement between experimental and calculated metrics (Figure A117, Table A8, the resulting *xyz* coordinates of the optimized structures are presented in Tables A56 and A57).

The molecular structures of the Ni(II) complexes are overall very similar to the previously reported Ni(II) dpb complexes in terms of bond length and angles.[41,103] However, both complexes show C–Ni–Cl angles of around 150° instead of 180° (Figure 3-9). The most remarkable feature is the marked deviation of the Cl^- coligand from the square planar coordination plane with τ_4 values of 0.336 for L^{NHPh} and 0.318 for L^{NHBn} (Figure 3-9). We also calculated the hypothetical complexes [Ni(L^{NHPh})F] and [Ni(L^{NHPh})H] having far smaller coligands along with much reduced τ_4 values of 0.19 and 0.11, respectively. Still, they are not completely planar (Figure A118, Table A10). Evidently, the rigid RNH–N^C^N–NHR (R = Ph or Bn) ligand scaffold does not provide enough space to accommodate even the smallest anionic coligand H^-. When replacing the NHR groups through OMe substituents on the N^C^N scaffold, the steric bulk of the binding pocket for the coligand even increased resulting in a higher τ_4 value of 0.411 for the DFT-optimized [Ni(L^{OMe})Cl] complex (Figure A118, Table A10). This occurs while the τ_4 value for the nearly completely planar complex [Ni(dpb)Cl] is 0.116, based on single crystal data.[41,103]

For the recently reported Pt(II) and Pd(II) complexes [M(L^{NHPh})Cl] and [M(L^{NHBn})Cl] (M = Pt or Pd) we found τ_4 values ranging from 0.239 to 0.296,[28] which are markedly smaller than for the Ni derivatives. However, the main reason for the strong deviation of the Cl^- coligand from the plane is the same in the Pt, Pd, and Ni complexes of these two chelate ligands.

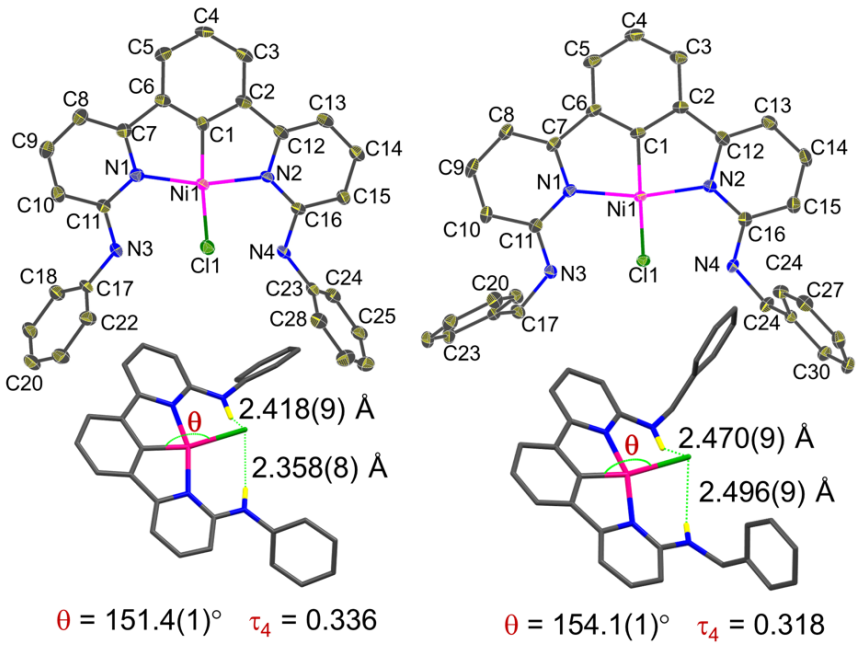


Figure 3-9. Molecular structures of the complexes [Ni(L^{NHR})Cl] (N^C^N = L^{NHPh}, top left and L^{NHBn}, top right) from X-ray diffraction studies on single crystals (top, 50% displacement ellipsoids) and their side-on views featuring the deviation τ_4 from the square planar coordination (bottom).

Non-symmetric Ni–Cl···H–N hydrogen bonds (H bonds) were found ranging from about 2.36 to 2.49 Å with angles of around 123 to 138°, which represent medium-strong H bonds (Figure 3-9, Tables A8 and A9).[106] In contrast to our initial idea to govern the complex geometry through intramolecular H bonding, the herein found H bonds are not the cause of the geometric distortion of the two complexes, as shown by the comparative geometry optimization with F or H (or the replacement of the NHR function by OMe).

In both crystal structures, a characteristic head-to-tail stacking of the molecules was found (Figures A114 to A116), very similar to those observed for the previously reported [M(dpb)X] or [M(phbpy)Br] derivatives with M = Ni, Pd, and Pt.[28,32,41,95,103–105] Intimate π-stacking is only observable in [Ni(L^{NHPh})Cl] between the pyridine units of two neighboring molecules with an angle of 8.159°, a centroid-centroid distance of 3.613 Å, and shift distance of 1.242 Å (Figure 3-10). Metallophilic Ni···Ni interactions, as recently proposed for similar [Ni(N^C^N)(L)] complexes (L = thiophenol or thiadiazole),[111] were not found in our experimental structures.

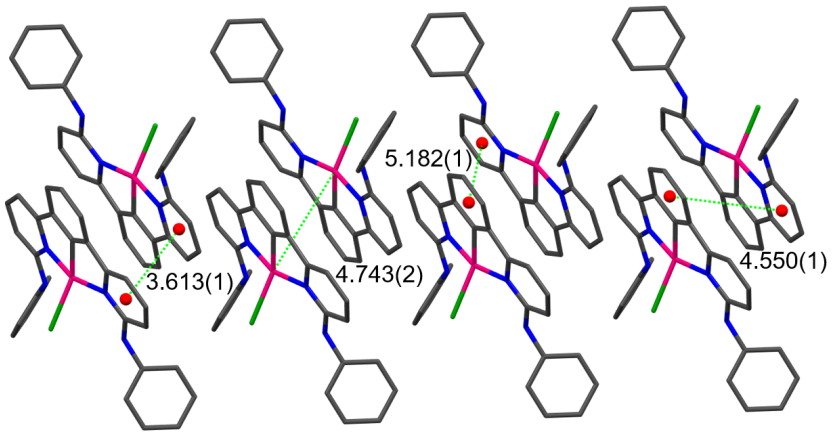


Figure 3-10. Intermolecular contacts and Ni···Ni distances (Å) in [Ni(L^{NHPh})Cl].

3.2.2. Experimental and theoretical properties of [Ni(L^{NHPh})Cl] and [Ni(L^{NHBn})Cl]

At a first glance, the cyclic voltammograms for the two complexes are very similar, each exhibiting two reduction peaks in the range of –2.2 to –2.8 V vs. the ferrocene/ferrocenium couple, and one oxidation wave at very similar potentials, slightly above 0 V (Figures 3-11 and full data in Table 3-6; cyclic voltammograms are presented in Figure A139). The DFT-calculated lowest unoccupied molecular orbitals (LUMO) are centered on the N^C^N ligand core with some contributions from Ni ($d_{x^2-y^2}$) and Cl for both complexes (Figure 3-12 and Tables A28 and A30).

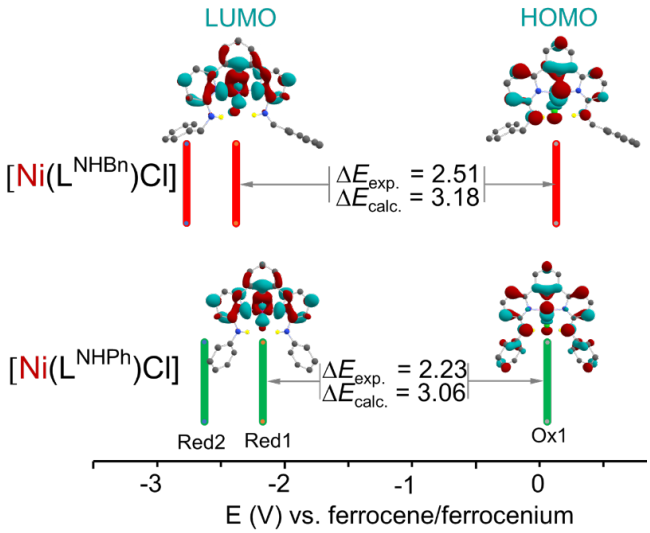


Figure 3-11. Selected experimental redox potentials (bars) and HOMO-LUMO gaps (Δ*E*exp.) from cyclic voltammetry along with DFT-calculated orbital compositions and energies of the HOMO and LUMO and the corresponding HOMO-LUMO gap (Δ*E*calc.).

Table 3-6. Redox potentials of the complexes.[a]

complex	E_{pc} (Red3)	E_{pc} (Red2)	E_{pc} (Red1)	E_{pa} (Ox1)	E_{pa} (Ox2)	E_{pa} (Ox3)	Δ*E* (Red1-Red2)	Δ*E* (Ox1-Red1)
[Ni(L^{NHPh})Cl]	–2.94 [b]	–2.63	–2.17	0.06	1.02	–	0.46	2.23
[Ni(L^{NHBn})Cl]	–3.30	–2.77	–2.38	0.13	0.81	1.20	0.39	2.51

[a] From cyclic voltammetry in 0.1 M n-Bu$_4$NPF$_6$/THF. Potentials in V vs. ferrocene/ferrocenium; cathodic peak potentials (E_{pc}) for irreversible reductions; anodic peak potentials (E_{pa}) for irreversible oxidations.

For the highest occupied molecular orbitals (HOMOs), the calculations show contributions of the pending phenyl cores for the L^{NHPh} complex, while this is not the case for the L^{NHBn} derivative (Figure 3-12, Tables A28 and A30), while all other contributions are very similar. This might explain the slightly higher oxidation potential for the L^{NHBn} complex.

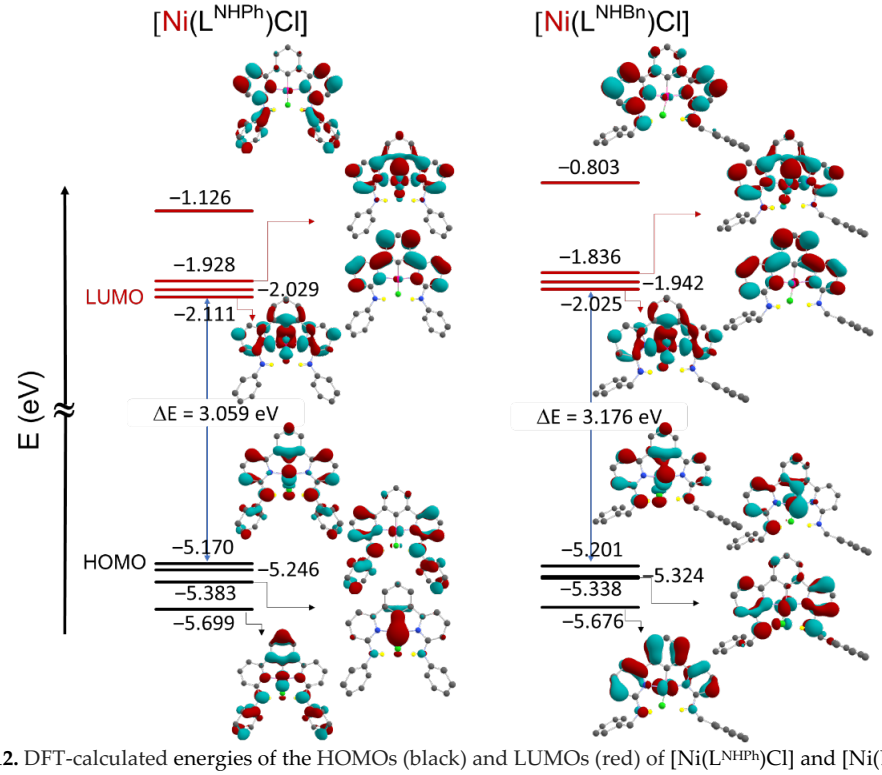


Figure 3-12. DFT-calculated energies of the HOMOs (black) and LUMOs (red) of [Ni(L^{NHPh})Cl] and [Ni(L^{NHBn})Cl].

The intense UV absorption bands of the complexes, peaking at 250 nm (L^{NHBn}) and 283 (L^{NHPh}) nm, also occur for the ligand precursors (Figure 3-13 and Table 3-7, Figures A158 and A159) and are assigned to transitions into singlet π–π* (LC) states. The bands in the visible range with maxima at 340 nm (L^{NHBn}) and 368 nm (L^{NHPh}) as well as the long-wavelength bands at around 425 nm, are attributed to transitions into mixed LC/metal-to-ligand charge transfer (MLCT) singlet states.

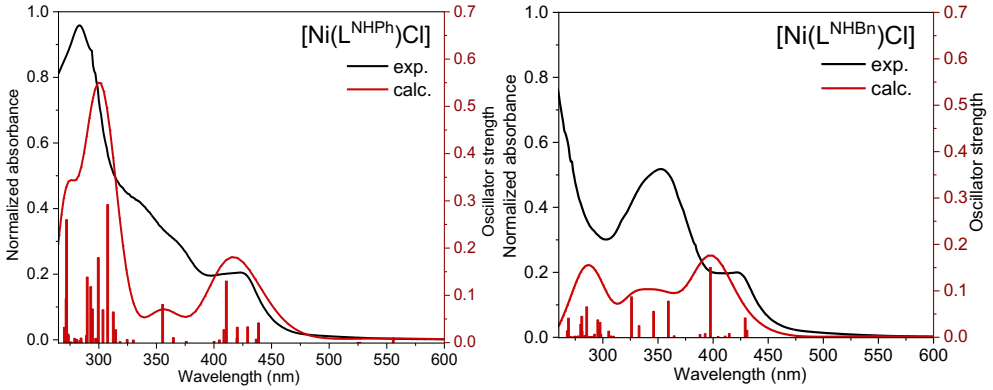


Figure 3-13. UV-vis absorption spectra of the complexes in THF solution at 298 K with calculated TD-DFT transitions (spectrum as line and sticks for individual transitions, in red).

Table 3-7. Selected experimental UV-vis absorption maxima of the complexes.[a]

complex	[Ni(L^{NHPh})Cl]	[Ni(L^{NHBn})Cl]
λ_3	283	250
λ_2	368	340
λ_1	427	423

Measured in THF at 298 K, absorption maxima λ in nm.

The TD-DFT calculated transitions match the observed absorption bands (Figure 3-13 and Tables 3-7, A44 and A45) for both the UV range and in the visible bands. The appearance of the long-wavelength bands is very similar to those of reported Ni and Pt complexes of dpb derivatives,[19,41–43,81,88,110–112] aligning with our assignment.

The Ni(II) complexes reported herein are only soluble in polar solvents and undergo decomposition over time, as indicated by the gradual diminution of the long-wavelength absorption bands which starts 10 minutes after sample preparation (Figure A157). However, complete disappearance of theses bands requires more than four hours in both cases. To gain insight into the decomposition pathway, time-dependent ^{1}H NMR studies were conducted (Figures 3-14 and A21). Over a period exceeding four months, no precipitation or formation of paramagnetic species was observed, although the solution color progressively changed from orange-yellow to green. This suggests that Ni remains coordinated to the ligand, despite the gradual disappearance of characteristic signals associated with the original complex and the emergence of new resonances. For [Ni(L^{NHPh})Cl], a new signal at 8.75 ppm appears after a few days, closely matching the chemical shift of the proton attached to the deprotonated carbon atom in the free HL^{NHPh} ligand (Figure 3-14). This observation suggests that the Ni–C bond in

[Ni(L^{NHPh})Cl] undergoes cleavage in solution, leading to protonation of the carbanion. In contrast, ^{1}H NMR spectra of [Ni(L^{NHBn})Cl] over time do not provide clear evidence for protonation of the deprotonated carbon (Figure A21). To further investigate the decomposition products, we attempted crystallization from solutions containing decomposed complexes. However, these efforts did not yield suitable crystals for structural elucidation.

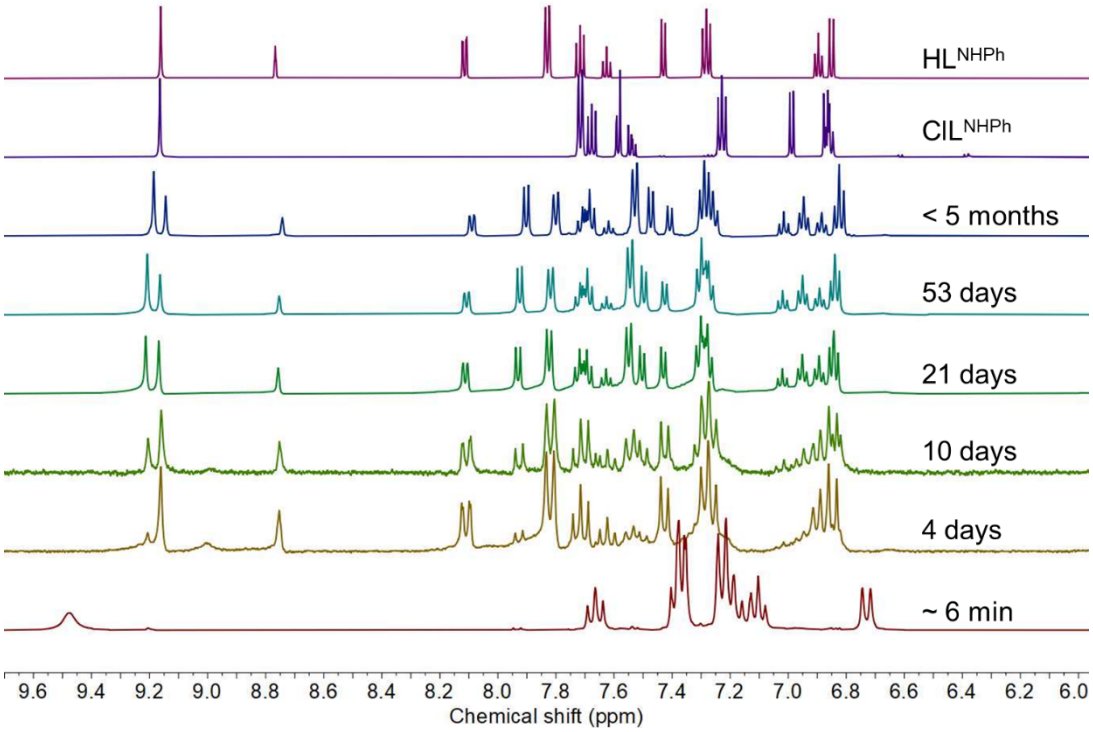


Figure 3-14. ^{1}H NMR spectra of [Ni(L^{NHPh})Cl] over time, with ^{1}H NMR spectra of HL^{NHPh} and ClL^{NHPh}, in DMSO-d_6 at RT.

Typically, Ni(II) complexes do not emit light in liquid solutions at RT; even at lower temperatures, they fail to show photoluminescence. However, when the herein reported complexes are within a frozen 2-methyltetrahydrofuran (2MeTHF) glassy matrix at 77 K, a clear luminescence with a vibrationally structured emission profile was detected (Figure 3-15).

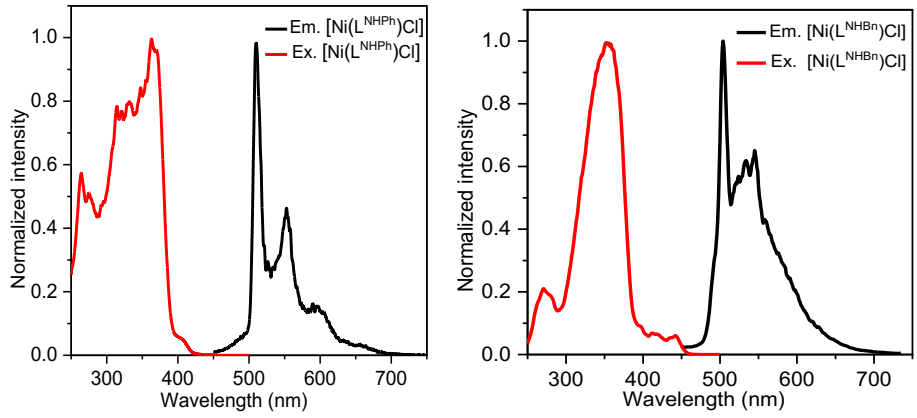


Figure 3-15. Excitation (red, λ_{em} = 525 nm) and emission (black, λ_{ex} = 350 nm) spectra of complexes at 77 K in 2MeTHF.

The notably high steady-state photoluminescence quantum yields of 30% for [Ni(L^{NHPh})Cl] and 40% for [Ni(L^{NHBn})Cl] (coupled with sizeable decay components with lifetimes in the ms range, i.e., 648 ms for [Ni(L^{NHPh})Cl] and 178 ms for [Ni(L^{NHBn})Cl], along with the nanosecond components discussed below), suggest a triplet nature of the emissive states (Figures A178 and A179). To the best of our knowledge, our present work represents the first instance in which Ni(II) complexes exhibit quantum yields exceeding 30% and lifetimes in the millisecond range. To date, only one pioneering study by *Yam* et al. reported lifetimes in the sub-microsecond regime for the [Ni(dpb)(carbazolate)] complex.[91] However, our compounds achieve longer lifetimes and measurable quantum yields. Not surprisingly, the Pt(II) and Pd(II) complexes carrying these same ligands behave quite as expected (i.e., in that the Pt(II) complexes emit both at RT and at 77 K with relatively high quantum yields). While the photophysical properties obtained in glassy matrices are remarkable, they are limited to one single temperature (77 K). To address this drawback and to investigate the photophysical properties of these complexes across a broader range of temperatures, the complexes were incorporated into poly(methyl methacrylate, PMMA) films, which typically provide a defined microenvironment for characterizing triplet emitters.

Interestingly, within the range spanning from 6 K to 300 K, we observed a temperature dependence in both emission spectra and the lifetimes (Figures 3-16, A180 to A199 and Table 3-8). Notably, increasing the temperature resulted in a less vibrationally structured emission profile and a shortening of the lifetimes for both complexes (Figure 3-16, Table 3-8). This observation suggests a progressive enhancement of the MLCT character pertaining the emissive triplet state, accompanied by successively faster spin-forbidden deactivation rates and shorter lifetimes.

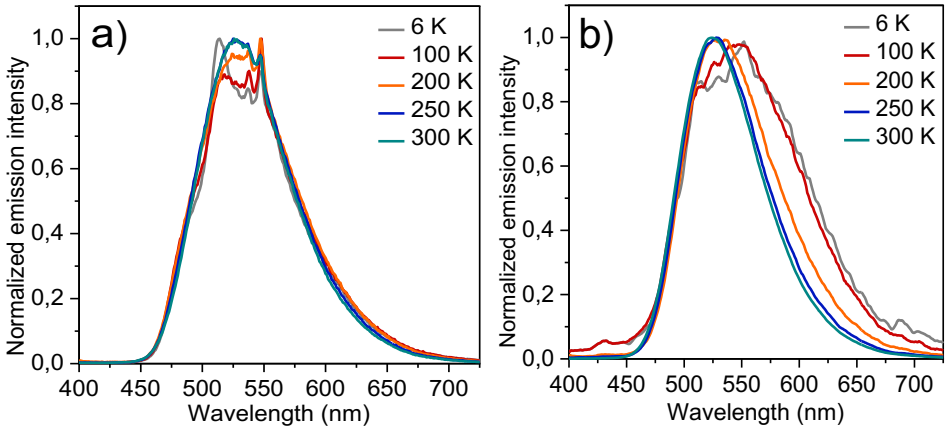


Figure 3-16. Photoluminescence spectra of [Ni(L^{NHPh})Cl] (a) and [Ni(L^{NHBn})Cl] (b) (λ_{ex} = 350 nm) at different temperatures within PMMA films (2.5%).

Remarkably, even at RT, lifetimes in the ms range (143 for [Ni(L^{NHPh})Cl] and 1.05 for [Ni(L^{NHBn})Cl], along with nanosecond components, vide infra) were achieved. The differences among the complexes can be attributed to the higher deactivation rates associated with the less rigid benzyl-substituted ligand. This

behavior was also observed at 77 K (vide supra). To the best of our knowledge, such quantum yields in PMMA films are unprecedented, particularly at room temperature, and clearly surpass the benchmark set by *Yam* et al. for the complex [Ni(dpb)(carbazolate)].[91]

Table 3-8. Selected photophysical data for the [Ni(N^C^N)Cl] complexes.[a]

		[Ni(L^{NHPh})Cl]	[Ni(L^{NHBn})Cl]
2MeTHF (77 K)	$\lambda_{em,\,max}$ (nm)	510	504
	$\Phi_L \pm 0.05$	0.30	0.40
	τ_{av_amp} (ns)	3.34 ± 0.01	3.63 ± 0.02
	τ_{av_amp} (ms)	648 ± 3	180 ± 10
PMMA (6 K)	τ_{av_amp} (ns)	1.91 ± 0.04	2.73 ± 0.02
	τ_{av_amp} (ms)	476 ± 6	93 ± 3
PMMA (100 K)	τ_{av_amp} (ns)	1.80 ± 0.05	2.69 ± 0.03
	τ_{av_amp} (ms)	464 ± 6	74 ± 3
PMMA (200 K)	τ_{av_amp} (ns)	1.69 ± 0.04	2.46 ± 0.05
	τ_{av_amp} (ms)	161 ± 5	16 ± 1
PMMA (250 K)	τ_{av_amp} (ns)	1.51 ± 0.03	2.24 ± 0.04
	τ_{av_amp} (ms)	163 ± 4	10.4 ± 0.2
PMMA (300 K)	τ_{av_amp} (ns)	1.41 ± 0.04	2.18 ± 0.02
	τ_{av_amp} (ms)	143 ± 5	1.05 ± 0.01
	$\Phi_L \pm 0.05$	0.03 ± 0.02	0.04 ± 0.02

[a] In a frozen glassy matrix (2MeTHF) at 77 K or immersed in a PMMA matrix at different temperatures (where short and long lifetimes were detected). Φ_L: photoluminescence quantum yields. (τ_{av_amp}: amplitude-weighted average lifetimes from multi-exponential decays). Raw time-resolved photoluminescence decay are shown in the appendix, Figures A178 to A199.

In addition to the long decay components (with lifetimes in the ms range) observed across the temperature range, a short lifetime was also detected (between 1.5 and 2 ns) both in the glassy matrix and in the PMMA films across the investigated temperature range (Table 3-8, Figures A178 to A201). This result is consistent with fluorescence originating from the singlet manifold while sensing a restricted roto-vibrational freedom in a rigid environment (either glassy solvent matrix or PMMA). These results were further validated through theoretical calculations (vide infra). To ensure that this emission does not originate from residual ligand, the ligand alone was measured at 77 K. Neither the emission spectra nor the lifetimes resemble those of the complexes, confirming that both the emission as well as the long and short lifetimes arise from the complexes (Figure 3-17).

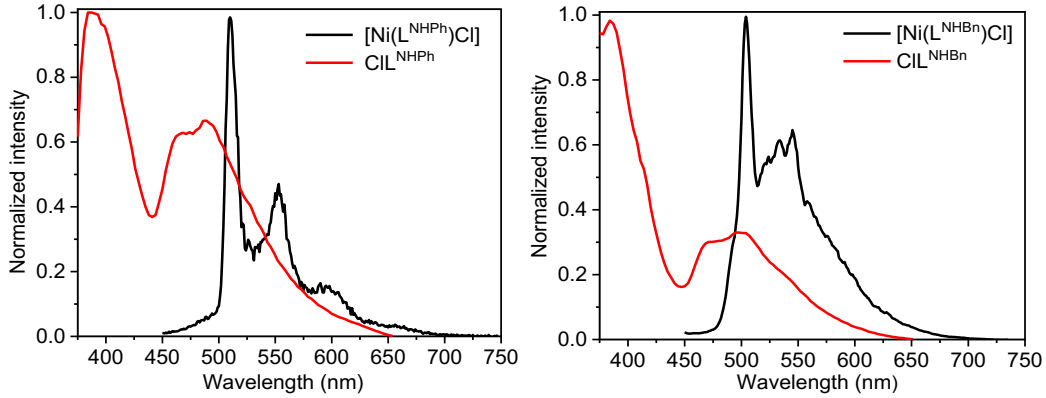


Figure 3-17. Emission spectra of complexes (black) and their respective ligands (red) in 2MeTHF at 77 K (c = 10^{-5} M), λ_{ex} = 350 nm.

The initial idea of this study was to rigidify the coordination sphere around the Ni(II) centers through the N–H···Cl···H–N hydrogen bonds. However, we found that these ligands do not provide enough space for the Cl coligand. Nonetheless, the experimental molecular structures align very well with the DFT-calculated S_0 ground state geometries. However, these differ significantly from the DFT-calculated T_1 geometries (Figure 3-18), in which the Ni–N bonds stretch by about 0.3 Å. We hypothesize that the photoluminescence from an excited triplet state is related to the fact that the ground-state geometry is effectively locked-in by a restrictive environment suppressing the expansion of the Ni–N bonds.

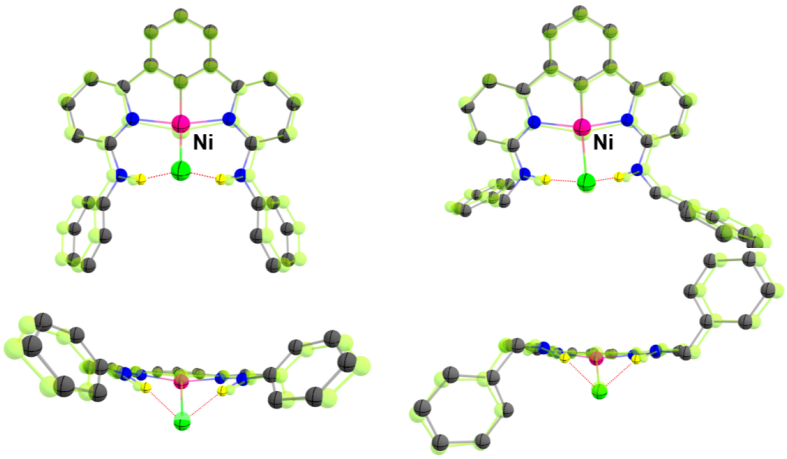


Figure 3-18. DFT-calculated geometries of the complexes in the S_0 (black) and T_1 (green) states.

To investigate this scenario in more detail, we performed a scan of the first five singlet and triplet states using TD-DFT in the Tamm-Dancoff approximation,[112] varying the Ni–N bond lengths of the central [Ni(N^C^N)Cl] unit. Figure 3-19 shows potential curves obtained with the PBE0 exchange-correlation functional[113] and the SDD basis set.[114] For both [Ni(L^{NHPh})Cl] and [Ni(L^{NHBn})Cl], it can be seen that population of the T_1–T_4 or S_1–S_4 states leads to a substantial Ni–N bond stretch. For the T_1–T_3 states conical intersections with the S_0 ground state are clearly visible, enabling non-radiative decay and thus quenching the phosphorescence. In the case of the T_4 state, the curves suggest that there may well be an energetically accessible crossing with the S_0 state (or at least a very small gap) at a Ni–N distance beyond 2.45 Å. On the other hand, the S_1 state is well separated from the T_4 state and is therefore likely to be fluorescent. In a rigid environment that restricts the geometry to the Franck-Condon region (i.e. around 2.0 Å), the T_5 and the S_4 state could both contribute to the luminescence as well. In fact, a geometry optimization of [Ni(L^{NHBn})Cl] in the S_4 state with the Ni–N bonds constrained to their ground state lengths yields a emission wavelengths of 514 nm and 485 nm for the vertical and adiabatic transitions, respectively. The optimized T_5 state of [Ni(L^{NHBn})Cl] gives an adiabatic (vertical) emission of 490 nm (556 nm). Thus, the theoretical S_4 and the T_5 results match the experimental emission wavelengths quite well. Similarly, the optimized T_5 state of [Ni(L^{NHPh})Cl] corresponds to an adiabatic (vertical) emission wavelength of 502 nm (568 nm), while the constraint-optimized S_4 state with ground

state Ni–N bond lengths yields 485 nm (514 nm). The main electronic configurations contributing to the T_5 state are HOMO→LUMO+1 (45% / 44%) and HOMO-1→LUMO (33% / 34%) excitations for [Ni(L^{NHPh})Cl] and [Ni(L^{NHBn})Cl], respectively (Tables 3-9 and 3-10). The S_4 state is mainly composed of the HOMO-13→LUMO+3 (48%) and HOMO-9→LUMO+3 (35%) excited configurations for [Ni(L^{NHPh})Cl], and the HOMO-14→LUMO+2 (48%) and HOMO-8→LUMO+2 (29%) for [Ni(L^{NHBn})Cl]. A visualization of the most relevant orbitals participating on the description of the S_1, S_4, and T_5 states can be found in Figures 3-20 and 3-21.

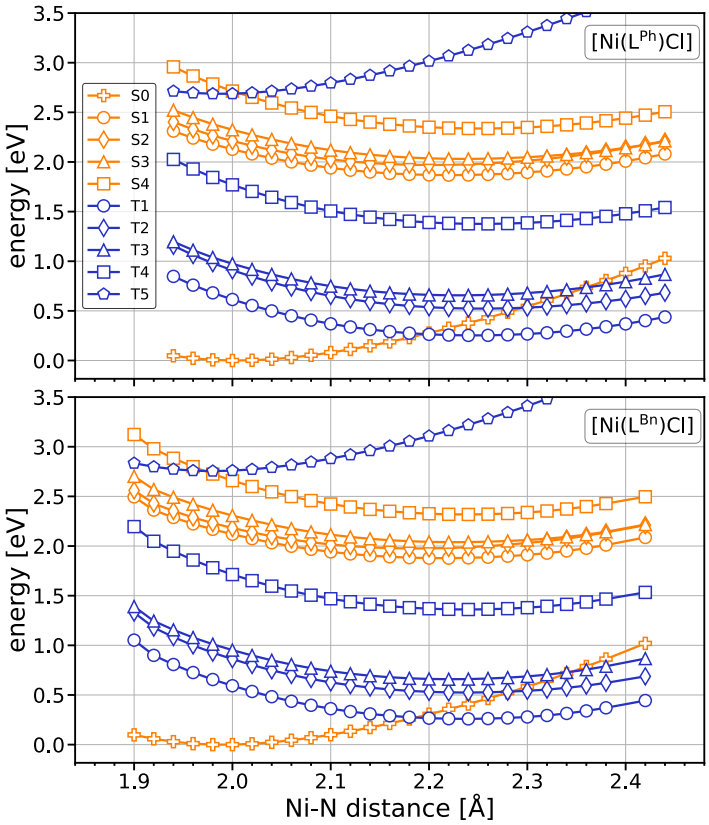


Figure 3-19. Ground and excited states energies for fixed Ni–N distances of the central [Ni(N^C^N)Cl] unit from TD-DFT calculations using the Tamm-Dancoff Approximation (TDA)[112] in vacuum for both substituents, Ph (top) and Bn (bottom). Elongation of the Ni–N bonds promotes non-radiative transitions from T_1–T_3 to the S_0 ground state due to conical intersections, whereas the S_1 state should be emissive. In a rigid environment, where the Ni–N distance is kept at ca. 2.0 Å, luminescence could also occur from the T_5 and S_4 states.

Table 3-9. Characterization of selected TDA-calculated vertical excited states for the optimized ground state geometry of [Ni(L^{NHPh})Cl]. Only orbital transitions with a weight of at least 10% are listed.

state	oscillator strength (f_{osc})	λ (nm)	transitions (major contribution)
S_1	0.002	604.7	HOMO-2→LUMO+3 (70%)
			HOMO→LUMO+3 (14%)
S_4	0.001	464.7	HOMO-13→LUMO+3 (48%)
			HOMO-9→LUMO+3 (35%)
T_5	0.000	455.7	HOMO→LUMO+1 (45%)
			HOMO-1→LUMO (33%)

Table 3-10. Characterization of selected TDA-calculated excited states for the optimized ground state geometry of [Ni(L^{NHBn})Cl]. Only orbital transitions with a weight of at least 10% are listed.

state	oscillator strength (f_{osc})	λ (nm)	transitions (major contribution)
S_1	0.003	597.0	HOMO-2→LUMO+2 (60%)
			HOMO→LUMO+2 (20%)
S_4	0.001	466.5	HOMO-14→LUMO+2 (48%)
			HOMO-8→LUMO+2 (29%)
T_5	0.000	446.5	HOMO→LUMO+1 (44%)
			HOMO-1→LUMO (34%)
			HOMO-3→LUMO (10%)

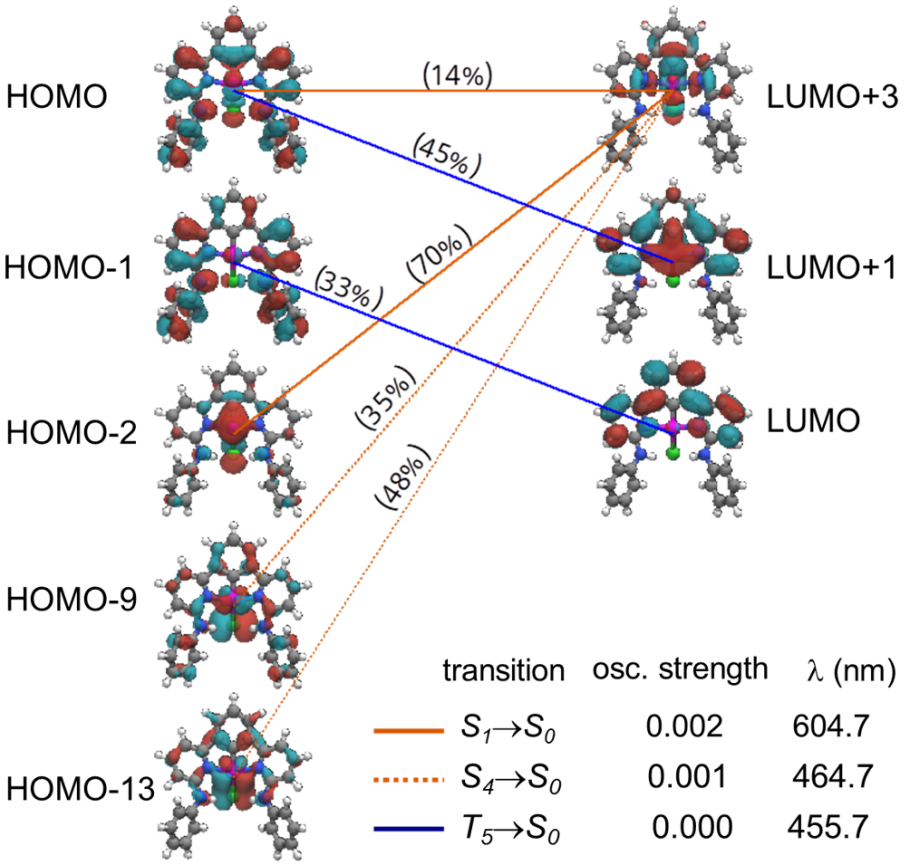


Figure 3-20. Main contributing orbitals to the $S_1 \rightarrow S_0$, $S_4 \rightarrow S_0$, and $T_5 \rightarrow S_0$ of [Ni(L^{NHPh})Cl] from TDA calculations as detailed in Table 3-9.

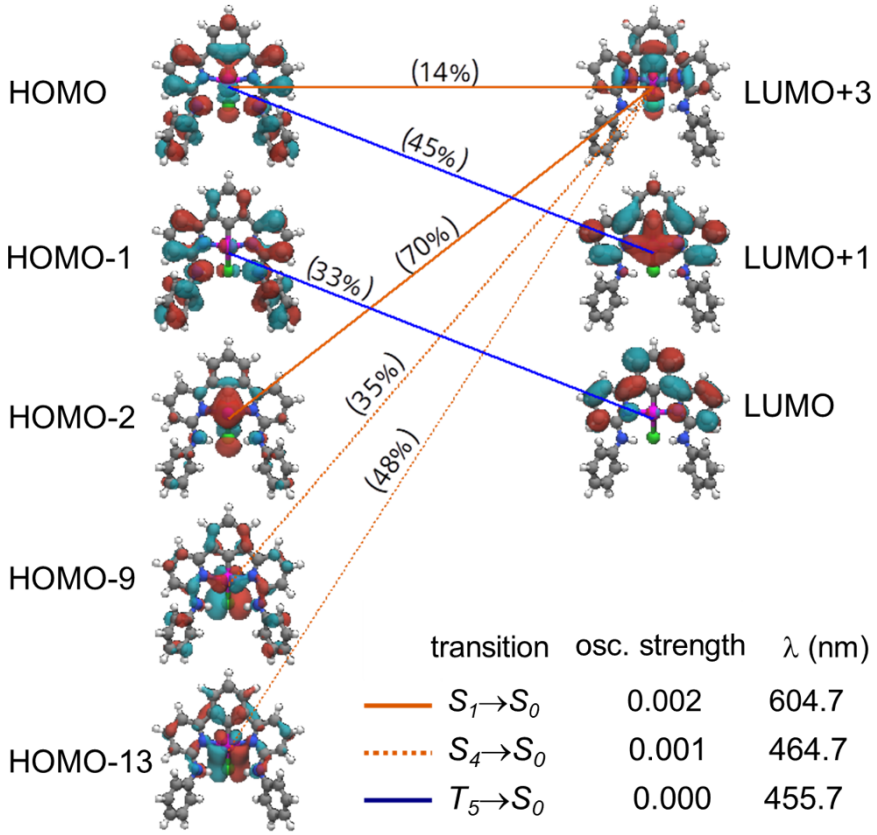


Figure 3-21. Main contributing orbitals to the $S_1 \rightarrow S_0$, $S_4 \rightarrow S_0$, and $T_5 \rightarrow S_0$ of [Ni(L^{NHBn})Cl] from TDA calculations as detailed in Table 3-10.

To further analyze the excited state dynamics, cryostat-supported nanosecond transient absorption spectroscopy was carried out. Rather than observing a long-lived species as identified in Figure 3-17, only a short-lived transient with excited state absorptions (ESA) at 400 and 580 nm and lifetimes of 722 ps for [Ni(L^{NHPh})Cl] and 1.94 ns for [Ni(L^{NHBn})Cl] were identified (Figures A228 to A231). These ESAs perfectly overlap with the ESAs seen for the free ligands (Figures A232 and A233). As such, it confirms that in contrast to low temperature emission studies, ESAs are ligand-centered and short-lived in nature. Although being unlikely, considering the care that we have taken in the sample preparation, we cannot rule out any chemical decomposition. In that particular case, ligand-based ESAs would stem from the free ligands in solution and/or the matrix upon decomposition. Long-lived emission, on the other hand, would originate from the phosphorescence of the intact complexes.

3.3. [M(L^{Bn})Cl] (M = Pt, Pd, Ni) complexes

3.3.1. Synthesis and structure of [M(L^{Bn})Cl] (M = Pt, Pd, Ni)

To asses how the rigidity of the structures would be affected by replicating the steric bulk of the coordination environment without the presence of NH···Cl···NH hydrogen bonds, the two ligand

precursors HL^{Bn} and ClL^{Bn} were synthesized through Suzuki cross coupling reactions in 82% and 72% yield (Figure 3-22, details in the experimental section). The Pt(II) and Pd(II) complexes [M(L^{Bn})Cl] were synthesized from $K_2[MCl_4]$ (M = Pt or Pd) through an established method of heating in glacial acetic acid,[92] in 62% and 60% yield (Figure 3-22, details in the experimental section). The Ni(II) complex was obtained by modifying an established procedure[96] including oxidative addition reaction of $[Ni(COD)_2]$ (COD = 1,5- cyclooctadiene) with the chlorinated ligand precursor ClL^{Bn} in 78% yield (Figure 3-22, details in the experimental section). The three Pt(II) (yellow), Pd(II) (pale yellow), and Ni(II) (orange-red) complexes were characterized by NMR spectroscopy, HR-ESI mass spectrometry, elemental (CHN) analysis, and single-crystal X-ray diffraction (XRD) (spectra and data in the experimental section and the appendix).

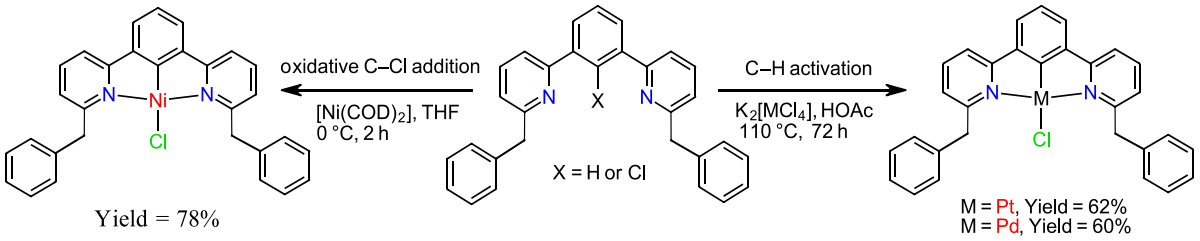


Figure 3-22. Synthesis of the [M(L^{Bn})Cl] (M = Pt, Pd, Ni) complexes.

The [M(L^{Bn})Cl] (M = Pt or Pd) complexes crystallize isostructural in the triclinic space group $P\bar{1}$ while for the [Ni(L^{Bn})Cl] complex, the structure was solved in the monoclinic space group $C2/c$ (Figure 3-23, Figures A119-A121, data in Table A11 and A12, appendix). The experimental data for the complexes were used to benchmark our DFT geometry-optimization using TPSSh/def2-TZVP/CPCM(THF) with good agreement between the experimental and calculated metrics (Figure A122, Table A12).

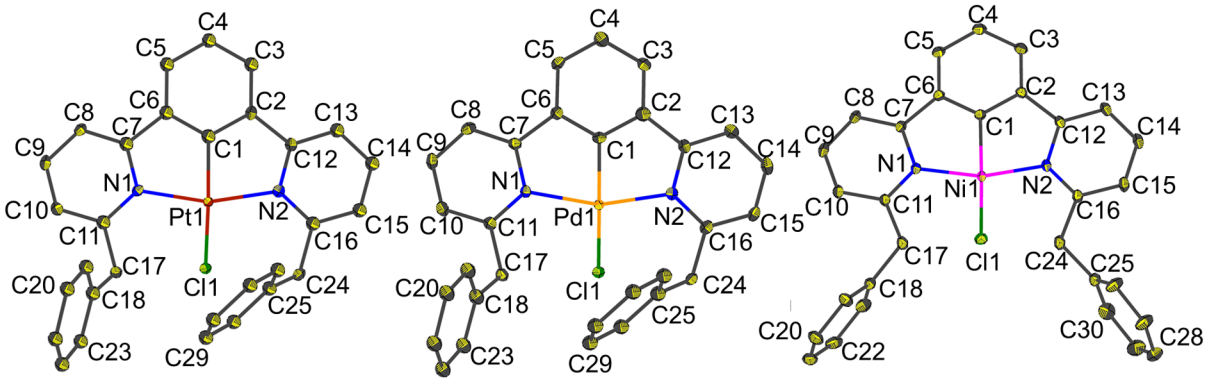


Figure 3-23. Molecular structures of the complexes [M(L^{Bn})Cl] (M = Pt, Pd, and Ni) from single crystal X-ray diffraction (top, 50% displacement ellipsoids). H atoms are omitted for clarity.

The crystal structures feature long metal-metal distances ranging from 5.11 (for the Ni complex) to 6.12 Å (for the Pt and Pd complexes) which are far beyond the sum of van der Waals radii; thus, no significant metallophilic M···M interactions were found. All the structures showed pronounced π···π stacking between the pyridine and phenyl units of two neighboring molecules with centroid distances ranging from 3.5 (for the Pt and Pd complexes) to 3.9 Å (for the Ni complex).

Very similar to our previous complexes [M(N^C^N)Cl] (N^C^N = L^{NHPh} or L^{NHBn}, M = Pt, Pd,[28] and Ni), all three complexes show marked distortion of the Cl^- coligand out of the coordination plane (Figure 3-23), resulting in τ_4 values of 0.35 to 0.44. The deviation of the C–M–Cl angle is bigger for the Ni complex (138°) compared with the Pd (150°) and Pt (152°) derivatives. This is due to the shorter M–C1 and M–Cl bond lengths in the case of the Ni complex. Generally, the τ_4 values for these new series of complexes are bigger than those reported for [M(N^C^N)Cl] (N^C^N = L^{NHPh} or L^{NHBn}, M = Pt, Pd, and Ni) complexes by about 0.1 showing the increased steric bulk of the binding pocket. Therefore, replacing the NHR groups of our previous complexes through benzyl substituents on the N^C^N ligand scaffold proves the negligible role of the M–Cl···H–N hydrogen bonding on the deviation from planar and emphasize the importance of steric bulk of the ortho-substituents as already predicted by the DFT-calculated [M(L^{OMe})Cl] complexes. This deviation along with the experimentally observed structural trends in the solid state are well reproduced by the DFT optimized structures.

3.3.2. Experimental and theoretical properties of [M(L^{Bn})Cl] (M = Pt, Pd, Ni)

Cyclic voltammograms showed a first irreversible reduction waves at around –2.30 V for Pt and Pd(II) complexes and at –2.15 V for Ni(II) derivatives (Figure 3-24, full data in Table 3-11; cyclic voltammograms are presented in Figure A140). The first wave is usually followed by a second and third irreversible reduction waves at low potentials (–2.41 V to –3.11 V). The reduction potentials are very similar to the NHR (R = Phenyl) substituted complexes but slightly less negative when compared to the NHR (R = Benzyl) substituted complexes.[28] The DFT-calculated LUMO orbitals represent exclusively the π* states of the N^C^N ligand core that is similar in energy for each of the complexes at around –2.35 eV for Pt(II) and Pd(II) complexes and –2.29 eV for Ni(II). The observed differences of the Ni(II) complex compared to the Pt(II) and Pd(II) derivatives (having less negative first reduction potential) is fully in line with the DFT-calculated LUMO and LUMO+1 energies (Figure 3-25 and Table A32). We thus assign the reduction processes as essentially taking place at the ligand center, in line with results for comparable complexes.[41,64,95,103] On the anodic side, first irreversible oxidation wave at 0.65 V for Pt(II) and in part poorly defined first oxidation waves at 0.73 V for Pd(II) and 0.08 V for Ni(II) are recorded (Table 3-11). Potentials for comparable NHR (R = Phenyl or Benzyl) substituted Pt and Pd(II) complexes are slightly higher,[28] pointing out the importance of the ortho-substituents and the

stabilizing influence of the amino function on the HOMO orbitals. The DFT-calculated HOMO orbitals of [M(L^{Bn})Cl] (M = Pt, Pd, and Ni) gain essential contributions from the metals and the central aryl group with some contributions from the Cl$^-$ coligand (Table A32). Previous reports on similar complexes indicate predominantly metal (M^{II}/M^{III}) based oxidation processes.[41,59,60,95] Our findings agree with this hypothesis while additionally highlighting significant contributions from different parts of the complexes.

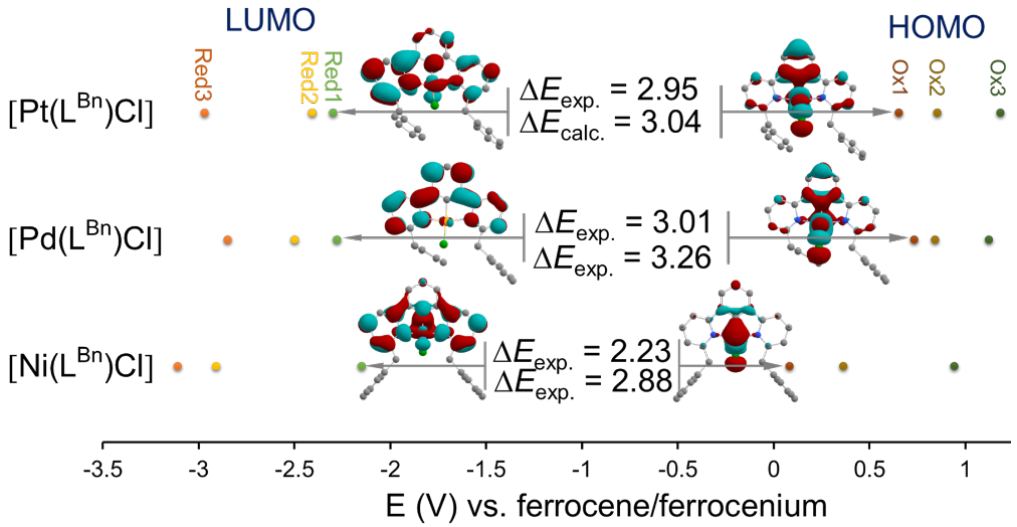


Figure 3-24. Selected experimental redox potentials (dots) and HOMO-LUMO gaps (Δ*E*exp.) from cyclic voltammetry together with DFT-calculated HOMO and LUMO compositions and HOMO-LUMO gaps (Δ*E*calc.) for the complexes.

Table 3-11. Redox potentials of the complexes [M(L^{Bn})Cl] (M = Pt, Pd, and Ni).[a]

complex	E_{pc} (Red3)	E_{pc} (Red2)	E_{pc} (Red1)	E_{pa} (Ox1)	E_{pa} (Ox2)	E_{pa} (Ox3)	Δ*E* (Red1-Red2)	Δ*E* (Ox1-Red1)
[Pt(L^{Bn})Cl]	–2.97	–2.41	–2.30	0.65	0.85	1.18	0.11	2.95
[Pd(L^{Bn})Cl]	–2.85	–2.50	–2.28	0.73	0.84	1.12	0.22	3.01
[Ni(L^{Bn})Cl]	–3.11	–2.91	–2.15	0.08	0.36	0.94	0.74	2.23

[a] From cyclic voltammetry in 0.1 M n-Bu$_4$NPF$_6$/THF. Potentials in V vs. ferrocene/ferrocenium; cathodic peak potentials (E_{pc}) for irreversible reductions; anodic peak potentials (E_{pa}) for irreversible oxidations.

The electrochemical gaps Δ*E* (Ox1-Red1) increase along the series Ni < Pt < Pd and thus qualitatively agree well with the calculated HOMO-LUMO gaps (Figure 3-24). The same behavior was also reported for the series of [M(Me$_2$dpb)Cl] and [M(N^C^N)Cl] (N^C^N = L^{NHPh} or L^{NHBn}, M = Pt, Pd, and Ni) complexes (Table 3-12). A comparison between the parent/unsubstituted [Pt(dpb)Cl] and the Me-substituted [Pt(Me$_2$dpb)Cl] complexes reveals a slight increase in the reported HOMO-LUMO gap for the [Pt(L^{Bn})Cl] complex by 0.46 and 0.36 V, respectively. Conversely, when compared to [Pt(L^{NHBn})Cl] and [Pt(L^{NHPh})Cl] complexes, the HOMO-LUMO gap for [Pt(L^{Bn})Cl] decreases by 0.4 and 0.27 V, respectively (Table 3-12). For [Pd(L^{Bn})Cl], this gap value decreases by 0.06, 0.25, and 0.37 V compared to [Pd(Me$_2$dpb)Cl], [Pd(L^{NHPh})Cl], and [Pd(L^{NHBn})Cl] complexes, respectively. Interestingly, the HOMO-

LUMO gap for [Ni(L^{Bn})Cl] matches that of [Ni(L^{NHPh})Cl], but decreases by 0.13, 0.16, and 0.28 V when compared with [Ni(Me$_2$dpb)Cl], [Ni(dpb)Cl], and Ni(L^{NHBn})Cl] complexes, respectively (Table 3-12).

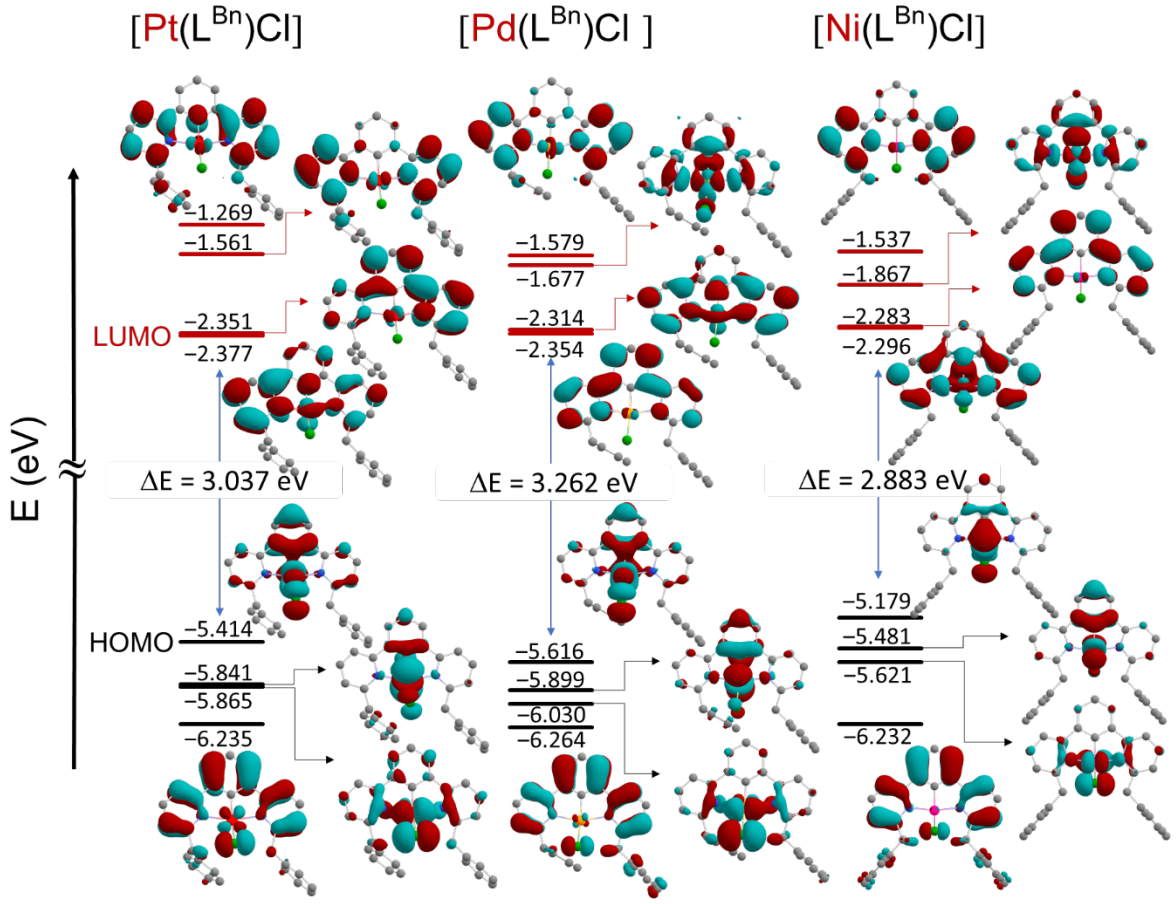


Figure 3-25. DFT-calculated energies of the HOMOs (black) and LUMOs (red) for the complexes; DFT calculations on TPSSh/def2-TZVP/CPCM(THF) level of theory.

Table 3-12. Redox potentials of [M(L^{Bn})Cl] (M = Pt, Pd, Ni), and comparable complexes.[a]

complex	$E_{1/2}$ (Red1)	E_{pa} (Ox1)	ΔE (Ox1-Red1)	Solvent
[Pt(L^{Bn})Cl]	–2.30 irr	0.65	2.95	THF
[Pd(L^{Bn})Cl]	–2.28 irr	0.73	3.01	THF
[Ni(L^{Bn})Cl]	–2.15 irr	0.08	2.23	THF
[Pt(L^{NHPh})Cl]	–2.29	0.93	3.22	THF
[Pd(L^{NHPh})Cl]	–2.31	0.95	3.26	THF
[Ni(L^{NHPh})Cl]	–2.17 irr	0.06	2.23	THF
[Pt(L^{NHBn})Cl]	–2.45	0.90	3.35	THF
[Pd(L^{NHBn})Cl]	–2.43	0.95	3.38	THF
[Ni(L^{NHBn})Cl]	–2.38 irr	0.13	2.51	THF
[Pt(Me$_2$dpb)Cl] [b]	–2.24	0.35	2.59	THF
[Pd(Me$_2$dpb)Cl] [b]	–2.34	0.74	3.07	THF
[Ni(Me$_2$dpb)Cl] [b]	–2.26 irr	0.10	2.36	THF
[Pt(dpb)Cl] [c]	–2.14	0.35	2.49	MeCN
[Ni(dpb)Cl] [e]	–2.33 irr	0.06	2.39	THF

[a] From cyclic voltammetry in 0.1 M n-Bu$_4$NPF$_6$/THF. Potentials in V vs. ferrocene/ferrocenium; accuracy of potentials: ±0.003 V. $E_{1/2}$: half-wave potential for reversible processes, E_{pc}: cathodic peak potentials for irreversible reductions, E_{pa}: anodic peak potentials for irreversible oxidations. [b] From reference [41]. [c] From reference [62]. [d] From reference [103]

The UV-vis absorption spectra of the complexes [M(L^{Bn})Cl] (M = Pt, Pd, and Ni) feature intense bands in the UV-range up to 308 nm. Since they also occur for the ligand precursors HL^{Bn} and ClL^{Bn}, we can assign them to transitions into excited singlet states with $^1\pi$–π^* (^{1}LC) character (Figure 3-26, data in Table 3-13). They are followed by medium intensity, structured absorption bands down to almost 570 nm. For the Ni complex, the long-wavelength absorption band show a maximum at 433 nm, which tails down to a cut-off at 544 nm (Figure 3-26). For the Pt complex, the maximum is blue-shifted to 421 nm and the cut-off shifts to 459 nm. For the Pd derivative, the maximum is even more blue-shifted to 381 nm and the cut-off appears at 406 nm. When taking these cut-off energies into account, an increasing series of the optical HOMO-LUMO gaps Ni (2.28) < Pt (2.70) < Pd (3.05) is observed. The electrochemical HOMO-LUMO gaps follow the same series, i.e. Ni (2.23) < Pt (2.95) < Pd (3.01) and are slightly smaller in case of Ni and Pd as expected but this is opposite for Pt complex by 0.25 eV.

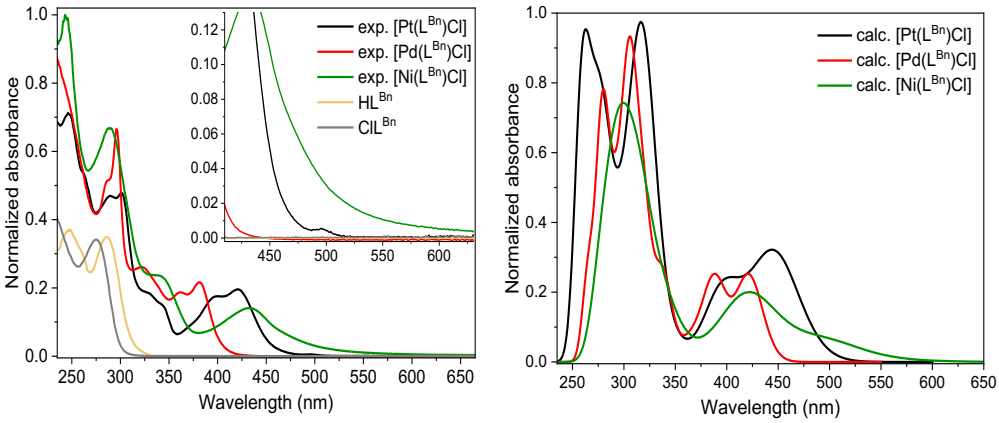


Figure 3-26. UV-vis absorption spectra of the complexes in THF at 298 K with calculated TD-DFT transitions.

Table 3-13. Selected UV-Vis absorption maxima of the complexes [M(L^{Bn})Cl] (M = Pt, Pd, and Ni). [a,b]

complex	[Pt(L^{Bn})Cl]	[Pd(L^{Bn})Cl]	[Ni(L^{Bn})Cl]
λ_9 (ε)[b]	246 (57.5)	245 (48.1)	244 (82.9)
λ_8 (ε)[b]	263 (42.8)	–	–
λ_7 (ε)[b]	289 (37.9)	286 (32.6)	289 (55.7)
λ_6 (ε)[b]	301 (38.6)	296 (42.4)	–
λ_5 (ε)[b]	330 (14.8)	321 (16.8)	–
λ_4 (ε)[b]	344 (11.8)	362 (12.2)	343 (19.3)
λ_3 (ε)[b]	399 (14.2)	381 (14.1)	–
λ_2 (ε)[b]	421 (15.8)	–	433 (11.8)
λ_1 (ε)[b]	496 (0.1)	–	–

[a] Measured in THF at 298 K. [b] Absorption maxima λ are given in nm, molar absorption coefficients ε are given in 10^3 L mol^{-1} cm^{-1}.

A closer look reveals low energy absorption bands with very low intensities at 496 nm for the Pt complex (Figure 3-26, Table 3-13, λ_1). The same features have been previously reported for [Pt(Me$_2$dpb)Cl] at 480 nm and [Pt(dpb)Cl] at 485 nm.[41,62,115] When comparing the [M(L^{Bn})Cl] (M = Pt, Pd,

and Ni) complexes with their NHR (R = Phenyl or Benzyl) substituted counterparts,[28] only a minimal effect on the absorption energies, approximately 10 nm, is observable.

TD-DFT calculated absorption spectra match qualitatively well with the experimental results (Figure 3-26, Figure A161, Table A46). They show low-energy absorption bands at 448 nm (Pt), 422 nm (Pd), and 424 nm with a broad shoulder at 501 nm (Ni) which are slightly red-shifted if compared with the experimental maxima (421, 381, 433 nm); the DFT-calculated broad shoulder at 501 nm for Ni(II) could explain the very long experimental cutoff until 544 nm. Long-wavelength bands in three complexes have been previously assigned to mixed ligand-centered (^{1}LC)/metal-to-ligand charge transfer (^{1}MLCT) states as supported by the calculation.[41,59,60,62,95,107] Additionally, the long-wavelength maximum of the Ni(II) complex appear at lower energies compared to those of Pt and Pd(II) derivatives, as corroborated by TD-DFT calculated spectra. This observation aligns with the lower experimental and DFT-calculated HOMO-LUMO gaps.

Photoluminescence spectroscopy revealed that the Pt(II) derivative is emissive at room temperature (RT) in both argon-purged CH_2Cl_2 solution and in the solid state with the emission maxima at 580 and 597 nm, respectively (Figure 3-27, Table 3-14; raw time-resolved photoluminescence decays and fitting parameters are shown in Figures A202 and A203). To investigate the formation of aggregates or excimers, the Pt(II) complex was incorporated into PMMA matrices at different concentrations. Increasing the concentration of PMMA matrices from 0.5% to 5% caused a red shift in the emission maximum from 496 nm to 544 nm, with corresponding changes in the emission profile, which closely resembled the spectrum recorded in CH_2Cl_2 solution and in the solid state at RT (Figure 3-28 and Table 3-14). These data suggest the presence of emissive molecular aggregates with increasing concentration in the PMMA matrices, indicating that the Pt(II) complex may emit primarily from aggregates in both the solid state and CH_2Cl_2 solution. However, upon concentration change of Pt(II) in CH_2Cl_2 solution, the emission spectrum did not change.

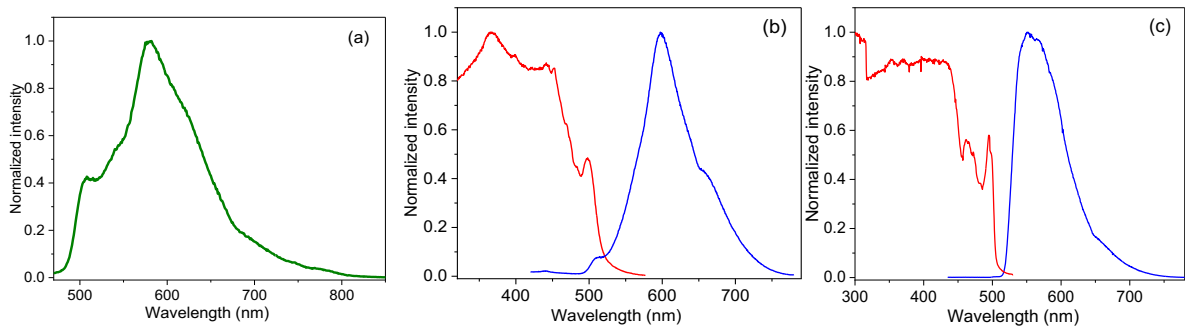


Figure 3-27. Emission spectra of [Pt(L^{Bn})Cl] in CH_2Cl_2 solution at 298 K (λ_{ex} = 376 nm) (a); emission (blue) and excitation (red) spectra of [Pt(L^{Bn})Cl] in solid state at 298 K (b) and at 77 K (c) (λ_{ex} = 400 nm).

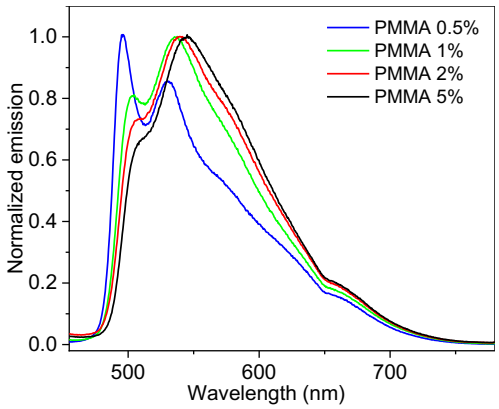


Figure 3-28. Photoluminescence spectra of [Pt(L^{Bn})Cl] at different concentrations within PMMA films at 298 K (λ_{ex} = 400 nm).

Table 3-14. Photophysical properties of [Pt(L^{Bn})Cl] complex at 298 K.

Medium	$\lambda_{em,\,max}$ (nm)	$\Phi_L \pm 0.02$	τ (μs)
CH_2Cl_2 (air)	580	n.d.	τ_1 = 0.324 ± 0.001 (55%) τ_2 = 0.049 ± 0.001 (45%) τ_{av_amp} = 0.2 ± 0.001
CH_2Cl_2 (Ar-purged)	580	n.d.	τ_1 = 2.650 ± 0.02 (29%) τ_2 = 0.847 ± 0.008 (71%) τ_{av_amp} = 1.367 ± 0.004
Crystalline state	512	n.d.	τ_1 = 2.077 ± 0.16 (36%) τ_2 = 0.733 ± 0.026 (64%) τ_{av_amp} = 0.944 ± 0.018
Solid state	597	-	0.89 (50%), 2.9 (40%), 0.24 (10%)
PMMA 0.5%	496	0.18	0.91 (51%), 3.26 (38%), 0.23 (11%)
PMMA 5%	544	0.12	1.1 (52%), 3.8 (33%), 0.31 (15%)

n.d. = not detected.

As expected, Pd(II) and Ni(II) complexes were not emissive at RT. This is attributed to the population of dissociative metal-centered (^{3}MC or d–d*) states, which provide non-radiative deactivation channels via conical intersections with the ground state. Consequently, these complexes are non-emissive in fluid solutions at RT. However, at 77 K, these complexes become emissive (Figure 3-29). At lower temperature, thermal population of the ^{3}MC states becomes inaccessible, and rigidification of the system prevents additional non-radiative vibrational pathways and/or solvent quenching. While this effect is somehow expected in both Pt(II) and Pd(II) complexes, it is surprising for Ni(II), where not only a defined emission spectrum is observed but also a high quantum yield (20%) along with lifetimes in the millisecond range (Table 3-15).

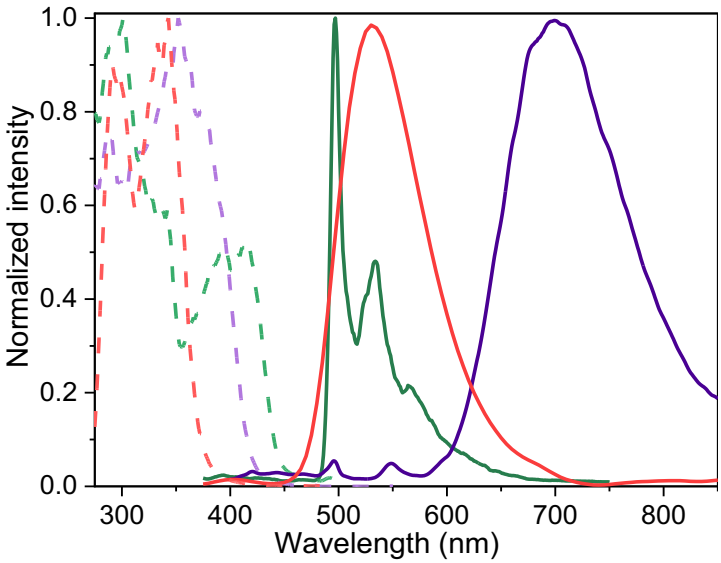


Figure 3-29. Photoluminescence emission (lines) and excitation (dash lines) spectra of the complexes [M(L^{Bn})Cl] (M = Pt: green, Pd: red and Ni: violet) in 2MeTHF at 77 K as a glassy matrix (λ_{ex} = 350 nm).

As observed in Figure 3-29, the Pt(II) complex exhibits typical emission spectra with the expected vibrational progression for this type of complex (λ_{max} = 497 nm). However, the Pd(II) complex shows a broad, red-shifted emission band (λ_{max} = 530 nm) compared to Pt(II) and some very minor peaks in the region of 500-600 nm. This is attributable to the formation of weakly coupled aggregated rather than monomeric species.[35,46,116] It is important to mention that this emission spectrum did not change upon varying the concentration of the complex in the glassy matrix (from 10^{-4} to 10^{-7}) indicating that this is not concentration-related but rather an outcome due to the stabilization and orientation of the complexes within the glassy matrix at 77 K. In case of the Ni(II) complex, the relatively broad band (λ_{max} = 699 nm) together with the notably high photoluminescence quantum yield coupled with the lifetime in the ms range are pointing to the triplet nature of the emissive state.

Table 3-15. Photophysical properties of [M(L^{Bn})Cl] (M = Pt, Pd, and Ni) complexes at 77 K.[a]

Complex	Φ_L ± 0.02	τ / μs[b,c]	k_r / 10^4s^{-1}	k_{nr} / 10^4s^{-1}
[Pt(L^{Bn})Cl]	0.10	τ_1 = 6.50 ± 0.06 (42%) τ_2 = 2.71 ± 46 (58%) τ_{av_amp} = 4.30 ± 0.01	2.3 ± 0.5	21.0 ± 0.5
[Pd(L^{Bn})Cl]	0.03	τ_1 = 204.7 ± 2.1 (64%) τ_2 = 100.3 ± 3.8 (36%) τ_{av_amp} = 167.5 ± 0.4	n.d.	0.57 ± 0.01
[Ni(L^{Bn})Cl]	0.20	τ_1 = 87200 ± 1500 (27%) τ_2 =9320 ± 230 (73%) τ_{av_amp} = 30020 ± 450	0.00067 ± 0.00008	0.003 ± 0.00008

[a] Photoluminescence Φ_L and lifetimes (τ) in frozen glassy matrices at 77 K. [b] For multiexponential decays, the amplitude-weighted average lifetimes are given. [c] Measured using phosphorescence lifetime imaging micro(spectro)scopy (PLIM). n.d. = not detected. Raw time-resolved photoluminescence decays and fitting parameters are shown in Figures A204 to A206, appendix.

As observed in Table 3-15, by going down in the group from Pt(II) to Ni(II), both k_r and k_{nr} decrease, mainly due to the different population of the ^{3}MC-states.

By means of photoluminescence lifetime imaging micro(spectro)scopy (PLIM), both the decay rates and the phosphorescence spectra of the crystalline phase of the Pt(II) complex were measured. The corresponding lifetime maps and emission spectra of the crystal are depicted in Figure 3-30. As expected, both Pd(II) and Ni(II) crystals did not show any measurable luminescence at crystalline state.

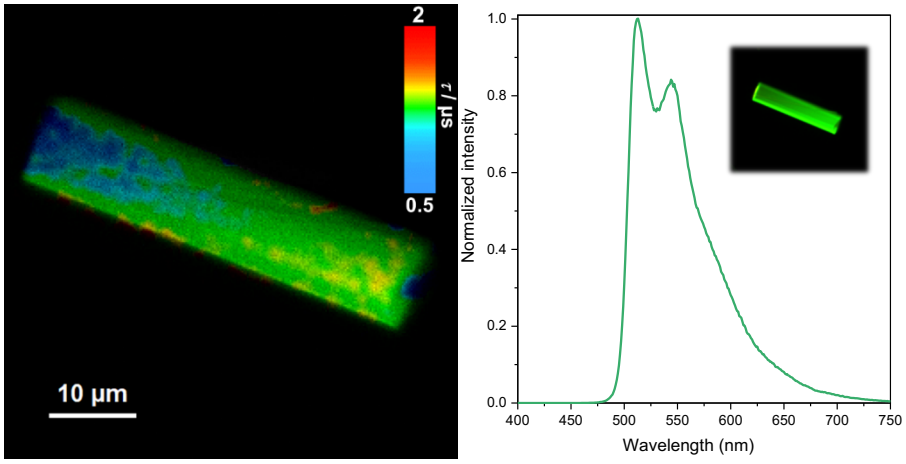


Figure 3-30. Time resolved photoluminescence micro(spectro)scopy imaging of the Pt(II) complex. Left: Photoluminescence lifetime map of the crystalline phase of the complex (λ_{ex} = 376 nm, low-pass cut-off filter 514 LP). Right: Photoluminescence spectra of the single crystal measured with the microscope, inset: photoluminescence micrograph. Raw time-resolved photoluminescence decays can be seen in the appendix, Figure A207.

The character of the emissive T_1 states for the complexes were assessed through excitation analysis using the TheoDORE package[110] (Figure 3-31). The resulting decomposition into MLCT (d–π*), ligand-to-metal-charge-transfer (LMCT), ligand'-to-ligand-charge-transfer (L'LCT), LC (π–π*), and metal-centered (MC) contributions is based on a partitioning defined in Figure 3-31. The highest MLCT character can be found for [Ni(L^{Bn})Cl] (34.4%), while [Pd(L^{Bn})Cl] has the lowest (30%), less than [Pt(L^{Bn})Cl] (34%). The high MLCT character of the excited state of the Ni derivative explains its high quantum yield and long lifetime, despite its high MC character (42%). For the Pt and Pd derivatives, the LC character is superior (39-36%) compared with the Ni derivative (5.1%). The L'LCT character decreases down the series from Pt to Ni, while the LMCT contribution increases.

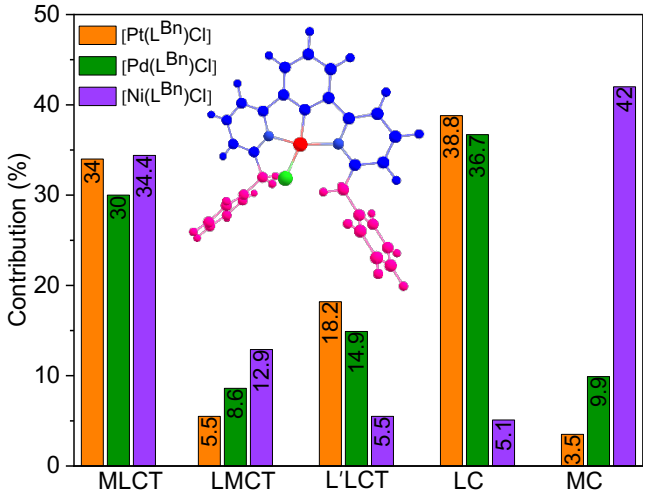


Figure 3-31. Decomposition of the T_1 state for the three calculated complexes into contributions originating from MLCT, LMCT, LC, L'LCT, or MC configurations determined with the package TheoDORE,[110] together with the partitioning of the [M(L^{Bn})Cl] complexes for the numerical analysis. L'LCT donates ligand-centered transitions between different parts of the tridentate ligand, while LC represents excitation within the same part.

The DFT-optimized S_0 geometries of the complexes generally exhibit good agreement with the experimental data from crystallography, displaying maximum deviations of 0.03 Å and 2.4° (Table A12). Notably, the C–M–Cl angle, constituting a significant portion of the observed distortion in the S_0 state, experiences further deviation in the T_1 excited state (Figure 3-32). This phenomenon is particularly pronounced in Pt(II) and Pd(II), where the deviation reaches 32.3° and 34.8°, respectively, compared to the S_0 state, whereas in Ni(II), the deviation is less pronounced at 17.6°. It is worth noting that other critical metrics surrounding the metal atoms exhibit minimal changes, with the pyridyl rings of the cyclometalated L^{Bn} ligand remaining coplanar in the complexes.

Thus, through replicating the steric bulk observed in previously reported complexes[28] while omitting NH···Cl···NH hydrogen bonds, our findings affirm the significant impact of non-covalent interactions of the second coordination sphere on reducing the conformational deviations between the S_0 and T_1 states. While the influence of steric bulk cannot be disregarded and may contribute to a certain level of rigidity. Our forthcoming investigations will probe deeper into the effects of steric bulk and varying strength of hydrogen bonds.

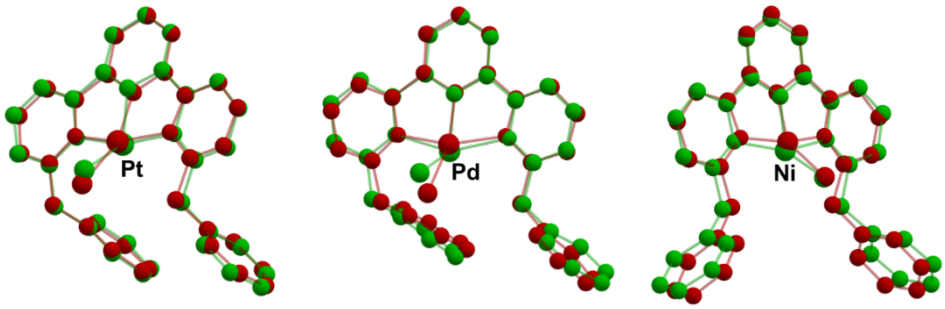


Figure 3-32. DFT-calculated geometries of [M(L^{Bn})Cl] (M = Pt, Pd, Ni) in the S_0 (red) and T_1 (green) states.

3.4. [M(L^{NHPh})OPh] and [M(L^{NHBn})OPh] (M = Pt or Pd) complexes

3.4.1. Synthesis and structure of [M(L^{NHPh})OPh] and [M(L^{NHBn})OPh] (M = Pt or Pd)

To further explore the influence of hydrogen bonding on photophysical properties, it becomes essential to create environments that enable stronger and more directional hydrogen bonds. In this context, we report the synthesis of a series of Pt(II) and Pd(II) complexes, [M(L^{NHPh})OPh] and [M(L^{NHBn})OPh], derived from their pre-designed chloride-coordinated counterparts. The complexes [M(L^{NHPh})OPh] and [M(L^{NHBn})OPh] (M = Pt or Pd) were obtained via a two-step procedure (Figure 3-33).[117] First, the metal(II) chloride precursors were converted to their nitrate derivatives by reaction with $AgNO_3$ under light exclusion. Subsequently the nitrate derivatives were treated with an excess of KOPh in $CHCl_3$, yielding the desired products in 86% to 99% yields (Figure 3-33, details in the experimental section).

The new Pt(II) and Pd(II) complexes were fully characterized. The ^{1}H and ^{13}C NMR spectra confirmed the complete set of expected signals. HR-ESI mass spectrometry and single-crystal XRD further validated the structural integrity of the complexes (spectra and crystallographic data are provided in the appendix).

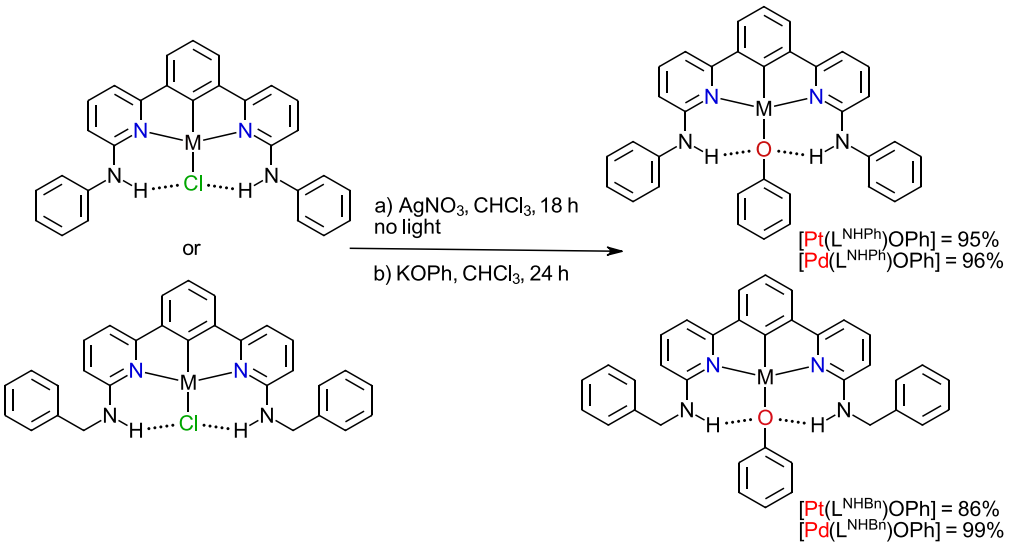


Figure 3-33. Synthesis of [M(L^{NHPh})OPh] and [M(L^{NHBn})OPh] (M = Pt or Pd) complexes.

The [M(L^{NHBn})OPh] (M = Pt or Pd) complexes crystallized isostructurally in the monoclinic space group $P2_1/c$ whereas the [Pd(L^{NHPh})OPh] complex crystallized in the triclinic space group $P\bar{1}$ and [Pt(L^{NHPh})OPh] crystallized in the monoclinic space group $C2/c$ (Figures A123 to A126, data in Tables A13 to A15, appendix). Experimental data for the complexes were employed to benchmark DFT geometry optimizations using TPSSh/def2-TZVP/CPCM(THF). A good agreement was observed between the experimental and calculated metrics (Tables A14 and A15).

In all crystal structures, head to tail stacking of molecules was found, leading to moderate π···π interactions between the pyridyl and phenyl or pyridyl units of adjacent molecules, with centroid-centroid distances of approximately 3.55 Å (Figures A123 to A126). The structures feature long metal-metal distances exceeding 6.90 Å, well beyond the sum of van der Waals radii. The shortest metal-metal distance was observed in [Pd(L^{NHPh})OPh], measuring 4.63 Å. The molecular structures of the OPh-coordinated complexes are overall comparable to their previously reported chloride-coordinated analogs ([M(L^{NHPh})Cl] and [M(L^{NHBn})Cl]) in terms of bond length and angles.[28] However, the OPh-coordinated complexes exhibit nearly linear C–M–O angles (~178°), contrasting with the more bent C–M–Cl angles (160° to 167°) observed in the chloride-coordinated complexes. The deviation of the coligand from the square planar geometry in the Cl-coordinated complexes is no longer apparent when Cl is replaced with OPh. Instead, oxygen aligns within the coordination plane, resulting in τ_4 values of 0.14 to 0.16, significantly smaller than the values reported for the Cl-coordinated analogs (0.25 to 0.29). This structural adjustment leads to shorter non-symmetric M–O···H–N hydrogen bonds between the pending aniline moieties and the OPh coligand, with H···O distances ranging from 1.81 to 1.91 Å and O···H–N angles spanning from 157° to 172° (Figure 3-34). These non-symmetric hydrogen bonds were successfully reproduced in the DFT-optimized structures in solution (using CPCM model, Tables A14 and A15). In contrast, non-symmetric M–Cl···H–N hydrogen bonds in the Cl-coordinated complexes feature longer H···Cl distances (2.23 to 2.38 Å).

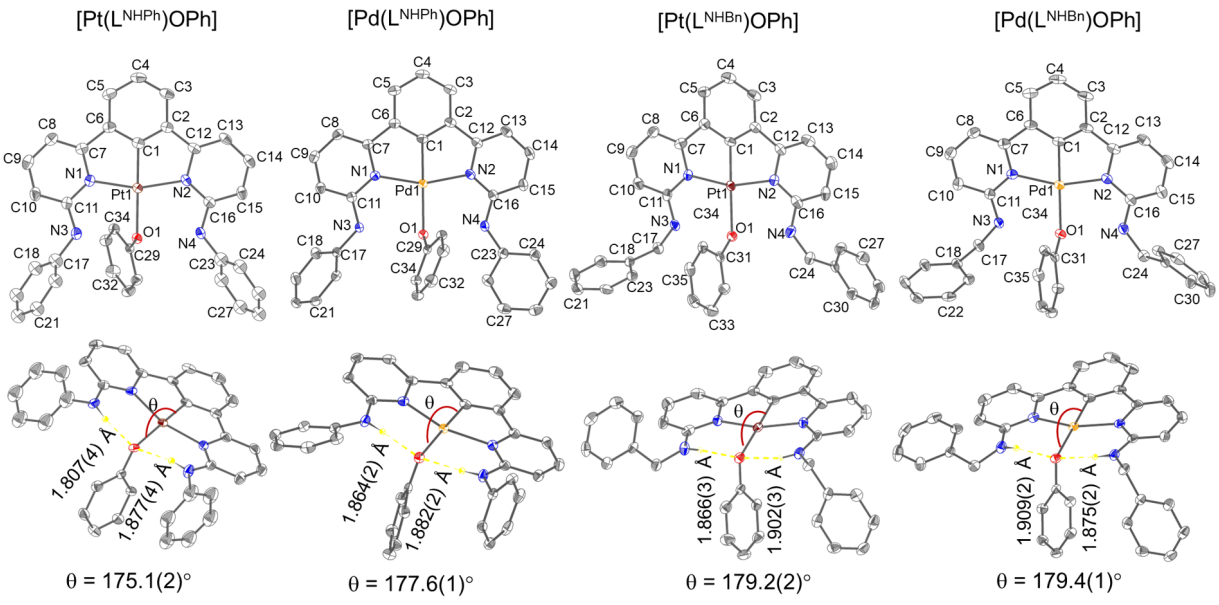


Figure 3-34. Molecular structures of the complexes from X-ray diffractometry on single crystals (top, displacement ellipsoids at 50%) and their side-on views featuring the C–M–O angle and O···H distances.

This observation contradicts our previous conclusion for the Cl-coordinated complexes, where we suggested that hydrogen bonding played a negligible role in coligand deviations and attributed the

deviations primarily to steric bulk from ortho-substituted aniline groups. However, DFT calculations on hypothetical [M(L^{NHPh})F] and [M(L^{NHPh})H] complexes (M = Pt or Pd), featuring significantly smaller coligands, revealed τ_4 values of 0.14 to 0.17.[28] These observations refines our understanding of the geometric effects in such systems and highlights the subtle interplay between steric and electronic factors in determining the coordination geometry.

3.4.2. Experimental and theoretical properties of [M(L^{NHPh})OPh] and [M(L^{NHBn})OPh] (M = Pt or Pd)

Cyclic voltammetry measurements revealed irreversible and in part poorly defined oxidations in the range of 0.39 to 1.32 V (Figure 3-35; full data in Table 3-16; cyclic voltammograms are presented in Figures A141 and A142). The first oxidation potentials in each series of complexes (L^{NHPh} and L^{NHBn}) are nearly identical, occurring at 0.39 V and approximately 0.62 V, respectively. Reports for similar complexes suggest that these processes are primarily metal-centered (M^{II}/M^{III}) oxidation.[28,29,41,59,60,62,64,65,95,118] The DFT-calculated frontier molecular orbital landscapes (Figures 3-36 and 3-37, data in Tables A34 and A35) indicate almost invariant HOMO orbitals with contributions from the OPh coligand, the N^C^N ligand framework and the pending NHPh or NHBn substituents, alongside notable metal-centered character.

All complexes showed a reversible first reduction process within the range of –2.45 to –2.56 V, typically followed by an irreversible second reduction wave at lower potentials (–3.02 to –3.17 V). Notably, [Pd(L^{NHPh})OPh] deviates from this pattern, showing only a single irreversible reduction wave at –2.54 V. The DFT-calculated LUMO orbitals are primarily localized on the π* orbitals of the N^C^N ligand core, suggesting ligand-centered reduction processes, consistent with reports for similar complexes.[28,29,41,59,60,62,64,65,118] The LUMOs also incorporate increasing contributions from the pending NHPh or NHBn substituents, beginning with LUMO+2 for Pt(II) derivatives and LUMO+4 for Pd(II) derivatives (Figures 3-36 and 3-37, data in Tables A34 and A35).

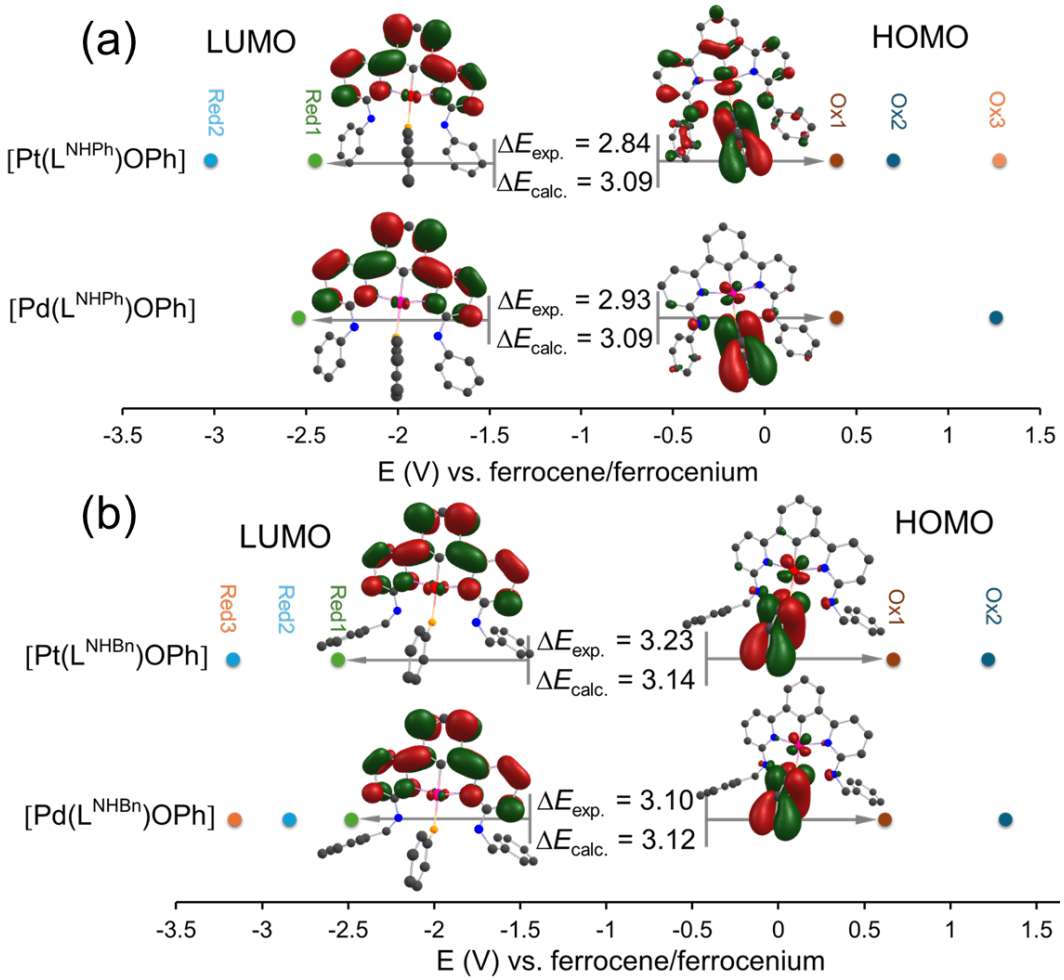


Figure 3-35. Selected experimental redox potentials (dots) and HOMO-LUMO gaps (Δ*E*exp.) from cyclic voltammetry together with DFT-calculated HOMO and LUMO compositions and HOMO-LUMO gaps (Δ*E*calc.) for the complexes.

Table 3-16. Redox potentials of the complexes.[a]

complex	E_{pc} (Red3)	E_{pc} (Red2)	$E_{1/2}$ (Red1)	E_{pa} (Ox1)	E_{pa} (Ox2)	E_{pa} (Ox3)	Δ*E* (Red1-Red2)	ΔE_{echem}[b]	ΔE_{calc}[c]
[Pt(L^{NHPh})OPh]	–	–3.02	–2.45	0.39	0.70	1.28	0.57	2.84	3.09
[Pd(L^{NHPh})OPh]	–	–	–2.54	0.39	1.26	–	–	2.93	3.09
[Pt(L^{NHBn})OPh]	–	–3.17	–2.56	0.67	1.22	–	0.61	3.23	3.14
[Pd(L^{NHBn})OPh]	–3.16	–2.84	–2.48	0.62	1.32	–	0.36	3.10	3.12

[a] From cyclic voltammetry in 0.1 M n-Bu$_4$NPF$_6$/THF. Potentials in V vs. ferrocene/ferrocenium; accuracy of potentials: ±0.003 V. E_{pc}: cathodic peak potentials for irreversible reductions, E_{pa}: anodic peak potentials for irreversible oxidations. [b] Electrochemical HOMO–LUMO gap ($\Delta E_{echem} = E_{Ox1} - E_{Red1}$). [c] ΔE_{calc} = DFT-calculated HOMO-LUMO gap; TPSSh/def2-TZVP/CPCM(THF).

A comparison of the potentials between the chloride-coordinated analogs ([M(L^{NHPh})Cl] and [M(L^{NHBn})Cl] complexes[28] reveals similar values. However, the OPh complexes show a cathodic shift in oxidation potentials, consistent with the stronger σ-donor ability of OPh relative to Cl. This cathodic shift is particularly pronounced in the L^{NHPh} complexes, where the first oxidation occurs at 0.39 V. The electrochemical HOMO-LUMO gaps (ΔE_{echem}) range from 2.84 to 3.23 eV, consistent with the DFT-calculated values. This gap is slightly smaller for L^{NHPh} complexes and uniformly smaller when compared to their chloride-coordinated counterparts (3.22 to 3.38 eV).[28]

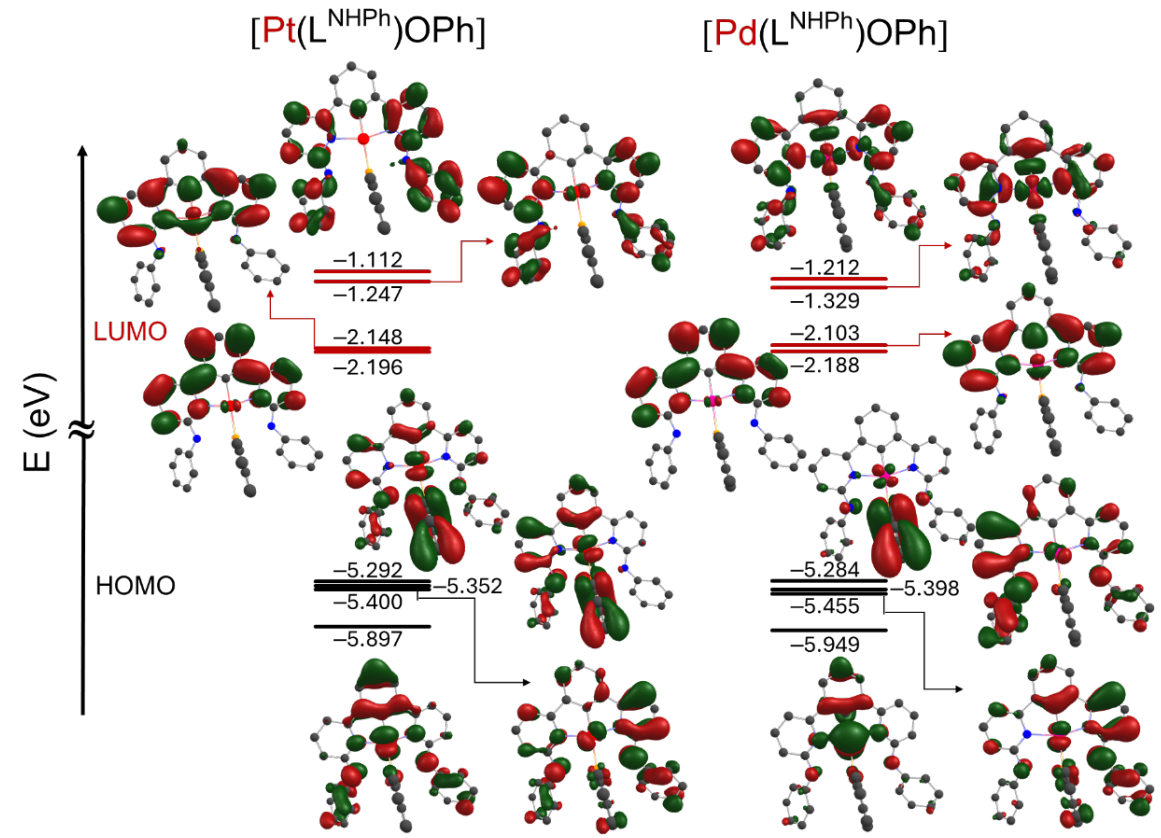


Figure 3-36. DFT-calculated energies of the HOMOs (black) and LUMOs (red) for [M(L^{NHPh})OPh] (M = Pt and Pd); DFT calculations on TPSSh/def2-TZVP/CPCM(THF) level of theory.

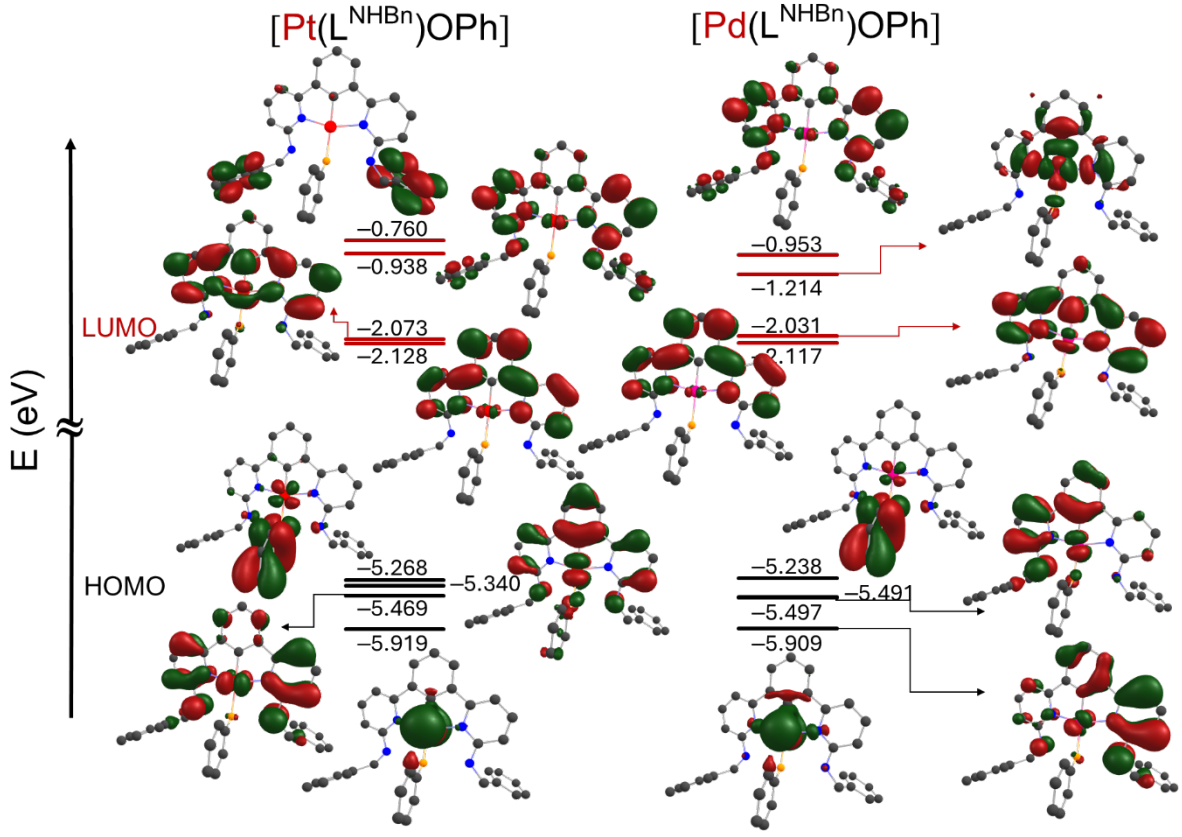


Figure 3-37. DFT-calculated energies of the HOMOs (black) and LUMOs (red) for [M(L^{NHBn})OPh] (M = Pt and Pd); DFT calculations on TPSSh/def2-TZVP/CPCM(THF) level of theory.

The UV-vis absorption spectra of the complexes exhibit absorption bands extending to nearly 430 nm, with intense maxima observed at approximately 282 nm for the Pt(II) complexes and 266 nm for their Pd(II) counterparts. In the visible range, medium intensity double bands with maxima between 394–419 nm for Pt(II) complexes and 376–395 nm for Pd(II) complexes were observed (Figure 3-38 and Table 3-17; Figure A162). The UV-bands in both Pt(II) and Pd(II) complexes are attributed to transitions into singlet ^{1}LC (π–π*) excited states, while the bands at longer wavelength suggest a mixed ^{1}LC/metal-to-ligand charge transfer (^{1}MLCT) character, as reported for related compounds.[28,35,41,62,64,65,95,118] TD-DFT calculated absorption spectra align closely with the experimental data, reinforcing these assignments (Figure 3-38; Tables 3-17 and A47). The calculated $S_0 \rightarrow S_n$ transitions for absorptions beyond 319 nm reveal their predominantly ^{1}LC/^{1}MLCT nature, consistent with previous studies on related systems.[28,41,60,65,95,118] Experimentally and computationally Pt(II) complexes exhibit a slight red-shift of the long-wavelength absorption energies relative to Pd (II) complexes.

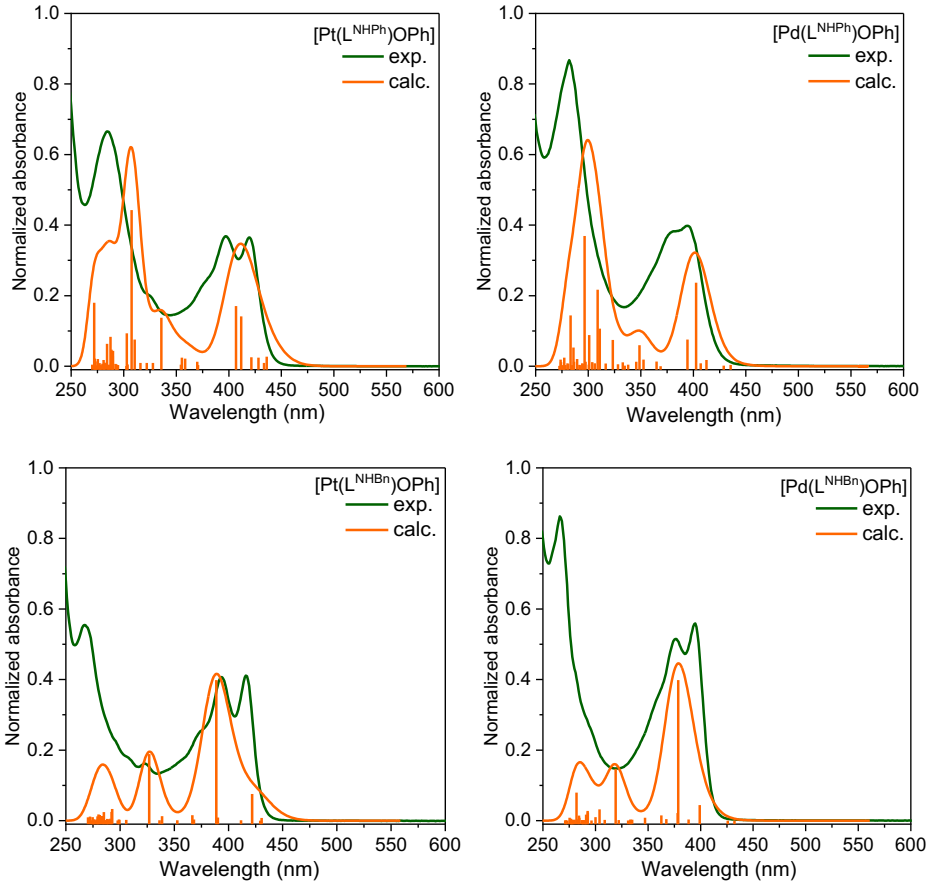


Figure 3-38. Experimental (green) UV-vis absorption spectra of the complexes in THF solution at 298 K with TD-DFT calculated transitions (calculated spectra as solid lines with sticks for individual transitions, in orange (TPSSh/def2-TZVP/CPCM(THF) level of theory).

Replacing the Cl coligand in the previously reported complexes[28] with OPh results in a negligible red-shift of 2–3 nm for the long wavelength absorptions. This minor shift hardly aligns with the slightly

reduced electrochemical HOMO-LUMO gaps (ΔE_{echem}) determined from cyclic voltammetry for the OPh-coordinated complexes (2.84 to 3.23 eV) compared to their Cl-coordinated analogs (3.22 to 3.38 eV).

The optical HOMO-LUMO gap (ΔE_{opt}) extrapolated from the lowest energy absorption bands, exceeds ΔE_{echem}, as anticipated, since the electrochemistry probes the molecule in its ground state. However, in the case of [Pt(L^{NHBn})OPh], the opposite trend is observed with ΔE_{echem} exceeding ΔE_{opt} by 0.25 eV. This behavior, previously reported for the Cl-coordinated derivatives, has been attributed to hindered electrochemical responses.[28]

Table 3-17. Selected UV-Vis absorption maxima of the complexes in THF at 298 K.

complex	[Pt(L^{NHPh})OPh]	[Pd(L^{NHPh})OPh]	[Pt(L^{NHBn})OPh]	[Pd(L^{NHBn})OPh]
λ_3 (ε)[a]	284 (33.7)	282 (41.5)	267 (25.2)	266 (28.2)
λ_2 (ε)[a]	397 (21.6)	379 (22.1)	394 (20.5)	376 (17.4)
λ_1 (ε)[a]	419 (21.6)	394 (22.4)	416 (20.6)	395 (18.6)
ΔE_{opt}[b]	2.96	3.15	2.98	3.14

[a] Absorption maxima λ are in nm, and molar absorption coefficients ε are in 10^3 L mol^{-1} cm^{-1}. [b] Optical HOMO-LUMO gap extrapolated from the lowest energy absorption band in eV.

3.5. [M(L^R)X] (M = Pt, Pd, Ni; R = Me, Me_2, Cl, F; X = Cl or Br) complexes

3.5.1. Synthesis and structure of [M(L^R)X] (M = Pt, Pd, Ni; R = Me, Me_2, Cl, F; X = Cl or Br)

To expand the discussion in this section, complexes synthesized and characterized by Dr. Lukas Kletsch, a former doctoral researcher in the group of Prof. Dr. Axel *Klein*, are incorporated. Specifically, [Ni(L^{Cl})Br], [M(L^F)X] (M = Pt, Pd, Ni; X = Cl or Br) were prepared and characterized by Dr. Kletsch.

To investigate how structural variations influence the photophysical behavior and the luminescence efficiency of the complexes, ligand precursors HL^{Me}, $L^{Me}Cl$, HL^{Me2}, HL^{Cl}, and HL^F were synthesized via modification of established methods including Suzuki cross coupling or Negishi cross-coupling reactions, yielding between 55 and 79% (Figure 3-39, details in the experimental section).

The N^C^N cyclometalated Ni(II) complexes [Ni(L^{Cl})Br] and [Ni(L^F)Br] were synthesized from $NiBr_2$ and HL^{Cl} or HL^F with 26% and 71% yield, respectively, using the previously reported base-assisted C–H deprotonation method.[41,103] Attempts to react $NiBr_2$ or $NiCl_2$ with HL^{Me} or HL^{Me2} using the same method failed, resulting in the isolation of only the unreacted ligand precursor. Further attempts using oxidative addition reaction of [Ni($COD)_2$] (COD = 1,5-cyclooctadiene) with the chlorinated ligand precursor $L^{Me}Cl$ yielded [Ni(L^{Me})Cl] in 63% by modifying an established procedure (Figure 3-39, details in the experimental section).[104]

The Pt(II) and Pd(II) complexes [M(N^C^N)Cl] were synthesized from $K_2[MCl_4]$ (M = Pt or Pd) and the ligand precursors HL^{Me}, HL^{Me2}, HL^{Cl}, and HL^{F} by heating in glacial acetic acid following an established method,[92] with yields ranging from 27% to 80% (Figure 3-39, details in the experimental section). Using the same reaction protocol to synthesis $[Pd(L^{Me2})Cl]$ resulted in less than 10% yield, and further workup for isolating a pure product was not successful. By modifying the previously reported method,[58] using $Pd(OAc)_2$ as the Pd precursor in acidic condition (HOAc) and adding KCl, the yield increased to 38% without requiring further purification. The complexes were characterized by NMR spectroscopy as well as HR-ESI mass spectrometry, and elemental (CHN) analysis confirmed their composition (spectra and data in the experimental section and the appendix).

While the Pt(II) complex $[Pt(L^{F})Cl]$ (1,3-bis(2-pyridyl)-4,6-difluorobenzene) has been previously reported,[64] its photophysical properties were re-examined under identical experimental conditions to facilitate direct comparison with its Ni(II) and Pd(II) analogues. In case of $[M(L^{Me2})Cl]$ complexes, although the synthesis of the Pt(II) and Pd(II) complexes was successful, the corresponding Ni(II) complex, $[Ni(L^{Me2})Cl]$, could not be synthesized. To address this limitation, DFT calculations were employed to predict its structural and photophysical properties.

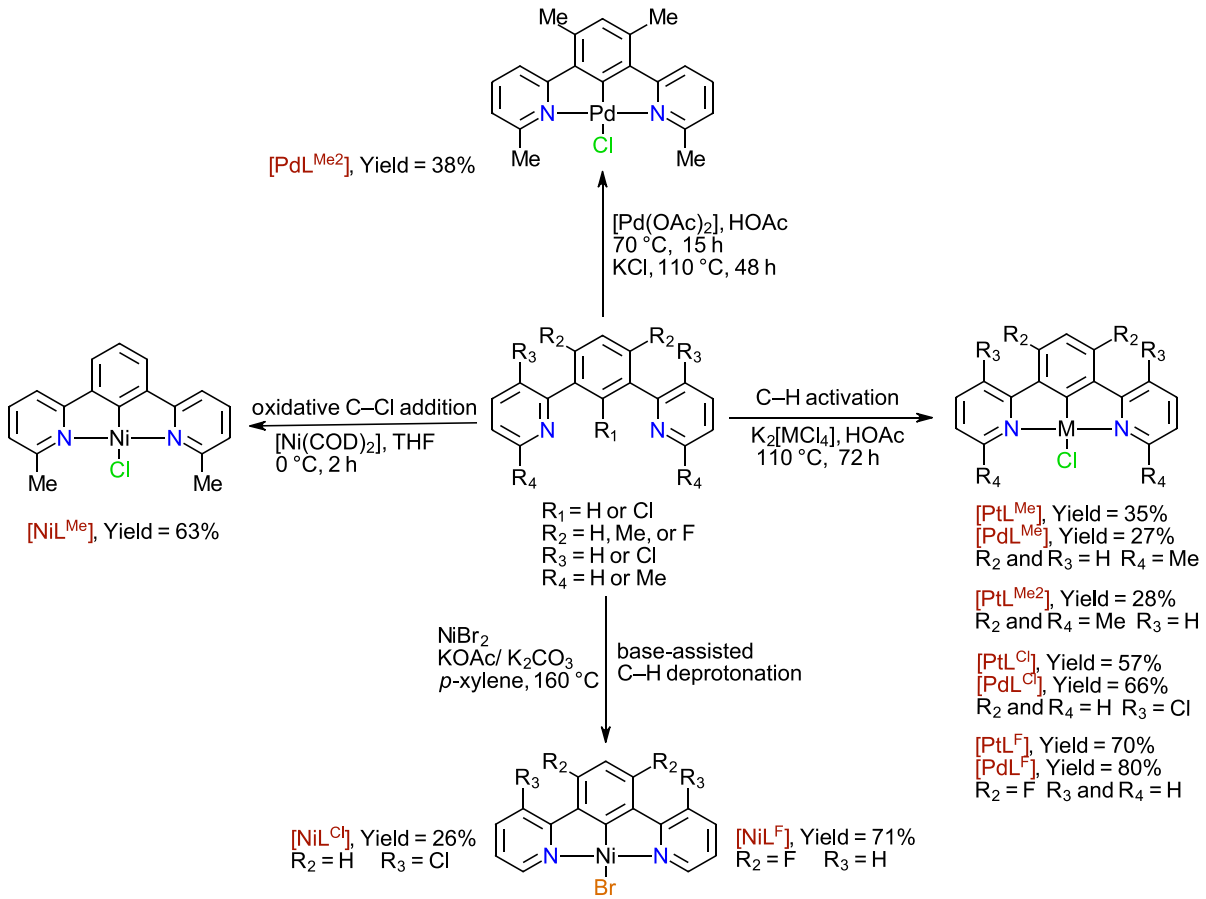


Figure 3-39. Synthesis of $[M(L^{R})X]$ (M = Pt, Pd, Ni; R = Me, Me2, Cl, F; X = Cl or Br)complexes.

The structure of complexes [M(L^{Me})Cl] (M = Pt, Pd, and Ni) and [Ni(L^{Cl})Br] were determined by single-crystal XRD (Figure 3-40). The [M(L^{Me})Cl] (M = Pt, Pd, and Ni) complexes crystallize isostructurally within the orthorhombic space group *P*bca, similar to the previously reported [Ni(Me_2dpb)Cl].CH_2Cl_2 but different from its Pt(II) and Pd(II) derivatives.[41,115] In contrast, [Ni(L^{Cl})Br] crystallize in the triclinic space group $P\bar{1}$ and [Pt(L^{F})Cl] is observed in the monoclinic space group $P2_1/n$ (Figures A127–A131). Comprehensive structural refinement details and selected structural parameters are listed in Tables A16–A21 (appendix) along with the data for the previously characterized [Pt(L^{F})Cl] structure.[64] The DFT-optimized geometries, calculated using TPSSh/def2-TZVP with CPCM solvation (THF) are in good agreement in terms of bond lengths and angles with the experimental data (Figures A127–A134, Tables A17–A21; the resulting *xyz* coordinates of the optimized structures are presented in Tables A62–A65, appendix).

All structures show a head-to-tail molecular stacking arrangement (Figures A127 to A131), a feature commonly observed in [M(N^C^N)X] or [M(C^N^N)X] derivatives where M = Pt(II), Pd(II), and Ni(II).[59,60,91,95,104] This arrangement are indicative of moderate π···π interaction between the pyridyl and phenyl or pyridyl units of adjacent molecules, with centroid-centroid distances around 3.80 Å (Figures A127 to A131). The metal-metal distances vary, while [Ni(L^{Cl})Br] shows a distance of 4.21 Å, the [M(L^{Me})Cl] (M = Pt, Pd, and Ni) complexes exhibit longer distances ranging from 4.93 to 5.02 Å. Notably, the structure of [Pt(L^{F})Cl] shows a metal-metal distance of 4.47 Å, contrasting with the earlier report of 3.42 Å.[64] Additionally, our measurement of the C–Pt–Cl angle at 178.3°is closer to linearity compared to the previously reported angle of 173.8°,[64] which can be attributed to slight variations in crystal packing interactions.

The crystal structures of the methyl-substituted complexes reveal a distorted square planar coordination with a significant deviation of the chloride ligand from the N–C–N–M plane. This distortion is quantitatively described by τ_4 values, which range from 0.295 for [Pt(L^{Me})Cl] to 0.318 for [Pd(L^{Me})Cl and 0.369 for [Ni(L^{Me})Cl]. This deviation is primarily attributed to the steric bulk of the methyl substituents in the ortho positions to the pyridyl N coordination sites. DFT-calculated geometries for the [M(L^{Me2})Cl] (M = Pt, Pd, Ni) further highlight increased distortion, with τ_4 values rising to 0.350 for [Pt(L^{Me2})Cl], 0.389 for [Pd(L^{Me2})Cl], and 0.435 for [Ni(L^{Me2})Cl]. Interestingly, within each series, the Ni(II) complexes exhibit the highest distortion, following the trend Ni > Pd > Pt. This distortion is not unique to herein reported complexes; similarly cyclometalated systems such as [M(L^{NHPh})Cl] or [M(L^{NHBn})Cl] (M = Pt and Pd) with bulky aniline moieties at the ortho-positions of the pyridyl rings, have demonstrated comparable deviations from square planar geometry.[28] The remaining complexes with less steric hinderance show minimal distortion, as confirmed by their DFT-

calculated geometries. Bond distances, specifically M–C, M–N, and M–X bonds are consistent with those reported for unsubstituted [M(dpb)X] complexes (M = Pt, Pd, Ni; X = Cl or Br).

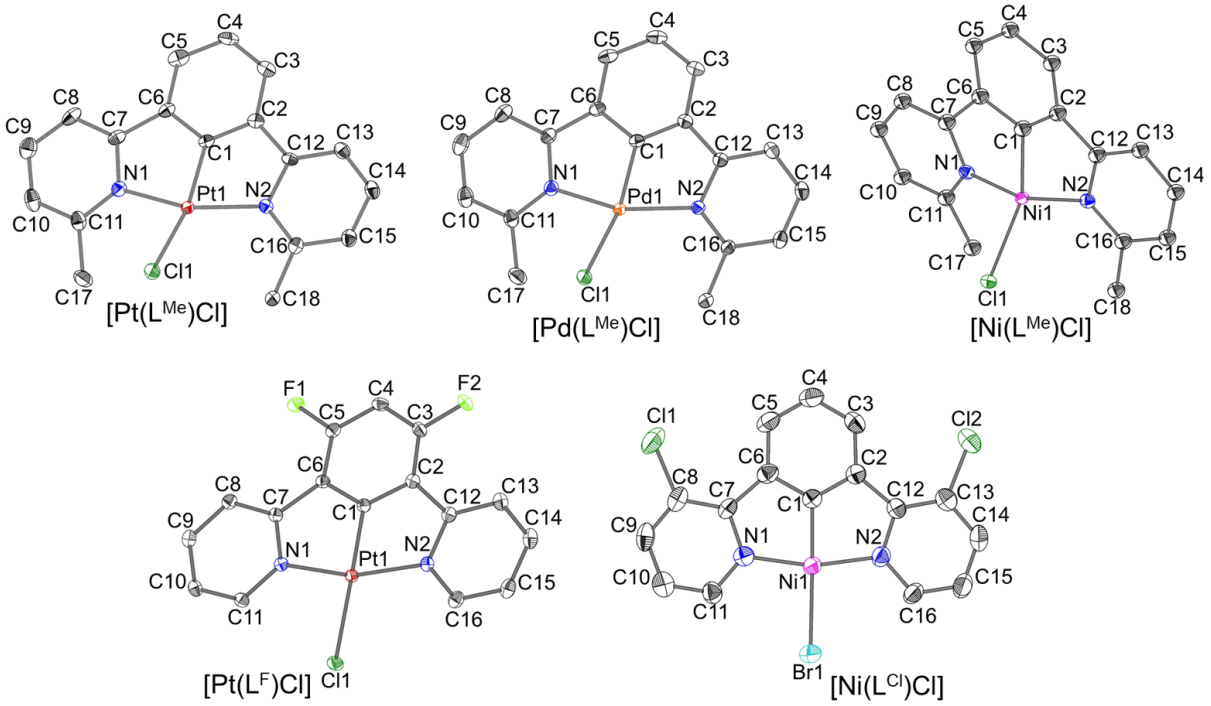


Figure 3-40. Molecular structures of the complexes from X-ray diffractometry on single crystals (displacement ellipsoids at 50%); H atoms are omitted for clarity.

3.5.2. Experimental and theoretical properties of [M(L^R)X] (M = Pt, Pd, Ni; R = Me, Me$_2$, Cl, F)

All complexes except [M(L^F)Cl] (M = Pt and Pd) display an irreversible first reduction between –2.06 to –2.36 V vs. the ferrocene/ferrocenium couple ($FeCp_2/FeCp_2^+$) (Figure 3-41; full data in Table 3-18; cyclic voltammograms in Figures A143–A146,). The first reduction of [M(L^F)Cl] (M = Pt and Pd) is reversible, indicating that the chloride dissociation does not occur on the timescale of the CV measurement. Subsequent reduction events are observed in all complexes, with second, third or even fourth reductions occurring at potentials ranging from –2.28 to –3.10 V. DFT calculations reveal that the LUMOs in these complexes are predominantly π*-type orbitals localized on the N^C^N ligands. The calculated LUMO energies are consistent across each series of complexes, with values around –2.4 V for the Me-substituted and –2.6 to –2.7 V for Cl- or F-substituted ligands (for details, see Figures A151–A154 and Tables A36–A39). In view of similar complexes,[41,64,95,103] we assign these reduction process to ligand-centered (π*) reductions.

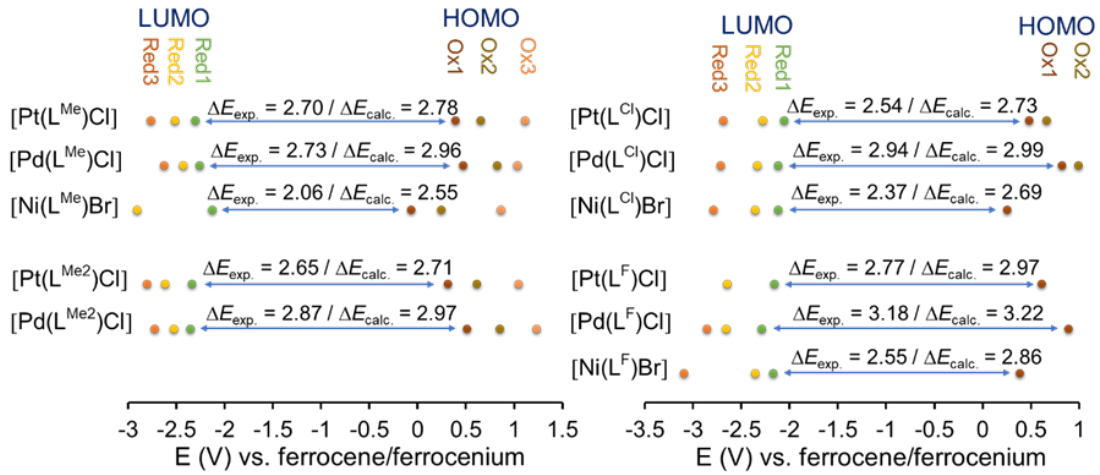


Figure 3-41. Selected experimental redox potentials (dots) and HOMO-LUMO gaps (Δ*E*exp.) from cyclic voltammetry together with DFT-calculated HOMO-LUMO gaps (Δ*E*calc.) for the complexes.

Table 3-18. Redox potentials of the complexes.[a]

complex	E_{pc} (Red3)	E_{pc} (Red2)	$E_{1/2}$ (Red1)	E_{pa} (Ox1)	E_{pa} (Ox2)	E_{pa} (Ox3)	ΔE (Red1–Red2)	ΔE_{echem}[b]	ΔE_{calc}[c]
[Pt(L^{Me})Cl]	–2.77	–2.52	–2.31	0.39	0.65	1.11	0.21	2.70	2.78
[Pd(L^{Me})Cl]	–2.63	–2.43	–2.26	0.47[d]	0.82	1.03	0.17	2.73	2.96
[Ni(L^{Me})Cl]	-	–2.91	–2.13	–0.07	0.24	0.86	0.78	2.06	2.55
[Pt(L^{Me2})Cl]	–2.81	–2.62	–2.34	0.31	0.61	1.04	0.28	2.65	2.71
[Pd(L^{Me2})Cl]	–2.73	–2.53	–2.36	0.51[d]	0.85	1.23	0.17	2.87	2.97
[Pt(L^{Cl})Cl]	–2.69[d]	–2.28	–2.06	0.48	0.66	-	0.22	2.54	2.73
[Pd(L^{Cl})Cl]	–2.72[d]	–2.34	–2.12	0.82[d]	0.99	-	0.22	2.94	2.99
[Ni(L^{Cl})Br]	–2.79	–2.36	–2.12	0.25[d]	-	-	0.24	2.37	2.69
[Pt(L^{F})Cl]	-	–2.65[d]	–2.16	0.61	-	-	0.49	2.77	2.97
[Pd(L^{F})Cl]	–2.86[d]	–2.66[d]	–2.29	0.89[d]	-	-	0.37	3.18	3.22
[Ni(L^{F})Br]	–3.10	–2.36	–2.17	0.38[d]	-	-	0.19	2.55	2.86

[a] From cyclic voltammetry in 0.1 M n-Bu$_4$NPF$_6$/THF. Potentials in V vs. ferrocene/ferrocenium; accuracy of potentials: ±0.003 V. E_{pc}: cathodic peak potentials for irreversible reductions, E_{pa}: anodic peak potentials for irreversible oxidations. [b] Electrochemical HOMO-LUMO gap ($\Delta E_{echem} = E_{Ox1} - E_{Red1}$). [c] ΔE_{calc} = DFT-calculated HOMO-LUMO gap; TPSSh/def2-TZVP/CPCM(THF). [d] Reversible, $E_{1/2}$ given.

Cyclic voltammograms revealed significant differences in the oxidation behavior among the three metals, with oxidation potentials increasing in the order Ni < Pt < Pd, consistent with previous studies on homologous series of metal complexes.[41,59,60,95] Singlet-point DFT calculations indicate that the HOMOs involve contributions from the metal d_{yz} orbitals, the phenyl group of the cyclometalating ligand, and the p_z orbitals of the chloride coligand (Figures A151–A154, Tables A36–A39). While the nature of the HOMOs is similar across the metal series, the orbital energies increase in the order Ni < Pt < Pd, paralleling the observed oxidation potentials. This suggest that the oxidation process involves not only metal-centered M(II)/ M(III) oxidation but also significant contributions from the ligands. Furthermore, complexes with electron-withdrawing substituents (e.g., F or Cl) show higher oxidative potentials than their Me-substituted counterparts, reflecting their electron deficient nature at the metal

center. This trend is also supported by DFT calculations, which show that electron-withdrawing groups stabilize the HOMOs, thus hindering the oxidation process (Figures A151−A154).

The electrochemical HOMO-LUMO gap varies from 2.06 to 3.18 eV, with a consistent trend of decreasing gap sizes in the order Pd > Pt > Ni for each series of complexes (Figure 3-41). Substitutions with F or Cl leads to larger gaps (e.g., 3.18 to 2.94 eV for Pd(II) complexes) compared to Me substitution (2.87 to 2.73 eV for Pd(II) complexes), likely due to greater stabilization of the HOMOs by the electron-withdrawing groups. These experimental trends are mirrored by DFT calculations, which also predict a decrease in the HOMO-LUMO gap along the series [M-L^{F}] > [M-L^{Cl}] > [M-L^{Me}] ≈ [M-L^{Me2}]. Interestingly, the electrochemical HOMO-LUMO gap for the [Pt-L^{Cl}] complex is smaller than that of its Me-substituted analogue, a trend that is likewise reproduced in the DFT calculations.

The UV-vis absorption spectra of the complexes exhibit intense absorption bands in the 235 to 300 nm range, accompanied by weaker, broader bands extending up to approximately 550 nm (Figure 3-42, data in Table 3-19). TD-DFT calculations using the TPSSh functional with the def2-TZVP basis set and a CPCM solvation model (THF) display qualitative agreement with the experimental results (Figures A163 and A164). The absorption profile of the [Pt(L^{F})Cl] complex has been previously reported and interpreted in earlier studies.[64] Based on TD-DFT calculations and comparisons with analogue complexes, the UV absorption bands in all the complexes can primarily be assigned to π–π* transitions. The weaker, long wavelength bands are attributed to mixed ligand-centered (LC) and metal-to-ligand charge-transfer (MLCT) transitions.[28,59,60,74,95,115] Within each series of complexes, the energy of the longest-wavelength absorption maximum follows the trend Ni < Pt < Pd. This progression mirrors both the experimentally observed and DFT-calculated HOMO-LUMO gaps, reaffirming the correlation between the optical transitions and the electronic structure.

Introducing electron-donating groups on the phenyl or pyridine rings ([M(L^{Me})Cl] or [M(L^{Me2})Cl]) results in lowering of the MLCT transition energies in the Pt complexes. For example, the parent [Pt(dpb)Cl] complex shows a long-wavelength absorption maxima at 401 nm in CH_2Cl_2.[63,64] In contrast, red-shifted maxima are observed in [Pt(L^{Me})Cl] (420 nm) and [Pt(L^{Me2})Cl] (418 nm). In the case of Ni complexes, [Ni(L^{Me})Cl] and the parent [Ni(dpb)X] (X = Cl, Br, and I)[103] display the long wavelength maxima in the range of 432 to 437 nm in THF. Electron-withdrawing substituents on the pyridine rings in the [M(L^{Cl})X] (X = Cl or Br) series cause only minor shifts in the long-wavelength absorption, with maxima at 394 nm for [Pt(L^{Cl})Cl] and 447 nm for [Ni(L^{Cl})Br]. However, broad shoulders appear at 425 nm for the Pt complex and 485 nm for its Ni analogue, indicating subtle changes in the MLCT/LC transitions. Notably, when electron-withdrawing groups are introduced on the phenyl ring in the [M(L^{F})X] (X = Cl or Br) complexes, a pronounced blue shift is observed. For example, the [Pt(L^{F})Cl] complex absorbs at 374 nm, while the Pd complex shifts further to 350 nm. In contrast, the [Ni(L^{F})Br]

complex exhibits a red shift, with the lowest-energy absorption band appearing at 461 nm, compared to the parent [Ni(dpb)Br] in CH_2Cl_2.[103]

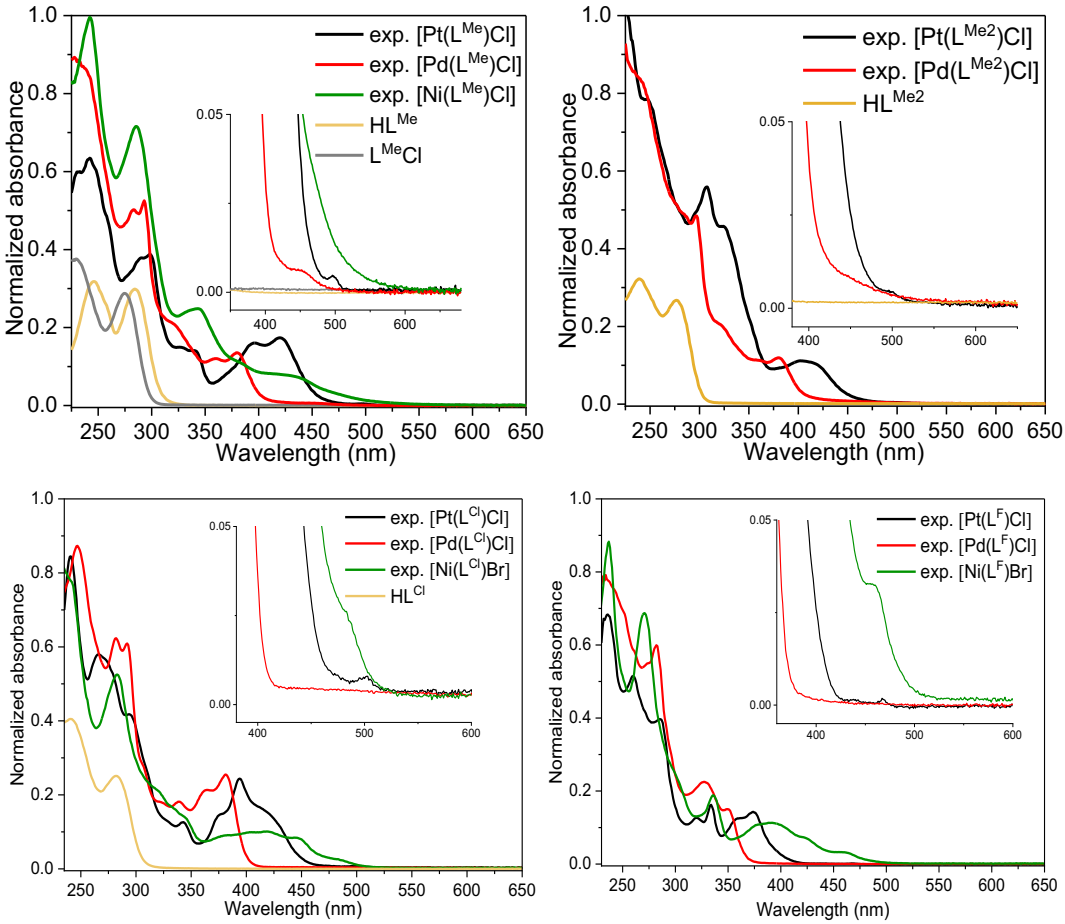


Figure 3-42. UV-vis absorption spectra of the complexes in THF solution at 298 K.

The optical band gaps (ΔE_{opt}), derived from the long-wavelength absorption maxima range from 2.56 to 3.54 eV (Table 3-19). The electrochemically determined gaps (ΔE_{echem}) (Table 3-18) are notably smaller than ΔE_{opt}, as expected given that electrochemical measurements reflect ground state properties.

Table 3-19. UV-vis absorption maxima of the complexes in THF solution at 298 K.[a]

complex	λ_1 (ε)	λ_2 (ε)	λ_3 (ε)	λ_4 (ε)	λ_5 (ε)	λ_6 (ε)	λ_7 (ε)	ΔE_{opt} [b]
[Pt(L^{Me})Cl]	242 (36.2)	290 (18.1)	298 (18.3)	328 (7.6)	340 (7.4)	396 (9.6)	420 (10.2)	2.95
[Pd(L^{Me})Cl]	238 (43.2)	283 (24.2)	293 (19.0)	321^{sh} (12.4)	360 (6.9)	380 (7.5)	-	3.26
[Ni(L^{Me})Cl]	242 (44.8)	285 (38.7)	-	-	344 (13.2)	-	436 (4.8)	2.84
[Pt(L^{Me2})Cl]	248 (38.2)	-	307 (22.3)	324^{sh} (19.2)	-	402 (7.7)	418 (7.3)	2.97
[Pd(L^{Me2})Cl]	242 (39.4)	-	297 (19.7)	321^{sh} (9.4)	361 (7.2)	380 (7.9)	-	3.26
[Pt(L^{Cl})Cl]	240 (24.5)	266 (15.6)	294 (12.8)	343 (5.6)	375 (6.1)	394 (7.5)	425^{sh} (6.2)	2.92
[Pd(L^{Cl})Cl]	247 (25.2)	282 (16.5)	292 (16.3)	339 (6.3)	363 (7.1)	382 (7.7)	-	3.25
[Ni(L^{Cl})Br]	242 (23.4)	283 (13.2)	320^{sh} (7.2)	345^{sh} (6.3)	409 (4.8)	447 (4.5)	485^{sh} (3.2)	2.56
[Pt(L^{F})Cl]	236 (40.8)	260 (30.8)	286 (23.8)	320 (7.7)	333 (9.7)	360 (7.5)	374 (8.6)	3.32
[Pd(L^{F})Cl]	234 (40.7)	283 (31.1)	-	328 (11.7)	350 (7.8)	-	-	3.54
[Ni(L^{F})Br]	237 (4.3)	270 (34.2)	300^{sh} (10.8)	336 (9.4)	389 (8.2)	425^{sh} (7.3)	461 (4.9)	2.69

[a] Absorption maxima λ in nm; molar absorption coefficients ε in 10^3 L mol^{-1} cm^{-1}; sh = shoulder. [b] Optical HOMO-LUMO gap extrapolated from the long wavelength absorptions in eV.

The photoluminescence properties of the complexes were investigated in liquid CH_2Cl_2 solution at 298 K and in frozen glassy THF matrices at 77 K (Figure 3-43, data in Tables 3-20 and 3-21 and Figures A208-A227, appendix). The Pt(II) complexes exhibit emission at 298 K with λ_{max} ranging from 471 to 508 nm, depending on the substituents on the ligands (Table 3-22). For instance, increasing the number of electron-donating methyl groups results in a red shift of the emission maxima, from 498 nm for [Pt(L^{Me})Cl] to 508 nm for [Pt(L^{Me2})Cl]. Comparatively, the parent [Pt(dpb)Cl] complex shows maxima at 491, 524, and 562 nm under similar conditions.[63,64] The electron-withdrawing fluorine substituents in [Pt(L^{F})Cl] blue-shift the emission to 471 nm. While [Pt(L^{Cl})Cl], with chlorine substituents, displays a slightly red-shifted λ_{max} at 506 nm.

At 77 K, the Pt(II) complexes exhibit structured multi-band emissions, indicative of vibronic coupling between metal and ligand vibrational modes. For instance, [Pt(L^{F})Cl] shows a blue-shifted spectrum, with the first emission peak at 467 nm and additional maxima extending to 572 nm. The quantum yields increase under inert conditions (Ar-purged CH_2Cl_2) at 298 K and at 77 K, reflecting the suppression of non-radiative decay pathways. For example, [Pt(L^{Me})Cl] displays Φ_L = 0.46 at 77 K, with lifetimes extending from 263 ns in aerated solution at 298 K to 4.628 μs at 77 K. Similarly, Φ_L increases to 0.97 for [Pt(L^{F})Cl] and [Pt(L^{Cl})Cl], with lifetimes of 5.703 μs and 118.120 μs, respectively. Conversely, the Pd(II) and Ni(II) complexes exhibit no detectable emission at 298 K, likely due to rapid non-radiative decay via metal-centered (^{3}MC) states. However, at 77 K in a frozen glassy THF matrices, they exhibit phosphorescence (Figure 3-43 and data in Tables 3-20 and 3-21; Figures A216-A227). Pd(II) complexes generally show blue-shifted emissions compared to their Pt(II) counterparts.[28,41,58] However, [Pd(L^{Me})Cl] and [Pd(L^{Me2})Cl] exhibit structured emissions over a broad range, indicative of mixed MLCT and LC transitions.

At 77 K, detectable emission was observed for Ni(II) complexes (Figure 3-43 and data in Tables 3-20 and 3-21; Figures A224-A226, appendix). [Ni(L^{Me})Cl] displays an unstructured band at 510 nm with Φ_L of 0.2 and a long lifetime of 68.1 ms. However, [Ni(L^{Cl})Br] and [Ni(L^{F})Br] exhibit extremely weak emissions (Φ_L < 0.02) with lifetimes of 194.2 μs and 8.7 μs, respectively. Notably, [Ni(dpb)Cl], was reported as non-emissive at 298 K in solution and solid state, as well as at 77 K in glassy matrices.[28,41,103] Recent studies by *Wenger et al.*,[74] reported that in solution at 293 K, the MLCT excited state of [Ni(dpb)Cl] decays within 0.7 ps (in CH_3CN) and 0.9 ps (in CH_2Cl_2), followed by rapid decay via the ^{3}MC state within 9.2 ps (CH_3CN) and 14 ps (CH_2Cl_2). At 77 K, however, we observed weak, structured emission with a peak at 467 nm, highlighting the role of temperature in suppressing non-radiative pathways (Figure 3-43 and data in Tables 3-20, 3-21 and 3-22; Figure A227, appendix).

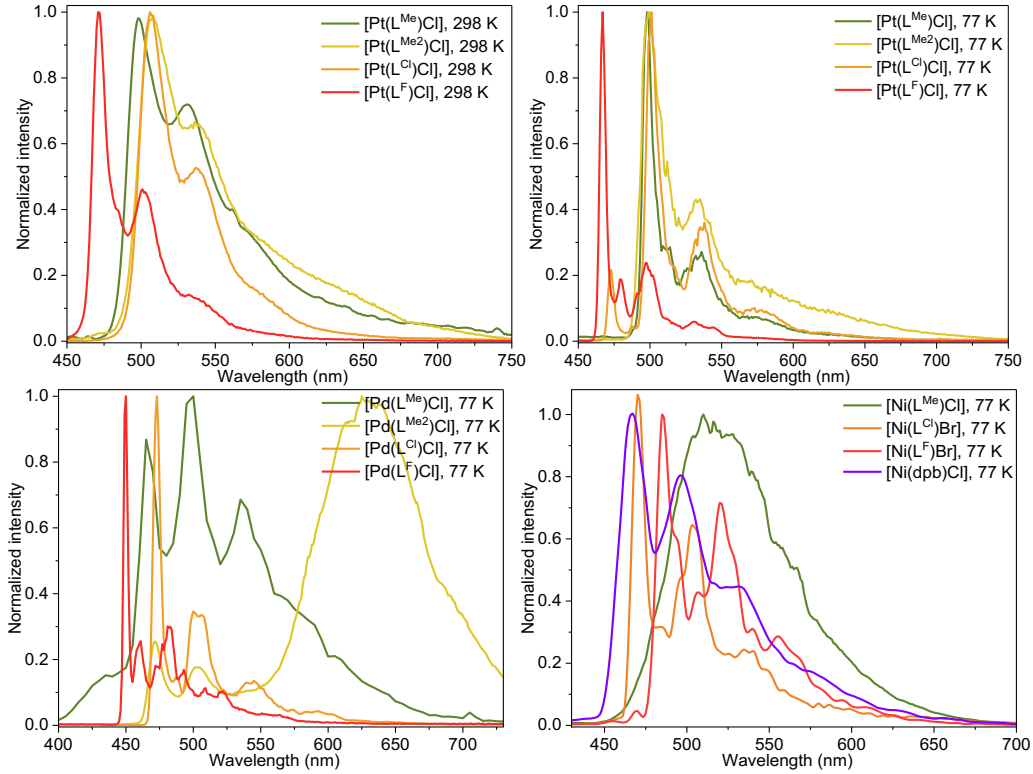


Figure 3-43. Photoluminescence emission spectra of the Pt(II) complexes in liquid CH_2Cl_2 at 298 K and in THF at 77 K (λ_{ex} = 350 nm) and Pd(II) and Ni(II) complexes in THF at 77 K (λ_{ex} = 350 nm); all solutions were optically diluted (concentration = 10^{-5} M). All maxima are listed in Table 3-22.

Radiative (k_r) and non-radiative (k_{nr}) rate constants were estimated from the obtained Φ_L and excited state lifetimes (Table 3-21). The Pt(II) complexes exhibit efficient radiative decay with [Pt(L^{Me})Cl] showing a balance between k_r (9.94×10^4 s^{-1}) and k_{nr} (11.7×10^4 s^{-1}) at 77 K. In [Pt(L^{Me2})Cl], k_{nr} increases slightly (12.0×10^4 s^{-1}), while k_r decreases to 6.2×10^4 s^{-1}, reflecting less efficient emission due to the additional methyl groups. The [Pt(L^F)Cl] complex demonstrates an exceptionally high k_r (17.0×10^4 s^{-1}) and a nearly negligible k_{nr} ($\leq 0.05 \times 10^4$ s^{-1}), consistent with highly efficient emission at 77 K. Interestingly, [Pt(L^{Cl})Cl], while exhibiting the lowest k_r (0.82×10^4 s^{-1}), maintains minimal non-radiative losses ($k_{nr} \leq 0.04 \times 10^4$ s^{-1}).

Among the Pd(II) complexes, [Pd(L^{Me})Cl] and [Pd(L^{Me2})Cl] display low k_r ($\leq 1 \times 10^4$ s^{-1}) and high k_{nr} values, leading to weak emission. However, [Pd(L^{Cl})Cl] is a notable exception, with $k_r = 0.84 \times 10^4$ s^{-1} and $\Phi_L = 0.97$ at 77 K, suggesting that radiative decay is more favorable in this particular complex.

The Ni(II) complexes, by contrast, exhibit the weakest luminescence, with extremely low k_r and dominant non-radiative decay. For example, [Ni(L^{Me})Cl] has a k_r of just 2.9 s^{-1} at 77 K, with $k_{nr} = 0.0012 \times 10^4$ s^{-1}, indicating minimal radiative decay. Even [Ni(L^F)Cl], which exhibits a slight improvement in k_r ($\leq 0.4 \times 10^4$ s^{-1}), is dominated by high k_{nr} (11.2×10^4 s^{-1}), resulting in very weak emission. Similarly, [Ni(dpb)Cl] shows negligible radiative decay ($k_r \leq 0.02 \times 10^4$ s^{-1}), further highlighting the challenges of achieving efficient emission in Ni(II) complexes.

Table 3-20. Photoluminescence data for the complexes.[a,b]

complex	$\Phi_{L\text{-Air}}$	$\Phi_{L\text{-Argon}}$	$\Phi_{L\text{-77 K}}$	τ_{air}/ ns	τ_{Ar}/ μs	$\tau_{77\ K}$/ μs
[Pt(L^{Me})Cl]	≤0.02	≤0.02	0.46 ± 0.03	τ_1 = 369 ± 2 (66%) τ_2 = 60 ± 4 (34%) τ_{av_amp} = 263 ± 5	τ_1 = 0.90 ± 0.01 (52%) τ_2 = 3.58 ± 0.01 (48%) τ_{av_amp} = 2.180 ± 0.07	τ_1 = 5.601 ± 0.08 (62%) τ_2 = 3.02 ± 0.2 (38%) τ_{av_amp} = 4.63 ± 0.02
[Pd(L^{Me})Cl]	-	-	≤0.02	-	-	τ_1 = 183± 3 (12%) τ_2 = 17.7 ± 0.2 (88%) τ_{av_amp} = 38.3 ± 0.4
[Ni(L^{Me})Cl]	-	-	0.20 ± 0.02	-	-	τ_1 = 110000 ± 4000 (51%) τ_2 = 25200 ± 1600 (49%) τ_{av_amp} = 68100 ± 1200
[Pt(L^{Me2})Cl]	≤0.02	≤0.02	0.34 ± 0.02	τ_1 = 264 ± 5 (10%) τ_2 = 49.3 ± 0.6 (90%) τ_{av_amp} = 70.1 ± 0.6	τ_1 = 4.31 ± 0.05 (88%) τ_2 = 1.47 ± 0.29 (12%) τ_{av_amp} = 3.952 ± 0.03	τ_1 = 7.8 ± 0.3 (17%) τ_2 = 5.02 ± 0.07 (83%) τ_{av_amp} = 5.484 ± 0.006
[Pd(L^{Me2})Cl]	-	-	≤0.02	-	-	τ_1 = 193± 2 (64%) τ_2 = 94 ± 3 (36%) τ_{av_amp} = 156.6 ± 0.4
[Pt(L^{Cl})Cl]	≤0.05	0.43 ± 0.02	0.97 ± 0.03	424.5 ± 0.3	2.034 ± 0.002	118.1 ± 0.2
[Pd(L^{Cl})Cl]	-	-	0.97 ± 0.03	-	-	τ_1 = 121.0 ± 0.5 (92%) τ_2 = 45 ± 6 (8%) τ_{av_amp} = 114.9 ± 0.3
[Ni(L^{Cl})Br]	-	-	≤0.02	-	-	τ_1 = 330 ± 20 (14%) τ_2 = 172 ± 2 (86%) τ_{av_amp} = 194.2 ± 0.4
[Pt(L^{F})Cl]	≤0.06	0.60 ± 0.03	0.97 ± 0.03	496.1 ± 0.1	0.957 ± 0.004	5.703 ± 0.004
[Pd(L^{F})Cl]	-	-	0.18 ± 0.02	-	-	τ_1 = 111 ± 10 (10%) τ_2 = 272 ± 1 (90%) τ_{av_amp} = 255.1 ± 0.6
[Ni(L^{F})Br]	-	-	≤0.02	-	-	τ_1 = 13.3 ± 0.9 (14%) τ_2 = 8.0 ± 0.2 (86%) τ_{av_amp} = 8.7 ± 0.01
[Ni(dpb)Cl]	-	-	≤0.02	-	-	τ_1 = 176 ± 4 (92%) τ_2 = 480 ± 50 (8%) τ_{av_amp} = 200.0 ± 1.4

[a] Photoluminescence Φ_L and lifetimes (τ) under different conditions: Liquid CH_2Cl_2 solution under air (Air) atmosphere or Ar-purged (Argon) (both c ≈ 10^{-5} M), and frozen glassy matrices at 77 K (THF). [b] For multi-exponential decays, the amplitude-weighted average lifetimes are given. Raw time-resolved photoluminescence decays and fitting parameters are shown in Figures A208 to A227, appendix.

Table 3-21. Radiative and non-radiative rate constants (k_r and k_{nr}) of the complexes.[a]

complex	$k_{r,Air}$ / 10^4 s^{-1}	$k_{nr,Air}$ / 10^4 s^{-1}	$k_{r,Ar}$ / 10^4 s^{-1}	$k_{nr,Ar}$ / 10^4 s^{-1}	$k_{r,77\ K}$ / 10^4 s^{-1}	$k_{nr,77\ K}$ / 10^4 s^{-1}
[Pt(L^{Me})Cl]	≤15	373 – 380	≤2	45 – 46	9.94 ± 0.7	11.7 ± 0.7
[Pd(L^{Me})Cl]	-	-	-	-	≤1	2.56 ± 0.06
[Ni(L^{Me})Cl]	-	-	-	-	2.9 ± 0.3 × 10^{-4}	0.00120 ± 0.00004
[Pt(L^{Me2})Cl]	≤58	1398 – 1426	≤1	25 – 26	6.2 ± 0.4	12.0 ± 0.4
[Pd(L^{Me2})Cl]	-	-	-	-	≤0.01	0.62 ± 0.01
[Pt(L^{Cl})Cl]	12 ± 5 (or ≤17)	224 ± 5	21.1 ± 1.0	28 ± 1	0.82 ± 0.03	≤0.04
[Pd(L^{Cl})Cl]	-	-	-	-	0.84 ± 0.03	≤0.05
[Ni(L^{Cl})Br]	-	-	-	-	≤0.02	0.5 ± 0.01
[Pt(L^{F})Cl]	12 ± 4 (or ≤16)	189 ± 4	63 ± 3	42 ± 3	17.0 ± 0.5	≤0.05
[Pd(L^{F})Cl]	-	-	-	-	0.070 ± 0.008	0.32 ± 0.01
[Ni(L^{F})Br]	-	-	-	-	≤0.4	11.2 ± 0.2
[Ni(dpb)Cl]	-	-	-	-	≤0.02	0.49 ± 0.01

[a] For conditions, see Table 3-20.

Table 3-22. λ_{max} of the emission spectra of the complexes under different conditions.

complex	λ_{max} (CH_2Cl_2, RT) / nm	λ_{max} (THF, 77 K) / nm
[Pt(L^{Me})Cl]	498, 531, 576^{sh}	498, 512, 535, 574^{sh}
[Pd(L^{Me})Cl]	–	466, 498, 536, 570^{sh}, 610^{sh}
[Ni(L^{Me})Cl]	–	510
[Pt(L^{Me2})Cl]	508, 537, 584^{sh}	499, 533, 570^{sh}
[Pd(L^{Me2})Cl]	–	472, 502, 625
[Pt(L^{Cl})Cl]	506, 538, 582^{sh}	501, 538, 574^{sh}
[Pd(L^{Cl})Cl]	–	473, 501, 545, 593^{sh}
[Ni(L^{Cl})Br]	–	470, 504, 535, 589^{sh}
[Pt(L^{F})Cl]	471, 501, 537^{sh}	467, 480, 497, 530, 545, 572^{sh}
[Pd(L^{F})Cl]	–	450, 460, 482, 515, 557^{sh}
[Ni(L^{F})Br]	–	486, 521, 555, 610^{sh}
[Ni(dpb)Cl]	–	467, 496, 532, 577^{sh}

sh = shoulder.

3.6. [M(L^{Qu})Cl] (M = Pt, Pd, Ni) complexes

3.6.1. Synthesis and structure of [M(L^{Qu})Cl] (M = Pt, Pd, Ni)

To expand the discussion in this section, [Ni(L^{Qu})Cl] complex synthesized and characterized by Dr. Lukas Kletsch, a former doctoral researcher in the group of Prof. Dr. Axel Klein, is incorporated.

Building on our ongoing efforts to design efficient triplet emitters, the π-system of the complexes was extended by incorporating quinoline units into the N^C^N ligand framework, leading to the synthesis of [M(L^{Qu})Cl] (M = Pt, Pd, Ni; L^{Qu} = bis(2-pyridyl)/2-quinolyl)benzene) complexes (Figure 3-44). The ligand precursors HL^{Qu} and ClL^{Qu} were synthesized via Suzuki cross coupling reactions, achieving yields of 76% and 87%, respectively (Figure 3-44, details in the experimental section). The corresponding Pt(II) and Pd(II) complexes [M(L^{Qu})Cl] were synthesized from $K_2[MCl_4]$ (M = Pt or Pd) using a well stablished method involving heating in glacial acetic acid,[92] yielding 68% and 65%, respectively (Figure 3-44, details in the experimental section). The Ni(II) complex was obtained through a modified procedure,[96] involving the oxidative addition of $[Ni(COD)_2]$ (COD = 1,5- cyclooctadiene) with the chlorinated ligand precursor ClL^{Qu}, resulting in a quantitative yield (Figure 3-44, details in the experimental section). The three Pt(II) (orange-red), Pd(II) (yellow), and Ni(II) (red) complexes have been thoroughly characterized by NMR spectroscopy, HR-ESI mass spectrometry, elemental analysis (CHN), and single-crystal XRD (spectra and data in the experimental section and the appendix). While the Pt(II) complex [Pt(L^{Qu})Cl] has been previously reported,[119,120] its photophysical properties were re-examined under identical experimental conditions to facilitate direct comparison with its Ni(II) and Pd(II) counterparts.

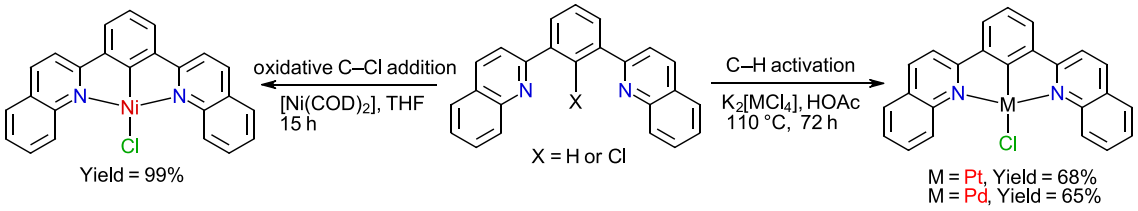


Figure 3-44. Synthesis of [M(L^{Qu})Cl] (M = Pt, Pd, Ni) complexes.

The complexes [Pt(L^{Qu})Cl] and [Pd(L^{Qu})Cl] were crystallized by slow cooling of hot saturated DMSO solutions, while single crystals of [Ni(L^{Qu})Cl] were grown via layering of a saturated CH_2Cl_2 solution with n-pentane. All three complexes crystallized isostructurally in the monoclinic space group $P2_1/c$ (Figures A135 to A137, data in Tables A22 and A23, appendix), resembling the previously reported complexes [M(dpb)X] (M = Pt, Pd, Ni; X = Cl, Br, I; Hdpb = 1,3-di-pyridyl-benzene)[92,94,103] with the $P2_1/n$ space group.

Each complex exhibits a distorted square planar geometry due to the significant out-of-plane distortion of the chloride coligand relative to the $N^{quinoline}$–$C^{benzene}$–$N^{quinoline}$–M coordination plane (Figure 3-45). The distortion is quantitatively reflected in the τ_4 values: Pt (0.305), Pd (0.321), and Ni (0.354). These values contrast with the nearly planar geometry of [Ni(dpb)Cl][103] (τ_4 = 0.121) and [Pt(dpb)Cl][92] (τ_4 = 0.141), based on single crystal data. A similar feature has been previously reported for [M($L^{NHPh\ or\ NHBn}$)Cl],[28] [M(L^{Bn})Cl], and [M(L^{Me})Cl][41] (M = Pt, Pd, and Ni) complexes. Among the three complexes, the distortion in [Ni(L^{Qu})Cl] is most pronounced, supported by shorter M–$C^{benzene}$ and M–Cl bond lengths: Pt(II): 1.92 and 2.44 Å; Pd(II): 1.91 and 2.45 Å; Ni(II): 1.82 and 2.28 Å. Despite the distortion, the remainder of the structure, the $N^{quinoline}$–$C^{benzene}$–$N^{quinoline}$–M coordination, is nearly planar. This planarity facilitates head-to-tail stacking of molecules and pronounced intermolecular π···π stacking interactions between the pyridyl and phenyl units of adjacent molecules. The centroid-centroid distances for these interactions are 3.51 Å (Pt and Pd complexes) and 3.72 Å (Ni complex) (Figures A135 to A137). In contrast, no significant metallophilic M···M interactions were observed. The metal-metal distances are ~5.56 Å (Pt and Pd complexes) and 5.27 Å (Ni complex) longer than those reported for [M(dpb)Cl] complexes (~4.90 Å for the Pt(II) and Pd(II)[62] and 4.80 Å for the Ni(II)[103]). This preference of interactions between the pyridyl and phenyl rings rather than between the metal centers is quite typical of reported symmetrical [M(NCN)X] (M = Pt, Pd, and Ni; X = Cl, Br, I) complexes.[121]

Geometry optimization of the three complexes using TPSSh/def2-TZVP with CPCM solvation (THF) shows very good agreement with the experimental data (Table A23). The resulting *xyz* coordinates of the optimized structures are presented in Tables A67 and A66.

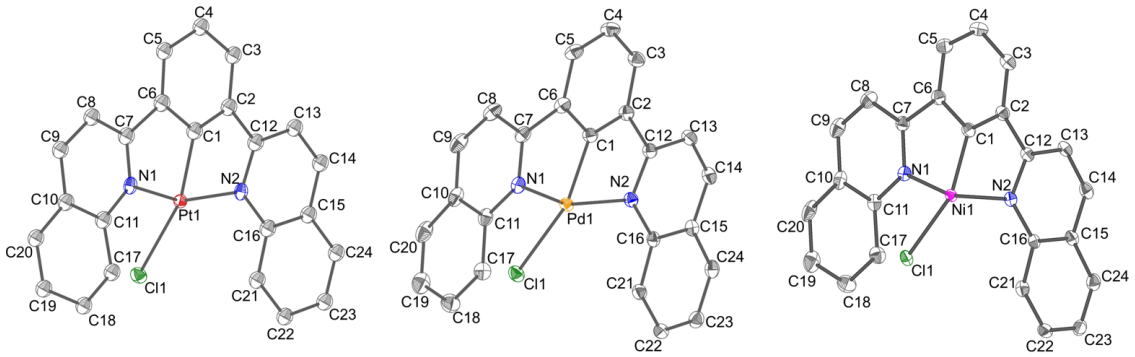


Figure 3-45. Molecular structures of the complexes [M(L^{Qu})Cl] (M = Pt, Pd, Ni) with numbering from single crystal X-ray diffraction (50% displacement ellipsoids), H atoms omitted for clarity.

3.6.2. Experimental and theoretical properties of [M(L^{Qu})Cl] (M = Pt, Pd, Ni)

All complexes exhibit an irreversible oxidative wave at potentials ranging from +0.21 V to +1.14 V vs. the ferrocene/ferrocenium couple ($FeCp_2/FeCp_2^+$) (Figure 3-46, full data in Table 3-23; cyclic voltammograms are presented in Figures A147 and A148). The Ni(II) complex shows a notably low oxidation potential of +0.21 V, assignable to a M(II)/M(III) redox pair based on similar reports.[41,59,60,65,95,96,103,104,122] The corresponding oxidative processes for the Pt(II) and Pd(II) derivatives are shifted to higher potentials of +1.01 and +1.14 V, respectively.

The first reduction potentials for all complexes lie around –1.90 V, followed by two or three additional reductions at lower potentials (down to –3.18 V), which can be attributed to ligand-centered (π–π*) reductions. Compared with the free ligands, the first reduction in the complexes is shifted to higher potentials by approximately 0.55 V, for all the derivatives.

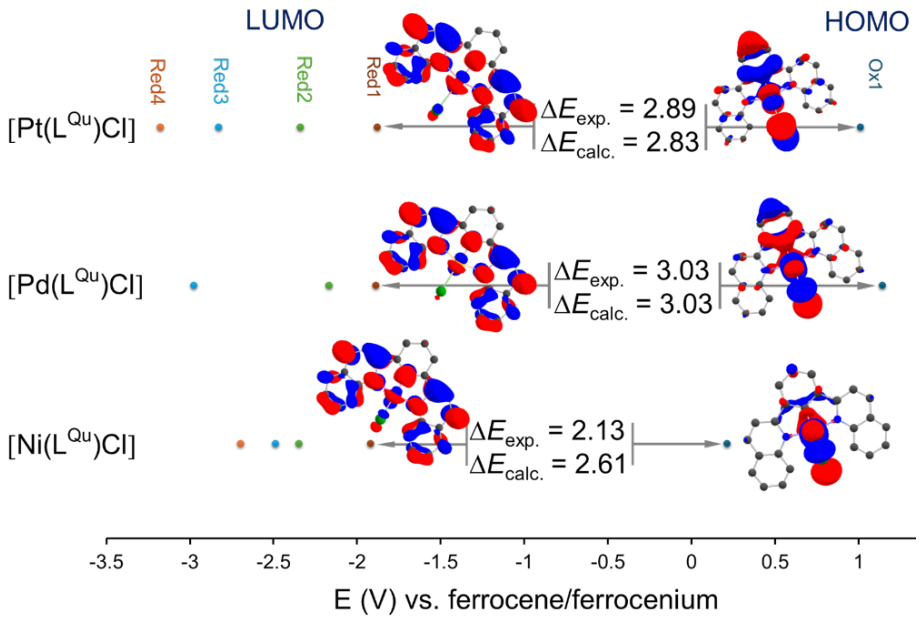


Figure 3-46. Selected experimental redox potentials (dots) and HOMO-LUMO gaps (Δ*E*exp.) from cyclic voltammetry together with DFT-calculated HOMO and LUMO compositions and HOMO-LUMO gaps (Δ*E*calc.) for the complexes.

Table 3-23. Redox potentials of the complexes [M(L^{Qu})Cl] (M = Pt, Pd, Ni).[a]

complex	E_{pc} ($_{Red4}$)	E_{pc} ($_{Red3}$)	E_{pc} ($_{Red2}$)	E_{pc} ($_{Red1}$)	E_{pa} ($_{Ox1}$)	ΔE ($_{Red1\text{-}Red2}$)	ΔE_{echem}	ΔE_{calc}
HL^{Qu}	–3.29	–3.08	–2.69	–2.44[d]	–	0.25	–	–
ClL^{Qu}	–3.29	–2.99	–2.73[d]	–2.49[d]	–	0.24	–	–
[Pt(L^{Qu})Cl]	–3.18	–2.83	–2.34[d]	–1.88[d]	1.01	0.46	2.89	2.83
[Pd(L^{Qu})Cl]	–	–2.98	–2.17	–1.89	1.14	0.28	3.03	3.03
[Ni(L^{Qu})Cl]	–2.70	–2.49	–2.35	–1.92	0.21	0.43	2.13	2.61

[a] From cyclic voltammetry in 0.1 M n-Bu_4NPF_6/THF. Potentials in V vs. ferrocene/ferrocenium; accuracy of potentials: ±0.003 V. E_{pc}: cathodic peak potentials for irreversible reductions, E_{pa}: anodic peak potentials for irreversible oxidations. [b] Electrochemical HOMO-LUMO gap ($\Delta E_{echem} = E_{Ox1} - E_{Red1}$). [c] ΔE_{calc} = DFT-calculated HOMO-LUMO gap; TPSSh/def2-TZVP/CPCM(THF). [d] Reversible, $E_{1/2}$ given.

DFT-calculated frontier molecular orbitals of the optimized structures reveal that the HOMO orbitals are predominantly localized on the metal centers, the central aryl group and partially on the chloride coligand (Figure 3-47, Table A40). The metal contribution to the HOMO increases from approximately 35% for Pt(II) and Pd(II) to 55% for the Ni(II) complex, supporting our assignment of the oxidative waves and the lower oxidation potential observed for Ni(II) in the cyclic voltammograms. The HOMOs are stabilized in the order Pd(II) > Pt(II) > Ni(II). In contrast, the LUMO orbitals show less variance across the series and are predominantly localized on the quinoline and phenyl units (Figure 3-47, Table A40).

The calculated HOMO-LUMO gaps ($\Delta E_{calc.}$) follow the trend Ni(II) < Pt(II) < Pd(II), ranging from 2.61 eV for [Ni(L^{Qu})Cl] to 3.03 eV for [Pd(L^{Qu})Cl], and correlate well with the experimental electrochemical gaps ($\Delta E_{echem.}$). This trend is consistent with previously reported complexes.[28,41,95] For [Ni(L^{Qu})Cl], the HOMO-LUMO gap is slightly smaller than that of [Ni(dpb)Cl][103] by 0.26 V, attributed to the expanded π-surface of the N^C^N ligand unit which enhances ligand-centered reduction (π-accepting properties). This effect shifts the first reduction from –2.33 V for [Ni(dpb)Cl] to –1.92 V for [Ni(L^{Qu})Cl]. In contrast, the HOMO-LUMO gap of [Pt(dpb)Cl] is 2.49 eV,[62] smaller than that of [Pt(L^{Qu})Cl] by 0.40 V, likely due to greater stabilization of the 5d orbitals in Pt compared with the 3d orbitals in Ni, mediated by the weaker σ-donor capacity of the N^C^N ligand in L^{Qu}. For [Pt(L^{Qu})Cl], two previous reports[119,120] provide calculated HOMO-LUMO gap as 3.19 and 3.85 eV. Neither study reports the experimental electrochemical gap. In contrast, our DFT-calculated HOMO-LUMO gap of 2.83 eV is significantly smaller and aligns very well with our experimental electrochemical gap of 2.89 eV.

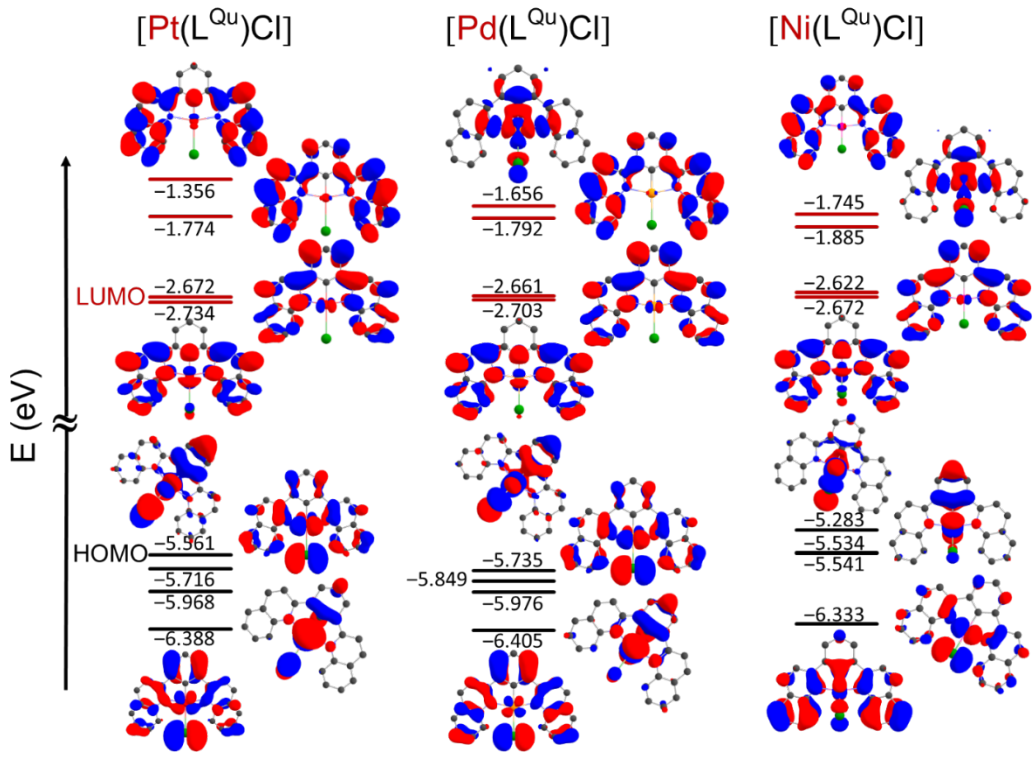


Figure 3-47. DFT-calculated energies of the highest occupied (HOMO, black) and lowest unoccupied (LUMO, red) molecular orbitals for [M(L^{Qu})Cl] (M = Pt, Pd, Ni); DFT calculations on TPSSh/def2-TZVP/CPCM(THF) level of theory.

The UV-vis absorption spectra of the [M(L^{Qu})Cl] complexes (M = Pt, Pd, Ni) exhibit intense absorption bands up to approximately 300 nm, which can be attributed to ligand-centered transitions into $^1\pi$–π^* excited singlet states. These bands are consistent with the absorption features observed for the ligand precursors HL^{Qu} and ClL^{Qu} (Figure 3-48, data in Table 3-24). In addition to these high energy bands, weaker absorption bands or shoulders are observed in the range 314–350 nm for Pt(II) and Pd(II) and at 352 nm for Ni(II). These are followed by broad, low-intensity absorption bands with maxima at 430 nm (Pt), 392 nm (Pd), and 439 nm (Ni). By comparison with absorption profiles reported for similar complexes,[28,41,59,60,65,95,96,103,104,122] the long-wavelength bands are assigned to transitions into states with mixed ligand-centered (^{1}LC) and metal-to-ligand-charge-transfer (^{1}MLCT) character or metal-perturbed LC character (^{1}MP-LC). The energy of the long-wavelength absorption band increases along the series Ni(II) < Pt(II) < Pd(II) and is in agreement with the experimentally determined and DFT-calculated HOMO-LUMO gaps.

TD-DFT calculations provide qualitative agreement with the experimental absorption spectra and support these assignments (Figure 3-48 and Table 3-24, Figure A165 and Table A48, appendix). The calculated low-energy absorption bands appear at 460 nm (Pt), 434 nm (Pd), and 479 nm (Ni), which are red-shifted relative to the experimental maxima (430, 392, 439 nm, respectively). The low-energy $S_0 \rightarrow S_n$ transitions (> 350 nm), involve excitation from filled orbitals with

metal, metalated central phenyl ring, and Cl^- contributions into π* orbitals that are localized over the entire N^C^N ligand unit, supporting the interpretation of ^{1}MP-LC excited states.

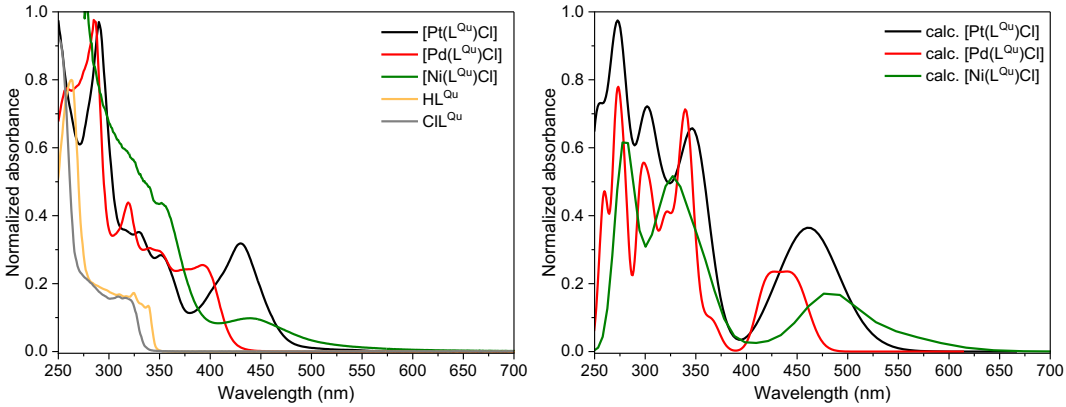


Figure 3-48. UV-vis absorption spectra of the complexes in THF solution at 298 K with TD-DFT calculated transitions (TPSSh/def2-TZVP/CPCM(THF) level of theory).

Table 3-24. Selected experimental UV-Vis absorption maxima of the complexes.[a]

complex	[Pt(L^{Qu})Cl]	[Pd(L^{Qu})Cl]	[Ni(L^{Qu})Cl]
λ_7 (ε)[b]	–	260 (33.7)	–
λ_6 (ε)[b]	–	285 (44.6)	–
λ_5 (ε)[b]	290 (44.5)	319 (18.3)	–
λ_4 (ε)[b]	314 (15.3)	339 (13.9)	–
λ_3 (ε)[b]	329 (15.3)	350 (13.8)	278 (46.2)
λ_2 (ε)[b]	351 (13.1)	373 (13.1)	352 (18.4)
λ_1 (ε)[b]	430 (15.2)	392 (13.4)	439 (8.4)
ΔE_{opt}[c]	2.88	3.16	2.82

[a] Measured in THF at 298 K. [b] Absorption maxima λ are given in nm, and molar absorption coefficients ε are given in 10^3 L mol^{-1} cm^{-1}. [c] Optical HOMO-LUMO gap extrapolated from the lowest energy absorption band in eV.

The expanded π-system of quinoline substituted N^C^N ligand is expected to include a red shift in the long-wavelength absorption bands due to enhanced π-acceptor properties relative to unsubstituted pyridine-based ligands. This trend is evident when comparing the [M(L^{Qu})Cl] complexes with their parent/unsubstituted [M(dpb)Cl] complexes.[62,103,115] The ^{1}MP-LC bands of [Pt(dpb)Cl] and [Ni(dpb)Cl] appear at 401 and 437 nm, respectively, while the corresponding bands for [Pt(L^{Qu})Cl] and [Ni(L^{Qu})Cl] are slightly red-shifted to 430 and 439 nm, respectively. The isoquinoline-substituted Pt(II) complexes absorb the ^{1}MP-LC band at around 450 nm, indicating that the longest-wavelength band is associated with the expanded π-surface of the isoquinoline unit.[121] When comparing the [M(L^{Qu})Cl] complexes with the NHR (R = Phenyl or Benzyl) or benzyl-functionalized analogs,[28] minimal effects on the absorption energies (shifts < 15 nm) are observed.

The optical HOMO-LUMO gaps $\Delta E_{opt.}$ extrapolated from the lowest-energy absorption bands for Pd(II) and Ni(II) are larger (3.16 and 2.82 eV, respectively) than their electrochemical and calculated HOMO-

LUMO gaps ($\Delta E_{echem.}$: 3.03 and 2.13 eV; $\Delta E_{calc.}$: 3.03 and 2.61 eV, respectively). In contrast, for the Pt(II) complex, $\Delta E_{opt.}$, $\Delta E_{echem.}$, and $\Delta E_{calc.}$ are nearly identical at approximately 2.89 eV. This suggests minimal structural reorganization between the ground state (S_0) and the lowest triplet excited state (T_1) for Pt(II) compared with Pd(II) and Ni(II), where reorganization effects appear more pronounced (Figure 3-49, Table A23).

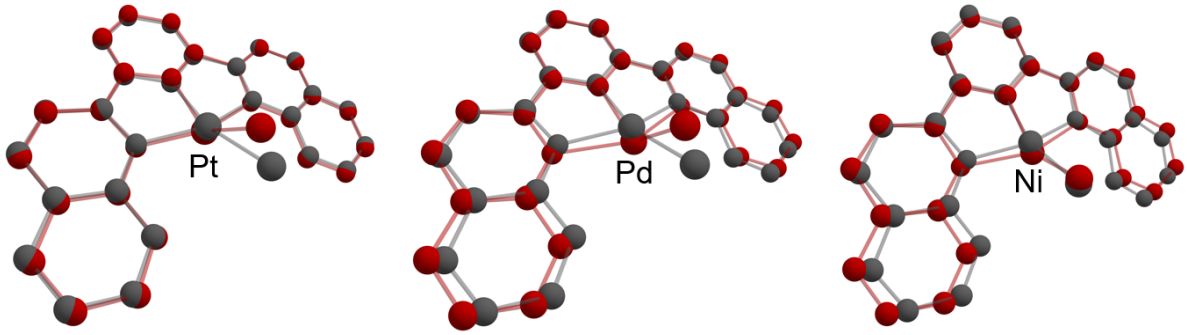


Figure 3-49. DFT-calculated geometries of [M(L^{Qu})Cl] (M = Pt, Pd, Ni) in the S_0 (black) and T_1 (red) states.

4. Conclusion and Outlook

In this study, cyclometalated complexes [M(N^C^N)Cl] (M = Pd and Pt) with hydrogen bond donors R = NH(C_6H_5) (HL^{NHPh}) or R = NH($C_6H_5CH_2$) (HL^{NHBn}) allowing for intramolecular hydrogen bonding with the Cl^- coligand were synthesized and characterized with respect to their structural, electrochemical and photophysical properties (Figure 4-1). We expected to minimize the usually occurring geometry distortion in the T_1 triplet excited state if compared with the S_0 singlet ground state. X-ray diffractometry on single crystals showed that the complexes adopt a square planar geometry around the metal, as expected for d^8-configured complexes, but with a marked out of plane distortion of the Cl^- coligand (with τ_4 values of around 0.2). We first assumed that the observed intramolecular hydrogen bonding involving the ligand-NH function and the Cl^- coligand is the reason for this distortion. However, DFT geometry-optimization for the model complexes [M(N^C^N)F] and [M(N^C^N)H] showed this distortion for the far smaller F^- and H^- coligands. Even more importantly, the model complexes [$M(L^{OMe})$Cl] bearing OMe substituents at the ortho-pyridyl positions also showed a distortion of the Cl^- coligand, even though no hydrogen bond is present. Thus, the bulkiness of the ortho-substituents in the herein reported [M(N^C^N)Cl] are the main cause for the out-of-plane distortion of the Cl^- coligands.

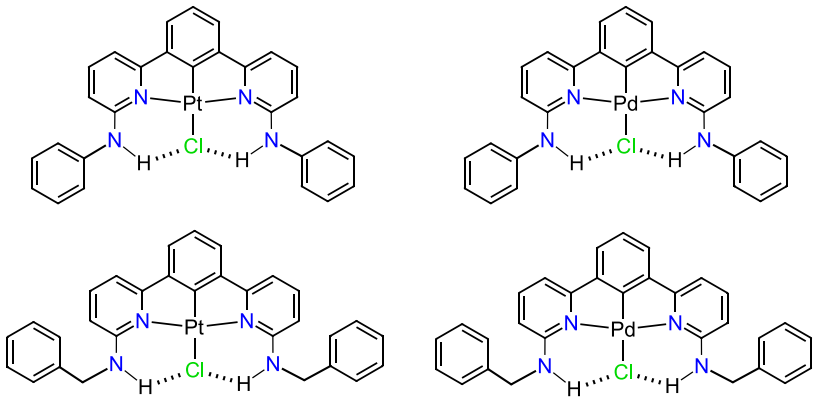


Figure 4-1. Cyclometalated complexes of [$M(L^{NHPh})$Cl] (up) and [$M(L^{NHBn})$Cl] (down).

As expected for homoleptic complexes with Pt(II) and Pd(II), the long-wavelength UV-vis absorption energies increase from Pt to Pd, paralleling the electrochemical HOMO-LUMO gaps. The Pt complexes are intense triplet emitters in solution at 298 K (λ_{max} = 520 nm) and reach a Φ_L of 0.63 at 77 K. The Pd derivatives showed vibronically structured phosphorescence bands in frozen glassy matrices at 77 K, very similar both in energy and in shape to those of the Pt complexes. However, they are essentially non-emissive at 298 K. The DFT-optimized electronic structures of the complexes show very similar

geometries for their S_0 and T_1 states as a result of the pre-distorted ground state (Figure 4-2). This, according to our initial expectations, should hamper non-radiative pathways. Nevertheless, the Pd(II) complexes did not show luminescence at 298 K, despite the similar geometries for T_1 and S_0. However, conical intersections between T_1 and S_0 are not the only non-radiative pathways. Moreover, the introduction of the NHR groups generally reduced the photoluminescence efficiency of the two Pt(II) complexes compared with the parent [Pt(dpb)Cl] derivative. This could be due to the marked red-shifted photoluminescence of the [M(N^C^N)Cl] complexes compared with non-substituted dpb derivatives, which would increase the non-radiative relaxation (energy-gap law). Furthermore, the involvement of the NHR groups might open non-radiative pathways in addition to those of the N^C^N scaffold. Further detailed study of their vibronic evolution and fate after initial excitation can help to get a more clear picture of the excited states.

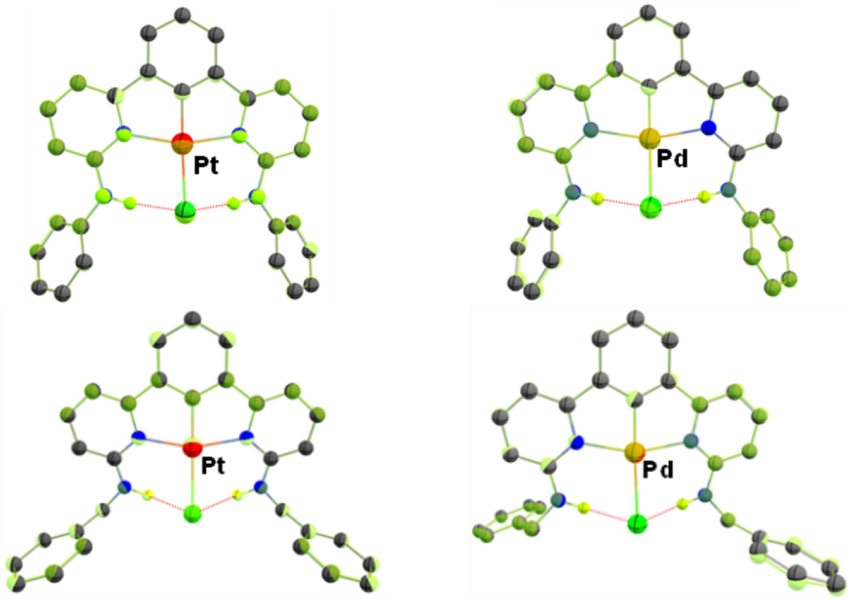


Figure 4-2. DFT-calculated geometries of [M(L^{NHPh})Cl] (up) and [M(L^{NHBn})Cl] (down) in the S_0 (black) and T_1 (green) states.

In continue of the study to replace precious transition metals like Pt by abundant base metals such as Ni towards efficient triplet emitters, the Ni(II) analogues of [M(L^{NHPh})Cl] and [M(L^{NHBn})Cl] complexes were synthesized and studied (Figure 4-3).

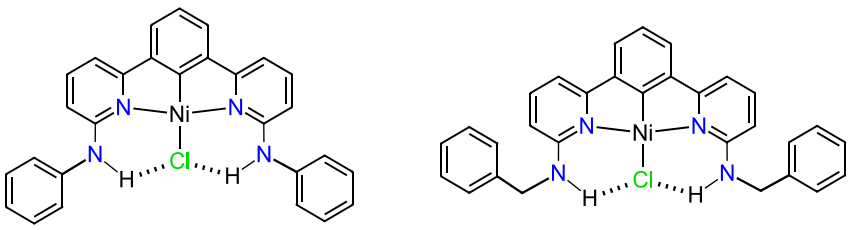


Figure 4-3. Cyclometalated complexes of [Ni(L^{NHPh})Cl] (left) and [Ni(L^{NHBn})Cl] (right).

The two cyclometalated complexes containing pendent hydrogen bond donor amine groups show a marked deviation of the Cl^- coligand from the ideally planar coordination, with τ_4 values of 0.35 and 0.33, respectively. We found that the steric strain of the ligand, rather than the observed N–H···Cl···H–N hydrogen bonding interactions of the NH function with the Cl^- coligand, is responsible for this observation. Importantly, the experimental molecular geometries from X-ray diffractometry agree very well with the DFT-calculated S_0 conformation. However, the excited T_1 state geometry involves significantly elongated Ni–N bonds (Figure 4-4).

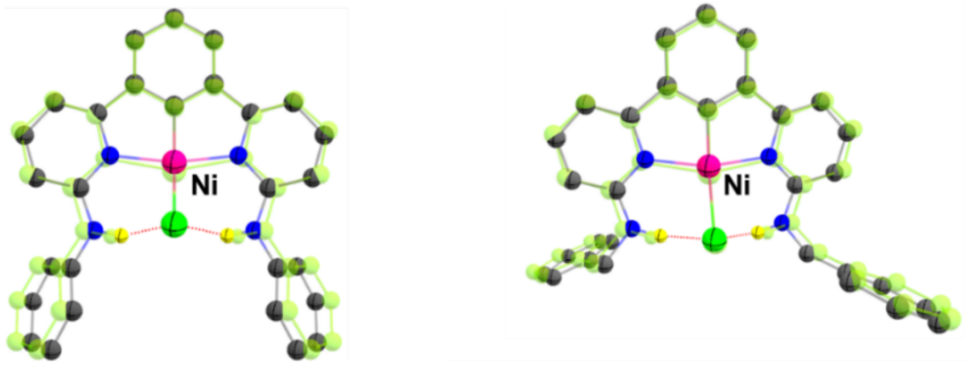


Figure 4-4. DFT-calculated geometries of [Ni(L^{NHPh})Cl] (left) and [Ni(L^{NHBn})Cl] (right) in the S_0 (black) and T_1 (green) states.

In solution, both complexes show long-wavelength absorption bands at around 425 nm, and the experimental spectra are reproduced by TD-DFT calculations. At 77 K in frozen 2MeTHF glassy matrices, the complexes display structured emission spectra with lifetimes in the nanosecond and millisecond range. To ensure that the emission does not originate from residual ligand, the ligand alone was measured at 77 K. Neither the emission spectra nor the lifetimes resemble those of the complexes, confirming that both the emission as well as the long and short lifetimes arise from the complexes (Figure 4-5).

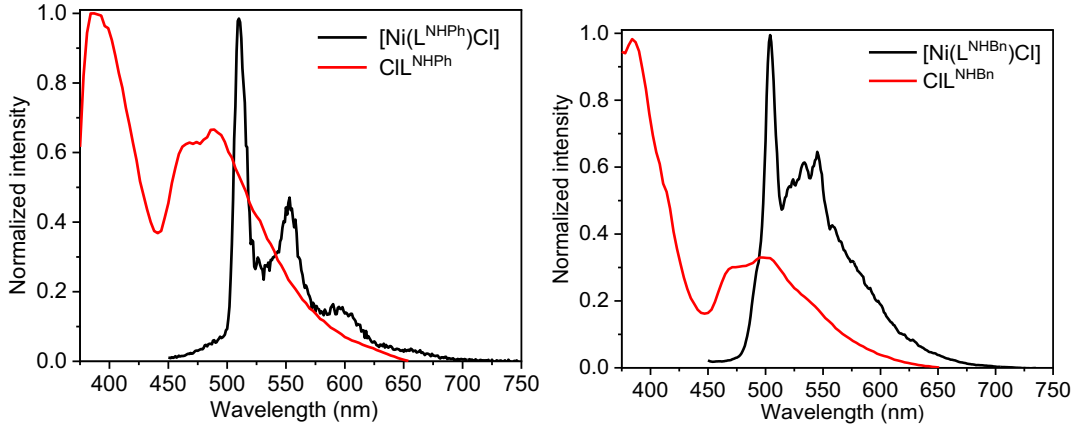


Figure 4-5. Emission spectra of complexes (black) and their respective ligands (red) in 2MeTHF at 77 K (c = 10^{-5} M), λ_{ex} = 350 nm.

Further investigations into the excited state dynamics using cryostat-supported nanosecond transient absorption spectroscopy did not reveal long-lived species. Instead, only short-lived transients with excited state absorptions (ESA) at 400 and 580 nm were identified with lifetimes of 722 ps for [Ni(L^{NHPh})Cl] and 1.94 ns for [Ni(L^{NHBn})Cl], resembling the ESAs of the free ligands. This suggests that, in contrast to the low temperature phosphorescence studies, the ESAs are ligand-centered and short-lived. However, potential chemical decomposition cannot be ruled out. In that particular case, ligand-based ESAs would stem from the free ligands in solution and/or the matrix upon decomposition. Long-lived emission, on the other hand, would originate from the phosphorescence of the intact complexes. Additionally a detailed theoretical analysis of the potential energy landscapes of the first ten excited states of the Ni(II) complexes revealed that the lowest triplet states decay non-radiatively due to conical intersections with the ground state. Contributions to the luminescence could originate from the S_1, S_4, or T_5 states. The theoretical emission wavelengths from the T_5 state agree particularly well with the experimental results. Moreover, if the elongation of the Ni–N bonds is suppressed in a rigid environment, the theoretical S_4 emission wavelengths also lie close to the experimental results.

To further probe the role of hydrogen bonding in enhancing the rigidity of structures and its controlling aspect over the extents of excited state distortions, a set of [M(N^C^N)Cl] complexes (M = Pt, Pd, and Ni) in which the two ortho-positions of the pyridyl rings were substituted with benzyl groups (Bn), N^C^N = L^{Bn}, instead of NHR functionalities in the previous complexes were synthesized (Figure 4-6).

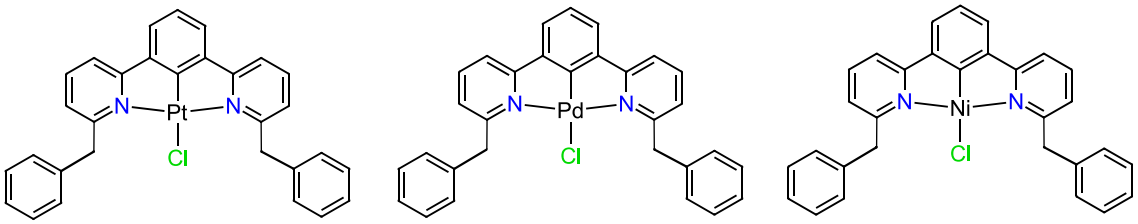


Figure 4-6. Cyclometalated complexes of [M(L^{Bn})Cl].

Single-crystal X-ray diffraction revealed distorted square planar coordination with significant out-of-plane tilting of the Cl^- coligand, particularly for Ni(II). This distortion is reflected in the excited state geometries, where the C–M–Cl angle experiences further deviation in the T_1 state—by 32.3° and 34.8° for Pt(II) and Pd(II), respectively, and 17.6° for Ni(II)—suggesting that steric bulk alone can induce structural distortion. It is worth noting that other critical metrics surrounding the metal atoms exhibit minimal changes, with the pyridyl rings of the cyclometalated L^{Bn} ligand remaining coplanar in the complexes.

Photophysical studies show that the Pt(II) complex emits at RT in both solution and solid state. When incorporating into PMMA matrices at varying concentrations, the emission maximum shifted from

496 nm to 544 nm as the concentration increased from 0.5% to 5%. This shift and changes in the emission profile suggest the formation of emissive molecular aggregates. In contrast, the Pd(II) and Ni(II) complexes are non-emissive at RT due to faster non-radiative deactivation via ^{3}MC sates. However, at 77 K, these complexes exhibit emission, with the Ni(II) complex showing particularly high quantum yield (Φ_L = 20%), suggesting a reduced rate of non-radiative deactivation due to rigidified structure (Figure 4-7).

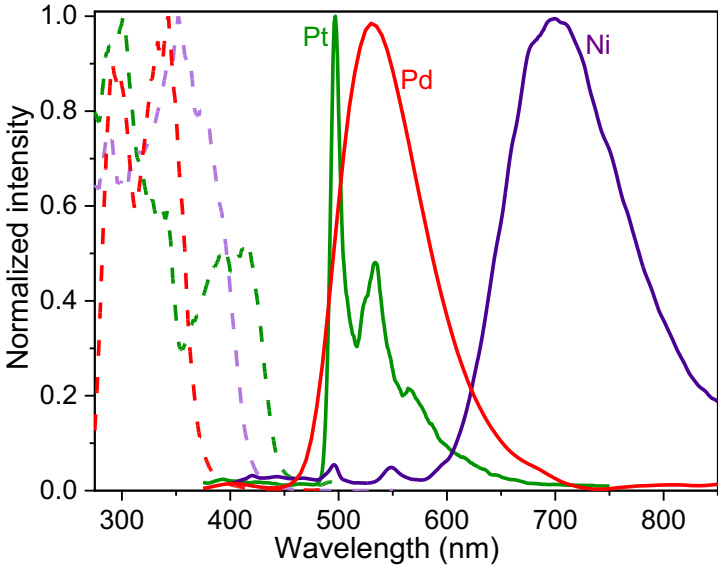


Figure 4-7. Photoluminescence emission (lines) and excitation (dash lines) spectra of [M(L^{Bn})Cl] complexes in 2MeTHF at 77 K as a glassy matrix (λ_{ex} = 350 nm).

When comparing theses findings with [M(L^{NHPh})Cl] and [M(L^{NHBn})Cl] complexes featuring the M–Cl···H–N hydrogen bonds, it is evident that while hydrogen bonding has been shown to stabilize the excited states and improve photoluminescence in Ni(II) systems, the new approach using steric bulk alone can also minimize excited state distortions to some level and enhance rigidity. This study confirms that modifications in the second coordination sphere, whether through non-covalent interactions like hydrogen bonding or through steric effects, play a critical role in controlling the photophysical behavior of transition metal complexes.

To further explore and refine the influence of hydrogen bonding on photophysical properties, a series of Pt(II) and Pd(II) complexes, [M(L^{NHPh})OPh] and [M(L^{NHBn})OPh], derived from their pre-designed chloride-coordinated counterparts were synthesized (Figure 4-8).

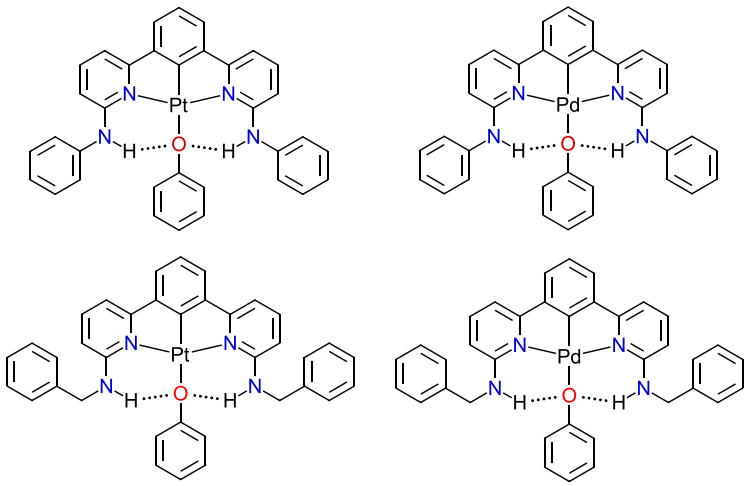


Figure 4-8. Cyclometalated complexes of [M(L^{NHPh})OPh] (up) and [M(L^{NHBn})OPh] (down).

Their crystal structures revealed the formation of strong and well-defined N–H···O···H–N hydrogen bonds between the OPh coligand and the amine groups positioned ortho to the pyridyl rings. By embedding phenolate at the fourth coordination site of the N^C^N cyclometalated Pt(II) and Pd(II) complexes, a secondary coordination sphere was established, enhancing the molecular planarity compared to their chloride-coordinated analogs (Figure 4-9). This structural refinement underscores the potential of such built-in hydrogen motifs to influence the overall coordination geometry and molecular architecture.

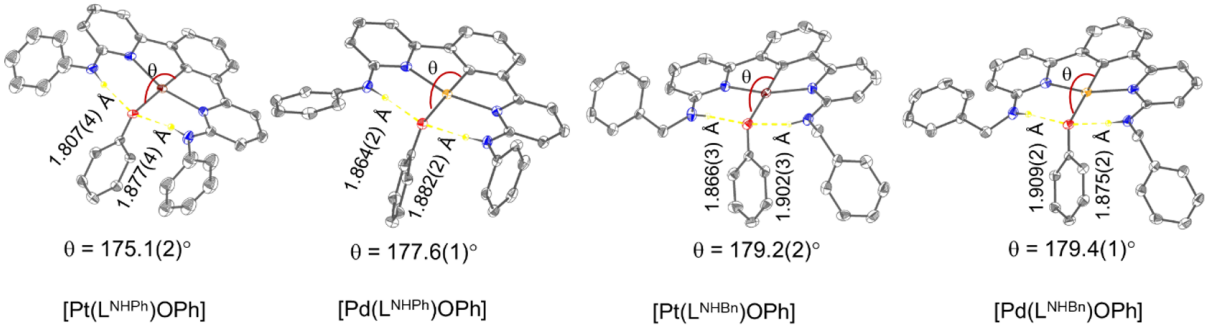


Figure 4-9. Side-on view molecular structures of [M(L^{NHPh})OPh] and [M(L^{NHBn})OPh] complexes from X-ray diffractometry on single crystals featuring the C–M–O angle and O···H distances.

While photophysical studies of these systems are ongoing, electrochemical measurements via cyclic voltammetry revealed cathodic shifts in oxidation potentials, consistent with the stronger σ-donor character of the OPh^- coligand relative to Cl^-. These results highlight the potential of targeted hydrogen bonding motifs to modulate electronic structure and coordination geometry.

To extend the study on the influence of electronic and steric effects, a series of [M(N^C^N)X] complexes (M = Pt, Pd, Ni; X = Cl or Br) using dpb derivatives substituted with electron-donating (Me) or electron-withdrawing (F or Cl) groups were synthesized (Figure 4-10).

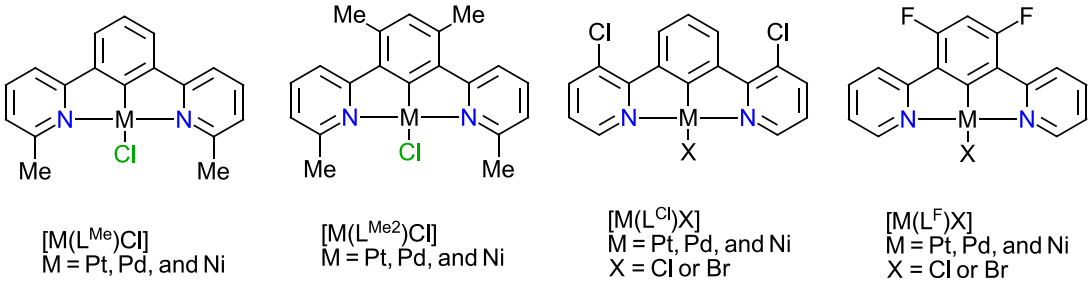


Figure 4-10. Cyclometalated complexes with electron-donating (Me) or electron-withdrawing (F or Cl) groups.

A combination of experimental techniques along with DFT calculations, was used to elucidate how ligand substitution and metal identity affect the electronic and photophysical behaviour of these complexes. X-ray diffraction and DFT-optimized geometries confirmed the expected square planar coordination around the metal centers for all complexes. However, the Me-substituted complexes displayed significant out-of-plane distortion of the chloride coligand ($\tau_4 \approx 0.3$), which is attributed to the steric bulk of the ortho-methyl groups. In contrast, F- and Cl-substituted complexes exhibited minimal distortion ($\tau_4 \approx 0.1$). The energy of the longest-wavelength absorption maxima follows the trend Ni < Pt < Pd, consistent with both electrochemical and DFT-calculated HOMO-LUMO gaps. Introducing electron-donating Me groups caused red shifts in the absorption maxima (e.g., from 401 nm for [Pt(dpb)Cl] to 420 nm for [Pt(L^{Me})Cl]), while electron-withdrawing substituents led to blue shifts. Photoluminescence studies revealed that the Pt(II) complexes are highly efficient triplet emitters, particularly at low temperatures, with quantum yields approaching unity for [Pt(L^{Cl})Cl] and [Pt(L^{F})Cl]. While Pd(II) complexes exhibited less intense, structured phosphorescence at 77 K, indicating mixed MLCT and LC transitions. These results demonstrate that in case of Pt(II) and Pd(II) complexes, the introduction of electron-donating groups led to red-shifted emission and lower quantum yields, while electron-withdrawing groups produced blue-shifted emission with enhanced radiative decay rates. Ni(II) complexes showed weak luminescence due to rapid non-radiative deactivation via ^{3}MC states, in agreement with previous studies.

Finally, as an alternative approach to enhance structural rigidity and phosphorescence efficiency, quinoline (Qu) units were incorporated into the N^C^N ligand framework, synthesizing [M(L^{Qu})Cl] (M = Pt, Pd, Ni; L^{Qu} = bis(2-pyridyl)/2-quinolyl)benzene) complexes (Figure 4-11).

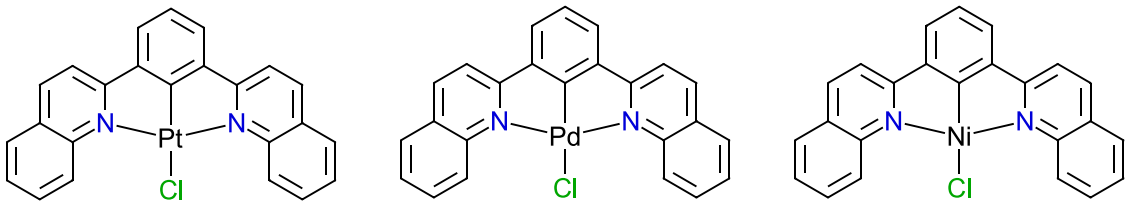


Figure 4-11. Cyclometalated complexes of [M(L^{Qu})Cl].

While photophysical studies are still underway, initial findings provide valuable structural insights. X-ray crystallographic data revealed distorted square planar geometries across all three complexes, primarily due to significant out-of-plane distortion of the Cl^- coligand. This distortion was most pronounced for [Ni(L^{Qu})Cl], with a τ_4 value of 0.354. Similar features have reported for [M($L^{NHPh\ or\ NHBn}$)Cl], [M(L^{Bn})Cl], and [M(L^{Me})Cl] (M = Pt, Pd, and Ni) complexes. Despite this distortion, the remainder of the molecular framework remained nearly planar, enabling head-to-tail stacking and strong intermolecular π···π stacking interactions between pyridyl and phenyl units of neighboring molecules (Figure 4-12). Notably, no significant metallophilic M···M interactions were observed, consistent with the larger metal-metal distances. Structurally, the quinoline functionalized N^C^N ligands induced minimal reorganization between the ground state (S_0) and the lowest triplet excited state (T_1) for the Pt(II) complex, whereas Pd(II) and Ni(II) derivatives, exhibited more pronounced reorganization effects.

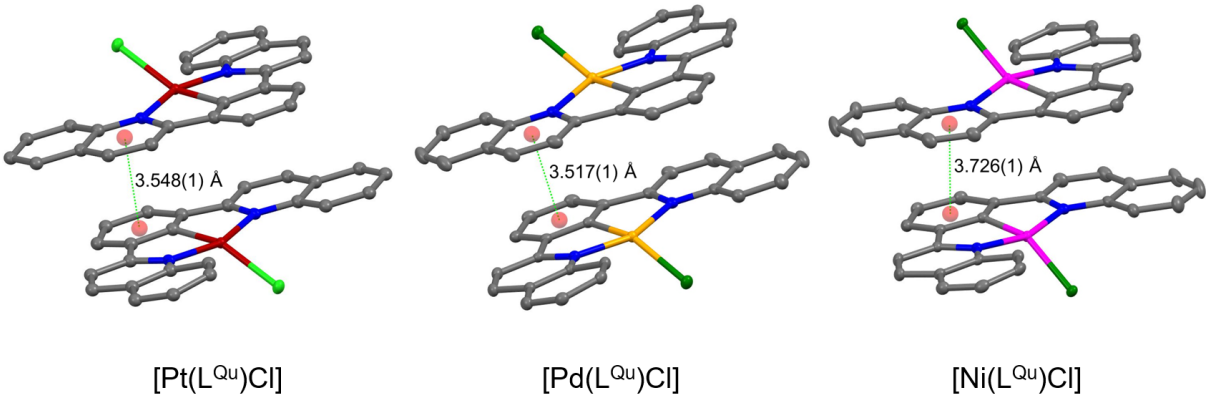


Figure 4-12. The packing of complexes from X-ray diffractometry on single crystals featuring the intermolecular interactions.

Furthermore, the introduction of quinoline units resulted in slight red shifts in the long-wavelength absorption bands of the complexes, attributed to the enhanced π-acceptor properties of quinoline compared to unsubstituted pyridine-based ligands. These finding underscore the potential of quinoline functionalized N^C^N ligands to influence structural, electronic, and photophysical properties, laying the groundwork for further studies on their phosphorescence efficiency and application in photonic materials.

Future ideas to tune the emitter properties within the cyclomatalated Pt, Pd, and Ni complexes, should explore how different steric and electronic modifications influence molecular rigidity, excited state dynamics, and photophysical properties. In particular, systemic variations in ligand design—such as fine-tuning steric bulk (Figure 4-13), introducing alternative hydrogen-bond donors/acceptors (Figure 4-14), or modifying electronic properties through tetradentate or even bidentate ligands (Figure 4-15)—could provide deeper insights into optimizing emission efficiency and excited state life time. Extending these concepts to other transition metals beyond Ni(II), including earth-abundant alternatives, may further contribute to the rational design of next generation phosphorescent materials for optoelectronic applications.

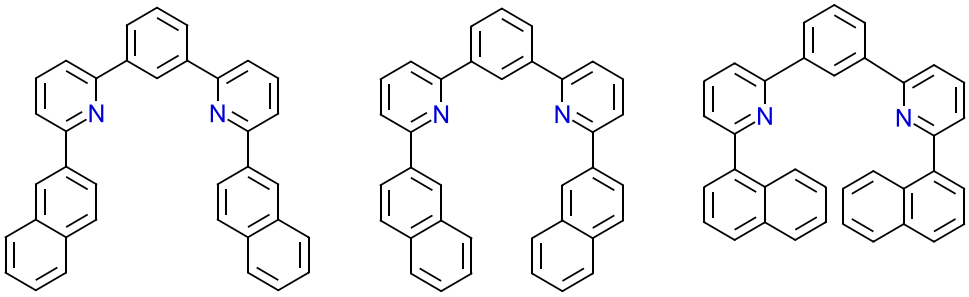


Figure 4-13. Structure of tridentate cyclometalating ligands for steric and electronic modifications.

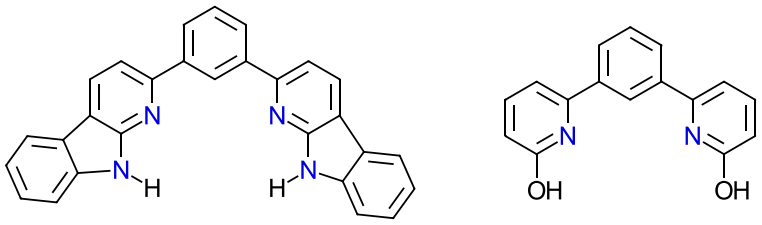


Figure 4-14. Structure of tridentate cyclometalating ligands bearing different hydrogen bonds.

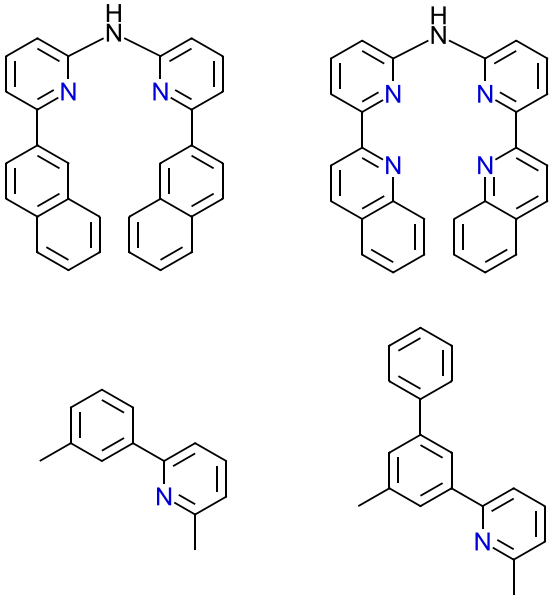


Figure 4-15. Structure of tetradentate (up) and bidentate (down) cyclometalating ligands for steric and electronic modifications.

5. Experimental Section

5.1. Materials and methods

Commercially available chemicals were obtained from *BLDPharm*, *ACROS*, *Sigma Aldrich*, *Carbolution*, *TCI*, and *Alpha Aesar* and used as received without further purification. Dry tetrahydrofuran (THF) was freshly distilled over a Na/K alloy (3:7), *p*-xylene was freshly distilled over sodium. Other dry solvents were soured from commercial argon-flushed bottles containing molecular sieves or dried over activated molecular sieves in *Schlenk* flasks prior to use.

Air and moisture sensitive reactions were conducted under an inert argon atmosphere using *Schlenk*-techniques. Glassware was thoroughly dried by heating under vacuum and subsequently cooled and flushed with argon to ensure inert conditions.

NMR spectroscopy. ^{1}H, ^{13}C, and ^{19}F spectra were recorded on a *Bruker* Avance II 300 MHz (^{1}H: 300 MHz, ^{13}C: 75 MHz, ^{19}F: 282 MHz) equipped with a double resonance (BBFO) 5 mm observe probe head with z-gradient coil, *Bruker* Avance III 500 MHz (^{1}H: 500 MHz, ^{13}C: 126 MHz), and Bruker Avance II 600 MHz spectrometer (^{1}H: 600 MHz, ^{13}C: 151 MHz) with a triple resonance (TBI) 5 mm inverse probe head with z-gradient coil using a triple resonance (*Bruker*, Rheinhausen, Germany). The unambiguous assignment of the ^{1}H and ^{13}C resonances was obtained from ^{1}H NOESY, ^{1}H COSY, ^{1}H ^{13}C HSQC, and ^{1}H ^{13}C HMBC experiments. All 2D NMR experiments were performed using standard pulse sequences from the *Bruker* pulse program library. Chemical shifts were referenced to tetramethylsilane (TMS) for ^{1}H and ^{13}C spectra (δ = 0.00 ppm) or to the respective solvent shift for ^{1}H and ^{13}C spectra using residual ^{1}H and ^{13}C solvent signals and to α,α,α-trifluorotoluene (TFT, δ = –63.7 ppm) for ^{19}F spectra. All data was processed and visualized using the software MestReNova 14.2.2.

UV/vis absorption spectroscopy. UV/vis absorption spectra were recorded on a Cary 50 and a Cary 60 spectrophotometer by Varian (*Varian Medical Systems*, Darmstadt, Germany) at ambient temperature using quartz glass cuvettes with an optical path length of 1 cm. All spectra are baseline corrected. The spectra were plotted using Origin 2021.

Mass spectroscopy. High resolution electrospray ionization **(**HR-ESI) spectra were measured at the *Thermo Scientific* LTQ OrbitrapXL mass spectrometer via electron spray ionization and a FTMS Analyzer. Simulations were performed using ISOPRO 3.0. EI(+) mass spectra were measured using a *Thermo Scientific* Exactive GC Orbitrap analyser mass spectrometer (*Thermo Fisher Scientific GmbH*, Dreieich, Germany) or a Finnigan MAT 95 spectrometer (*Finnigan Instrument Corporation*, Bremen, Germany) with an ionisation energy of 70 eV. The spectra were simulated using ISOPRO 3.0.

Cyclic Voltammetry (CV). CV measurements were carried out in 0.1 M *n*-Bu_4NPF_6 solution in THF (tetrahydrofuran) with a scan rate of 100 mV/s using a three-electrode configuration (glassy carbon working electrode, Pt counter electrode, Ag/AgCl reference) and an Autolab PGSTAT30 or μStat400 potentiostat by *Metrohm* (*Metrohm*, Filderstadt, Germany). The potentials were referenced against the ferrocene/ferrocenium redox couple as internal standard. The data was analyzed and plotted using Origin 2021.

Crystal structure determination. The measurements were performed using a *Bruker* D8 Venture, including a *Bruker* Photon 100 CMOS detector, a *Bruker* **D8 Quest** (*Bruker*, Rheinhausen, Germany) or an IPDS II T diffractometer (*STOE & Cie.,* Darmstadt, Germany) at 293 K or 100 K using Mo-Kα radiation (λ = 0.71073 Å). The crystal data was collected using X-AREA[123] or APEX3 v2015.5–2.[124] The structures were solved by dual space methods using SHELXT (*Sheldrick* 2015)[125] and the refinement was carried out with SHELXL 2017 employing full-matrix least-squares methods on $F_0^2 \geq 2\sigma(F_0^2)$.[126] The numerical absorption corrections (X-RED32v1.31)[127] were performed after optimizing the crystal shapes using XSHAPE V1.06.[128] The non-hydrogen atoms were refined with anisotropic displacement parameters without any constraints. The hydrogen atoms were included by using appropriate riding models.. The illustration of crystal structures was performed using Diamond. The data of the structural solutions and refinements are available at https://summary.ccdc.cam.ac.uk/ structures of the Cambridge Crystallographic Data Centre (CCDC).

Elemental analyses. The elemental analysis results were obtained using a *HEKAtech* CHNS EuroEA 3000 analyzer (HEKAtech, Wegberg, Germany).

Photophysical measurements. Steady-state excitation and emission spectra were recorded on a FluoTime 300 spectrometer from *PicoQuant* equipped with a 300 W ozone-free Xe lamp (250-1100 nm), a 10 W Xe flash-lamp (250-1100 nm, pulse width ca. 1 μs) with repetition rates of 0.1 – 300 Hz, a double-grating excitation monocromator (Czerny-Turner type, grating with 1200 lines/mm, blazed wavelength: 300 nm), diode lasers (pulse width < 20 ps) operated by a computer-controlled laser driver PDL-828 "Sepia II" (repetition rate up to 80 MHz, burst mode for slow and weak decays), two emission monochromators (*Czerny-Turner*, selectable between double-grating blazed at 500 nm with 2.7 nm/mm dispersion and 1200 lines/mm, or single-grating blazed at 1250 nm with 5.4 nm/mm dispersion and 600 lines/mm) with adjustable slit width between 25 μm and 7 mm, Glan-Thompson polarizers for excitation (after the Xe-lamps) and emission (after the sample). Different sample holders (Peltier-cooled mounting unit ranging from –15 to 110 °C or an adjustable front-face sample holder), along with two detectors (namely a PMA Hybrid-07 from PicoQuant with transit time spread FWHM < 50 ps, 200 – 850 nm, or a H10330C-45-C3 NIR detector with transit time spread FWHM 0.4 ns, 950 to 1400 nm from Hamamatsu) were used. Steady-state spectra and photoluminescence lifetimes were recorded in

TCSPC mode by a *PicoHarp* 300 (minimum base resolution 4 ps) or in MCS mode by a *TimeHarp* 260 (where up to several ms can be traced). Emission and excitation spectra were corrected for source intensity (lamp and grating) by standard correction curves. For samples with lifetimes in the ns order, an instrument response function calibration (IRF) was performed using a diluted Ludox® dispersion. Lifetime analysis was performed using the commercial EasyTau 2 software (*PicoQuant*). The quality of the fit was assessed by minimizing the reduced chi squared function (χ^2) and visual inspection of the weighted residuals and their autocorrelation. For the low temperature measurements (up to 6K), a Cryostat model DE-204S (ARS) with two DT-670B-SD thermocouples attached, coupled to a Helium ARS-4HW Compressor (ARS) was used. Temperature was controlled using a Cryogenic Temperature Controller (*Lake Shore*, Model 335).

Luminescence micrographs were acquired using an optical microscope (IX 73 from Olympus), equipped with a X-CiteQ Lamp module (*Excelitas Technologies*) as excitation source and a UI-5580SE (IDS) digital camera. Different band pass (BP) and low pass (LP) cubes were using accordingly.

Luminescence quantum yields were measured with a Hamamatsu Photonics absolute PL quantum yield measurement system (C9920-02) equipped with a L9799-01 CW Xenon light source (150 W), monochromator, C7473 photonic multi-channel analyzer, integrating sphere and employing U6039-05 PLQY measurement software (Hamamatsu Photonics). All cuvettes used were round quartz cuvettes and the solvents were of spectrometric grade (Uvasol®, Merck, Darmstadt, Germany).

Nanosecond transient absorption (nsTA) experiments were recorded with the EOS TAPPS detection unit from Ultrafast systems using two independent pulsed laser sources. While the pump pulse is also generated by an amplified Ti:sapphire CPA-2101 laser system from Clark:MXR Inc., the probe pulse is generated by a pulsed supercontinuum laser (output 350 – 2,200 nm, repetition rate of 2,100 Hz, and 1 ns pulse width). The electronic setup allows for time delays up to 400 μs between the pump and probe pulse. The excitation wavelength of 365 nm were generated by a noncolinear optical para-metric amplifier (NOPA, Clark:MXR Inc.). For the nsTA measurements, global analysis and fitting of the transient data was carried out utilizing the open-source software GloTarAn, which is a free, Java-based graphical user interface to the R-package TIMP.[129–131] Global analysis was performed on the TA data sets using a sequential model. The instrument response function (IRF) and dispersion (chirp of the white light pulse) were modelled and taken into account during the fitting procedure. The nsTA data sets were corrected for scattered light as well. Cryostat supported measurements between 297 and 80 K were conducted using an Optistat DN2 cryostat from Oxford Instruments in 2-methyltetrahydrofuran (MeTHF, SIGMA-ALDRICH, anhydrous, ≥ 99%).

Quantum chemical calculations using density functional theory (DFT). All DFT calculations were performed using the Gaussian 16 suite of programs.[132] For all atoms, def2-TZVP basis sets, as well as

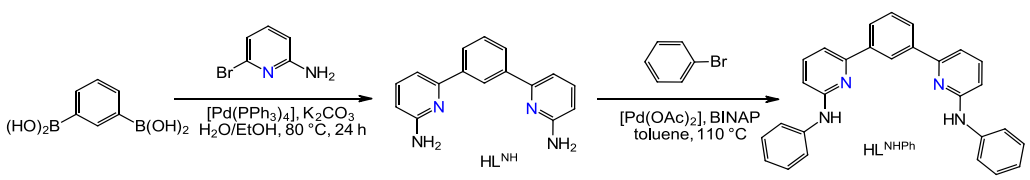
the corresponding def2-ECPs for Pt and Pd (ecp-46 and ecp-28) were used for the core electrons.[114,133] In case of [M(L^{NHPh})Cl] and [M(L^{NHBn})Cl] complexes, the LanL2DZ [134] basis set was used with effective core potentials ecp(10/18) for Ni, ecp(28/18) for Pd, ecp(60/18) for Pt by Hay and Wadt,[135–137] while the 6-31G(d)[9] basis set was used for non-metallic elements. The S_0 and T_1 geometries of all compounds were optimized with the hybrid functional TPSSh, using *Grimm´s* D3 dispersion correction and the conductor-like polarizable continuum model (CPCM) parametrized for THF as an approximate solvation model.[138–141] Geometry optimization of all complexes was followed by frequency calculations and yielded no imaginary modes, thus confirming the energetically minimal nature of the stationary points. Orbital isosurfaces were extracted from the singlet point calculation and plotted using the visualization software Chemcraft at isovalue of 0.3.

To obtain the UV-vis absorption spectrum of the complexes, TD-DFT calculations of the 45 lowest excited singlet states were performed at the optimized S_0 geometry. Molecular orbitals and electronic properties were extracted from the single point calculations. The emission spectra were calculated using the Franck-Condon approximation according to the method of Barone et al.[142,143] and frequency analysis calculations of optimized geometries in the S_0 and T_1 states. The TD-DFT calculation output was further evaluated using the software package TheoDORE to analyze relative MLCT, L'MCT, LC, LL'CT, and MC contributions to the emissive T_1 states, using the implemented standard algorithm for molecular partitioning of transition metal complexes employing Openbabel.[110]

Structural Distortion Calculations Using Time-Dependent Density Functional Theory (TD-DFT) with the Tamm-Dancoff Approximation (TDA): All calculations were performed using the Gaussian 16 suite of programs[132] with the PBE0 exchange-correlation functional[113] including the D3 version of Grimme's dispersion with Becke-Johnson damping[139] for the van-der-Waals interaction. The SDD basis set, which applies an effective core potential for the metal atoms,[114] was used for all elements, including nickel. Here, no PCM solvation models were used to simulate a solvent. Molecular orbitals were visualized using VMD[144] with an isovalue of 0.02. Geometrical optimizations in the ground state S_0 were carried out with Kohn-Sham DFT for scans, where the two-central nickel-nitrogen bonds were fixed at increasing values. For each resulting geometry a TD-DFT calculation with TDA[112] was conducted.

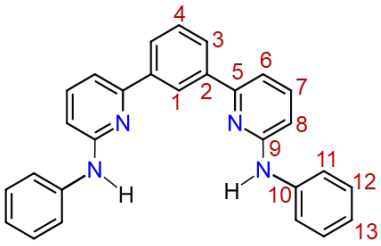
5.2. Experimental procedures

5.2.1. Syntheses of the N^C^N ligand precursor HL^{NHPh}



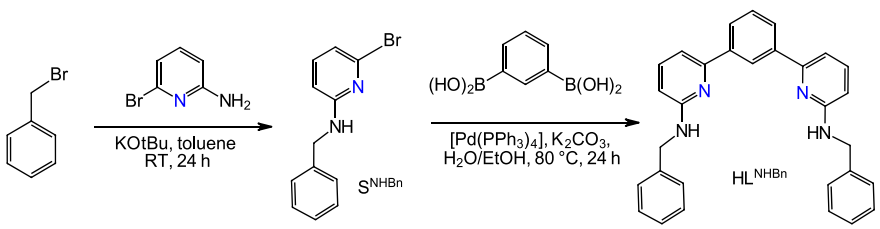
Synthesis of HL^{NH}. 1,3-phenylenediboronic acid (0.23 g, 1.40 mmol), 2-amino-6-bromopyridine (0.35 g, 2.00 mmol), [Pd(PPh$_3$)$_4$] (0.07 g, 3.00 mol%), and K$_2$CO$_3$ (0.55 g, 4.00 mmol) were mixed and dissolved in 15 mL H$_2$O/EtOH (1:1, degassed). The solution was stirred for 24 h at 80 °C under an argon atmosphere. After allowing the reaction mixture to cool to room temperature, the mixture was filtered and diluted with 30 mL EtOAc. The resulting solution was washed with brine (5 × 20 mL), separated and dried over anhydrous Na$_2$SO$_4$. After evaporation of the solvent, the residue was washed with n-hexane (*n*-Hex) to give an off-yellow precipitate. Recrystallization from CH$_2$Cl$_2$ produced off-white and pure amorphous material. Yield: 0.184 g (0.7 mmol, 70%). ^{1}H NMR (600 MHz, CD$_2$Cl$_2$, 298 K): δ /ppm = 8.57 (t, *J* = 1.7 Hz, 1H, H1), 7.95 (dd, *J* = 7.7, 1.8 Hz, 2H, H3), 7.53 (t, *J* = 7.8 Hz, 2H, H7), 7.50 (t, *J* = 7.7 Hz, 1H, H4), 7.19 (dd, *J* = 7.5, 0.4 Hz, 2H, H6), 6.50 (d, *J* = 8.0, 2H, H8), 4.66 (s, 4H, NH$_2$). ^{13}C NMR (151 MHz, CD$_2$Cl$_2$, 298 K): δ /ppm = 159.09 (C9), 156.17 (C5), 140.36 (C2), 138.89 (C7), 129.16 (C4), 127.37 (C3), 125.66 (C1), 111.11 (C6), 107.67 (C8). HR-EI MS(+): calcd. for C$_{16}$H$_{14}$N$_4$ m/z = 262.12130; found m/z = 262.12081 [M]$^+$. Elemental analysis calcd. (%) for C$_{16}$H$_{14}$N$_4$, M = 262.31 g mol^{-1}: C, 73.26; H, 5.38; N, 21.36. Found C, 73.34; H, 5.33; N, 21.29.

Synthesis of HL^{NHPh}. To a solution of Pd(OAc)$_2$ (0.03 g, 10.00 mol%), and *rac*-BINAP (0.14 g, 20.00 mol%) in dry toluene (50 mL) we added HL^{NH} (0.30 g, 1.14 mmol), bromobenzene (0.29 mL, 2.74 mmol), and KOtBu (0.26 g, 2.28 mmol). The solution was stirred at 110 °C under an argon atmosphere for 3 d. The solution was filtered to remove residual KOtBu and then concentrated under vacuo to afford the crude product, which was further purified by flash chromatography using *n*-Hex:EtOAc (7:3 v/v). Yield: 0.298 g (0.72 mmol, 63%).



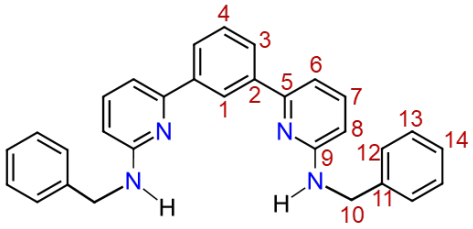
^{1}H NMR (600 MHz, DMSO-*d*$_6$, 298 K): δ /ppm = 9.16 (s, 2H, NH), 8.77 (t, *J* = 1.6 Hz, 1H, H1), 8.12 (dd, *J* = 7.7, 1.8 Hz, 2H, H3), 7.86–7.80 (m, 4H, H11), 7.74–7.69 (m, 2H, H7), 7.63 (t, *J* = 9.7, 1H, H4), 7.43 (d, *J* = 7.5 Hz, 2H, H6), 7.31–7.26 (m, 4H, H12), 6.89 (t, *J* = 7.3 Hz, 2H, H13), 6.85 (d, *J* = 8.2 Hz, 2H, H8). ^{13}C NMR (151 MHz, DMSO-*d*$_6$, 298 K): δ /ppm = 155.58 (C9), 153.88 (C5), 141.68 (C10), 139.55 (C2), 138.27 (C7), 129.16 (C4), 128.61 (C12), 126.61 (C3), 124.35 (C1), 120.49 (C13), 118.10 (C11), 110.50 (C6), 109.82 (C8). HR-EI MS(+): calcd. for C$_{28}$H$_{22}$N$_4$ m/z = 414.18390; found m/z = 414.18139 [M]$^+$. Elemental analysis calcd. (%) for C$_{28}$H$_{22}$N$_4$, M = 414.5 g mol^{-1}: C, 81.13; H, 5.35; N, 13.52. Found C, 81.16; H, 5.38; N, 13.52.

5.2.2. Synthesis of the N^C^N ligand precursor HL^{NHBn}



Synthesis of S^{NHBn}. To a solution of 2-amino-6-bromopyridine (17.34 mmol, 3.00 g), and KOtBu (19.00 mmol, 2.14 g) in dry toluene (50 mL), benzyl bromide (20.80 mmol, 2.50 mL) was added and the solution stirred at room temperature for 24 h. The mixture was extracted with EtOAc and the extracts washed with brine (3 × 50 mL). The combined organic layers were dried over Na_2SO_4. After evaporation of the solvent, the product was purified by column chromatography with *n*-Hex:EtOAc (9:1 v/v). Yield: 3.88 g (14.7 mmol, 85%). ^{1}H NMR (300 MHz, acetone-d_6, 298 K): δ /ppm = 7.43–7.28 (m, 5H), 7.25 (t, *J* = 7.5 Hz, 1H), 6.68 (dd, *J* = 7.4, 0.6 Hz, 1H), 6.61 (s, 1H, NH), 6.51 (dd, *J* = 8.2, 0.7 Hz, 1H), 4.54 (d, *J* = 6.0 Hz, 2H). ^{13}C NMR (75 MHz, acetone-d_6, 298 K): δ /ppm = 160.03, 140.77, 140.71, 140.15, 129.17, 128.32, 127.68, 115.62, 107.18, 45.62.

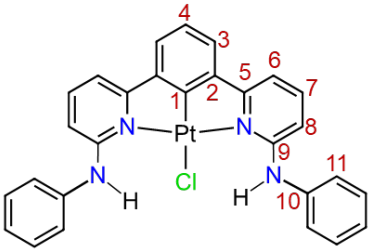
Synthesis of HL^{NHBn}. 1,3-phenylenediboronic acid (0.88 g, 5.32 mmol), S^{NHBn} (2.00 g, 7.60 mmol), $[Pd(PPh_3)_4]$ (0.26 g, 3.00 mol%), and K_2CO_3 (2.10 g, 15.20 mmol) were mixed and dissolved in 50 mL H_2O/EtOH (1:1, degassed). The solution was stirred for 24 h at 80 °C under an argon atmosphere. After allowing the reaction mixture to cool to room temperature, the mixture was filtered and diluted with 60 mL EtOAc. The resulting solution was washed with brine (5 × 20 mL), separated and dried over anhydrous Na_2SO_4. The crude product was purified by column chromatography with *n*-Hex:EtOAc (8:2 v/v). Yield: 1.19 g (2.7 mmol, 71%). ^{1}H NMR (600 MHz, DMSO-d_6, 298 K): δ /ppm = 8.58 (t, *J* = 1.5 Hz, 1H, H1), 7.97 (dd, *J* = 7.7, 1.7 Hz, 2H, H3), 7.49 (t, *J* = 8.0 Hz, 2H, H7), 7.47 (t, *J* = 7.8 Hz, 1H, H4), 7.40 (d, *J* = 7.1 Hz, 4H, H12), 7.30 (t, *J* = 7.6 Hz, 4H, H13), 7.24–7.16 (m, 4H, H14 and NH), 7.08 (d, *J* = 7.3 Hz, 2H, H6), 6.53 (d, *J* = 8.3 Hz, 2H, H8), 4.59 (d, *J* = 5.7 Hz, 4H, H10). ^{13}C NMR (151 MHz, DMSO-d_6, 298 K): δ /ppm = 158.24 (C9), 153.78 (C5), 140.91 (C11), 139.55 (C2), 137.63 (C7), 128.59 (C4), 128.18 (C13), 127.34 (C12), 126.48 (C14), 126.27 (C3), 124.15 (C1), 108.08 (C6), 107.46 (C8), 44.27 (C10). HR-EI MS(+): calcd. for $C_{30}H_{26}N_4$ m/z = 442.21520; found m/z = 442.21441 $[M]^+$. Elemental analysis calcd. (%) for $C_{30}H_{26}N_4$, M = 442.55 g mol^{-1}: C, 81.42; H, 5.92; N, 12.66. Found C, 81.38; H, 5.98; N, 12.69.



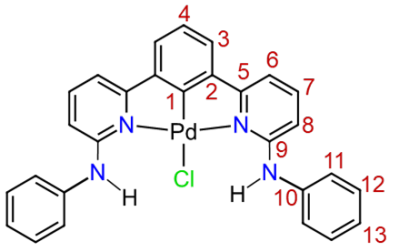
5.2.3. Synthesis of $[M(L^{NHPh})Cl]$ and $[M(L^{NHBn})Cl]$ (M = Pt or Pd) complexes

Modifying a previously reported method,[92] a mixture of 1.0 eq. $K_2[PtCl_4]$ or $K_2[PdCl_4]$ and 1.0 eq. of the proto-ligands HL^{NHPh} or HL^{NHBn} suspended in 8 mL glacial acetic acid and stirred at 110 °C for 3 d. The crude products were filtered off, washed with MeOH, H_2O, EtOH and Et_2O. Further purification was done by crystallizing the products in DMSO and washing the crystals with cold acetone.

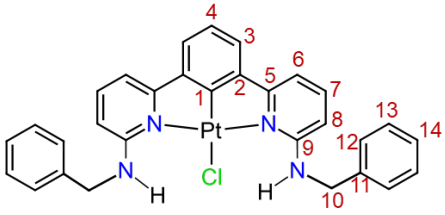
[Pt(L^{NHPh})Cl]. From $K_2[PtCl_4]$ 0.11 g (0.27 mmol), HL^{NHPh} 0.11 g (0.27 mmol). Yield 0.13 g (0.20 mmol, 72%) yellow solid. ^{1}H NMR (500 MHz, DMSO-d_6, 298 K): δ /ppm = 10.85 (s, 2H, NH), 7.74 (t, J = 8.0 Hz, 2H, H7), 7.56 (d, J = 7.7 Hz, 2H, H3), 7.44 (t, J = 7.8 Hz, 4H, H12), 7.34 (d, J = 7.3 Hz, 2H, H6), 7.30 (d, J = 7.7 Hz, 4H, H11), 7.23 (m, J = 11.4, 4.2 Hz, 3H, H4,13), 6.80 (d, J = 8.5 Hz, 2H, H8). ^{13}C NMR (126 MHz, DMSO-d_6, 313 K): δ /ppm = 164.02 (C9), 159.39 (C5), 141.66 (C10), 140.36 (C2), 138.11 (C7), 129.59 (C12), 125.14 (C3), 123.94 (C4), 123.91 (C13), 123.05 (C11), 109.02 (C6), 108.76 (C8), 40.14 (C1). HR-ESI MS(+): calcd. for $[C_{28}H_{21}N_4Pt]^+$ m/z = 608.14108; found m/z = 608.14160 $[M\text{-}Cl]^+$. Elemental analysis calcd. (%) for $C_{28}H_{21}ClN_4Pt$, M = 644.02 g mol^{-1}: C, 52.22; H, 3.29; N, 8.70. Found C, 52.21; H, 3.22; N, 8.72.



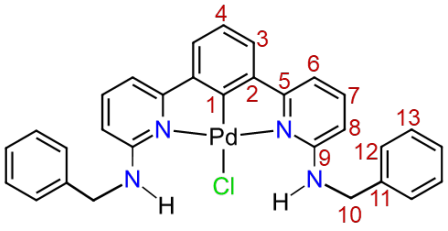
[Pd(L^{NHPh})Cl]. From $K_2[PdCl_4]$ 0.10 g (0.29 mmol), HL^{NHPh} 0.12 g (0.29 mmol). Yield 0.10 g (0.18 mmol, 62%) bright-yellow solid. ^{1}H NMR (600 MHz, DMSO-d_6, 313 K): δ /ppm = 10.62 (s, 2H, NH), 7.73 (t, J = 8.0 Hz, 2H, H7), 7.55 (d, J = 7.7 Hz, 2H, H3), 7.47–7.40 (m, 4H, H12), 7.31 (dd, J = 7.4, 1.1 Hz, 2H, H6), 7.29 (dd, J = 8.3, 0.8 Hz, 4H, H11), 7.24 (t, J = 7.7 Hz, 1H, H4), 7.23–7.19 (m, 2H, H13), 6.86–6.78 (dd, J = 8.5, 1.1 Hz, 2H, H8). ^{13}C NMR (151 MHz, DMSO-d_6, 313 K): δ /ppm = 161.97 (C9), 158.50 (C5), 143.87 (C10), 140.37 (C2), 138.32 (C7), 129.44 (C12), 125.16 (C3), 124.72 (C4), 124.04 (C13), 122.64 (C11), 108.85 (C6), 108.52 (C8), 40.06 (C1). HR-ESI MS(+): calcd. for $[C_{28}H_{21}N_4Pd]^+$ m/z = 519.08062; found m/z = 519.08142 $[M\text{-}Cl]^+$. Elemental analysis calcd. (%) for $C_{28}H_{21}ClN_4Pd$, M = 555.37 g mol^{-1}: C, 60.55; H, 3.81; N, 10.09. Found C, 60.53; H, 3.80; N, 10.02.



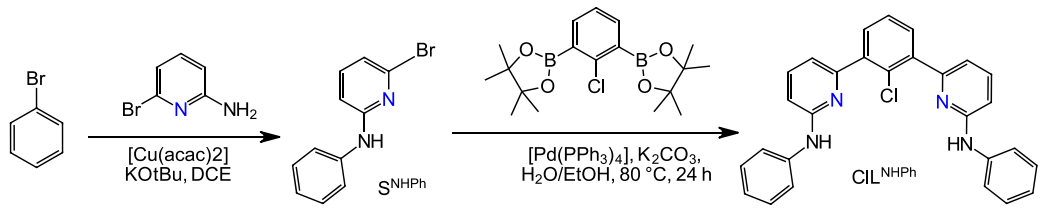
[Pt(L^{NHBn})Cl]. From $K_2[PtCl_4]$ 0.06 g (0.14 mmol), HL^{NHBn} 0.06 g (0.14 mmol). Yield 0.08 g (0.11 mmol, 79%) orange-yellow solid. ^{1}H NMR (600 MHz, DMSO-d_6, 298 K): δ /ppm = 9.71 (t, J = 6.2 Hz, 2H, NH), 7.62 (t, J = 7.9 Hz, 2H, H7), 7.45 (d, J = 7.7 Hz, 2H, H3), 7.42 (d, J = 7.5 Hz, 4H, H12), 7.35 (t, J = 7.7 Hz, 4H, H13), 7.26 (t, J = 7.3 Hz, 2H, H14), 7.16 – 7.10 (m, 3H, H4 and H6), 6.44 (d, J = 8.6 Hz, 2H, H8), 4.49 (d, J = 6.2 Hz, 4H, H10). ^{13}C NMR (151 MHz, DMSO-d_6, 298 K): δ /ppm = 163.73 (C9), 161.20 (C5), 150.20 (C2), 141.95 (C11), 139.96 (C7), 137.87 (C3), 128.54 (C12), 127.15 (C13), 123.78 (C14), 123.74 (C4), 107.60 (C6), 107.30 (C8), 45.27 (C10), 40.05 (C1). HR-ESI MS(+): calcd. for $[C_{30}H_{25}N_4Pt]^+$ m/z = 636.17240; found m/z = 636.17334 $[M\text{-}Cl]^+$. Elemental analysis calcd. (%) for $C_{30}H_{25}ClN_4Pt$, M = 672.08 g mol^{-1}: C, 53.61; H, 3.75; N, 8.34. Found C, 53.67; H, 3.77; N, 8.39.



[Pd(L^{NHBn})Cl]. From $K_2[PdCl_4]$ 0.09 g (0.27 mmol), HL^{NHBn} 0.12 g (0.27 mmol). Yield 0.12 g (0.20 mmol, 74%) yellow solid. ^{1}H NMR (600 MHz, DMSO-d_6, 298 K): δ /ppm = 9.47 (t, *J* = 6.4 Hz, 2H, NH), 7.61 (dd, *J* = 8.3, 7.6 Hz, 2H, H7), 7.45 (d, *J* = 7.7 Hz, 2H, H3), 7.42 (dd, *J* = 8.0, 0.9 Hz, 4H, H12), 7.38–7.33 (m, 4H, H13), 7.28–7.23 (m, 2H, H14), 7.14 (dd, *J* = 9.7, 5.7 Hz, 1H, H4), 7.10 (dd, *J* = 7.4, 1.1 Hz, 2H, H6), 6.44 (dd, *J* = 8.7, 1.0 Hz, 2H, H8), 4.45 (d, *J* = 6.4 Hz, 4H, H10). ^{13}C NMR (151 MHz, DMSO-d_6, 298 K): δ /ppm = 164.22 (C9), 161.69 (C5), 160.49 (C2), 144.09 (C11), 139.87 (C7), 138.02 (C3), 128.35 (C12), 127.00 (C13), 124.93 (C14), 123.73 (C4), 107.31 (C6), 106.94 (C8), 45.06 (C10), 40.06 (C1). HR-ESI MS(+): calcd. for $[C_{30}H_{25}N_4Pd]^+$ m/z = 547.11199; found m/z = 547.11188 $[M\text{-}Cl]^+$. Elemental analysis calcd. (%) for $C_{30}H_{25}ClN_4Pd$, M = 583.42 g mol^{-1}: C, 61.76; H, 4.32; N, 9.60. Found C, 61.78; H, 4.31; N, 9.58.



5.2.4. Synthesis of the ligand precursor ClL^{NHPh}

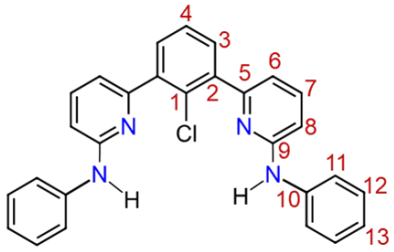


Synthesis of 2,2′-(2-chloro-1,3-phenylene)bis(4,4,5,5-tetramethyl-1,3,2-dioxaborolane) or 2-chloro-1,3-phenyldiboronic acid, pinacol ester).. To a solution of 1,3-dibromo-2-chlorobenzene (1.00 mmol, 0.27 g), B_2Pin_2 (3.00 mmol, 0.76 g), and KOAc (5.00 mmol, 0.49 g), in 6 mL 1,4-dioxane was added $[Pd(PPh_3)_2Cl_2]$ (6.00 mol%, 0.04 g) under inert condition. After three freeze-thaw cycles to remove trace amount of oxygen, the reaction mixture stirred at 102 °C for 12 h. The mixture was cooled down and 10 mL EtOAc was added to quench the reaction. The organic phase was washed with brine solution (3 × 20 mL) and dried over anhydrous Na_2SO_4. After evaporation of the solvent, crude product was purified by column chromatography using CH_2Cl_2 as an eluent to give white crystals. Yield: 0.27 g (0.75 mmol, 75%). ^{1}H NMR (300 MHz, acetone-d_6, 298 K): δ /ppm = 7.68 (d, *J* = 7.4 Hz, 2H), 7.29 (t, *J* = 7.4 Hz, 1H), 1.35 (s, 24H).

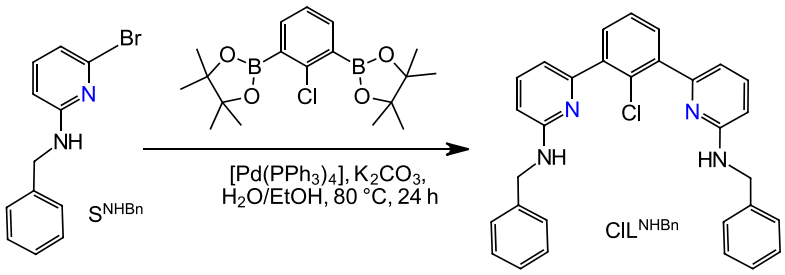
Synthesis of S^{NHPh}. To a solution of 2-amino-6-bromopyridine (17.34 mmol, 3.00 g), and KOtBu (19.00 mmol, 2.14 g) in 1,2-dichlorethane (50 mL) were added phenylboronic acid (27.74 mmol, 3.40 g) and Cu(II) acetyl acetonate (17.34 mmol, 4.54 g). The solution was heated under reflux (80 °C) for 1 d. Then the reaction mixture was washed with brine (3 × 50 mL). The combined organic layers were dried over Na_2SO_4 and the product (S^{Ph}) was purified by column chromatography with *n*-Hex:EtOAc (9:1 v/v). Yield: 0.66 g (2.60 mmol, 15%). ^{1}H NMR (300 MHz, acetone-d_6, 298 K): δ /ppm = 8.43 (s, 1H, NH), 7.65

(dd, *J* = 8.7, 1.1 Hz, 2H), 7.38 (dd, *J* = 8.2, 7.5 Hz, 1H), 7.34–7.26 (m, 2H), 7.02–6.95 (m, 1H), 6.88 (dd, *J* = 7.5, 0.6 Hz, 1H), 6.81 (d, *J* = 8.2 Hz, 1H).

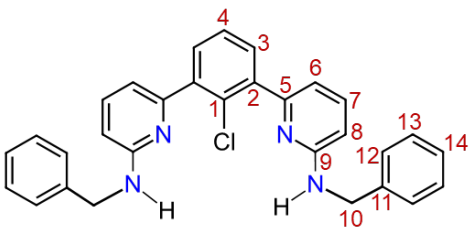
Synthesis of ClL^{NHPh}. 2,2′-(2-chloro-1,3-phenylene)bis(4,4,5,5-tetramethyl-1,3,2-dioxaborolane) (0.96 g, 2.63 mmol), S^{Ph} (0.94 g, 3.75 mmol), [Pd(PPh$_3$)$_4$] (0.13 g, 3.00 mol%), and K$_2$CO$_3$ (1.04 g, 7.51 mmol) were mixed in 40 mL H$_2$O/EtOH (1:1, degassed). The solution was stirred for 24 h at 80 °C under an argon atmosphere. After allowing the reaction mixture to cool to room temperature, the mixture was extracted with CH$_2$Cl$_2$. The extract was washed with brine (2 × 40 mL), separated and dried over anhydrous Na$_2$SO$_4$. The crude product was purified by column chromatography with *n*-Hex:EtOAc (7:3 v/v). Yield: 0.55 g (1.22 mmol, 65%). ^{1}H NMR (600 MHz, DMSO-*d*$_6$, 298 K): δ /ppm = 9.16 (s, 2H, NH), 7.72 (dd, *J* = 8.6, 1.0 Hz, 4H, H11), 7.68 (dd, *J* = 8.2, 7.5 Hz, 2H, H7), 7.60–7.51 (m, 3H, H3 and H4), 7.25–7.20 (m, 4H, H12), 6.99 (d, *J* = 7.2 Hz, 2H, H6), 6.90–6.83 (m, 4H, H8 and H13). ^{13}C NMR (151 MHz, DMSO-*d*$_6$, 298 K): δ /ppm = 155.37 (C9), 154.63 (C5), 141.60 (C10), 140.69 (C2), 137.44 (C7), 130.83 (C3), 129.30 (C1), 128.61 (C12), 126.93 (C4), 120.41 (C13), 117.98 (C11), 115.01 (C6), 109.62 (C8). HR-ESI MS(+): calcd. for [C$_{28}$H$_{22}$ClN$_4$]$^+$ m/z = 449.15275; found m/z = 449.15248 [M+H]$^+$. Elemental analysis calcd. (%) for C$_{28}$H$_{21}$ClN$_4$, M = 448.95 g mol^{-1}: C, 74.91; H, 4.71; N, 12.48. Found C, 74.23; H, 4.68; N, 12.49.



5.2.5. Synthesis of the ligand precursor ClL^{NHBn}



Synthesis of ClL^{NHBn}. 2,2′-(2-chloro-1,3-phenylene)bis(4,4,5,5-tetramethyl-1,3,2-dioxaborolane) (1.95 g, 5.34 mmol), S^{NHBn} (2.00 g, 7.60 mmol), [Pd(PPh$_3$)$_4$] (0.26 g, 3.00 mol%), and K$_2$CO$_3$ (2.10 g, 15.20 mmol) were mixed and dissolved in 50 mL H$_2$O/EtOH (1:1, degassed). The solution was stirred for 24 h at 80 °C under an argon atmosphere. After allowing the reaction mixture to cool to ambient temperature, the mixture was extracted with CH$_2$Cl$_2$. The extract was washed with brine (2 × 40 mL), separated and dried over anhydrous Na$_2$SO$_4$. The crude product was purified by column chromatography with *n*-Hex:EtOAc (6:4 v/v). Yield: 1.17 g (2.50 mmol, 65%). ^{1}H NMR (600 MHz,

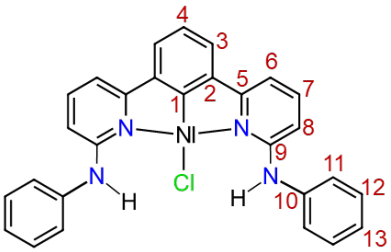


DMSO-d_6, 298 K): δ /ppm = 7.46 (dd, J = 8.3, 7.3 Hz, 2H, H7), 7.41–7.38 (m, 3H, H4 and H3), 7.37–7.34 (m, 4H, H12), 7.33–7.27 (m, 4H, H13), 7.21 (t, J = 7.3 Hz, 2H, H14), 7.15 (t, J = 6.0 Hz, 2H, NH), 6.70 (dd, J = 7.3, 0.5 Hz, 2H, H6), 6.52 (d, J = 8.3 Hz, 2H, H8), 4.49 (d, J = 6.0 Hz, 4H, H10). ^{13}C NMR (151 MHz, DMSO-d_6, 298 K): δ /ppm = 158.26 (C9), 154.92 (C5), 140.86 (C11), 140.61 (C2), 136.79 (C7), 130.52 (C3), 129.32 (C1), 128.15 (C13), 127.39 (C12), 126.51 (C14), 126.37 (C4), 112.45 (C6), 107.00 (C8), 44.22 (C10). HR-ESI MS(+): calcd. for $[C_{30}H_{25}ClN_4]^+$ m/z = 477.18405; found m/z = 477.18403 $[M+H]^+$. Elemental analysis calcd. (%) for $C_{30}H_{25}ClN_4$, M = 477.0 g mol^{-1}: C, 75.54; H, 5.28; N, 11.75. Found C, 75.51; H, 5.27; N, 11.75.

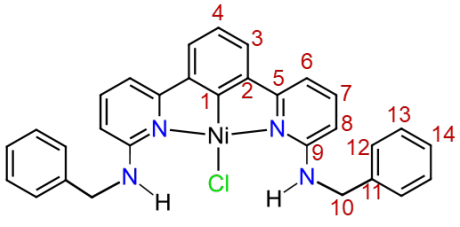
5.2.6. Synthesis of [Ni(L^{NHPh})Cl] and [Ni(L^{NHBn})Cl] complexes

Under an inert atmosphere, 1.00 eq. of the halogenated derivatives of the ligands ClL^{NHPh} or ClL^{NHBn} was dissolved in 8 mL of dry THF. The reaction mixture was transferred in an ice bath at 0°C and 1.30 eq. of [Ni(COD)$_2$] was added. The solution turned from yellow to dark orange with red-orange precipitation during 2 h. Then the solvent was removed and the residue was washed with dry MeCN to remove unreacted ligand and dried under vacuum.

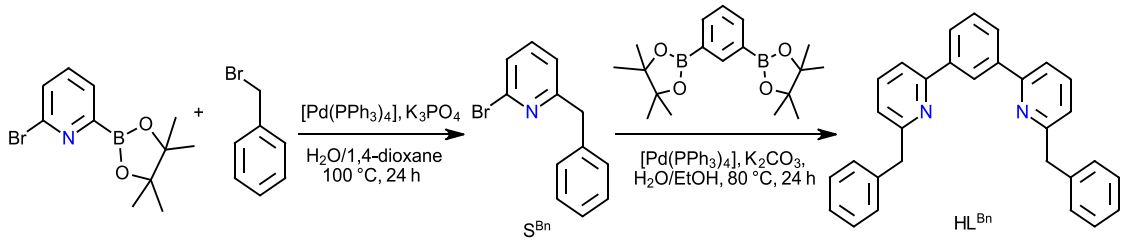
[Ni(L^{NHPh})Cl]. From [Ni(COD)$_2$] 0.29 g (0.83 mmol) and ClL^{NHPh} 0.29 g (0.64 mmol). Yield 0.20 g (0.38 mmol, 59%) deep orange solid. ^{1}H NMR (300 MHz, DMSO-d_6, 298 K): δ /ppm = 9.48 (s, 2H, NH), 7.66 (t, J = 7.9 Hz, 2H, H7), 7.45–7.33 (m, 6H, H3 and H12), 7.29–7.14 (m, 7H, H6 and H11 and H4), 7.10 (t, J = 7.4 Hz, 2H, H13), 6.73 (d, J = 8.5 Hz, 2H, H8). HR-ESI MS(+): calcd. for $[C_{28}H_{20}N_4Ni]^+$ m/z = 470.10300; found m/z = 470.10360 $[M-H-Cl]^+$. Elemental analysis calcd. (%) for $C_{28}H_{21}ClN_4Ni$, M = 507.64 g mol^{-1}: C, 66.25; H, 4.17; N, 11.04. Found C, 66.21; H, 4.15; N, 11.07.



[Ni(L^{NHBn})Cl]. From [Ni(COD)$_2$] 0.24 g (0.88 mmol) and ClL^{NHBn} 0.32 g (0.68 mmol). Yield 0.24 g (0.46 mmol, 67%) deep orange solid. ^{1}H NMR (600 MHz, DMSO-d_6, 298 K): δ /ppm = 8.12 (t, J = 5.6 Hz, 2H, NH), 7.54 (t, J = 8.0 Hz, 2H, H7), 7.45 (d, J = 7.4 Hz, 4H, H12), 7.37–7.31 (m, 4H, H13), 7.30–7.22 (m, 4H, H14 and H3), 7.09 (t, J = 7.6 Hz, 1H, H4), 6.98 (d, J = 7.2 Hz, 2H, H6), 6.26 (d, J = 8.5 Hz, 2H, H8), 4.42 (d, J = 6.2 Hz, 4H, H10). HR-ESI MS(+): calcd. for $[C_{30}H_{24}N_4Ni]^+$ m/z = 498.13494; found m/z = 498.13490 $[M-H-Cl]^+$. Elemental analysis calcd. (%) for $C_{30}H_{25}ClN_4Ni$, M = 535.69 g mol^{-1}: C, 67.26; H, 4.70; N, 10.46. Found C, 67.18; H, 4.71; N, 10.47.



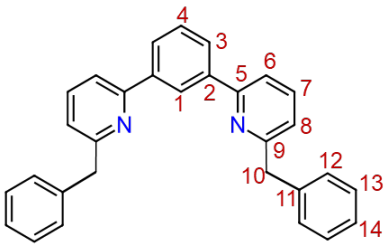
5.2.7. Synthesis of the ligand precursor HL^{Bn}



Synthesis of 2,2′-(1,3-phenylene)bis,(4,4,5,5-tetramethyl-1,3,2-dioxaborolane) (or 1,3-Phenyldiboronic acid, pinacol ester). To a solution of 1,3-dibromobenzene (4.20 mmol, 1.00 g), B_2Pin_2 (12.70 mmol, 3.20 g), and KOAc (21.20 mmol, 2.10 g), in 15 mL 1,4-dioxane was added $[Pd(PPh_3)_2Cl_2]$ (6.00 mol%, 0.18 g) under inert condition. After three freeze-thaw cycles to remove trace amount of oxygen, the reaction mixture stirred at 102 ˚C for 12 h. The mixture was cooled down and 10 mL EtOAc was added to quench the reaction. The organic phase was washed with brine solution (3 × 10 mL) and dried over anhydrous Na_2SO_4. After evaporation of the solvent, crude product was purified by column chromatography using CH_2Cl_2 as an eluent to give white crystals. Yield: 1.42 g (3.90 mmol, 92%). ^{1}H NMR (300 MHz, $CDCl_3$, 298 K): δ /ppm = 8.27 (s, 1H), 7.89 (dd, *J* = 7.4, 1.4 Hz, 2H), 7.37 (td, *J* = 7.4, 0.8 Hz, 1H), 1.33 (s, 24H).

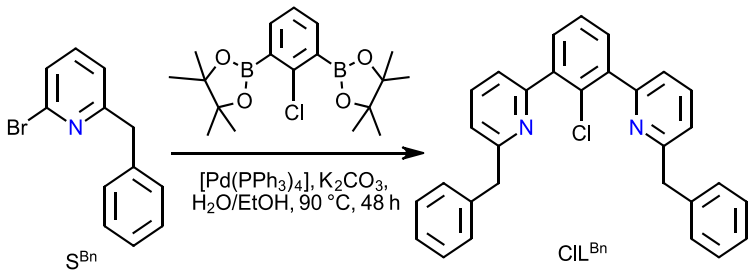
Synthesis of S^{Bn}. 2-Bromopyridine-6-boronic acid pinacol ester (0.50 g, 1.76 mmol), benzyl bromide (0.19 mL, 1.60 mmol), $[Pd(PPh_3)_4]$ (0.11 g, 6.00 mol%), and K_3PO_4 (0.68 g, 3.20 mmol) were mixed and dissolved in 25 mL H_2O/1,4-dioxane (1:1, degassed). The solution was stirred for 24 h at 100 °C under an argon atmosphere. After allowing the reaction mixture to cool to room temperature, the mixture was filtered and diluted with 15 mL EtOAc. The resulting solution was washed with brine (2 × 20 mL), separated and dried over anhydrous Na_2SO_4. The crude product was purified by column chromatography with *n*-Hex:EtOAc (9:1 v/v). Yield: 0.24 g (0.97 mmol, 60%). ^{1}H NMR (500 MHz, acetone-d_6, 298 K): δ /ppm = 7.57 (t, *J* = 7.7 Hz, 1H), 7.39 (dd, *J* = 7.9, 0.7 Hz, 1H), 7.30 (d, *J* = 4.5 Hz, 4H), 7.24 – 7.19 (m, 2H), 4.09 (s, 2H). ^{13}C NMR (126 MHz, acetone-d_6, 298 K): δ /ppm = 163.39, 141.91, 140.22, 139.86, 129.78, 129.28, 127.19, 126.32, 122.92, 44.38.

Synthesis of HL^{Bn}. 1,3-phenyldiboronic acid bis(pinacol)ester (0.41 g, 1.23 mmol), S^{Bn} (0.44 g, 1.76 mmol), $[Pd(PPh_3)_4]$ (0.12 g, 6.00 mol%), and K_2CO_3 (0.49 g, 3.52 mmol) were mixed and dissolved in 20 mL H_2O/EtOH (1:1, degassed). The solution was stirred for 24 h at 80 °C under an argon atmosphere. After allowing the reaction mixture to cool to room temperature, the mixture was filtered and diluted with 15 mL CH_2Cl_2. The resulting solution was washed with brine (3 × 20 mL), separated and dried over anhydrous Na_2SO_4. The crude product was purified by column

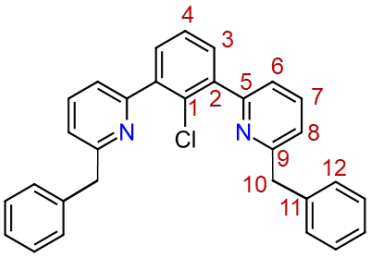


chromatography with *n*-Hex:EtOAc (8:2 v/v). Yield: 0.30 g (0.72 mmol, 82%). ^{1}H NMR (600 MHz, DMSO-d_6, 298 K): δ /ppm = 8.78 (t, *J* = 1.8 Hz, 1H, H1), 8.13 (dd, *J* = 7.7, 1.8 Hz, 2H, H3), 7.86 (dd, *J* = 7.8, 1.0 Hz, 2H, H6), 7.81 (t, *J* = 7.7 Hz, 2H, H7), 7.60 (t, *J* = 7.7 Hz, 1H, H4), 7.40 – 7.34 (m, 4H, H12), 7.34 – 7.26 (m, 4H, H13), 7.25 (dd, *J* = 7.5, 1.0 Hz, 2H, H8), 7.23 – 7.17 (m, 2H, H14), 4.19 (s, 4H, H10). ^{13}C NMR (151 MHz, DMSO-d_6, 298 K): δ /ppm = 160.44 (C9), 155.31 (C2), 139.79 (C11), 139.17 (C5), 137.83 (C7), 129.12 (C4), 128.97 (C12), 128.39 (C13), 127.12 (C3), 126.15 (C14), 124.80 (C1), 121.83 (C8), 117.92 (C6), 43.97 (C10). HR-ESI MS(+): calcd. for $[C_{30}H_{25}N_2]^+$ m/z = 413.20122; found m/z = 413.20091 $[M+H]^+$. Elemental analysis calcd. (%) for $C_{30}H_{24}N_2$, M = 412.52 g mol^{-1}: C, 87.35; H, 5.86; N, 6.79. Found C, 85.71; H, 5.72; N, 6.73.

5.2.8. Synthesis of the ligand precursor ClL^{Bn}



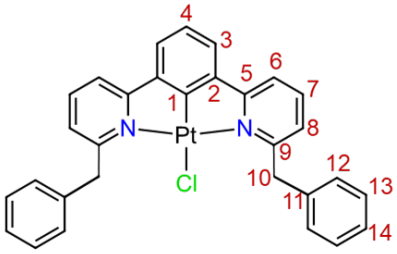
Synthesis of ClL^{Bn}. 2-chloro-1,3-Phenyldiboronic acid, pinacol ester (0.73 g, 2.00 mmol), S^{Bn} (0.71 g, 2.86 mmol), [Pd(PPh$_3$)$_4$] (0.20 g, 6.00 mol%), and K$_2$CO$_3$ (0.79 g, 5.72 mmol) were mixed and dissolved in 40 mL H$_2$O/EtOH (1:1, degassed). The solution was stirred for 48 h at 90 °C under an argon atmosphere. After allowing the reaction mixture to cool to ambient temperature, the mixture was extracted with CH_2Cl_2. The extract was washed with brine (2 × 30 mL), separated and dried over anhydrous Na_2SO_4. The crude product was purified by column chromatography with *n*-Hex:EtOAc (8:2 v/v). Yield: 0.46 g (1.03 mmol, 72%). ^{1}H NMR (500 MHz, DMSO-d_6, 298 K): δ /ppm = 7.81 (t, *J* = 7.7 Hz, 2H, H3), 7.59–7.51 (m, 3H, H6 and H4), 7.47 (dd, *J* = 7.8, 1.0 Hz, 2H, H7), 7.35–7.26 (m, 10H, H12, H13 and H8), 7.23–7.16 (m, 2H, H14), 4.15 (s, 4H, H10). ^{13}C NMR (151 MHz, acetone-d_6, 298 K): δ /ppm = 161.69 (C9), 157.68 (C2), 150.07 (C1), 141.71 (C5), 140.93 (C4), 137.42 (C11), 132.30 (C7), 129.90 (C12), 129.26 (C13), 127.53 (C3), 127.03 (C14), 123.22 (C8), 122.61 (C6), 45.17 (C10). HR-ESI MS(+): calcd. for $[C_{30}H_{24}ClN_2]^+$ m/z = 447.16225; found m/z = 447.16240 $[M+H]^+$. Elemental analysis calcd. (%) for $C_{30}H_{23}ClN_2$, M = 446.97 g mol^{-1}: C, 80.61; H, 5.19; N, 6.27. Found C, 80.90; H, 5.63; N, 6.34.



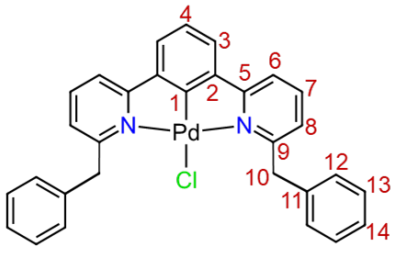
5.2.9. Synthesis of the complexes [M(L^{Bn})Cl] (M = Pt or Pd)

Modifying a previously reported method,[92] a mixture of 1.00 eq. $K_2[PtCl_4]$ or $K_2[PdCl_4]$ and 1.00 eq. of the proto-ligand HL^{Bn} suspended in 8 mL glacial acetic acid and stirred at 110 °C for 3 d. The crude products were filtered off, washed with glacial AcOH, MeOH, H_2O, EtOH and Et_2O. Further purification was done by crystallizing the products in DMSO and washing the crystals with cold acetone and then n-pentane.

[Pt(L^{Bn})Cl]. From $K_2[PtCl_4]$ 0.18 g (0.44 mmol), HL^{Bn} 0.18 g (0.44 mmol). Yield 0.16 g (0.27 mmol, 62%) orange-yellow solid. ^{1}H NMR (600 MHz, DMSO-d_6, 298 K): δ /ppm = 8.03 (t, J = 7.7 Hz, 2H, H7), 7.97 (dd, J = 7.9, 1.6 Hz, 2H, H8), 7.70 (d, J = 7.7 Hz, 2H, H3), 7.44–7.40 (m, 4H, H12), 7.38 (dd, J = 7.7, 1.5 Hz, 2H, H6), 7.29 (t, J = 7.7 Hz, 1H, H4), 7.24–7.19 (m, 4H, H13), 7.19–7.15 (m, 2H, H14), 5.27 (s, 4H, H10). ^{13}C NMR (151 MHz, DMSO-d_6, 313 K): δ /ppm = 165.93 (C9), 165.65 (C5), 140.95 (C2), 139.95 (C7), 139.27 (C11), 128.96 (C12), 128.45 (C13), 126.18 (C14), 125.05 (C6), 124.78 (C3), 123.35 (C4), 117.44 (C8), 43.36 (C10), 40.06 (C1). HR-ESI MS(+): calcd. for $[C_{30}H_{23}N_2Pt]^+$ m/z = 605.14823; found m/z = 605.14855 $[M\text{-}Cl]^+$. Elemental analysis calcd. (%) for $C_{30}H_{23}ClN_2Pt$, M = 642.05 g mol^{-1}: C, 56.12; H, 3.61; N, 4.36. Found C, 56.68; H, 3.61; N, 5.56.



[Pd(L^{Bn})Cl]. From $K_2[PdCl_4]$ 0.16 g (0.49 mmol), HL^{Bn} 0.20 g (0.49 mmol). Yield 0.16 g (0.29 mmol, 60%) yellow solid. ^{1}H NMR (600 MHz, DMSO-d_6, 298 K): δ /ppm = 8.02 (t, J = 7.8 Hz, 2H, H7), 7.95 (dd, J = 7.9, 1.4 Hz, 2H, H8), 7.69 (d, J = 7.7 Hz, 2H, H3), 7.44–7.39 (m, 4H, H12), 7.32 (dd, J = 7.7, 1.4 Hz, 2H, H6), 7.29 (t, J = 7.7 Hz, 1H, H4), 7.26–7.23 (m, 4H, H13), 7.22–7.18 (m, 2H, H14), 5.04 (s, 4H, H10). ^{13}C NMR (151 MHz, DMSO-d_6, 313 K): δ /ppm = 164.90 (C9), 163.11 (C5), 143.21 (2), 140.22 (7), 139.27 (C11), 128.99 (C12), 128.51 (C13), 126.26 (C14), 125.05 (C4), 125.01 (C6), 124.81 (C3), 117.32 (C8), 43.22 (C10), 40.06 (C1). HR-ESI MS(+): calcd. for $[C_{30}H_{23}N_2Pd]^+$ m/z = 516.09065; found m/z = 516.09156 $[M\text{-}Cl]^+$. Elemental analysis calcd. (%) for $C_{30}H_{23}ClN_2Pd$, M = 553.39 g mol^{-1}: C, 65.11; H, 4.19; N, 5.06. Found C, 66.61; H, 4.04; N, 5.28.

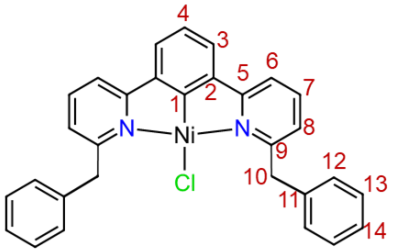


5.2.10. Synthesis of [Ni(L^{Bn})Cl] complex

Under an inert atmosphere, 1.00 eq. of the halogenated derivative of the ligand ClL^{Bn} was dissolved in 12 mL of dry THF. The reaction mixture was transferred in an ice bath at 0 °C and 1.30 eq. of $[Ni(COD)_2]$

was added. The solution turned from yellow to orange with red-orange precipitation during 2 h. Then the solvent was removed and the residue was washed with dry MeCN to remove unreacted ligand and dried under vacuum.

[Ni(L^{Bn})Cl]. From [Ni(COD)$_2$] 0.28 g (1.30 mmol), L^{Bn}Cl 0.36 g (0.79 mmol). Yield 0.31 g (0.62 mmol, 78%) deep orange solid. ^{1}H NMR (300 MHz, DMSO-*d*$_6$, 298 K): δ /ppm = 7.90 (t, *J* = 7.7 Hz, 2H, H7), 7.80 (dd, *J* = 7.9, 1.4 Hz, 2H, H8), 7.58 (d, *J* = 7.6 Hz, 2H, H3), 7.49–7.39 (m, 4H, H12), 7.34–7.19 (m, 7H, H6 and H4 and H13), 7.02 (dd, *J* = 7.6, 1.4 Hz, 2H, H14), 4.64 (s, 4H, H10). HR-ESI MS(+): calcd. for [C$_{30}$H$_{23}$N$_2$Ni]$^+$ m/z = 469.12092; found m/z = 469.12076 [M-Cl]$^+$. Elemental analysis calcd. (%) for C$_{30}$H$_{23}$ClN$_2$Ni, M = 505.66 g mol^{-1}: C, 71.26; H, 4.58; N, 5.54. Found C, 70.50; H, 4.55; N, 6.38.



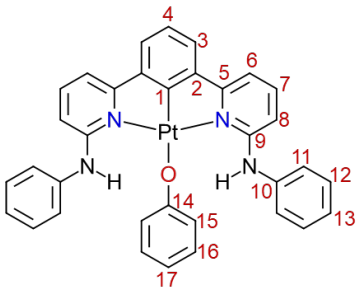
5.2.11. Synthesis of the complexes [M(L^{NHPh})NO$_3$] and [M(L^{NHBn})NO$_3$] (M = Pd or Pt)

A mixture of 1.00 eq. [M(L^{NHPh})Cl] or [M(L^{NHBn})Cl] and 2.00 eq. of AgNO$_3$ was suspended in 50 mL CHCl$_3$ and stirred at room temperature for 18 h, under strict exclusion of light. Then the mixture was filtered to remove precipitated AgCl. The crude product obtained after solvent removal was used in the next step without further purification.

5.2.12. Synthesis of the complexes [M(L^{NHPh})OPh] and [M(L^{NHBn})OPh] (M = Pt or Pd)

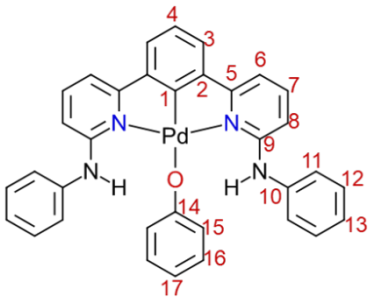
A mixture of 1.00 eq. [M(L^{NHPh})NO$_3$] or [M(L^{NHBn})NO$_3$] and 1.50 eq. of potassium phenolate was suspended in 50 mL CHCl$_3$ and stirred at room temperature for 24 h. After solvent removal, the crude product was further purified by sequential washings with acetone and n-pentane.

[Pt(L^{NHPh})OPh]. From [Pt(L^{NHPh})NO$_3$] 0.09 g (0.13 mmol), potassium phenolate 0.03 g (0.20 mmol). Yield 0.09 g (0.13 mmol, 95%) yellow solid. ^{1}H NMR (500 MHz, CD$_2$Cl$_2$, 298 K): δ /ppm = 11.86 (s, 2H, NH), 7.46 (m, 2H, H7), 7.34 (d, *J* = 7.7 Hz, 2H, H3), 7.31 – 7.27 (m, 4H, H12), 7.24 (dd, *J* = 8.6, 1.1 Hz, 2H, H6), 7.18 (dd, *J* = 8.1, 7.3 Hz, 1H, H17), 7.15 – 7.11 (m, 2H, H15), 7.07 – 7.03 (m, 2H, H16), 7.03 – 7.00 (m, 4H, H11), 6.95 (dd, *J* = 7.3, 1.3 Hz, 2H, H8), 6.70 – 6.66 (m, 1H, H4), 6.62 (dd, *J* = 8.6, 1.2 Hz, 2H, H13). ^{13}C NMR (126 MHz, CD$_2$Cl$_2$, 298 K): δ /ppm = 165.21 (C14), 165.03 (C9), 161.66 (C5), 152.59 (C1), 143.07 (C10), 139.67 (C2), 139.37 (C7), 129.72 (C12), 129.07 (C15), 125.49 (C3), 124.90 (C4), 123.68 (C13), 123.54 (C11),

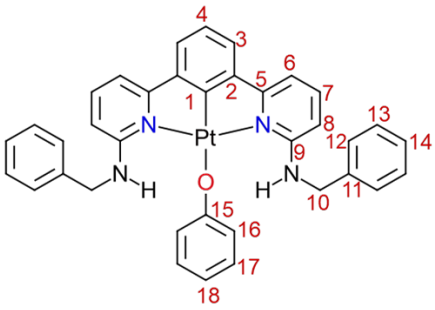


120.95 (C16), 117.80 (C17), 108.69 (C6), 108.00 (C8). HR-ESI MS(+): calcd. for $[C_{28}H_{21}N_4Pt]^+$ m/z = 607.13874; found m/z = 607.13876 $[M\text{-}OPh]^+$.

[Pd(L^{NHPh})Cl]. From $[Pd(L^{NHPh})NO_3]$ 0.12 g (0.21 mmol), potassium phenolate 0.04 g (0.32 mmol). Yield 0.13 g (0.20 mmol, 96%) yellow solid. ^1H NMR (500 MHz, CD_2Cl_2, 298 K): δ /ppm = 11.56 (s, 2H, NH), 7.46 (t, 2H *J* = 7.6 Hz, H7), 7.33 (d, *J* = 7.7 Hz, 2H, H3), 7.28 (t, *J* = 8.0 Hz, 4H, H12), 7.21 (d, *J* = 7.2 Hz, 2H, H6), 7.17 (t, *J* = 7.7 Hz, 1H, H17), 7.11 (t, *J* = 7.5 Hz, 2H, H15), 7.07 – 7.00 (m, 6H, H11 and H16), 6.93 (dd, *J* = 7.4, 1.1 Hz, 2H, H8), 6.66 (d, *J* = 6.7 Hz, 2H, H13), 6.63 (t, *J* = 7.2 Hz, 1H, H4). ^{13}C NMR (126 MHz, CD_2Cl_2, 298 K): δ /ppm = 167.26 (C14), 165.26 (C1), 163.26 (C9), 160.78 (C5), 145.01 (C10), 139.88 (C2), 139.52 (C7), 129.66 (C12), 129.28 (C15), 125.14 (C3), 124.91 (C4), 124.49 (C13), 123.48 (C11), 121.15 (C16), 116.97 (C17), 108.44 (C6), 107.69 (C8). HR-ESI MS(+): calcd. for $[C_{28}H_{21}N_4Pd]^+$ m/z = 518.08116; found m/z = 518.08128 $[M\text{-}OPh]^+$.

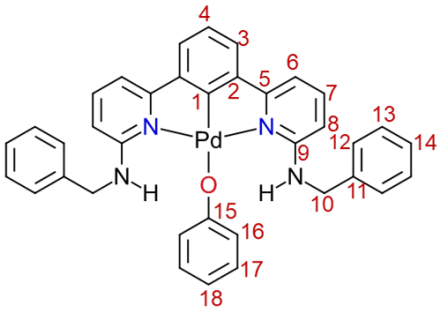


[Pt(L^{NHBn})OPh]. From $[Pt(L^{NHBn})NO_3]$ 0.07 g (0.10 mmol), potassium phenolate 0.02 g (0.15 mmol). Yield 0.06 g (0.09 mmol, 86%) yellow solid. ^1H NMR (500 MHz, CD_2Cl_2, 298 K): δ /ppm = 10.69 (t, *J* = 5.9 Hz, 2H, NH), 7.40 (t, *J* = 8.2 Hz, 2H, H7), 7.27 (t, *J* = 7.1 Hz, 4H, H13), 7.22 – 7.16 (m, 6H, H3 and H12), 7.13 (t, *J* = 7.7 Hz, 1H, H18), 7.05 (t, *J* = 8.2 Hz, 2H, H6), 7.02 (m, 4H, H16 and H17), 6.84 (dd, *J* = 7.3, 1.2 Hz, 2H, H14), 6.69 (t, *J* = 7.2 Hz, 1H, H4), 6.11 (dd, *J* = 8.6, 1.2 Hz, 2H, H8), 4.28 (d, *J* = 5.9 Hz, 4H, H10). ^{13}C NMR (126 MHz, CD_2Cl_2, 298 K): δ /ppm = 165.75 (C5), 165.10 (C9), 162.84 (C2), 152.72 (C1), 143.17 (C11), 141.31 (C15), 139.30 (C7), 138.51 (C13), 129.35 (C16), 128.83 (C3), 127.34 (C4), 123.42 (C14), 123.37 (C12), 120.47 (C17), 117.60 (C18), 107.20 (C6), 106.65 (C8), 47.06 (C10). HR-ESI MS(+): calcd. for $[C_{30}H_{25}N_4Pt]^+$ m/z = 635.17004; found m/z = 635.17093 $[M\text{-}OPh]^+$. Elemental analysis calcd. (%) for $C_{36}H_{30}N_4OPt$, M = 729.73 g mol^{-1}: C, 59.25; H, 4.14; N, 7.68. Found C, 57.60; H, 3.83; N, 7.06.



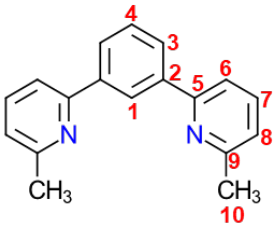
[Pd(L^{NHBn})OPh]. From $[Pd(L^{NHBn})NO_3]$ 0.21 g (0.35 mmol), potassium phenolate 0.07 g (0.52 mmol). Yield 0.22 g (0.34 mmol, 99%) pale-yellow solid. ^1H NMR (500 MHz, CD_2Cl_2, 298 K): δ /ppm = 10.37 (t, *J* = 6.0 Hz, 2H, NH), 7.39 (t, *J* = 7.9 Hz, 2H, H7), 7.28 (d, *J* = 7.7 Hz, 2H, H3), 7.23 – 7.17 (m, 8H, H12 and H13), 7.12 (t, *J* = 7.7 Hz, 1H, H18), 7.06 – 7.01 (m, 6H, H6 and H16 and H17), 6.82 (dd, *J* = 7.4, 1.1 Hz, 2H, H14), 6.63 (t, *J* = 7.2 Hz, 1H, H4), 6.11 (dd, *J* = 8.7, 1.1 Hz, 2H, H8), 4.26 (d, *J* = 6.0 Hz, 4H, H10). ^{13}C NMR

(126 MHz, CD_2Cl_2): δ /ppm = 167.38 (C5), 165.96 (C9), 163.17 (C2), 162.20 (C1), 145.13 (C11), 139.42 (C7), 138.77 (C15), 129.51 (C13), 128.80 (C16), 127.34 (C3), 127.28 (C4), 124.68 (C14), 123.29 (C12), 120.71 (C17), 116.75 (C18), 106.93 (C6), 106.22 (C8), 46.94 (C10). HR-ESI MS(+): calcd. for $[C_{30}H_{25}N_4Pd]^+$ m/z = 546.11246; found m/z = 546.11265 $[M\text{-}OPh]^+$. Elemental analysis calcd. (%) for $C_{36}H_{30}N_4OPt$, M = 641.07 g mol^{-1}: C, 67.45; H, 4.72; N, 8.74. Found C, 67.88; H, 5.24; N, 8.09.

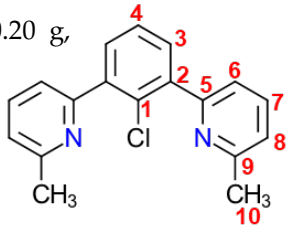


5.2.13. Synthesis of the N^C^N ligand precursors HL^{Me}, ClL^{Me}, HL^{Me2}, HL^{F}, and HL^{Cl}

Synthesis of HL^{Me}. 1,3-phenylenediboronic acid (1.35 g, 8.10 mmol), 2-bromo-6-methylpyridine (2.00 g, 11.60 mmol), $[Pd(PPh_3)_4]$ (0.40 g, 3.00 mol%), and K_2CO_3 (3.21 g, 23.00 mmol) were mixed and dissolved in 50 mL H_2O/EtOH (1:1, degassed). The solution was stirred for 24 h at 80 °C under an argon atmosphere. After allowing the reaction mixture to cool to room temperature, the mixture was filtered and diluted with 30 mL ethyl acetate (EtOAc). The resulting solution was washed with brine (5 × 20 mL), separated and dried over anhydrous Na_2SO_4. The crude product was purified by column chromatography with n-hexane (*n*-Hex):EtOAc (7:3 v/v). Yield: 0.88 g (3.40 mmol, 58%). ^{1}H NMR (600 MHz, DMSO-d_6, 298 K): δ /ppm = 8.71 (t, *J* = 1.8 Hz, 1H, H1), 8.10 (dd, *J* = 7.7, 1.8 Hz, 2H, H3), 7.84 (d, *J* = 7.7 Hz, 2H, H6), 7.79 (t, *J* = 7.7 Hz, 2H, H7), 7.59 (t, *J* = 7.7 Hz, 1H, H4), 7.25 (d, *J* = 7.4 Hz, 2H, H8), 2.57 (s, 6H, H10). ^{13}C NMR (151 MHz, DMSO-d_6, 298 K): δ /ppm = 157.78 (C9), 155.27 (C5), 139.30 (C2), 137.47 (C7), 129.05 (C4), 127.06 (C3), 124.62 (C1), 122.03 (C8), 117.52 (C6), 24.36 (C10). HR-ESI MS(+): calcd. for $[C_{18}H_{17}N_2]^+$ m/z = 261.13863; found m/z = 261.13870 $[M+H]^+$. Elemental analysis calcd. (%) for $C_{18}H_{16}N_2$, M = 260.33 g mol^{-1}: C, 83.04; H, 6.19; N, 10.76. Found C, 81.80; H, 6.07; N, 10.29.

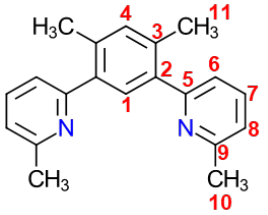


Synthesis of $L^{Me}Cl$. 2,2′-(2-chloro-1,3-phenylene)bis(4,4,5,5-tetramethyl-1,3,2-dioxaborolane) (0.90 g, 2.47 mmol), 2-bromo-6-methylpyridine (0.61 g, 3.53 mmol), $[Pd(PPh_3)_4]$ (0.20 g, 5.00 mol%), and K_2CO_3 (0.98 g, 7.06 mmol) were mixed in 50 mL H_2O/EtOH (1:1, degassed). The solution was stirred for 24 h at 90 °C under an argon atmosphere. After allowing the reaction mixture to cool to room temperature, the mixture was extracted with CH_2Cl_2. The extract was washed with brine (3 × 20 mL), separated and dried over anhydrous Na_2SO_4. The crude product was purified by column chromatography with *n*-Hex:EtOAc (8:2 v/v). Yield: 0.37 g (1.24 mmol, 70%). ^{1}H NMR (500 MHz, CD_2Cl_2, 298 K): δ /ppm = 7.66 (t, *J* = 7.7 Hz, 2H, H3), 7.55–7.51 (m, 2H, H6), 7.46–7.38 (m, 3H, H4 and H7), 7.18 (d, *J* = 7.7 Hz, 2H, H8),

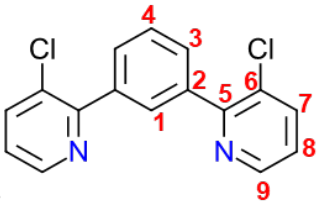


2.60 (s, 6H, H10). ^{13}C NMR (126 MHz, CD_2Cl_2, 298 K): δ /ppm = 158.65 (C9), 157.12 (C5), 141.17 (C2), 136.36 (C3), 131.56 (C6), 130.50 (C1), 126.95 (C4), 122.25 (C7), 122.23 (C8), 24.70 (C10). HR-ESI MS(+): calcd. for $[C_{18}H_{16}ClN_2]^+$ m/z = 295.09965; found m/z = 295.09981 $[M+H]^+$.

Synthesis of HL^{Me2}. Under inert conditions, a 250 mL Schlenk flask was filled with 70 mL of THF. Then a 2.50 M solution of n-butyl lithium (12.10 mL, 30.25 mmol) was transferred to the flask and cooled to –78 °C. A solution of 2-bromo-6-methylpyridine (4.90 g, 28.40 mmol) in 10 mL THF was slowly added dropwise and stirred for 1 h. A suspension of $ZnCl_2$ (5.15 g, 38.00 mmol; dried overnight at 140 °C under vacuum) in 50 mL THF was added to the reaction mixture and the reaction was warmed up to ambient temperature. Afterwards, $[Pd(PPh_3)_4]$ (0.55 g, 0.47 mmol) and 1,5-dibromo-2,4-dimethylbenzene (2.50 g, 9.47 mmol) were added to the solution, and heated under reflux for 17 h. The reaction was terminated by the addition of NH_4Cl (1.52 g, 28.4 mmol) in 10 mL H_2O. The mixture was extracted with EtOAc and washed with brine (3 × 20 mL), separated and dried over anhydrous Na_2SO_4. The crude product was purified by column chromatography with c-hexane:EtOAc (6:4 v/v). Yield: 2.15 g (7.46 mmol, 79%). ^{1}H NMR (500 MHz, $CDCl_3$, 298 K): δ /ppm = 7.59 (t, *J* = 7.7 Hz, 2H, H7), 7.41 (s, 1H, H4), 7.20 (s, 1H, H1), 7.18 (d, *J* = 10.4 Hz, 2H, H6), 7.07 (d, *J* = 7.6 Hz, 2H, H8), 2.59 (s, 6H, H10), 2.36 (s, 6H, H11). ^{13}C NMR (126 MHz, $CDCl_3$, 298 K): δ /ppm = 159.39 (C9), 157.83 (C5), 138.42 (C2), 136.34 (C7), 135.63 (C3), 133.23 (C6), 130.97 (C4), 121.22 (C1), 121.03 (C8), 24.76 (C10), 20.07 (C11). HR-EI MS(+): calcd. for $[C_{20}H_{19}N_2]^+$ m/z = 287.15; found m/z = 287.16 $[M–H]^+$. Elemental analysis calcd. (%) for $C_{20}H_{20}N_2$, M = 288.39 g mol^{-1}: C, 83.30; H, 6.99; N, 9.71. Found C, 82.29; H, 6.95; N, 9.25.

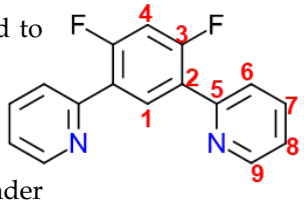


Synthesis of HL^{Cl}. 1,3-phenylenediboronic acid (0.83 g, 5.0 mmol), 2-bromo-3-chloropyridine (2.21 g, 12.0 mmol), $[Pd(PPh_3)_4]$ (0.35 g, 6.00 mol%), and K_2CO_3 (2.07 g, 15 mmol) were mixed and dissolved in 60 mL H_2O/EtOH (1:4, degassed). The solution was stirred for 24 h at 80 °C under an argon atmosphere. After allowing the reaction mixture to cool to room temperature, the mixture was filtered and diluted with 50 mL ethyl acetate (EtOAc). The resulting solution was washed with brine (3 × 50 mL), separated and dried over anhydrous $MgSO_4$. The crude product was purified by column chromatography with *c*-Hex:EtOAc (9:1 v/v). Yield: 0.82 g (2.70 mmol, 55%). ^{1}H NMR (300 MHz, DMSO-d_6, 298 K): δ /ppm = 8.66 (dd, *J* = 4.6, 1.4 Hz, 2H, H9), 8.08 (dd, *J* = 8.1, 1.4 Hz, 2H, H7), 7.99 (t, *J* = 1.6 Hz, 1H, H1), 7.80 (dd, *J* = 7.8, 1.5 Hz, 2H, H3), 7.64 (t, *J* = 7.8 Hz, 1H, H4), 7.47 (dd, *J* = 8.1, 4.6 Hz, 2H, H8). ^{13}C NMR (75 MHz, DMSO-d_6, 298 K): δ /ppm = 154.93 (C5), 148.09 (C9), 138.46 (C7), 137.64 (C6),



130.05 (C1), 129.63 (C3), 129.19 (C4), 127.80 (C2), 124.22 (C8). HR-EI MS(+): calcd. for $[C_{16}H_{10}N_2Cl]^+$ m/z = 265.05325; found m/z = 265.05264 $[M\text{-}Cl]^+$. Elemental analysis calcd. (%) for $C_{16}H_{10}N_2Cl_2$, M = 301.17 g mol^{-1}: C, 57.26; H, 2.70; N, 8.35. Found C, 57.15; H, 2.81; N, 7.64.

Synthesis of HL^F. Under inert conditions, a 250 mL Schlenk flask was filled with 140 mL of THF. Then a 2.50 M solution of n-butyl lithium (25.35 mL, 64.00 mmol) was transferred to the flask and cooled to –78 °C. A solution of 2-bromopyridine (5.85 mL, 60.00 mmol) in 20 mL THF was slowly added dropwise and stirred for 1 h.

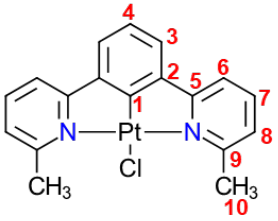


A suspension of $ZnCl_2$ (10.91 g, 80.00 mmol; dried overnight at 140 °C under vacuum) in 60 mL THF was added to the reaction mixture and the reaction was warmed up to ambient temperature. Afterwards, $[Pd(PPh_3)_4]$ (1.16 g, 1.00 mmol) and 1,5-dibromo-2,4-difluorobenzene (5.44 g, 20.00 mmol) were added to the solution, and heated under reflux for 17 h. The reaction was terminated by the addition of NH_4Cl (3.21 g, 60.00 mmol) in 10 mL H_2O. The mixture was extracted with CH_2Cl_2 and washed with brine (3 × 100 mL), separated and dried over anhydrous $MgSO_4$. The crude product was purified by column chromatography with c-hexane:EtOAc (4:1 v/v). Yield: 3.80 g (14.00 mmol, 71%). ^1H NMR (300 MHz, DMSO-d_6, 298 K): δ /ppm = 8.74 (ddd, *J* = 4.8, 1.9, 1.0 Hz, 2H, H9), 8.62 (t, *J* = 9.1 Hz, 1H, H1), 7.93 (td, *J* = 7.7, 1.9 Hz, 2H, H7), 7.83 (dt, *J* = 8.0, 1.2 Hz, 2H, H6), 7.55 (t, *J* = 11.2 Hz, 1H, H4), 7.43 (ddd, *J* = 7.4, 4.8, 1.2 Hz, 2H, H8). ^{13}C NMR (75 MHz, DMSO-d_6, 298 K): δ /ppm = 161.60 (d, *J* = 12.5 Hz, C3), 158.27 (d, *J* = 13.1 Hz, C5), 151.27 (t, *J* = 1.9 Hz, C2), 149.90 (C9), 137.12 (C7), 132.88 (t, *J* = 4.5 Hz, C1), 123.97 (t, *J* = 4.8 Hz, C6), 123.14 (C8), 105.51 (t, *J* = 27.7 Hz, C4). ^{19}F NMR (282 MHz, DMSO-d_6, 298 K): δ /ppm = –112.38 (t, *J* = 10.4 Hz, F). HR-EI MS(+): calcd. for $[C_{16}H_{10}N_2F_2]^+$ m/z = 268.08; found m/z = 268.00 $[M–H]^+$. Elemental analysis calcd. (%) for $C_{16}H_{10}N_2F_2$, M = 268.26 g mol^{-1}: C, 71.64; H, 3.76; N, 10.44. Found C, 71.27; H, 3.88; N, 10.13.

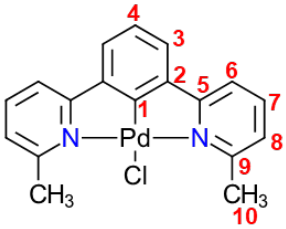
5.2.14. Synthesis of [M(N^C^N)Cl] (M = Pt or Pd; N^C^N = L^{Me}, L^{Me2}, L^F, L^{Cl}) complexes

Modifying a previously reported method,[92] a mixture of $K_2[PtCl_4]$ or $K_2[PdCl_4]$ and the proto-ligands HL^{Me}, HL^{Me2}, HL^{Cl}, or HL^F suspended in 8 mL glacial acetic acid and stirred at 110 °C for 3 d. The crude products were filtered off, washed with MeOH, H_2O, EtOH and Et_2O. Further purification was done either by solving the crude product in excess amount of CH_2Cl_2 and removing the unsolved impurities by filtration or by crystallizing the products in DMSO and washing the crystals with cold acetone.

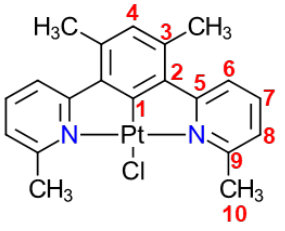
[Pt(L^{Me})Cl]. From $K_2[PtCl_4]$ 0.32 g (0.77 mmol, 1.00 eq.), HL^{Me} 0.20 g (0.77 mmol, 1.00 eq.). Yield 0.13 g (0.27 mmol, 35%) yellow solid. ^{1}H NMR (400 MHz, DMSO-d_6, 298 K): δ /ppm = 8.00 (t, J = 7.7 Hz, 2H, H7), 7.91 (d, J = 7.7 Hz, 2H, H6), 7.67 (d, J = 7.7 Hz, 2H, H3), 7.40 (d, J = 7.4 Hz, 2H, H8), 7.26 (t, J = 7.7 Hz, 1H, H4), 3.13 (s, 6H, H10). ^{13}C NMR (151 MHz, DMSO-d_6, 298 K): δ /ppm = 165.86 (C9), 163.66 (C5), 141.13 (C2), 139.64 (C7), 124.95 (C3), 124.56 (C8), 123.33 (C4), 116.87 (C6), 40.05 (C1), 26.56 (C10). HR-ESI MS(+): calcd. for $[C_{18}H_{15}N_2Pt]^+$ m/z = 453.08564; found m/z = 453.08549 $[M\text{-}Cl]^+$. Elemental analysis calcd. (%) for $C_{18}H_{15}ClN_2Pt$, M = 489.86 g mol^{-1}: C, 44.13; H, 3.09; N, 5.72. Found C, 43.03; H, 3.08; N, 5.44.



[Pd(L^{Me})Cl]. From $K_2[PdCl_4]$ 0.25 g (0.77 mmol, 1.00 eq.), HL^{Me} 0.20 g (0.77 mmol, 1.00 eq.). Yield 0.08 g (0.21 mmol, 27%) orange solid. ^{1}H NMR (600 MHz, DMSO-d_6, 298 K): δ /ppm = 7.98 (t, J = 7.7 Hz, 2H, H7), 7.91–7.88 (m, 2H, H6), 7.65 (d, J = 7.7 Hz, 2H, H3), 7.35 (dd, J = 7.6, 1.4 Hz, 2H, H8), 7.27 (t, J = 7.7 Hz, 1H, H4), 3.02 (s, 6H, H10). ^{13}C NMR (151 MHz, DMSO-d_6, 298 K): δ /ppm = 167.09 (C9), 163.25 (C5), 162.68 (C2), 143.31 (C7), 139.76 (C3), 124.90 (C8), 124.56 (C4), 116.69 (C6), 40.06 (C1), 26.50 (C10). HR-ESI MS(+): calcd. for $[C_{18}H_{15}N_2Pd]^+$ m/z = 364.02806; found m/z = 364.02847 $[M\text{-}Cl]^+$. Elemental analysis calcd. (%) for $C_{18}H_{15}ClN_2Pd$, M = 401.2 g mol^{-1}: C, 53.89; H, 3.77; N, 6.98. Found C, 52.74; H, 3.74; N, 6.58.

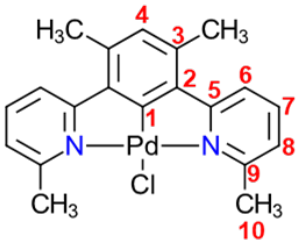


[Pt(L^{Me2})Cl]. From $K_2[PtCl_4]$ 0.36 g (0.87 mmol, 1.00 eq.), HL^{Me2} 0.30 g (1.04 mmol, 1.20 eq.). Yield 0.13 g (0.24 mmol, 28%) yellow solid. ^{1}H NMR (600 MHz, DMSO-d_6, 313 K): δ /ppm = 7.97 (t, J = 7.9 Hz, 2H, H7), 7.82 (d, J = 8.0 Hz, 2H, H6), 7.41–7.35 (m, 2H, H8), 6.94 (s, 1H, H4), 3.14 (s, 6H, H10), 2.65 (s, 6H, H11). ^{13}C NMR (151 MHz, DMSO-d_6, 313 K): δ /ppm = 166.05 (C9), 162.92 (C5), 139.00 (C2), 136.92 (C7), 136.06 (C3), 131.12 (C4), 123.78 (C8), 119.65 (C6), 40.06 (C1), 27.08 (C10), 21.64 (C11). HR-ESI MS(+): calcd. for $[C_{20}H_{19}N_2Pt]^+$ m/z = 481.11694; found m/z = 481.11676 $[M\text{-}Cl]^+$. Elemental analysis calcd. (%) for $C_{20}H_{19}ClN_2Pt$, M = 517.91 g mol^{-1}: C, 46.38; H, 3.70; N, 5.41. Found C, 45.87; H, 3.68; N, 5.32.

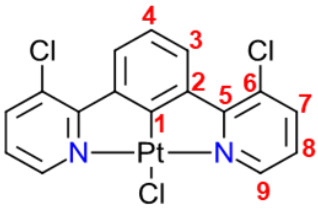


[Pd(L^{Me2})Cl]. A mixture of $[Pd(OAc)_2]$ 0.23 g (0.92 mmol, 1.06 eq.) and HL^{Me2} 0.25 g (0.87 mmol, 1.00 eq.) in 15 mL glacial acetic acid was stirred at 70 °C for 15 h. Then KCl (1.73 mmol, 2.00 eq.) was added to the reaction mixture. Upon addition of KCl, the color of reaction turned to orange with precipitation. The mixture heated under reflux condition for additional 48 h. The product was filtered off, washed with MeOH, H_2O, EtOH and Et_2O. Yield 0.14 g (0.33 mmol, 38%) pale yellow solid. ^{1}H NMR (600 MHz,

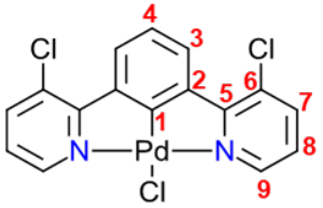
DMSO-d_6, 298 K): δ /ppm = 7.91 (t, J = 7.9 Hz, 2H, H7), 7.70 (d, J = 8.1 Hz, 2H, H6), 7.27 (dd, J = 7.7, 1.2 Hz, 2H, H8), 6.92 (s, 1H, H4), 2.94 (s, 6H, H10), 2.57 (s, 6H, H11). ^{13}C NMR (151 MHz, DMSO-d_6, 298 K): δ /ppm = 163.27 (C9), 161.59 (C5), 139.37 (C7), 138.81 (C2), 135.67 (C3), 132.76 (C4), 123.77 (C8), 119.66 (C6), 40.06 (C1), 26.33 (C10), 21.98 (C11). HR-ESI MS(+): calcd. for $[C_{20}H_{19}N_2Pd]^+$ m/z = 392.05936; found m/z = 392.05217 $[M\text{-}Cl]^+$. Elemental analysis calcd. (%) for $C_{20}H_{19}ClN_2Pd$, M = 429.26 g mol^{-1}: C, 55.96; H, 4.46; N, 6.53. Found C, 54.60; H, 4.85; N, 6.30.



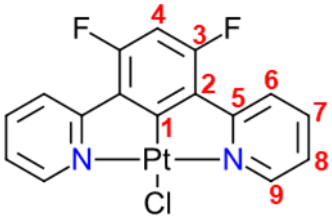
[Pt(L^{Cl})Cl]. From $K_2[PtCl_4]$ 0.14 g (0.33 mmol, 1.00 eq.), HL^{Cl} 0.10 g (0.33 mmol, 1.00 eq.). Yield 0.10 g (0.19 mmol, 57%) yellow solid. ^{1}H NMR (600 MHz, DMSO-d_6, 313 K): δ /ppm = 9.38 (dd, J = 5.5, 1.4 Hz, 2H, H7), 8.43 (d, J = 8.0 Hz, 2H, H3), 8.37 (dd, J = 8.3, 1.4 Hz, 2H, H9), 7.62 (dd, J = 8.2, 5.5 Hz, 2H, H8), 7.38 (t, J = 8.0 Hz, 1H, H4). ^{13}C NMR (151 MHz, DMSO-d_6, 313 K): δ /ppm = 161.05 (C5), 150.63 (C8), 142.79 (C9), 140.12 (C2), 129.76 (C3), 128.55 (C7), 124.58 (C6), 122.63 (C4), 40.06 (C1). HR-ESI MS(+): calcd. for $[C_{16}H_9Cl_2N_2Pt]^+$ m/z = 492.97639; found m/z = 492.97678 $[M\text{-}Cl]^+$. Elemental analysis calcd. (%) for $C_{16}H_9Cl_3N_2Pt$, M = 530.69 g mol^{-1}: C, 36.21; H, 1.71; N, 5.28. Found C, 36.22; H, 1.35; N, 5.14.



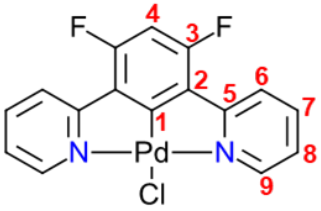
[Pd(L^{Cl})Cl]. From $K_2[PdCl_4]$ 0.11 g (0.33 mmol, 1.00 eq.), HL^{Cl} 0.10 g (0.33 mmol, 1.0 eq.). Yield 0.97 g (0.22 mmol, 66%) yellow solid. ^{1}H NMR (500 MHz, DMSO-d_6, 313 K): δ /ppm = 9.13 (dd, J = 5.3, 1.4 Hz, 2H, H7), 8.41 (d, J = 8.1 Hz, 2H, H3), 8.31 (dd, J = 8.3, 1.5 Hz, 2H, H9), 7.59 (dd, J = 8.3, 5.4 Hz, 2H, H8), 7.38 (t, J = 8.1 Hz, 1H, H4). HR-ESI MS(+): calcd. for $[C_{16}H_9Cl_2N_2Pd]^+$ m/z = 403.91881; found m/z = 403.91900 $[M\text{-}Cl]^+$. Elemental analysis calcd. (%) for $C_{16}H_9Cl_3N_2Pd$, M = 442.04 g mol^{-1}: C, 43.47; H, 2.05; N, 6.34. Found C, 43.14; H, 1.71; N, 6.23.



[Pt(L^{F})Cl]. From $K_2[PtCl_4]$ 0.13 g (0.30 mmol, 1.00 eq.), HL^{F} 0.08 g (0.30 mmol, 1.0 eq.). Yield 0.10 g (0.20 mmol, 70%) yellow solid. ^{1}H NMR (300 MHz, CD_2Cl_2, 298 K): δ /ppm = 9.25 (td, J = 5.7 Hz, J_{PtH} = 41.0 Hz, 2H, H9), 7.99 (td, J = 7.9, 1.6 Hz, 2H, H7), 7.90 (d, J = 7.1 Hz, 2H, H6), 7.33 (ddd, J = 7.4, 5.7, 1.6 Hz, 2H, H8), 6.72 (t, J = 11.3 Hz, 1H, H4). ^{19}F NMR (282 MHz, CD_2Cl_2, 298 K): δ /ppm = –108.83 (d, J = 11.3 Hz, J_{PtF} = 54.0 Hz, F). HR-EI MS(+): calcd. for $[C_{16}H_9F_2N_2Pt]^+$ m/z = 462.03776; found m/z = 462.03762 $[M\text{-}Cl]^+$. Elemental analysis calcd. (%) for $C_{16}H_9ClF_2N_2Pt$, M = 497.78 g mol^{-1}: C, 38.61; H, 1.82; N, 5.63. Found C, 37.16; H, 1.67; N, 5.57.

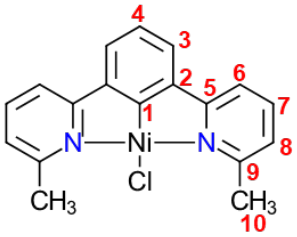


[Pd(L^F)Cl]. From $K_2[PdCl_4]$ 0.14 g (0.4 mmol, 1.0 eq.), HL^F 0.11 g (0.40 mmol, 1.00 eq.). Yield 0.16 g (0.30 mmol, 80%) yellow solid. ^{1}H NMR (300 MHz, CD_2Cl_2, 298 K): δ /ppm = 9.06 (d, *J* = 5.7 Hz, 2H, H9), 7.97–7.87 (m, 4H, H6 and H7), 7.32 (ddd, *J* = 7.3, 5.5, 1.8 Hz, 2H, H8), 6.69 (t, *J* = 11.3 Hz, 1H, H4). ^{19}F NMR (282 MHz, CD_2Cl_2, 298 K): δ /ppm = –108.59 (d, *J* = 11.4 Hz, F). HR-EI MS(+): calcd. for $[C_{16}H_9F_2N_2Pd]^+$ m/z = 372.97696; found m/z = 372.97666 $[M\text{-}Cl]^+$. Elemental analysis calcd. (%) for $C_{16}H_9ClF_2N_2Pd$, M = 409.13 g mol^{-1}: C, 46.97; H, 2.22; N, 6.85. Found C, 46.29; H, 2.10; N, 6.39.

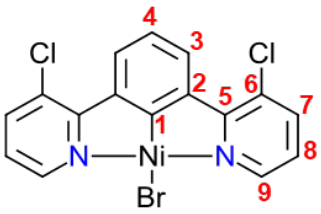


5.2.15. Synthesis of [Ni(N^C^N)X] (N^C^N = L^{Me}, L^F, L^{Cl}; X = Cl or Br) complexes

[Ni(L^{Me})Cl]. Under an inert atmosphere, L^{Me}Cl 0.33 g (1.12 mmol, 1.00 eq.) was dissolved in 15 mL of dry THF. The reaction mixture was transferred in an ice bath at 0 °C and 0.40 g $[Ni(COD)_2]$ (1.46 mmol, 1.30 eq.) was added. The solution transferred to room temperature and turned from yellow to orange with red precipitation during 4 h. Then the solvent was removed and the residue was washed with dry MeCN to remove unreacted ligand and dried under vacuum. Yield 0.25 g (0.71 mmol, 63%) red solid. ^{1}H NMR (300 MHz, DMSO-*d*$_6$, 298 K): δ /ppm = 7.87 (t, *J* = 7.7 Hz, 2H, H7), 7.73 (d, *J* = 7.7 Hz, 2H, H6), 7.53 (d, *J* = 7.6 Hz, 2H, H3), 7.28–7.15 (m, 3H, H8 and H4), 2.89 (s, 6H, H10). HR-ESI MS(+): calcd. for $[C_{18}H_{15}N_2Ni]^+$ m/z = 317.05832; found m/z = 317.05859 $[M\text{-}Cl]^+$. Elemental analysis calcd. (%) for $C_{18}H_{15}ClN_2Ni$, M = 353.5 g mol^{-1}: C, 61.16; H, 4.28; N, 7.93. Found C, 60.76; H, 4.19; N, 7.62.

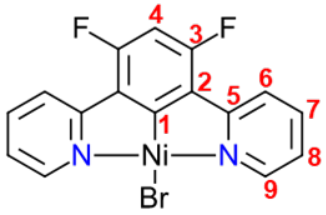


[Ni(L^{Cl})Br]. A Dean-Stark apparatus was equipped with 0.28 g (1.30 mmol, 1.30 eq.) $NiBr_2$, 0.10 g (1.00 mmol, 1.00 eq.) potassium acetate and 0.14 g (1.00 mmol, 1.00 eq.) potassium carbonate and dried under vacuum at 140°C for 1 h. Then HL^{Cl} 0.30 g (1.00 mmol, 1.00 eq.) and p-xylene (200 mL) were added, the reaction mixture was refluxed for 3 d then cooled down to rt. The solid was purified through filtration and extraction using p-xylene**.** Yield 0.11 g (0.30 mmol, 26%) orange solid. ^{1}H NMR (300 MHz, DMSO-*d*$_6$, 298 K): δ /ppm = 8.17 (s, 2H, H9), 8.04 (d, *J* = 8.1 Hz, 2H, H7), 7.83 (d, *J* = 8.3, 2H, H3), 7.17–7.02 (m, 3H, H8 and H4). HR-EI MS(+): calcd. for $[C_{16}H_9Cl_2N_2Ni]^+$ m/z = 358.94567; found m/z = 358.94540 $[M\text{-}Br]^+$. Elemental analysis calcd. (%) for $C_{16}H_9BrCl_2N_2Ni$, M = 438.76 g mol^{-1}: C, 43.80; H, 2.07; N, 6.38. Found C, 43.70; H, 2.33; N, 5.68.



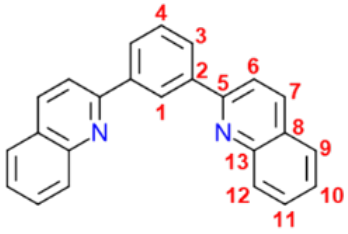
[Ni(L^F)Br]. A Dean-Stark apparatus was equipped with 0.28 g (1.30 mmol, 1.30 eq.) $NiBr_2$, 0.10 g (1.00 mmol, 1.00 eq.) potassium acetate and 0.14 g (1.00 mmol, 1.00 eq.) potassium carbonate and dried under vacuum at 140°C for 1 h. Then HL^F 0.27 g (1.00 mmol, 1.0 eq.) and p-xylene (200 mL) were added,

the reaction mixture was refluxed for 3 d then cooled down to rt. The solid was purified through filtration and extraction using p-xylene**.** Yield 0.29 g (0.70 mmol, 71%) orange solid. ^{1}H NMR (300 MHz, DMSO-d_6, 298 K): δ /ppm = 8.22 (d, J = 5.7 Hz, 2H, H9), 7.93 (td, J = 7.8, 1.6, Hz, 2H, H7), 7.47 (d, J = 7.9 Hz, 2H, H6), 7.16 (ddd, J = 7.3, 5.7, 1.4 Hz, 2H, H8), 6.94 (t, J = 11.0 Hz, 1H, H4). ^{19}F NMR (282 MHz, DMSO-d_6, 298 K): δ /ppm = –111.14 (d, J = 11.0 Hz, F). HR-EI MS(+): calcd. for $[C_{16}H_9F_2N_2Ni]^+$ m/z = 325.00818; found m/z = 325.0 $[M\text{-}Br]^+$. Elemental analysis calcd. (%) for $C_{16}H_9BrF_2N_2Ni$, M = 405.85 g mol^{-1}: C, 47.35; H, 2.24; N, 6.90. Found C, 49.22; H, 2.61; N, 6.30.



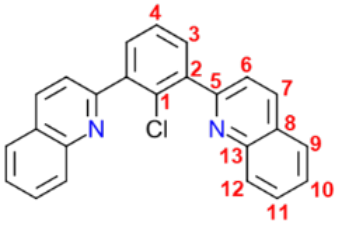
5.2.16. Synthesis of the N^C^N ligand precursors HL^{Qu}

Synthesis of HL^{Qu}. 1,3-phenyldiboronic acid bis(pinacol)ester (0.41 g, 1.23 mmol), 2-bromoquinoline (0.37 g, 1.76 mmol), $[Pd(PPh_3)_4]$ (0.12 g, 6.00 mol%), and K_2CO_3 (0.47 g, 3.52 mmol) were mixed and dissolved in 30 mL H_2O/EtOH (1:4, degassed). The solution was stirred for 24 h at 80 °C under an argon atmosphere. After allowing the reaction mixture to cool to room temperature, the mixture was filtered and diluted with 15 mL CH_2Cl_2. The resulting solution was washed with brine (3 × 20 mL), separated and dried over anhydrous Na_2SO_4. The crude product was purified by column chromatography with *n*-Hex:EtOAc (8:2 v/v). Yield: 0.22 g (0.67 mmol, 76%). ^{1}H NMR (300 MHz, DMSO-d_6, 298 K): δ /ppm = 9.13 (t, J = 1.8 Hz, 1H, H1), 8.52 (d, J = 8.6 Hz, 2H, H7), 8.41 (dd, J = 7.8, 1.8 Hz, 2H, H12), 8.31 (d, J = 8.6 Hz, 2H, H6), 8.16 (d, J = 8.2 Hz, 2H, H3), 8.04 (d, J = 8.1 Hz, 2H, H9), 7.82 (td, J = 8.4, 1.5 Hz, 2H, H10), 7.75 (t, J = 7.8 Hz, 1H, H4), 7.63 (td, J = 8.1, 1.2 Hz, 2H, H11). ^{13}C NMR (75 MHz, DMSO-d_6, 298 K): δ /ppm = 155.94 (C5), 147.57 (C13), 139.35 (C2), 137.32 (C12), 130.00 (C3), 129.47 (C1), 129.15 (C11), 128.44 (C7), 127.85 (C9), 127.11 (C8), 126.58 (C4), 125.98 (C10), 119.01 (C6). HR-ESI MS(+): calcd. for $[C_{24}H_{17}N_2]^+$ m/z = 333.13863; found m/z = 333.13843 $[M+H]^+$. Elemental analysis calcd. (%) for $C_{24}H_{16}N_2$, M = 332.40 g mol^{-1}: C, 86.72; H, 4.85; N, 8.43. Found C, 86.91; H, 5.03; N, 8.06.



5.2.17. Synthesis of the ligand precursor ClL^{Qu}

Synthesis of ClL^{Qu}. 2-chloro-1,3-Phenyldiboronic acid, pinacol ester (1.82 g, 5.00 mmol), 2-bromoquinoline (2.39 g, 2.86 mmol), $[Pd(PPh_3)_4]$ (0.35 g, 6.00 mol%), and K_2CO_3 (2.07 g, 15.00 mmol) were mixed and dissolved in 60 mL H_2O/EtOH (1:4, degassed). The solution was stirred for 24 h at 90 °C under an argon atmosphere. After allowing the reaction mixture to cool to ambient temperature, the mixture was extracted with EtOAc. The extract was washed with brine (2 × 50 mL), separated and dried over anhydrous Na_2SO_4. The crude

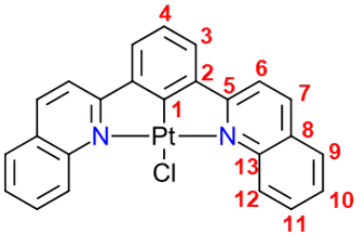


product was purified by column chromatography with *c*-Hex:EtOAc (4:1 v/v). Yield: 1.60 g (3.80 mmol, 87%). ^{1}H NMR (500 MHz, CD_2Cl_2, 298 K): δ /ppm = 8.26 (d, *J* = 8.5 Hz, 2H, H12), 8.15 (d, *J* = 8.4 Hz, 2H, H7), 7.92 (d, *J* = 8.1 Hz, 2H, H9), 7.77 (dt, *J* = 8.3, 3.3 Hz, 4H, H6 and H11), 7.73 (d, *J* = 7.6 Hz, 2H, H3), 7.61 (t, *J* = 7.1 Hz, 2H, H10), 7.57 (t, *J* = 7.6 Hz, 1H, H4). ^{13}C NMR (75 MHz, CD_2Cl_2, 298 K): δ /ppm = 157.68 (C5), 148.09 (C13), 140.92 (C2), 135.58 (C12), 131.72 (C3), 130.64 (C1), 129.62 (C11), 129.55 (C7), 127.60 (C9), 127.17 (C8), 126.97 (C4), 126.79 (C10), 122.92 (C6). HR-ESI MS(+): calcd. for $[C_{24}H_{16}ClN_2]^+$ m/z = 367.09965; found m/z = 367.09976 $[M+H]^+$. Elemental analysis calcd. (%) for $C_{24}H_{15}ClN_2$, M = 366.85 g mol^{-1}: C, 78.58; H, 4.12; N, 7.64. Found C, 78.42; H, 4.13; N, 7.55.

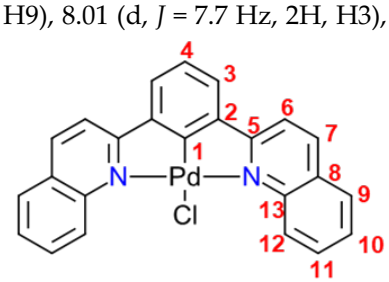
5.2.18. Synthesis of the complexes [M(L^{Qu})Cl] (M = Pt or Pd)

Modifying a previously reported method,[92] a mixture of 1.00 eq. $K_2[PtCl_4]$ or $K_2[PdCl_4]$ and 1.00 eq. of the proto-ligand HL^{Qu} suspended in 8 mL glacial acetic acid and stirred at 110 °C for 3 d. The crude products were filtered off, washed with glacial acetic acid, MeOH, H_2O, EtOH and Et_2O. Further purification was done by washing the crude products with DMSO, acetone and then n-pentane.

[Pt(L^{Qu})Cl]. From $K_2[PtCl_4]$ 0.18 g (0.44 mmol), HL^{Qu} 0.15 g (0.44 mmol). Yield 0.15 g (0.30 mmol, 68%) red solid. ^{1}H NMR (500 MHz, DMSO-d_6, 313 K): δ /ppm = 9.82 (d, *J* = 8.9 Hz, 2H, H7), 8.85 (d, *J* = 8.6 Hz, 2H, H12), 8.36 (d, *J* = 8.5 Hz, 2H, H6), 8.13 (dd, *J* = 7.5, 1.3 Hz, 2H, H9), 8.08 (d, *J* = 7.7 Hz, 2H, H3), 7.93 (td, *J* = 7.9, 1.3 Hz, 2H, H10), 7.74 (td, *J* = 7.1, 1.8 Hz, 2H, H11), 7.48 (t, *J* = 7.7 Hz, 1H, H4). HR-ESI MS(+): calcd. for $[C_{24}H_{15}N_2Pt]^+$ m/z = 526.08564; found m/z = 525.08589 $[M-Cl]^+$. Elemental analysis calcd. (%) for $C_{24}H_{15}ClN_2Pt$, M = 561.92 g mol^{-1}: C, 51.30; H, 2.69; N, 4.99. Found C, 50.98; H, 2.11; N, 4.22.



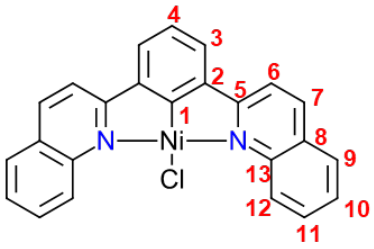
[Pd(L^{Qu})Cl]. From $K_2[PdCl_4]$ 0.16 g (0.49 mmol), HL^{Qu} 0.16 g (0.49 mmol). Yield 0.16 g (0.32 mmol, 65%) yellow solid. ^{1}H NMR (500 MHz, DMSO-d_6, 313 K): δ /ppm = 9.41 (d, *J* = 9.0 Hz, 2H, H7), 8.82 (d, *J* = 8.5 Hz, 2H, H12), 8.37 (d, *J* = 8.6 Hz, 2H, H6), 8.12 (d, *J* = 8.1 Hz, 2H, H9), 8.01 (d, *J* = 7.7 Hz, 2H, H3), 7.92 (t, *J* = 8.8 Hz, 2H, H10), 7.74 (t, *J* = 7.4 Hz, 2H, H11), 7.46 (t, *J* = 7.7 Hz, 1H, H4). HR-ESI MS(+): calcd. for $[C_{24}H_{15}N_2Pd]^+$ m/z = 436.02806; found m/z = 436.02830 $[M-Cl]^+$. Elemental analysis calcd. (%) for $C_{24}H_{15}ClN_2Pd$, M = 473.26 g mol^{-1}: C, 60.01; H, 3.19; N, 5.92. Found C, 66.61; H, 2.69; N, 5.11.



5.2.19. Synthesis of [Ni(L^{Qu})Cl] complex

Under an inert atmosphere, 1.00 eq. of the halogenated derivative of the ligand ClL^{Qu} was dissolved in 12 mL of dry THF. The reaction mixture was transferred in an ice bath at 0 °C and 1.30 eq. of [Ni(COD)$_2$] was added. The reaction was stirred overnight at room temperature and then treated with *n*-pentane (20 mL). After removal of the solvent, the remaining solid was washed with additional *n*-pentane (2 × 20 mL). The solvent was removed and the solid subsequently dried under reduced pressure.

[Ni(L^{Qu})Cl]. From [Ni(COD)$_2$] 0.36 g (1.30 mmol), ClL^{Qu} 0.38 g (1.00 mmol). Yield 0.42 g (1.00 mmol, >99%) red solid. ^{1}H NMR (300 MHz, DMSO-*d*$_6$, 298 K): δ /ppm = 8.50 (d, *J* = 8.4 Hz, 2H), 8.08 (t, *J* = 7.8 Hz, 6H), 7.84 (d, *J* = 8.4 Hz, 3H), 7.76 (d, *J* = 6.9 Hz, 2H), 7.68 (t, *J* = 7.0 Hz, 2H). HR-ESI MS(+): calcd. for [$C_{24}H_{15}N_2Ni$]$^+$ m/z = 389.05832; found m/z = 389.05864 [M-Cl]$^+$. Elemental analysis calcd. (%) for $C_{24}H_{15}ClN_2Ni$, M = 424.54 g mol^{-1}: C, 67.74; H, 3.55; N, 6.58. Found C, 67.70; H, 3.55; N, 6.43.



6. References

(1) Williams, J. A. G. Photochemistry and Photophysics of Coordination Compounds: Platinum. *Photochemistry and Photophysics of Coordination Compounds II*; Balzani, V., Campagna, S., Eds.; Springer: Berlin, Heidelberg, **2007**; 205–268.

(2) Mauro, M.; Aliprandi, A.; Septiadi, D.; Kehr, N. S.; De Cola, L. When Self-Assembly Meets Biology: Luminescent Platinum Complexes for Imaging Applications. *Chem. Soc. Rev.* **2014**, *43* (12), 4144–4166.

(3) Jaffe, H. H.; Miller, A. L. The Fates of Electronic Excitation Energy. *J. Chem. Educ.* **1966**, *43* (9), 469.

(4) Jablonski, A. Efficiency of Anti-Stokes Fluorescence in Dyes. *Nature* **1933**, *131* (3319), 839–840.

(5) Turro, N. J.; Ramamurthy, V.; Scaiano, J. C. *Principles of Molecular Photochemistry: An Introduction*; University Science Books: Sausalito, Calif, **2009**.

(6) Sarma, D. D. Nature of Dependence of Spin-Orbit Splittings on Atomic Number. *Proc. Indian Acad. Sci. - Chem. Sci.* **1981**, *90* (1), 19–26.

(7) Housecroft, C. E.; Constable, E. C. Over the LEC Rainbow: Colour and Stability Tuning of Cyclometallated Iridium(III) Complexes in Light-Emitting Electrochemical Cells. *Coord. Chem. Rev.* **2017**, *350*, 155–177.

(8) Li, K.; Tong, G. S. M.; Wan, Q.; Cheng, G.; Tong, W.-Y.; Ang, W.-H.; Kwong, W.-L.; Che, C.-M. Highly Phosphorescent Platinum(II) Emitters: Photophysics, Materials and Biological Applications. *Chem. Sci.* **2016**, *7* (3), 1653–1673.

(9) Tong, G. S.-M.; Che, C.-M. Emissive or Nonemissive? A Theoretical Analysis of the Phosphorescence Efficiencies of Cyclometalated Platinum(II) Complexes. *Chem. – Eur. J.* **2009**, *15* (29), 7225–7237.

(10) Baggaley, E.; Weinstein, J. A.; Williams, J. A. G. Lighting the Way to See inside the Live Cell with Luminescent Transition Metal Complexes. *Coord. Chem. Rev.* **2012**, *256* (15), 1762–1785.

(11) Zhong, F.; Yuan, X.; Zhao, J.; Wang, Q. Visible Light-Harvesting Tricarbonyl Re(I) Complex: Synthesis and Application in Intracellular Photodynamic Effect and Luminescence Imaging. *Sci. China Chem.* **2016**, *59* (1), 70–77.

(12) Gareth Williams, J. A.; Develay, S.; Rochester, D. L.; Murphy, L. Optimising the Luminescence of Platinum(II) Complexes and Their Application in Organic Light Emitting Devices (OLEDs). *Coord. Chem. Rev.* **2008**, *252* (23), 2596–2611.

(13) Eastwood, D.; Gouterman, M. Porphyrins: XVIII. Luminescence of (Co), (Ni), Pd, Pt Complexes. *J. Mol. Spectrosc.* **1970**, *35* (3), 359–375.

(14) McGuire, R.; McGuire, M. C.; McMillin, D. R. Platinum(II) Polypyridines: A Tale of Two Axes. *Coord. Chem. Rev.* **2010**, *254* (21), 2574–2583.

(15) McMillin, D. R.; Moore, J. J. Luminescence that Lasts from $[Pt(Trpy)Cl]^+$ Derivatives (Trpy=2,2′;6′,2″-Terpyridine). *Coord. Chem. Rev.* **2002**, *229* (1), 113–121.

(16) Crites, D. K.; Cunningham, C. T.; McMillin, D. R. Remarkable Substituent Effects on the Photophysics of $[Pt(4'-X-Trpy)Cl]^+$ Systems (Trpy = 2,2′; 6′,2″-Terpyridine). *Inorganica Chim. Acta* **1998**, *273* (1), 346–353.

(17) Castellano, F. N.; Pomestchenko, I. E.; Shikhova, E.; Hua, F.; Muro, M. L.; Rajapakse, N. Photophysics in Bipyridyl and Terpyridyl Platinum(II) Acetylides. *Coord. Chem. Rev.* **2006**, *250* (13), 1819–1828.

(18) Liu, X.-J.; Feng, J.-K.; Meng, J.; Pan, Q.-J.; Ren, A.-M.; Zhou, X.; Zhang, H.-X. A Theoretical Investigation of Substituent Effects on the Absorption and Emission Properties of a Series of Terpyridylplatinum(II) Acetylide Complexes. *Eur. J. Inorg. Chem.* **2005**, *2005* (10), 1856–1866.

(19) Hua, F.; Kinayyigit, S.; Cable, J. R.; Castellano, F. N. Platinum(II) Diimine Diacetylides: Metallacyclization Enhances Photophysical Properties. *Inorg. Chem.* **2006**, *45* (11), 4304–4306.

(20) Hua, F.; Kinayyigit, S.; Cable, J. R.; Castellano, F. N. Green Photoluminescence from Platinum(II) Complexes Bearing Silylacetylide Ligands. *Inorg. Chem.* **2005**, *44* (3), 471–473.

(21) Wilson, M. H.; Ledwaba, L. P.; Field, J. S.; McMillin, D. R. Push–Pull Effects and Emission from Ternary Complexes of Platinum(II), Substituted Terpyridines, and the Strong-Field Cyanide Ion. *Dalton Trans.* **2005**, No. 16, 2754–2759.

(22) Law, A. S.-Y.; Lee, L. C.-C.; Lo, K. K.-W.; Yam, V. W.-W. Aggregation and Supramolecular Self-Assembly of Low-Energy Red Luminescent Alkynylplatinum(II) Complexes for RNA Detection, Nucleolus Imaging, and RNA Synthesis Inhibitor Screening. *J. Am. Chem. Soc.* **2021**, *143* (14), 5396–5405.

(23) Liu, L.; Wang, X.; Hussain, F.; Zeng, C.; Wang, B.; Li, Z.; Kozin, I.; Wang, S. Multiresponsive Tetradentate Phosphorescent Metal Complexes as Highly Sensitive and Robust Luminescent Oxygen Sensors: Pd(II) versus Pt(II) and 1,2,3-Triazolyl versus 1,2,4-Triazolyl. *ACS Appl. Mater. Interfaces* **2019**, *11* (13), 12666–12674.

(24) Parasram, M.; Gevorgyan, V. Visible Light-Induced Transition Metal-Catalyzed Transformations: Beyond Conventional Photosensitizers. *Chem. Soc. Rev.* **2017**, *46* (20), 6227–6240.

(25) Yam, V. W.-W.; Law, A. S.-Y. Luminescent d^8 Metal Complexes of Platinum(II) and Gold(III): from Photophysics to Photo-functional Materials and Probes. *Coord. Chem. Rev.* **2020**, *414*, 213298.

(26) Xu, G.-X.; Mak, E. C.-L.; Lo, K. K.-W. Photo-functional Transition Metal Complexes as Cellular Probes, Bioimaging Reagents and Phototherapeutics. *Inorg. Chem. Front.* **2021**, *8* (20), 4553–4579.

(27) Zhen, X.; Qu, R.; Chen, W.; Wu, W.; Jiang, X. The Development of Phosphorescent Probes for In-itro and In-vivo Bioimaging. *Biomater. Sci.* **2021**, *9* (2), 285–300.

(28) Niazi, M.; Maisuls, I.; Strassert, C. A.; Klein, A. Molecular Rigidification of Cyclometalated N^C^N Pt(II)- and Pd(II)-Based Triplet Emitters. *Organometallics* **2024**, *43* (14), 1547–1556.

(29) Krause, M.; von der Stück, R.; Brünink, D.; Buss, S.; Doltsinis, N. L.; Strassert, C. A.; Klein, A. Platinum and Palladium Complexes of Tridentate −C^N^N (Phen-ide)-Pyridine-Thiazol Ligands – A Case Study Involving Spectroelectrochemistry, Photoluminescence Spectroscopy and TD-DFT Calculations. *Inorganica Chim. Acta* **2021**, *518*, 120093.

(30) Fleetham, T.; Ji, Y.; Huang, L.; Fleetham, T. S.; Li, J. Efficient and Stable Single-Doped White OLEDs Using a Palladium-Based Phosphorescent Excimer. *Chem. Sci.* **2017**, *8* (12), 7983–7990.

(31) Bryant, M. J.; Skelton, J. M.; Hatcher, L. E.; Stubbs, C.; Madrid, E.; Pallipurath, A. R.; Thomas, L. H.; Woodall, C. H.; Christensen, J.; Fuertes, S.; Robinson, T. P.; Beavers, C. M.; Teat, S. J.; Warren, M. R.; Pradaux-Caggiano, F.; Walsh, A.; Marken, F.; Carbery, D. R.; Parker, S. C.; McKeown, N. B.; Malpass-Evans, R.; Carta, M.; Raithby, P. R. A Rapidly-Reversible Absorptive and Emissive Vapochromic Pt(II) Pincer-Based Chemical Sensor. *Nat. Commun.* **2017**, *8* (1), 1800.

(32) Cheung, T.-C.; Cheung, K.-K.; Peng, S.-M.; Che, C.-M. Photoluminescent Cyclometallated Diplatinum(II,II) Complexes: Photophysical Properties and Crystal Structures of $[PtL(PPh_3)]ClO_4$ and $[Pt_2L_2(\mu\text{-Dppm})][ClO_4]_2$ (HL = 6-Phenyl-2,2′-Bipyridine, Dppm = $Ph_2PCH_2PPh_2$). *J. Chem. Soc. Dalton Trans.* **1996**, No. 8, 1645–1651.

(33) Chan, A. K.-W.; Ng, M.; Wong, Y.-C.; Chan, M.-Y.; Wong, W.-T.; Yam, V. W.-W. Synthesis and Characterization of Luminescent Cyclometalated Platinum(II) Complexes with Tunable Emissive Colors and Studies of their Application in Organic Memories and Organic Light-Emitting Devices. *J. Am. Chem. Soc.* **2017**, *139* (31), 10750–10761.

(34) Doherty, R. E.; Sazanovich, I. V.; McKenzie, L. K.; Stasheuski, A. S.; Coyle, R.; Baggaley, E.; Bottomley, S.; Weinstein, J. A.; Bryant, H. E. Photodynamic Killing of Cancer Cells by a Platinum(II) Complex with Cyclometallating Ligand. *Sci. Rep.* **2016**, *6* (1), 22668.

(35) Eskelinen, T.; Buss, S.; Petrovskii, S. K.; Grachova, E. V.; Krause, M.; Kletsch, L.; Klein, A.; Strassert, C. A.; Koshevoy, I. O.; Hirva, P. Photophysics and Excited State Dynamics of Cyclometalated [M(Phbpy)(CN)] (M = Ni, Pd, Pt) Complexes: A Theoretical and Experimental Study. *Inorg. Chem.* **2021**, *60* (12), 8777–8789.

(36) Lai, S.-W.; Cheung, T.-C.; Chan, M. C. W.; Cheung, K.-K.; Peng, S.-M.; Che, C.-M. Luminescent Mononuclear and Binuclear Cyclometalated Palladium(II) Complexes of 6-Phenyl-2,2′-Bipyridines: Spectroscopic and Structural Comparisons with Platinum(II) Analogues. *Inorg. Chem.* **2000**, *39* (2), 255–262.

(37) Zhang, J.; Zhang, Z.; Su, M.; Xu, X.; Gao, R.; Yu, B.; Yan, X. Cyclometalated *N* -Difluoromethylbenzimidazolylidene Platinum(II) Complexes with Built-in Secondary

Coordination Spheres: Photophysical Properties and Bioimaging. *Inorg. Chem.* **2024**, *63* (48), 22782–22791.

(38) Krause, M.; Kourkoulos, D.; González-Abradelo, D.; Meerholz, K.; Strassert, C. A.; Klein, A. Luminescent Pt(II) Complexes of Tridentate Cyclometalating 2,5-Bis(Aryl)-Pyridine Ligands. *Eur. J. Inorg. Chem.* **2017**, *2017* (44), 5215–5223.

(39) Sivchik, V.; Sarker, R. K.; Liu, Z.-Y.; Chung, K.-Y.; Grachova, E. V.; Karttunen, A. J.; Chou, P.-T.; Koshevoy, I. O. Improvement of the Photophysical Performance of Platinum-Cyclometalated Complexes in Halogen-Bonded Adducts. *Chem. Weinh. Bergstr. Ger.* **2018**, *24* (44), 11475–11484.

(40) Poirier, S.; Lynn, H.; Reber, C.; Tailleur, E.; Marchivie, M.; Guionneau, P.; Probert, M. R. Variation of M···H–C Interactions in Square-Planar Complexes of Nickel(II), Palladium(II), and Platinum(II) Probed by Luminescence Spectroscopy and X-Ray Diffraction at Variable Pressure. *Inorg. Chem.* **2018**, *57* (13), 7713–7723.

(41) Kletsch, L.; Jordan, R.; Köcher, A. S.; Buss, S.; Strassert, C. A.; Klein, A. Photoluminescence of Ni(II), Pd(II), and Pt(II) Complexes [M(Me_2dpb)Cl] Obtained from C–H Activation of 1,5-Di(2-Pyridyl)-2,4-Dimethylbenzene (Me_2dpbH). *Molecules* **2021**, *26* (16), 5051.

(42) Fleetham, T.; Li, G.; Li, J. Phosphorescent Pt(II) and Pd(II) Complexes for Efficient, High-Color-Quality, and Stable OLEDs. *Adv. Mater.* **2017**, *29* (5), 1601861.

(43) Zhang, Y.; Wang, Y.; Song, J.; Qu, J.; Li, B.; Zhu, W.; Wong, W.-Y. Near-Infrared Emitting Materials via Harvesting Triplet Excitons: Molecular Design, Properties, and Application in Organic Light Emitting Diodes. *Adv. Opt. Mater.* **2018**, *6* (18), 1800466.

(44) Lai, P.-N.; Brysacz, C. H.; Alam, M. K.; Ayoub, N. A.; Gray, T. G.; Bao, J.; Teets, T. S. Highly Efficient Red-Emitting Bis-Cyclometalated Iridium Complexes. *J. Am. Chem. Soc.* **2018**, *140* (32), 10198–10207.

(45) Saito, D.; Ogawa, T.; Yoshida, M.; Takayama, J.; Hiura, S.; Murayama, A.; Kobayashi, A.; Kato, M. Intense Red-Blue Luminescence Based on Superfine Control of Metal–Metal Interactions for Self-Assembled Platinum(II) Complexes. *Angew. Chem. Int. Ed.* **2020**, *59* (42), 18723–18730.

(46) Maisuls, I.; Wang, C.; Suburu, M. E. G.; Wilde, S.; Daniliuc, C.-G.; Brünink, D.; Doltsinis, N. L.; Ostendorp, S.; Wilde, G.; Kösters, J.; Resch-Genger, U.; Strassert, C. A. Ligand-Controlled and Nanoconfinement-Boosted Luminescence Employing Pt(II) and Pd(II) Complexes: from Color-Tunable Aggregation-Enhanced Dual Emitters towards Self-Referenced Oxygen Reporters. *Chem. Sci.* **2021**, *12* (9), 3270–3281.

(47) Wenger, O. S. Vapochromism in Organometallic and Coordination Complexes: Chemical Sensors for Volatile Organic Compounds. *Chem. Rev.* **2013**, *113* (5), 3686–3733.

(48) Kobayashi, A.; Kato, M. Vapochromic Platinum(II) Complexes: Crystal Engineering toward Intelligent Sensing Devices. *Eur. J. Inorg. Chem.* **2014**, *2014* (27), 4469–4483.

(49) Walden, M. T.; Pander, P.; Yufit, D. S.; Dias, F. B.; Williams, J. A. G. Homoleptic Platinum(II) Complexes with Pyridyltriazole Ligands: Excimer-Forming Phosphorescent Emitters for Solution-Processed OLEDs. *J. Mater. Chem. C* **2019**, *7* (22), 6592–6606.

(50) Bizzarri, C.; Spuling, E.; Knoll, D. M.; Volz, D.; Bräse, S. Sustainable Metal Complexes for Organic Light-Emitting Diodes (OLEDs). *Coord. Chem. Rev.* **2018**, *373*, 49–82.

(51) Glaser, F.; Wenger, O. S. Recent Progress in the Development of Transition-Metal Based Photoredox Catalysts. *Coord. Chem. Rev.* **2020**, *405*, 213129.

(52) Zhong, J.-J.; Yang, C.; Chang, X.-Y.; Zou, C.; Lu, W.; Che, C.-M. Platinum(II) Photo-Catalysis for Highly Selective Difluoroalkylation Reactions. *Chem. Commun.* **2017**, *53* (64), 8948–8951.

(53) McCusker, J. K. Electronic Structure in the Transition Metal Block and its Implications for Light Harvesting. *Science* **2019**, *363* (6426), 484–488.

(54) Aliprandi, A.; Mauro, M.; De Cola, L. Controlling and Imaging Biomimetic Self-Assembly. *Nat. Chem.* **2016**, *8* (1), 10–15.

(55) Kasera, A.; Biswas, J. P.; Ali Alshehri, A.; Ahmed Al-Thabaiti, S.; Mokhtar, M.; Maiti, D. Transition Metal Pincer Complexes: A Series of Potential Catalysts in C-H Activation Reactions. *Coord. Chem. Rev.* **2023**, *475*, 214915.

(56) He, F.; Zois, K. P.; Tzeli, D.; Danopoulos, A. A.; Braunstein, P. N-Heterocyclic Carbenes as Bridgehead Donors in Metal Pincer Complexes. *Coord. Chem. Rev.* **2024**, *514*, 215757.

(57) Gafurov, Z. N.; Kantyukov, A. O.; Kagilev, A. A.; Kagileva, A. A.; Sakhapov, I. F.; Mikhailov, I. K.; Yakhvarov, D. G. Recent Advances in Chemistry of Unsymmetrical Phosphorus-Based Pincer Nickel Complexes: from Design to Catalytic Applications. *Molecules* **2021**, *26* (13), 4063.

(58) Theiss, T.; Buss, S.; Maisuls, I.; López-Arteaga, R.; Brünink, D.; Kösters, J.; Hepp, A.; Doltsinis, N. L.; Weiss, E. A.; Strassert, C. A. Room-Temperature Phosphorescence from Pd(II) and Pt(II) Complexes as Supramolecular Luminophores: The Role of Self-Assembly, Metal–Metal Interactions, Spin–Orbit Coupling, and Ligand-Field Splitting. *J. Am. Chem. Soc.* **2023**, *145* (7), 3937–3951.

(59) Von Der Stück, R.; Schmitz, S.; Klein, A. C–X vs C–H Activation for the Synthesis of the Cyclometalated Complexes [Pd(YPhbpy)X] (HPhbpy = 6-Phenyl-2,2′-Bipyridine; X/Y = (Pseudo)Halides). *Inorg. Chem. Res.* **2021**, *5* (2), 173–192.

(60) von der Stück, R.; Krause, M.; Brünink, D.; Buss, S.; Doltsinis, N. L.; Strassert, C. A.; Klein, A. Luminescent Pd(II) Complexes with Tridentate − Aryl-Pyridine-(Benzo)Thiazole Ligands. *Z. Für Anorg. Allg. Chem.* **2022**, *648* (1), e202100278.

(61) Esteruelas, M. A.; Moreno-Blázquez, S.; Oliván, M.; Oñate, E. N,C,N-Pincers in Platinum Bimetallic Complexes: Influence of the Pincer and Bridging Ligands on the Metal–Metal Bond and the Photophysical Properties. *Inorg. Chem.* **2024**, *63* (31), 14482–14494.

(62) Williams, J. A. G.; Beeby, A.; Davies, E. S.; Weinstein, J. A.; Wilson, C. An Alternative Route to Highly Luminescent Platinum(II) Complexes: Cyclometalation with N^C^N-Coordinating Dipyridylbenzene Ligands. *Inorg. Chem.* **2003**, *42* (26), 8609–8611.

(63) Farley, S. J.; Rochester, D. L.; Thompson, A. L.; Howard, J. A. K.; Williams, J. A. G. Controlling Emission Energy, Self-Quenching, and Excimer Formation in Highly Luminescent N^C^N-Coordinated Platinum(II) Complexes. *Inorg. Chem.* **2005**, *44* (26), 9690–9703.

(64) Wang, Z.; Turner, E.; Mahoney, V.; Madakuni, S.; Groy, T.; Li, J. Facile Synthesis and Characterization of Phosphorescent Pt(N^C^N)X Complexes. *Inorg. Chem.* **2010**, *49* (24), 11276–11286.

(65) Jordan, R.; Maisuls, I.; Nair, S. S.; Dietzek-Ivanšić, B.; Strassert, C. A.; Klein, A. Enhanced Luminescence Properties through Heavy Ancillary Ligands in [Pt(C^N^C)(L)] Complexes, L = $AsPh_3$ and $SbPh_3$. *Dalton Trans.* **2023**, *52* (48), 18220–18232.

(66) Sanning, J.; Ewen, P. R.; Stegemann, L.; Schmidt, J.; Daniliuc, C. G.; Koch, T.; Doltsinis, N. L.; Wegner, D.; Strassert, C. A. Scanning-Tunneling-Spectroscopy-Directed Design of Tailored Deep-Blue Emitters. *Angew. Chem. Int. Ed.* **2015**, *54* (3), 786–791.

(67) Hebenbrock, M.; González-Abradelo, D.; Hepp, A.; Meadowcroft, J.; Lefringhausen, N.; Strassert, C. A.; Müller, J. Influence of the Ancillary Ligands on the Luminescence of Platinum(II) Complexes with a Triazole-Based Tridentate C^N^N Luminophore. *Inorganica Chim. Acta* **2021**, *516*, 119988.

(68) Ogawa, T.; Sameera, W. M. C.; Yoshida, M.; Kobayashi, A.; Kato, M. Phosphorescence Properties of Anionic Cyclometalated Platinum(II) Complexes with Fluorine-Substituted Tridentate Diphenylpyridine in the Solid State. *Chem. Phys. Lett.* **2020**, *739*, 137024.

(69) Sheelakumari, S. P.; Cappellari, M. V.; Rivas Aiello, M. B.; Hepp, A.; Strassert, C. A. Synthesis and Photophysical Evaluation of Isoleptic Pt(II) and Pd(II) Complexes Utilizing N^N^N Ligands as Luminophoric Chelators with Different Ancillary Ligands. *Inorganics* **2024**, *12* (2), 58.

(70) Kulikova, M. V.; Balashev, K. P.; Erzin, Kh. Synthesis and Photophysical Properties of a Series of Biscyclometalated Platinum(II) Complexes on the Basis of a Tridentate 2,6-Diphenylpyridine. *Russ. J. Gen. Chem.* **2003**, *73* (12), 1839–1845.

(71) Lu, W.; Chan, M. C. W.; Cheung, K.-K.; Che, C.-M. π-π Interactions in Organometallic Systems. Crystal Structures and Spectroscopic Properties of Luminescent Mono-, Bi-, and Trinuclear Trans-

Cyclometalated Platinum(II) Complexes Derived from 2,6-Diphenylpyridine. *Organometallics* **2001**, *20* (12), 2477–2486.

(72) Lai, S.-W.; Chan, M. C.-W.; Cheung, T.-C.; Peng, S.-M.; Che, C.-M. Probing d^8–d^8 Interactions in Luminescent Mono- and Binuclear Cyclometalated Platinum(II) Complexes of 6-Phenyl-2,2′-Bipyridines. *Inorg. Chem.* **1999**, *38* (18), 4046–4055.

(73) Prokhorov, A. M.; Hofbeck, T.; Czerwieniec, R.; Suleymanova, A. F.; Kozhevnikov, D. N.; Yersin, H. Brightly Luminescent Pt(II) Pincer Complexes with a Sterically Demanding Carboranyl-Phenylpyridine Ligand: A New Material Class for Diverse Optoelectronic Applications. *J. Am. Chem. Soc.* **2014**, *136* (27), 9637–9642.

(74) Ogawa, T.; Wenger, O. S. Nickel(II) Analogues of Phosphorescent Platinum(II) Complexes with Picosecond Excited-State Decay. *Angew. Chem. Int. Ed.* **2023**, *62* (46), e202312851.

(75) Ogawa, T.; Sinha, N.; Pfund, B.; Prescimone, A.; Wenger, O. S. Molecular Design Principles to Elongate the Metal-to-Ligand Charge Transfer Excited-State Lifetimes of Square-Planar Nickel(II) Complexes. *J. Am. Chem. Soc.* **2022**, *144* (48), 21948–21960.

(76) Ting, S. I.; Garakyaraghi, S.; Taliaferro, C. M.; Shields, B. J.; Scholes, G. D.; Castellano, F. N.; Doyle, A. G. ^{3}d-d Excited States of Ni(II) Complexes Relevant to Photoredox Catalysis: Spectroscopic Identification and Mechanistic Implications. *J. Am. Chem. Soc.* **2020**, *142* (12), 5800–5810.

(77) Andrews, L. J. Radiationless Decay in Rhodium(I) and Iridiuum(I) Complexes. Polarization and Solvent Relaxation Studies. *J. Phys. Chem.* **1979**, *83* (25), 3203–3209.

(78) Yarnell, J. E.; Davydenko, I.; Dorovatovskii, P. V.; Khrustalev, V. N.; Timofeeva, T. V.; Castellano, F. N.; Marder, S. R.; Risko, C.; Barlow, S. Positional Effects from σ-Bonded Platinum(II) on Intersystem Crossing Rates in Perylenediimide Complexes: Synthesis, Structures, and Photophysical Properties. *J. Phys. Chem. C* **2018**, *122* (25), 13848–13862.

(79) Imoto, H.; Tanaka, S.; Kato, T.; Watase, S.; Matsukawa, K.; Yumura, T.; Naka, K. Highly Efficient Solid-State Phosphorescence of Platinum Dihalide Complexes with 9-Phenyl-9-Arsafluorene Ligands. *Organometallics* **2016**, *35* (3), 364–369.

(80) Grant, G. J. Pnictogen–Thiacrown Complexes with Pt(II) and Pd(II). *Dalton Trans.* **2012**, *41* (29), 8745.

(81) Beckmann, J.; Bolsinger, J.; Duthie, A.; Finke, P.; Lork, E.; Lüdtke, C.; Mallow, O.; Mebs, S. Mesityltellurenyl Cations Stabilized by Triphenylpnictogens $[MesTe(EPh_3)]^+$ (E = P, As, Sb). *Inorg. Chem.* **2012**, *51* (22), 12395–12406.

(82) Gangadharappa, S. C.; Maisuls, I.; Schwab, D. A.; Kösters, J.; Doltsinis, N. L.; Strassert, C. A. Compensation of Hybridization Defects in Phosphorescent Complexes with Pnictogen-Based

Ligands—A Structural, Photophysical, and Theoretical Case-Study with Predictive Character. *J. Am. Chem. Soc.* **2020**, *142* (51), 21353–21367.

(83) Buss, S.; Ketter, L.; Brünink, D.; Schwab, D.; Klenner, S.; Hepp, A.; Kösters, J.; Schmidt, T. J.; Pöttgen, R.; Doltsinis, N. L.; Strassert, C. A. Antiprotozoal Pt(II) Complexes as Luminophores Bearing Monodentate P/As/Sb-Based Donors: An X-Ray Diffractometric, Photoluminescence, and ^{121}Sb-Mössbauer Spectroscopic Study with TD-DFT-Guided Interpretation and Predictive Extrapolation toward Bi. *Inorg. Chem.* **2024**, *63* (22), 10114–10126.

(84) Feuerstein, W.; Breher, F. Synthetic Access to a Phosphorescent Non-Palindromic Pincer Complex of Palladium by a Double Oxidative Addition – Comproportionation Sequence. *Chem. Commun.* **2020**, *56* (83), 12589–12592.

(85) Wegeberg, C.; Wenger, O. S. Luminescent First-Row Transition Metal Complexes. *JACS Au* **2021**, *1* (11), 1860–1876.

(86) Wenger, O. S. Photoactive Complexes with Earth-Abundant Metals. *J. Am. Chem. Soc.* **2018**, *140* (42), 13522–13533.

(87) Carrasco, R.; Cano, J.; Ottenwaelder, X.; Aukauloo, A.; Journaux, Y.; Ruiz-García, R. Molecular and Electronic Structure of Square-Planar Nickel(II) and Nickel(III) π-Cation Radical Complexes with a Tetradentate *o*-Phenylenedioxamidate Redox-Active Ligand. *Dalton Trans.* **2005**, No. 15, 2527.

(88) Blanchard, S.; Neese, F.; Bothe, E.; Bill, E.; Weyhermüller, T.; Wieghardt, K. Square Planar vs Tetrahedral Coordination in Diamagnetic Complexes of Nickel(II) Containing Two Bidentate π-Radical Monoanions. *Inorg. Chem.* **2005**, *44* (10), 3636–3656.

(89) Bruce-Smith, I. F.; Zakharov, B. A.; Stare, J.; Boldyreva, E. V.; Pulham, C. R. Structural Properties of Nickel Dimethylglyoxime at High Pressure: Single-Crystal X-Ray Diffraction and DFT Studies. *J. Phys. Chem. C* **2014**, *118* (42), 24705–24713.

(90) Gao, M.; To, W.-P.; Tong, G. S. M.; Du, L.; Low, K.-H.; Tang, Z.; Lu, W.; Che, C.-M. Dinuclear Cyclometalated Pincer Nickel(II) Complexes with Metal-Metal-to-Ligand Charge Transfer Excited States and Near-Infrared Emission. *Angew. Chem. Int. Ed.* **2025**, *64* (2), e202414411.

(91) Wong, Y.-S.; Tang, M.-C.; Ng, M.; Yam, V. W.-W. Toward the Design of Phosphorescent Emitters of Cyclometalated Earth-Abundant Nickel(II) and Their Supramolecular Study. *J. Am. Chem. Soc.* **2020**, *142* (16), 7638–7646.

(92) Cárdenas, D. J.; Echavarren, A. M.; Ramírez de Arellano, M. C. Divergent Behavior of Palladium(II) and Platinum(II) in the Metalation of 1,3-Di(2-Pyridyl)Benzene. *Organometallics* **1999**, *18* (17), 3337–3341.

(93) Zvirzdinaite, M.; Garbe, S.; Arefyeva, N.; Krause, M.; von der Stück, R.; Klein, A. Palladium(II) Complexes of Ambidentate and Potentially Cyclometalating 5-Aryl-3-(2′-Pyridyl)-1,2,4-Triazine Ligands. *Eur. J. Inorg. Chem.* **2017**, *2017* (13), 2011–2022.

(94) Soro, B.; Stoccoro, S.; Minghetti, G.; Zucca, A.; Cinellu, M. A.; Gladiali, S.; Manassero, M.; Sansoni, M. Synthesis of the First C-2 Cyclopalladated Derivatives of 1,3-Bis(2-Pyridyl)Benzene. Crystal Structures of [Hg(N-C-N)Cl], [Pd(N-C-N)Cl], and $[Pd_2(N\text{-}C\text{-}N)_2(\mu\text{-}OAc)]_2[Hg_2Cl_6]$. Catalytic Activity in the Heck Reaction. *Organometallics* **2005**, *24* (1), 53–61.

(95) Payen, L.; Kletsch, L.; Lapić, T.; Wickleder, M.; Klein, A. C–H Metalation of Terpyridine Stereoisomers with Ni(II), Pd(II), and Pt(II). *Inorganics* **2023**, *11* (4), 174.

(96) Vogt, N.; Sandleben, A.; Kletsch, L.; Schäfer, S.; Chin, M. T.; Vicic, D. A.; Hörner, G.; Klein, A. Role of the X Coligands in Cyclometalated [Ni(Phbpy)X] Complexes (HPhbpy = 6-Phenyl-2,2′-Bipyridine). *Organometallics* **2021**, *40* (11), 1776–1785.

(97) Mousa, A. H.; Chakrabarti, K.; Isapour, G.; Bendix, J.; Wendt, O. F. Enhancing the Stability of Aromatic PCN Pincer Nickel Complexes by Incorporation of Pyridine as the Nitrogen Side Arm. *Eur. J. Inorg. Chem.* **2020**, *2020* (45), 4270–4277.

(98) Garbe, S.; Krause, M.; Klimpel, A.; Neundorf, I.; Lippmann, P.; Ott, I.; Brünink, D.; Strassert, C. A.; Doltsinis, N. L.; Klein, A. Cyclometalated Pt Complexes of CNC Pincer Ligands: Luminescence and Cytotoxic Evaluation. *Organometallics* **2020**, *39* (5), 746–756.

(99) Parthiban, M.; Thangaraj, K.; Vinothkumar, K.; Baskaran, S.; Rajakannu, P. Intra-Molecular Hydrogen Bonding Interactions Controlled the Formation of *Cis*- and *Trans*-Pt (II) Emitters: Tuning the Emission Wavelength through Tuning the Functionality. *J. Mol. Struct.* **2025**, *1326*, 141097.

(100) Dahl, E. W.; Szymczak, N. K. Hydrogen Bonds Dictate the Coordination Geometry of Copper: Characterization of a Square-Planar Copper(I) Complex. *Angew. Chem. Int. Ed.* **2016**, *55* (9), 3101–3105.

(101) Takeda, K.; Sasaki, T.; Hayashi, J.; Kagami, S.; Shirotani, I.; Yakushi, K. X-Ray and Optical Studies of One-Dimensional Bis(Dimethylglyoximato)Pd(II), $Pd(Dmg)_2$ at High Pressures. *J. Phys. Conf. Ser.* **2010**, *215*, 012065.

(102) Hsu, C.-W.; Zhao, Y.; Yeh, H.-H.; Lu, C.-W.; Fan, C.; Hu, Y.; Robertson, N.; Lee, G.-H.; Sun, X. W.; Chi, Y. Efficient Pt(II) Emitters Assembled from Neutral Bipyridine and Dianionic Bipyrazolate: Designs, Photophysical Characterization and the Fabrication of Non-Doped OLEDs. *J. Mater. Chem. C* **2015**, *3* (41), 10837–10847.

(103) Kletsch, L.; Hörner, G.; Klein, A. Cyclometalated Ni(II) Complexes [Ni(N∧C∧N)X] of the Tridentate 2,6-Di(2-Pyridyl)Phen-Ide Ligand. *Organometallics* **2020**, *39* (15), 2820–2829.

(104) Sandleben, A.; Vogt, N.; Hörner, G.; Klein, A. Redox Series of Cyclometalated Nickel Complexes [Ni((R)Ph(R′)Bpy)Br]+/0/–/2– (H–(R)Ph(R′)Bpy = Substituted 6-Phenyl-2,2′-Bipyridine). *Organometallics* **2018**, *37* (19), 3332–3341.

(105) Karlen, T.; Ludi, A.; Guedel, H. U.; Riesen, H. One-Dimensional Migration of ^{3}MLCT (Metal-to-Ligand Charge Transfer) Excitation Energy in Chloro(6-Phenyl-2,2′-Bipyridine)Palladium($^{+}$). *Inorg. Chem.* **1991**, *30* (10), 2249–2250.

(106) Steiner, T. The Hydrogen Bond in the Solid State. *Angew. Chem. Int. Ed.* **2002**, *41* (1), 48–76.

(107) Kalinowski, J.; Fattori, V.; Cocchi, M.; Williams, J. A. G. Light-Emitting Devices Based on Organometallic Platinum Complexes as Emitters. *Coord. Chem. Rev.* **2011**, *255* (21), 2401–2425.

(108) Baggaley, E.; Botchway, S. W.; Haycock, J. W.; Morris, H.; Sazanovich, I. V.; Williams, J. A. G.; Weinstein, J. A. Long-Lived Metal Complexes Open up Microsecond Lifetime Imaging Microscopy under Multiphoton Excitation: From FLIM to PLIM and Beyond. *Chem. Sci.* **2014**, *5* (3), 879–886.

(109) Kirse, T. M.; Lüke, J.; Maisuls, I.; Hepp, A.; Strassert, C. A. Comparison of Phosphorescent Pt(II) Complexes with C^N^N vs N^N^N Chelators and Caffeine-Based NHC-Co-Ligands. *Photochem. Photobiol.* **2023**, *99* (2), 616–623.

(110) Plasser, F. TheoDORE: A Toolbox for a Detailed and Automated Analysis of Electronic Excited State Computations. *J. Chem. Phys.* **2020**, *152* (8), 084108.

(111) Zheng, Q.; Borsley, S.; Nichol, G. S.; Duarte, F.; Cockroft, S. L. The Energetic Significance of Metallophilic Interactions. *Angew. Chem. Int. Ed.* **2019**, *58* (36), 12617–12623.

(112) Hirata, S.; Head-Gordon, M. Time-Dependent Density Functional Theory within the Tamm–Dancoff Approximation. *Chem. Phys. Lett.* **1999**, *314* (3), 291–299.

(113) Adamo, C.; Barone, V. Toward Reliable Density Functional Methods without Adjustable Parameters: The PBE0 Model. *J. Chem. Phys.* **1999**, *110* (13), 6158–6170.

(114) Andrae, D.; Häußermann, U.; Dolg, M.; Stoll, H.; Preuß, H. Energy-Adjusted Ab Initio Pseudopotentials for the Second and Third Row Transition Elements. *Theor. Chim. Acta* **1990**, *77* (2), 123–141.

(115) Schulze, B.; Friebe, C.; Jäger, M.; Görls, H.; Birckner, E.; Winter, A.; Schubert, U. S. Pt(II) Phosphors with Click-Derived 1,2,3-Triazole-Containing Tridentate Chelates. *Organometallics* **2018**, *37* (1), 145–155.

(116) Zou, C.; Lin, J.; Suo, S.; Xie, M.; Chang, X.; Lu, W. Palladium(II) N-Heterocyclic Allenylidene Complexes with Extended Intercationic Pd···Pd Interactions and MMLCT Phosphorescence. *Chem. Commun.* **2018**, *54* (42), 5319–5322.

(117) Martínez-Prieto, L. M.; Cámpora, J. Nickel and Palladium Complexes with Reactive σ-Metal-Oxygen Covalent Bonds. *Isr. J. Chem.* **2020**, *60* (3–4), 373–393.

(118) Friedel, J.; Krause, M.; Jordan, R.; Maisuls, I.; Brünink, D.; Schwab, D.; Doltsinis, N. L.; Strassert, C. A.; Klein, A. Triplet Emitting C^N^C Cyclometalated Dibenzo[*c,h*]Acridine Pt(II) Complexes. *Molecules* **2022**, *27* (22), 8054.

(119) Ortiz, R. J.; Garcia-Torres, E.; Brothwood, P. L.; Williams, J. A. G.; Herbert, D. E. Site-Selective Ligand Functionalization Reverses Hypsochromic Luminescence Shifts in Platinum(II) Complexes of Benzannulated NCN-Coordinating Ligands. *Chem. Weinh. Bergstr. Ger.* **2025**, *31* (6), e202403766.

(120) Nkabinde, S. V.; Kinunda, G.; Jaganyi, D.; Mambanda, A. Nucleophilic Substitution of Chloride from the [Pt(Chlorido)(NNN)/(NCN)]$^+$, (NNN) = *Bis*(2-Pyridyl/2-Quinolyl)Pyridine, (NCN) = *Bis*(2-Pyridyl/2-Quinolyl)Benzene) Complexes by Azoles. *Results Chem.* **2021**, *3*, 100218.

(121) Salthouse, R. J.; Sil, A.; Gildea, L. F.; Yufit, D. S.; Williams, J. A. G. Platinum(II) Complexes of Nonsymmetrical NCN-Coordinating Ligands: Unimolecular and Excimeric Luminescence Properties and Comparison with Symmetrical Analogues. *Inorg. Chem.* **2023**, *62* (31), 12356–12371.

(122) Jordan, R.; Schäfer, S. A.; Sander, N.; Maisuls, I.; Hamacher, C.; Friedel, J.; Strassert, C. A.; Klein, A. Assessing the Character of the C_6F_5 Ligand from the Electrochemical and Photophysical Properties of [Ni(C_6F_5)2(N∧N)] Complexes. *Inorg. Chem.* **2024**, *63* (24), 11079–11091.

(123) STOE; STOE & Cie GmbH: Darmstadt, Germany, **2006**.

(124) APEX3 − Software Suite for Crystallographic Programs; Bruker AXS, Inc.: Madison, WI, USA, **2015**.

(125) Sheldrick, G. M. Crystal Structure Refinement with SHELXL. *Acta Crystallogr. Sect. C Struct. Chem.* **2015**, *71* (Pt 1), 3–8.

(126) Sheldrick, G. M. A Short History of SHELX. *Acta Crystallogr. A* **2008**, *64* (Pt 1), 112–122.

(127) X-RED32, v1.31; STOE & Cie GmbH: Darmstadt, Germany, **2001**.

(128) X-SHAPE, v1.06; STOE & Cie GmbH: Darmstadt, Germany, **1999**.

(129) van Stokkum, I. H. M.; Larsen, D. S.; van Grondelle, R. Global and Target Analysis of Time-Resolved Spectra. *Biochim. Biophys. Acta BBA - Bioenerg.* **2004**, *1657* (2), 82–104.

(130) Snellenburg, J. J.; Laptenok, S.; Seger, R.; Mullen, K. M.; Stokkum, I. H. M. van. Glotaran: A Java-Based Graphical User Interface for the R Package TIMP. *J. Stat. Softw.* **2012**, *49*, 1–22.

(131) Mullen, K. M.; Stokkum, I. H. M. van. TIMP: An R Package for Modeling Multi-Way Spectroscopic Measurements. *J. Stat. Softw.* **2007**, *18*, 1–46.

(132) Frisch, M. J.; Trucks, G. W.; Schlegel, H. B.; Scuseria, G. E.; Robb, M. A.; Cheeseman, J. R.; Scalmani, G.; Barone, V.; Petersson, G. A.; Nakatsuji, H.; Li, X.; Caricato, M.; Marenich, A. V.;

Bloino, J.; Janesko, B. G.; Gomperts, R.; Mennucci, B.; Hratchian, H. B.; Ortiz, J. V.; Izmaylov, A. F.; Sonnenberg, J. L.; Williams-Young, D.; Ding, F.; Lipparini, F.; Egidi, F.; Goings, J.; Peng, B.; Petrone, A.; Henderson, T.; Ranasinghe, D.; Zakrewski, V. G.; Gao, J.; Rega, N.; Zheng, G.; Liang, W.; Hada, M.; Ehara, M.; Toyota, K.; Fukuda, R.; Hasegawa, J.; Ishida, M.; Nakajima, T.; Honda, Y.; Kitao, O.; Nakai, H.; Vreven, T.; Throssell, K.; Montgomery, J. A.; Peralta, J. E.; Ogliaro, F.; Bearpark, M. J.; Heyd, J. J.; Brothers, E. N.; Kudin, K. N.; Staroverov, V. N.; Keith, T. A.; Kobayashi, R.; Normand, J.; Raghavachari, K.; Rendell, A. P.; Burant, J. C.; Iyengar, S. S.; Tomasi, J.; Cossi, M.; Millam, J. M.; Klene, M.; Adamo, C.; Cammi, R.; Ochterski, J. W.; Martin, R. L.; Morokuma, K.; Farkas, O.; Foresman, J. B.; Fox, D. J. Gaussian 16, Rev. A.03; Gaussian, Inc.: Wallingford, CT, **2016**. 2016.

(133) Weigend, F.; Ahlrichs, R. Balanced Basis Sets of Split Valence, Triple Zeta Valence and Quadruple Zeta Valence Quality for H to Rn: Design and Assessment of Accuracy. *Phys. Chem. Chem. Phys.* **2005**, *7* (18), 3297–3305.

(134) Roy, L. E.; Hay, P. J.; Martin, R. L. Revised Basis Sets for the LANL Effective Core Potentials. *J. Chem. Theory Comput.* **2008**, *4* (7), 1029–1031.

(135) Rohlfing, C. M.; Hay, P. J.; Martin, R. L. An Effective Core Potential Investigation of Ni, Pd, and Pt and their Monohydrides. *J. Chem. Phys.* **1986**, *85* (3), 1447–1455.

(136) Hay, P. J.; Wadt, W. R. *Ab Initio* Effective Core Potentials for Molecular Calculations. Potentials for K to Au Including the Outermost Core Orbitals. *J. Chem. Phys.* **1985**, *82* (1), 299–310.

(137) Hay, P. J.; Wadt, W. R. *Ab Initio* Effective Core Potentials for Molecular Calculations. Potentials for the Transition Metal Atoms Sc to Hg. *J. Chem. Phys.* **1985**, *82* (1), 270–283.

(138) Staroverov, V. N.; Scuseria, G. E.; Tao, J.; Perdew, J. P. Comparative Assessment of a New Nonempirical Density Functional: Molecules and Hydrogen-Bonded Complexes. *J. Chem. Phys.* **2003**, *119* (23), 12129–12137.

(139) Grimme, S.; Ehrlich, S.; Goerigk, L. Effect of the Damping Function in Dispersion Corrected Density Functional Theory. *J. Comput. Chem.* **2011**, *32* (7), 1456–1465.

(140) Cossi, M.; Rega, N.; Scalmani, G.; Barone, V. Energies, Structures, and Electronic Properties of Molecules in Solution with the C-PCM Solvation Model. *J. Comput. Chem.* **2003**, *24* (6), 669–681.

(141) Barone, V.; Cossi, M. Quantum Calculation of Molecular Energies and Energy Gradients in Solution by a Conductor Solvent Model. *J. Phys. Chem. A* **1998**, *102* (11), 1995–2001.

(142) Barone, V.; Bloino, J.; Biczysko, M.; Santoro, F. Fully Integrated Approach to Compute Vibrationally Resolved Optical Spectra: From Small Molecules to Macrosystems. *J. Chem. Theory Comput.* **2009**, *5* (3), 540–554.

(143) Barone, V.; Bloino, J.; Biczysko, M. Vibrationally-Resolved Electronic Spectra in GAUSSIAN 09.

(144) Humphrey, W.; Dalke, A.; Schulten, K. VMD: Visual Molecular Dynamics. *J. Mol. Graph.* **1996**, *14* (1), 33–38.

7. Appendix

7.1. NMR spectra

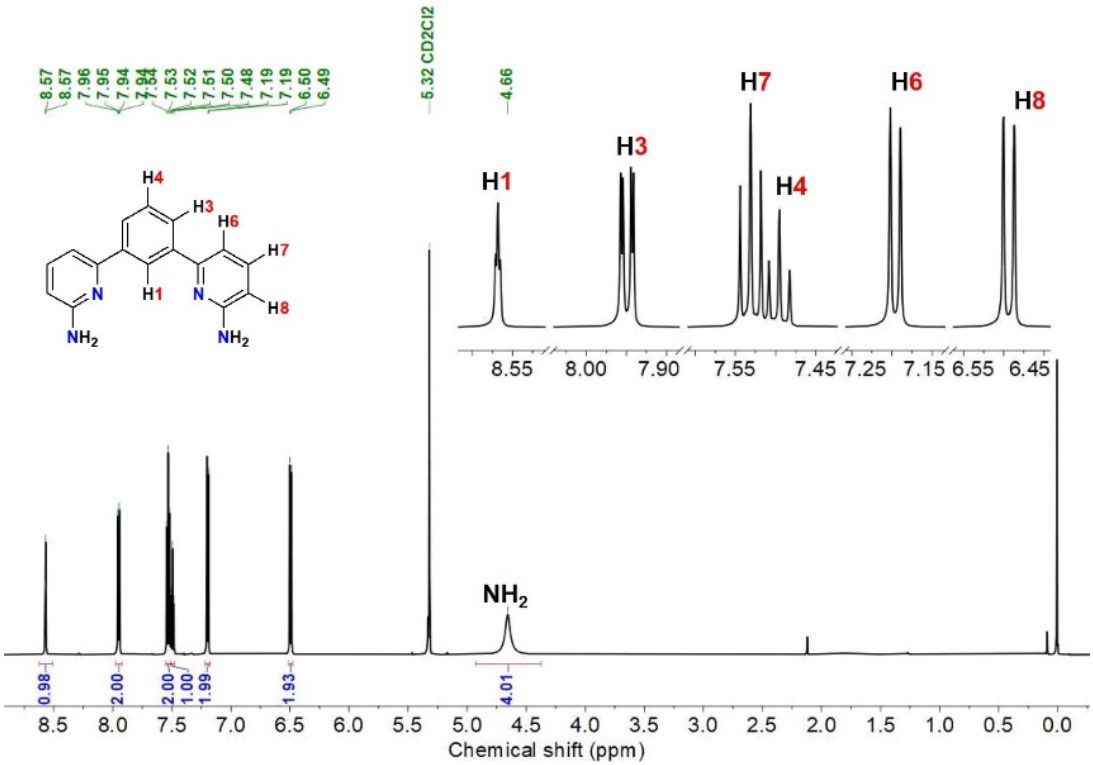


Figure A1. 600 MHz ^{1}H NMR spectrum of HL^{NH_2} in CD_2Cl_2 at RT.

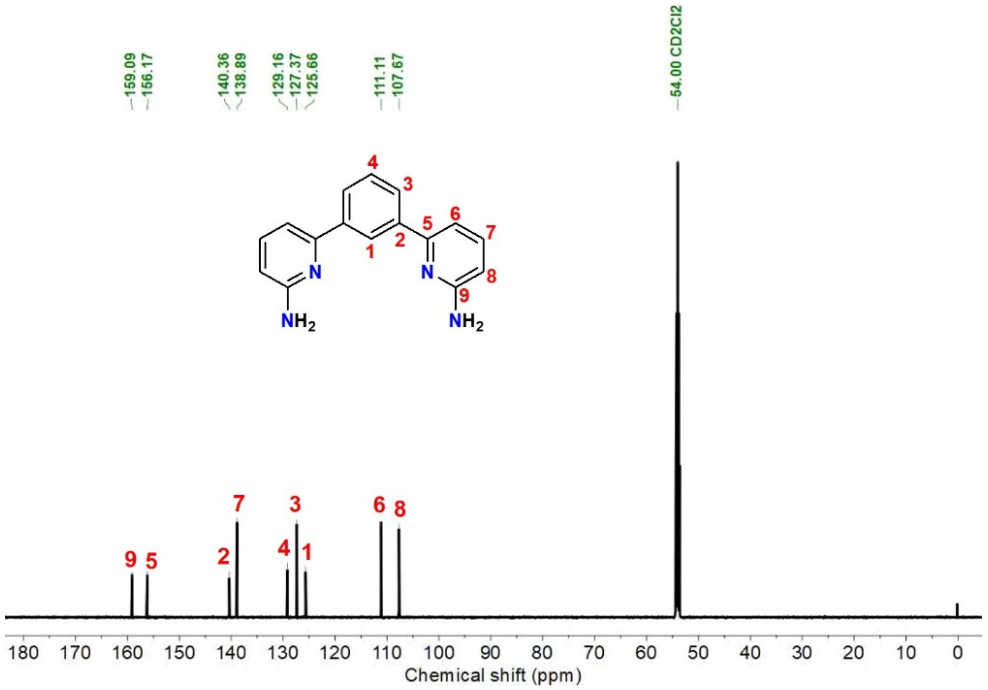


Figure A2. 151 MHz ^{13}C NMR spectrum of HL^{NH_2} in CD_2Cl_2 at RT.

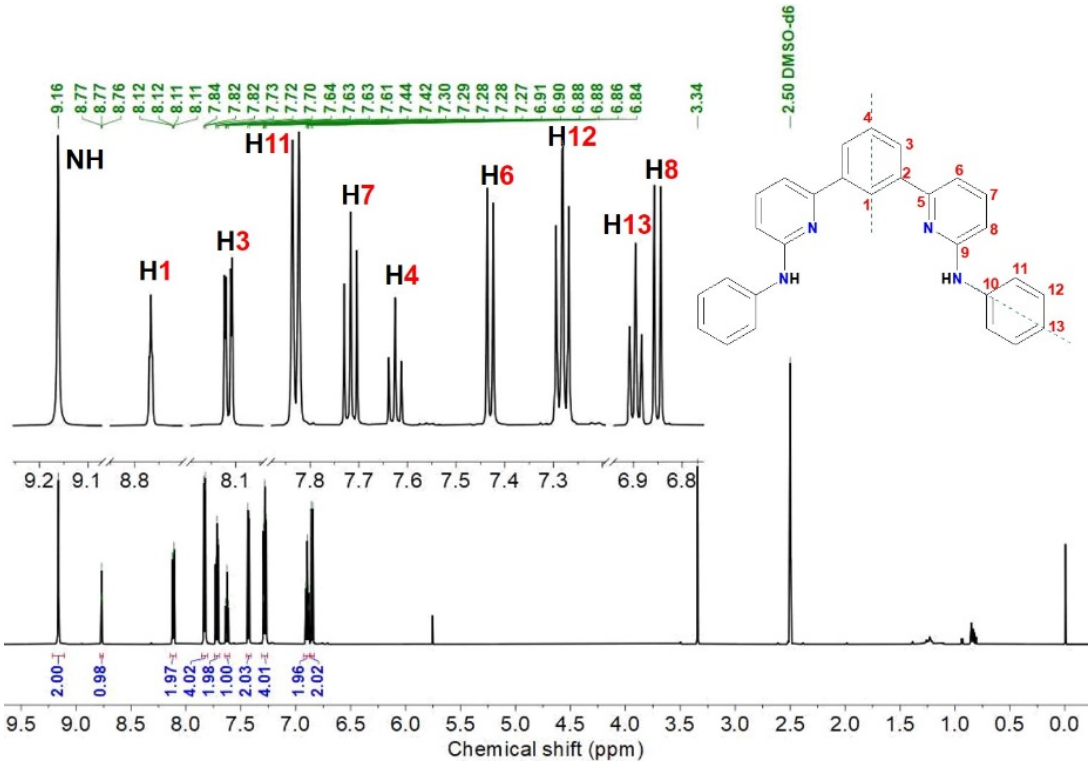


Figure A3. 600 MHz ^{1}H NMR spectrum of HL^{NHPh} in DMSO-d_6 at RT.

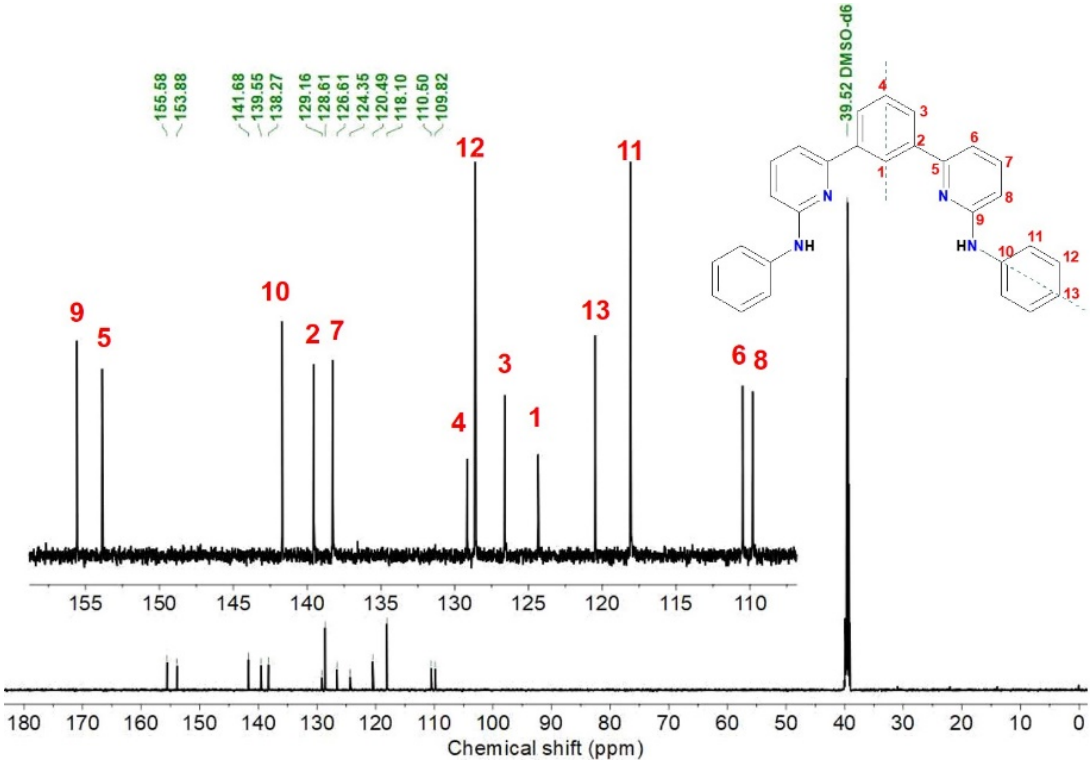


Figure A4. 151 MHz ^{13}C NMR spectrum of HL^{NHPh} in DMSO-d_6 at RT.

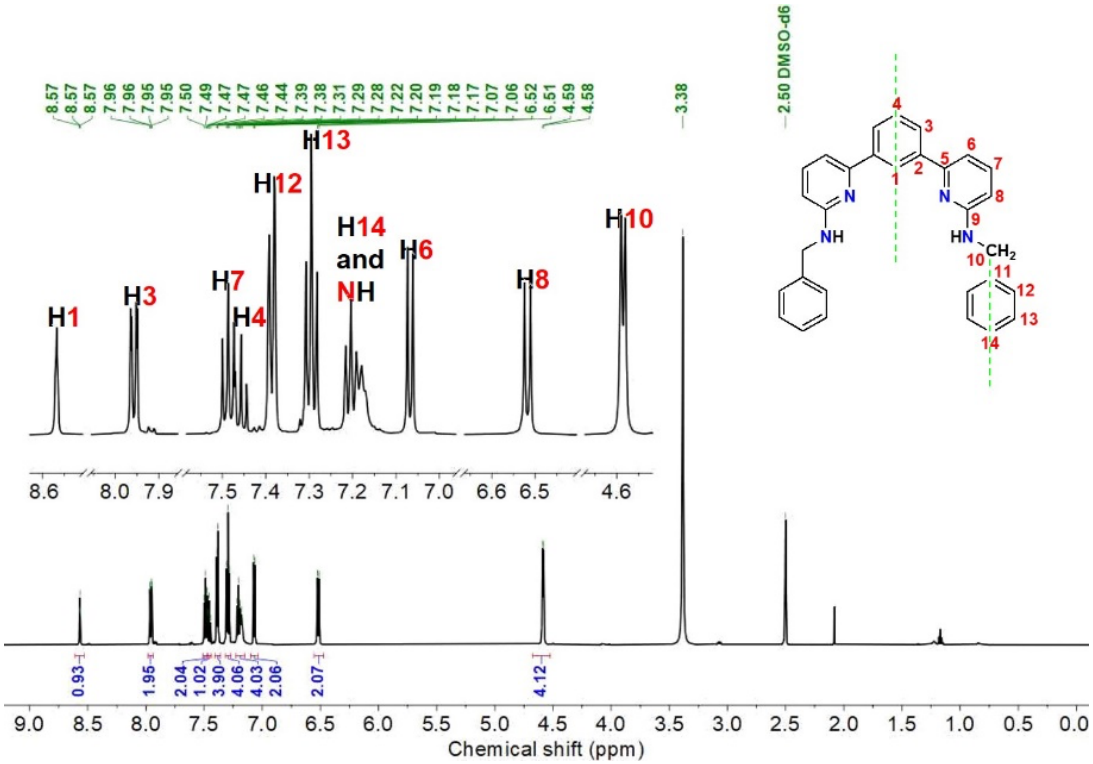


Figure A5. 600 MHz ^{1}H NMR spectrum of HL^{NHBn} in DMSO-d_6 at RT.

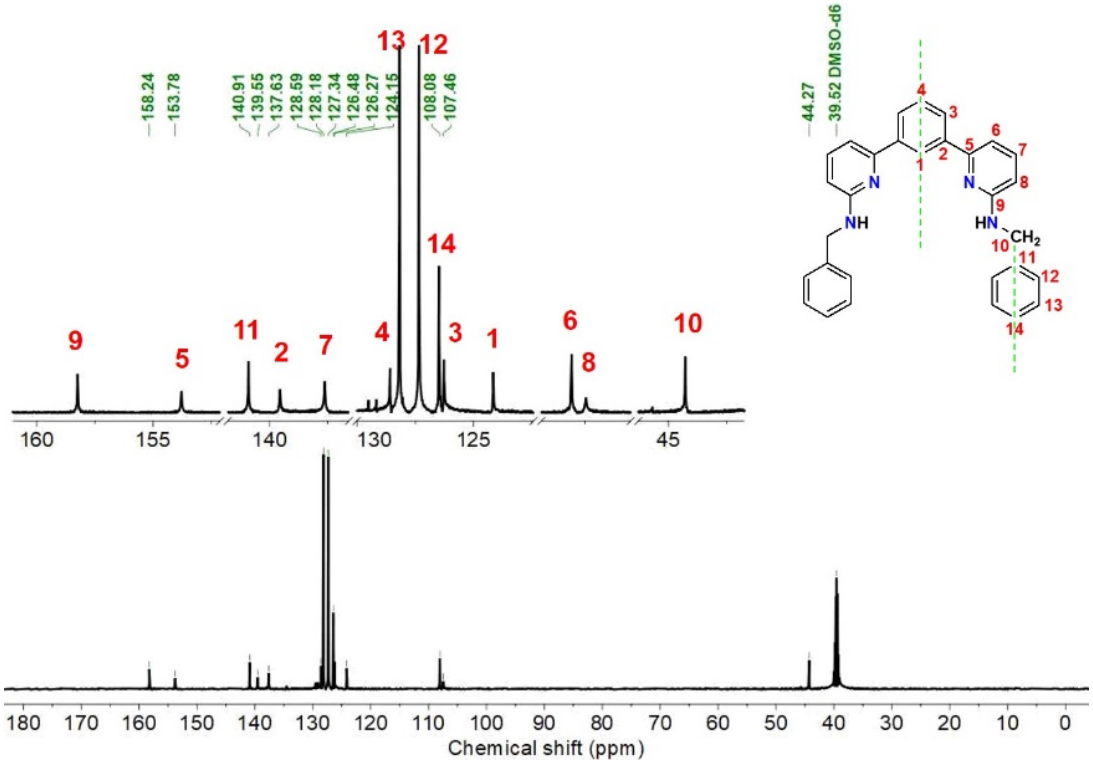


Figure A6. 151 MHz ^{13}C NMR spectrum of HL^{NHBn} in DMSO-d_6 at RT.

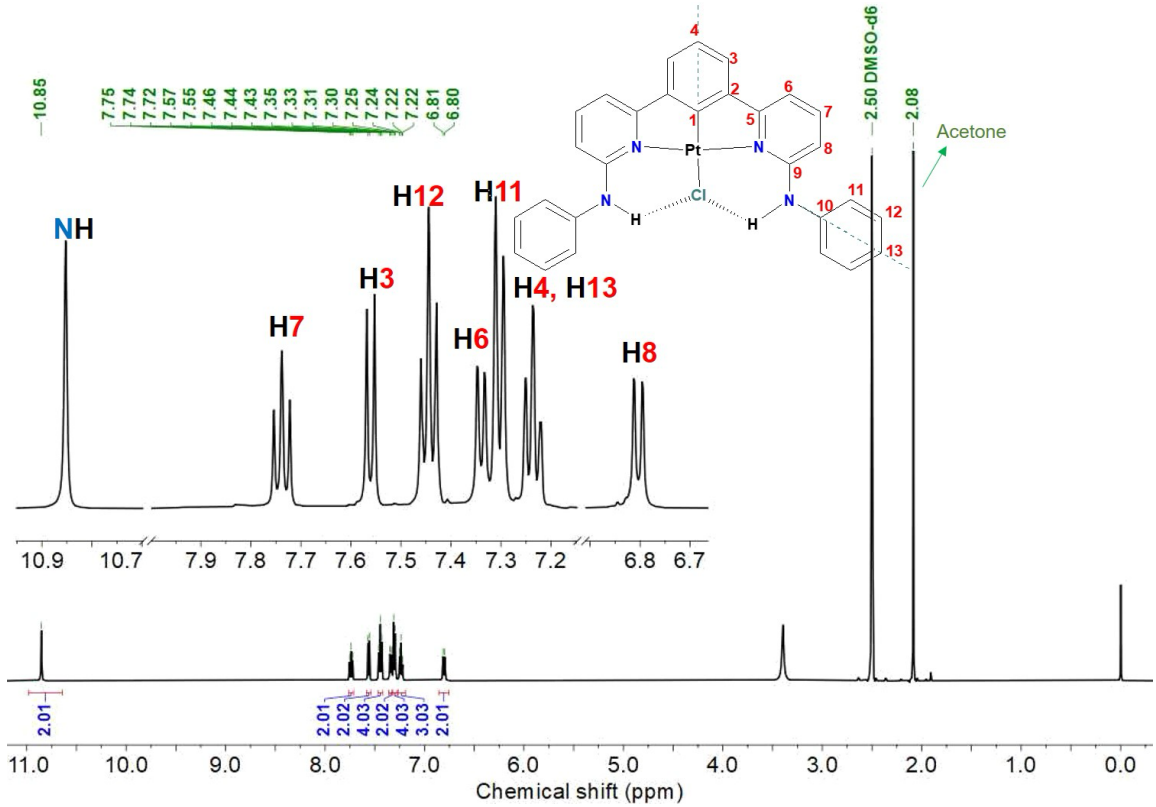


Figure A7. 500 MHz ^{1}H NMR spectrum of [Pt(L^{NHPh})Cl] in DMSO-d_6 at RT.

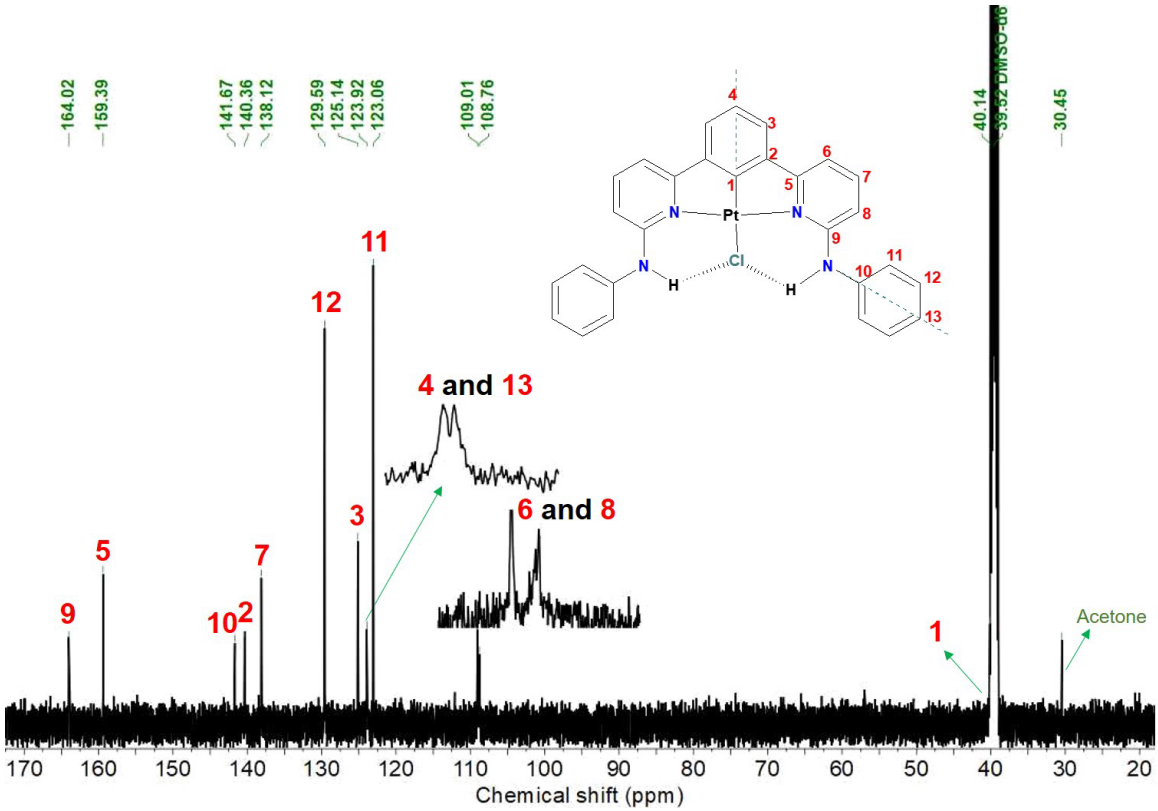


Figure A8. 126 MHz ^{13}C NMR spectrum of [Pt(L^{NHPh})Cl] in DMSO-d_6 at 313 K.

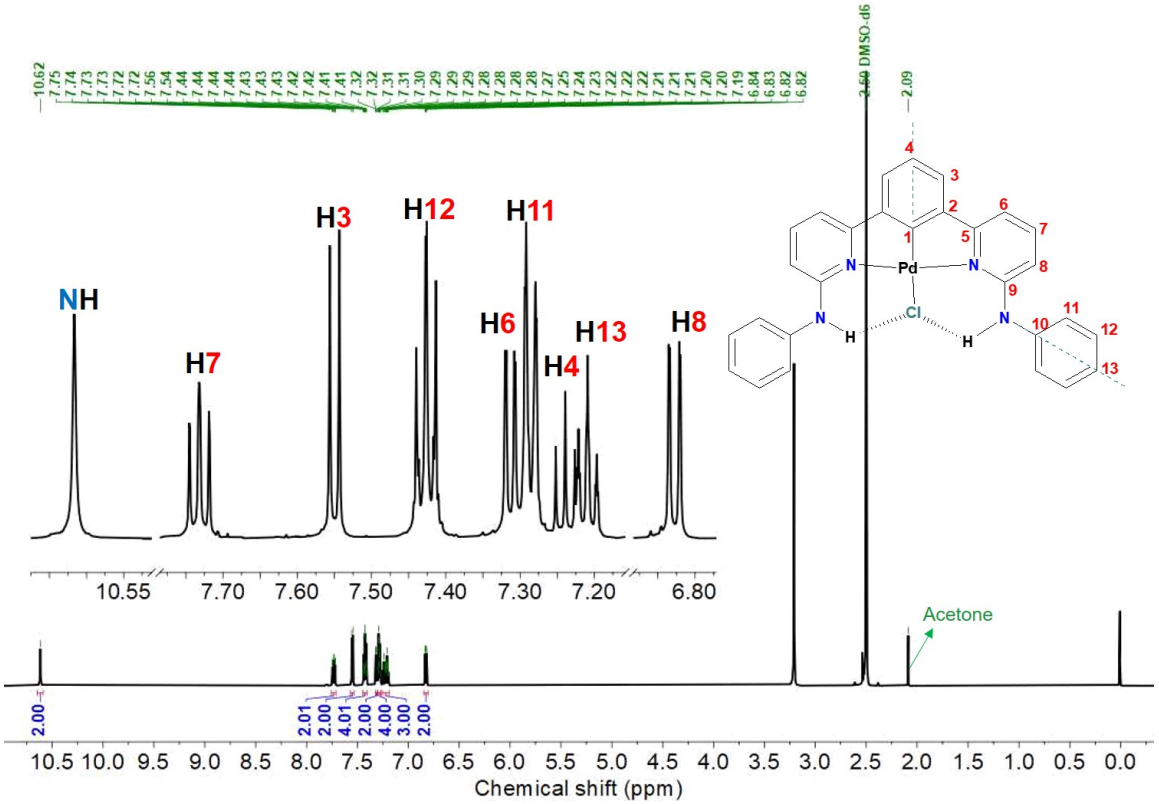


Figure A9. 600 MHz ^{1}H NMR spectrum of [Pd(L^{NHPh})Cl] in DMSO-d_6 at 313 K.

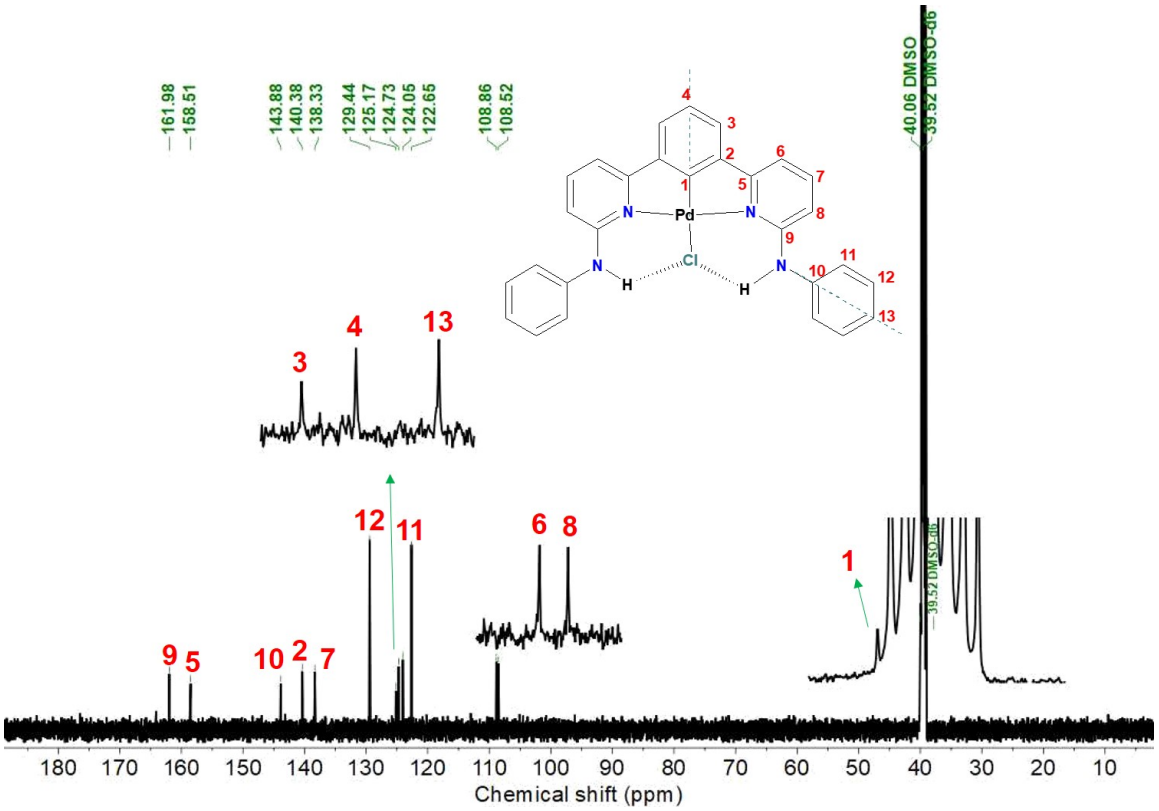


Figure A10. 151 MHz ^{13}C NMR spectrum of [Pd(L^{NHPh})Cl] in DMSO-d_6 at 313 K.

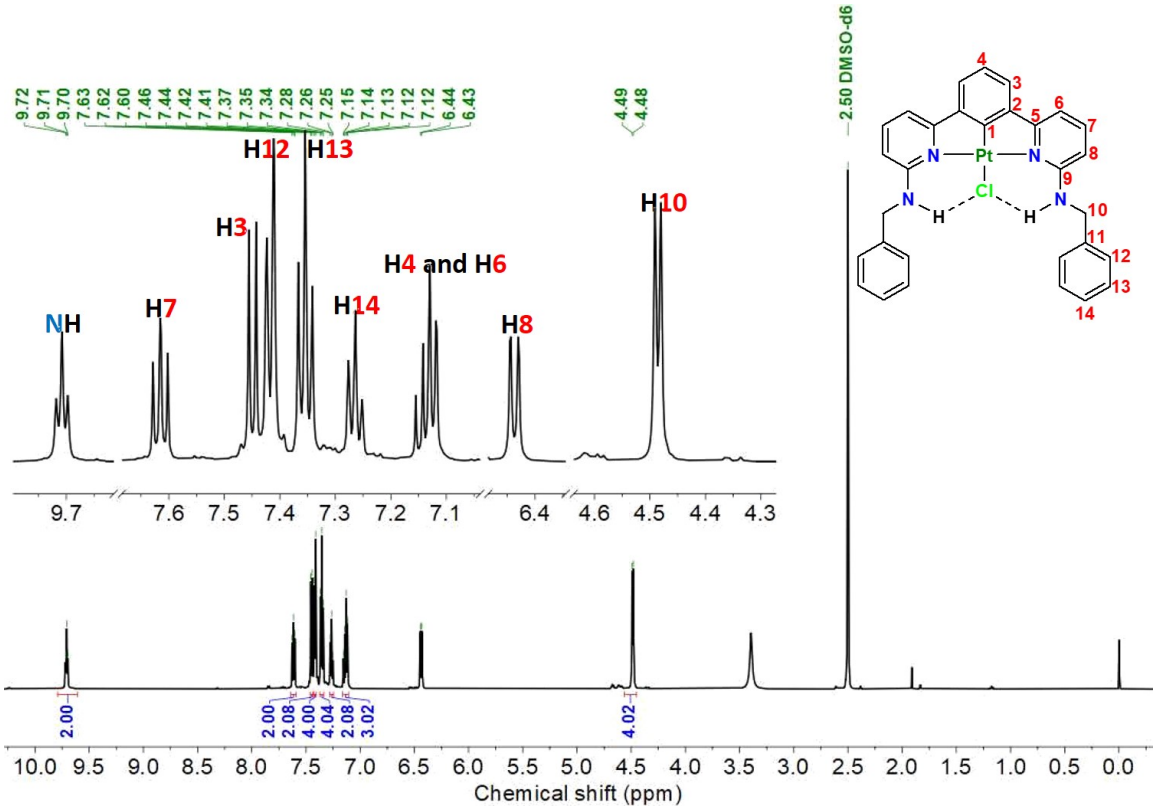


Figure A11. 600 MHz ^{1}H NMR spectrum of [Pt(L^{NHBn})Cl] in DMSO-d_6 at RT.

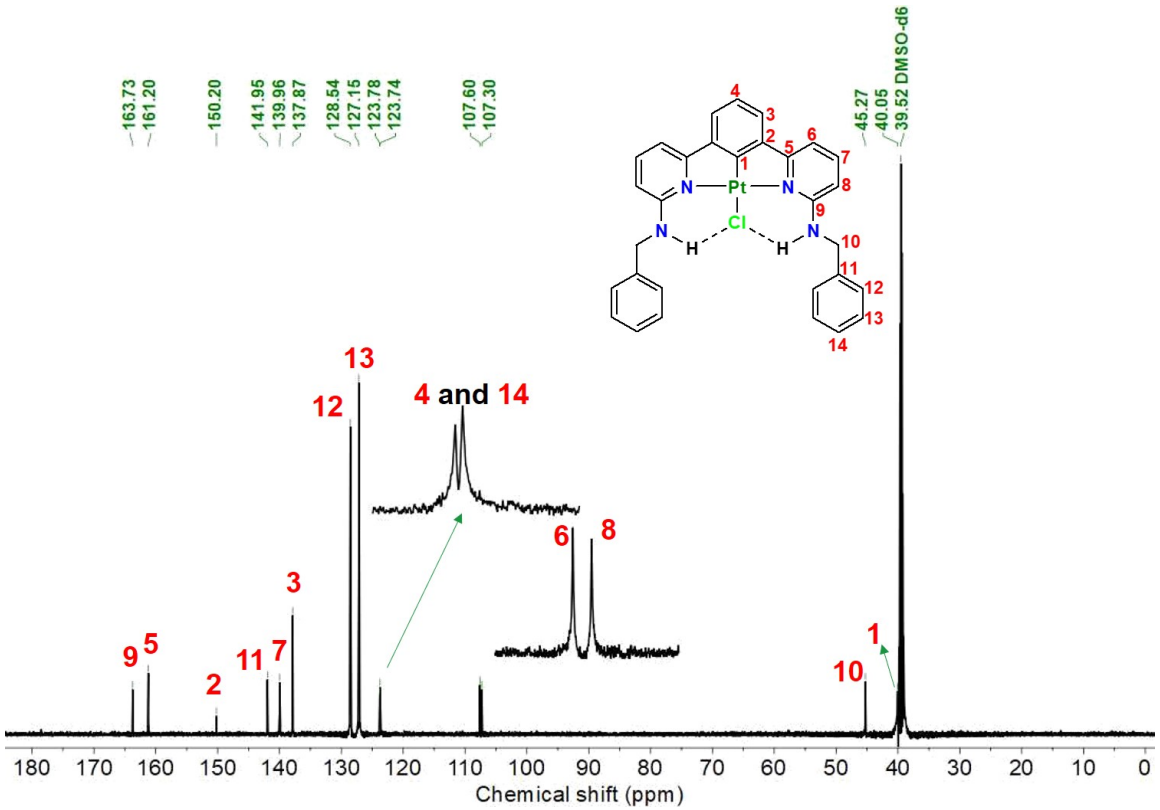


Figure A12. 151 MHz ^{13}C NMR spectrum of [Pt(L^{NHBn})Cl] in DMSO-d_6 at RT.

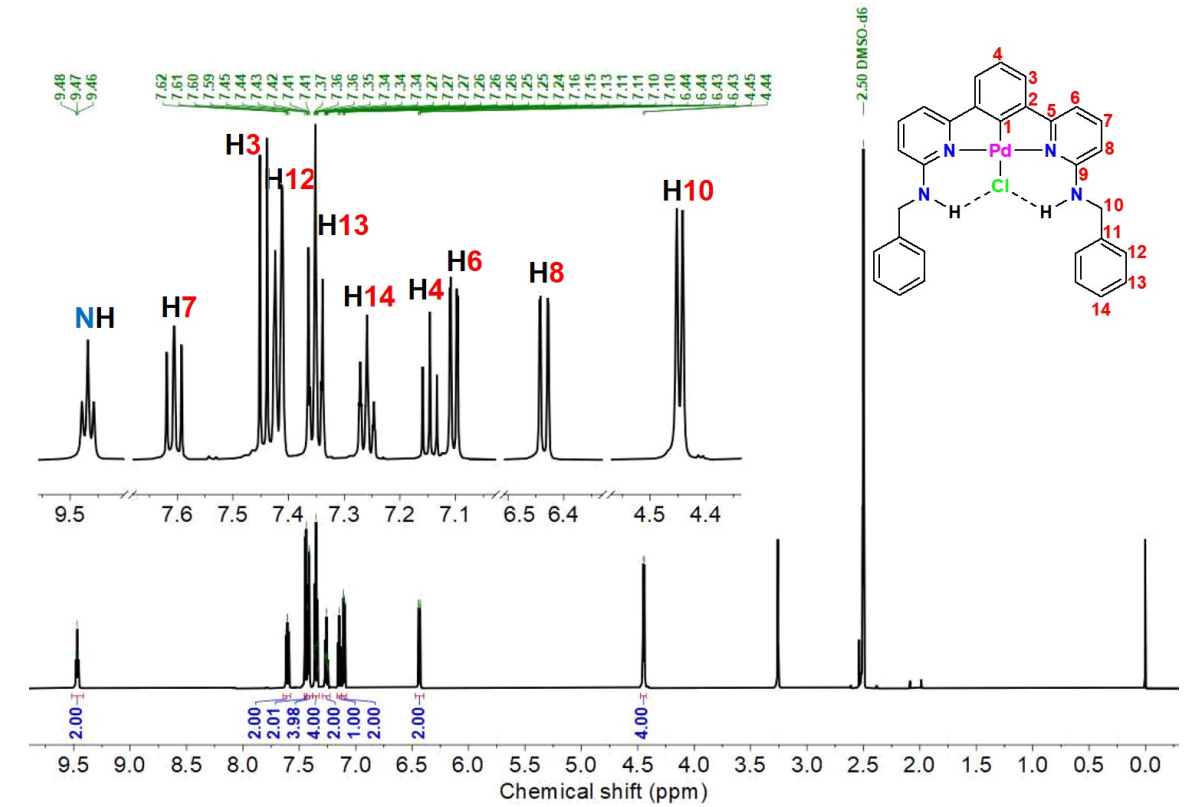


Figure A13. 600 MHz ^{1}H NMR spectrum of [Pd(L^{NHBn})Cl] in DMSO-d_6 at RT.

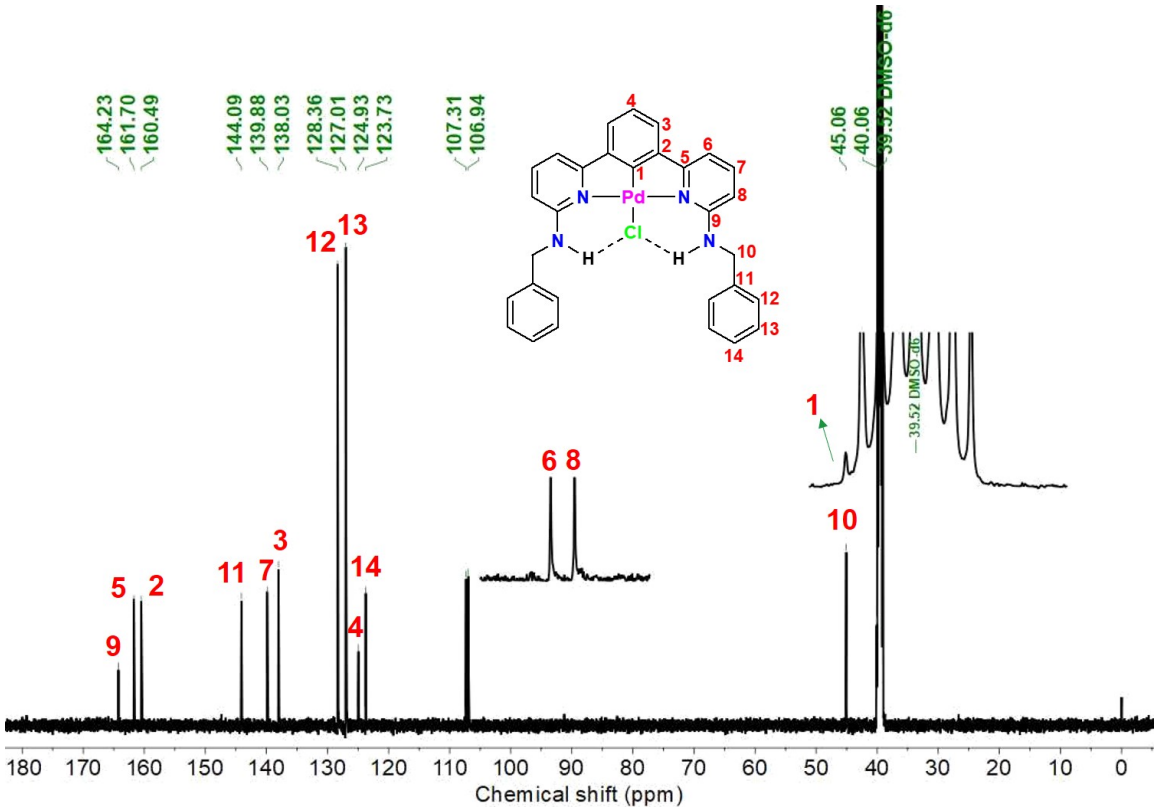


Figure A14. 151 MHz ^{13}C NMR spectrum of [Pd(L^{NHBn})Cl] in DMSO-d_6 at RT.

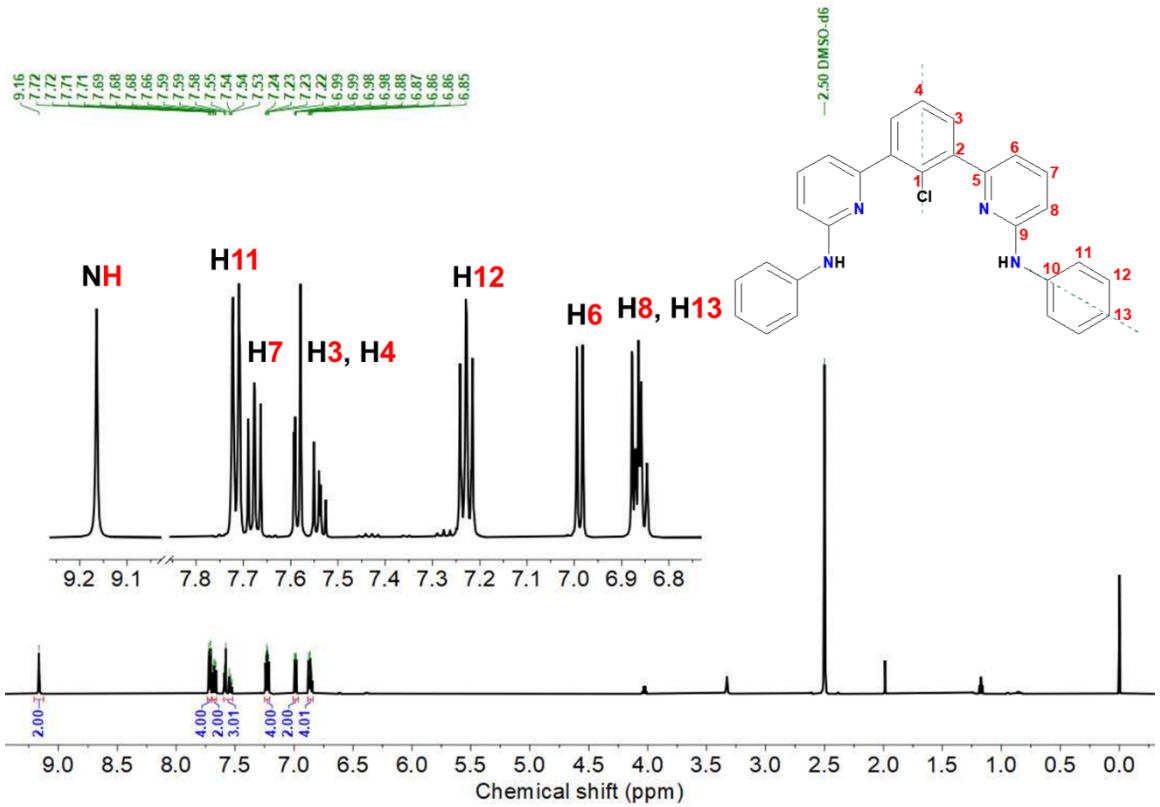


Figure A15. 600 MHz ^{1}H NMR spectrum of ClL^{NHPh} in DMSO-d_6 at RT.

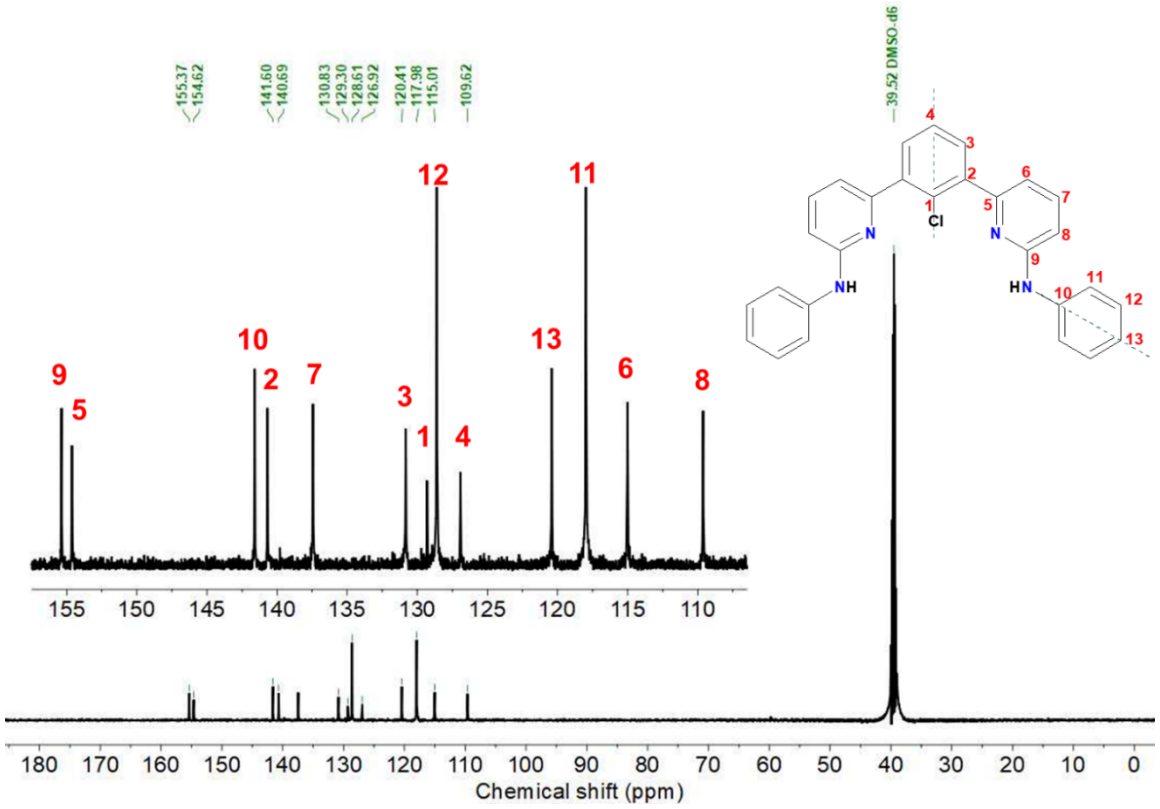


Figure A16. 151 MHz ^{13}C NMR spectrum of ClL^{NHPh} in DMSO-d_6 at RT.

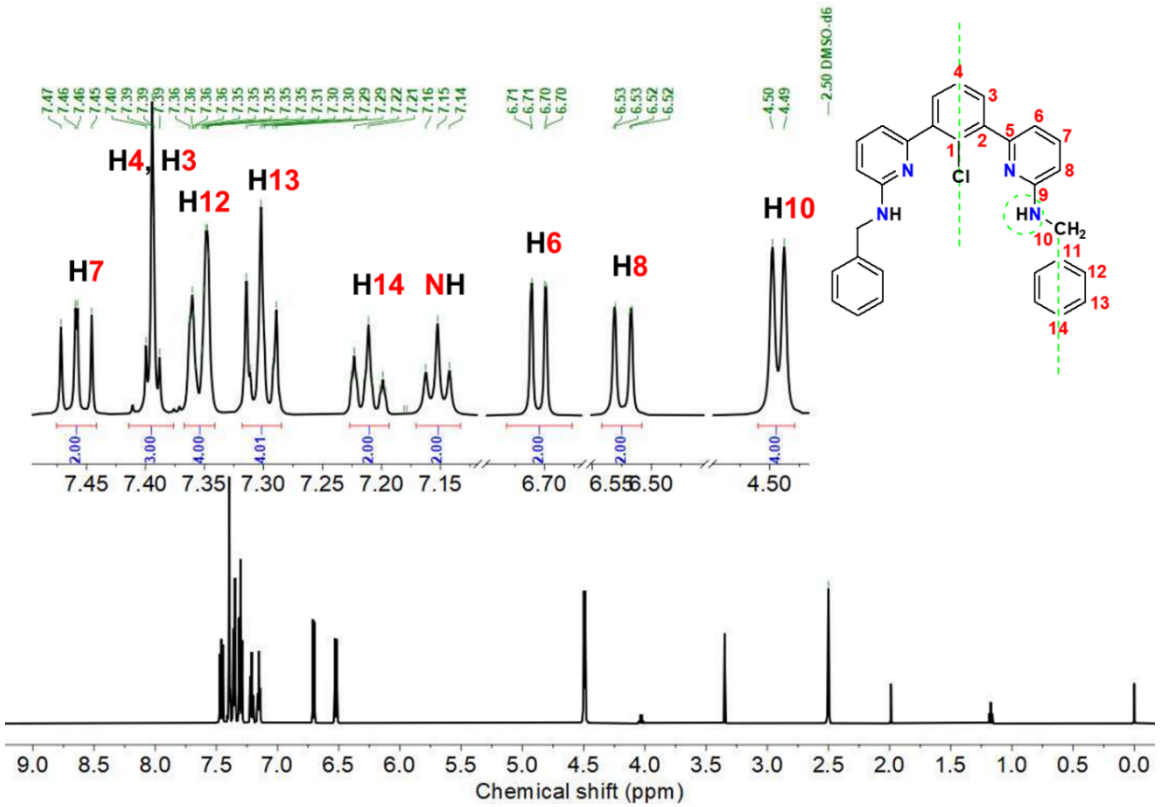


Figure A17. 600 MHz ^{1}H NMR spectrum of ClL^{NHBn} in DMSO-*d*$_6$ at RT.

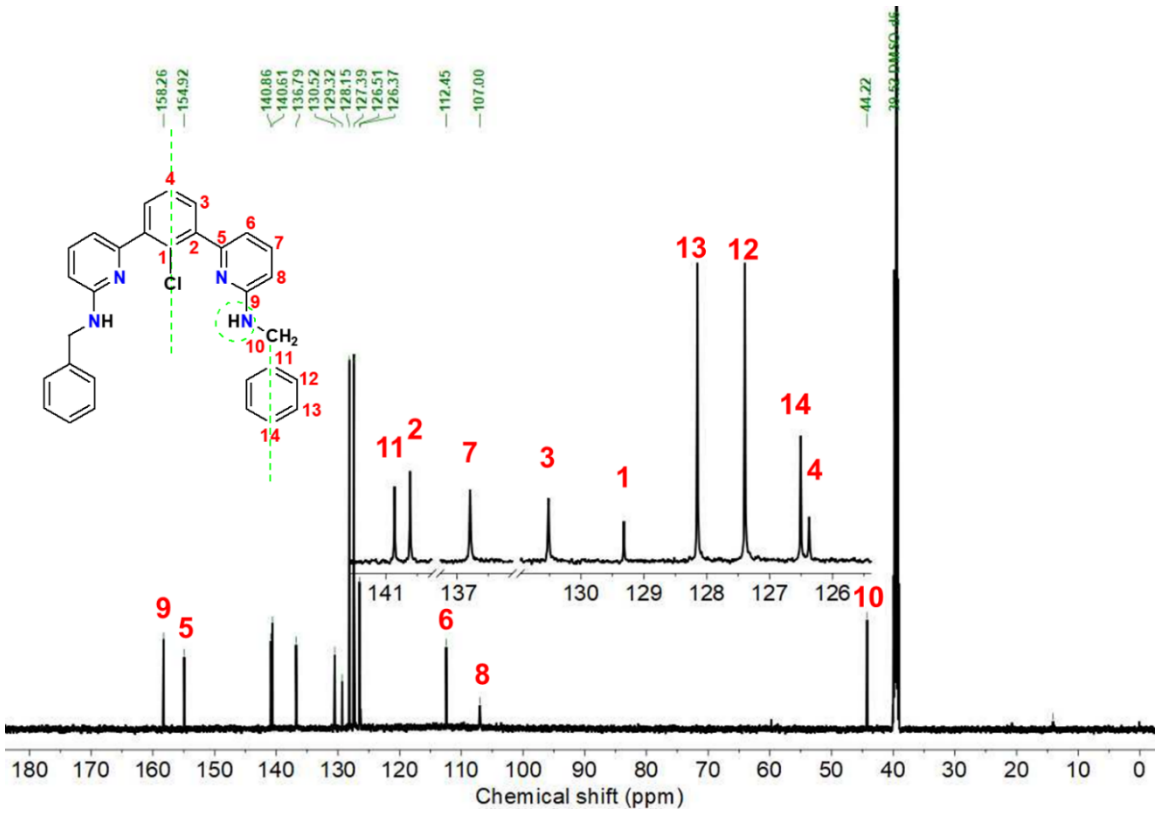


Figure A18. 151 MHz ^{13}C NMR spectrum of ClL^{NHBn} in DMSO-*d*$_6$ at RT.

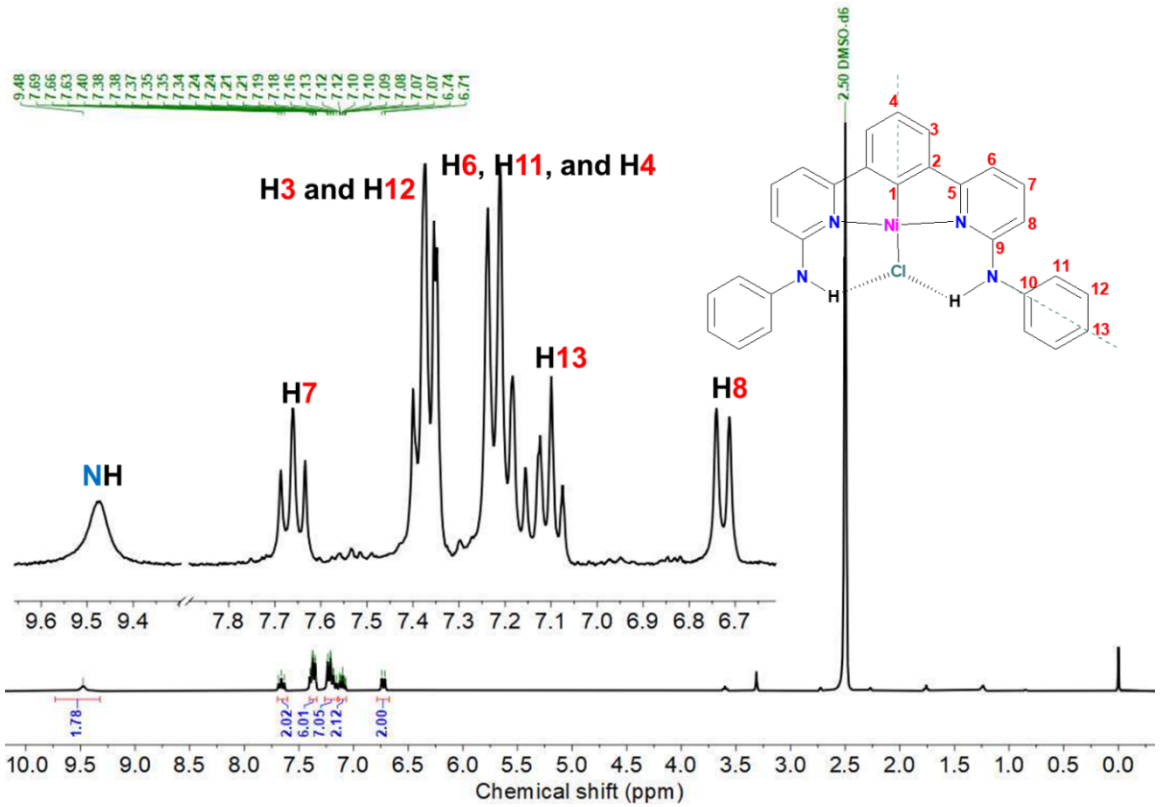


Figure A19. 300 MHz ^{1}H NMR spectrum of [Ni(L^{NHPh})Cl] in DMSO-d_6 at RT.

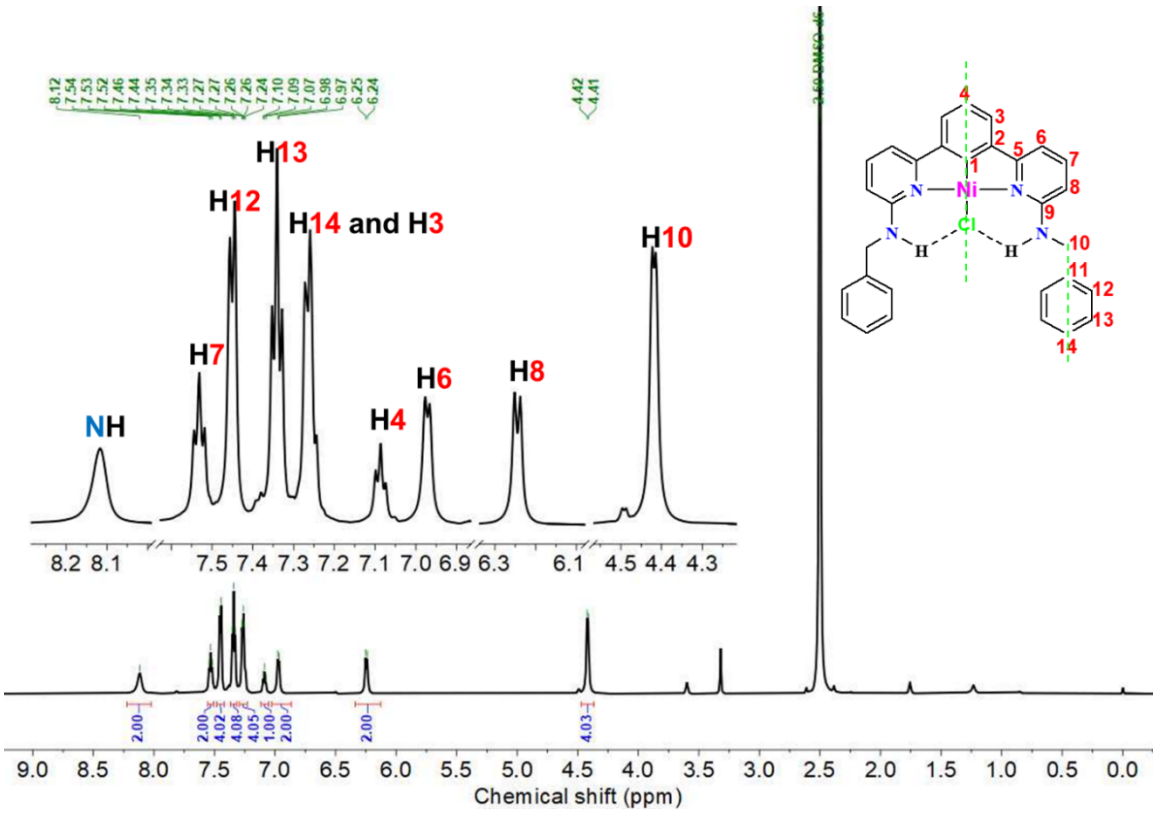


Figure A20. 600 MHz ^{1}H NMR spectrum of [Ni(L^{NHBn})Cl] in DMSO-d_6 at RT.

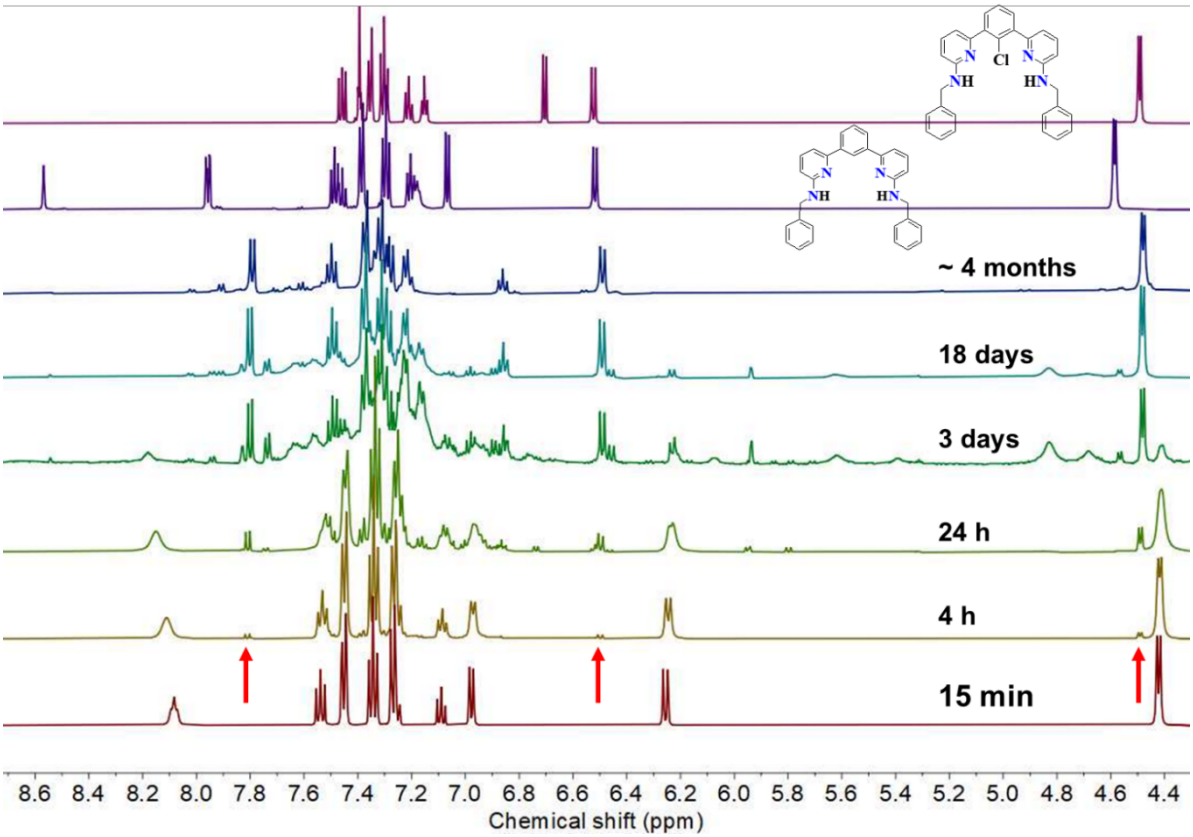


Figure A21. ^{1}H NMR spectra of [Ni(L^{NHBn})Cl] over time, alongside with ^{1}H NMR spectra of HL^{NHBn} and ClL^{NHBn}, in DMSO-d_6 at RT.

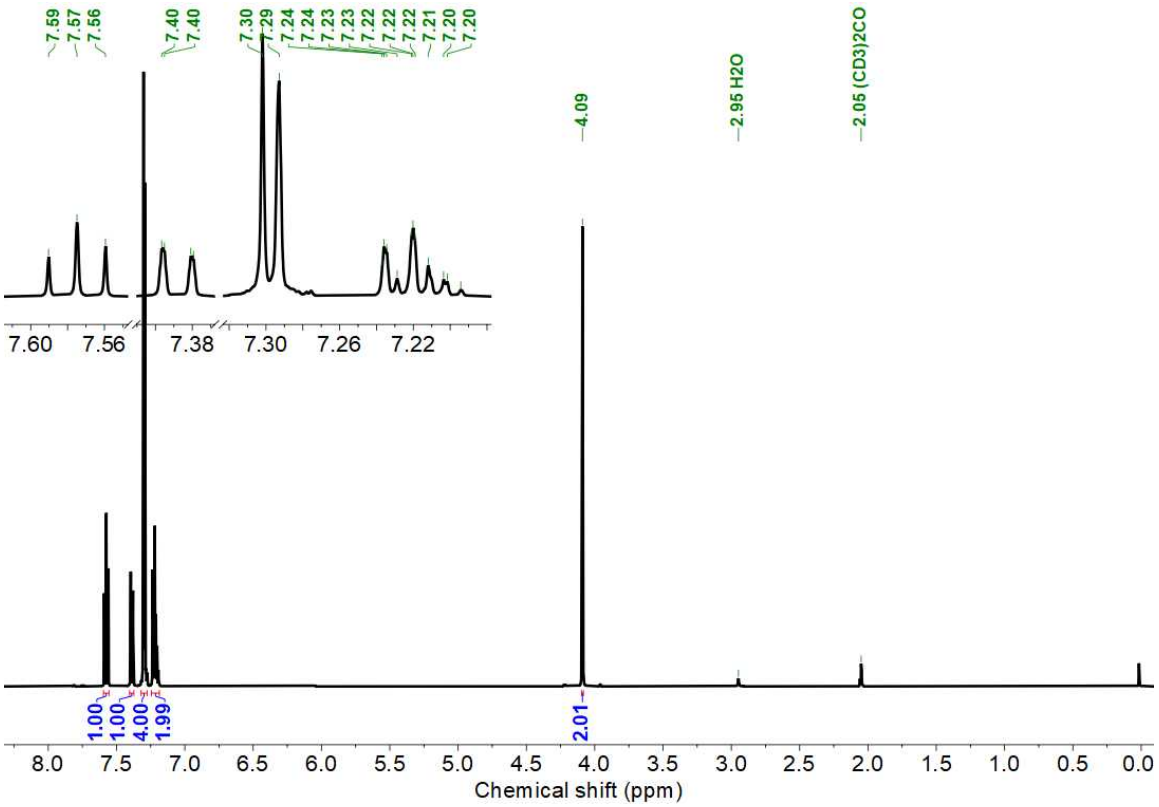


Figure A22. 500 MHz ^{1}H NMR spectrum of S^{Bn} in acetone-d_6 at RT.

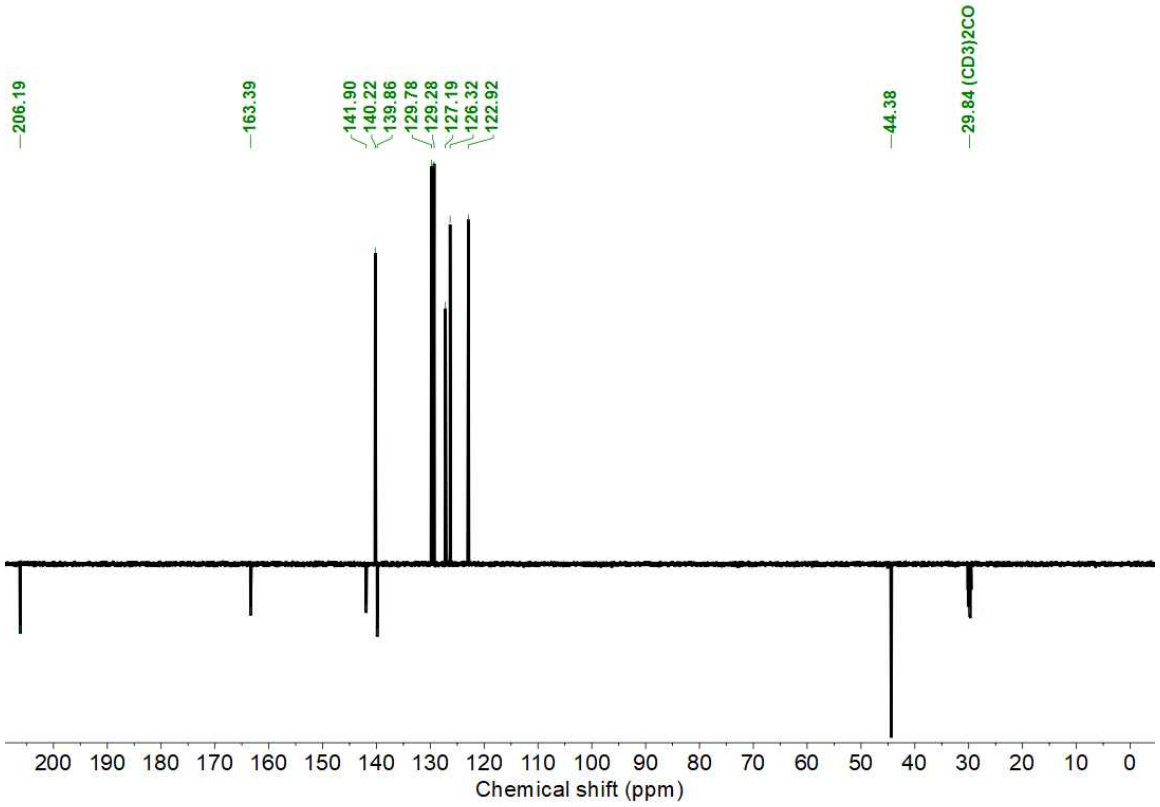


Figure A23. 126 MHz ^{13}C NMR spectrum of S^{Bn} in acetone-d_6 at RT.

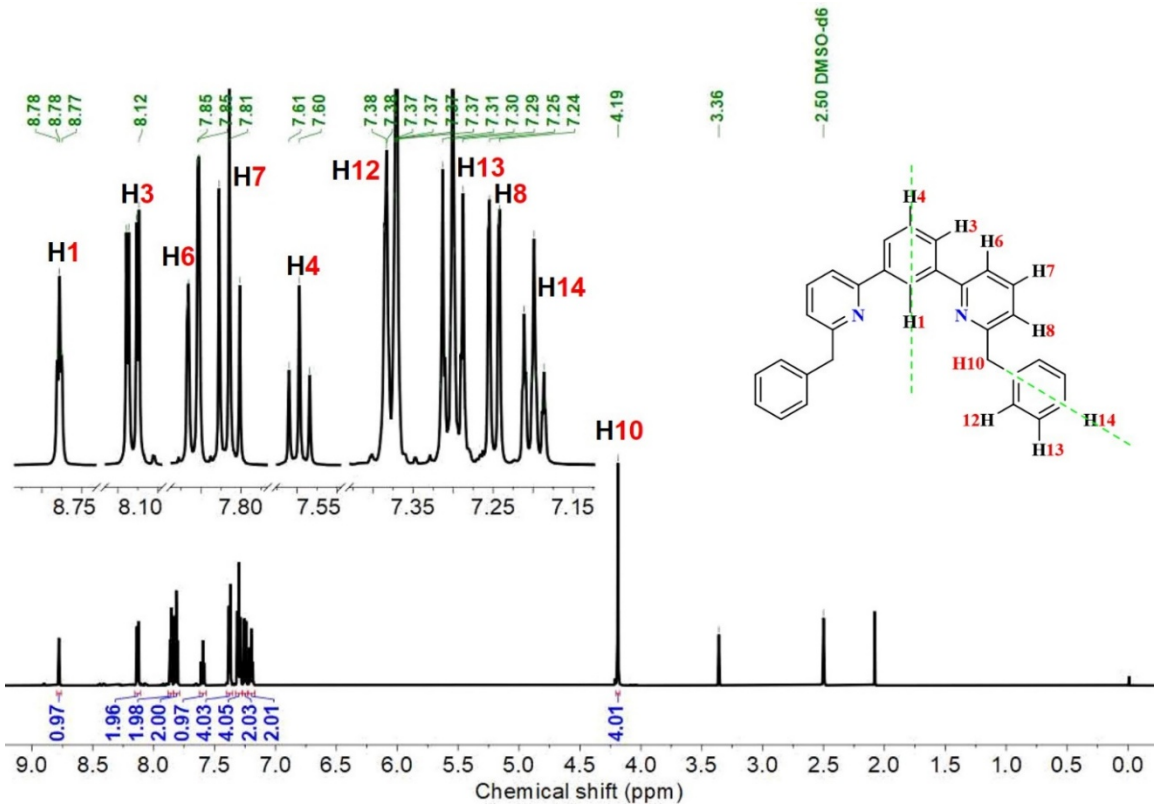


Figure A24. 600 MHz ^{1}H NMR spectrum of HL^{Bn} in DMSO-*d*$_6$ at RT.

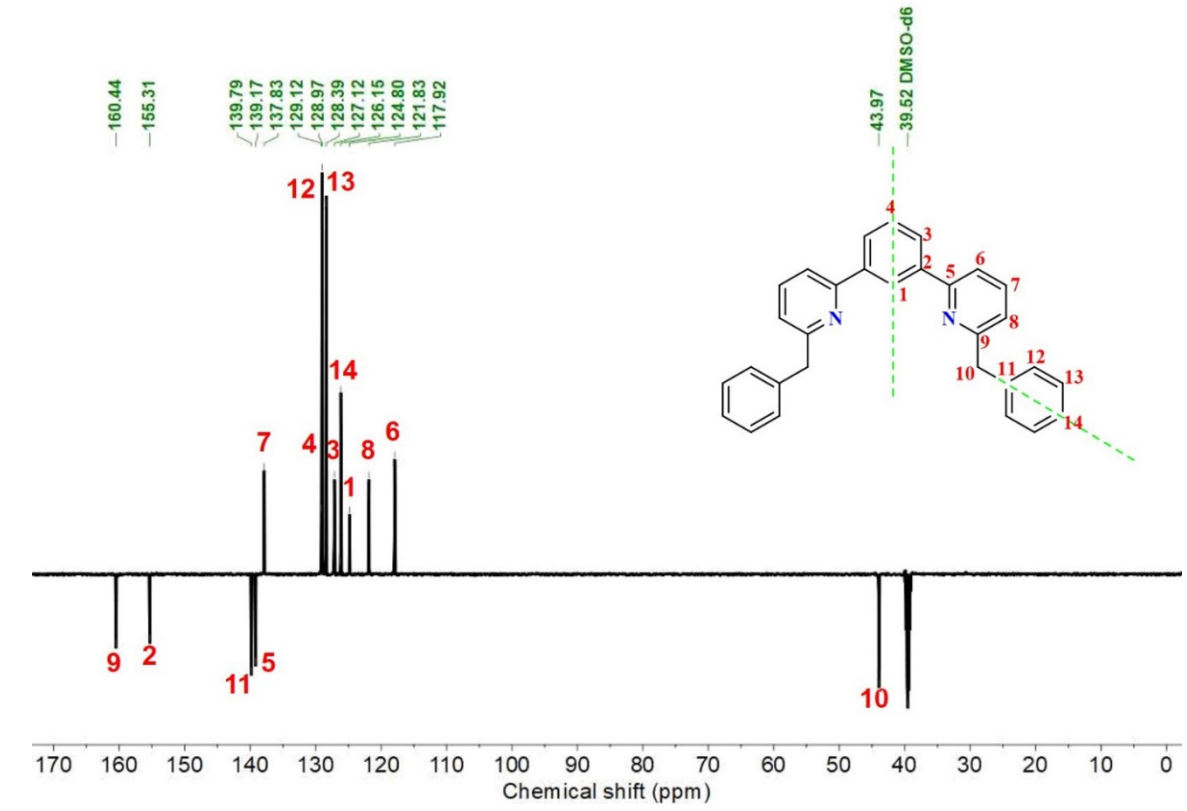


Figure A25. 151 MHz ^{13}C NMR spectrum of HL^{Bn} in DMSO-*d*$_6$ at RT.

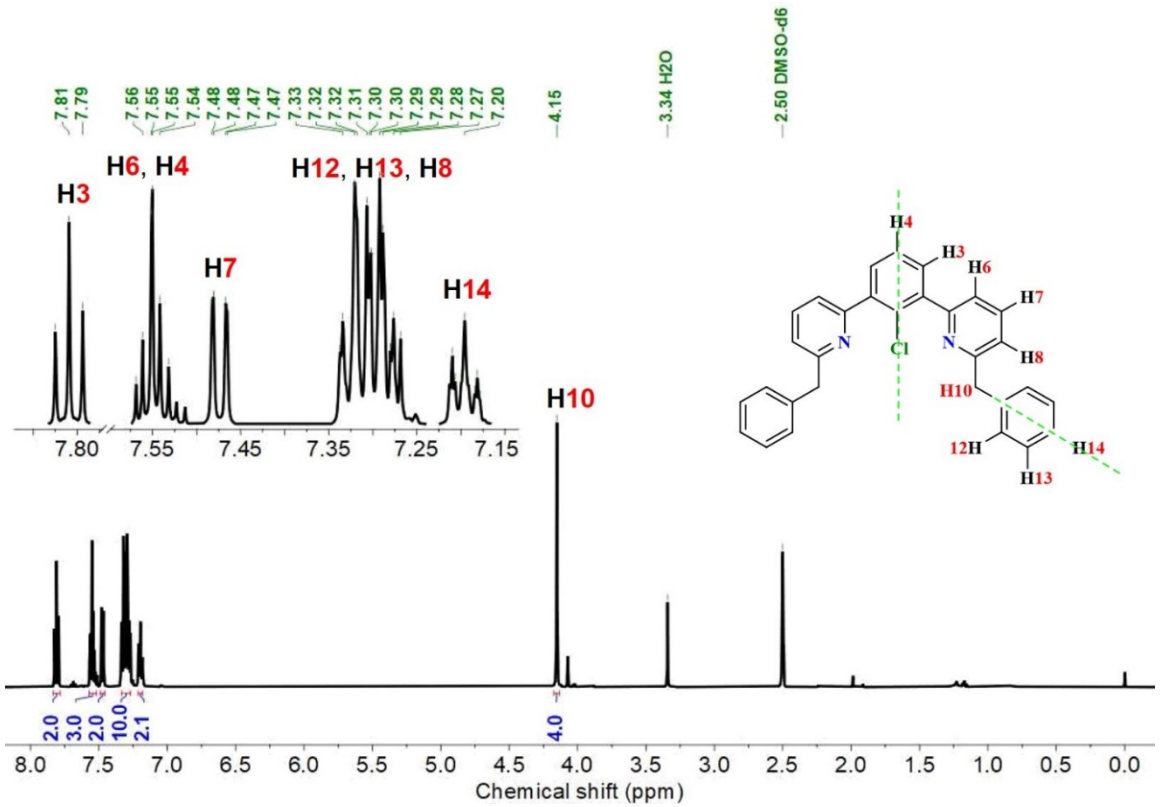


Figure A26. 500 MHz ^{1}H NMR spectrum of ClL^{Bn} in DMSO-d_6 at RT.

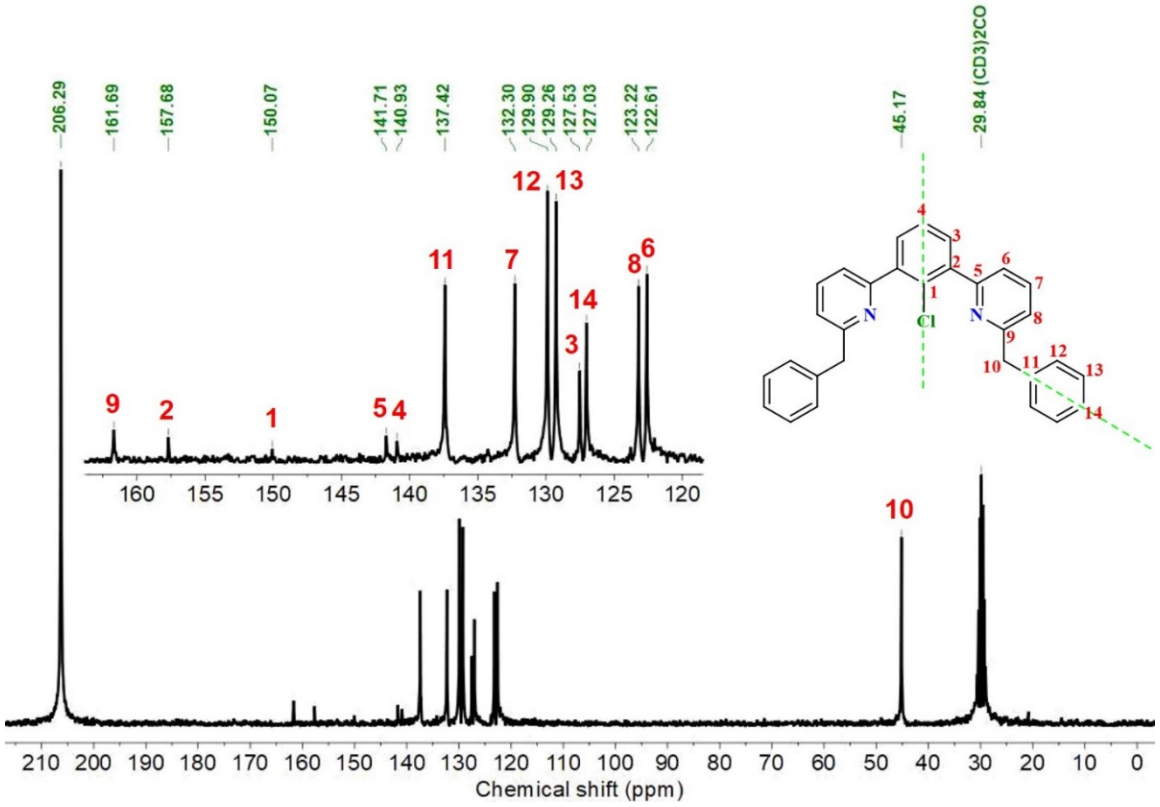


Figure A27. 151 MHz ^{13}C NMR spectrum of ClL^{Bn} in acetone-d_6 at RT.

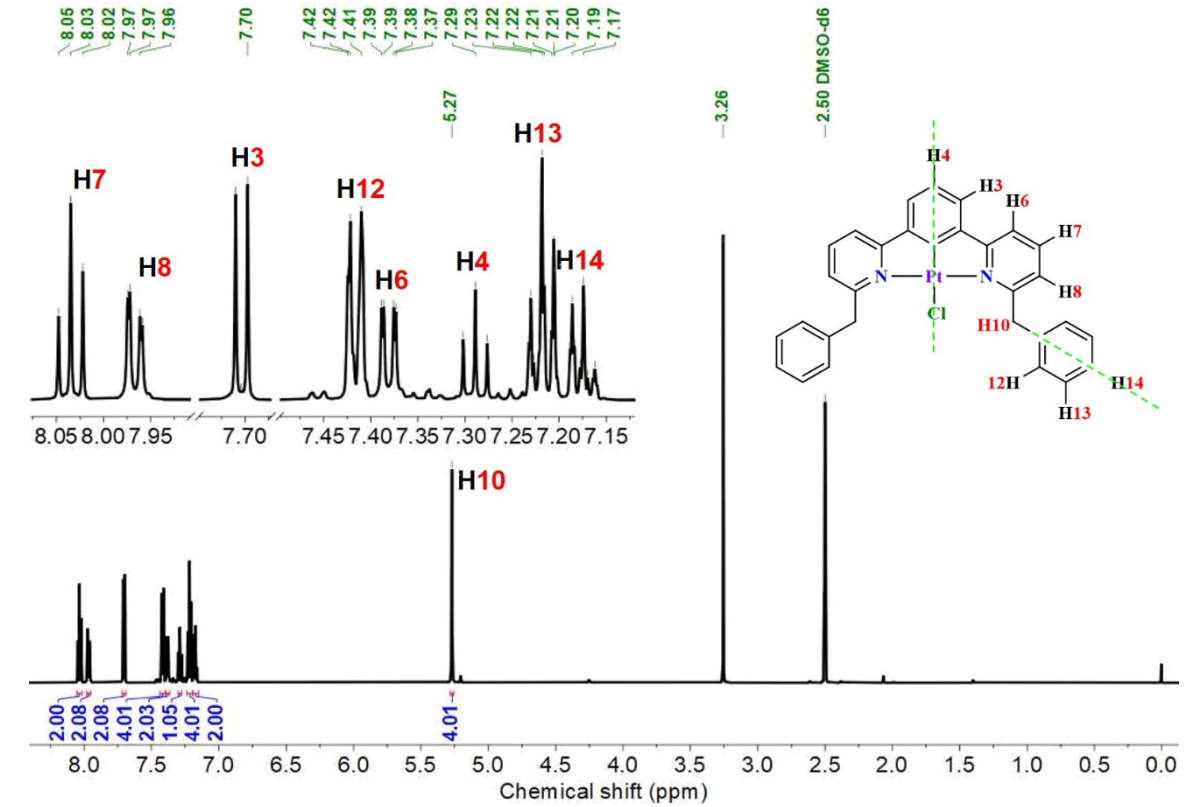


Figure A28. 600 MHz ^{1}H NMR spectrum of [Pt(L^{Bn})Cl] in DMSO-*d*$_6$ at RT.

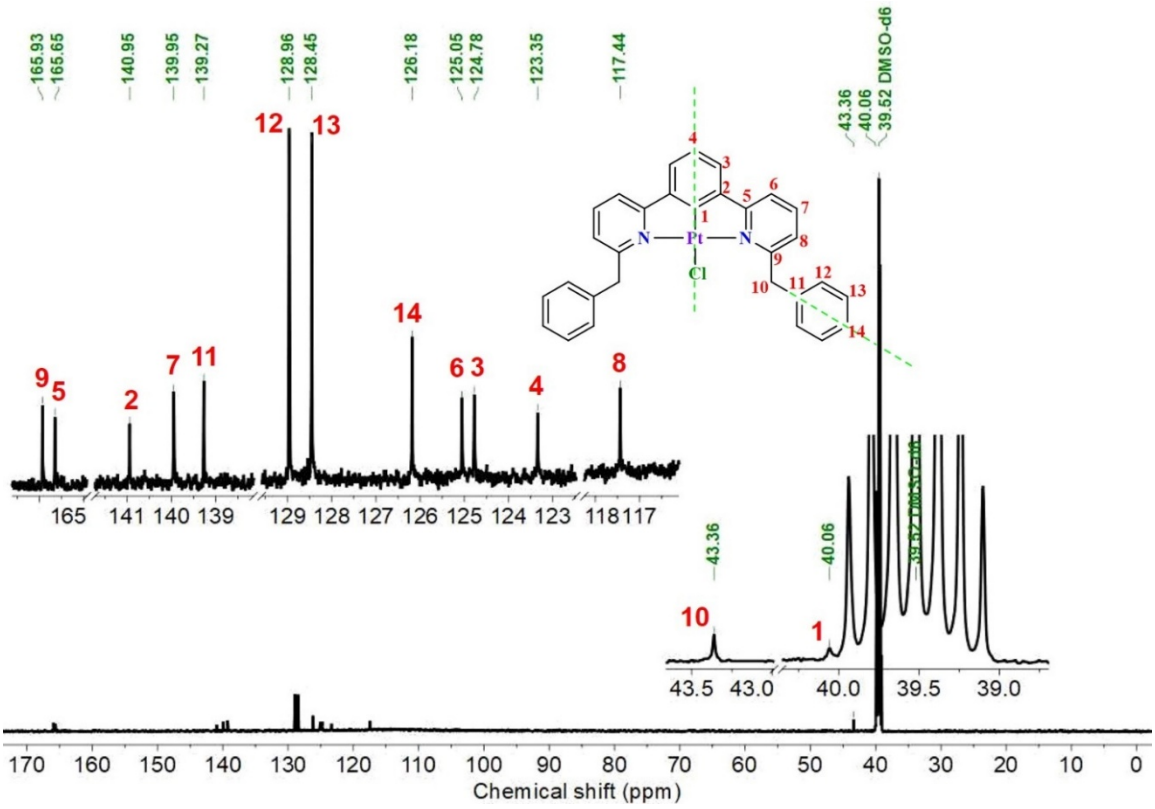


Figure A29. 151 MHz ^{13}C NMR spectrum of [Pt(L^{Bn})Cl] in DMSO-*d*$_6$ at 313 K.

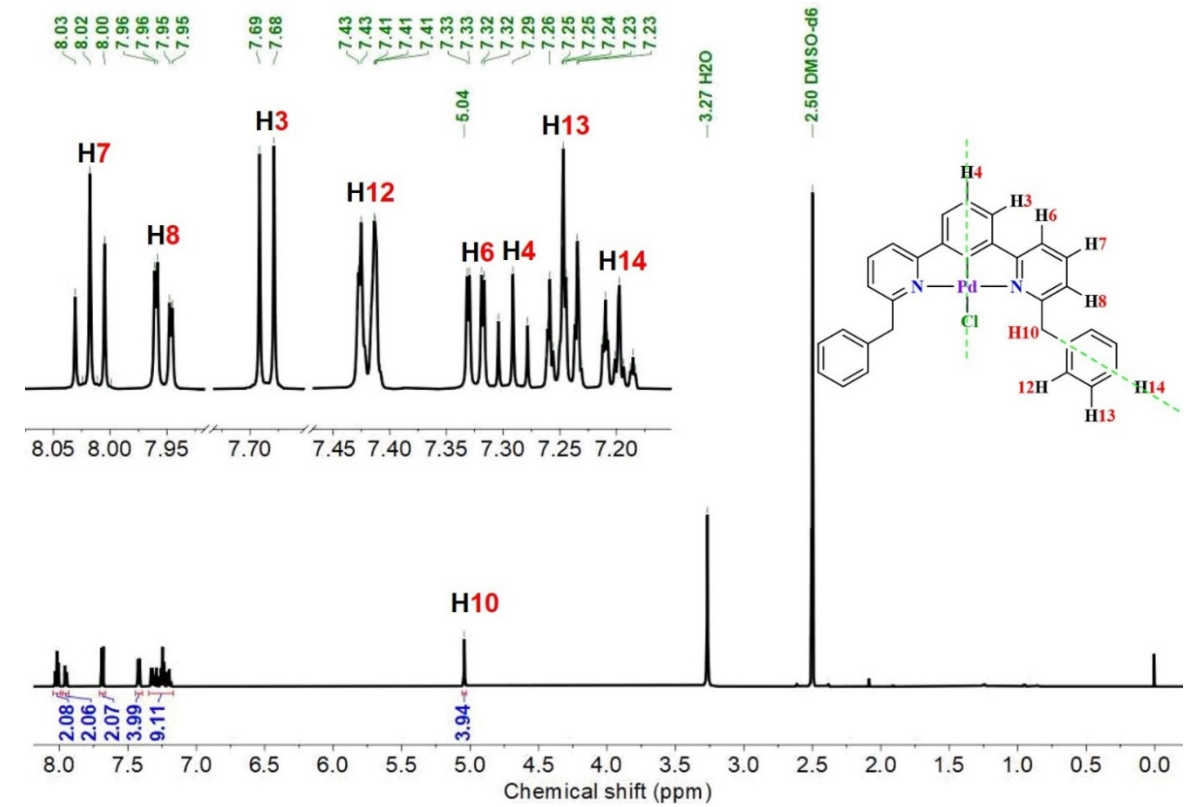


Figure A30. 600 MHz ^{1}H NMR spectrum of [Pd(L^{Bn})Cl] in DMSO-*d*$_6$ at RT.

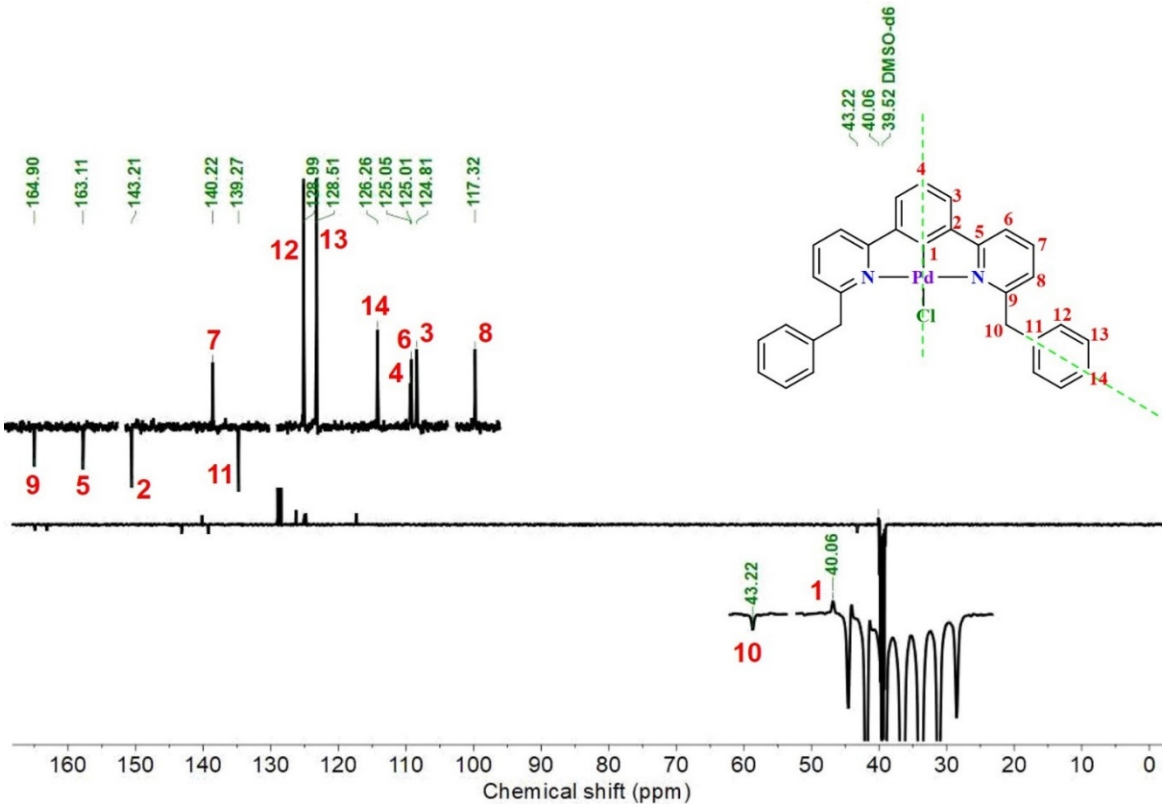


Figure A31. 151 MHz ^{13}C NMR spectrum of [Pd(L^{Bn})Cl] in DMSO-*d*$_6$ at 313 K.

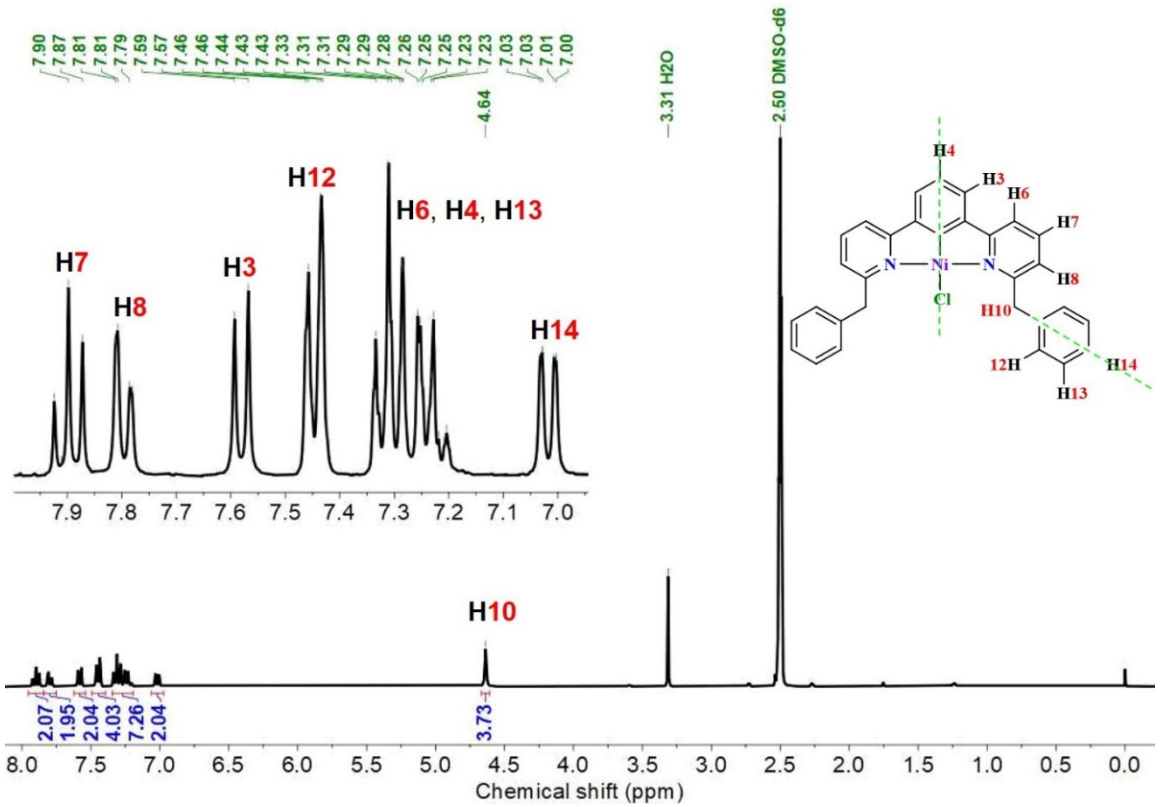


Figure A32. 300 MHz ^{1}H NMR spectrum of [Ni(L^{Bn})Cl] in DMSO-d_6 at RT.

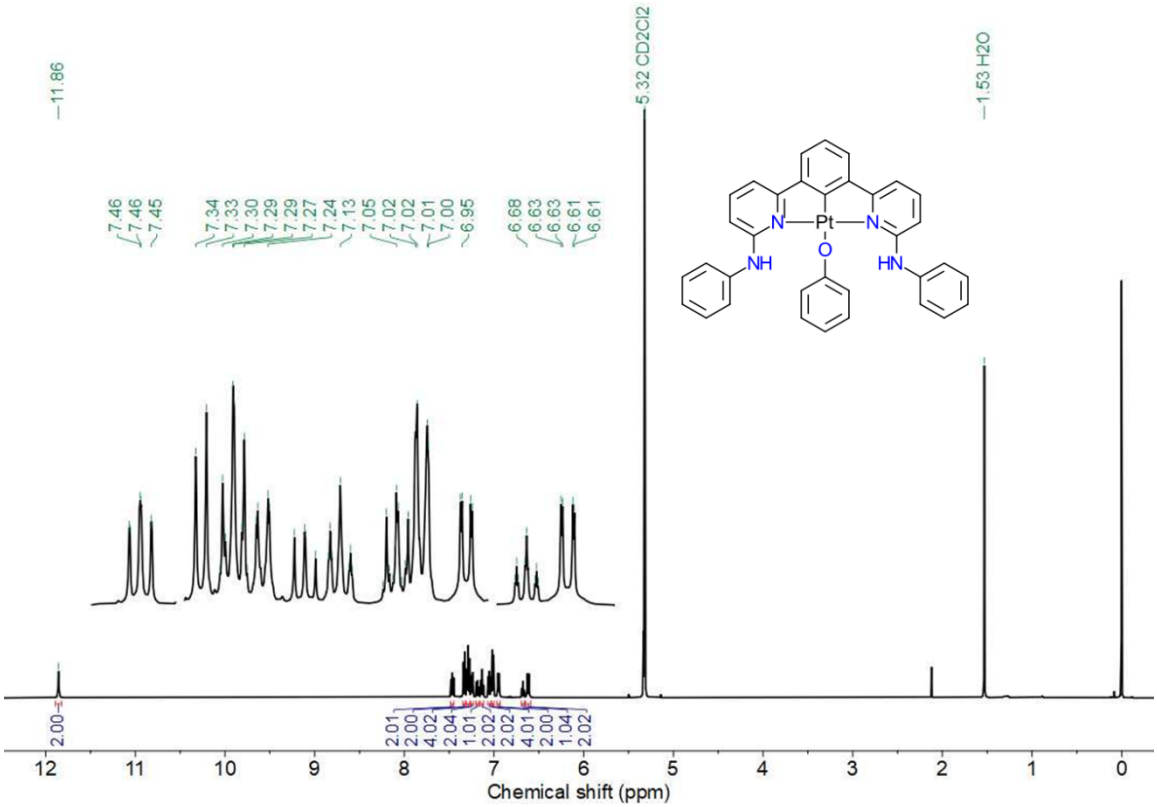


Figure A33. 500 MHz ^{1}H NMR spectrum of [Pt(L^{NHPh})OPh] in CD_2Cl_2 at RT.

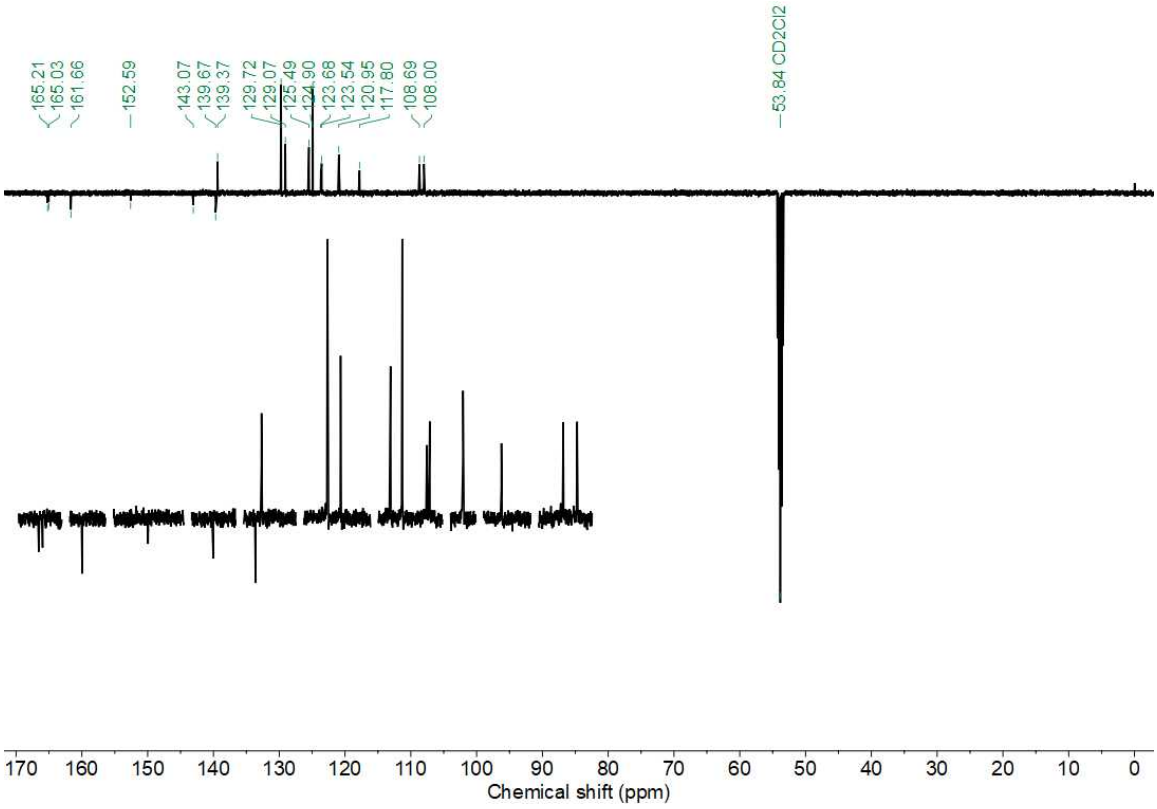


Figure A34. 126 MHz ^{13}C NMR spectrum of [Pt(L^{NHPh})OPh] in CD_2Cl_2 at RT.

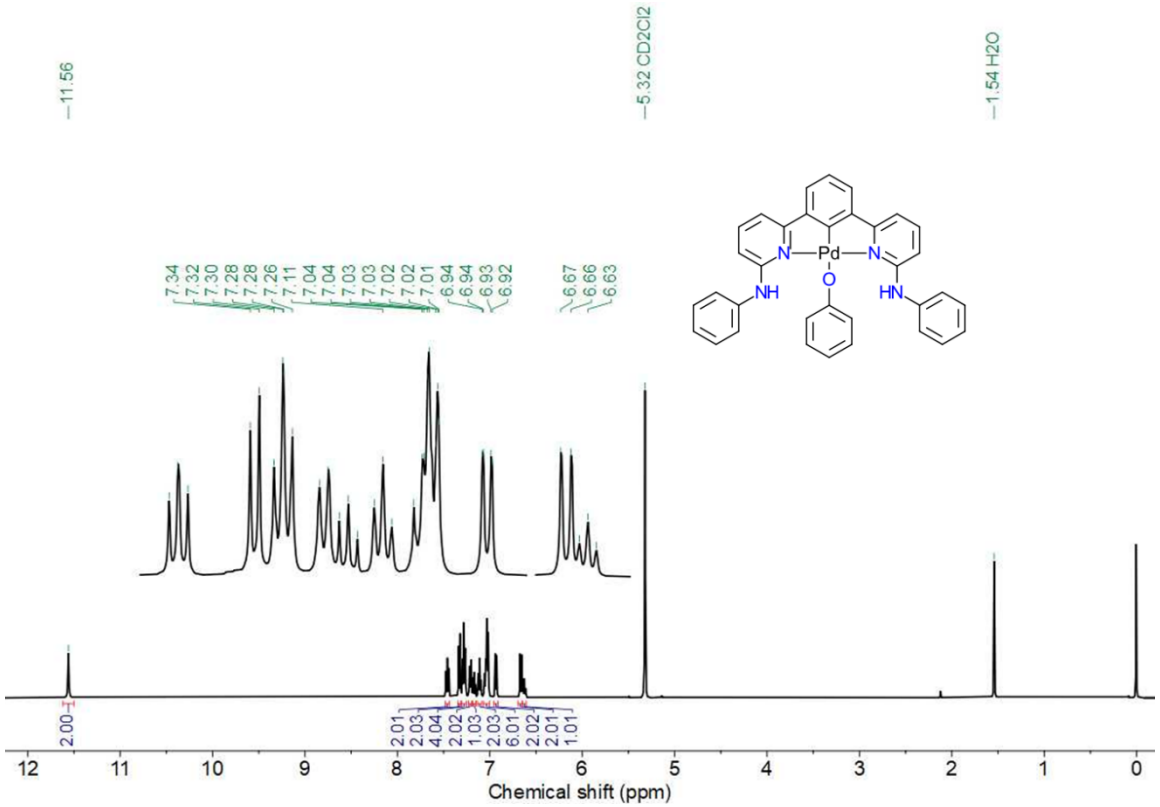


Figure A35. 500 MHz ^{1}H NMR spectrum of [Pd(L^{NHPh})OPh] in CD_2Cl_2 at RT.

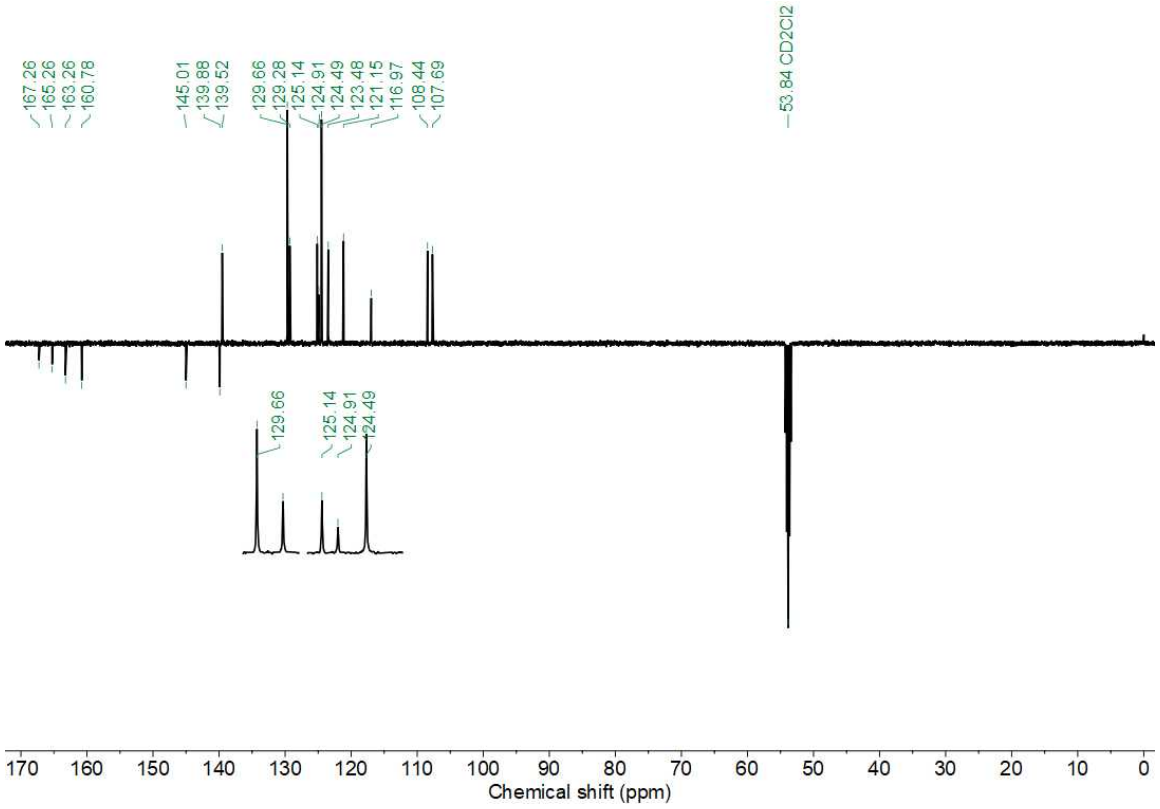


Figure A36. 126 MHz ^{13}C NMR spectrum of [Pd(L^{NHPh})OPh] in CD_2Cl_2 at RT.

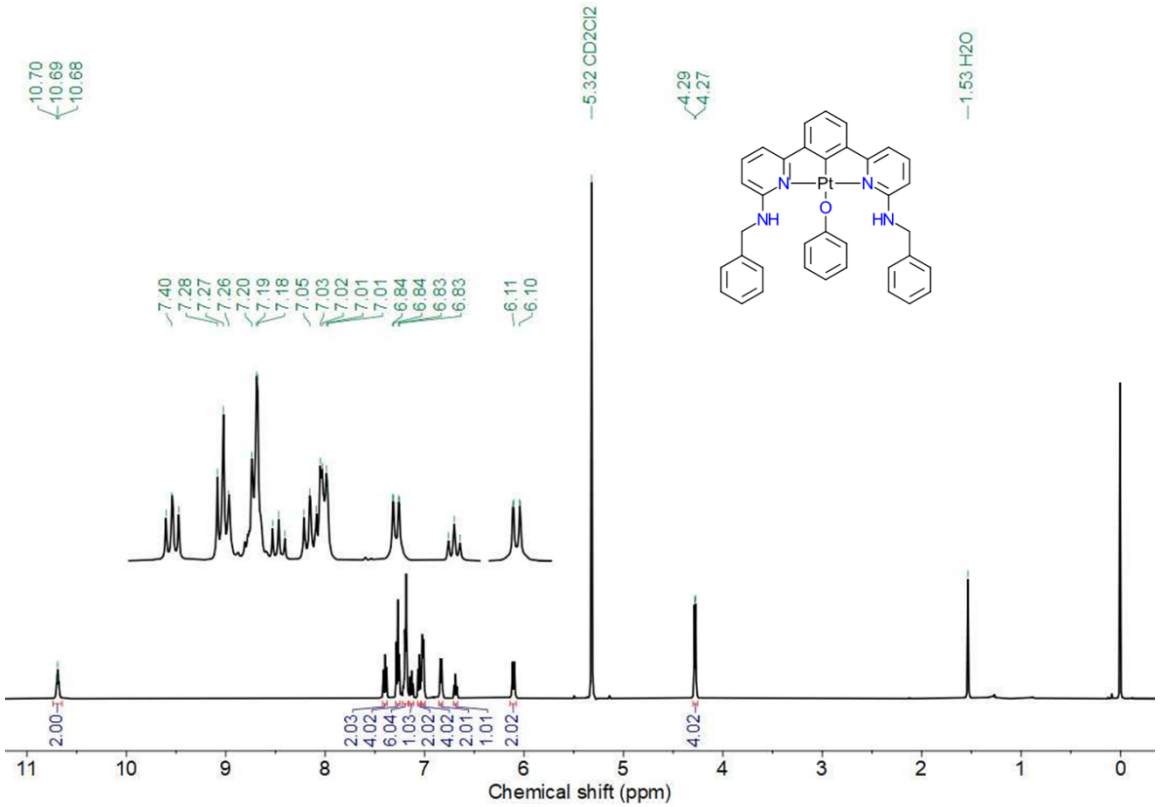


Figure A37. 500 MHz ^{1}H NMR spectrum of [Pt(L^{NHBn})OPh] in CD_2Cl_2 at RT.

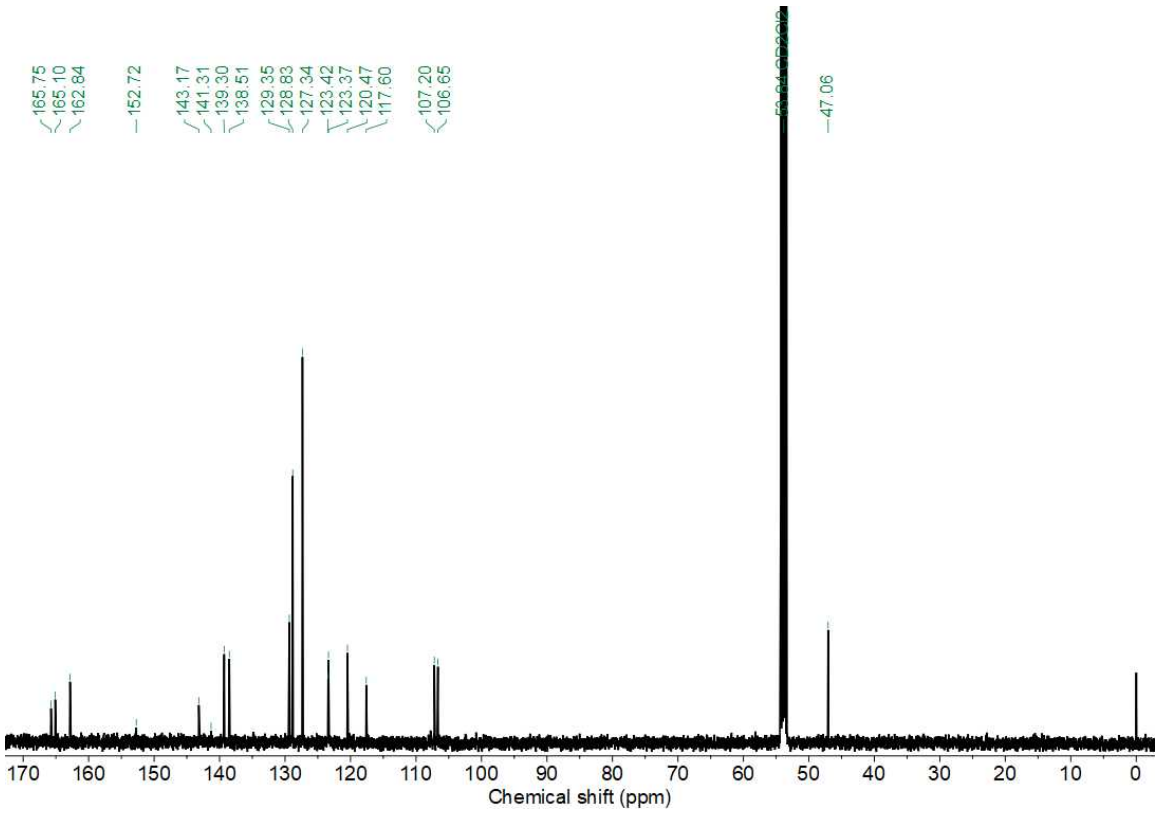


Figure A38. 126 MHz ^{13}C NMR spectrum of [Pt(L^{NHBn})OPh] in CD_2Cl_2 at RT.

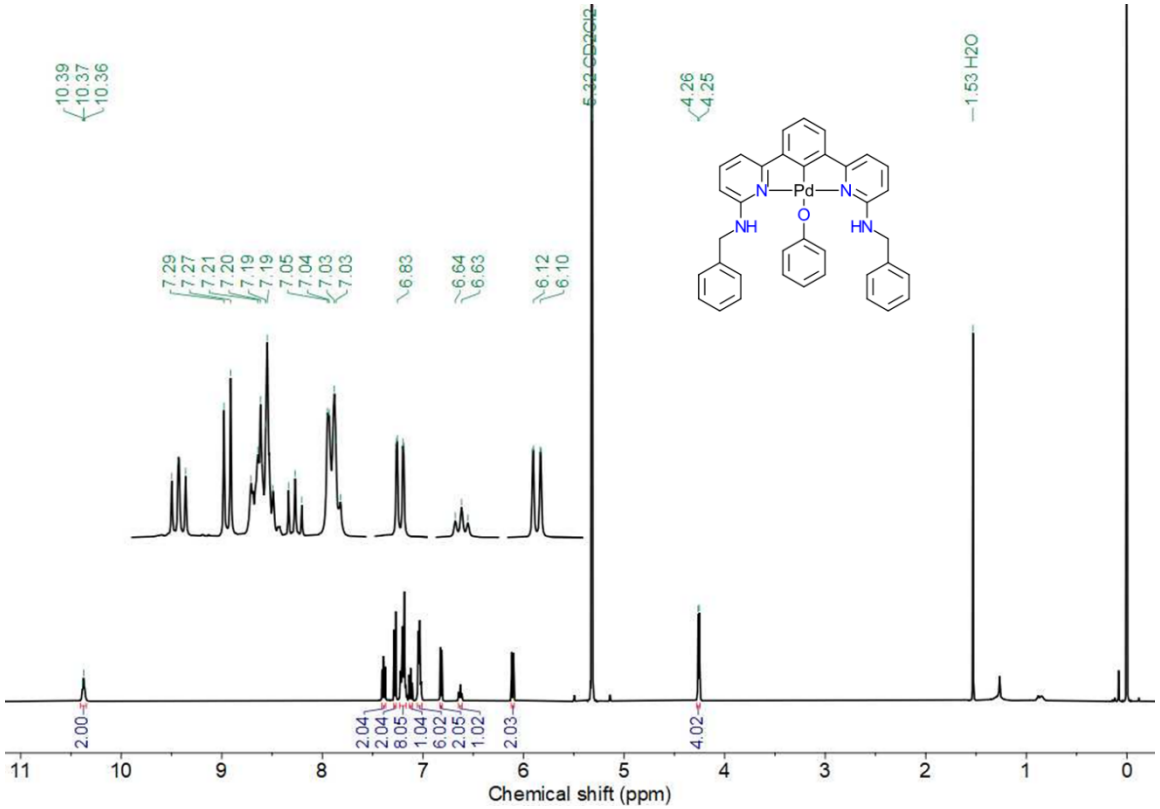


Figure A39. 500 MHz ^{1}H NMR spectrum of [Pd(L^{NHBn})OPh] in CD_2Cl_2 at RT.

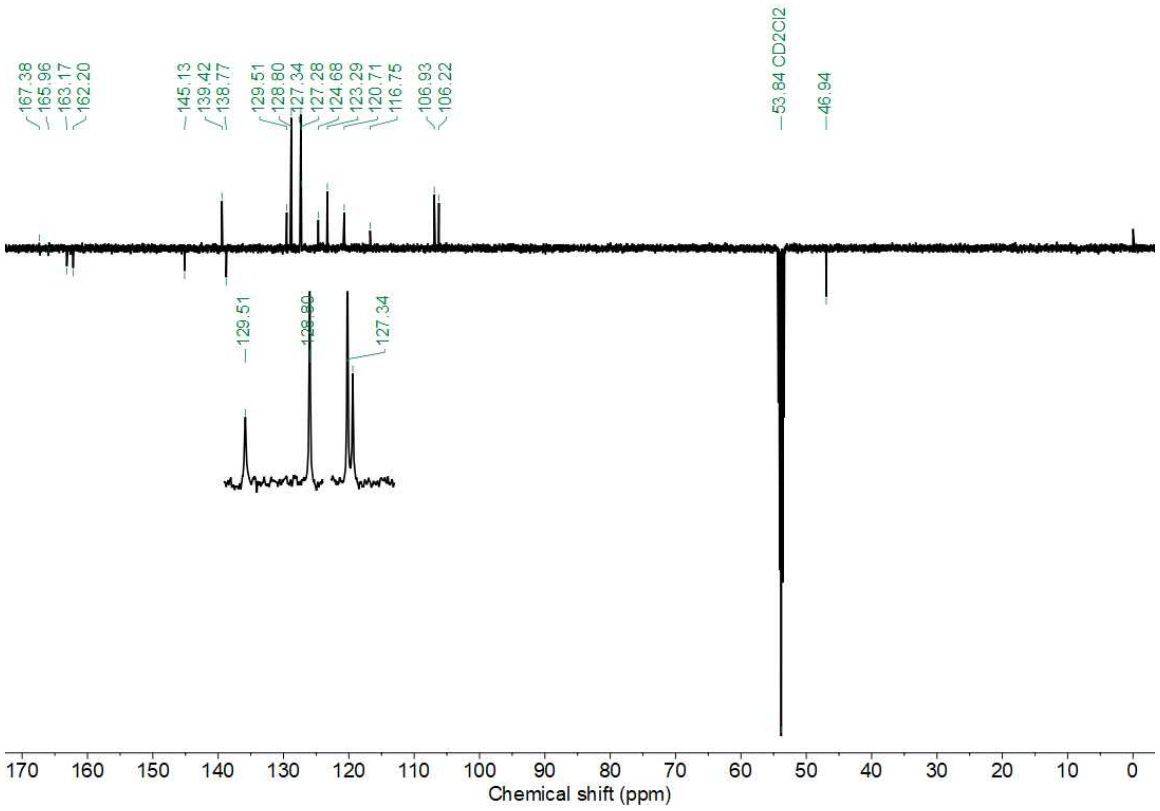


Figure A40. 126 MHz ^{13}C NMR spectrum of [Pd(L^{NHBn})OPh] in CD_2Cl_2 at RT.

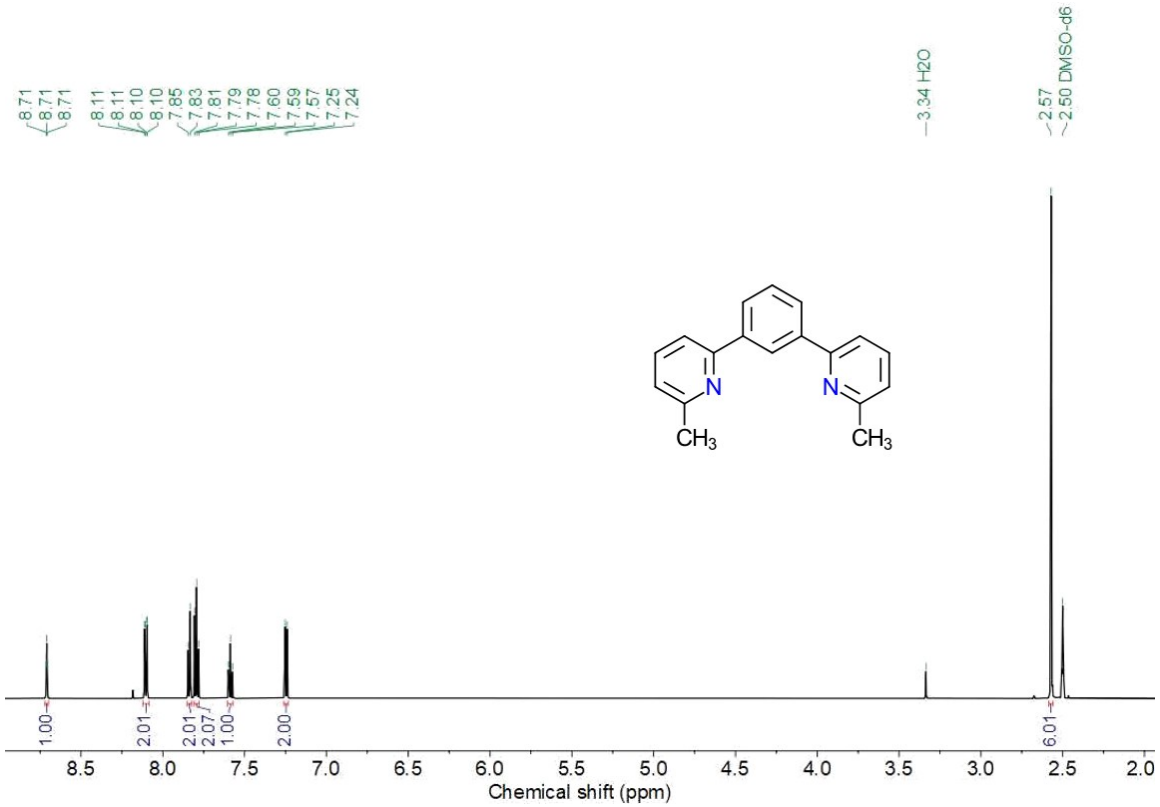


Figure A41. 600 MHz ^{1}H NMR spectrum of HL^{Me} in DMSO-*d*$_6$ at RT.

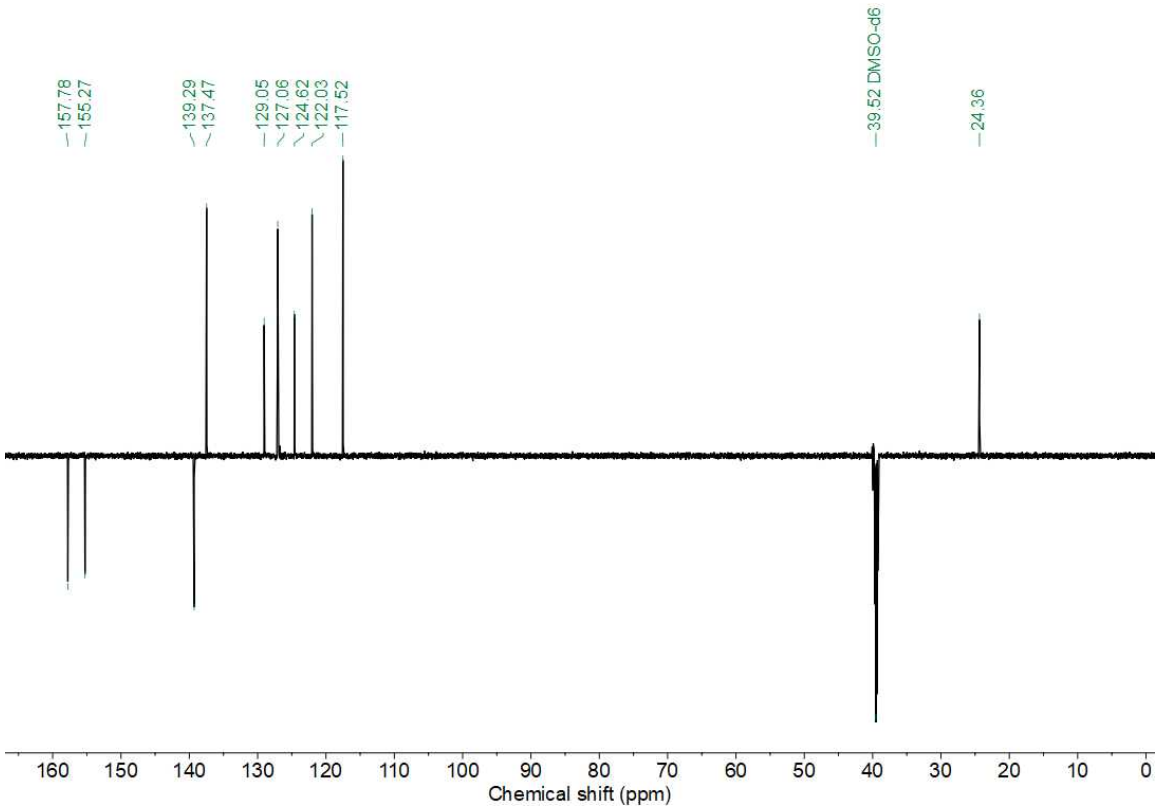


Figure A42. 151 MHz ^{13}C NMR spectrum of HL^{Me} in DMSO-*d*$_6$ at RT.

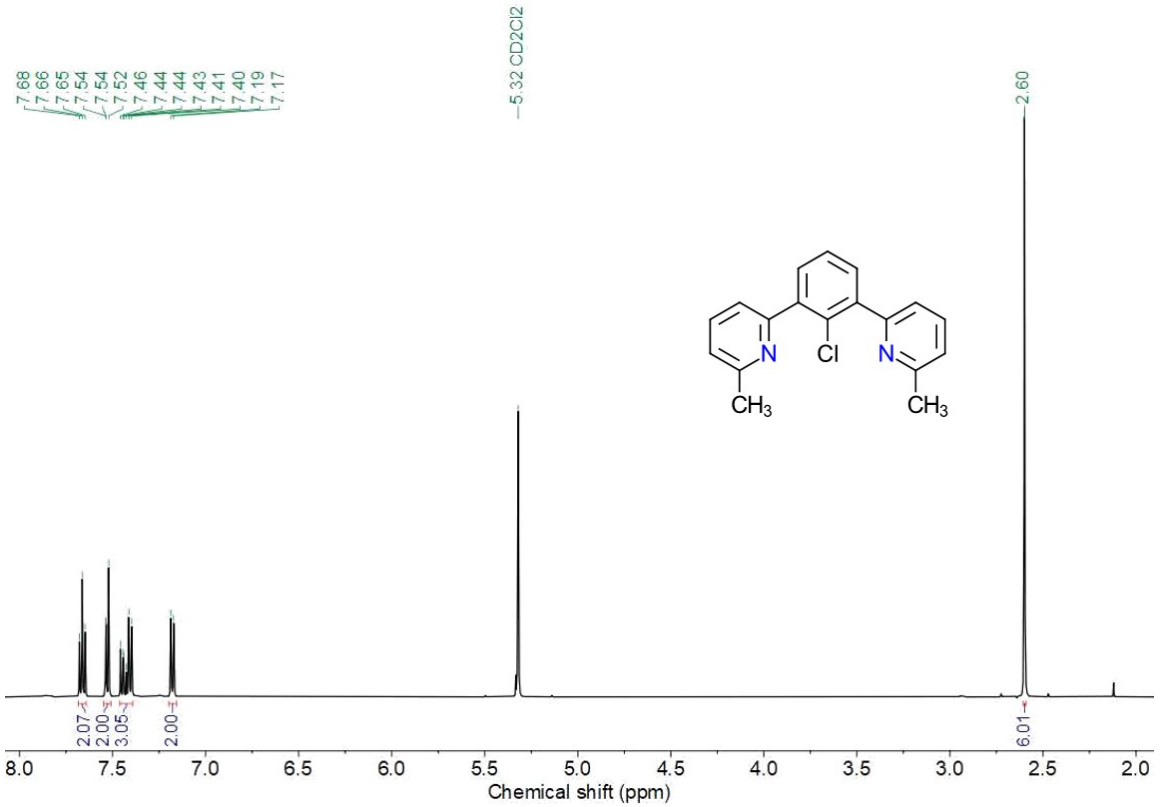


Figure A43. 500 MHz ^{1}H NMR spectrum of L^{Me}Cl in CD_2Cl_2 at RT.

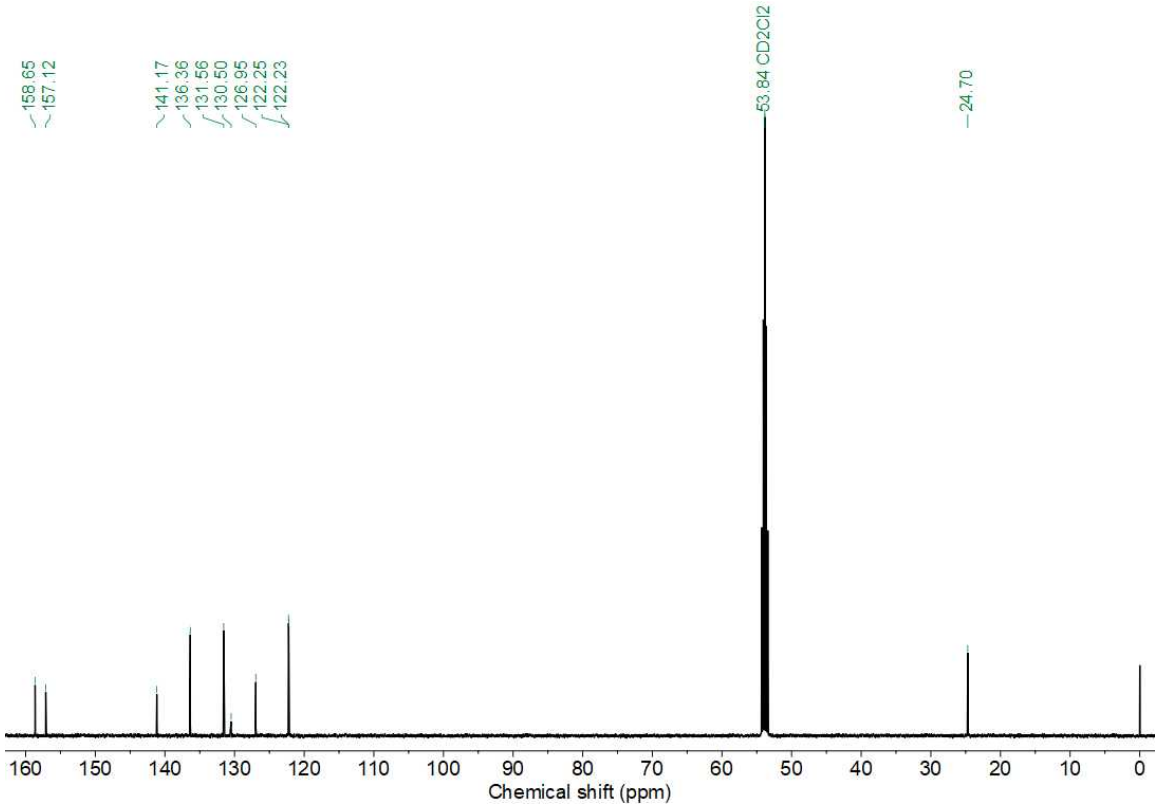


Figure A44. 126 MHz ^{13}C NMR spectrum of L^{Me}Cl in CD_2Cl_2 at RT.

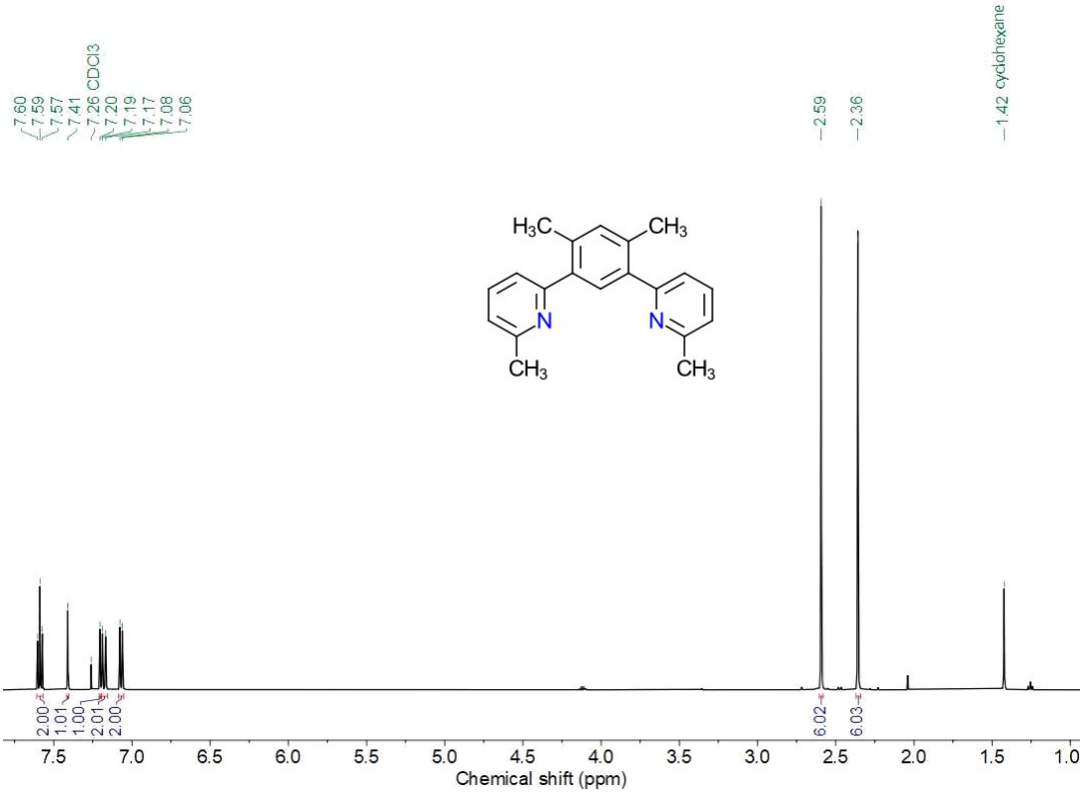


Figure A45. 500 MHz ^{1}H NMR spectrum of HL^{Me2} in $CDCl_3$ at RT.

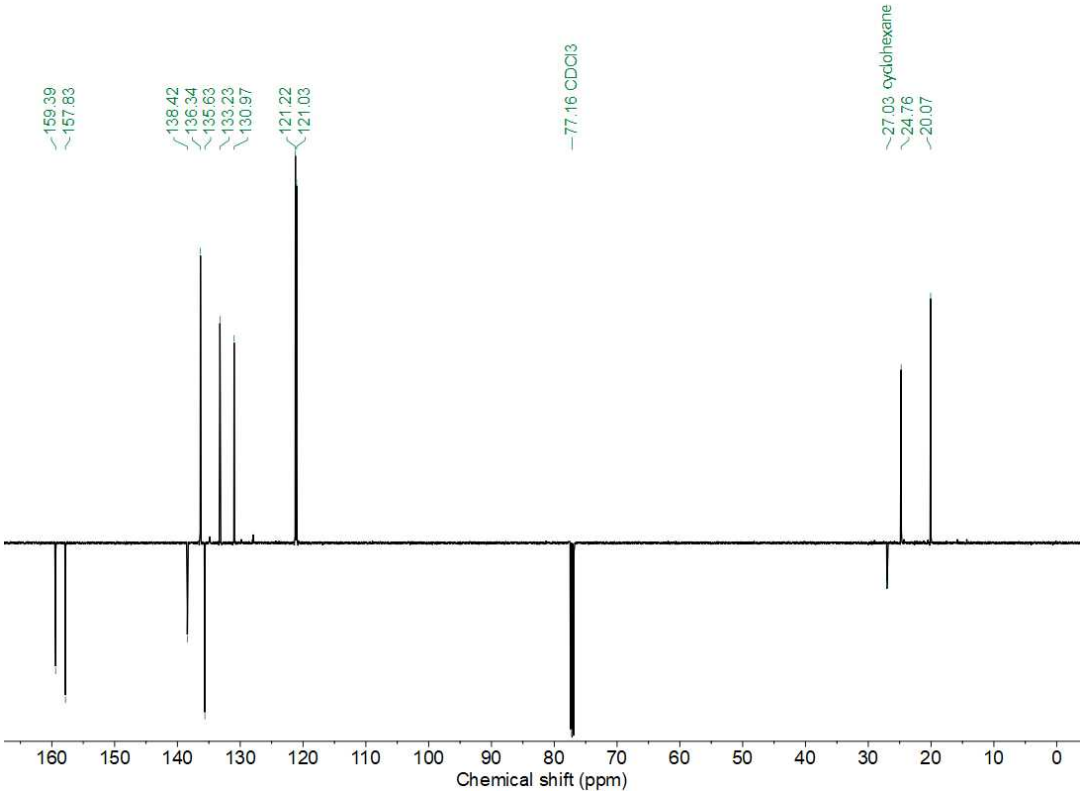


Figure A46. 126 MHz ^{13}C NMR spectrum of HL^{Me2} in $CDCl_3$ at RT.

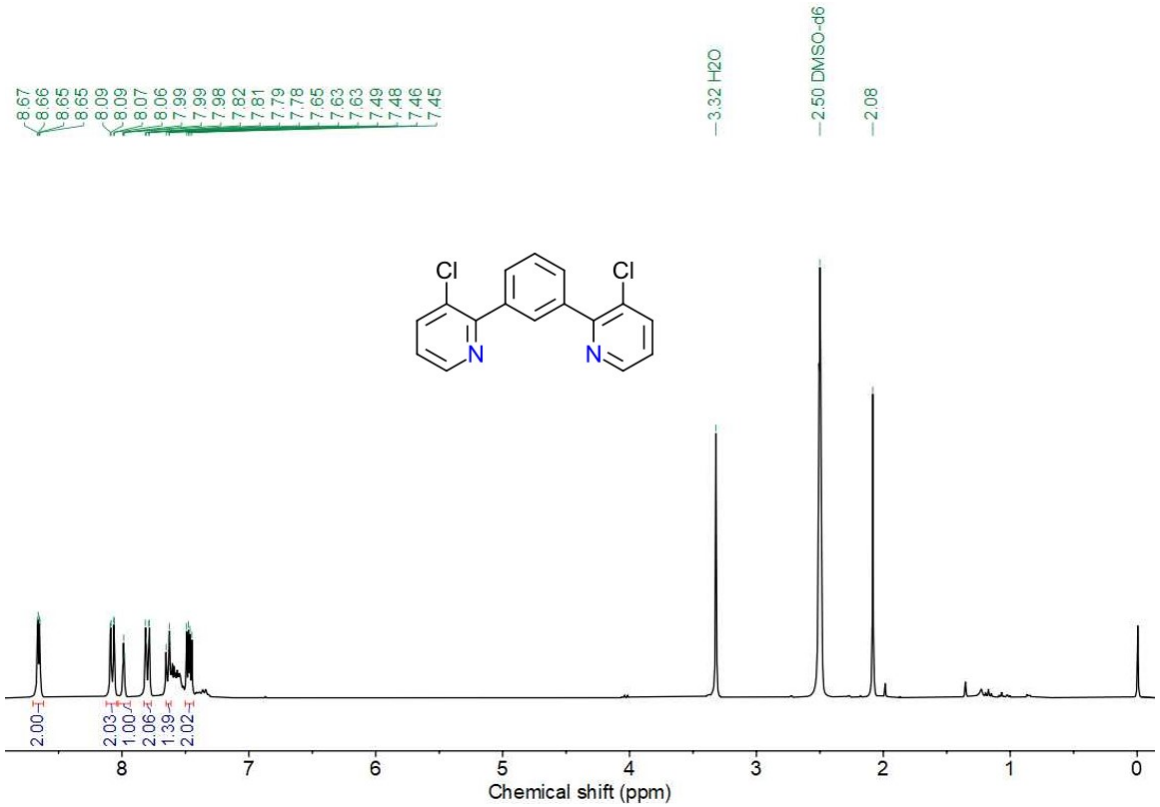


Figure A47. 300 MHz ^{1}H NMR spectrum of HL^{Cl} in DMSO-d_6 at RT.

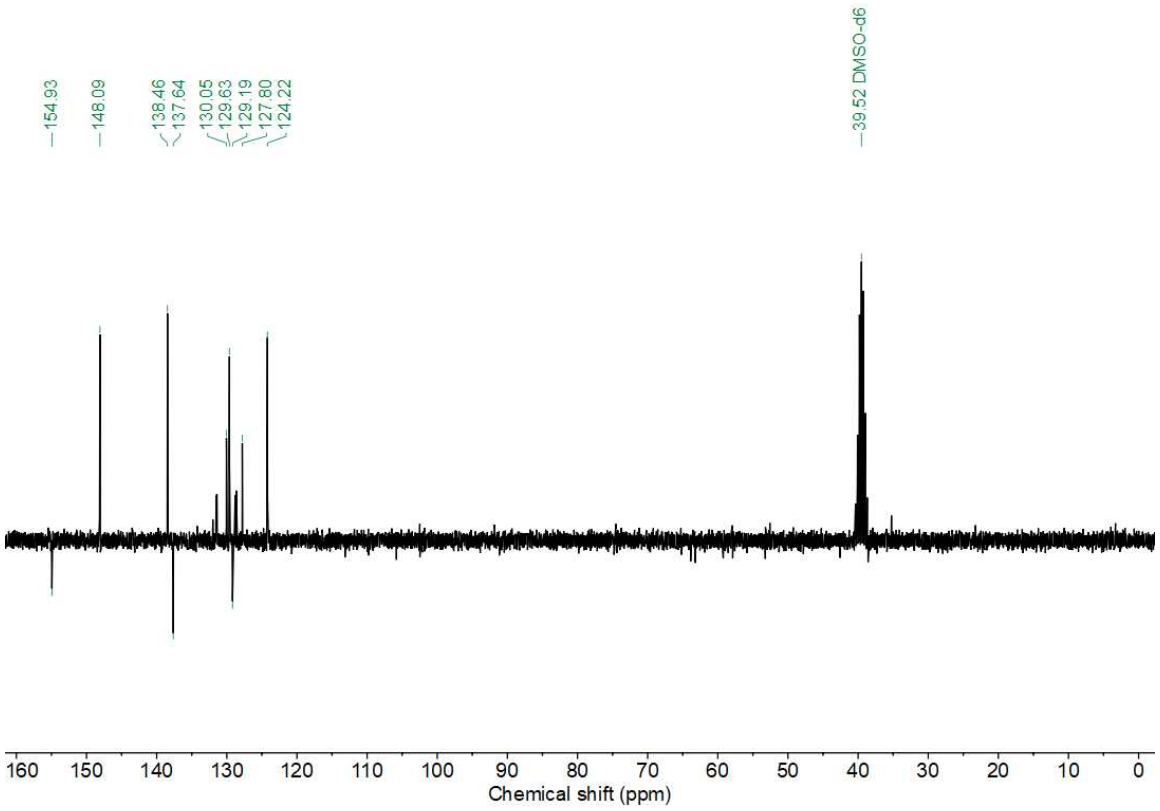


Figure A48. 75 MHz ^{13}C NMR spectrum of HL^{Cl} in DMSO-d_6 at RT.

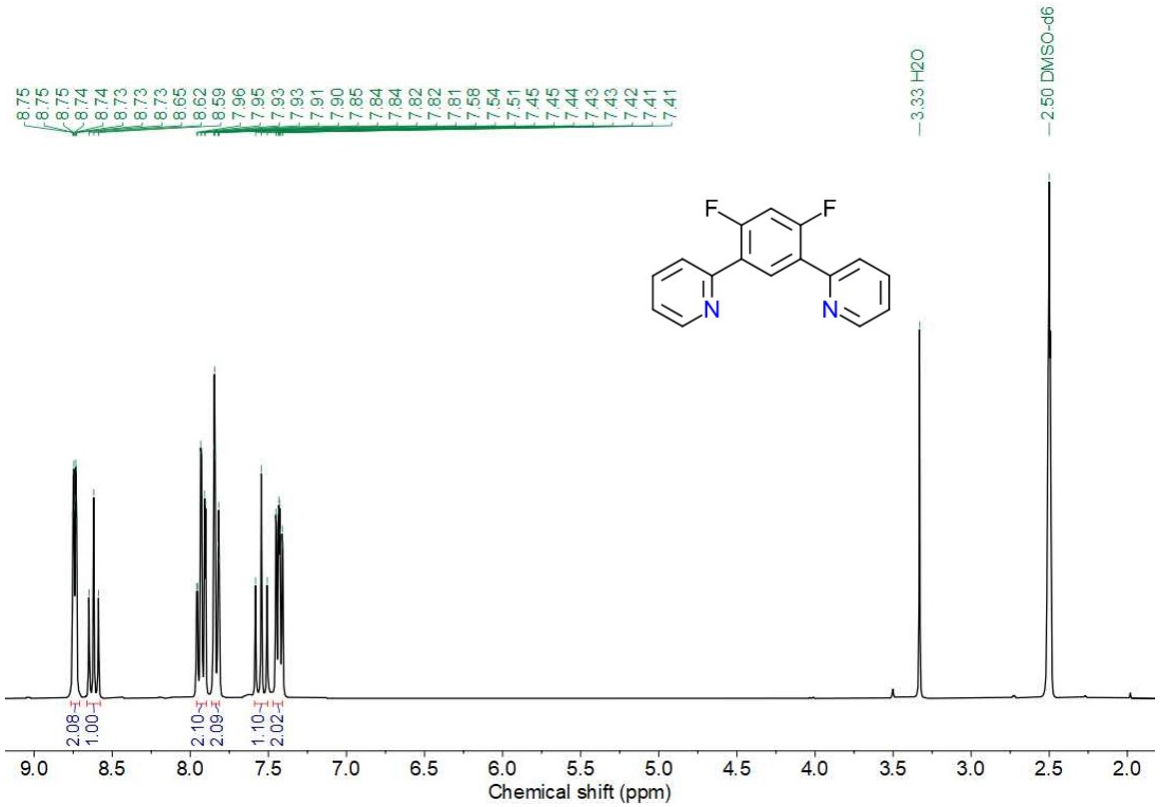


Figure A49. 300 MHz ^{1}H NMR spectrum of HL^{F} in DMSO-*d*$_6$ at RT.

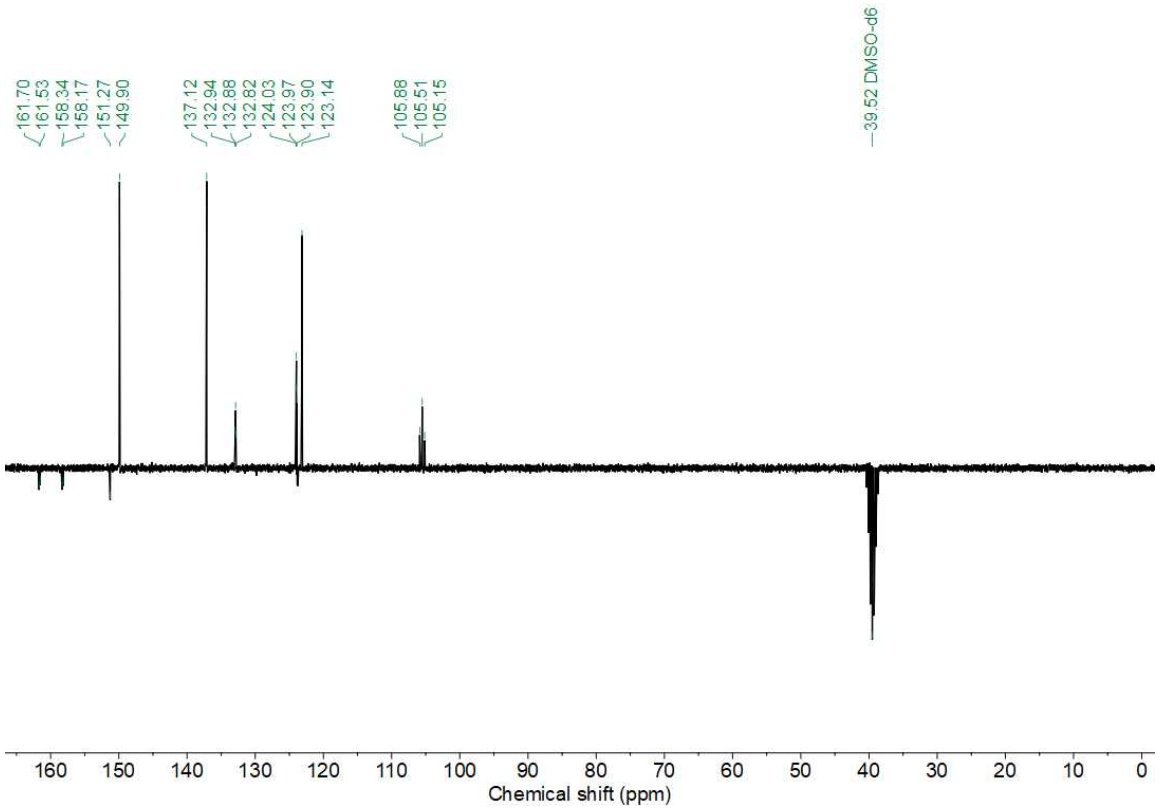


Figure A50. 75 MHz ^{13}C NMR spectrum of HL^{F} in DMSO-*d*$_6$ at RT.

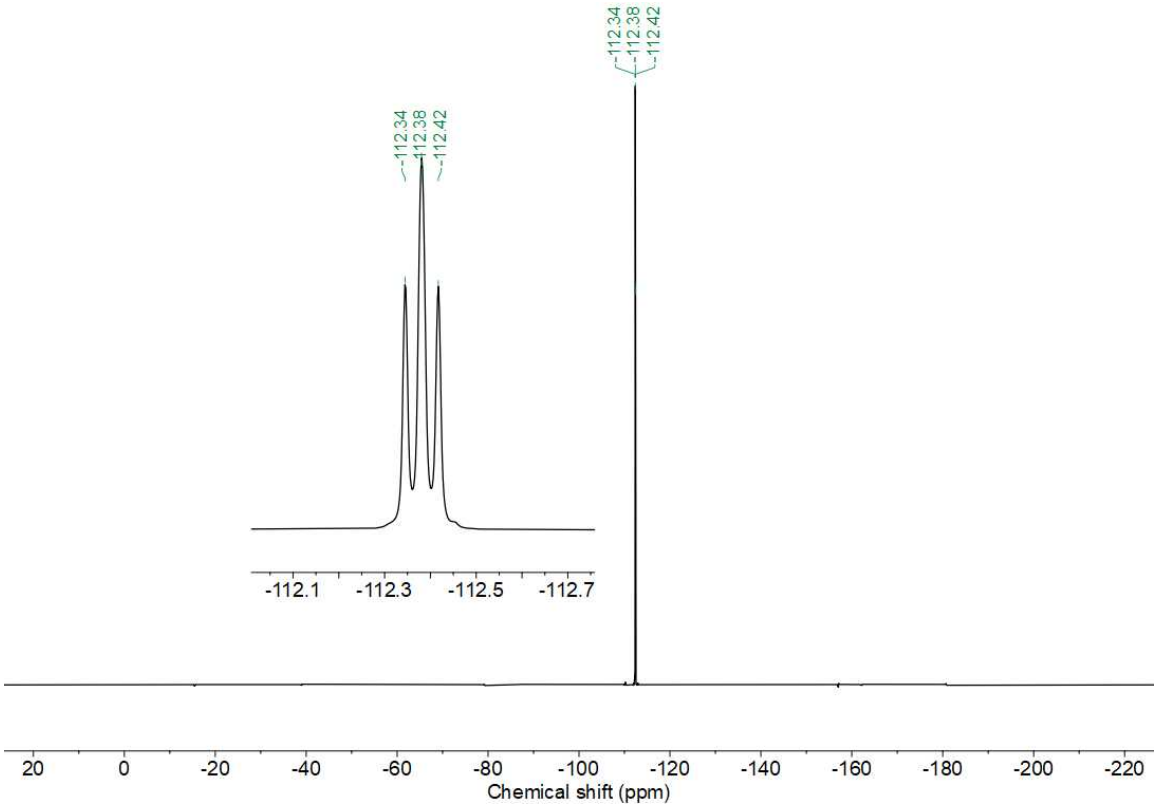


Figure A51. 282 MHz ^{19}F NMR spectrum of HL^F in DMSO-d_6 at RT.

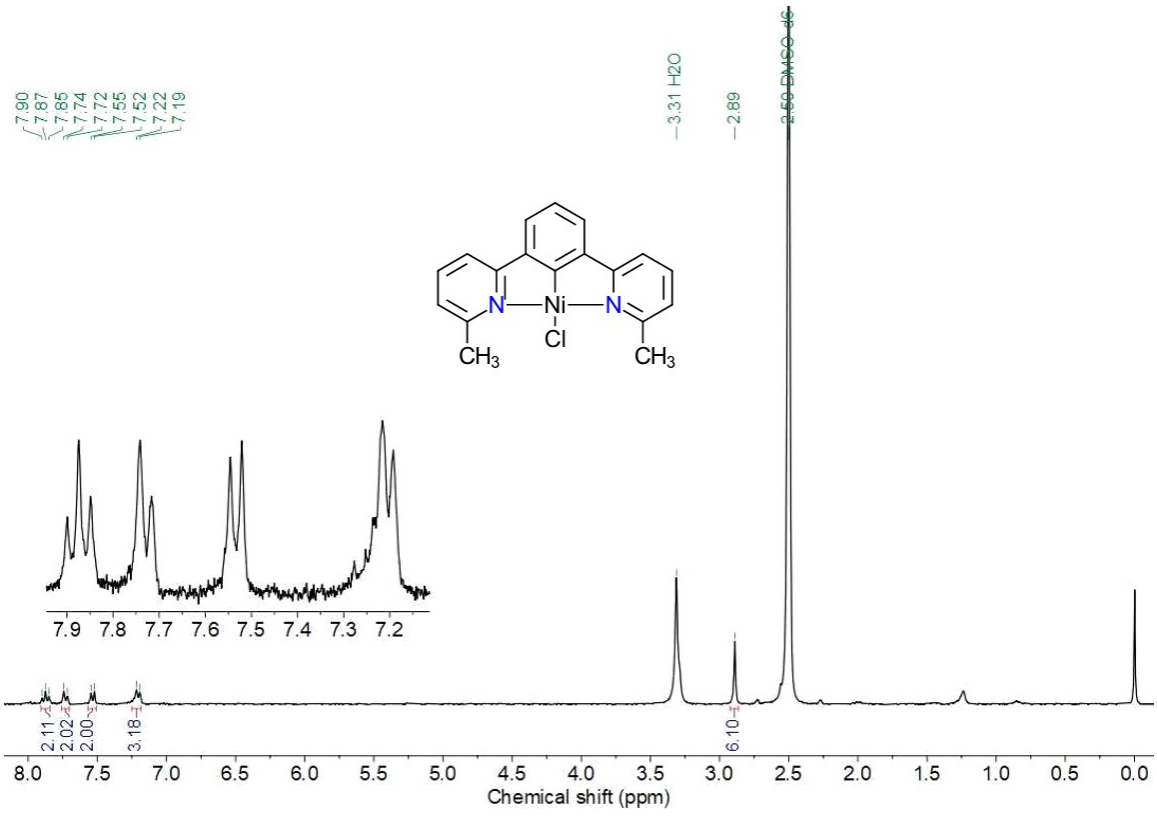


Figure S52. 300 MHz ^1H NMR spectrum of [Ni(L^{Me})Cl] in DMSO-d_6 at RT.

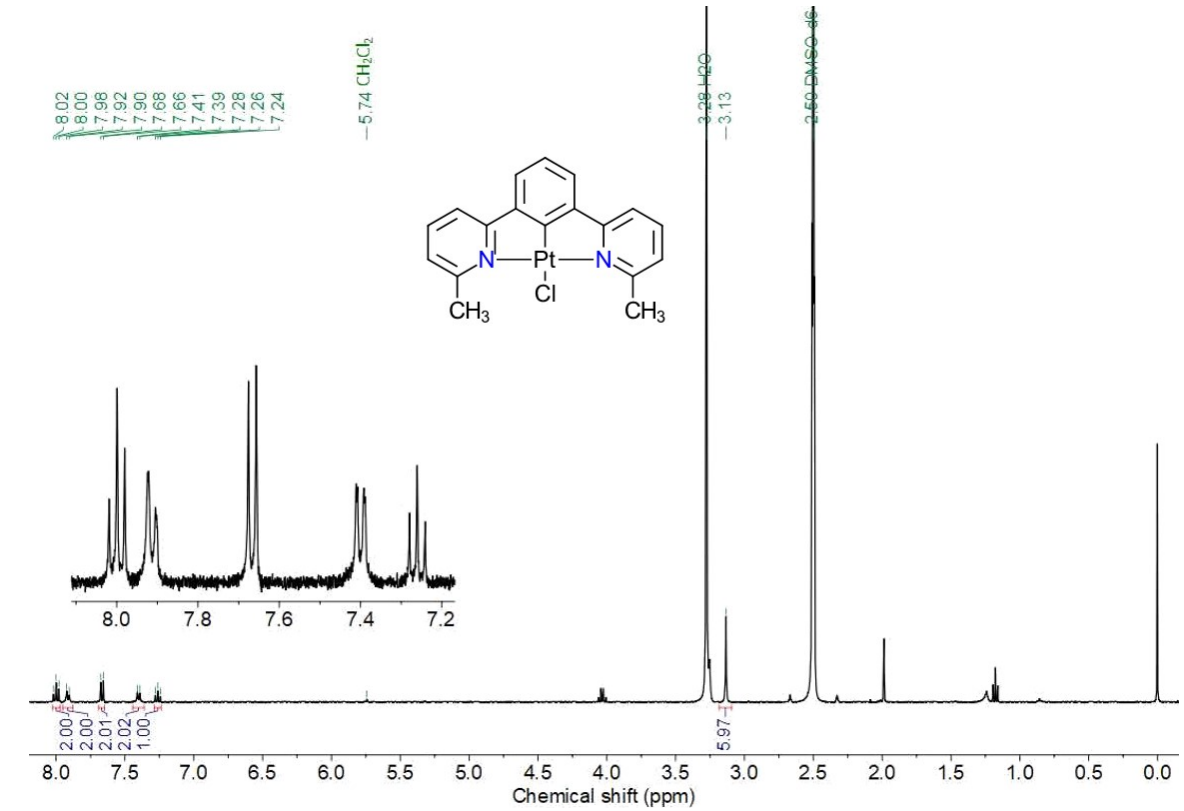


Figure A53. 400 MHz ^{1}H NMR spectrum of [Pt(L^{Me})Cl] in DMSO-*d*$_6$ at RT.

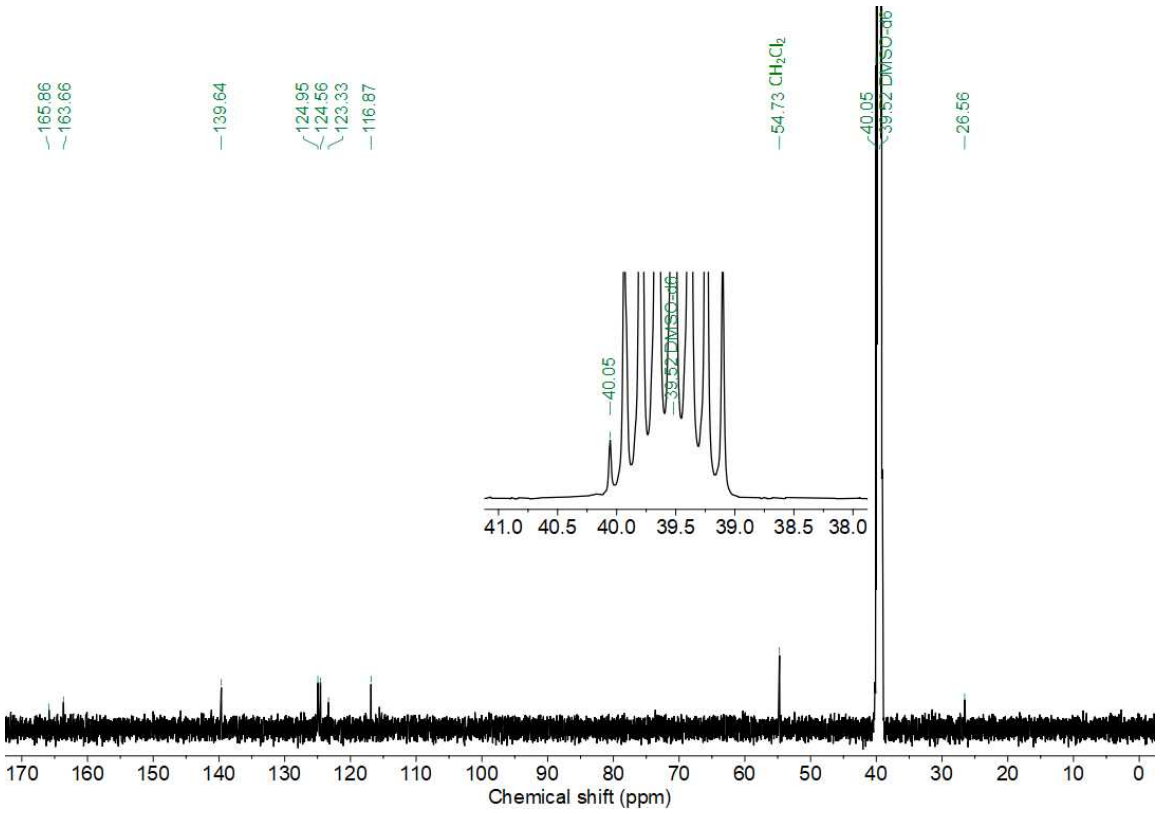


Figure A54. 151 MHz ^{13}C NMR spectrum of [Pt(L^{Me})Cl] in DMSO-*d*$_6$ at RT.

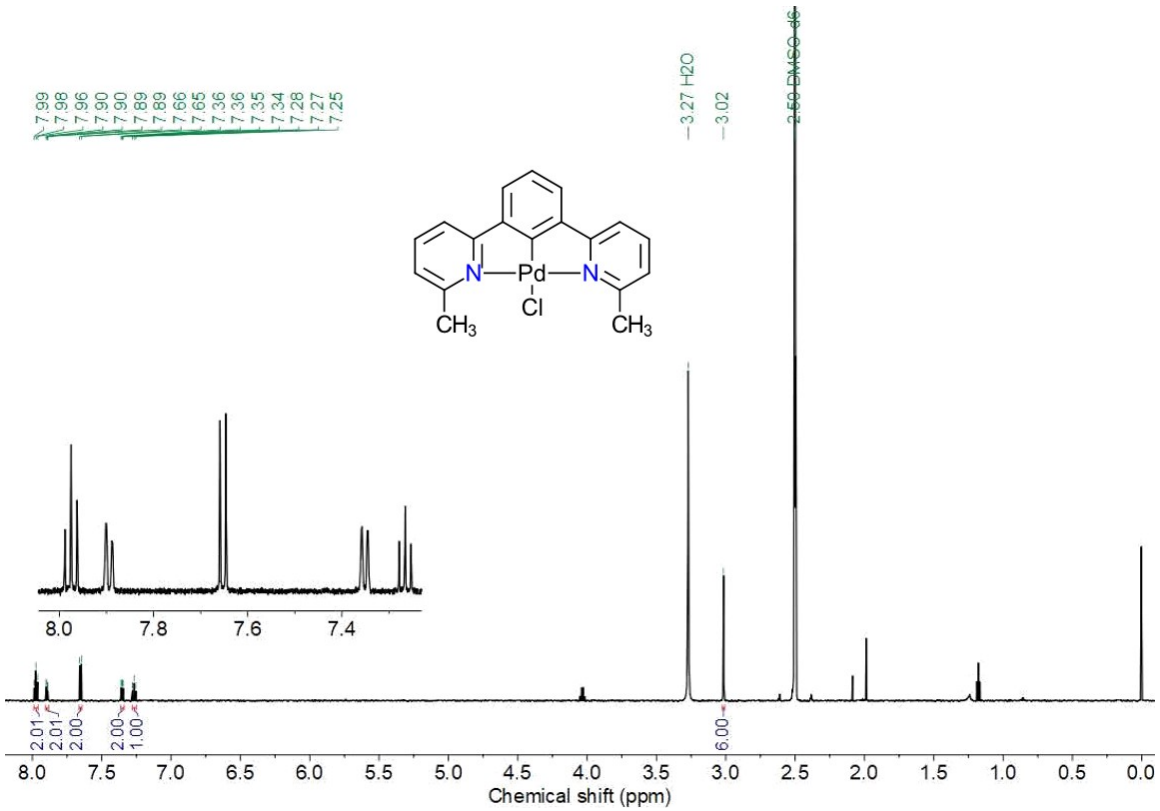


Figure A55. 600 MHz ^{1}H NMR spectrum of [Pd(L^{Me})Cl] in DMSO-d_6 at RT.

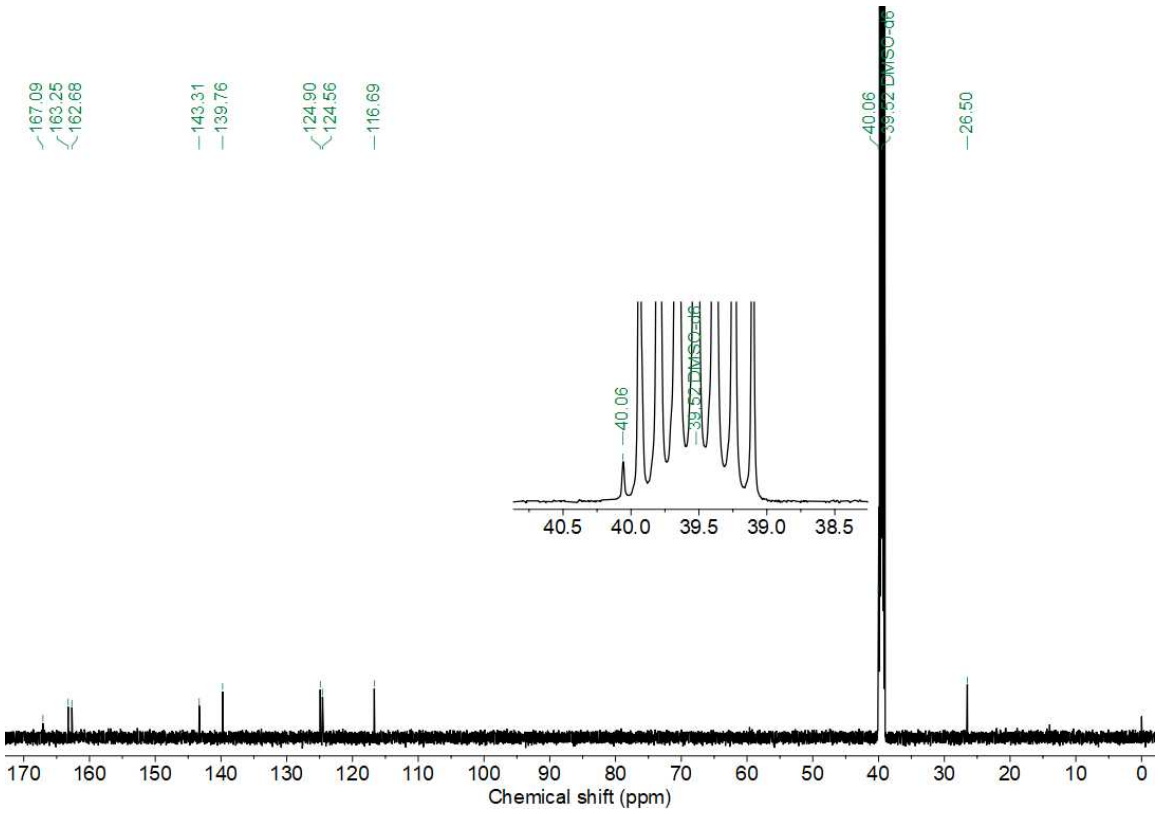


Figure A56. 151 MHz ^{13}C NMR spectrum of [Pd(L^{Me})Cl] in DMSO-d_6 at RT.

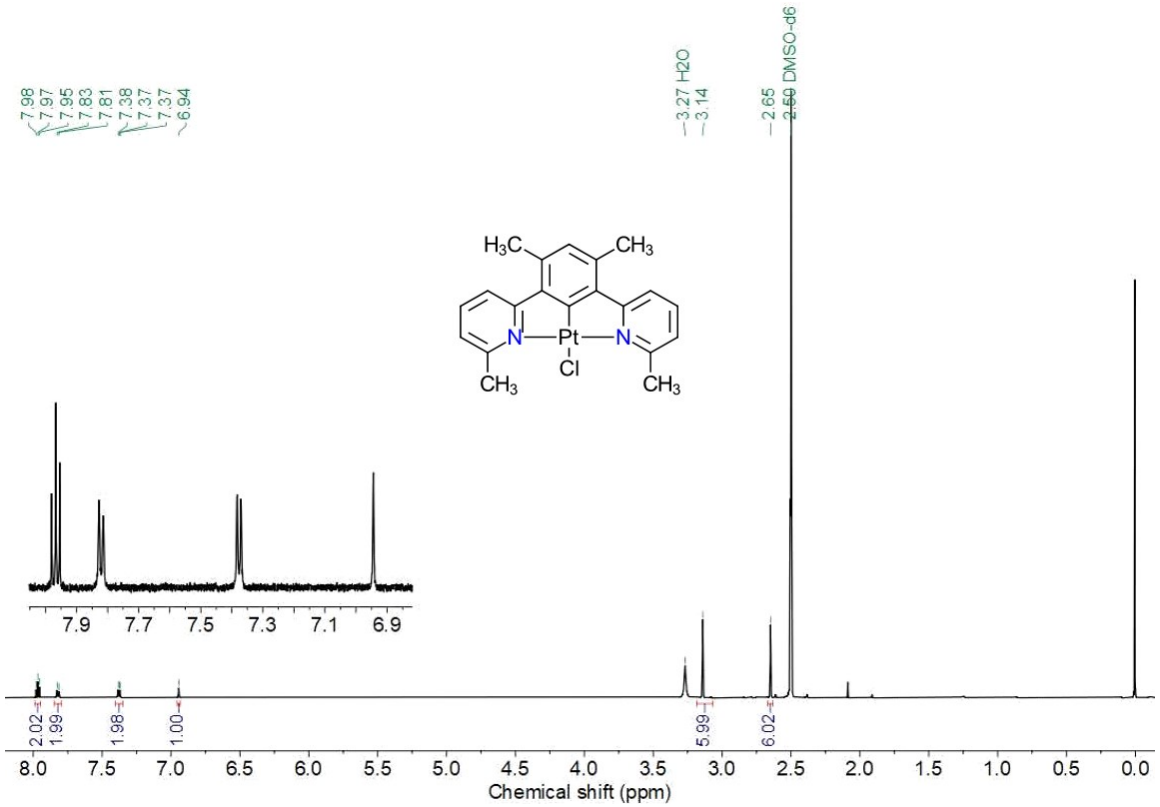


Figure A57. 600 MHz ^{1}H NMR spectrum of [Pt(L^{Me2})Cl] in DMSO-d_6 at 313 K.

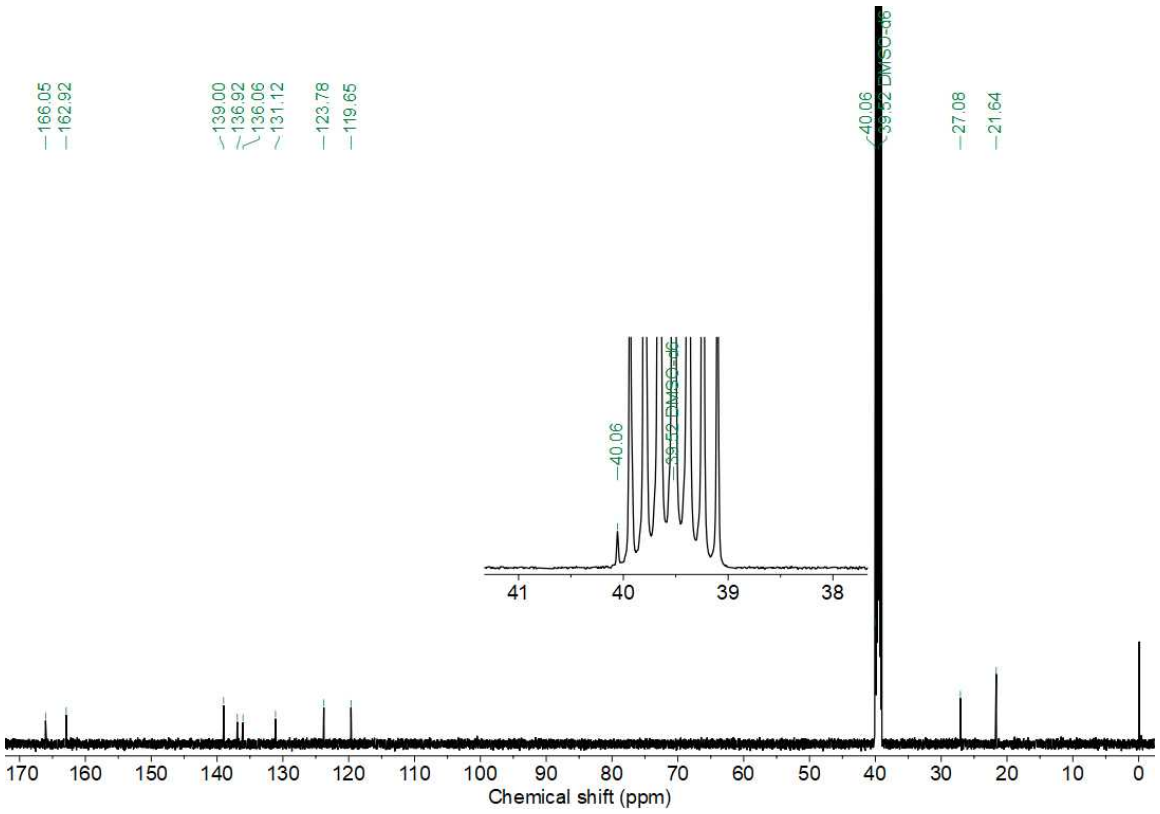


Figure A58. 151 MHz ^{13}C NMR spectrum of [Pt(L^{Me2})Cl] in DMSO-d_6 at 313 K.

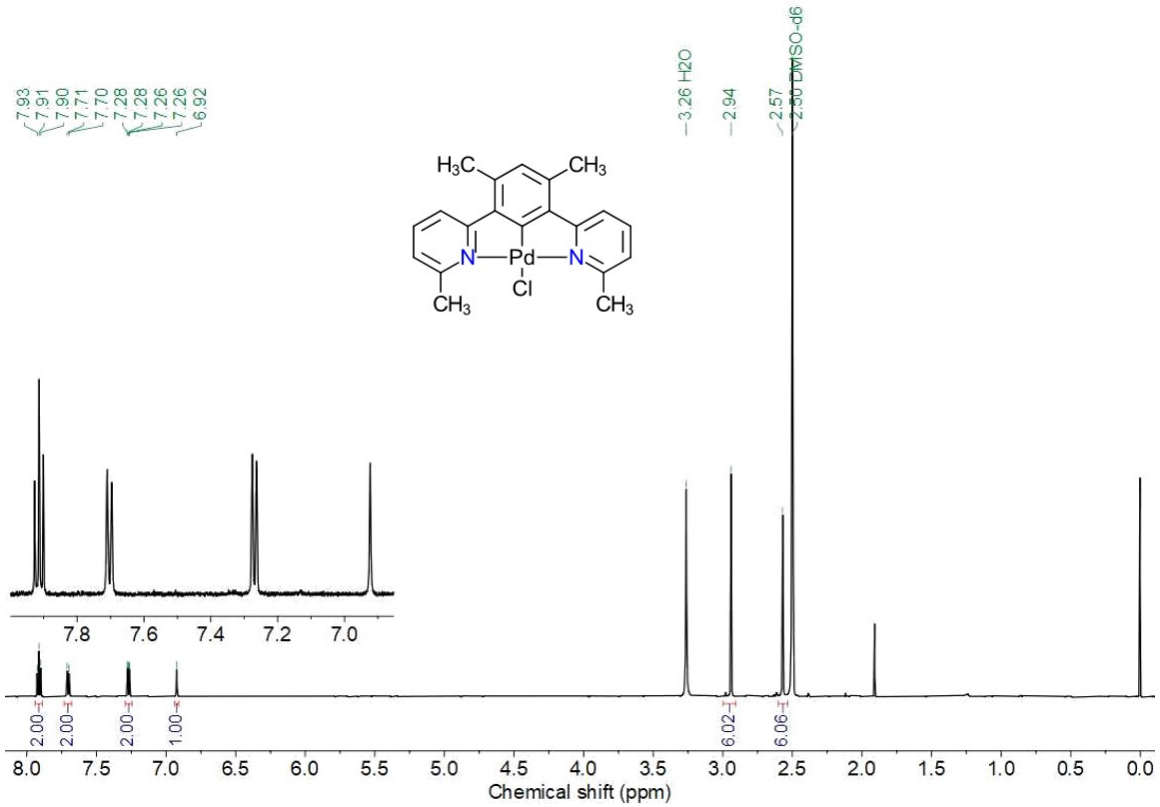


Figure A59. 600 MHz ^{1}H NMR spectrum of [Pd(L^{Me2})Cl] in DMSO-d_6 at RT.

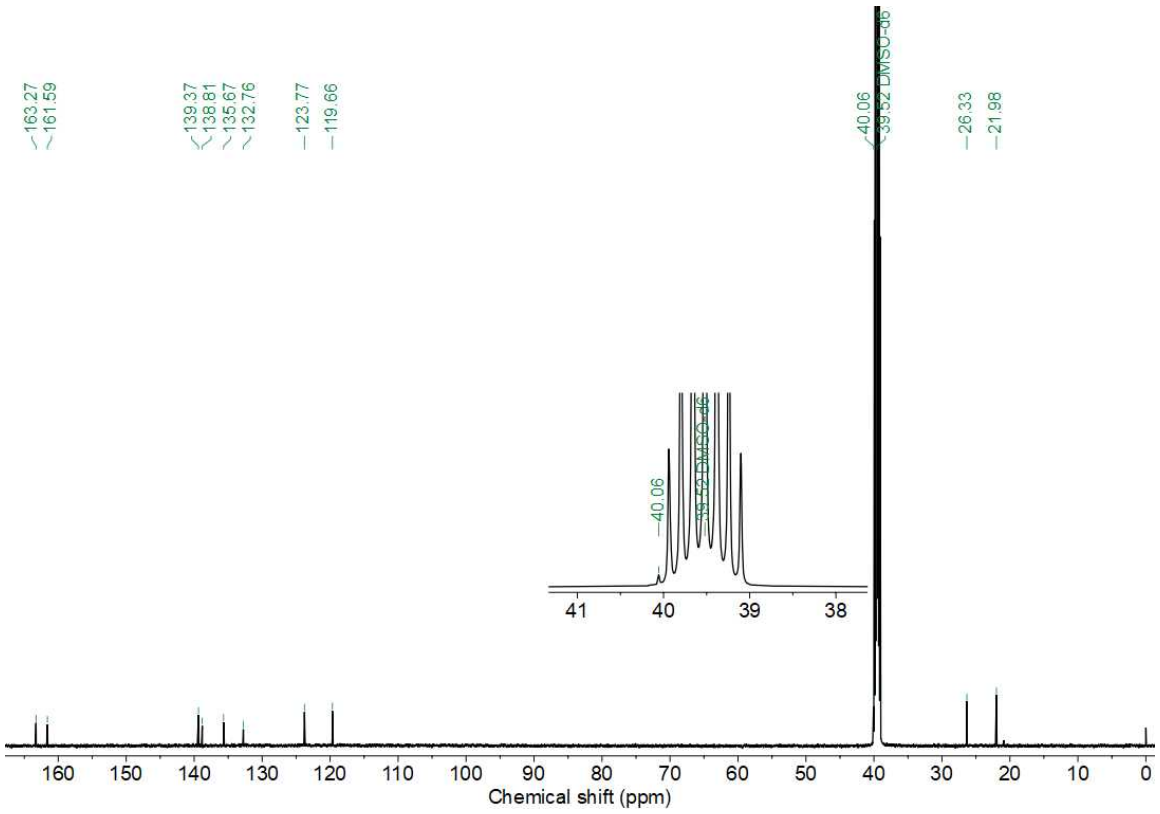


Figure A60. 151 MHz ^{13}C NMR spectrum of [Pd(L^{Me2})Cl] in DMSO-d_6 at RT.

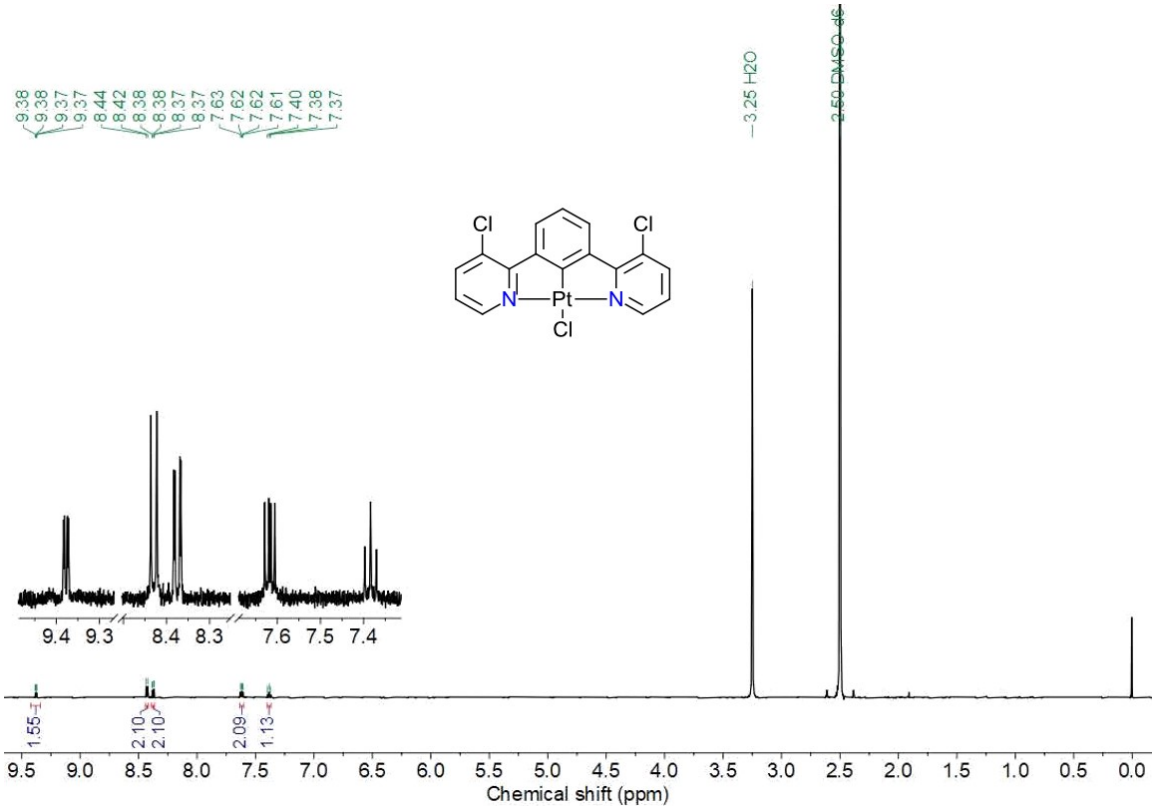


Figure A61. 600 MHz ^{1}H NMR spectrum of [Pt(L^{Cl})Cl] in DMSO-d_6 at 313 K.

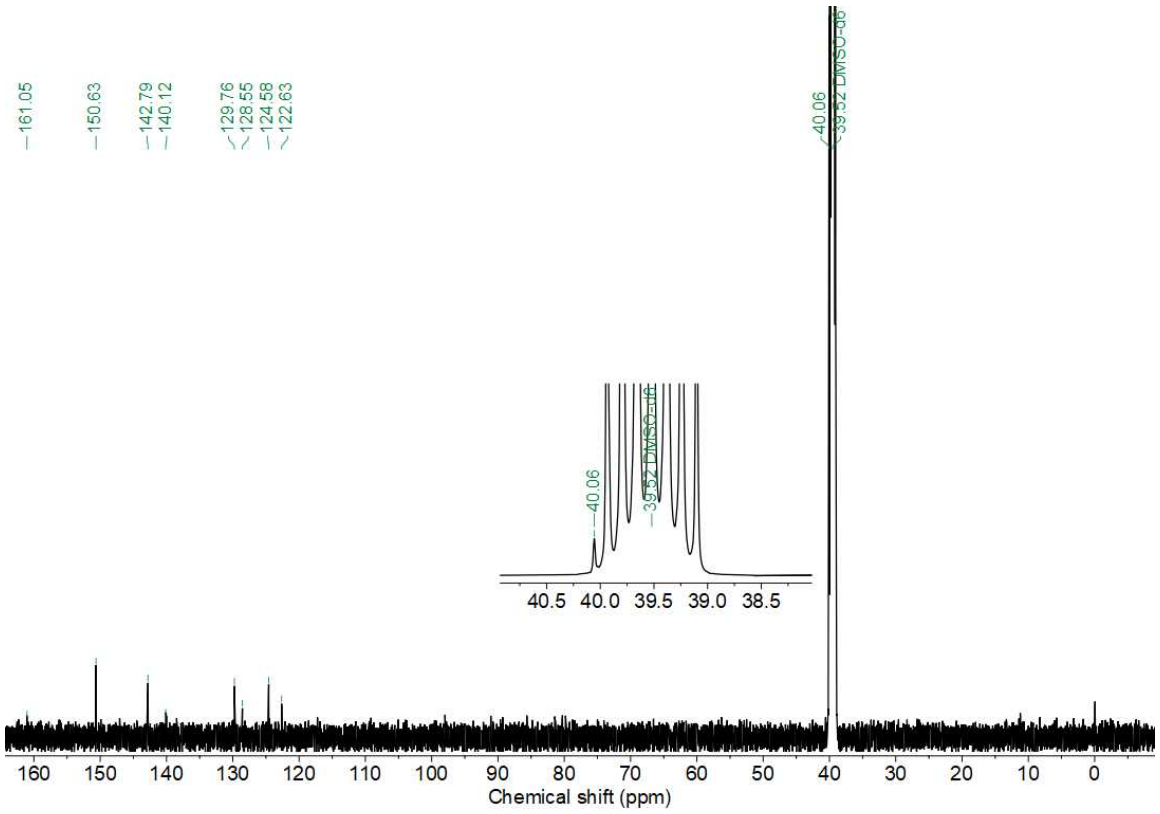


Figure S62. 151 MHz ^{13}C NMR spectrum of [Pt(L^{Cl})Cl] in DMSO-d_6 at 313 K.

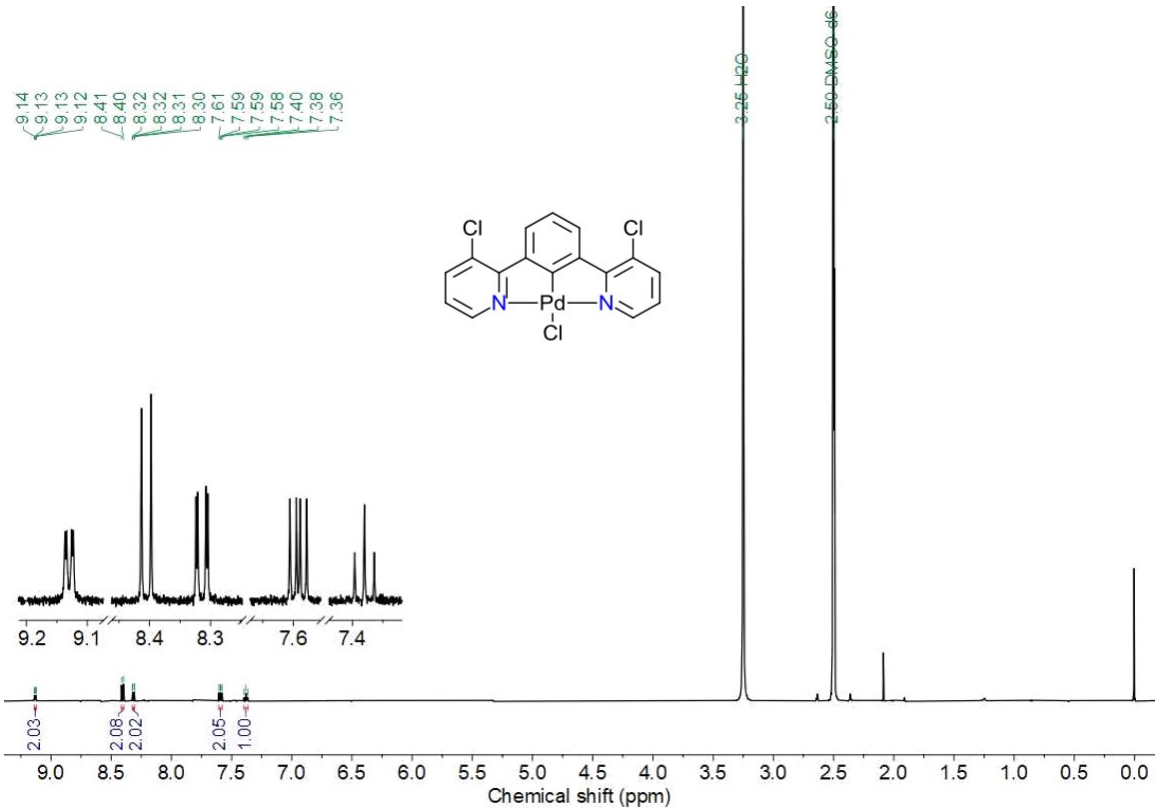


Figure A63. 500 MHz ^{1}H NMR spectrum of [Pd(L^{Cl})Cl] in DMSO-d_6 at 313 K.

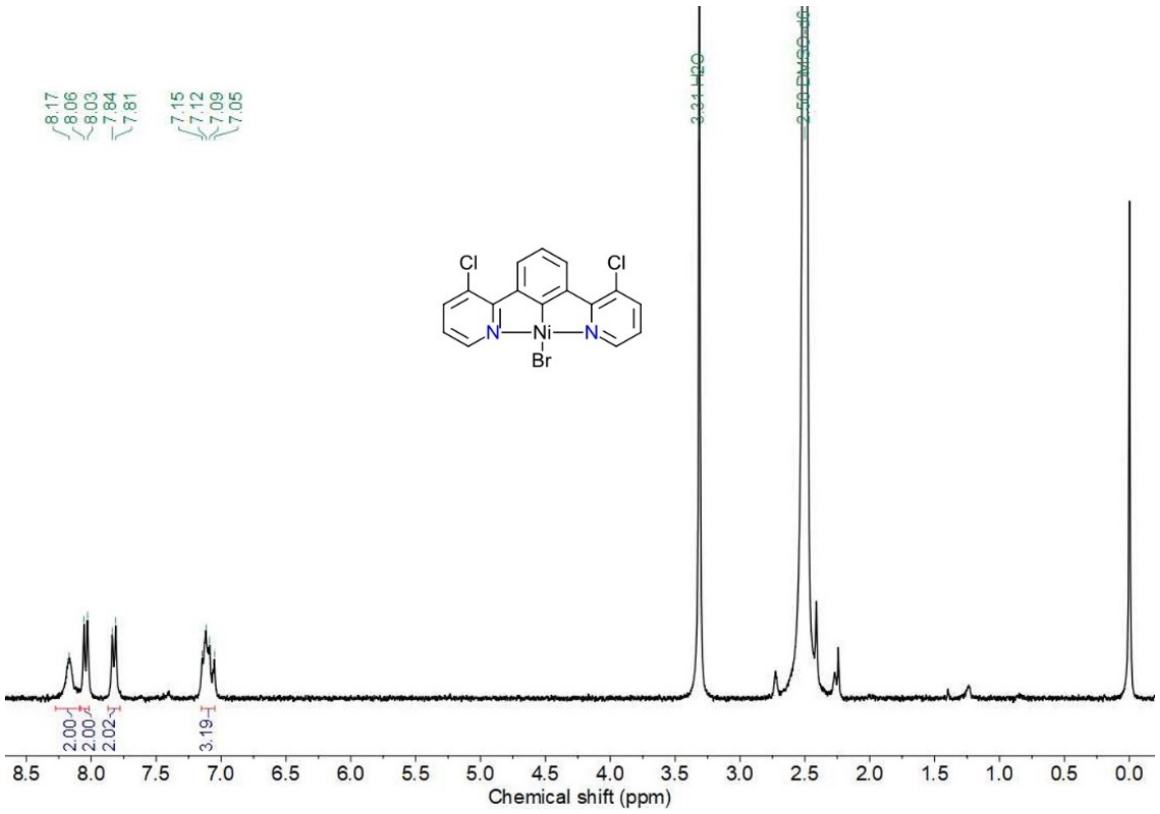


Figure A64. 300 MHz ^{1}H NMR spectrum of [Ni(L^{Cl})Br] in DMSO-d_6 at RT

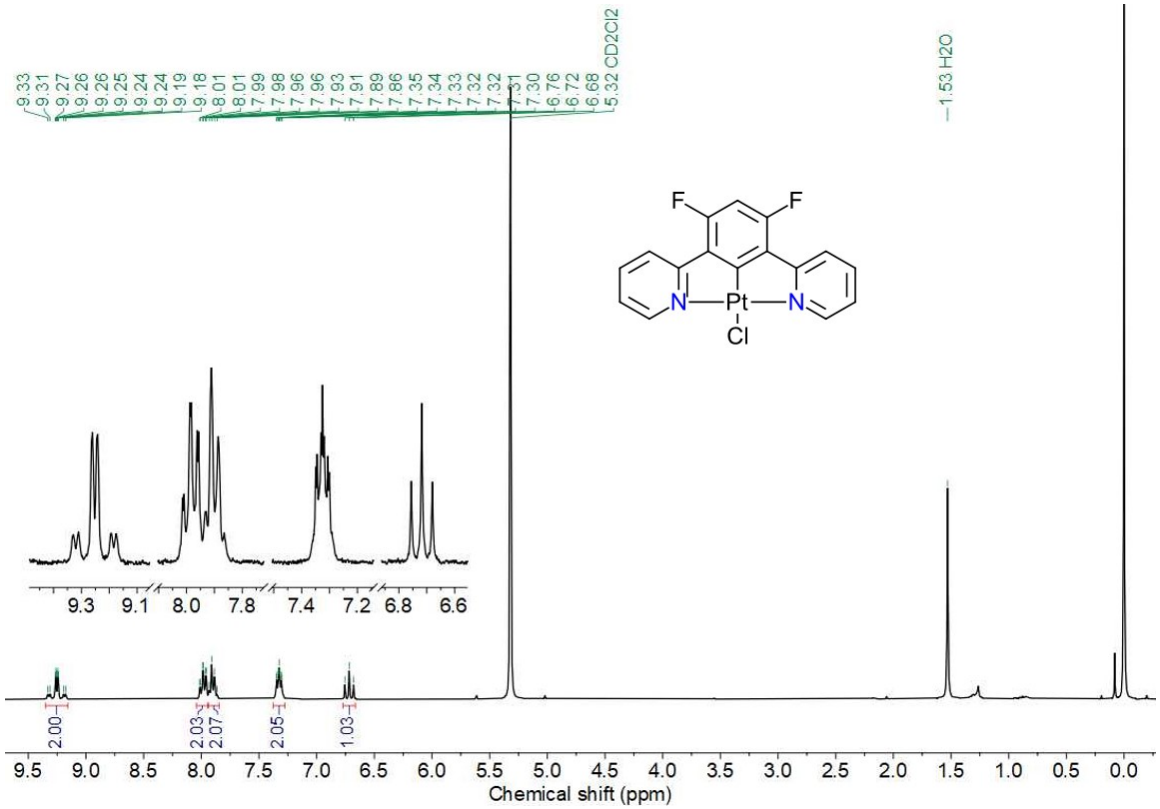


Figure A65. 300 MHz ^{1}H NMR spectrum of [Pt(L^{F})Cl] in CD_2Cl_2 at RT.

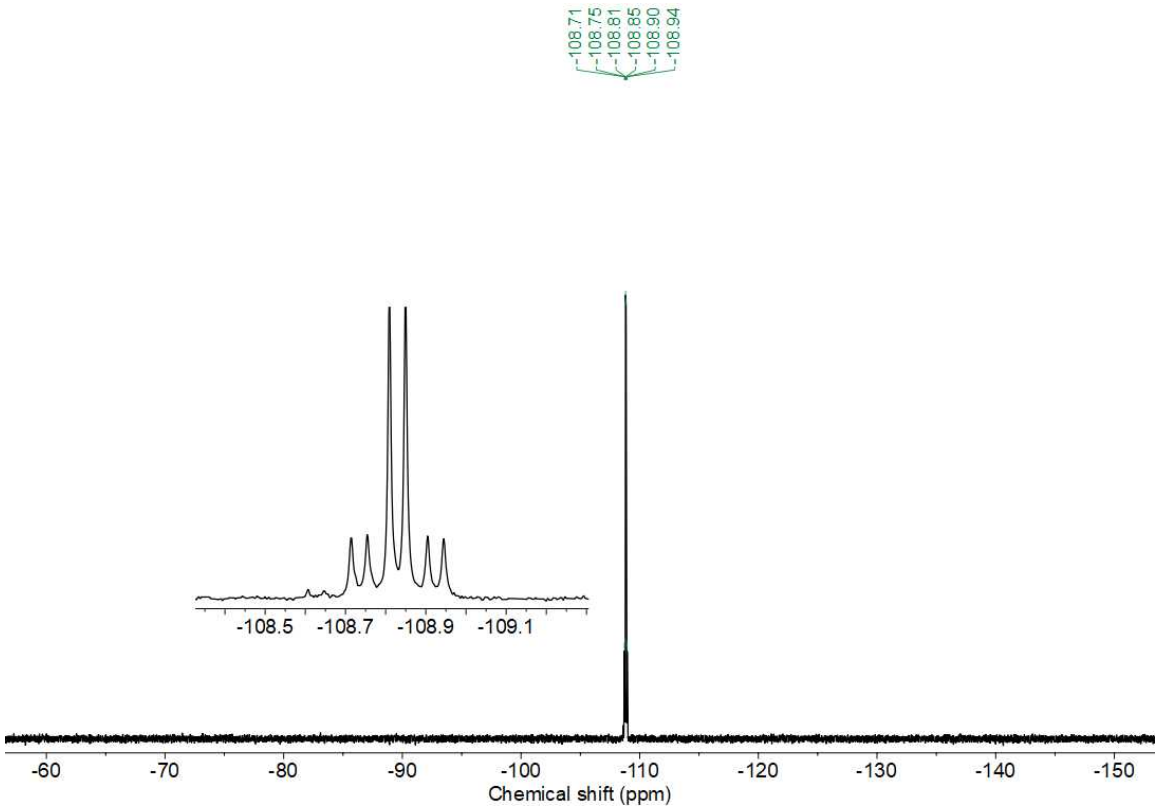


Figure A66. 282 MHz ^{19}F NMR spectrum of [Pt(L^{F})Cl] in CD_2Cl_2 at RT.

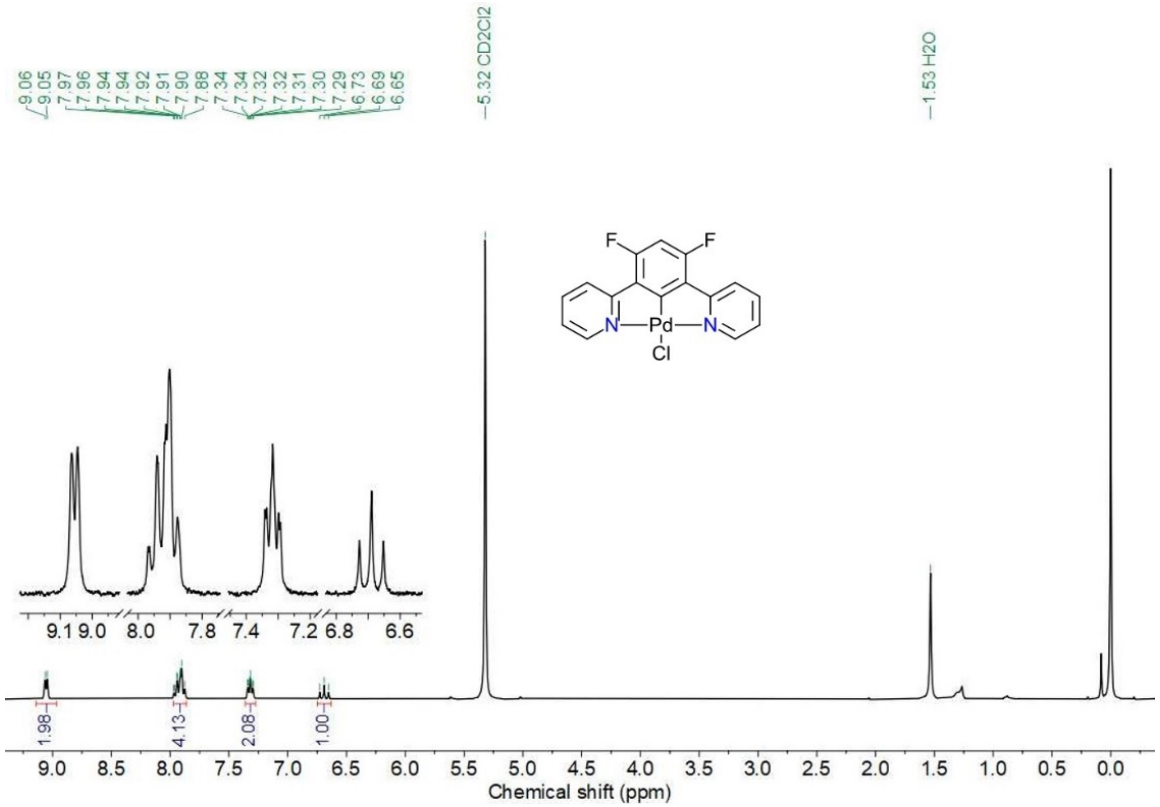


Figure A67. 300 MHz ^{1}H NMR spectrum of [Pd(L^{F})Cl] in CD_2Cl_2 at RT.

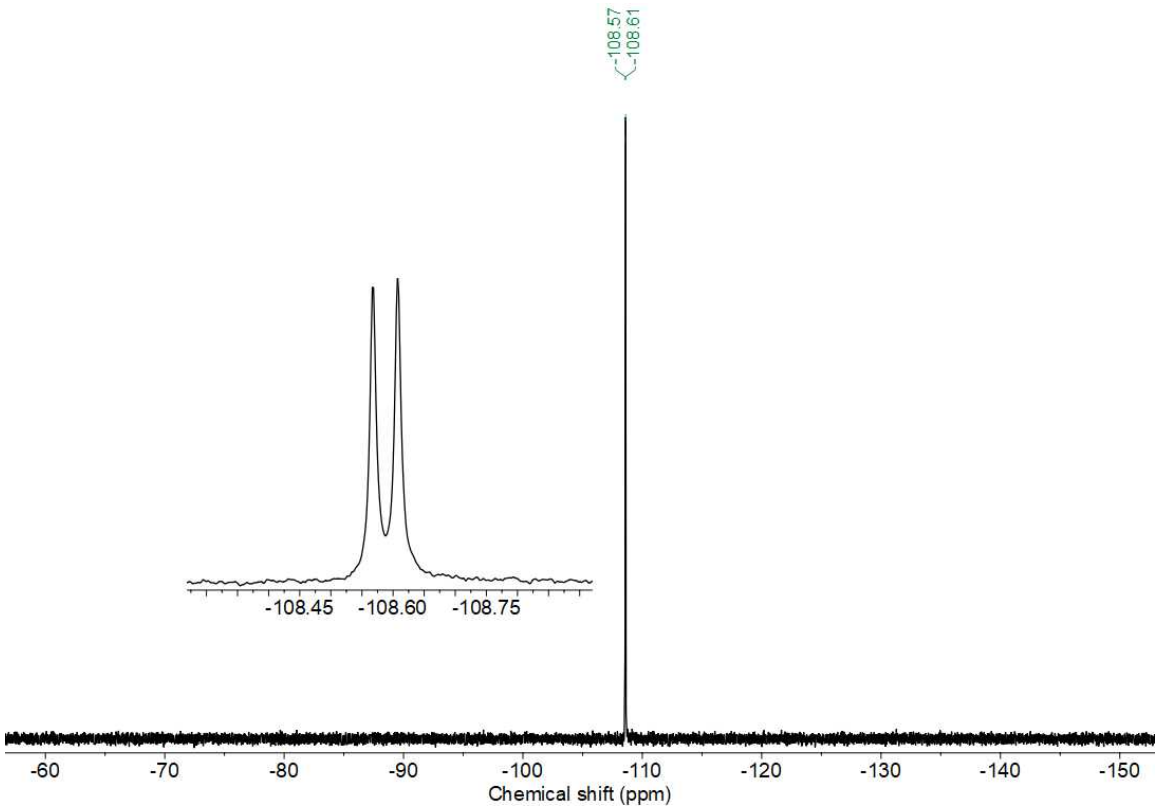


Figure A68. 282 MHz ^{19}F NMR spectrum of [Pd(L^{F})Cl] in CD_2Cl_2 at RT.

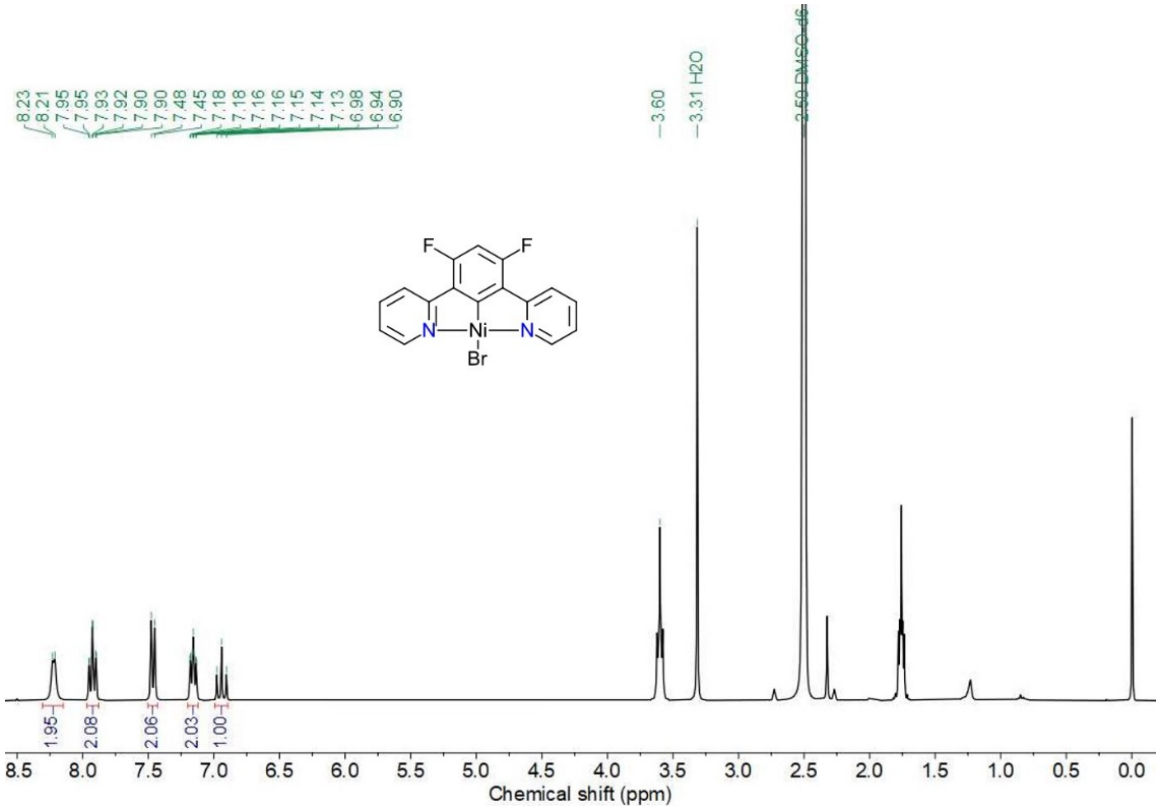


Figure A69. 300 MHz ^{1}H NMR spectrum of [Ni(L^{F})Br] in DMSO-*d*$_6$ at RT.

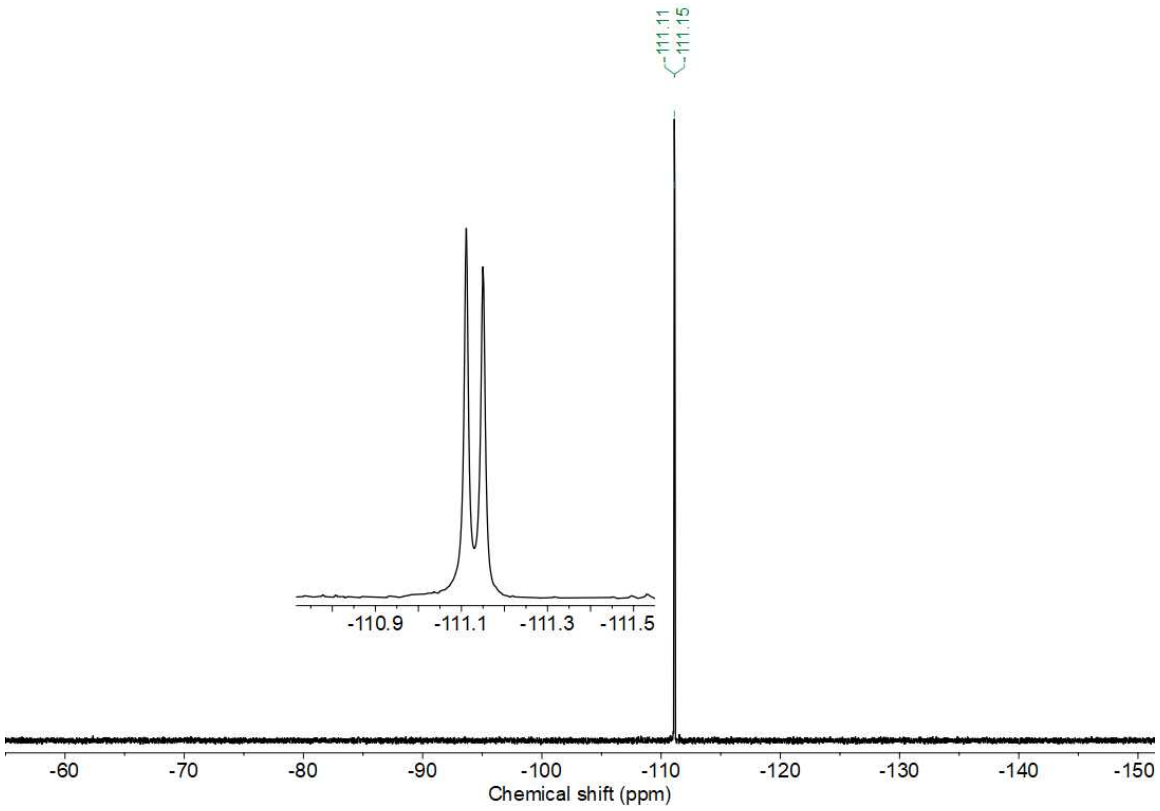


Figure A70. 282 MHz ^{19}F NMR spectrum of [Ni(L^{F})Br] in DMSO-*d*$_6$ at RT.

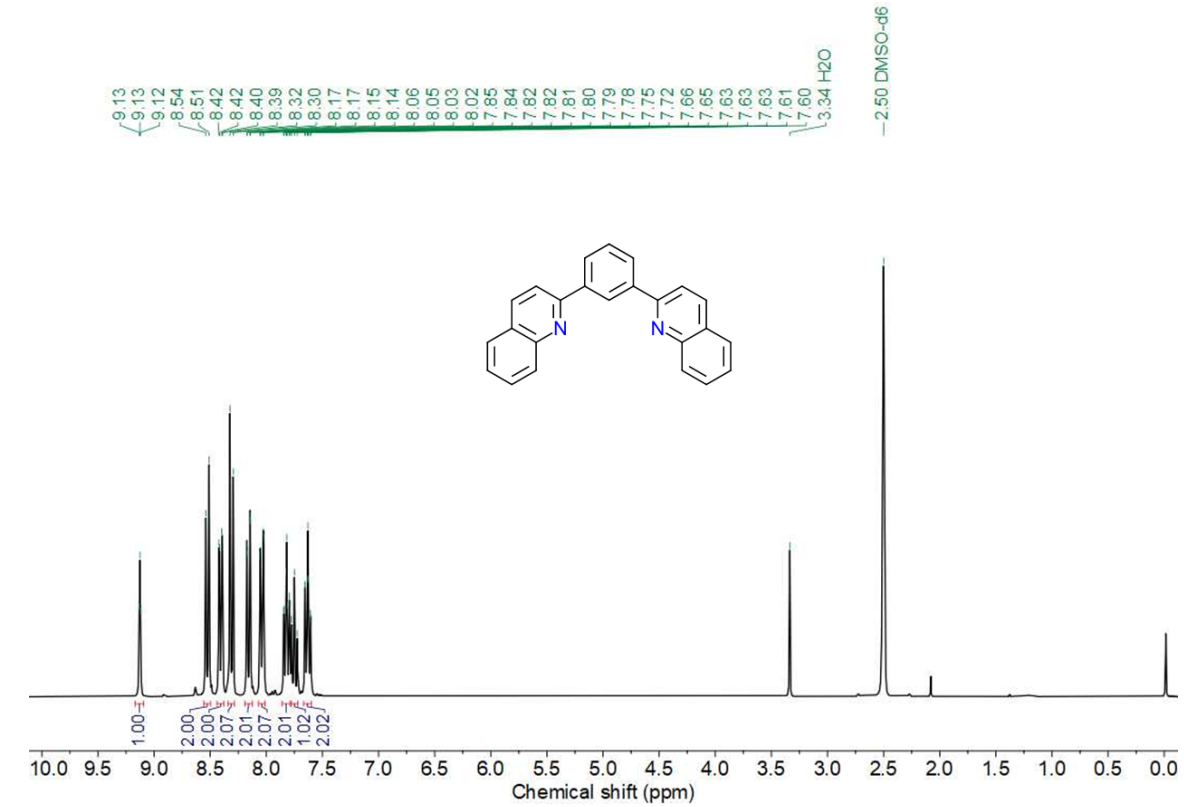


Figure A71. 300 MHz ^{1}H NMR spectrum of HL^{Qu} in DMSO-*d*$_6$ at RT.

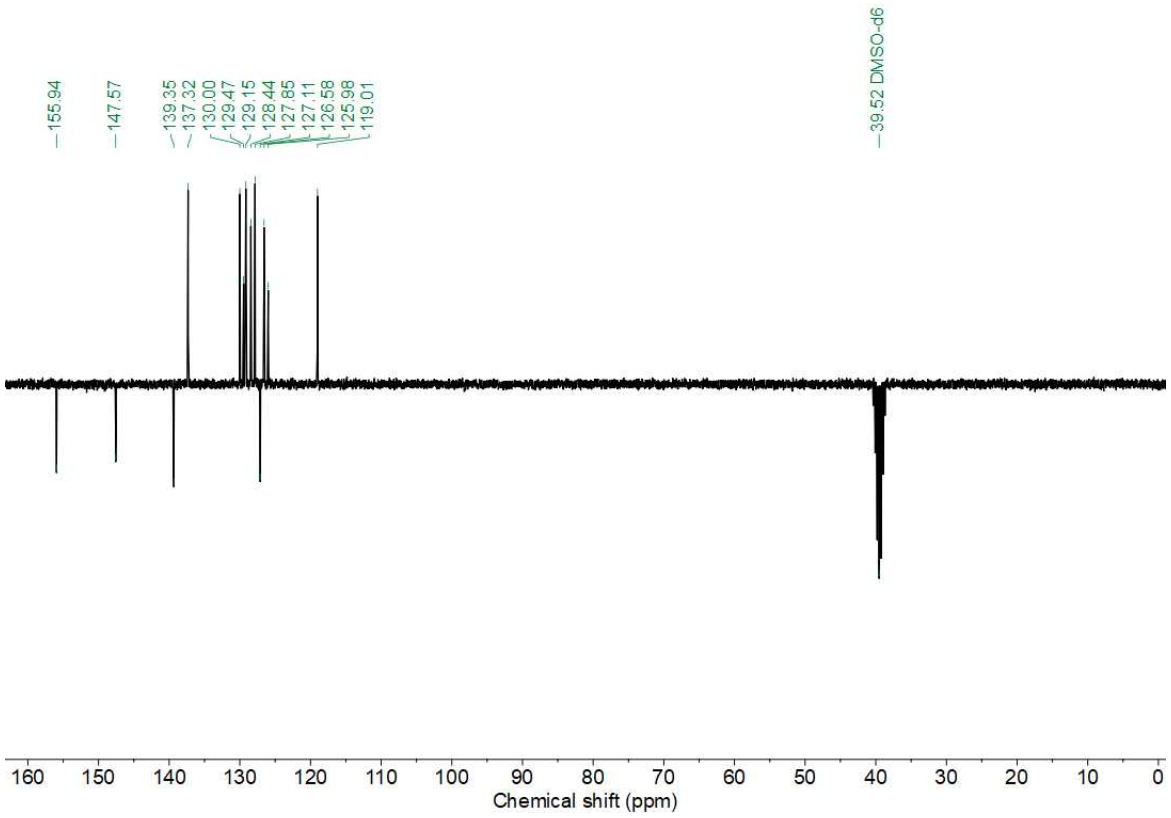


Figure A72. 75 MHz ^{13}C NMR spectrum of HL^{Qu} in DMSO-*d*$_6$ at RT.

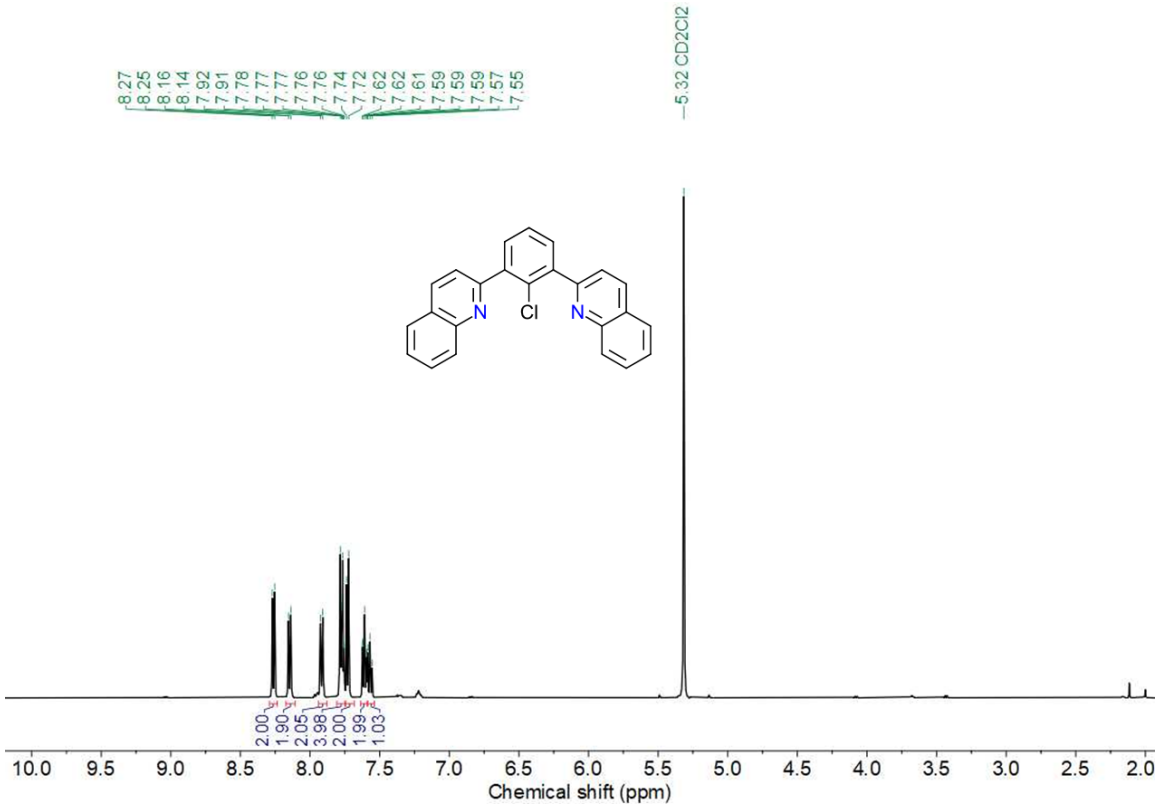


Figure A73. 500 MHz ^{1}H NMR spectrum of ClL^{Qu} in CD_2Cl_2 at RT.

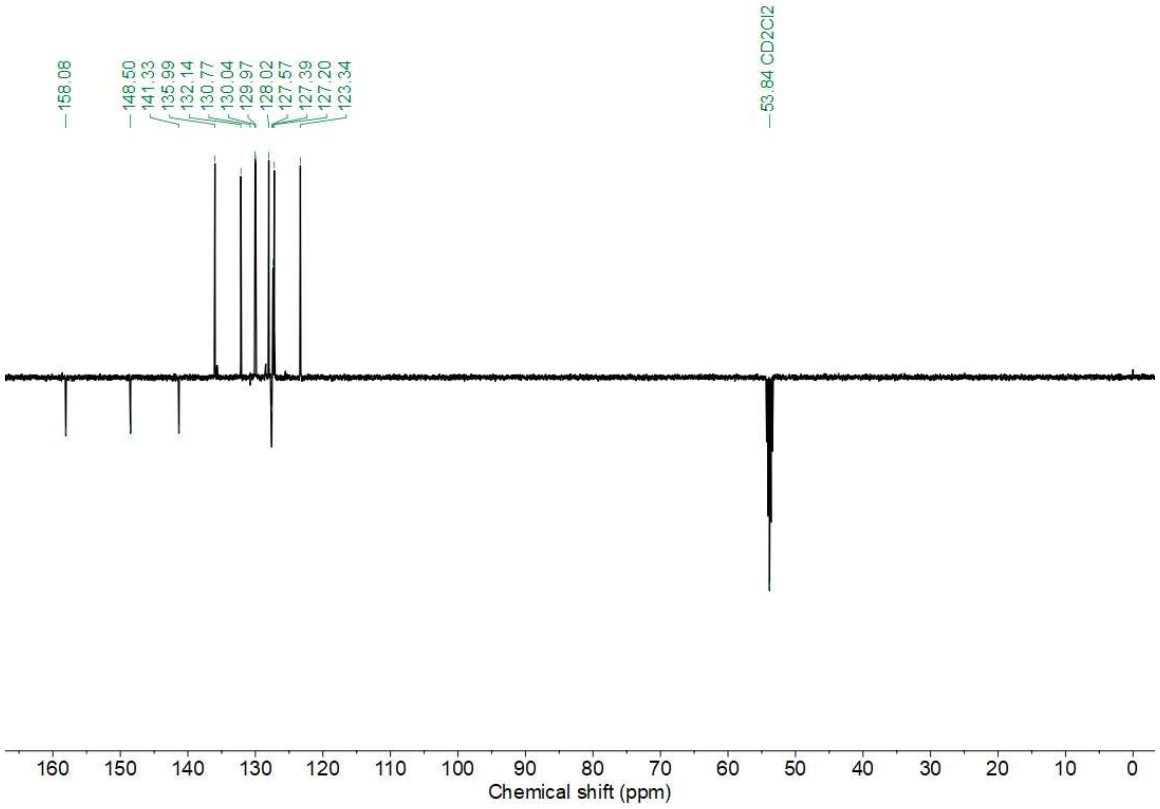


Figure A74. 75 MHz ^{13}C NMR spectrum of ClL^{Qu} in CD_2Cl_2 at RT.

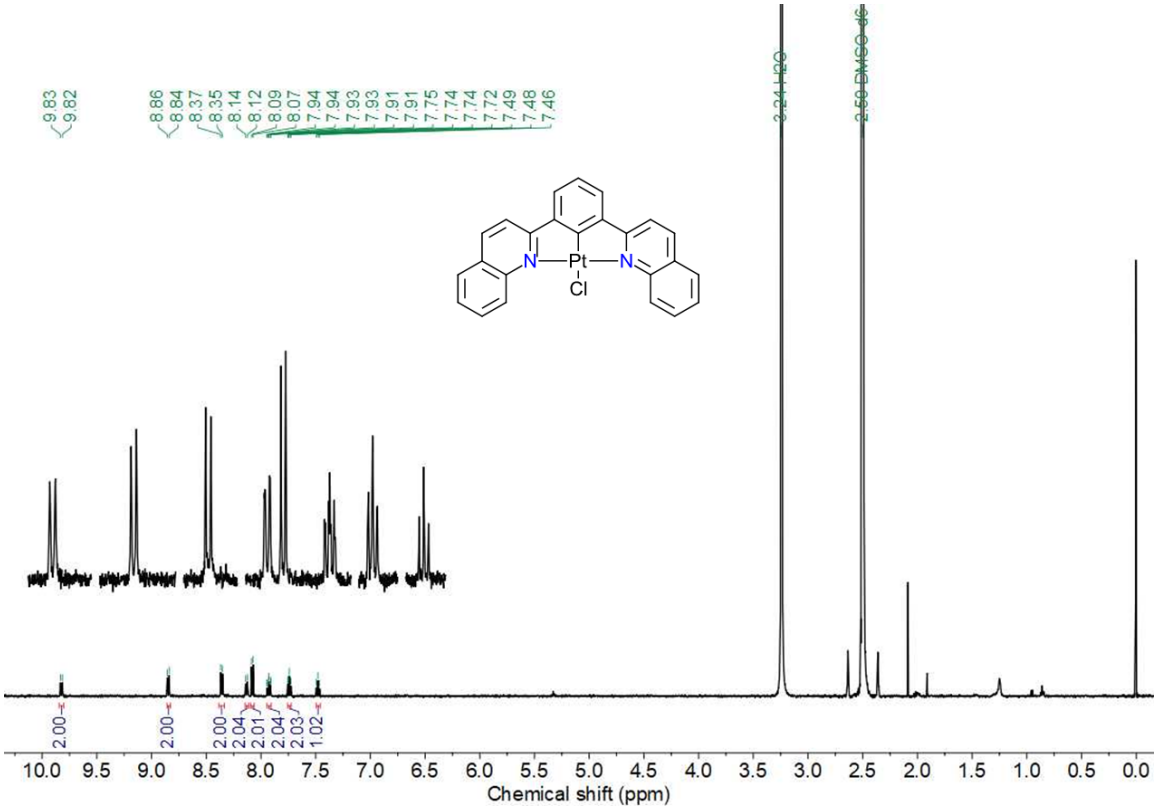


Figure A75. 500 MHz ^{1}H NMR spectrum of [Pt(L^{Qu})Cl] in DMSO-d_6 at 313 K.

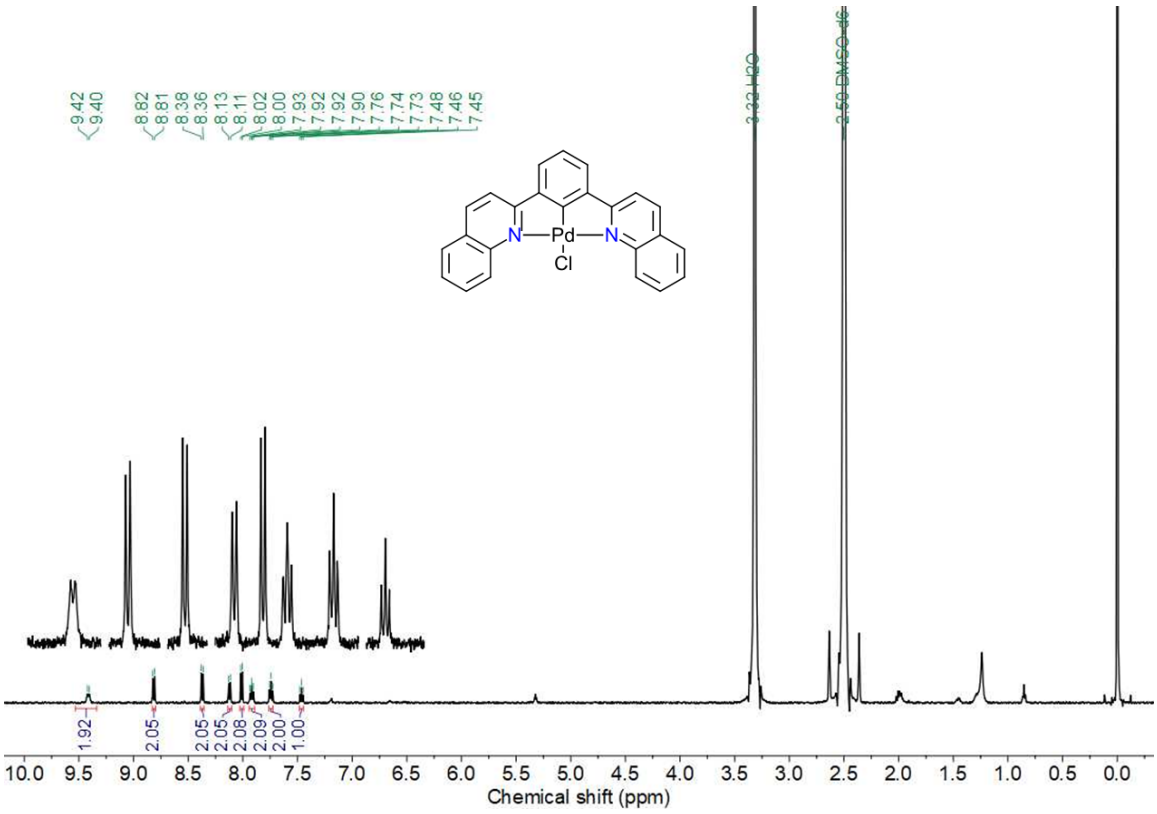


Figure A76. 500 MHz ^{1}H NMR spectrum of [Pd(L^{Qu})Cl] in DMSO-d_6 at 313 K.

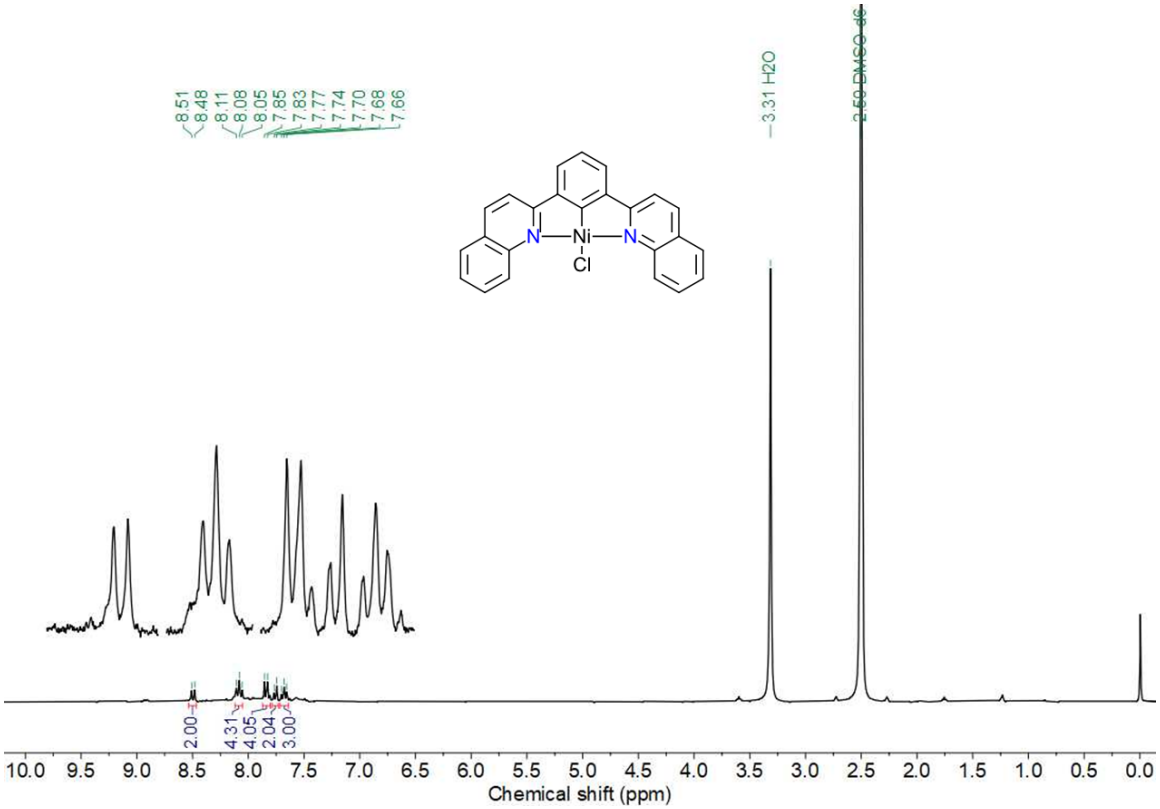


Figure A77. 300 MHz ^{1}H NMR spectrum of [Ni(L^{Qu})Cl] in DMSO-d_6 at RT.

7.2. Mass spectra

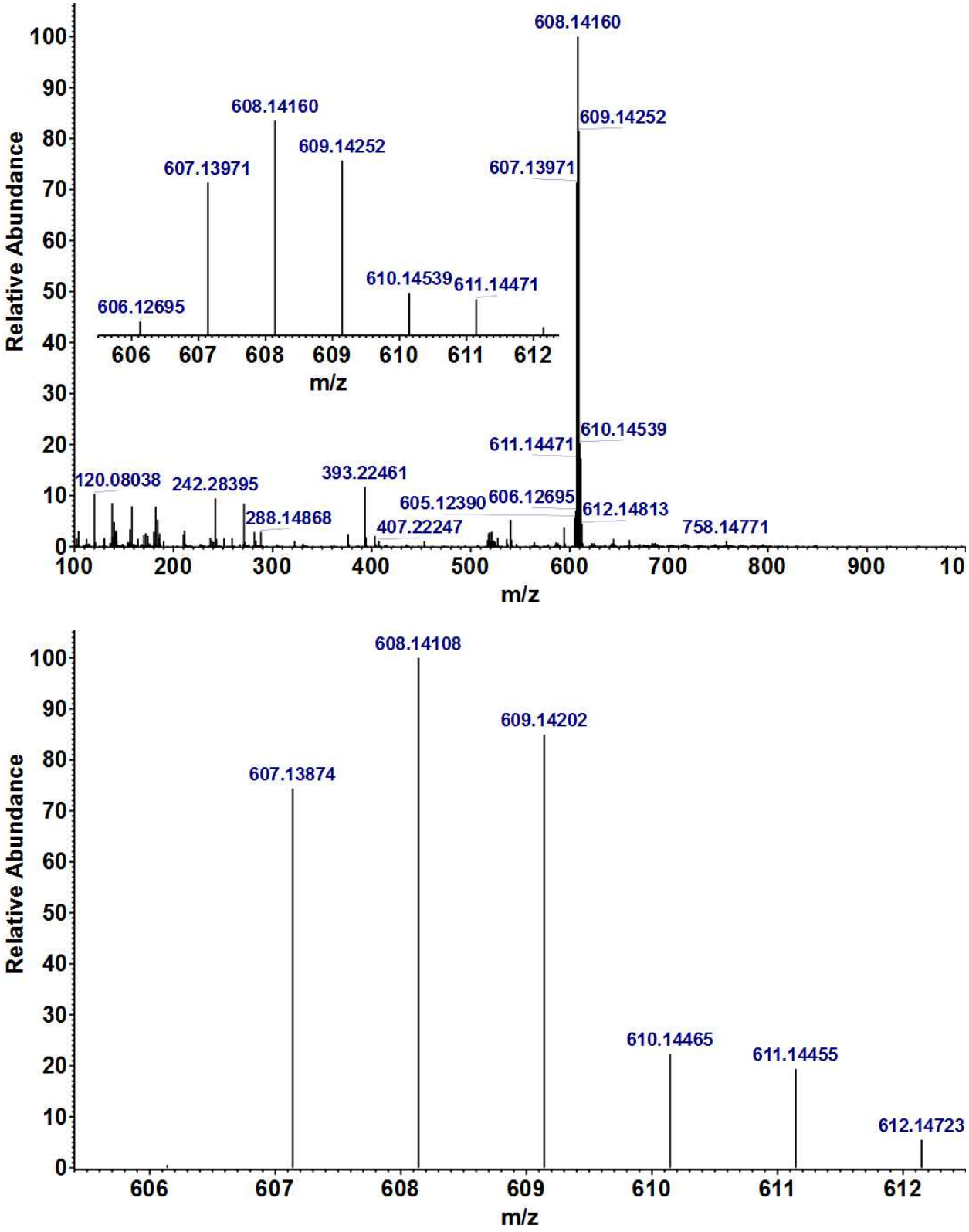


Figure A78. High-resolution ESI-MS(+) spectrum of [Pt(L^{NHPh})Cl] (top) and calculated pattern for $[C_{28}H_{21}N_4Pt]^+$ = $[M–Cl]^+$ (bottom).

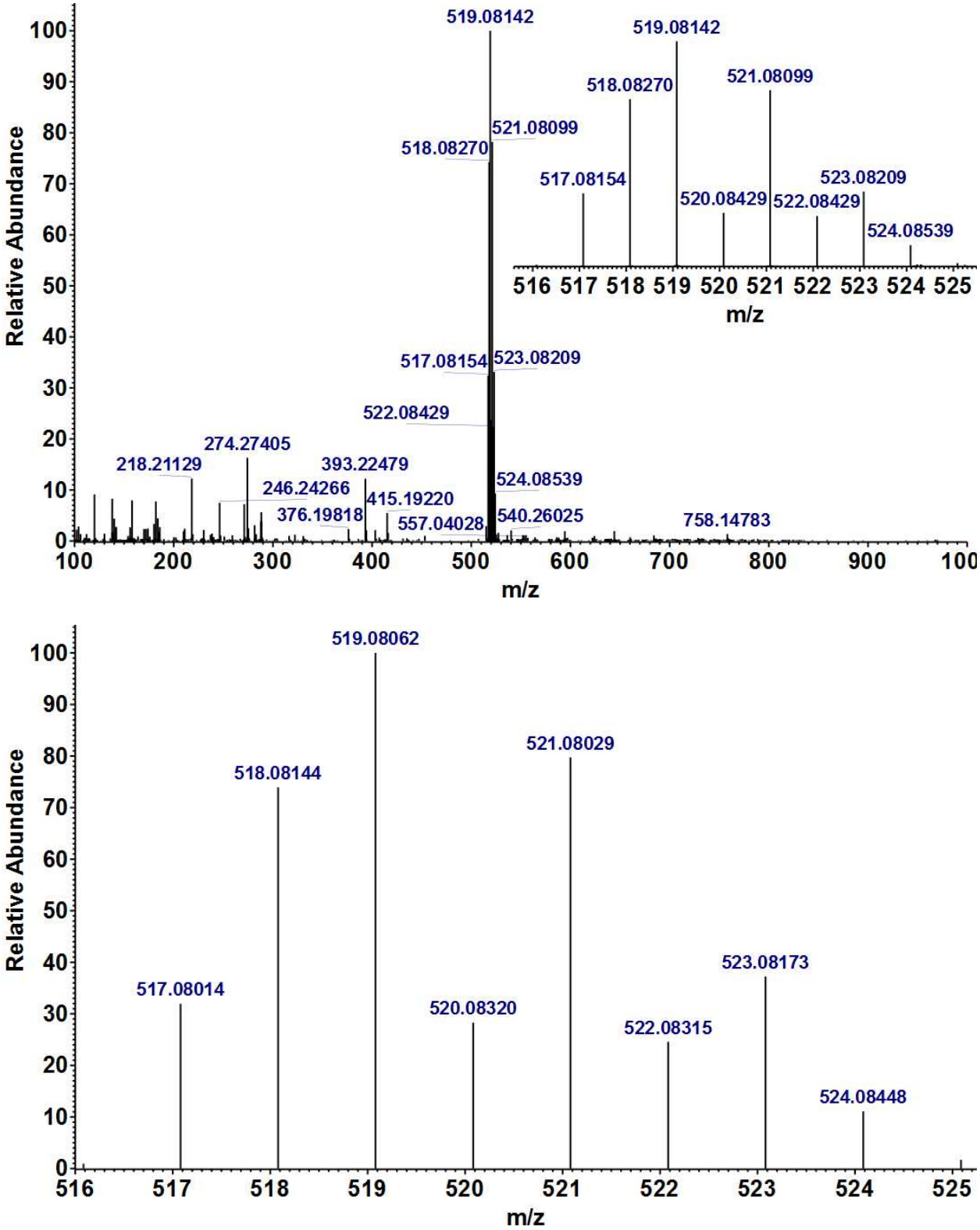


Figure A79. High-resolution ESI-MS(+) spectrum of [Pd(L^{NHPh})Cl] (top) and calculated pattern for $[C_{28}H_{21}N_4Pd]^+ = [M–Cl]^+$ (bottom).

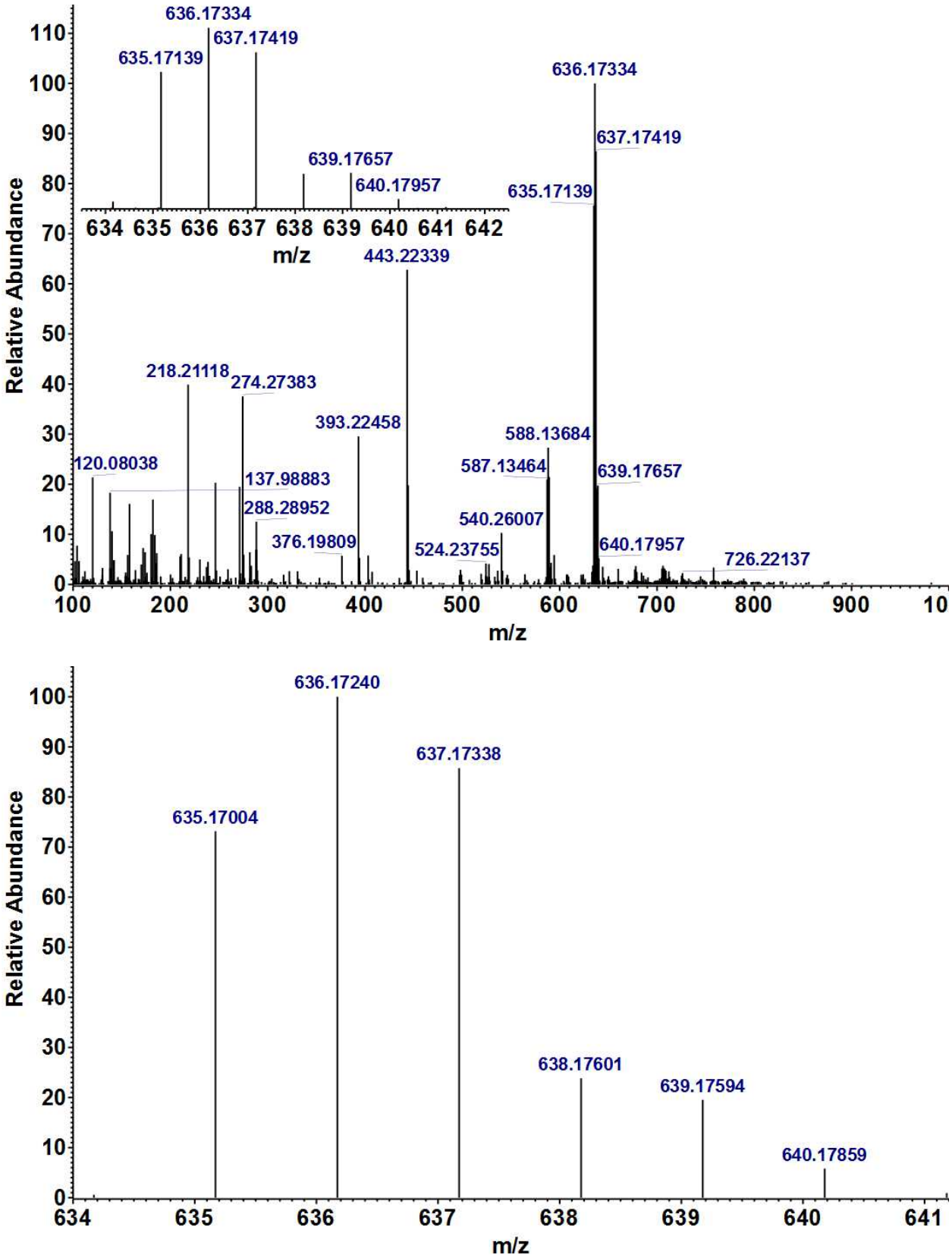


Figure A80. High-resolution ESI-MS(+) spectrum of [Pt(L^{NHBn})Cl] (top) and calculated pattern for $[C_{30}H_{25}N_4Pt]^+$ = $[M–Cl]^+$ (bottom).

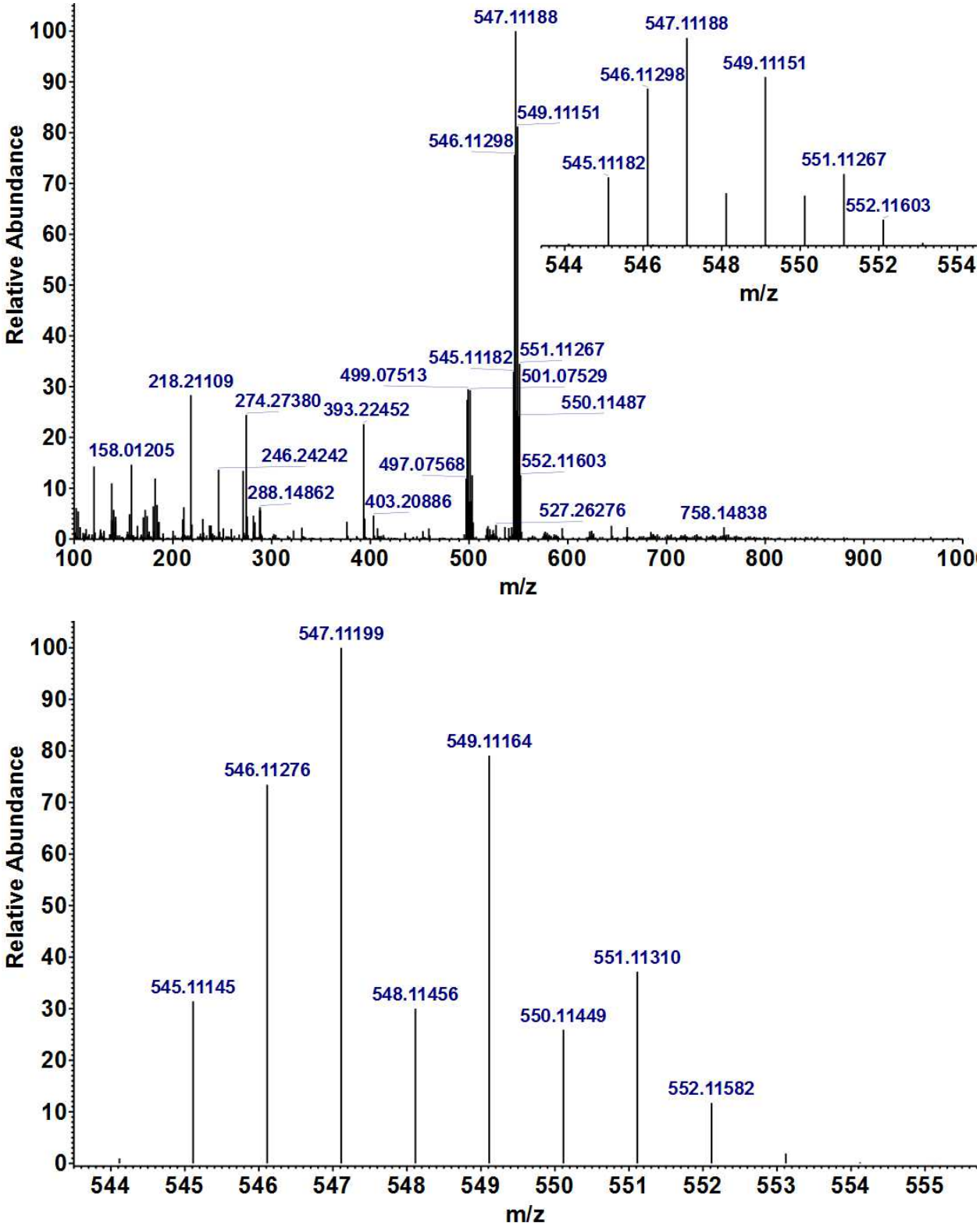


Figure A81. High-resolution ESI-MS(+) spectrum of [Pd(L^{NHBn})Cl] (top) and calculated pattern for $[C_{30}H_{25}N_4Pd]^+ = [M–Cl]^+$ (bottom).

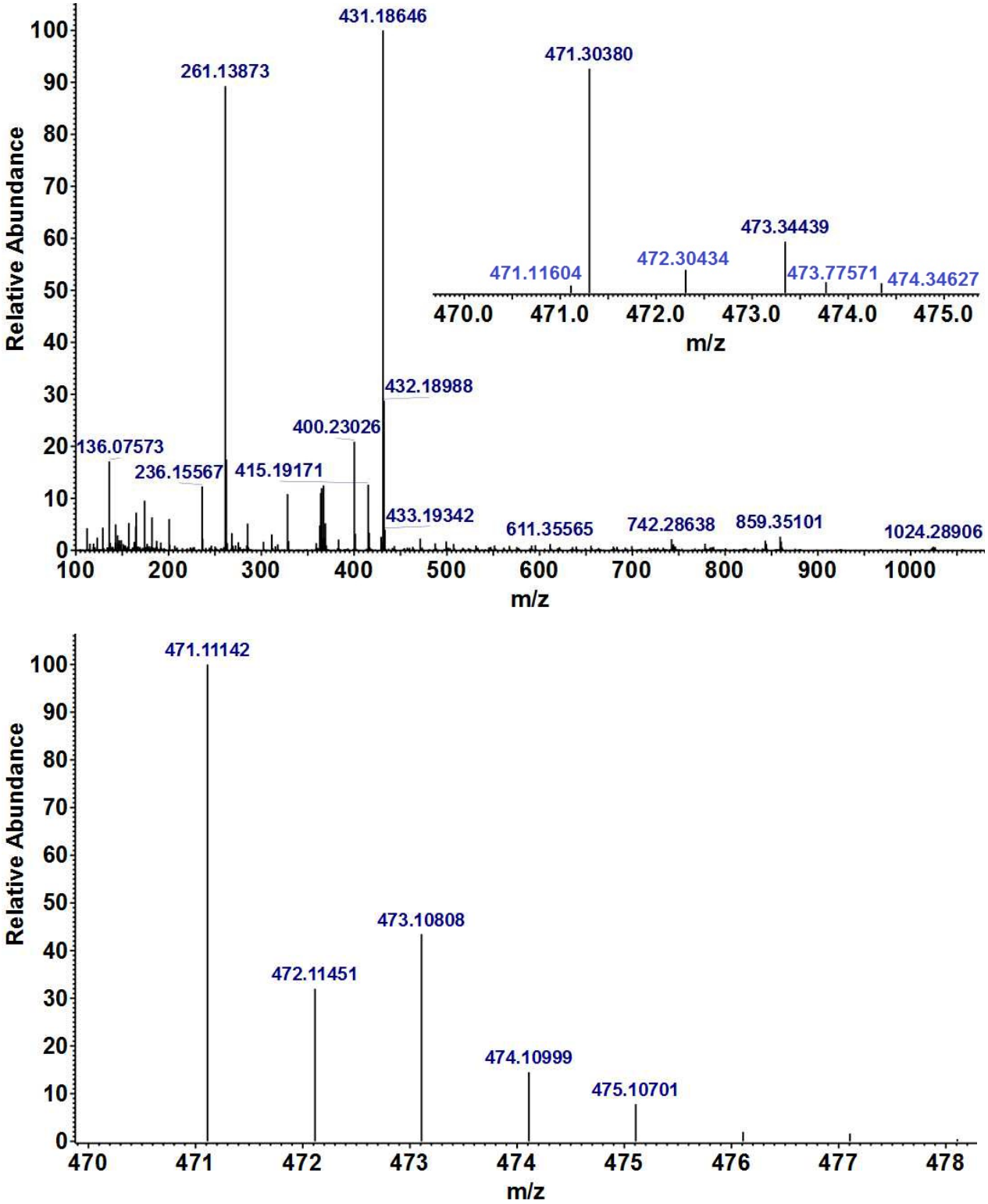


Figure A82. High-resolution ESI-MS(+) spectrum of [Ni(L^{NHPh})Cl] (top) and calculated pattern for $[C_{28}H_{21}N_4Ni]^+$ = $[M–Cl]^+$ (bottom).

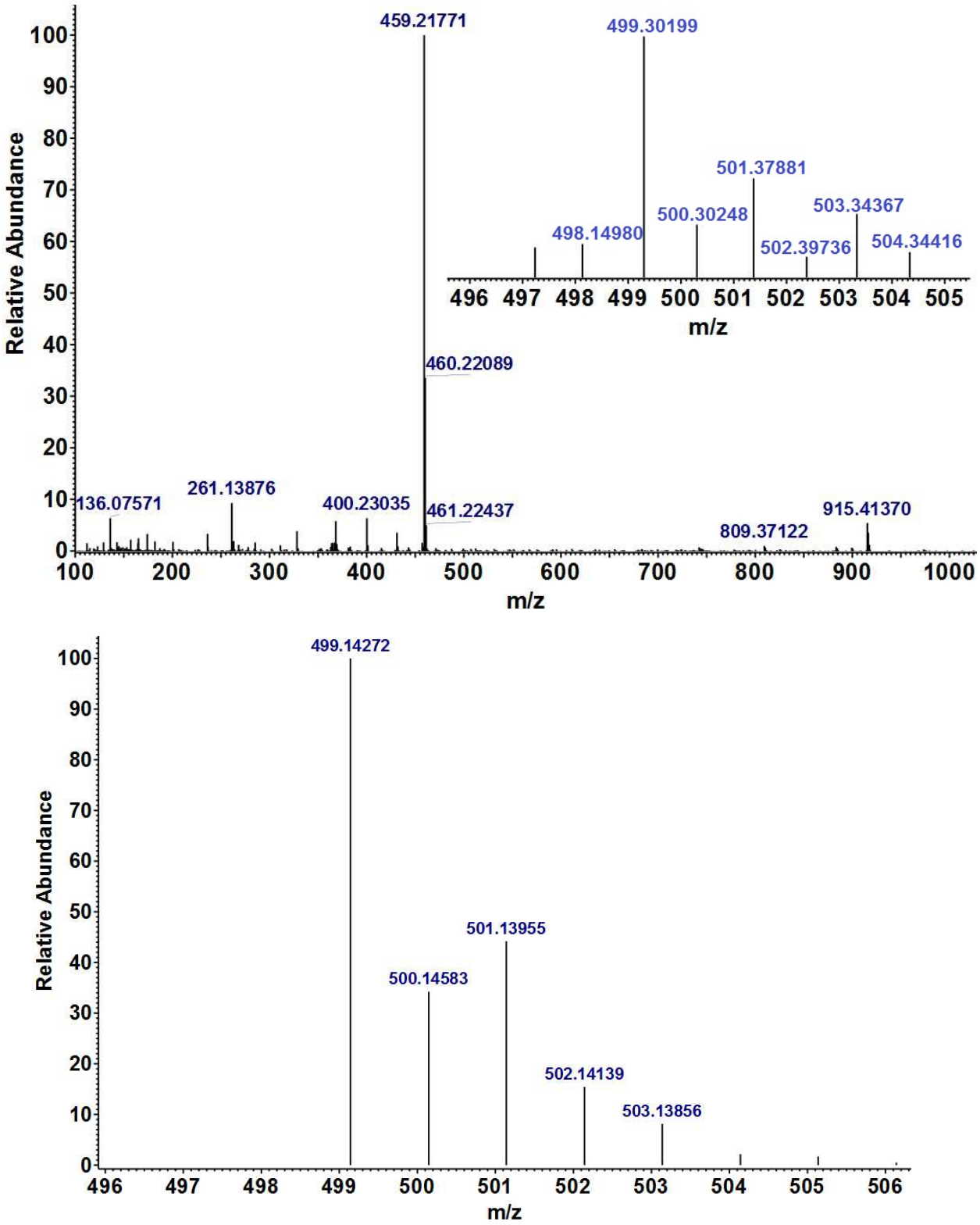


Figure A83. High-resolution ESI-MS(+) spectrum of [Ni(L^{NHBn})Cl] (top) and calculated pattern for $[C_{30}H_{25}N_4Ni]^+$ = $[M–Cl]^+$ (bottom).

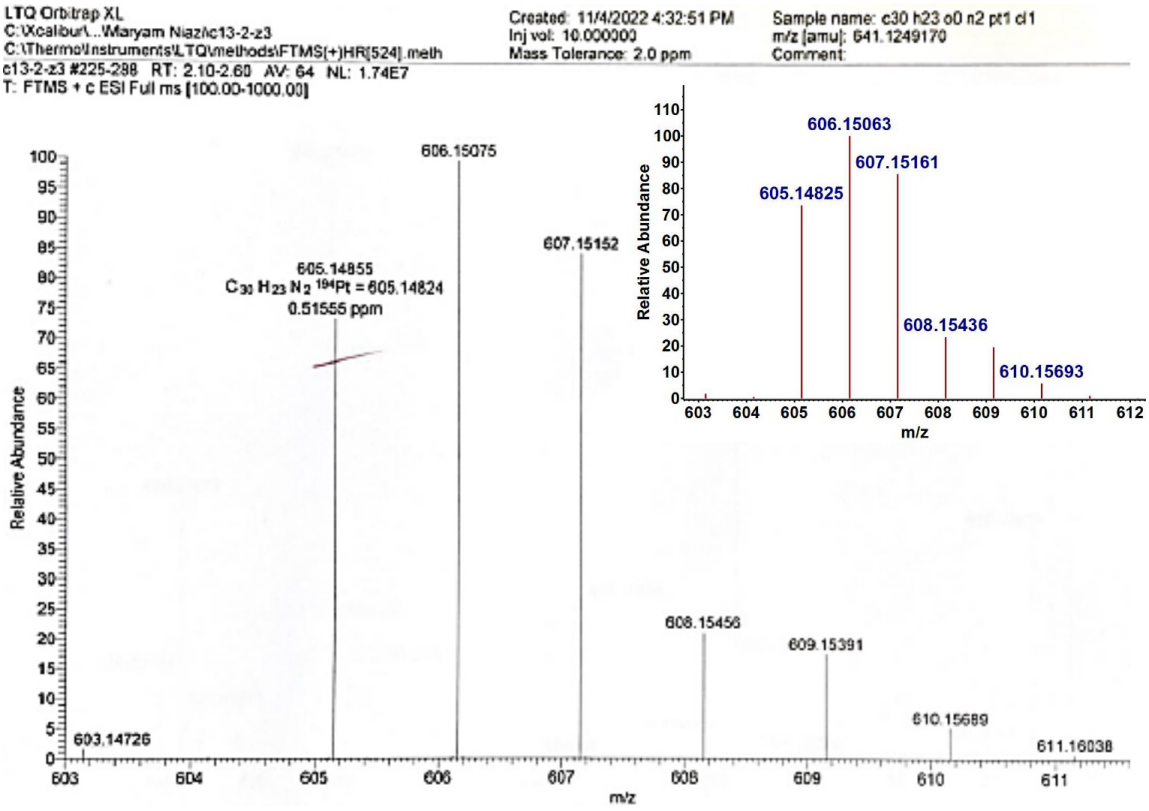


Figure A84. High-resolution ESI-MS(+) spectrum of [Pt(L^{Bn})Cl] (black) and calculated pattern for $[C_{30}H_{23}N_2Pt]^+$ = $[M\text{-}Cl]^+$ (red).

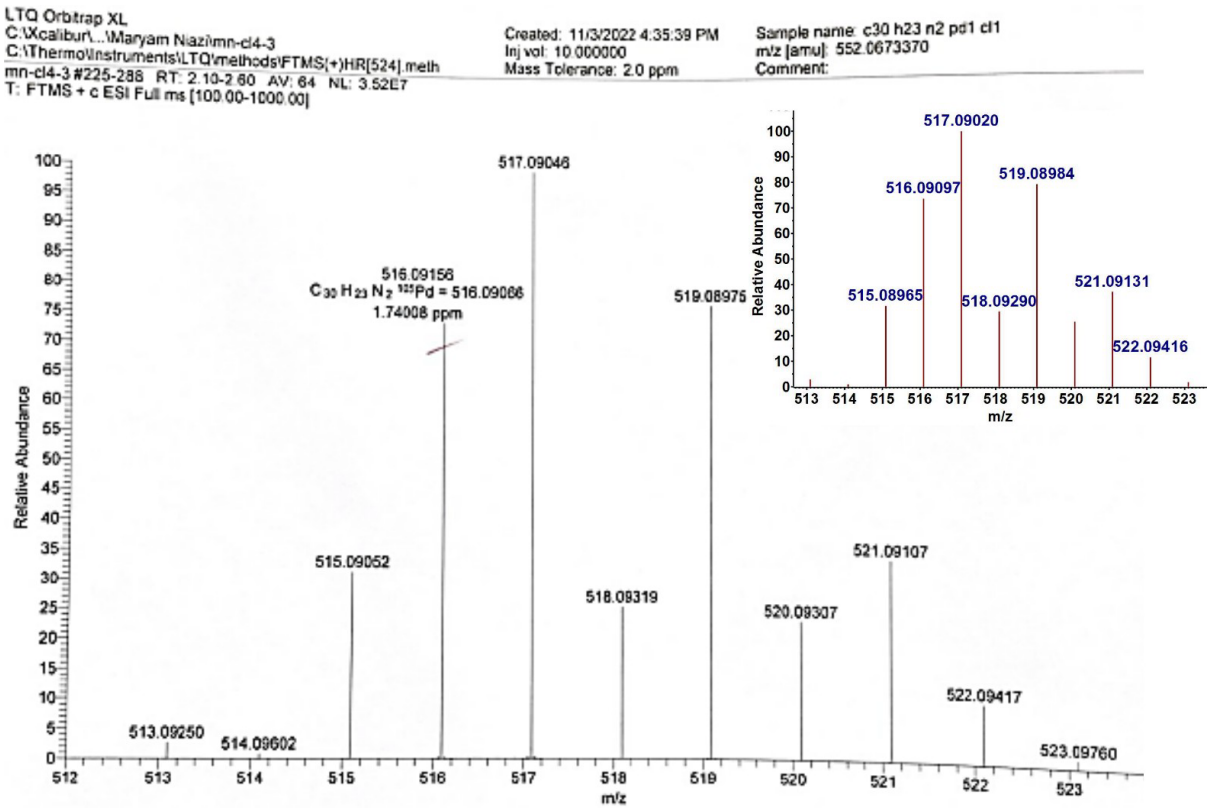


Figure A85. High-resolution ESI-MS(+) spectrum of [Pd(L^{Bn})Cl] (black) and calculated pattern for $[C_{30}H_{23}N_2Pd]^+$ = $[M\text{-}Cl]^+$ (red).

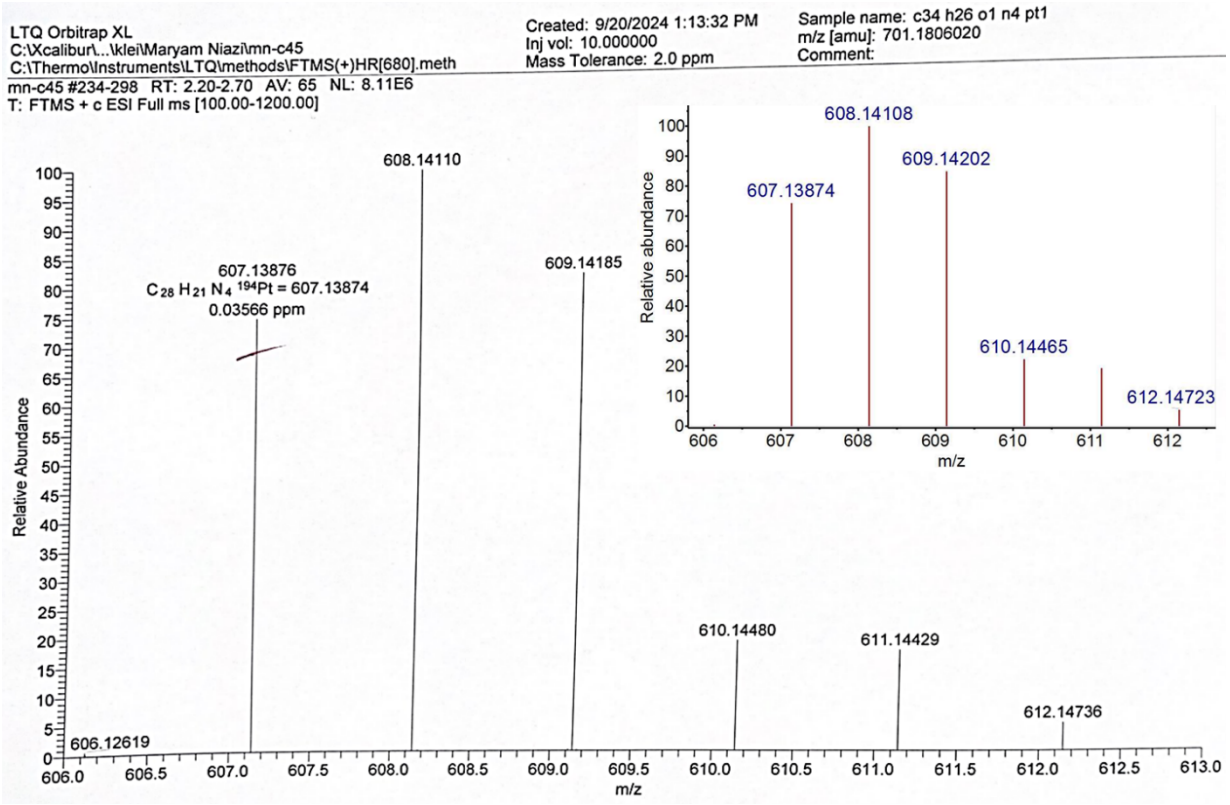


Figure A86. High-resolution ESI-MS(+) spectrum of [Pt(L^{NHPh})OPh] (black) and calculated pattern for $[C_{28}H_{21}N_4Pt]^+$ = $[M\text{-}OPh]^+$ (red).

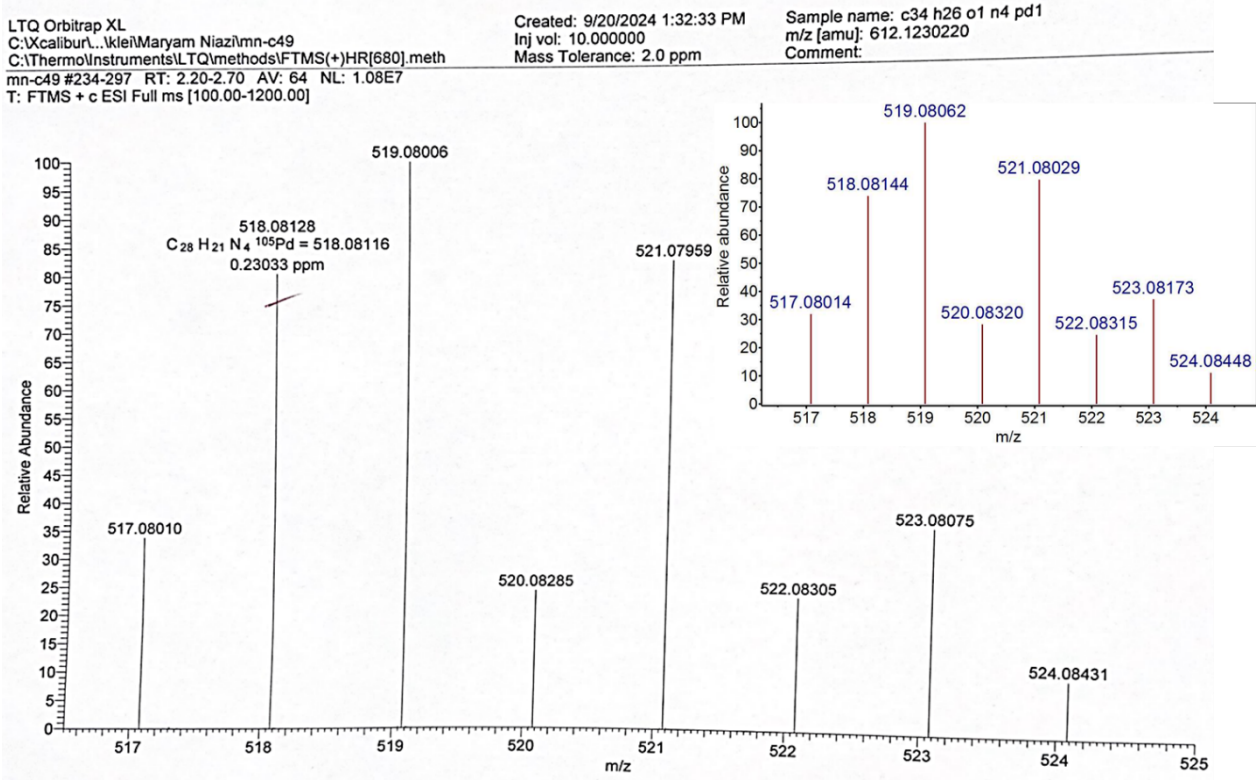


Figure A87. High-resolution ESI-MS(+) spectrum of [Pd(L^{NHPh})OPh] (black) and calculated pattern for $[C_{28}H_{21}N_4Pd]^+$ = $[M\text{-}OPh]^+$ (red).

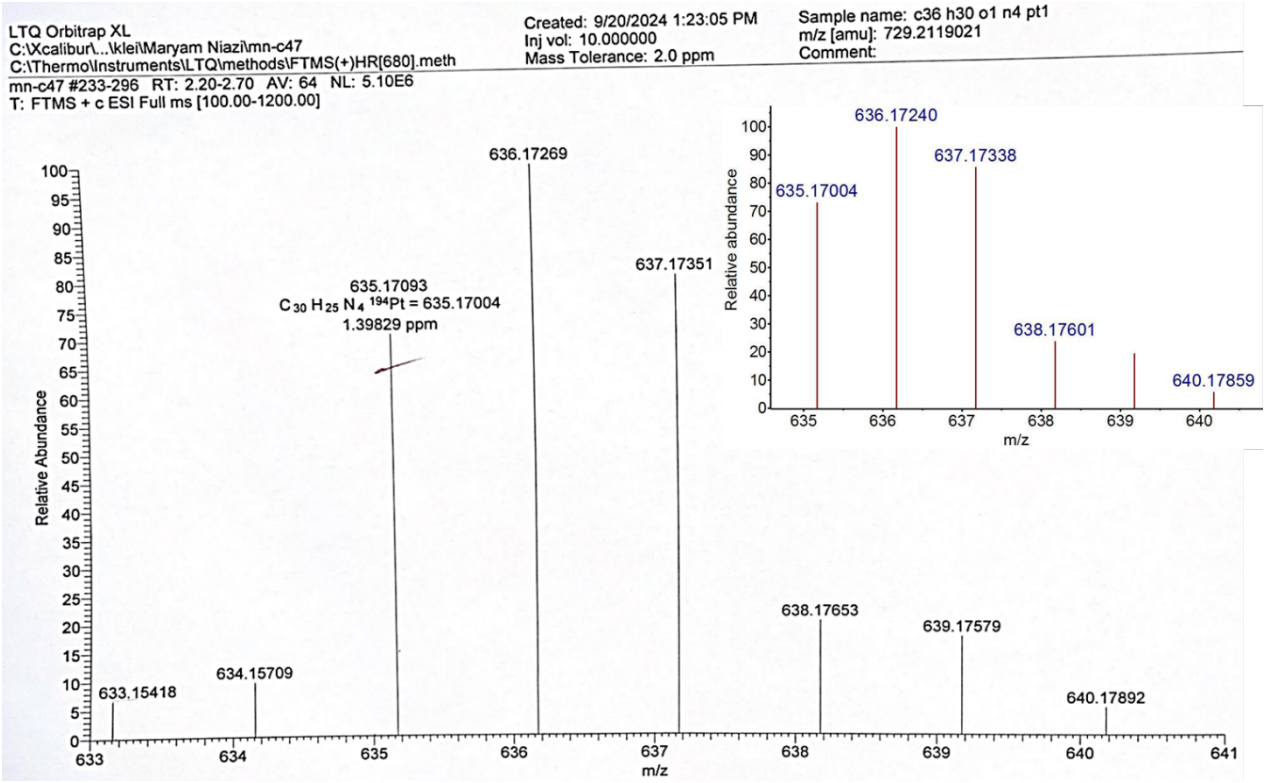


Figure A88. High-resolution ESI-MS(+) spectrum of [Pt(L^{NHBn})OPh] (black) and calculated pattern for $[C_{30}H_{25}N_4Pt]^+$ = [M-OPh]$^+$ (red).

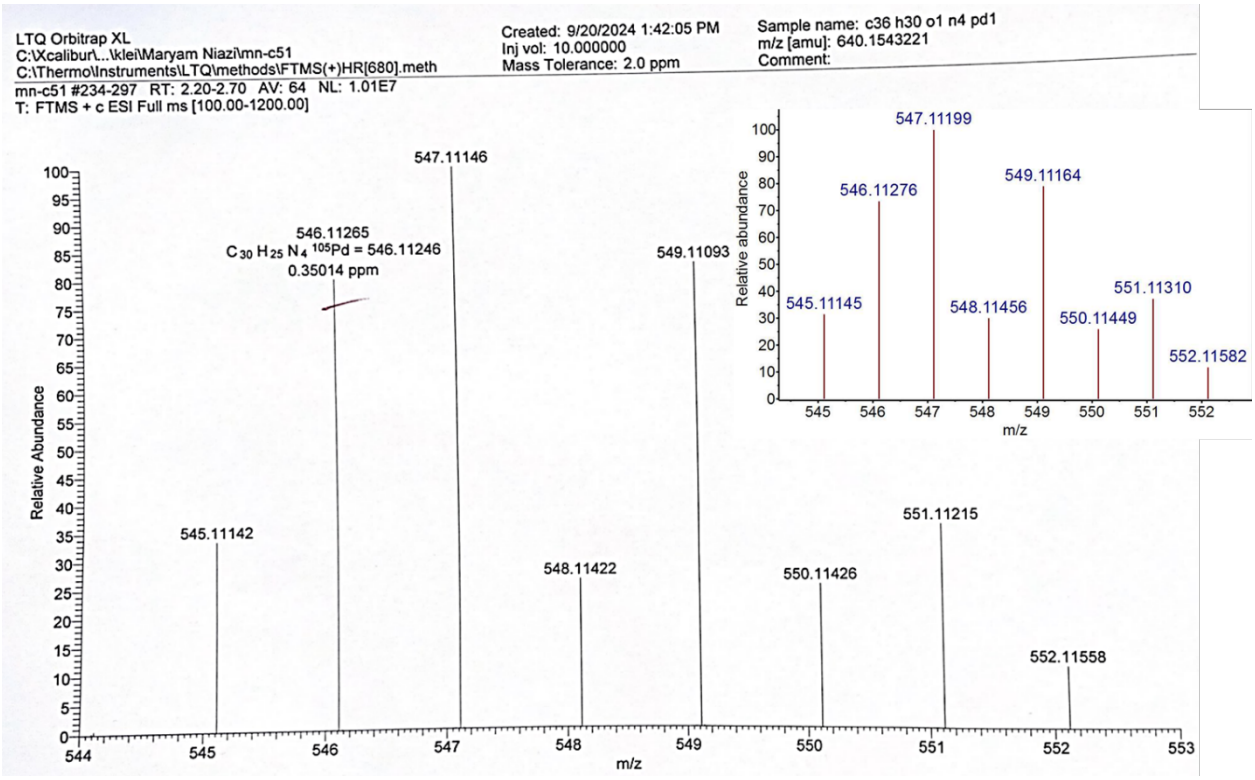


Figure A89. High-resolution ESI-MS(+) spectrum of [Pd(L^{NHBn})OPh] (black) and calculated pattern for $[C_{30}H_{25}N_4Pd]^+$ = [M-OPh]$^+$ (red).

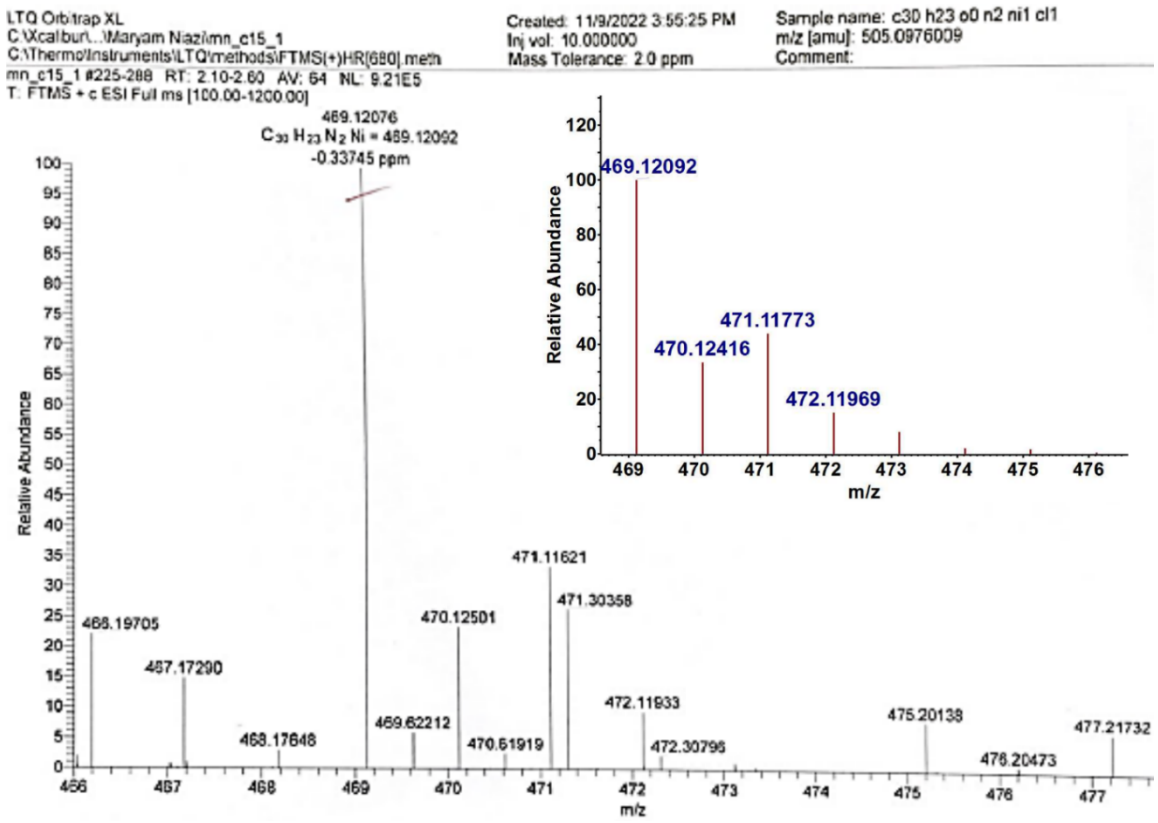


Figure A90. High-resolution ESI-MS(+) spectrum of [Ni(L^{Bn})Cl] (black) and calculated pattern for $[C_{30}H_{23}N_2Ni]^+$ = $[M\text{-}Cl]^+$ (red).

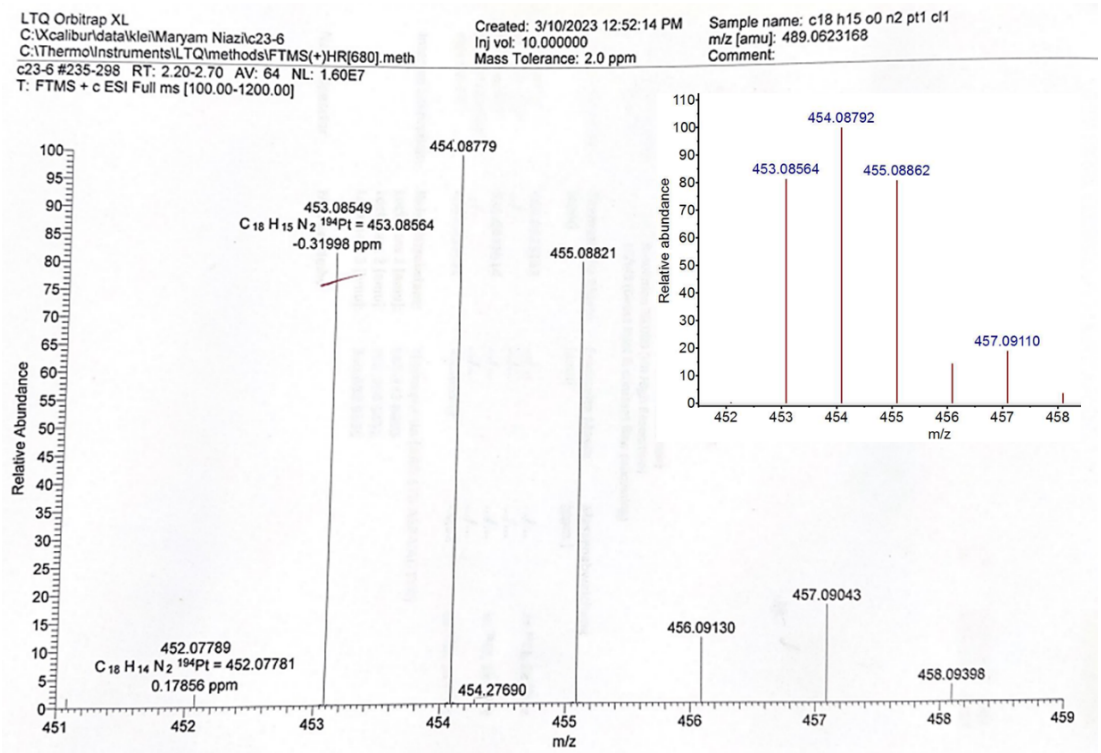


Figure A91. High-resolution ESI-MS(+) spectrum of [Pt(L^{Me})Cl] (black) and calculated pattern for $[C_{18}H_{15}N_2Pt]^+$ = $[M–Cl]^+$ (red).

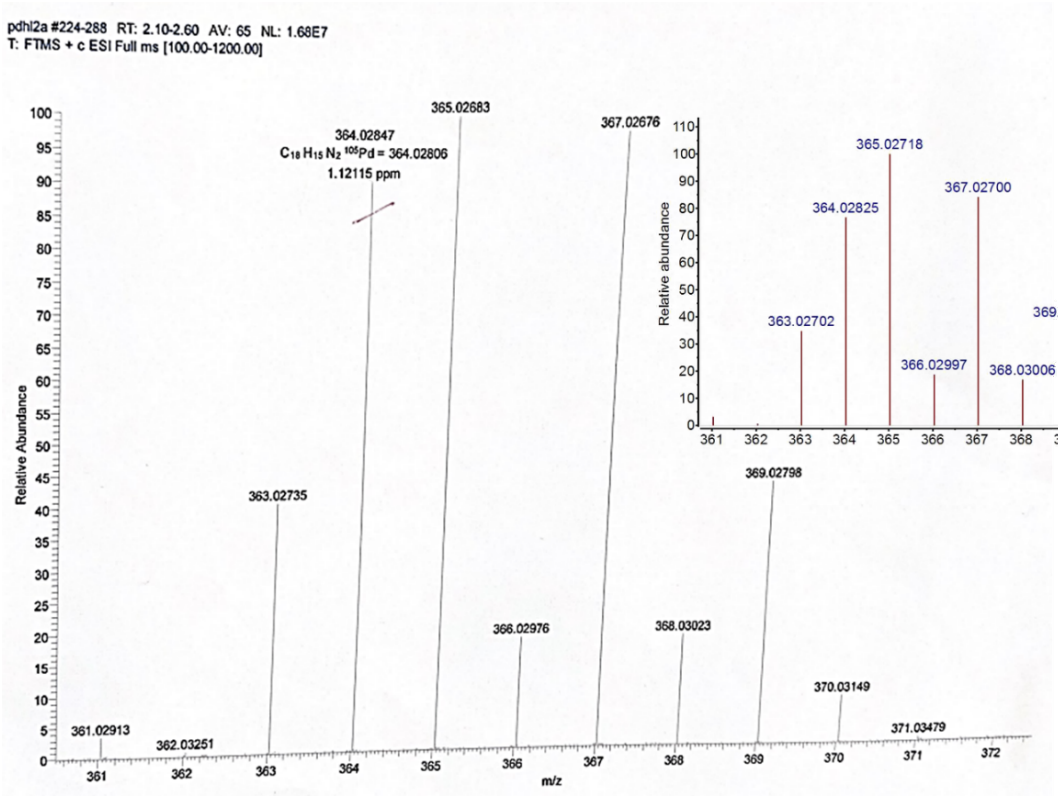


Figure A92. High-resolution ESI-MS(+) spectrum of [Pd(L^{Me})Cl] (black) and calculated pattern for [$C_{18}H_{15}N_2Pd$]$^+$ = [M–Cl]$^+$ (red).

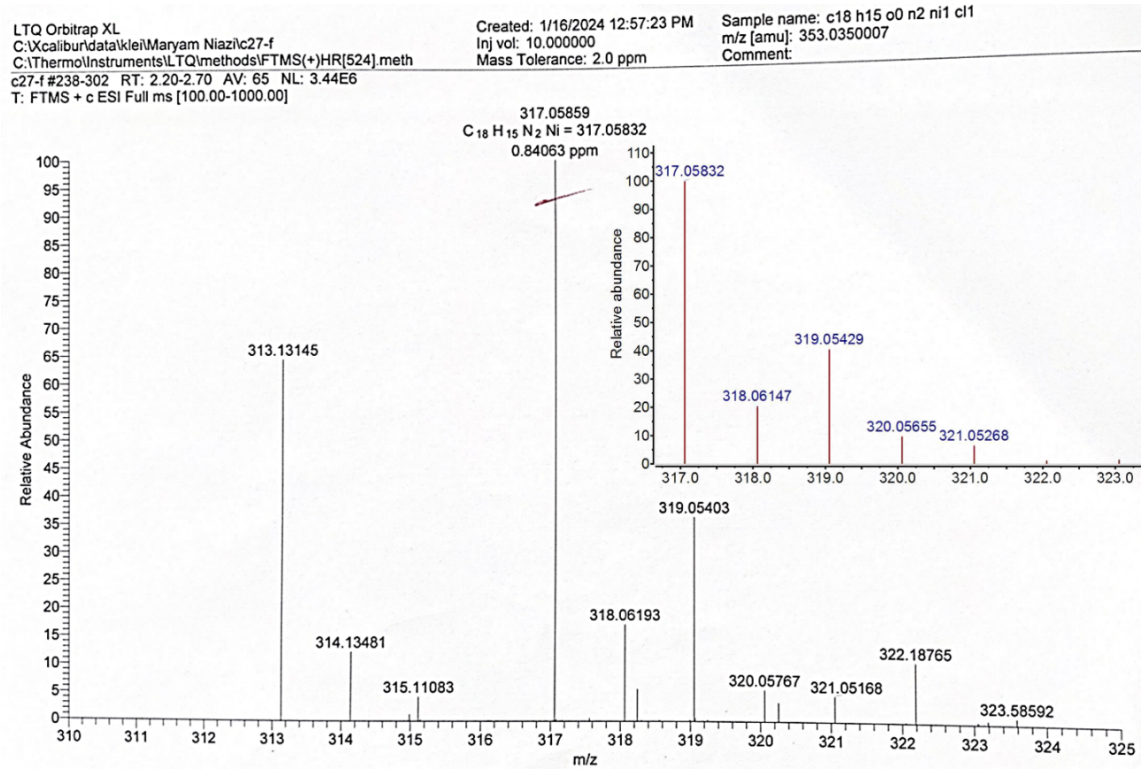


Figure A93. High-resolution ESI-MS(+) spectrum of [Ni(L^{Me})Cl] (black) and calculated pattern for [$C_{18}H_{15}N_2Ni$]$^+$ = [M–Cl]$^+$ (red).

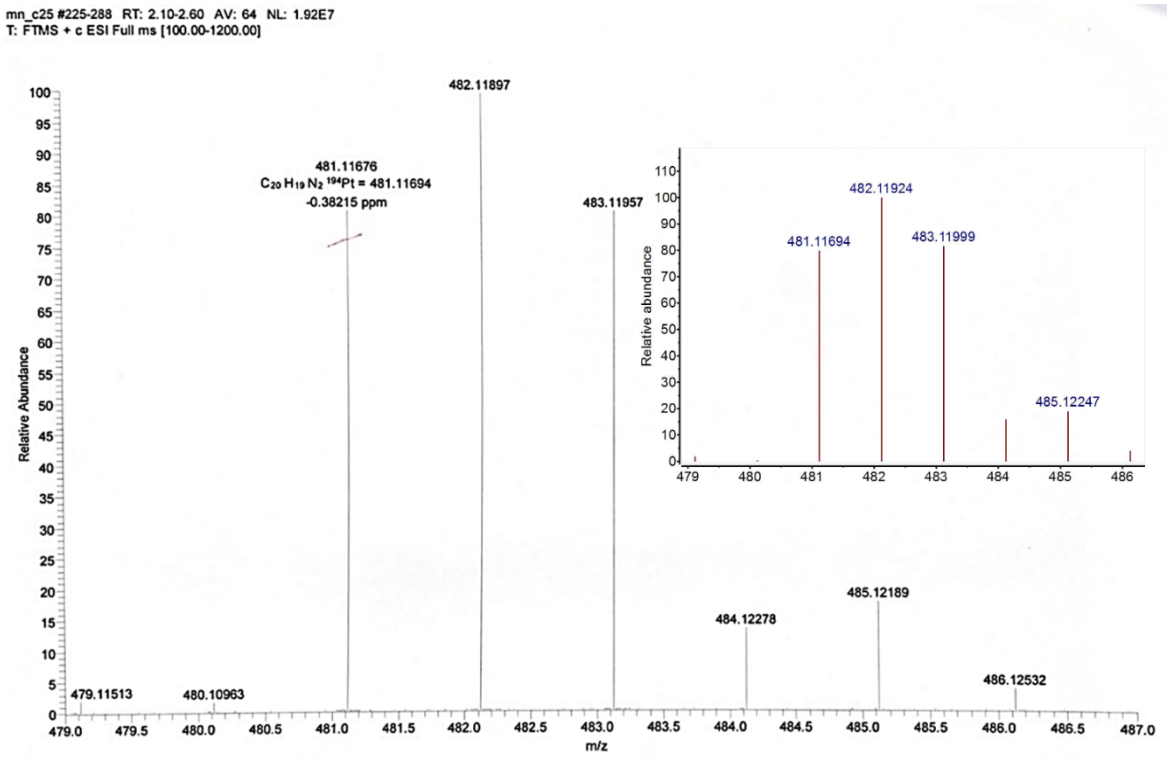


Figure A94. High-resolution ESI-MS(+) spectrum of [Pt(L^{Me2})Cl] (black) and calculated pattern for $[C_{20}H_{19}N_2Pt]^+$ = $[M–Cl]^+$ (red).

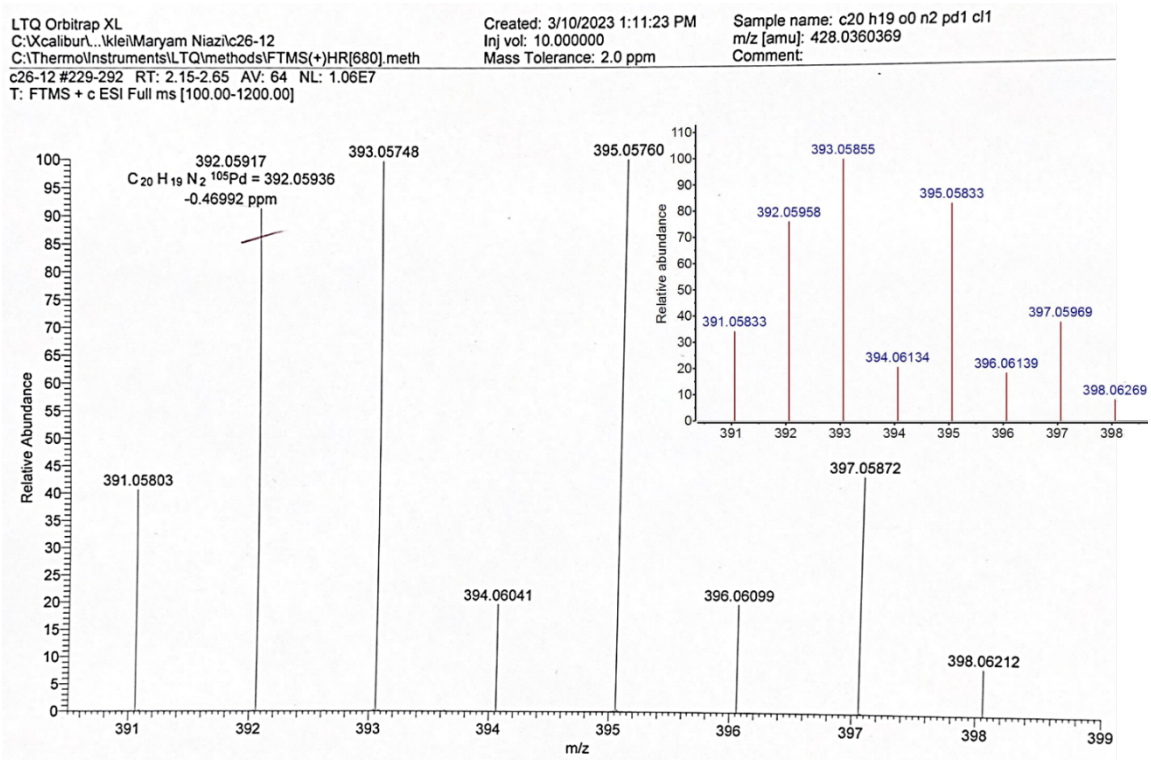


Figure A95. High-resolution ESI-MS(+) spectrum of [Pd(L^{Me2})Cl] (black) and calculated pattern for $[C_{20}H_{19}N_2Pd]^+$ = $[M–Cl]^+$ (red).

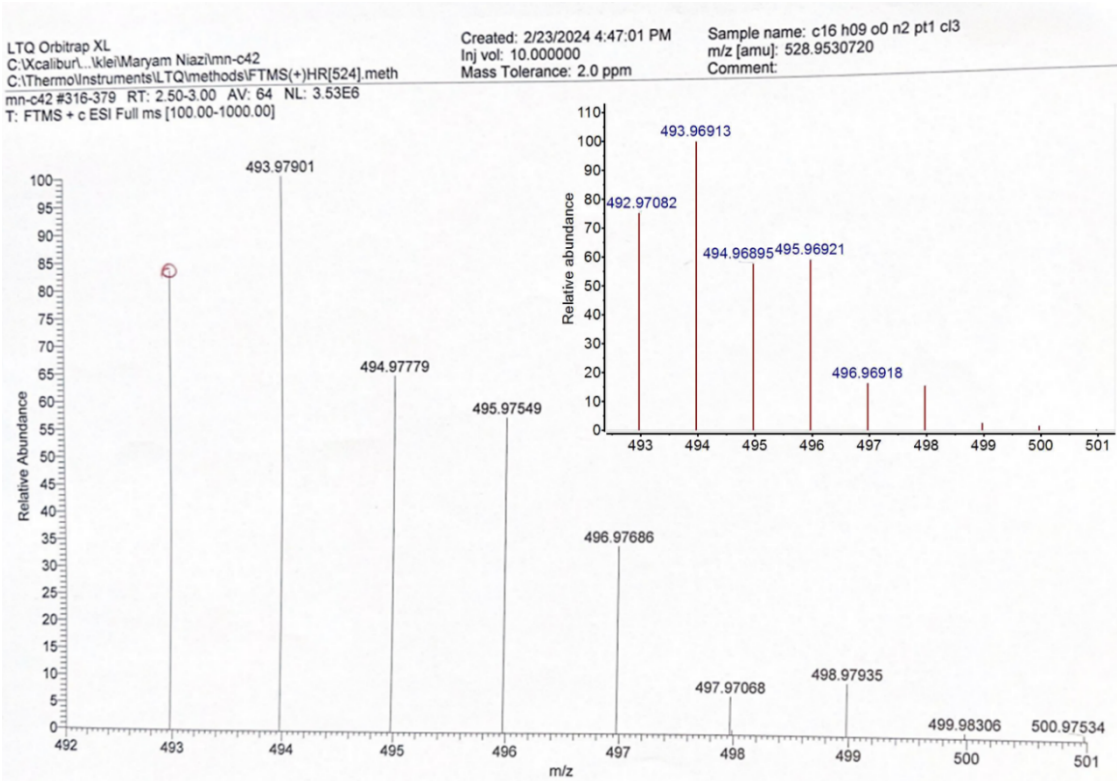


Figure A96. High-resolution ESI-MS(+) spectrum of [Pt(L^{Cl})Cl] (black) and calculated pattern for $[C_{16}H_9Cl_2N_2Pt]^+$ = $[M–Cl]^+$ (red).

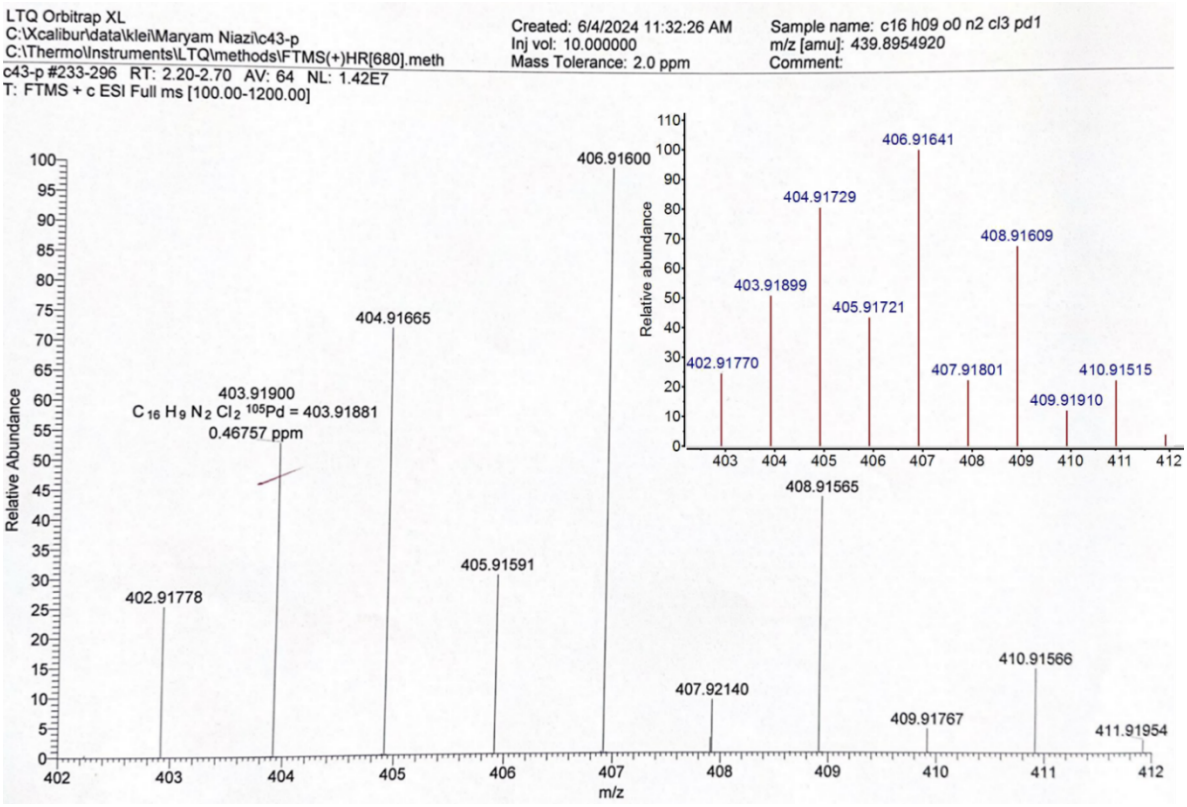


Figure A97. High-resolution ESI-MS(+) spectrum of [Pd(L^{Cl})Cl] (black) and calculated pattern for $[C_{16}H_9Cl_2N_2Pd]^+$ = $[M–Cl]^+$ (red).

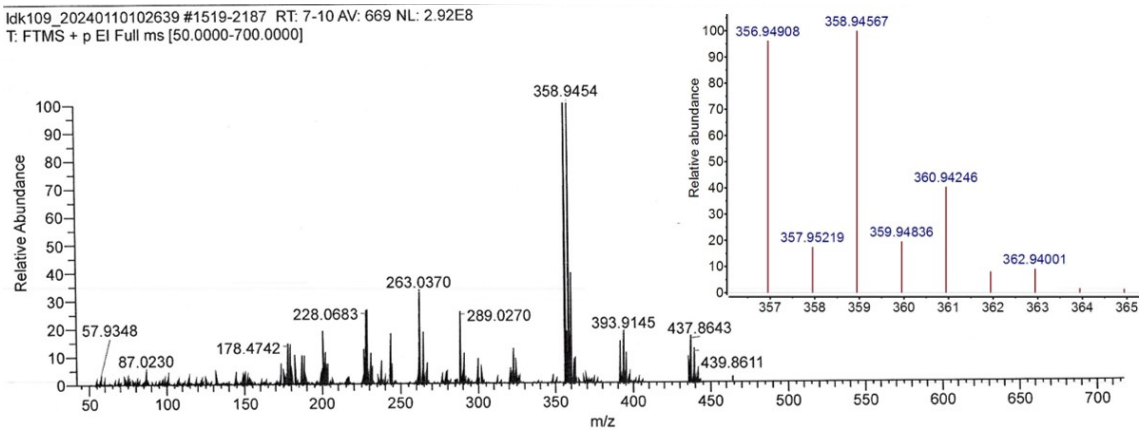


Figure A98. EI-MS(+) spectrum of [Ni(L^{Cl})Br] (black) and calculated pattern for $[C_{16}H_9Cl_2N_2Ni]^+$ = $[M–Br]^+$ (red).

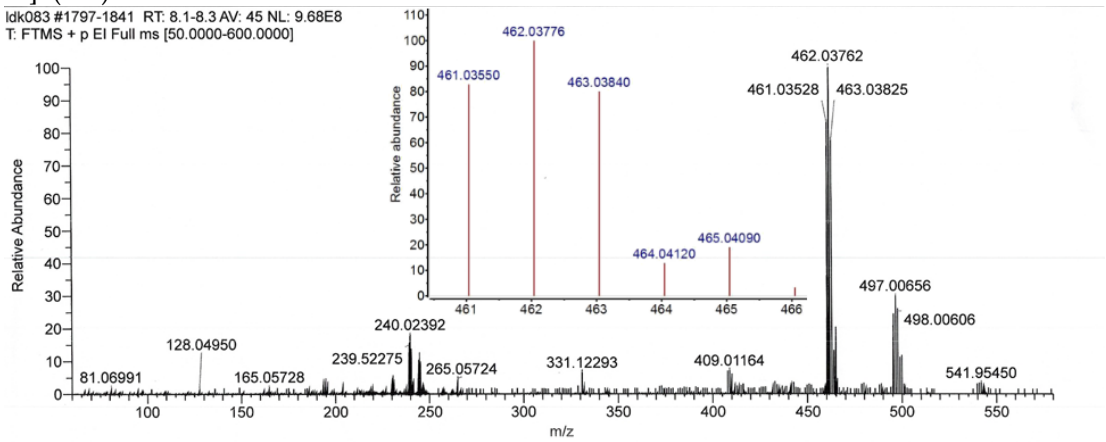


Figure A99. EI-MS(+) spectrum of [Pt(L^{F})Cl] (black) and calculated pattern for $[C_{16}H_9F_2N_2Pt]^+$ = $[M–Cl]^+$ (red).

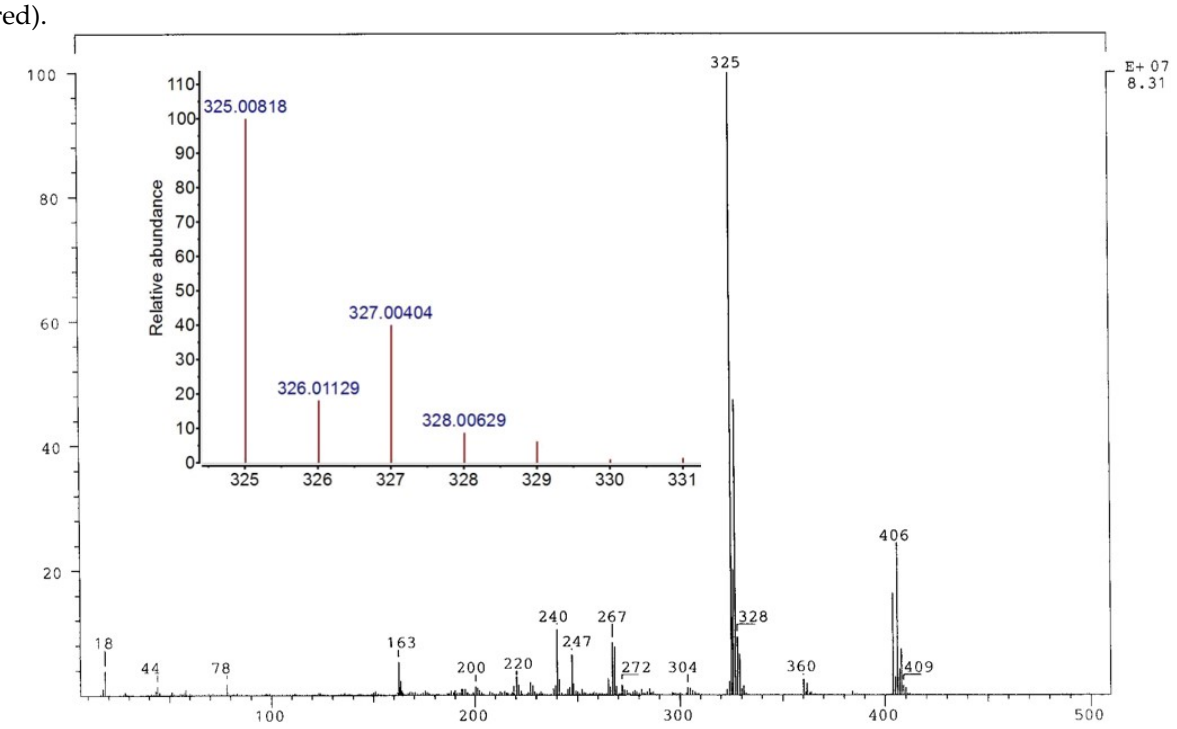


Figure A100. EI-MS(+) spectrum of [Ni(L^{F})Br] (black) and calculated pattern for $[C_{16}H_9F_2N_2Ni]^+$ = $[M–Br]^+$ (red).

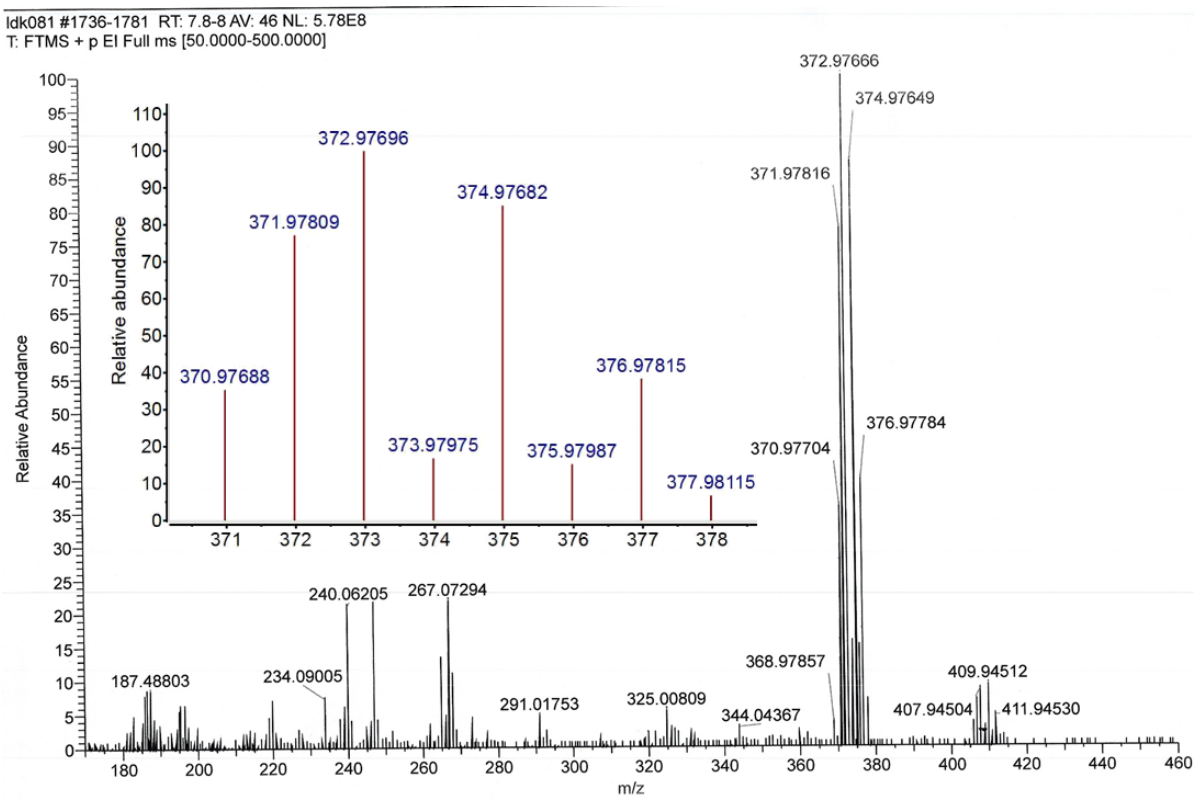


Figure A101. EI-MS(+) spectrum of [Pd(L^F)Cl] (black) and calculated pattern for $[C_{16}H_9F_2N_2Pd]^+$ = $[M–Cl]^+$ (red).

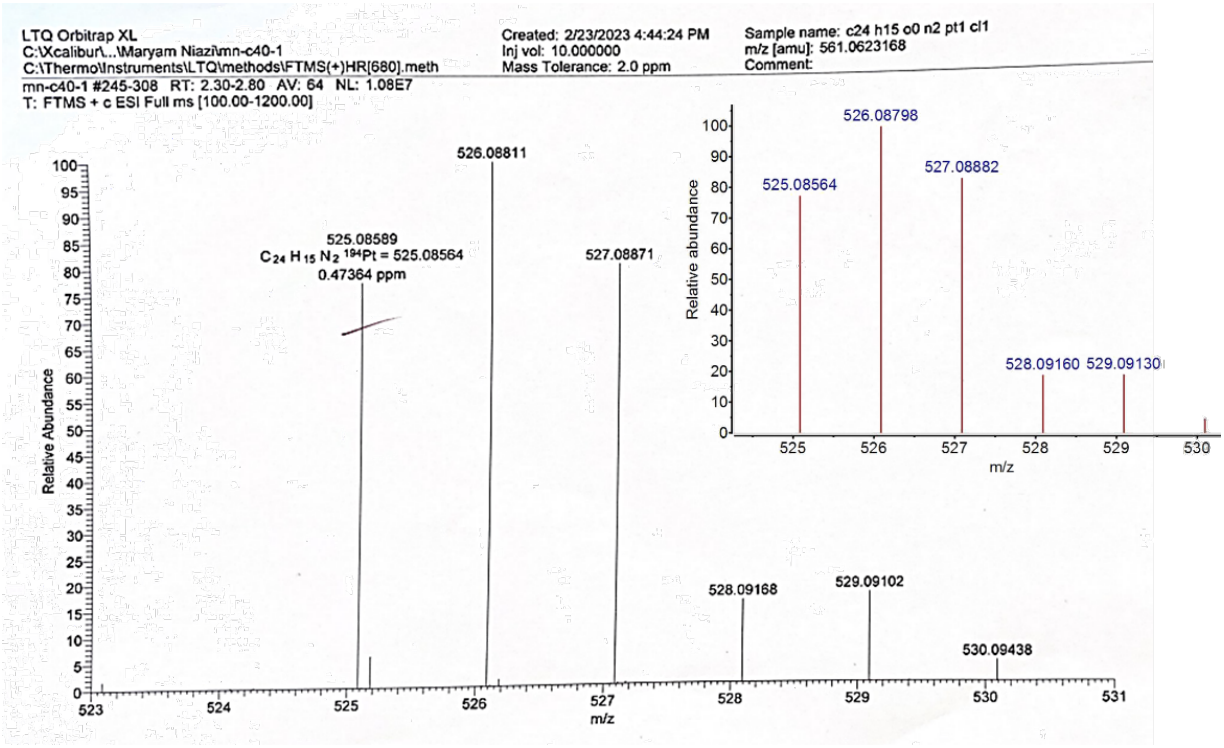


Figure A102. High-resolution ESI-MS(+) spectrum of [Pt(L^{Qu})Cl] (black) and calculated pattern for $[C_{24}H_{15}N_2Pt]^+$ = $[M\text{-}Cl]^+$ (red).

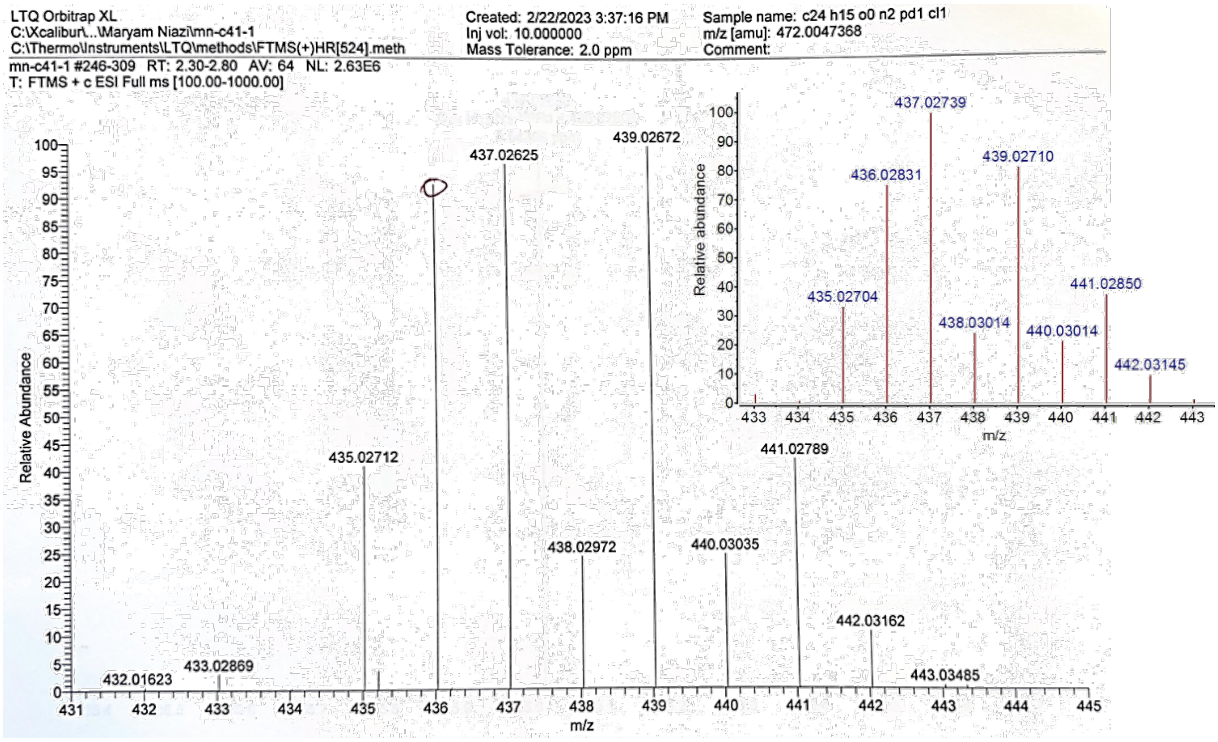


Figure A103. High-resolution ESI-MS(+) spectrum of [Pd(L^{Qu})Cl] (black) and calculated pattern for $[C_{24}H_{15}N_2Pd]^+$ = $[M\text{-}Cl]^+$ (red).

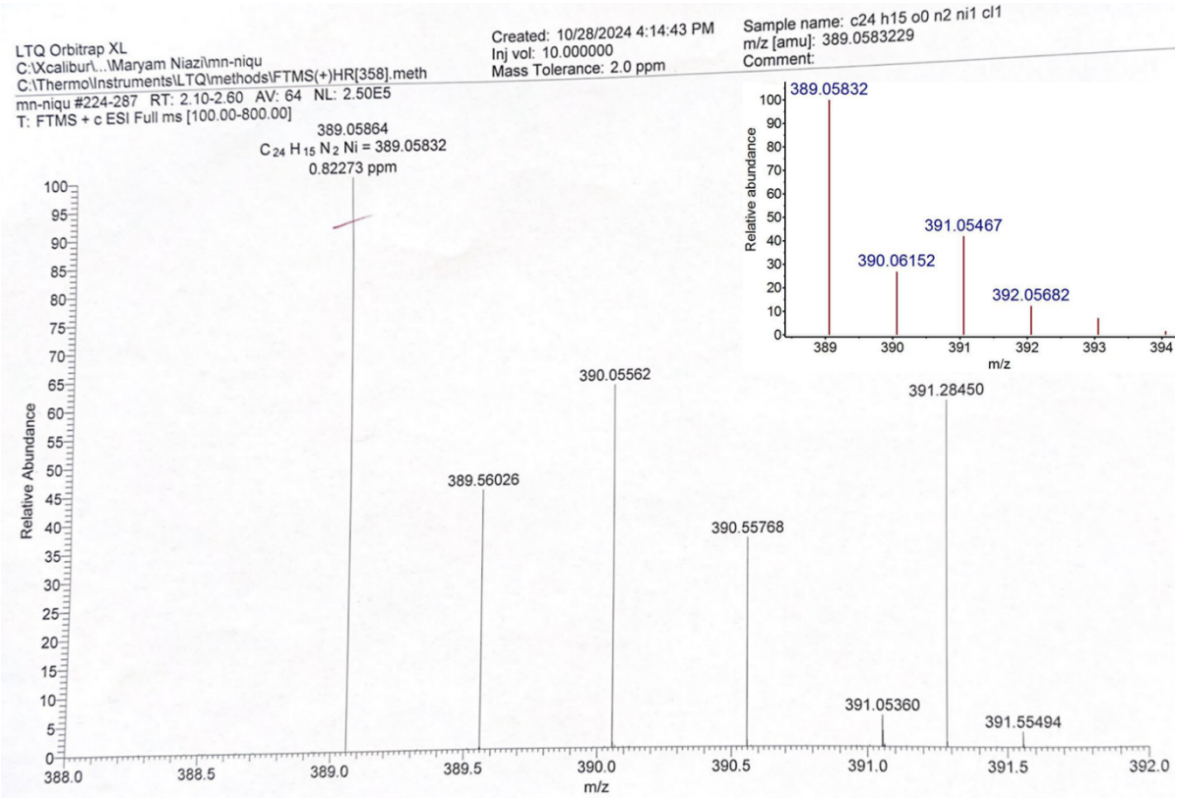


Figure A104. High-resolution ESI-MS(+) spectrum of [Ni(L^{Qu})Cl] (black) and calculated pattern for $[C_{24}H_{15}N_2Ni]^+$ = $[M\text{-}Cl]^+$ (red).

7.3. Single crystal XRD and calculated structural data

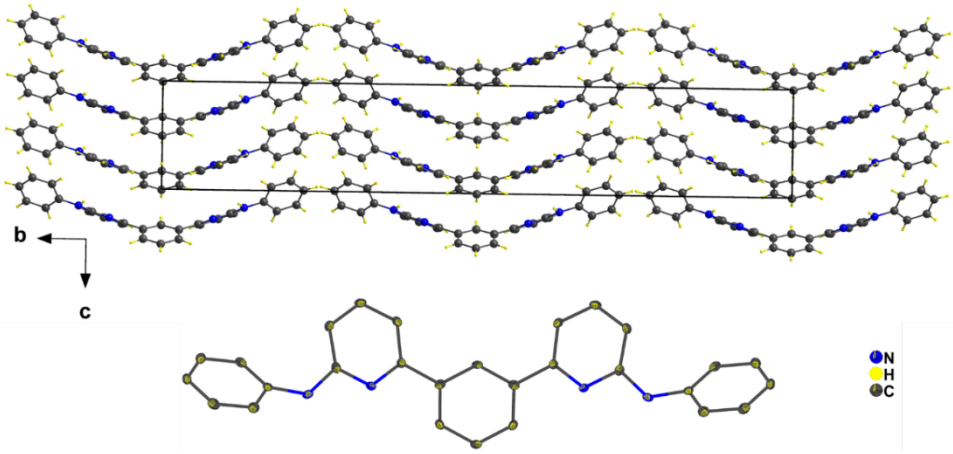


Figure A105. Crystal structure of HL^{NHPh} from single crystal X-ray diffractometry (XRD), viewed along the crystallographic *a* axis (top) and molecular structure with atoms as 50% ellipsoids (bottom).

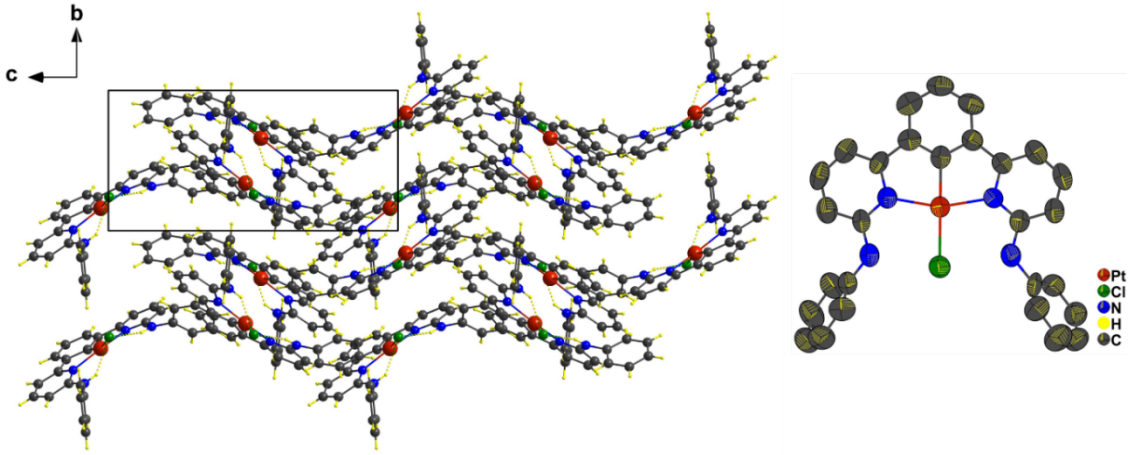


Figure A106. Crystal structure of [Pt(L^{NHPh})Cl] (left) from single crystal X-ray diffractometry (XRD), viewed along the crystallographic *a* axis (left) and molecular structure with atoms as 50% ellipsoids.

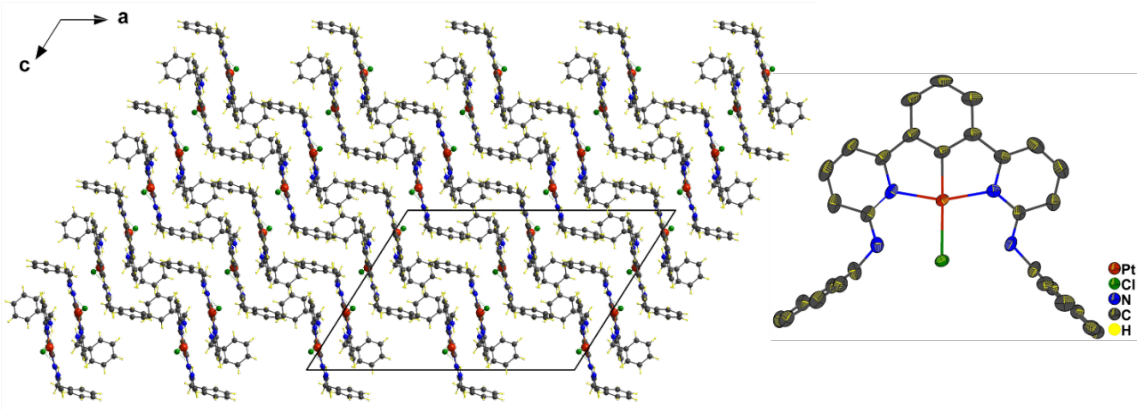


Figure A107. Crystal structure of [Pt(L^{NHBn})Cl] (left) from single crystal X-ray diffractometry (XRD), viewed along the crystallographic *b* axis (left) and molecular structure with atoms as 50% ellipsoids.

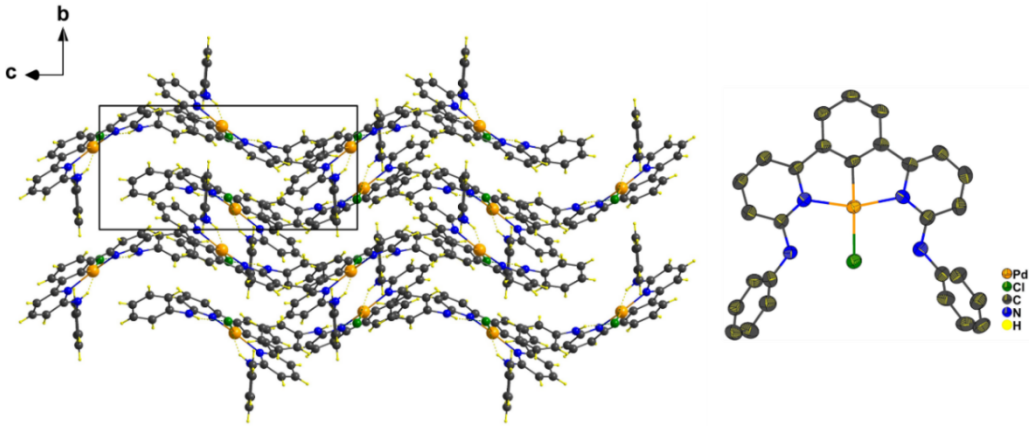


Figure A108. Crystal structure of [Pd(L^{NHPh})Cl] (left) from single crystal X-ray diffractometry (XRD), viewed along the crystallographic *a* axis (left) and molecular structure with atoms as 50% ellipsoids.

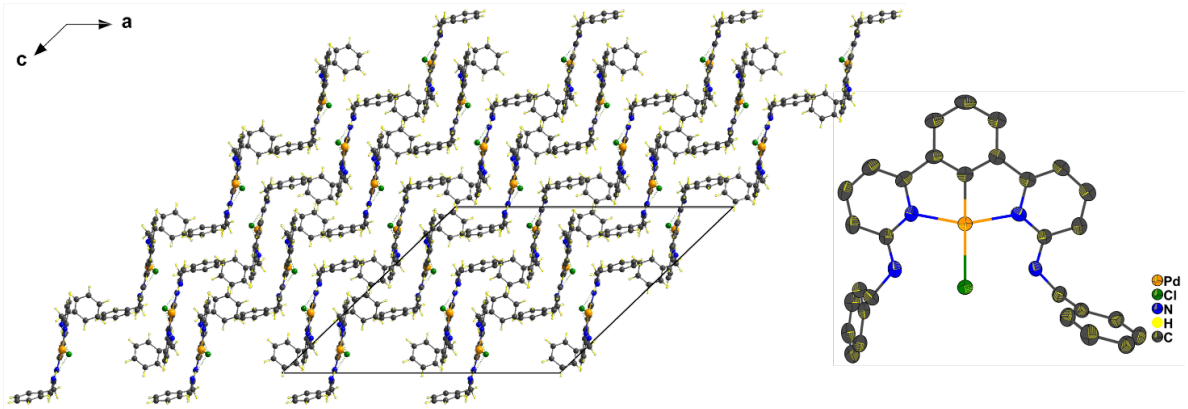


Figure A109. Crystal structure of [Pd(L^{NHBn})Cl] (left) from single crystal X-ray diffractometry (XRD), viewed along the crystallographic *b* axis (left) and molecular structure with atoms as 50% ellipsoids.

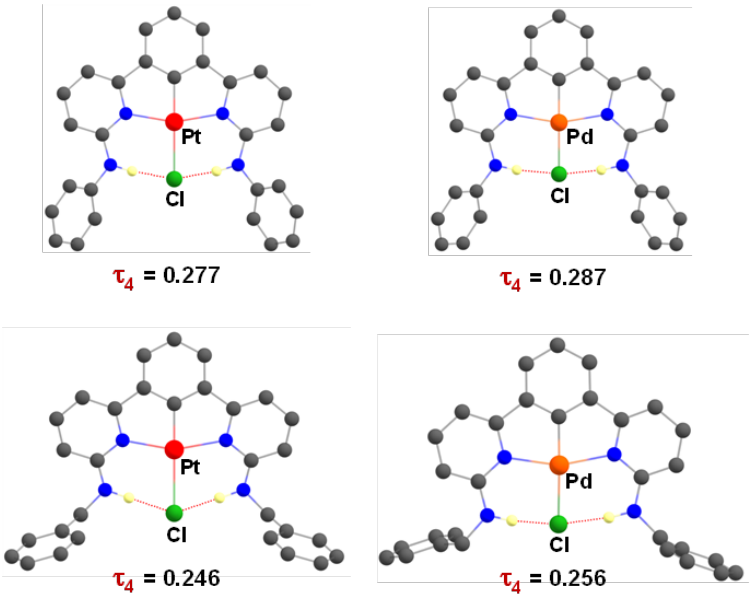


Figure A110. DFT-calculated molecular structures of [M(N^C^N)Cl] (M = Pt or Pd; N^C^N = L^{NHPh} (top) and L^{NHBn} (bottom)) in the S_0 ground state, featuring the deviation τ_4 from the square planar coordination.

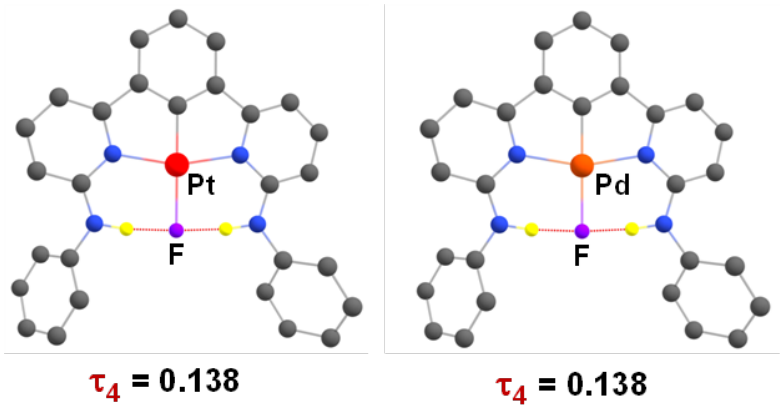


Figure A111. DFT-calculated molecular structures of [M(L^{NHPh})F] (M = Pt or Pd) in the S_0 ground state, featuring the deviation τ_4 from the square planar coordination.

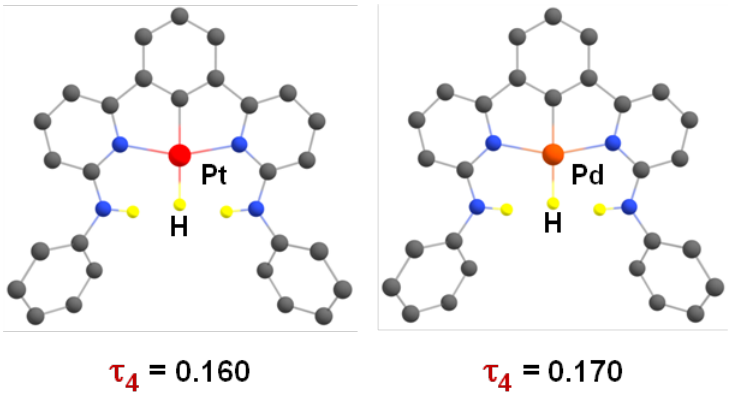


Figure A112. DFT-calculated molecular structures of [M(L^{NHPh})H] (M = Pt or Pd) in the S_0 ground state, featuring the deviation τ_4 from the square planar coordination.

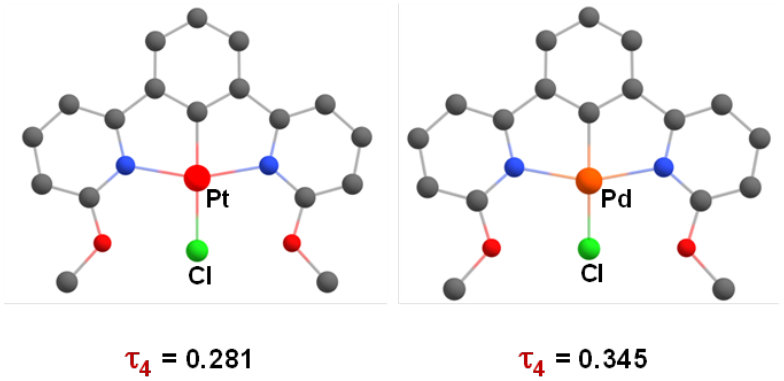


Figure A113. DFT-calculated molecular structures of [M(L^{OMe})Cl] (M = Pt or Pd) in the S_0 ground state, featuring the deviation τ_4 from the square planar coordination.

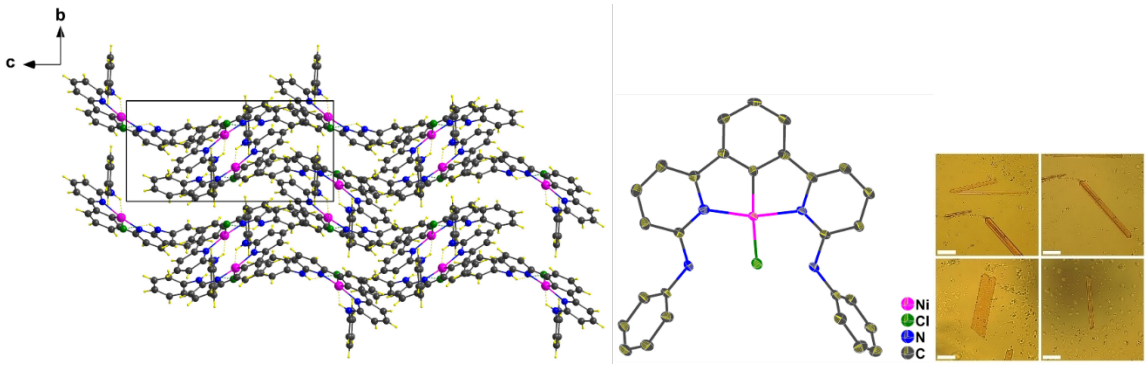


Figure A114. Crystal structure of [Ni(L^{NHPh})Cl] from single crystal X-ray diffractometry (XRD), viewed along the crystallographic *a* axis (left), molecular structure with atoms as 50% ellipsoids, H atoms omitted for clarity (center), and photoluminescence micrographs of the complex in the crystal state at 298 K, scale bar = 20 μm (right).

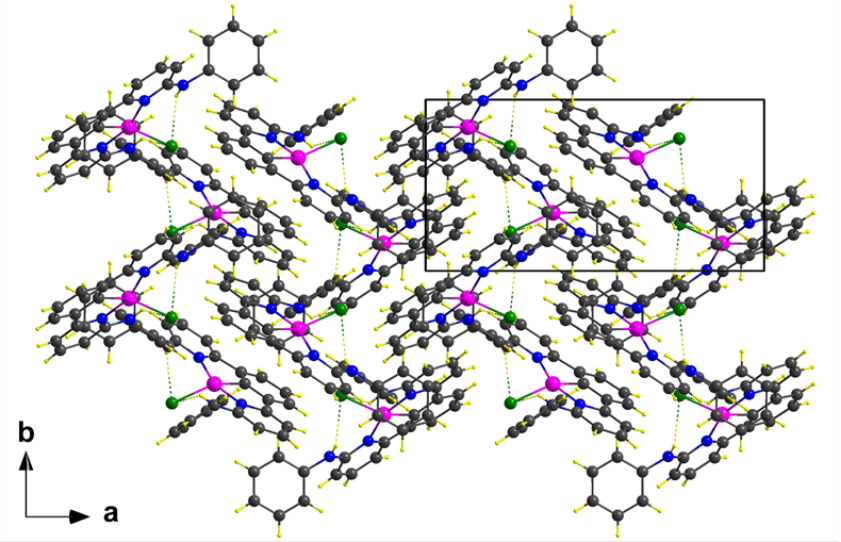


Figure A115. Crystal structure of [Ni(L^{NHPh})Cl] from single crystal X-ray diffractometry (XRD), viewed along the crystallographic *c* axis.

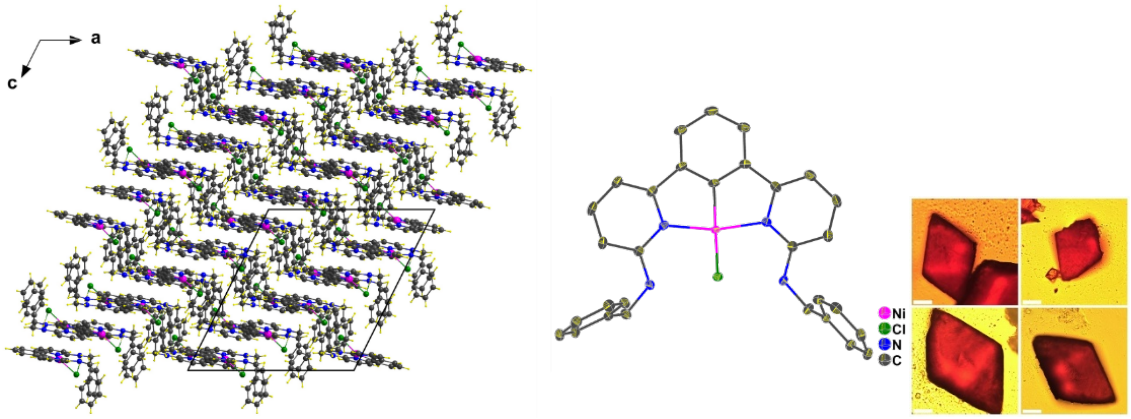


Figure A116. Crystal structure of [Ni(L^{NHBn})Cl] from single crystal XRD, viewed along the crystallographic *b* axis (left), molecular structure with atoms as 50% ellipsoids, H atoms omitted for clarity (center), and photoluminescence micrographs of the complex in the crystal state at 298 K, scale bar = 20 μm (right).

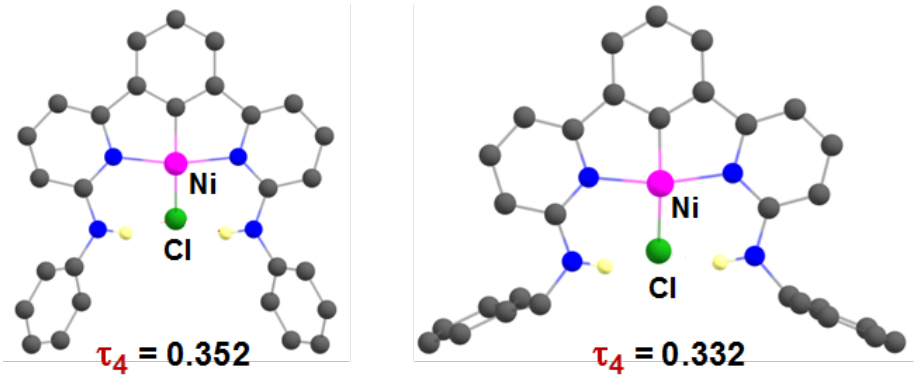


Figure A117. DFT-calculated molecular structures of [Ni(L^{NHPh})Cl] (left), [Ni(L^{NHBn})Cl] (right), in the S_0 ground state, featuring the deviation τ_4 from square planar coordination (for square planar, $\tau_4 = 0$; for tetrahedral, $\tau_4 = 1$).

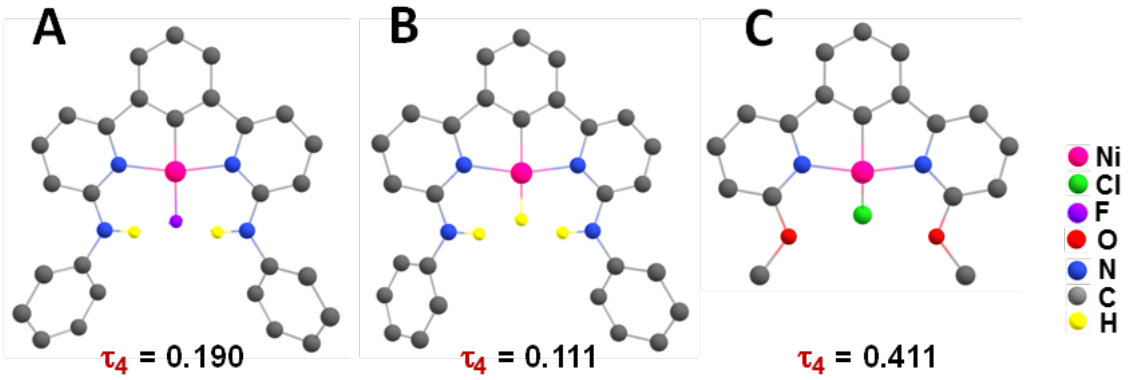


Figure A118. DFT-calculated molecular structures of [Ni(L^{NHPh})F] (A), [Ni(L^{NHPh})H] (B), and [Ni(L^{OMe})Cl] (C) in the S_0 ground state, featuring the deviation τ_4 from square planar coordination (for square planar, $\tau_4 = 0$; for tetrahedral, $\tau_4 = 1$).

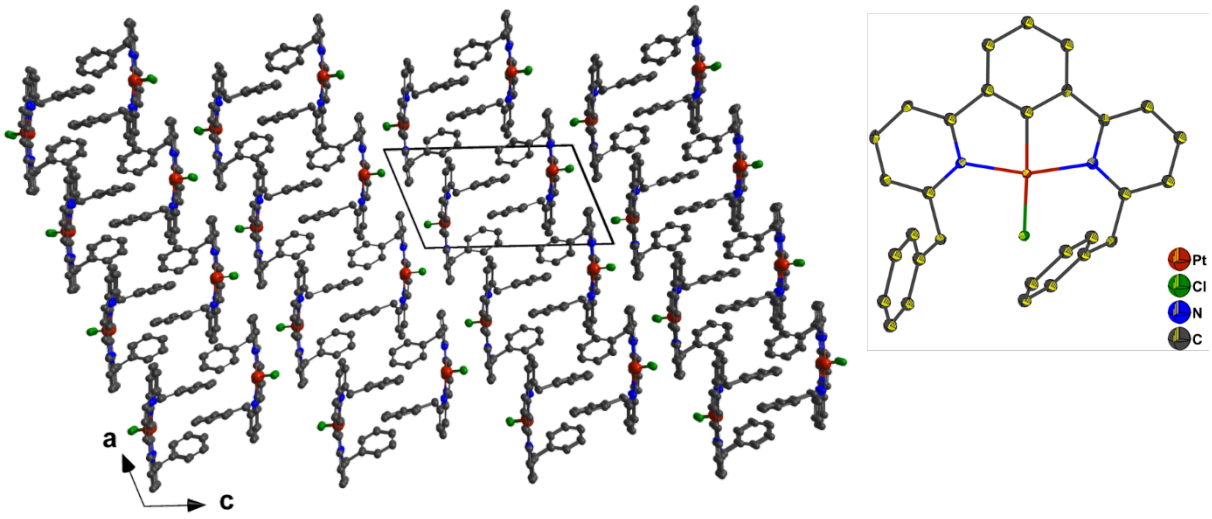


Figure A119 Crystal structure of [Pt(L^{Bn})Cl] from single crystal XRD, viewed along the crystallographic *b* axis (left) and molecular structure with atoms as 50% ellipsoids (right), H atoms omitted for clarity.

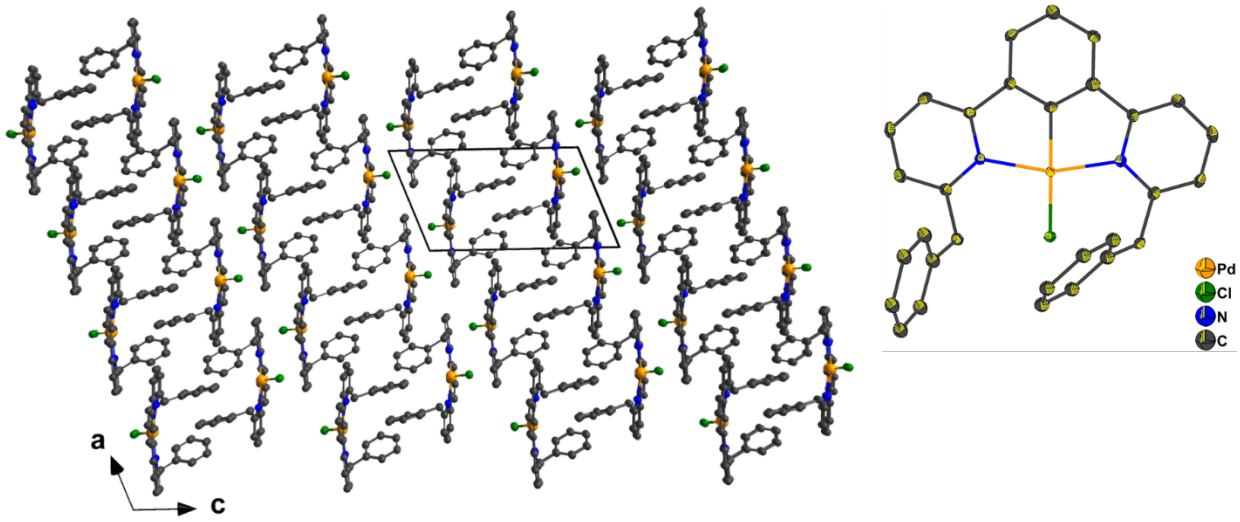


Figure A120. Crystal structure of [Pd(L^{Bn})Cl] from single crystal XRD, viewed along the crystallographic *b* axis (left) and molecular structure with atoms as 50% ellipsoids (right), H atoms omitted for clarity.

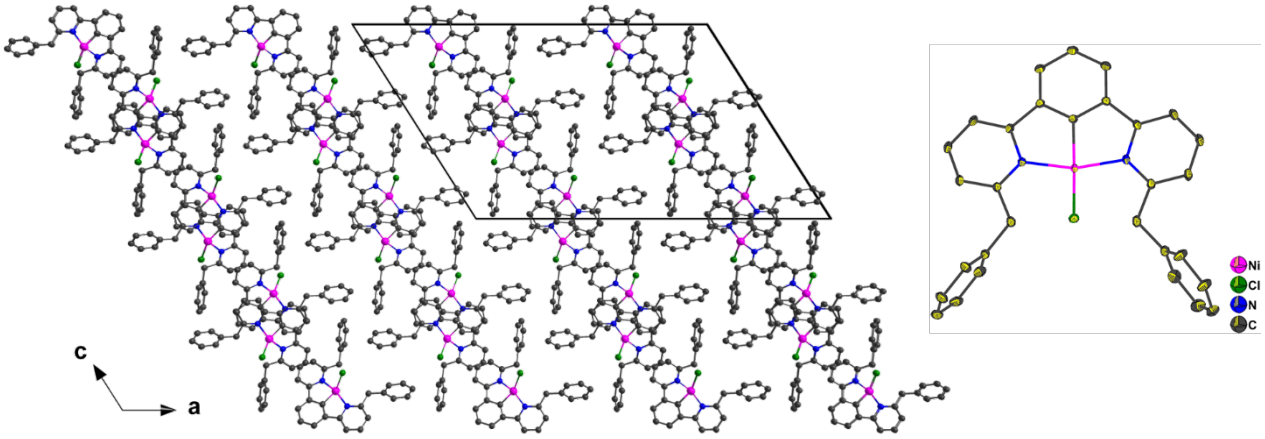


Figure A121. Crystal structure of [Ni(L^{Bn})Cl] from single crystal XRD, viewed along the crystallographic *b* axis (left) and molecular structure with atoms as 50% ellipsoids (right), H atoms omitted for clarity.

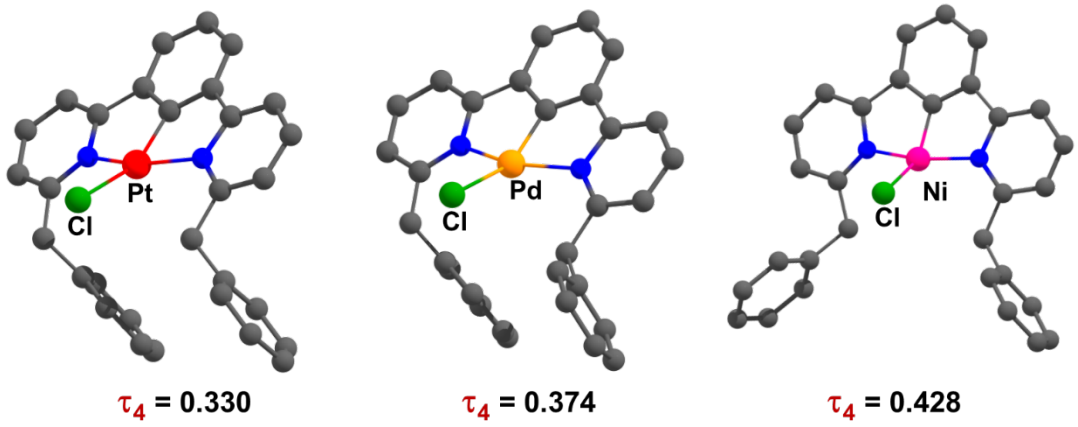


Figure A122. DFT-calculated molecular structures of [M(L^{Bn})Cl] (M = Pt, Pd, and Ni) in the S_0 ground state, featuring the deviation τ_4 from the square planar coordination (for perfect square planar, $\tau_4 = 0$; for perfect tetrahedral $\tau_4 = 1$).

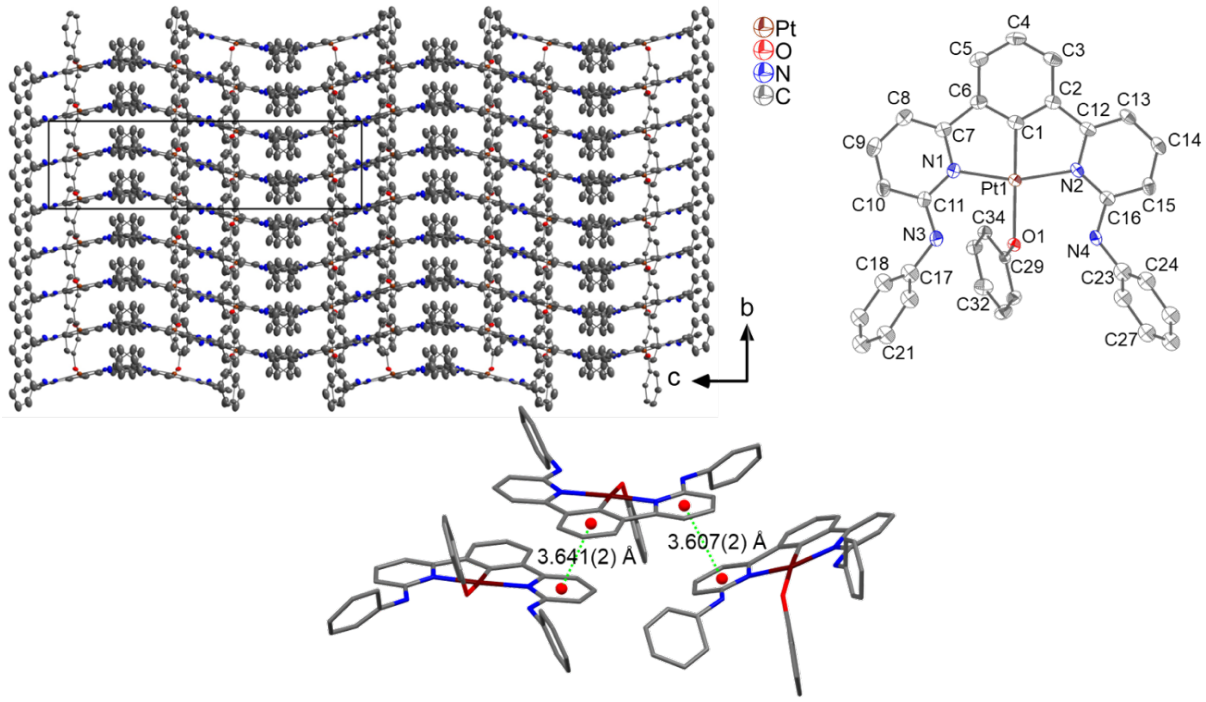


Figure A123. Crystal structure of [Pt(L^{NHPh})OPh] from single crystal XRD, viewed along the crystallographic *a* axis (left) and molecular structure with atoms as 50% ellipsoids (right), H atoms omitted for clarity, along with extended view of the packing of the complex showing the intermolecular interactions (down).

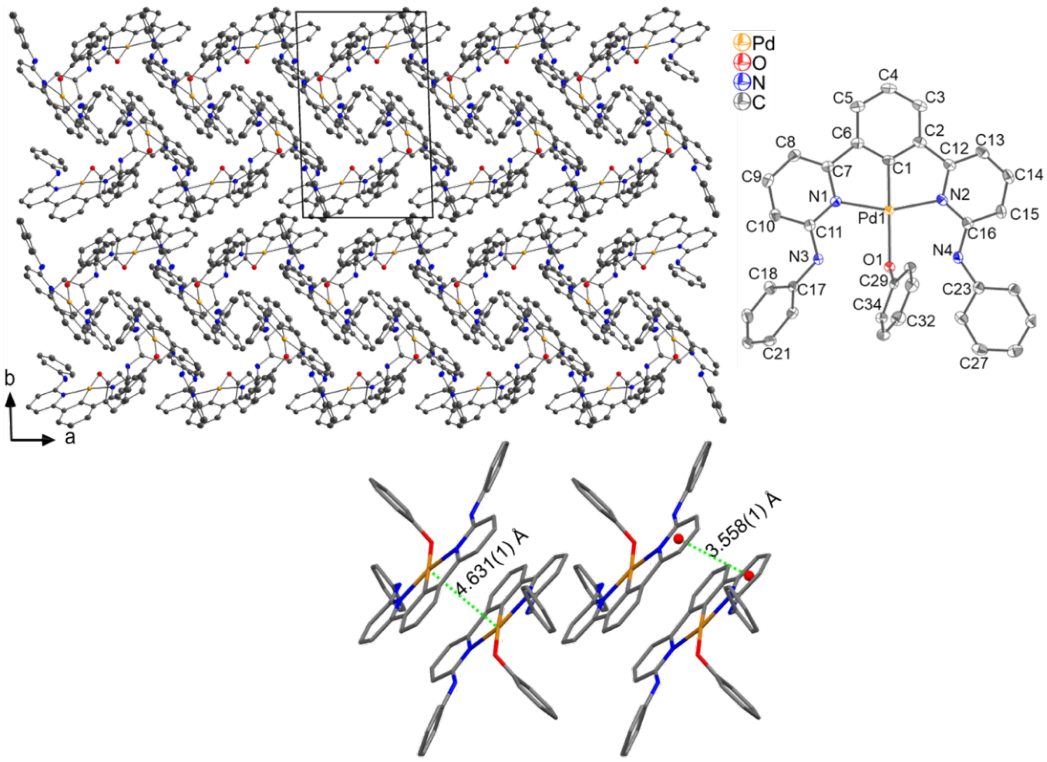


Figure A124. Crystal structure of [Pd(L^{NHPh})OPh] from single crystal XRD, viewed along the crystallographic *c* axis (left) and molecular structure with atoms as 50% ellipsoids (right), H atoms omitted for clarity, along with extended view of the packing of the complex showing the intermolecular interactions (down).

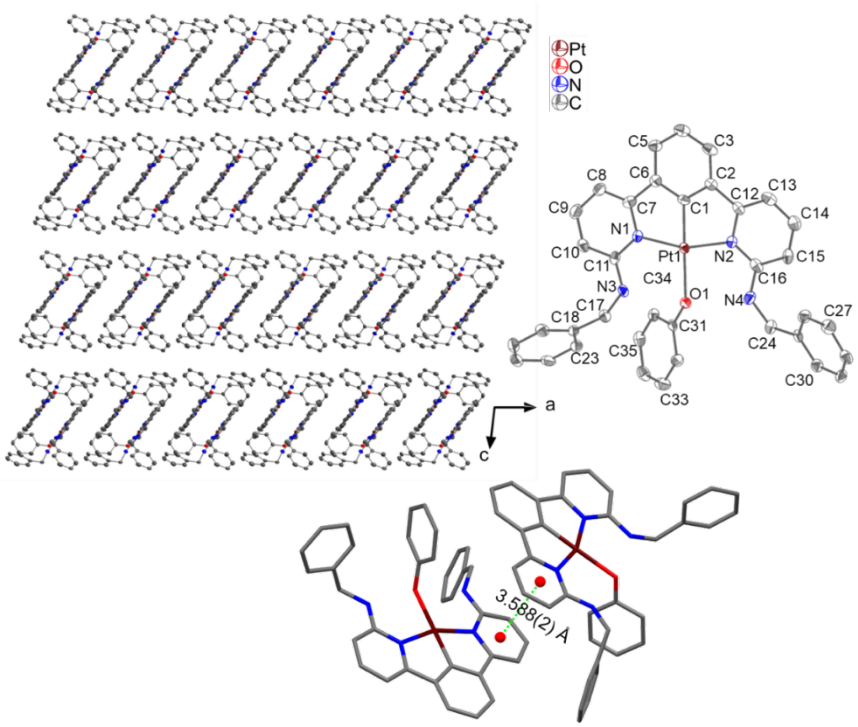


Figure A125. Crystal structure of [Pt(L^{NHBn})OPh] from single crystal XRD, viewed along the crystallographic *b* axis (left) and molecular structure with atoms as 50% ellipsoids (right), H atoms omitted for clarity, along with extended view of the packing of the complex showing the intermolecular interactions (down).

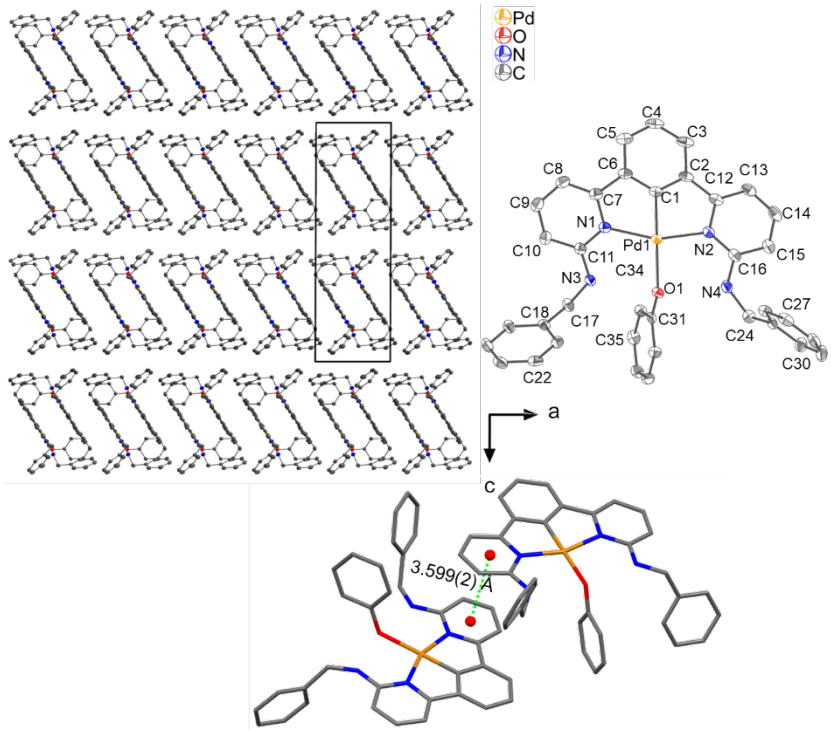


Figure A126. Crystal structure of [Pd(L^{NHBn})OPh] from single crystal XRD, viewed along the crystallographic *b* axis (left) and molecular structure with atoms as 50% ellipsoids (right), H atoms omitted for clarity, along with extended view of the packing of the complex showing the intermolecular interactions (down).

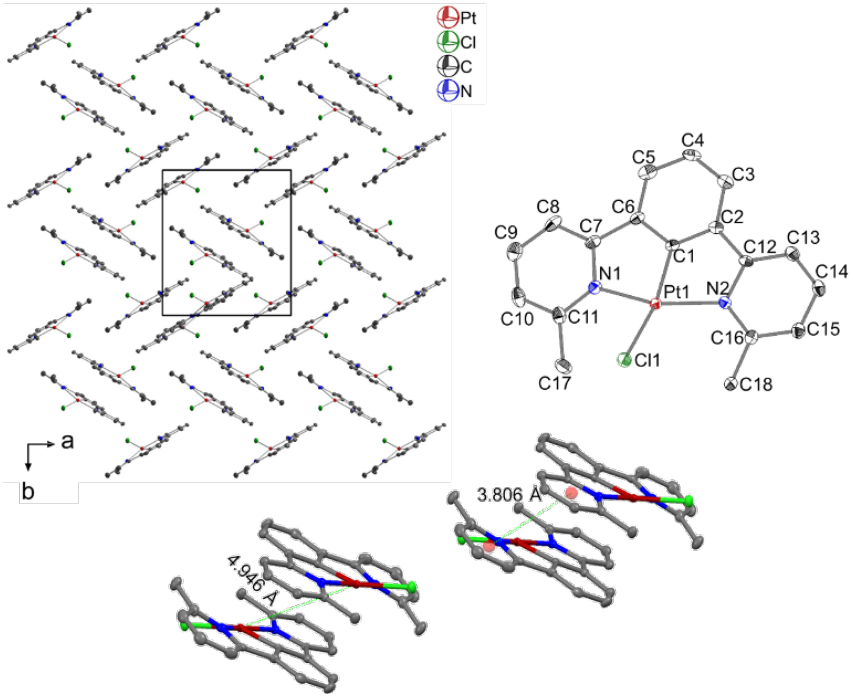


Figure A127. Crystal structure of [Pt(L^{Me})Cl] from single crystal XRD, viewed along the crystallographic *c* axis (left) and molecular structure with atoms as 50% ellipsoids (right), H atoms omitted for clarity, along with extended view of the packing of the complex showing the intermolecular interactions (down).

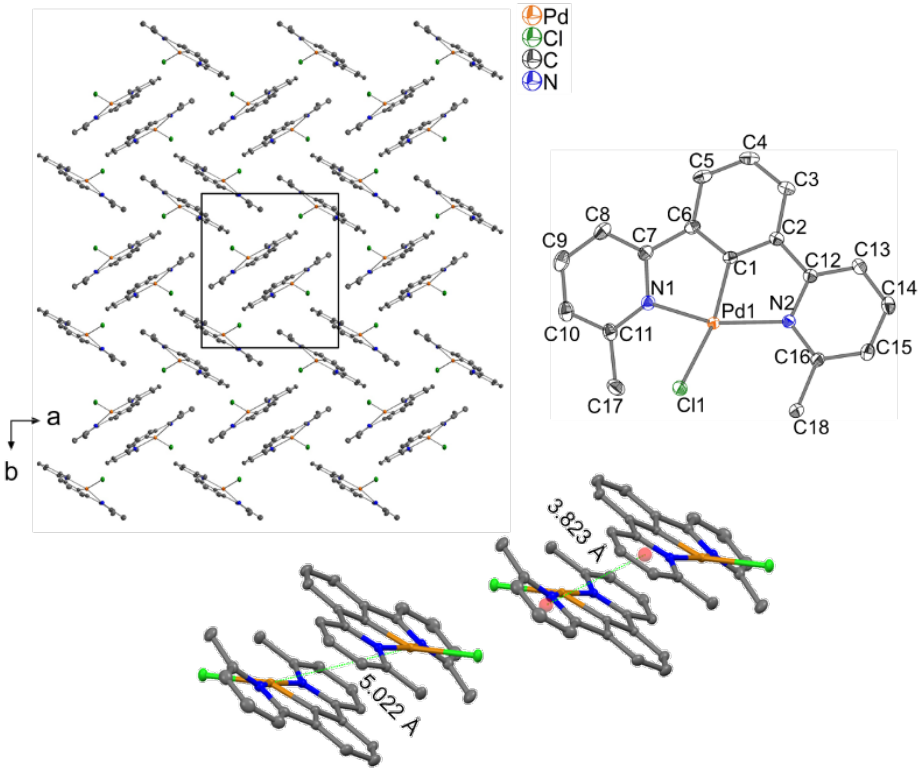


Figure A128. Crystal structure of [Pd(L^{Me})Cl] from single crystal XRD, viewed along the crystallographic *c* axis (left) and molecular structure with atoms as 50% ellipsoids (right), H atoms

omitted for clarity, along with extended view of the packing of the complex showing the intermolecular interactions (down).

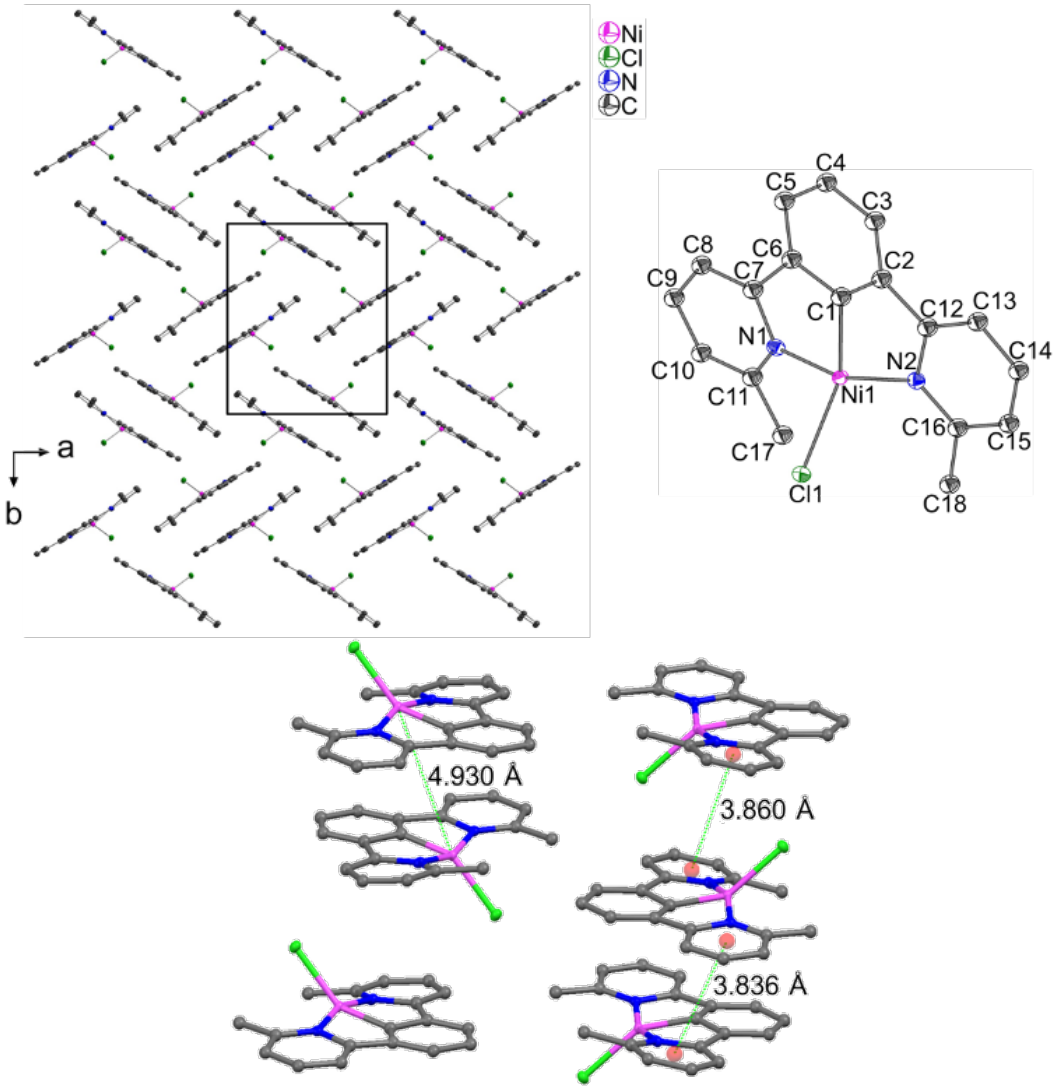


Figure A129. Crystal structure of [Ni(L^{Me})Cl] from single crystal XRD, viewed along the crystallographic *c* axis (left) and molecular structure with atoms as 50% ellipsoids (right), H atoms omitted for clarity, along with extended view of the packing of the complex showing the intermolecular interactions (down).

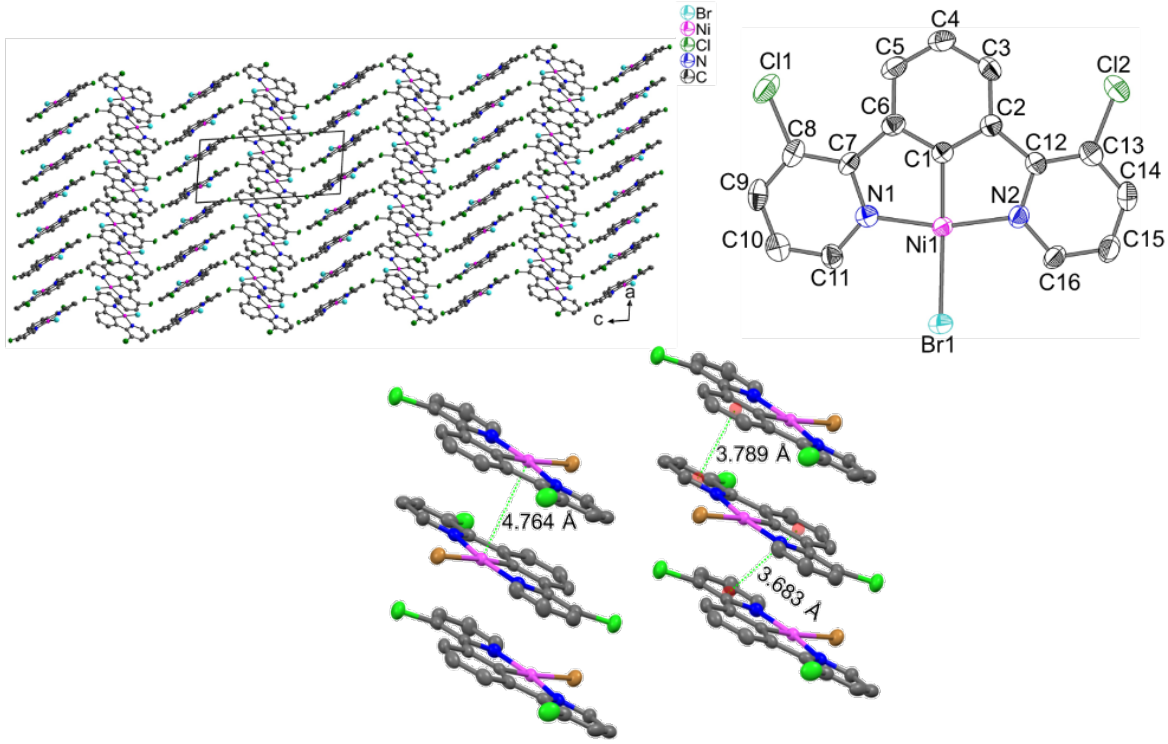


Figure A130. Crystal structure of [Ni(L^{Cl})Br] from single crystal XRD, viewed along the crystallographic *b* axis (left) and molecular structure with atoms as 50% ellipsoids (right), H atoms omitted for clarity, along with extended view of the packing of the complex showing the intermolecular interactions (down).

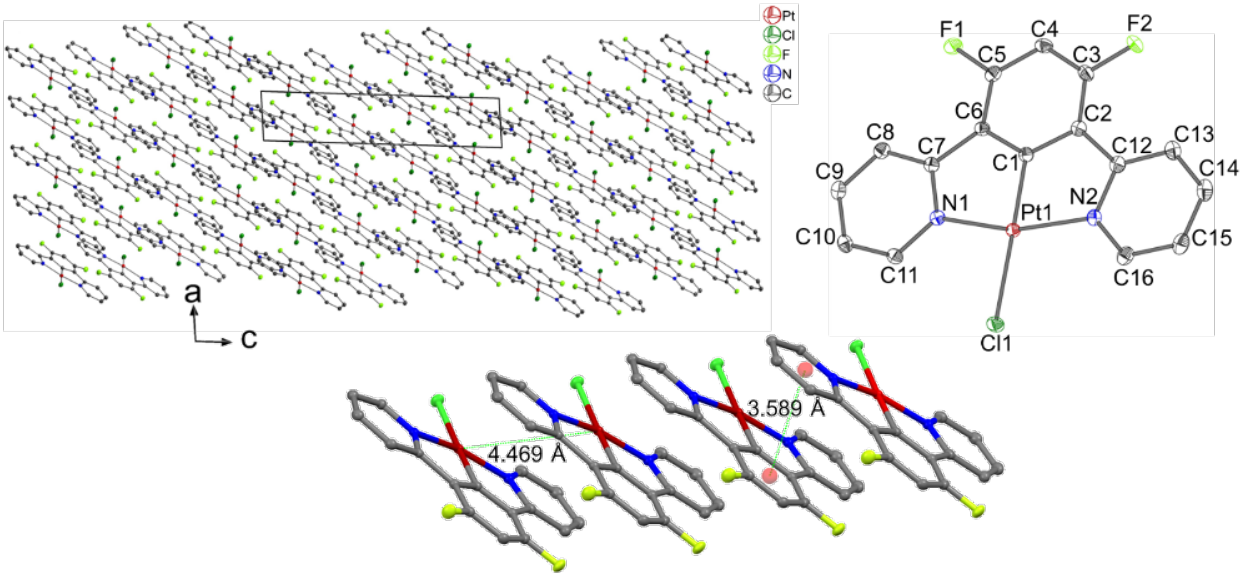


Figure A131. Crystal structure of [Pt(L^{F})Cl] from single crystal XRD, viewed along the crystallographic *b* axis (left) and molecular structure with atoms as 50% ellipsoids (right), H atoms omitted for clarity.

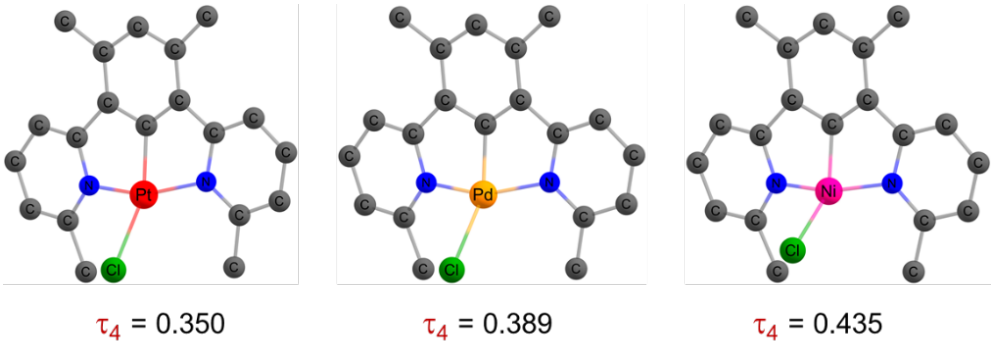


Figure A132. DFT-calculated molecular structures of [M(L^{Me2})Cl] (M = Pt, Pd, and Ni) in the S_0 ground state, featuring the deviation τ_4 from the square planar coordination (for perfect square planar, $\tau_4 = 0$; for perfect tetrahedral $\tau_4 = 1$).

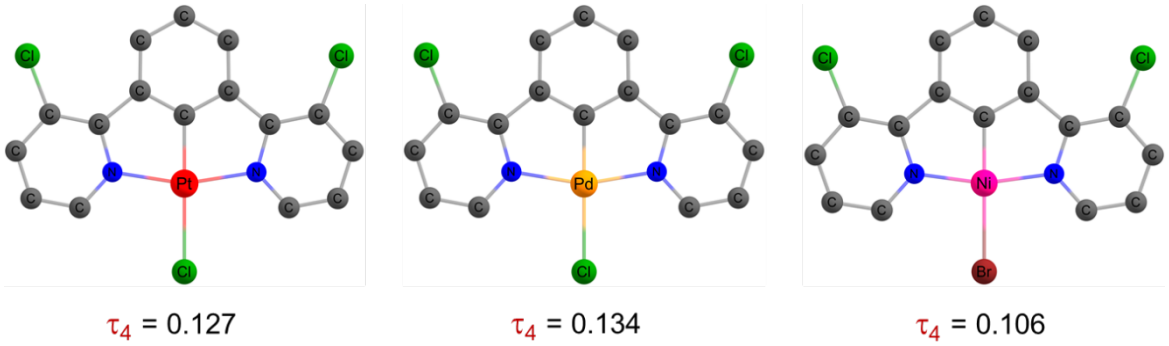


Figure A133. DFT-calculated molecular structures of [M(L^{Cl})X] (M = Pt, Pd, and Ni; X = Cl or Br) in the S_0 ground state, featuring the deviation τ_4 from the square planar coordination (for perfect square planar, $\tau_4 = 0$; for perfect tetrahedral $\tau_4 = 1$).

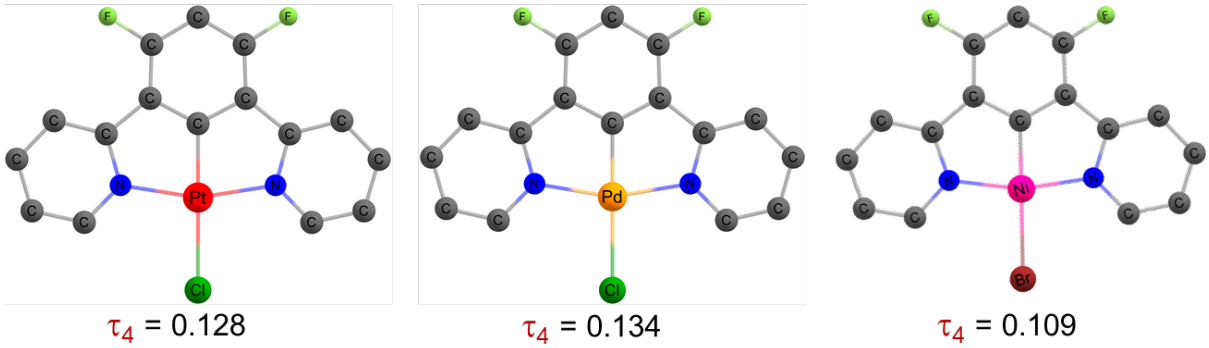


Figure A134. DFT-calculated molecular structures of [M(L^{F})X] (M = Pt, Pd, and Ni; X = Cl or Br) in the S_0 ground state, featuring the deviation τ_4 from the square planar coordination (for perfect square planar, $\tau_4 = 0$; for perfect tetrahedral $\tau_4 = 1$).

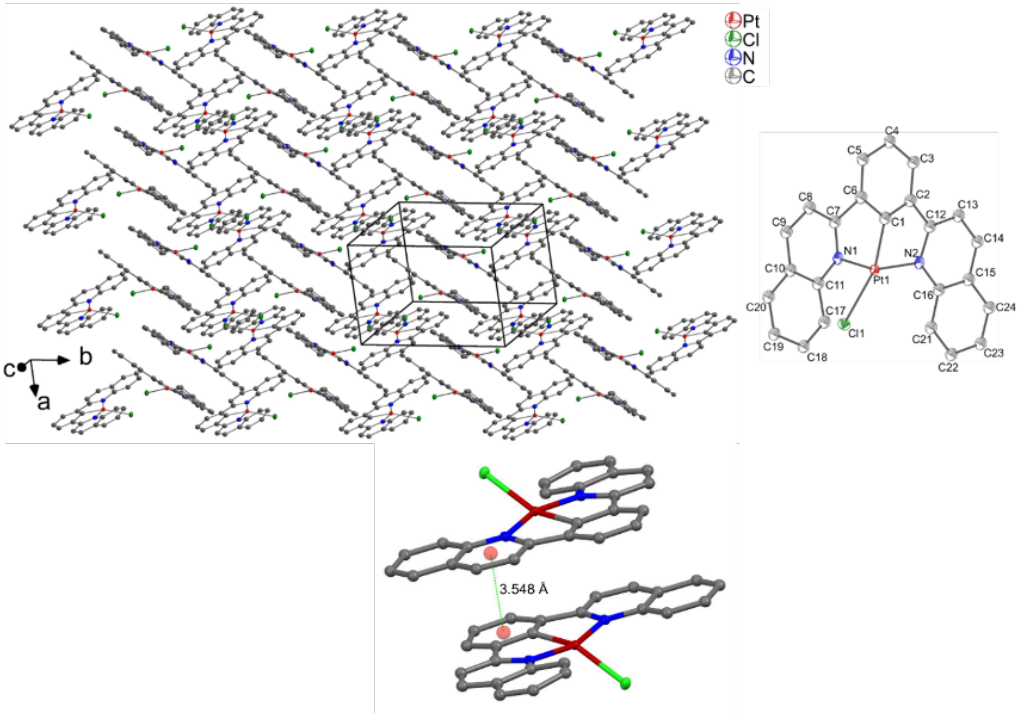


Figure A135. Crystal structure of [Pt(L^{Qu})Cl] from single crystal XRD, viewed along the crystallographic tilted *c* axis (left) and molecular structure with atoms as 50% ellipsoids (right), H atoms omitted for clarity, along with extended view of the packing of the complex showing the intermolecular interactions (down).

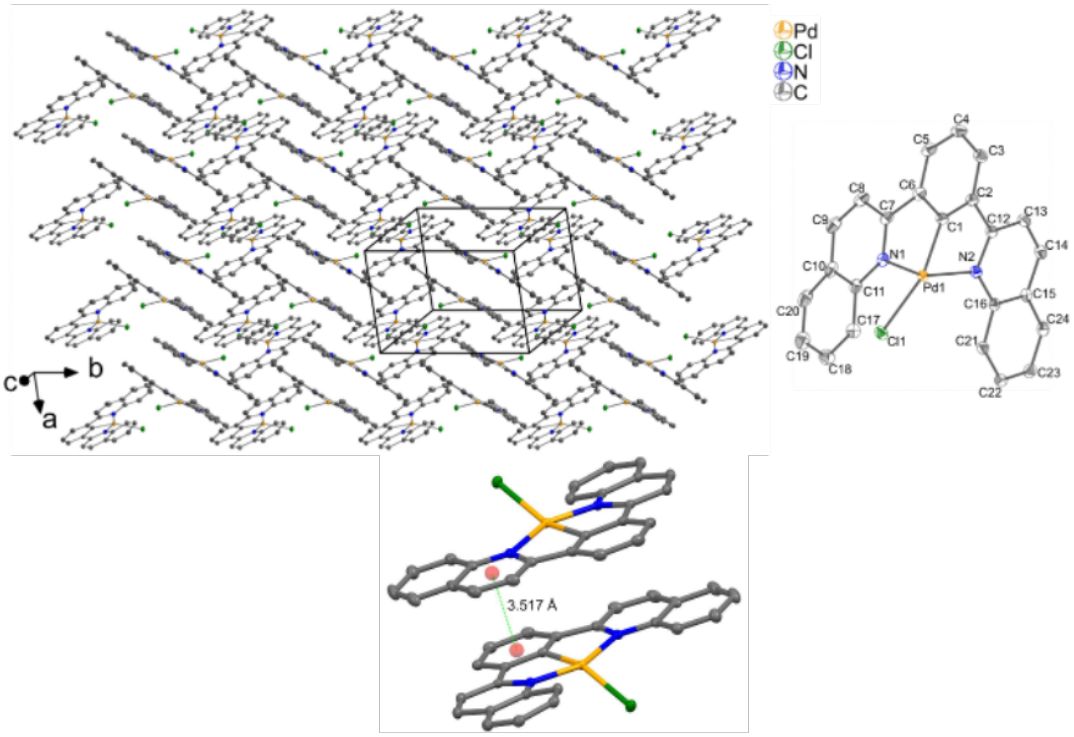


Figure A136. Crystal structure of [Pd(L^{Qu})Cl] from single crystal XRD, viewed along the crystallographic tilted *c* axis (left) and molecular structure with atoms as 50% ellipsoids (right), H atoms omitted for clarity, along with extended view of the packing of the complex showing the intermolecular interactions (down).

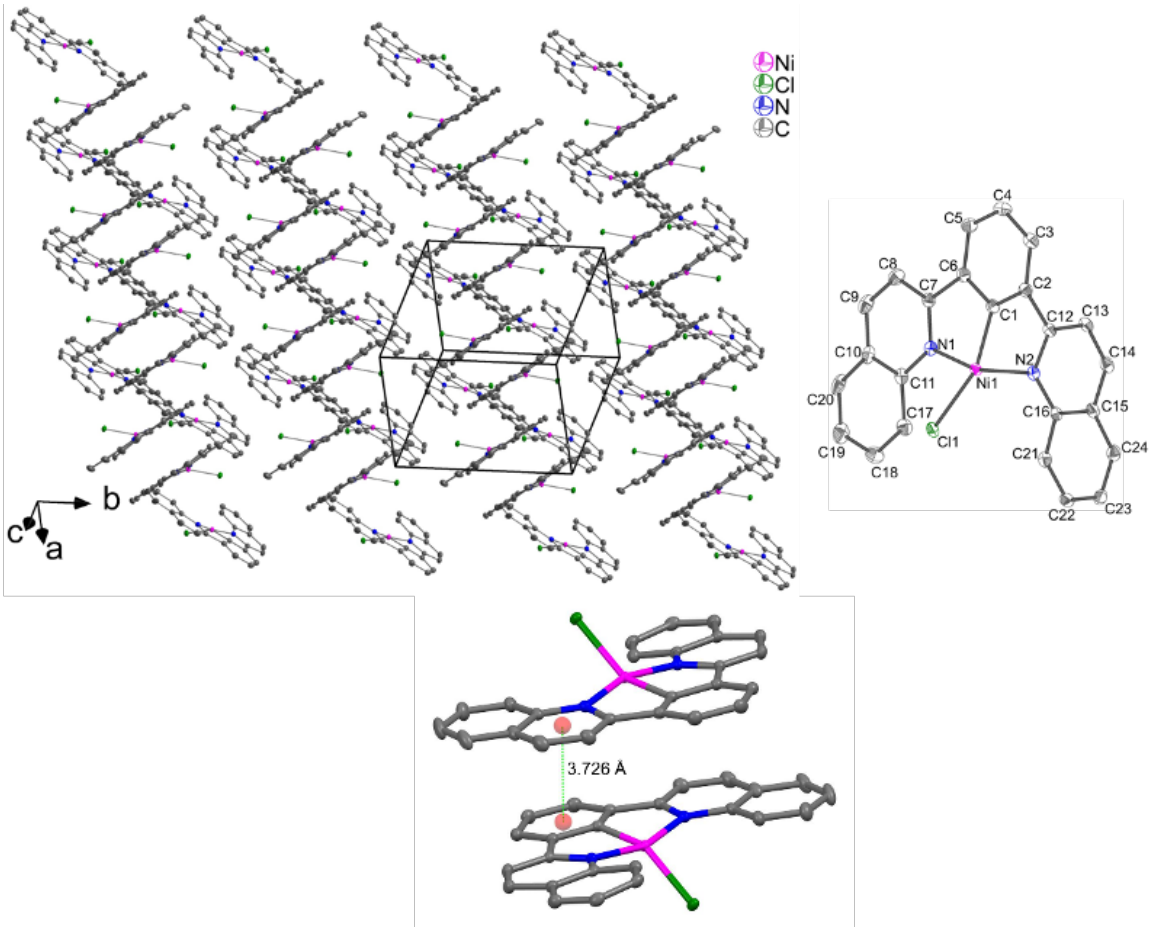


Figure A137. Crystal structure of [Ni(L^{Qu})Cl] from single crystal XRD, viewed along the crystallographic tilted *c* axis (left) and molecular structure with atoms as 50% ellipsoids (right), H atoms omitted for clarity, along with extended view of the packing of the complex showing the intermolecular interactions (down).

Table A1. Crystal data and structure refinement for the [M(N^C^N)Cl] (M = Pt or Pd; N^C^N = L^{NHPh} or L^{NHBn}) and HL^{NHPh}.[a]

	[Pt(L^{NHPh})Cl]	[Pd(L^{NHPh})Cl]	[Pt(L^{NHBn})Cl]	[Pd(L^{NHBn})Cl]	HL^{NHPh}
Empirical formula	$C_{28}H_{21}ClN_4Pt$	$C_{28}H_{21}ClN_4Pd$	$C_{30}H_{25}ClN_4Pt$	$C_{30}H_{25}ClN_4d$	$C_{28}H_{22}N_4$
Formula weight	644.03	555.37	672.09	583.39	414.51
Temperature/K	293(2)	293(2)	100(2)	293(2)	100(2)
Crystal system	monoclinic	monoclinic	monoclinic	monoclinic	orthorhombic
Space group	$P2_1/n$	$P2_1/c$	$C2/c$	$C2/c$	$Ccm2_1$
a/Å	16.805(2)	16.7442(1)	27.9688(2)	28.000(4)	6.5671(5)
b/Å	8.1951(6)	8.0798(1)	10.5896(6)	10.5717(19)	42.579(4)
c/Å	17.427(2)	21.1724(1)	19.6701(1)	24.154(3)	7.3162(6)
α/°	90	90	90	90	90
β/°	103.581(11)	127.405(1)	122.413(2)	136.264(6)	90
γ/°	90	90	90	90	90
Volume/Å^3	2333.0(5)	2275.37(1)	4918.2(5)	4942.9(1)	2045.8(3)
Z	4	4	8	8	4
ρ_{calc} g/cm^3	1.834	1.621	1.815	1.568	1.346
μ/mm^{-1}	6.154	0.959	5.841	0.886	0.081
F(000)	1248.0	1117.0	2616.2	2368.0	872.3
Crystal size/mm^3	0.3 × 0.2 × 0.1	0.3 × 0.2 × 0.1	0.4 × 0.1 × 0.08	0.3 × 0.2 × 0.1	0.4 × 0.4 × 0.1
2Θ range for data collection/°	3.848 to 53.436	3.84 to 52	4.22 to 56.58	3.44 to 53.574	3.82 to 56.56
Index ranges	–21 ≤ h ≤ 21, –9 ≤ k ≤ 10, –20 ≤ l ≤ 22	–22 ≤ h ≤ 22, –9 ≤ k ≤ 11, –29 ≤ l ≤ 29	–37 ≤ h ≤ 33, –13 ≤ k ≤ 14, –22 ≤ l ≤ 26	–35 ≤ h ≤ 32, –13 ≤ k ≤ 13, –28 ≤ l ≤ 30	–8 ≤ h ≤ 8, –56 ≤ k ≤ 55, –9 ≤ l ≤ 8
Reflections collected	26093	36791	34321	31593	10282
Independent reflections	4928 [R_{int} = 0.0929, R_{sigma} = 0.0579]	4464 [R_{int} = 0.1348, R_{sigma} = 0.0685]	6003 [R_{int} = 0.0358, R_{sigma} = 0.0235]	5259 [R_{int} = 0.1554, R_{sigma} = 0.0834]	2378 [R_{int} = 0.0543, R_{sigma} = 0.0445]
Data/restraints/parameters	4928/0/308	4464/0/329	6003/0/325	5259/0/426	2378/1/194
Goodness-of-fit on F^2	1.029	1.030	1.024	1.006	1.049
Final R indexes [I>=2σ (I)]	R_1 = 0.0451, wR_2 = 0.1041	R_1 = 0.0423, wR_2 = 0.0934	R_1 = 0.0199, wR_2 = 0.0445	R_1 = 0.0452, wR_2 = 0.0994	R_1 = 0.0502, wR_2 = 0.1188
Final R indexes [all data]	R_1 = 0.0828, wR_2 = 0.1283	R_1 = 0.0647, wR_2 = 0.1060	R_1 = 0.0227, wR_2 = 0.0458	R_1 = 0.0785, wR_2 = 0.1144	R_1 = 0.0539, wR_2 = 0.1217
Largest diff. peak/hole / e Å^{-3}	1.28/–1.28	0.91/–1.22	1.86/–0.98	1.06/–1.05	0.30/–0.40
CCDC	2194596	2195590	2195363	2194597	2194775

[a] From X-ray diffraction on single crystals, measured using MoKα (λ = 0.71073) radiation.

Table A2. Selected experimental and DFT-calculated geometries for [M(L^{NHPh})Cl] (M = Pt or Pd).[a]

	[Pt(L^{NHPh})Cl]			[Pd(L^{NHPh})Cl]		
	XRD	DFT [a]		XRD	DFT [a]	
bond lengths / Å		S_0	T_1		S_0	T_1
M–C1	1.914(1)	1.920	1.924	1.912(5)	1.924	1.924
M–N1	2.087(8)	2.110	2.109	2.108(4)	2.145	2.121
M–N2	2.074(7)	2.110	2.109	2.101(5)	2.145	2.148
M–Cl	2.483(3)	2.603	2.617	2.496(2)	2.575	2.587
Cl···H1	2.235(3)	2.102	2.094	2.264(5)	2.115	2.076
Cl···H2	2.319(3)	2.102	2.094	2.322(4)	2.115	2.131
angles / °						
C1–M–Cl	162.6(3)	161.6	163.7	160.1(1)	161.7	162.9
C1–M–N1	80.1(4)	80.1	80.2	79.6(2)	79.5	80.1
C1–M–N2	80.0(3)	80.1	80.2	80.0(2)	79.5	79.5
N1–M–N2	159.0(3)	159.4	159.8	158.2(2)	157.9	158.6
N1–M–Cl	101.7(3)	100.3	100.1	99.8(1)	101.1	99.4
N2–M–Cl	99.3(2)	100.3	100.1	102.0(1)	101.1	102.1
N3–H1···Cl	162.4(6)	169.9	171.2	149.6(5)	172.0	172.1
N4–H2···Cl	144.0(7)	169.9	171.2	162.4(5)	172.0	174.1
M–N1–C7–C6	2.2(1)	3.2	4.0	5.4(3)	3.3	5.4
M–N2–C12–C2	–4.8(1)	–3.2	–4.0	–2.3(3)	–3.3	–3.0
M–C1–C6–C7	–7.8(1)	–7.7	–5.8	–11.8(4)	–8.2	–5.1
M–C1–C2–C12	11.9(1)	7.7	5.8	7.6(4)	8.2	6.8
τ_4	0.272	0.277	0.259	0.296	0.287	0.273

[a] DFT calculations on TPSSh/6-31G(d)/LanL2DZ ecp/CPCM(THF) level of theory.

Table A3. Selected experimental and DFT-calculated geometries for [M(L^{NHBn})Cl] (M = Pt or Pd).[a]

	[Pt(L^{NHBn})Cl]			[Pd(L^{NHBn})Cl]		
	XRD	DFT [a]		XRD	DFT [a]	
bond lengths / Å		S_0	T_1		S_0	T_1
M–C1	1.900(2)	1.924	1.900	1.914(4)	1.927	1.925
M–N1	2.086(2)	2.119	2.110	2.139(4)	2.155	2.158
M–N2	2.092(2)	2.119	2.110	2.121(4)	2.154	2.130
M–Cl	2.481(6)	2.576	2.570	2.489(1)	2.567	2.575
Cl···H1	2.316(3)	2.101	2.120	2.34(8)	2.104	2.117
Cl···H2	2.379(2)	2.101	2.120	2.38(4)	2.115	2.093
angles / °						
C1–M–Cl	166.8(1)	165.9	162.1	166.7(2)	166.0	167.4
C1–M–N1	80.2(1)	80.0	80.3	79.4(2)	79.4	79.3
C1–M–N2	80.1(1)	80.0	80.3	79.8(2)	79.4	80.0
N1–M–N2	159.5(1)	159.4	159.7	158.2(2)	157.9	158.5
N1–M–Cl	99.4(1)	100.3	100.2	101.6(1)	101.3	101.9
N2–M–Cl	101.1(1)	100.3	100.2	100.2(1)	100.7	99.5
N3–H1···Cl	141.8(3)	163.2	161.7	173.0(8)	169.2	170.3
N4–H2···Cl	131.7(3)	163.2	161.7	162.0(7)	165.3	163.5
M–N1–C7–C6	4.0(2)	2.7	4.8	1.6(7)	1.9	2.0
M–N2–C12–C2	–1.0(3)	–2.7	–4.8	–4.0(7)	–3.2	–4.2
M–C1–C6–C7	–8.6(3)	–6.3	1.0	–6.4(9)	–6.8	–5.8
M–C1–C2–C12	6.9(3)	6.3	–1.0	7.9(8)	6.9	4.4
τ_4	0.239	0.246	0.271	0.250	0.256	0.242

[a] DFT calculations on TPSSh/6-31G(d)/LanL2DZ ecp/CPCM(THF) level of theory.

Table A4. Selected DFT-calculated geometries for [M(L^{NHPh})F] (M = Pt or Pd) in the S_0 ground state.[a]

	[Pt(L^{NHPh})F]	[Pd(L^{NHPh})F]
bond lengths / Å	S_0	S_0
M–C1	1.910	1.912
M–N1	2.080	2.102
M–N2	2.081	2.102
M–F	2.139	2.113
F···H1	1.610	1.609
F···H2	1.610	1.609
angles / °		
C1–M–F	179.0	180.0
C1–M–N1	80.8	80.3
C1–M–N2	80.8	80.3
N1–M–N2	161.5	160.6
N1–M–F	99.2	99.7
N2–M–F	99.3	99.7
N3–H1···F	171.8	172.8
N4–H2···F	171.4	172.8
M–N1–C7–C6	3.1	3.8
M–N2–C12–C2	3.0	3.7
M–C1–C6–C7	–0.8	–0.2
M–C1–C2–C12	0.6	–0.2
τ_4	0.138	0.138

[a] DFT calculations on TPSSh/6-31G(d)/LanL2DZ ecp/CPCM(THF) level of theory.

Table A5. Selected DFT-calculated geometries for [M(L^{NHPh})H] (M = Pt or Pd) in the S_0 ground state.[a]

	[Pt(L^{NHPh})H]	[Pd(L^{NHPh})H]
bond lengths / Å	S_0	S_0
M–C1	1.959	1.959
M–N1	2.087	2.110
M–N2	2.087	2.110
M–H	1.735	1.736
H···H1	1.657	1.653
H···H2	1.657	1.653
angles / °		
C1–M–H	178.2	177.8
C1–M–N1	79.6	79.1
C1–M–N2	79.6	79.1
N1–M–N2	159.2	158.2
N1–M–H	100.4	100.9
N2–M–H	100.4	100.9
N3–H1···H	163.1	165.0
N4–H2···H	163.1	165.0
M–N1–C7–C6	1.3	1.4
M–N2–C12–C2	–1.3	–1.4
M–C1–C6–C7	–0.8	–1.0
M–C1–C2–C12	0.8	1.0
τ_4	0.160	0.170

[a] DFT calculations on TPSSh/6-31G(d)/LanL2DZ ecp/CPCM(THF) level of theory.

Table A6. Selected DFT-calculated geometries for [M(L^{OMe})Cl] (M = Pt or Pd) in the S_0 ground state.[a]

	[Pt(L^{OMe})Cl]	[Pt(L^{OMe})Cl]
bond lengths / Å	S_0	S_0
M–C1	1.926	1.928
M–N1	2.101	2.124
M–N2	2.101	2.124
M–Cl	2.525	2.529
angles / °		
C1–M–Cl	162.0	154.8
C1–M–N1	79.6	79.0
C1–M–N2	79.6	79.0
N1–M–N2	158.4	156.5
N1–M–Cl	100.8	101.7
N2–M–Cl	100.8	101.7
M–N1–C7–C6	4.8	6.0
M–N2–C12–C2	–4.8	–6.0
M–C1–C6–C7	–7.1	–9.8
M–C1–C2–C12	7.1	9.8
τ_4	0.281	0.345

[a] DFT calculations on TPSSh/6-31G(d)/LanL2DZ ecp/CPCM(THF) level of theory.

Table A7. Crystal data and structure refinement for [Ni(N^C^N)Cl] (N^C^N = L^{NHPh} and L^{NHBn}).[a]

	[Ni(L^{NHPh})Cl]	[Ni(L^{NHBn})Cl]
Empirical formula	$C_{28}H_{21}ClN_4Ni$	$C_{30}H_{25}ClN_4Ni$
Formula weight	507.652	535.706
Temperature/K	100(2)	100(2)
Crystal system	monoclinic	monoclinic
Space group	$P2_1/n$	$P2_1/n$
a/Å	16.5402(2)	16.7842(1)
b/Å	8.0937(8)	26.3802(2)
c/Å	17.2587(2)	18.1847(1)
α/°	90	90
β/°	105.007(3)	116.691(3)
γ/°	90	90
Volume/Å^3	2231.6(4)	7193.7(9)
Z	4	12
ρ_{calc} g/cm^3	1.511	1.484
μ/mm^{-1}	1.015	0.949
F(000)	1048.0	3336.0
Crystal size/mm^3	0.1 × 0.02 × 0.02	0.4 × 0.4 × 0.2
2Θ range for data collection/°	4.88 to 53.464	3.978 to 54.202
Index ranges	$-20 \le h \le 20$, $-10 \le k \le 10$, $-21 \le l \le 21$	$-21 \le h \le 21$, $-33 \le k \le 33$, $-23 \le l \le 23$
Reflections collected	58685	193511
Independent reflections	4729 [R_{int} = 0.1310, R_{sigma} = 0.0566]	15873 [R_{int} = 0.0967, R_{sigma} = 0.0396]
Data/restraints/parameters	4729/0/307	15873/0/973
Goodness-of-fit on F^2	1.025	1.107
Final R indexes [I>=2σ (I)]	R_1 = 0.0468, wR_2 = 0.0988	R_1 = 0.0536, wR_2 = 0.1292
Final R indexes [all data]	R_1 = 0.0783, wR_2 = 0.1166	R_1 = 0.0674, wR_2 = 0.1388
Largest diff. peak/hole / e Å^{-3}	0.57/–0.64	2.06/–0.96
CCDC	2246584	2252984

[a] From X-ray diffraction on single crystals, measured using MoKα (λ = 0.71073) radiation.

Table A8. Experimental and DFT-calculated geometries of the [Ni(N^C^N)Cl] (N^C^N = L^{NHPh} or L^{NHBn}) and [Ni(dpb)Cl] complexes.[a]

	[Ni(L^{NHPh})Cl]			[Ni(L^{NHBn})Cl]			[Ni(dpb)Cl]		
	XRD	DFT [a]		XRD [b]	DFT [a]		XRD [c]	DFT [a]	
bond lengths / Å		S_0	T_1		S_0	T_1		S_0	T_1
M–C1	1.821(4)	1.819	1.930	1.823(3)	1.820	1.932	1.836(7)	1.831	1.951
M–N1	1.987(3)	1.985	2.175	1.990(3)	1.992	2.191	1.932(6)	1.946	2.184
M–N2	1.980(3)	1.985	2.175	1.995(3)	1.993	2.183	1.936(5)	1.946	2.184
M–Cl	2.313(1)	2.397	2.352	2.278(3)	2.379	2.351	2.247(2)	2.292	2.329
Cl···H1	2.418(9)	2.147	2.366	2.479(9)	2.169	2.378	–	–	–
Cl···H2	2.358(8)	2.147	2.366	2.480(9)	2.174	2.414	–	–	–
angles / °									
C1–M–Cl	151.4(1)	149.1	130.2	154.9(1)	152.0	135.9	179.7(2)	179.9	175.7
C1–M–N1	82.0(1)	82.4	79.9	81.9(1)	82.2	79.6	81.6(3)	82.3	78.9
C1–M–N2	82.2(1)	82.4	79.9	82.1(1)	82.3	79.9	82.3(3)	82.3	78.9
N1–M–N2	161.2(1)	161.2	158.8	161.2(9)	161.2	158.4	163.9(2)	164.6	157.7
N1–M–Cl	98.2(9)	99.4	98.8	99.1(7)	99.2	99.7	98.2(2)	97.7	101.1
N2–M–Cl	100.6(1)	99.4	98.8	99.6(7)	99.5	99.7	97.9(2)	97.7	101.1
N3–H1···Cl	130.9(2)	158.8	159.9	125.2(4)	154.0	159.0	–	–	–
N4–H2···Cl	137.8(2)	158.8	159.9	124.3(4)	154.0	155.2	–	–	–
M–N1–C7–C6	6.5(3)	4.5	1.4	6.8(4)	4.7	1.4	0.4(7)	0.0	–0.04
M–N2–C12–C2	–5.1(3)	–4.5	–1.4	–4.9(4)	–3.5	–1.8	–1.5(7)	0.0	0.04
M–C1–C6–C7	–14.1(4)	–11.8	0.5	–10.0	–11.9	–0.2	–0.1(8)	0.001	–1.6
M–C1–C2–C12	10.0(4)	11.8	–0.5	9.9(4)	11.7	0.2	–0.0(8)	–0.001	1.6
τ_4	0.336	0.352	0.501	0.311	0.332	0.466	0.116	0.111	0.189

[a] DFT calculations on TPSSh/6-31G(d)/LanL2DZ ecp/CPCM(THF) level of theory. [b] Averaged values from three independent molecules in the unit cell. [c] From ref. 103.

Table A9. Selected experimental structural data for [Ni(L^{NHBn})Cl].[a]

	XRD [1]	XRD [2]	XRD [3]
bond lengths / Å			
M–C1	1.821(3)	1.826(3)	1.821(3)
M–N1	1.987(3)	2.005(3)	1.978(3)
M–N2	1.990(3)	1.996(3)	1.999(3)
M–Cl	2.278(8)	2.280(8)	2.277(7)
Cl···H1	2.470(9)	2.515(9)	2.453(9)
Cl···H2	2.496(9)	2.457(9)	2.488(9)
angles / °			
C1–M–Cl	154.1(1)	155.2(1)	155.5(1)
C1–M–N1	81.9(1)	81.8(1)	82.1(1)
C1–M–N2	82.2(1)	82.1(1)	82.1(1)
N1–M–N2	161.0(9)	161.2(9)	161.5(9)
N1–M–Cl	98.8(7)	100.0(7)	98.6(7)
N2–M–Cl	100.1(7)	98.8(7)	99.8(7)
N3–H1···Cl	125.9(4)	122.7(4)	127.0(4)
N4–H2···Cl	122.8(4)	126.3(4)	123.9(4)
M–N1–C7–C6	6.2(4)	5.7(4)	8.7(4)
M–N2–C12–C2	–4.1(4)	–5.2(4)	–5.5(4)
M–C1–C6–C7	–11.9(4)	–7.6(4)	–10.5(4)
M–C1–C2–C12	9.5(3)	12.1(4)	8.2(4)
τ_4	0.318	0.309	0.305

[a] Three independent molecules in the unit cell.

Table A10. Selected DFT-calculated geometries of the [Ni(N^C^N)X] Complexes in the S_0 ground state.[a]

	[Ni(L^{NHPh})F]	[Ni(L^{NHPh})H]	[Ni(L^{OMe})Cl]
bond lengths / Å	S_0	S_0	S_0
M–C1	1.817	1.843	1.822
M–N1	1.977	1.970	1.948
M–N2	1.977	1.970	1.948
M–X	1.903	1.590	2.360
X···H1	1.571	1.511	–
X···H2	1.571	1.511	–
angles / °			
C1–M–X	168.7	180.0	141.2
C1–M–N1	82.7	82.2	82.0
C1–M–N2	82.7	82.2	82.0
N1–M–N2	164.4	164.3	160.9
N1–M– X	97.7	97.8	99.5
N2–M– X	97.7	97.8	99.5
N3–H1···X	162.3	157.7	–
N4–H2···X	162.3	157.7	–
M–N1–C7–C6	3.3	2.1	7.8
M–N2–C12–C2	–3.3	2.1	–7.8
M–C1–C6–C7	–6.0	–0.2	–12.0
M–C1–C2–C12	6.0	–0.2	12.0
τ_4	0.190	0.111	0.411

[a] DFT calculations on TPSSh/6-31G(d)/LanL2DZ ecp/CPCM(THF) level of theory.

Table A11. Crystal data and structure refinement for the [M(L^{Bn})Cl] (M = Pt, Pd, and Ni).[a]

	[Pt(L^{Bn})Cl]	[Pd(L^{Bn})Cl]	[Ni(L^{Bn})Cl]
Empirical formula	$C_{30}H_{23}ClN_2Pt$	$C_{30}H_{23}ClN_2Pd$	$C_{30}H_{23}ClN_2Ni$
Formula weight	642.04	553.35	506.66
Temperature/K	100(2)	105(2)	100(2)
Crystal system	triclinic	triclinic	monoclinic
Space group	$P\bar{1}$	$P\bar{1}$	$C2/c$
a/Å	8.9466(4)	8.9694(4)	34.298(2)
b/Å	10.2921(5)	10.2495(4)	7.6309(5)
c/Å	14.5835(7)	14.5659(6)	22.2564(14)
α/°	95.206(2)	95.205(2)	90
β/°	107.337(2)	107.440(2)	122.523(2)
γ/°	113.192(2)	112.952(2)	90
Volume/Å^3	1144.63(10)	1143.06(8)	4911.6(6)
Z	2	2	8
ρ_{calc} g/cm^3	1.863	1.608	1.481
μ/mm^{-1}	6.269	0.951	1.030
F(000)	624.0	560.0	2268.1
Crystal size/mm^3	0.12 × 0.11 × 0.02	0.1 × 0.05 × 0.04	0.32 × 0.13 × 0.04
2Θ range for data collection/°	4.432 to 61.11	4.442 to 52.742	4.34 to 75.6
Index ranges	–12 ≤ h ≤ 12, –14 ≤ k ≤ 14, –20 ≤ l ≤ 20	–11 ≤ h ≤ 11, –12 ≤ k ≤ 12, –18 ≤ l ≤ 18	–58 ≤ h ≤ 58, –13 ≤ k ≤ 13, –38 ≤ l ≤ 38
Reflections collected	41592	17848	158153
Independent reflections	6952 [R_{int} = 0.0500, R_{sigma} = 0.0334]	4626 [R_{int} = 0.0390, R_{sigma} = 0.0337]	13165 [R_{int} = 0.0519, R_{sigma} = 0.0237]
Data/restraints/parameters	6952/0/175	4626/0/235	13165/0/326
Goodness-of-fit on F^2	1.044	1.049	1.028
Final R indexes [I>=2σ (I)]	R_1 = 0.0262, wR_2 = 0.0532	R_1 = 0.0321, wR_2 = 0.0688	R_1 = 0.0384, wR_2 = 0.0957
Final R indexes [all data]	R_1 = 0.0286, wR_2 = 0.0548	R_1 = 0.0355, wR_2 = 0.0707	R_1 = 0.0448, wR_2 = 0.1028
Largest diff. peak/hole / e Å^{-3}	1.72/–1.98	1.28/–0.78	1.79/–1.38
CCDC	2307143	2271328	2258876

[a] From X-ray diffraction on single crystals, measured using MoKα (λ = 0.71073) radiation.

Table A12. Experimental and DFT-calculated geometries of [M(L^{Bn})Cl] (M = Pt, Pd, Ni).[a]

	[Pt(L^{Bn})Cl]			[Pd(L^{Bn})Cl]			[Ni(L^{Bn})Cl]		
	XRD	DFT [a]		XRD	DFT [a]		XRD	DFT [a]	
bond lengths / Å		S_0	T_1		S_0	T_1		S_0	T_1
M–C1	1.907(4)	1.908	1.947	1.907(3)	1.903	2.044	1.811(8)	1.805	1.916
M–N1	2.073(3)	2.087	2.081	2.105(3)	2.112	2.318	1.945(1)	1.955	2.173
M–N2	2.065(2)	2.088	2.081	2.100(2)	2.114	2.330	1.941(1)	1.955	2.173
M–Cl	2.469(9)	2.505	2.446	2.492(8)	2.522	2.414	2.320(3)	2.325	2.273
Cl···H17a	2.512(8)	2.348	2.604	2.562(8)	2.419	2.918	2.505(2)	2.446	2.722
Cl···H24a	2.672(7)	2.664	2.634	2.718(7)	2.375	2.942	2.605(1)	2.446	2.722
angles / °									
C1–M–Cl	152.1(1)	154.0	121.7	150.3(1)	149.4	114.6	138.5(3)	139.2	121.6
C1–M–N1	80.2(1)	80.3	81.3	79.7(1)	79.8	76.7	82.4(5)	82.5	79.9
C1–M–N2	80.4(1)	80.4	80.9	79.7(1)	79.9	76.5	82.4(4)	82.5	79.9
N1–M–N2	158.6(1)	159.5	161.2	156.7(1)	157.8	152.8	159.8(3)	160.5	156.9
N1–M–Cl	103.5(8)	100.6	97.5	104.6(8)	100.9	97.4	102.6(3)	99.6	100.0
N2–M–Cl	97.9(9)	99.5	97.0	98.7(9)	101.1	97.5	97.7(2)	99.8	100.0
C17–H17a···Cl	142.0(1)	153.9	144.6	143.4(1)	155.5	146.1	149.3(1)	149.3	150.4
C24–H24a···Cl	122.2(1)	112.5	134.5	123.1(2)	162.4	144.6	143.7(1)	149.3	150.4
M–N1–C7–C6	3.2(3)	7.1	5.6	3.4(3)	7.4	5.1	5.4(1)	8.3	7.7
M–N2–C12–C2	–7.8(3)	–5.9	–5.9	–9.1(3)	–6.9	–6.0	–9.4(1)	–8.3	–7.7
M–C1–C6–C7	–12.1(4)	–9.9	12.2	–12.2(4)	–10.7	2.6	–15.1(1)	–13.5	–0.3
M–C1–C2–C12	13.5(4)	9.6	–11.6	13.7(4)	10.9	–2.4	17.4(1)	13.5	0.3
τ_4	0.349	0.330	0.547	0.376	0.374	0.657	0.438	0.428	0.578

[a] DFT calculations on TPSSh/def2-TZVP/CPCM(THF) level of theory.

Table A13. Crystal data and structure refinement for the complexes.[a]

	[Pt(L^{NHPh})OPh]	[Pd(L^{NHPh})OPh]	[Pt(L^{NHBn})OPh].$CHCl_3$	[Pd(L^{NHBn})OPh].CH_2Cl_2
Empirical formula	$C_{34}H_{26}N_4OPt$	$C_{34}H_{26}N_4OPd$	$C_{37}H_{31}Cl_3N_4OPt$	$C_{37}H_{32}Cl_2N_4OPd$
Formula weight	701.68	613.027	849.10	725.96
Temperature/K	100.0	100.0	104.0	100.0
Crystal system	monoclinic	triclinic	monoclinic	monoclinic
Space group	*C*2/c	$P\bar{1}$	$P2_1/c$	$P2_1/c$
a/Å	31.064(4)	9.5728(7)	8.8751(10)	8.2845(7)
b/Å	7.0143(8)	15.5830(14)	13.8856(13)	14.3767(12)
c/Å	25.939(4)	18.2332(16)	26.943(3)	26.465(2)
α/°	90	103.748(3)	90	90
β/°	105.462(8)	95.295(3)	96.659(5)	90.213(3)
γ/°	90	90.642(3)	90	90
Volume/$Å^3$	5447.4(12)	2629.2(4)	3297.9(6)	3152.1(5)
Z	8	4	4	4
ρ_{calc} g/cm^3	1.711	1.549	1.710	1.530
μ/mm^{-1}	5.187	0.742	4.535	0.796
F(000)	2752.0	1244.7	1672.0	1480.0
Crystal size/mm^3	0.05 × 0.02 × 0.01	0.06 × 0.04 × 0.026	0.09 × 0.06 × 0.04	0.05 × 0.05 × 0.02
2Θ range for data collection/°	5.442 to 56.702	3.94 to 56.6	4.228 to 56.634	4.184 to 56.636
Index ranges	–41 ≤ h ≤ 41, –9 ≤ k ≤ 9, –34 ≤ l ≤ 34	–12 ≤ h ≤ 12, –20 ≤ k ≤ 20, –24 ≤ l ≤ 24	–11 ≤ h ≤ 11, –18 ≤ k ≤ 18, –32 ≤ l ≤ 35	–11 ≤ h ≤ 11, –19 ≤ k ≤ 19, –35 ≤ l ≤ 35
Reflections collected	117808	179814	56317	215476
Independent reflections	6795 [R_{int} = 0.0557, R_{sigma} = 0.0201]	13078 [R_{int} = 0.0415, R_{sigma} = 0.0166]	8171 [R_{int} = 0.0699, R_{sigma} = 0.0425]	7825 [R_{int} = 0.0846, R_{sigma} = 0.0226]
Data/restraints/parameters	6795/0/295	13078/0/721	8171/0/415	7825/0/414
Goodness-of-fit on F^2	1.089	1.040	1.046	1.120
Final R indexes [I>=2σ (I)]	R_1 = 0.0368, wR_2 = 0.0928	R_1 = 0.0252, wR_2 = 0.0602	R_1 = 0.0367, wR_2 = 0.0796	R_1 = 0.0331, wR_2 = 0.0693
Final R indexes [all data]	R_1 = 0.0425, wR_2 = 0.0957	R_1 = 0.0283, wR_2 = 0.0625	R_1 = 0.0479, wR_2 = 0.0861	R_1 = 0.0425, wR_2 = 0.0732
Largest diff. peak/hole / e $Å^{-3}$	2.94/–1.98	0.51/–0.42	1.56/–1.96	0.56/–0.39
CCDC	2418229	2410716	2384707	2410986

[a] From X-ray diffraction on single crystals, measured using MoKα (λ = 0.71073) radiation.

Table A14. Experimental and DFT-calculated geometries of [M(L^{NHPh})OPh] (M = Pt and Pd).[a]

	[Pt(L^{NHPh})OPh]			[Pd(L^{NHPh})OPh]		
	XRD	DFT [a]		XRD	DFT [a]	
bond lengths / Å		S_0	T_1		S_0	T_1
M–C1	1.910(5)	1.910	1.903	1.909(2)	1.907	1.910
M–N1	2.066(4)	2.079	2.056	2.098(1)	2.099	2.090
M–N2	2.065(5)	2.081	2.088	2.105(1)	2.103	2.093
M–O	2.163(4)	2.185	2.196	2.170(1)	2.170	2.179
O···H1	1.887(4)	1.715	1.675	1.882(2)	1.722	1.721
O···H2	1.807(4)	1.731	1.778	1.864(2)	1.745	1.761
angles / °						
C1–M– O	175.1(2)	175.7	175.3	177.6(1)	175.3	176.2
C1–M–N1	80.6(2)	80.4	81.2	79.9(1)	80.0	80.2
C1–M–N2	80.7()	80.4	80.3	80.1(1)	80.0	80.2
N1–M–N2	160.8(2)	160.4	161.2	160.0(1)	159.4	159.9
N1–M– O	100.2(2)	99.5	97.7	99.5(1)	99.9	99.5
N2–M– O	98.8(2)	99.9	100.9	100.5(1)	100.4	100.3
N3–H1··· O	158.4(3)	170.6	170.4	169.0(2)	171.5	172.1
N4–H2··· O	170.3(3)	163.0	162.2	172.4(1)	164.0	163.4
M–N1–C7–C6	0.8(5)	4.1	4.7	3.9(1)	4.6	4.5
M–N2–C12–C2	0.0(5)	0.5	0.6	2.7(1)	0.7	–0.1
M–C1–C6–C7	–7.0(6)	–5.7	–3.9	–3.1(2)	–6.0	–4.8
M–C1–C2–C12	7.2(6)	4.8	4.6	3.3(2)	5.4	4.1
τ_4	0.171	0.170	0.167	0.159	0.179	0.170

[a] DFT calculations on TPSSh/def2-TZVP/CPCM(THF) level of theory.

Table A15. Experimental and DFT-calculated geometries of [M(L^{NHBn})OPh] (M = Pt and Pd).[a]

	[Pt(L^{NHBn})OPh]		[Pd(L^{NHBn})OPh]		
	XRD	DFT[a]	XRD	DFT [a]	
bond lengths / Å		S_0		S_0	T_1
M–C1	1.906(5)	1.911	1.913(2)	1.907	1.902
M–N1	2.073(3)	2.080	2.102(2)	2.100	2.076
M–N2	2.078(3)	2.082	2.098(2)	2.099	2.101
M–O	2.179(3)	2.187	2.169(2)	2.173	2.182
O···H1	1.902(3)	1.731	1.875(2)	1.744	1.708
O···H2	1.866(3)	1.740	1.909(2)	1.748	1.784
angles / °					
C1–M– O	179.2(2)	176.3	179.4(1)	175.8	176.0
C1–M–N1	80.3(2)	80.4	80.0(1)	80.0	80.6
C1–M–N2	80.4(2)	80.3	80.1(1)	79.9	79.8
N1–M–N2	160.6(1)	160.4	160.0(1)	159.4	160.1
N1–M– O	100.3(1)	99.6	100.2(1)	100.1	98.6
N2–M– O	99.0(1)	99.9	99.7(1)	101.2	101.2
N3–H1··· O	165.7(3)	166.9	170.8(1)	168.0	168.6
N4–H2··· O	162.5(3)	166.8	156.8(1)	167.6	167.8
M–N1–C7–C6	–0.3(4)	–1.9	2.3(3)	0.7	1.9
M–N2–C12–C2	0.4(4)	0.7	–0.2(2)	–2.3	–2.3
M–C1–C6–C7	0.2(5)	5.0	1.2(3)	–5.4	–3.3
M–C1–C2–C12	4.4(5)	–4.9	2.4(3)	5.5	4.9
τ_4	0.143	0.165	0.146	0.176	0.170

[a] DFT calculations on TPSSh/def2-TZVP/CPCM(THF) level of theory.

Table A16. Crystal data and structure refinement for the [M(L^{Me})Cl] (M = Pt, Pd, Ni) and [Ni(L^{Cl})Br].[a]

	[Pt(L^{Me})Cl]	[Pd(L^{Me})Cl]	[Ni(L^{Me})Cl]	[Ni(L^{Cl})Br]	[Pt(L^{F})Cl]
Empirical formula	$C_{18}H_{15}ClN_2Pt$	$C_{18}H_{15}ClN_2Pd$	$C_{18}H_{15}ClN_2Ni$	$C_{16}H_9BrCl_2N_2Ni$	$C_{16}H_9ClF_2N_2Pt$
Formula weight	489.86	401.20	353.48	438.77	497.79
Temperature/K	293(2)	293(2)	100(0)	293(2)	100(2)
Crystal system	orthorhombic	orthorhombic	orthorhombic	triclinic	monoclinic
Space group	*P*bca	*P*bca	*P*bca	$P\bar{1}$	$P2_1/n$
a/Å	12.2247(4)	12.2794(3)	11.8117(8)	8.0719(5)	4.4686(2)
b/Å	13.8495(4)	13.8378(4)	14.0954(9)	9.9861(6)	13.7363(5)
c/Å	17.6942(4)	17.6772(5)	17.9063(10)	18.2862(11)	21.6322(8)
α/°	90	90	90	91.040(5)	90
β/°	90	90	90	97.112(5)	94.8200(10)
γ/°	90	90	90	98.510(5)	90
Volume/Å^3	2995.73(15)	3003.71(14)	2981.2(3)	1445.55(15)	1323.13(9)
Z	8	8	8	4	4
ρ_{calc} g/cm^3	2.172	1.774	1.575	2.016	2.499
μ/mm^{-1}	9.540	1.410	1.477	4.470	10.826
F(000)	1848.0	1593.8	1456.0	864.0	928.0
Crystal size/mm^3	0.15 × 0.03 × 0.01	0.34 × 0.07 × 0.04	0.1 × 0.06 × 0.02	0.3 × 0.2 × 0.1	0.48 × 0.02 × 0.02
2Θ range for data collection/°	5 to 61.06	4.6 to 68.72	5.042 to 56.66	4.126 to 58.386	3.778 to 56.578
Index ranges	$-17 \le h \le 17$, $-19 \le k \le 18$, $-20 \le l \le 25$	$-18 \le h \le 19$, $-17 \le k \le 21$, $-28 \le l \le 28$	$-15 \le h \le 15$, $-18 \le k \le 18$, $-23 \le l \le 23$	$-11 \le h \le 11$, $-13 \le k \le 13$, $-23 \le l \le 25$	$-5 \le h \le 5$, $-18 \le k \le 18$, $-28 \le l \le 28$
Reflections collected	63412	79343	86716	15995	25735
Independent reflections	4577 [R_{int} = 0.0785, R_{sigma} = 0.0318]	6297 [R_{int} = 0.0652, R_{sigma} = 0.0292]	3711 [R_{int} = 0.1258, R_{sigma} = 0.0356]	7450 [R_{int} = 0.0593, R_{sigma} = 0.0759]	3223 [R_{int} = 0.0220, R_{sigma} = 0.0129]
Data/restraints/parameters	4577/0/201	6297/0/201	3711/0/99	7450/0/398	3223/0/199
Goodness-of-fit on F^2	1.023	1.047	1.074	0.990	1.095
Final R indexes [I>=2σ (I)]	R_1 = 0.0279, wR_2 = 0.0507	R_1 = 0.0241, wR_2 = 0.0497	R_1 = 0.0487, wR_2 = 0.1021	R_1 = 0.0442, wR_2 = 0.1013	R_1 = 0.0116, wR_2 = 0.0279
Final R indexes [all data]	R_1 = 0.0403, wR_2 = 0.0573	R_1 = 0.0317, wR_2 = 0.0554	R_1 = 0.0711, wR_2 = 0.1147	R_1 = 0.0947, wR_2 = 0.1326	R_1 = 0.0120, wR_2 = 0.0282
Largest diff. peak/hole / e Å^{-3}	1.41/–1.87	0.63/–0.70	1.11/–0.80	1.54/–1.04	0.47/–0.83
CCDC	2236404	2236405	2333978	2343467	2394238

[a] From X-ray diffraction on single crystals, measured using MoKα (λ = 0.71073) radiation.

Table A17. Experimental and DFT-calculated geometries of [M(L^{Me})Cl] (M = Pt, Pd, and Ni).[a]

	[Pt(L^{Me})Cl]			[Pd(L^{Me})Cl]			[Ni(L^{Me})Cl]		
	XRD	DFT [a]		XRD	DFT [a]		XRD	DFT [a]	
bond lengths / Å		S_0	T_1		S_0	T_1		S_0	T_1
M–C1	1.911(4)	1.912	1.951	1.909(1)	1.904	2.043	1.814(3)	1.806	1.916
M–N1	2.065(4)	2.097	2.075	2.097(1)	2.111	2.309	1.954(3)	1.954	2.168
M–N2	2.073(4)	2.097	2.075	2.105(1)	2.111	2.308	1.966(3)	1.954	2.168
M–Cl	2.448(1)	2.476	2.466	2.465(4)	2.506	2.413	2.276(1)	2.308	2.273
angles / °									
C1–M–Cl	158.8(1)	160.5	114.3	157.0(1)	151.2	116.5	147.0(1)	141.5	120.9
C1–M–N1	80.3(2)	80.2	81.1	79.6(1)	79.8	76.8	82.1(1)	82.4	79.9
C1–M–N2	80.4(2)	80.2	81.1	80.0(1)	79.8	76.8	82.6(1)	82.4	79.9
N1–M–N2	159.6(1)	159.3	161.4	158.2(1)	157.5	153.1	161.0(1)	160.5	156.6
N1–M–Cl	98.2(1)	100.3	96.0	99.2(1)	101.2	98.0	98.2(1)	99.8	100.2
N2–M–Cl	102.2(1)	100.3	96.0	102.6(1)	101.2	98.0	100.7(1)	99.8	100.2
M–N1–C7–C6	9.9(5)	5.8	5.6	11.4(2)	6.8	7.1	12.0(4)	8.0	8.8
M–N2–C12–C2	–1.8(4)	–5.8	–5.9	–2.0(2)	–6.8	–7.1	–3.8(4)	–8.0	–8.2
M–C1–C6–C7	–9.3(5)	–8.4	12.2	–9.5(2)	–11.0	6.4	–12.2(4)	–13.5	–0.9
M–C1–C2–C12	10.2(5)	8.4	–11.6	9.8(2)	11.0	–6.4	12.1(4)	13.5	0.9
τ_4	0.295	0.285	0.547	0.318	0.364	0.641	0.369	0.411	0.585

[a] DFT calculations on TPSSh/def2-TZVP/CPCM(THF) level of theory.

Table A18. DFT-calculated geometries of [M(L^{Me2})Cl] (M = Pt, Pd, and Ni).[a]

	[Pt(L^{Me2})Cl]		[Pd(L^{Me2})Cl]		[Ni(L^{Me2})Cl]	
	DFT [a]		DFT [a]		DFT [a]	
bond lengths / Å	S_0	T_1	S_0	T_1	S_0	T_1
M–C1	1.913	1.961	1.910	2.047	1.809	1.922
M–N1	2.064	2.061	2.076	2.235	1.930	2.104
M–N2	2.064	2.061	2.076	2.235	1.930	2.104
M–Cl	2.512	2.469	2.525	2.425	2.323	2.285
angles / °						
C1–M–Cl	150.5	114.0	147.0	115.3	138.2	119.1
C1–M–N1	81.1	81.6	80.6	78.2	83.1	81.1
C1–M–N2	81.1	81.6	80.6	78.2	83.1	81.1
N1–M–N2	160.2	162.6	158.1	155.9	160.4	158.3
N1–M–Cl	99.9	95.3	100.9	97.3	99.8	99.7
N2–M–Cl	99.9	95.3	100.9	97.3	99.8	99.7
M–N1–C7–C6	5.2	7.7	5.5	15.3	7.6	13.5
M–N2–C12–C2	–5.2	–7.7	–5.5	–15.3	–7.6	–13.5
M–C1–C6–C7	–11.9	13.8	–13.4	17.1	–14.6	5.3
M–C1–C2–C12	11.9	–13.8	13.4	–17.0	14.6	–5.3
τ_4	0.350	0.591	0.389	0.630	0.435	0.586

[a] DFT calculations on TPSSh/def2-TZVP/CPCM(THF) level of theory.

Table A19. Experimental and DFT-calculated geometries for [M(L^{Cl})X] (M = Pt, Pd, and Ni; X = Cl or Br).[a, b]

	[Pt(L^{Cl})Cl]		[Pd(L^{Cl})Cl]		[Ni(L^{Cl})Br]		
	DFT [a]		DFT [a]		XRD [b]	DFT [a]	
bond lengths / Å	S_0	T_1	S_0	T_1		S_0	T_1
M–C1	1.907	1.884	1.905	1.882	1.845(6)	1.821	1.934
M–N1	2.035	2.047	2.045	2.063	1.940(4)	1.942	2.141
M–N2	2.035	2.047	2.045	2.028	1.935(4)	1.942	2.142
M–X	2.448	2.415	2.439	2.423	2.393(1)	2.426	2.444
angles / °							
C1–M–X	180.0	180.0	180.0	179.5	176.4(2)	180.0	171.3
C1–M–N1	81.0	82.1	80.6	80.7	82.8(2)	82.4	79.5
C1–M–N2	81.0	82.1	80.6	81.7	82.3(2)	82.4	79.5
N1–M–N2	162.1	164.2	161.1	162.4	164.9(2)	164.7	158.3
N1–M–X	99.0	97.9	99.4	98.8	97.5(1)	97.6	100.8
N2–M–X	99.0	97.9	99.4	98.8	97.7(1)	97.6	100.8
M–N1–C7–C6	0.0	0.0	0.0	0.0	3.3(6)	0.0	8.9
M–N2–C12–C2	–0.0	–0.0	–0.0	–0.0	–0.8(6)	–0.0	–8.9
M–C1–C6–C7	–0.0	–0.0	–0.0	0.0	–1.2(7)	–0.0	7.4
M–C1–C2–C12	0.0	0.0	0.0	–0.0	1.1(7)	0.0	–7.4
τ_4	0.127	0.112	0.134	0.128	0.133	0.106	0.216

[a] DFT calculations on TPSSh/def2-TZVP/CPCM(THF) level of theory. [b] Averaged values from two independent molecules in the unit cell.

Table A20. Experimental structural data for [Ni(L^{Cl})Br].[a]

	XRD [1]	XRD [2]
bond lengths / Å		
M–C1	1.825(5)	1.864(6)
M–N1	1.939(4)	1.941(1)
M–N2	1.925(4)	1.945(1)
M–X	2.394(1)	2.391(1)
angles / °		
C1–M–X	174.7(2)	178.1(2)
C1–M–N1	82.7(2)	82.9(2)
C1–M–N2	82.2(2)	82.3(2)
N1–M–N2	164.7(2)	165.1(2)
N1–M–X	97.4(1)	97.5(1)
N2–M–X	97.9(1)	97.4(2)
M–N1–C7–C6	4.4(6)	2.2(6)
M–N2–C12–C2	–0.8(6)	–0.8(6)
M–C1–C6–C7	–0.3(7)	–1.4(6)
M–C1–C2–C12	0.7(7)	1.5(6)
τ_4	0.146	0.119

[a] Two independent molecules in the unit cell.

Table A21. Experimental and DFT-calculated geometries for [M(L^F)X] (M = Pt, Pd, and Ni; X = Cl or Br).[a]

	[Pt(L^F)Cl]				[Pd(L^F)Cl]		[Ni(L^F)Br]	
	XRD	XRD [b]	DFT [a]		DFT [a]		DFT [a]	
bond lengths / Å			S_0	T_1	S_0	T_1	S_0	T_1
M–C1	1.908(2)	1.910(6)	1.911	1.893	1.910	1.895	1.826	1.948
M–N1	2.032(2)	2.043(5)	2.042	2.021	2.056	2.029	1.948	2.150
M–N2	2.034(2)	2.028(5)	2.042	2.058	2.056	2.067	1.948	2.150
M–X	2.393(1)	2.413(2)	2.437	2.425	2.426	2.420	2.408	2.437
angles / °								
C1–M–X	178.3(1)	173.8(2)	180.0	179.7	180.0	179.7	180.0	180.0
C1–M–N1	80.9(1)	81.4(2)	80.9	82.2	80.5	81.5	82.4	79.4
C1–M–N2	81.0(1)	80.8(2)	80.9	80.9	80.5	80.3	82.4	79.4
N1–M–N2	161.9(1)	162.1(2)	161.9	163.1	161.1	161.9	164.7	158.8
N1–M–X	99.1(1)	98.6(2)	99.1	98.0	99.5	98.8	97.6	100.6
N2–M–X	99.1(1)	99.0(2)	99.1	98.8	99.5	99.4	97.6	100.6
M–N1–C7–C6	–0.2(2)	–0.5(4)	0.0	–0.0	0.0	–0.0	0.0	0.0
M–N2–C12–C2	1.8(2)	–0.9(4)	0.0	0.0	0.0	0.0	0.0	0.0
M–C1–C6–C7	0.8(2)	1.5(5)	–0.0	–0.0	0.0	–0.0	0.0	0.0
M–C1–C2–C12	–1.1(2)	–5.4(5)	0.0	0.0	–0.0	–0.0	0.0	0.0
τ_4	0.140	0.171	0.128	0.122	0.134	0.130	0.109	0.150

[a] DFT calculations on TPSSh/def2-TZVP/CPCM(CH_2Cl_2) level of theory. [b] From ref 64.

Table A22. Crystal data and structure refinement for the [M(L^{Qu})Cl] (M = Pt, Pd, Ni).[a]

	[Pt(L^{Qu})Cl]	[Pd(L^{Qu})Cl]	[Ni(L^{Qu})Cl]
Empirical formula	$C_{24}H_{15}ClN_2Pt$	$C_{24}H_{15}ClN_2Pd$	$C_{24}H_{15}ClN_2Ni$
Formula weight	561.92	473.268	425.54
Temperature/K	100(2)	100(2)	100(2)
Crystal system	monoclinic	monoclinic	monoclinic
Space group	$P2_1/c$	$P2_1/c$	$P2_1/c$
a/Å	9.5087(4)	9.4854(7)	9.5913(4)
b/Å	12.9911(5)	13.0563(11)	12.4899(5)
c/Å	14.6122(6)	14.5885(12)	14.9938(6)
α/°	90	90	90
β/°	101.547(2)	102.471(3)	95.7960(10)
γ/°	90	90	90
Volume/Å^3	1768.49(12)	1764.1(3)	1786.99(13)
Z	4	4	4
ρ_{calc} g/cm^3	2.110	1.782	1.582
μ/mm^{-1}	8.098	1.216	1.247
F(000)	1072.0	941.0	872.0
Crystal size/mm^3	0.16 × 0.01 × 0.01	0.08 × 0.06 × 0.05	0.16 × 0.08 × 0.05
2Θ range for data collection/°	4.234 to 56.59	4.24 to 56.58	4.254 to 56.558
Index ranges	$-12 \le h \le 12$, $-17 \le k \le 17$, $-19 \le l \le 19$	$-12 \le h \le 11$, $-17 \le k \le 17$, $-19 \le l \le 19$	$-12 \le h \le 12$, $-16 \le k \le 16$, $-19 \le l \le 19$
Reflections collected	36433	41959	63244
Independent reflections	4396 [R_{int} = 0.0760, R_{sigma} = 0.0407]	4353 [R_{int} = 0.0448, R_{sigma} = 0.0224]	4419 [R_{int} = 0.0656, R_{sigma} = 0.0245]
Data/restraints/parameters	4396/0/109	4353/0/253	4419/0/253
Goodness-of-fit on F^2	1.075	1.045	1.094
Final R indexes [I>=2σ (I)]	R_1 = 0.0357, wR_2 = 0.0713	R_1 = 0.0199, wR_2 = 0.0481	R_1 = 0.0364, wR_2 = 0.0809
Final R indexes [all data]	R_1 = 0.0486, wR_2 = 0.0780	R_1 = 0.0220, wR_2 = 0.0503	R_1 = 0.0438, wR_2 = 0.0855
Largest diff. peak/hole / e Å^{-3}	2.01/–1.49	0.49/–0.57	0.70/–0.50
CCDC	2343058	2350065	2343468

[a] From X-ray diffraction on single crystals, measured using MoKα (λ = 0.71073) radiation.

Table A23. Experimental and DFT-calculated geometries of [M(L^{Qu})Cl] (M = Pt, Pd, Ni).[a]

	[Pt(L^{Qu})Cl]			[Pd(L^{Qu})Cl]			[Ni(L^{Qu})Cl]		
	XRD	DFT [a]		XRD	DFT [a]		XRD	DFT [a]	
bond lengths / Å		S_0	T_1		S_0	T_1		S_0	T_1
M–C1	1.916(6)	1.907	1.923	1.909(2)	1.904	2.038	1.824(2)	1.807	1.917
M–N1	2.080(5)	2.088	2.065	2.122(2)	2.115	2.325	1.985(2)	1.961	2.182
M–N2	2.091(5)	2.088	2.065	2.106(2)	2.115	2.326	1.975(2)	1.962	2.182
M–Cl	2.438(1)	2.479	2.440	2.452(5)	2.477	2.405	2.275(1)	2.279	2.259
Cl···H17	2.573(2)	2.456	3.046	2.516(2)	2.487	3.408	2.585(1)	2.602	3.064
Cl···H21	2.491(2)	2.456	3.046	2.622(2)	2.487	3.500	2.707(1)	2.603	3.064
angles / °									
C1–M–Cl	158.0(2)	157.7	119.7	157.2(5)	155.8	113.2	149.3(1)	146.3	123.8
C1–M–N1	79.9(2)	80.0	81.2	79.6(7)	79.4	76.4	81.9(1)	82.1	79.5
C1–M–N2	79.9(2)	80.0	81.2	79.3(7)	79.4	76.3	81.5(1)	82.1	79.5
N1–M–N2	159.0(2)	159.2	162.1	157.6(6)	157.2	152.3	160.8(1)	160.7	156.3
N1–M–Cl	99.0(2)	100.3	95.6	102.4(4)	101.4	97.4	100.8(1)	99.6	100.3
N2–M–Cl	101.9(2)	100.4	95.6	99.9(4)	101.4	97.5	98.4(1)	99.7	100.4
C17–H17··· Cl	125.3(3)	131.0	114.4	140.5(2)	133.3	117.6	125.4(1)	120.0	119.6
C17–H21··· Cl	138.0(3)	131.1	114.4	124.9(2)	133.3	117.6	115.2(1)	120.0	119.6
τ_4	0.305	0.306	0.555	0.321	0.333	0.670	0.354	0.376	0.567

[a] DFT calculations on TPSSh/def2-TZVP/CPCM(THF) level of theory.

7.4. Electrochemistry and DFT-calculated frontier molecular orbitals data

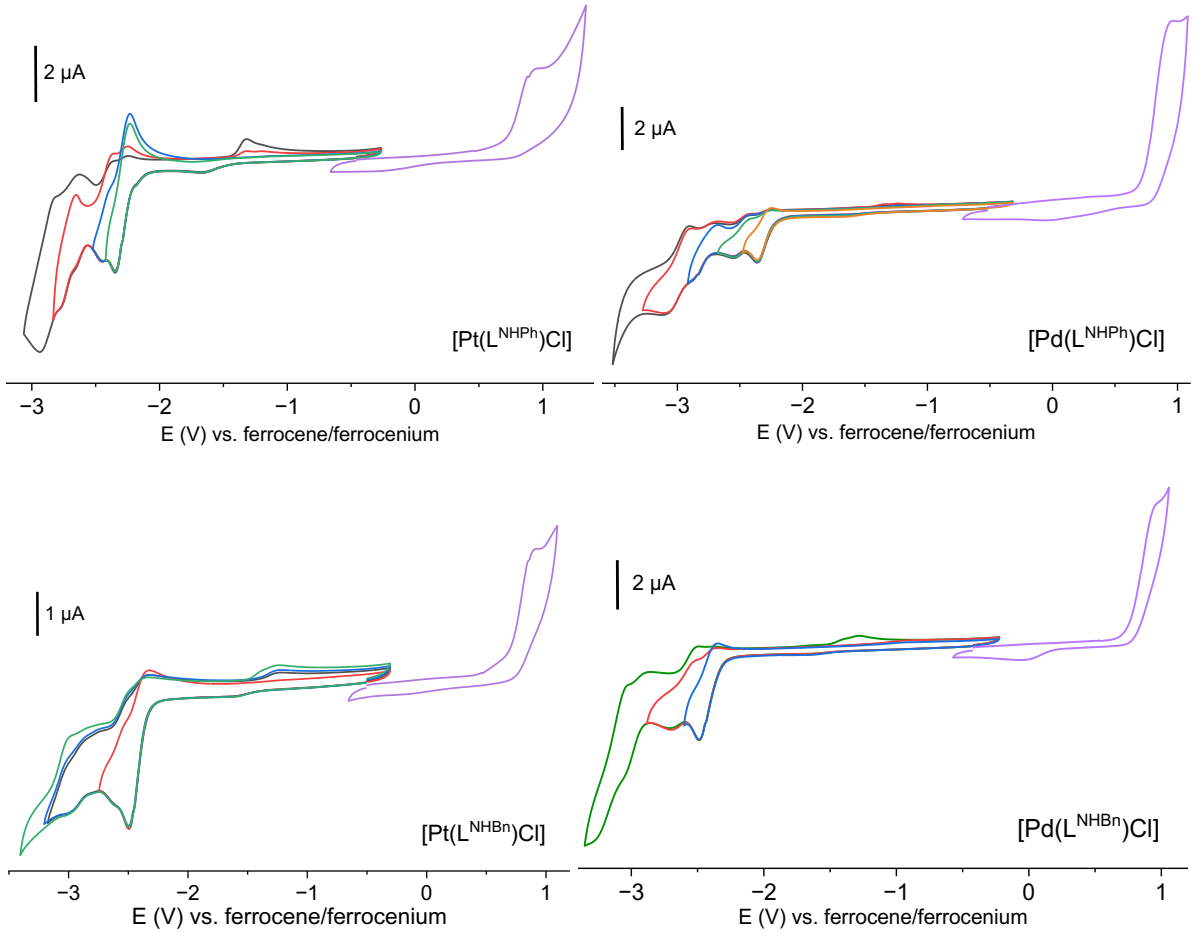


Figure A138. Cyclic voltammograms of the complexes [M(N^C^N)Cl] (M = Pt or Pd) in *n*-Bu_4NPF_6/THF.

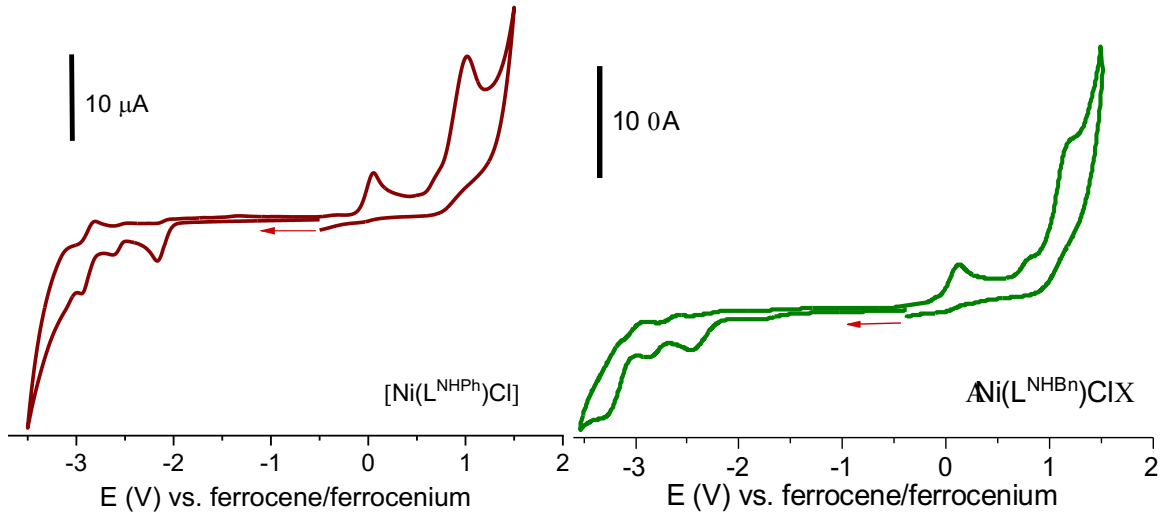


Figure A139. Cyclic voltammograms of the complexes [Ni(N^C^N)Cl] in *n*-Bu_4NPF_6/THF.

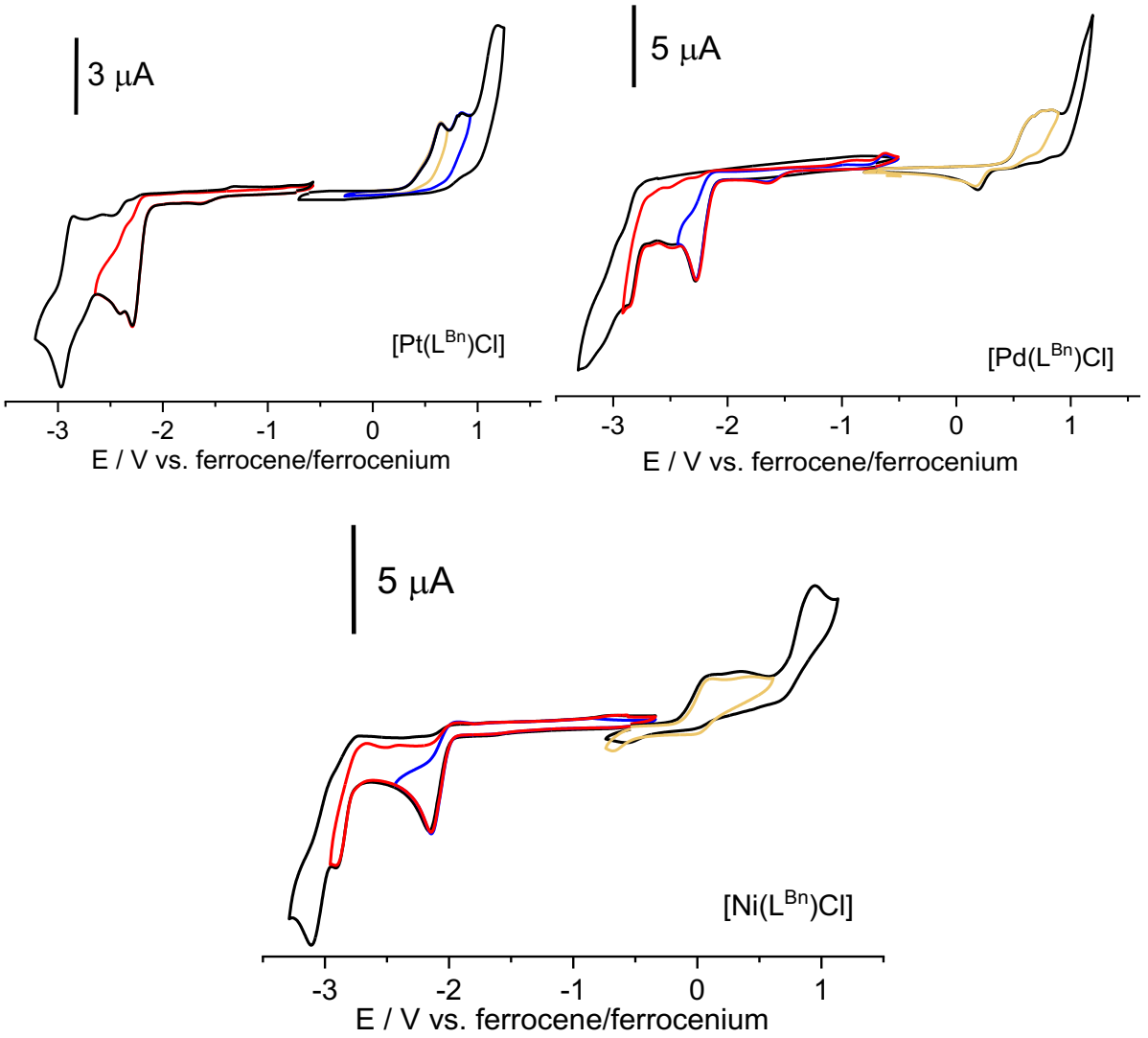


Figure A140. Cyclic voltammograms of the complexes [M(L^{Bn})Cl] (M = Pt, Pd, and Ni) in *n*-Bu_4NPF_6/THF.

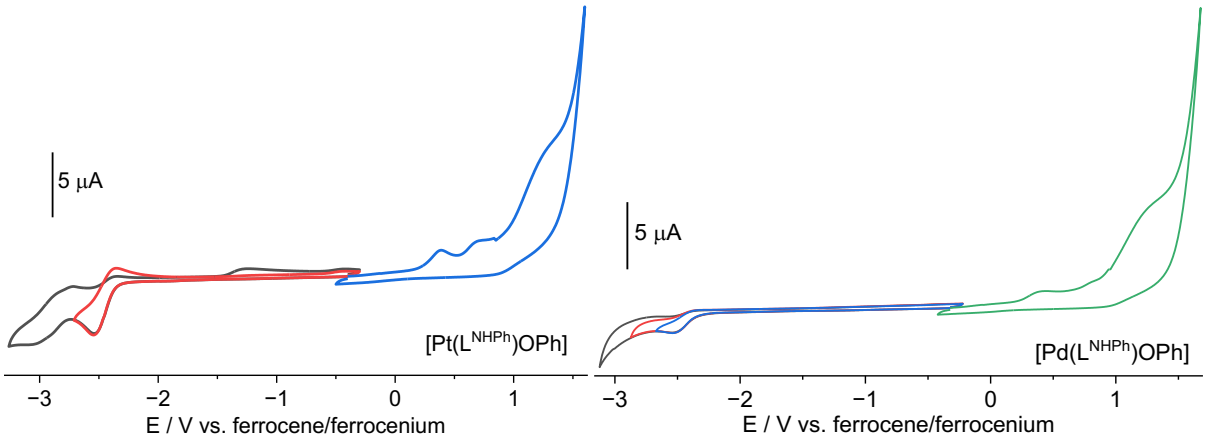


Figure A141. Cyclic voltammograms of the complexes [M(L^{NHPh})OPh] (M = Pt and Pd) in *n*-Bu_4NPF_6/THF.

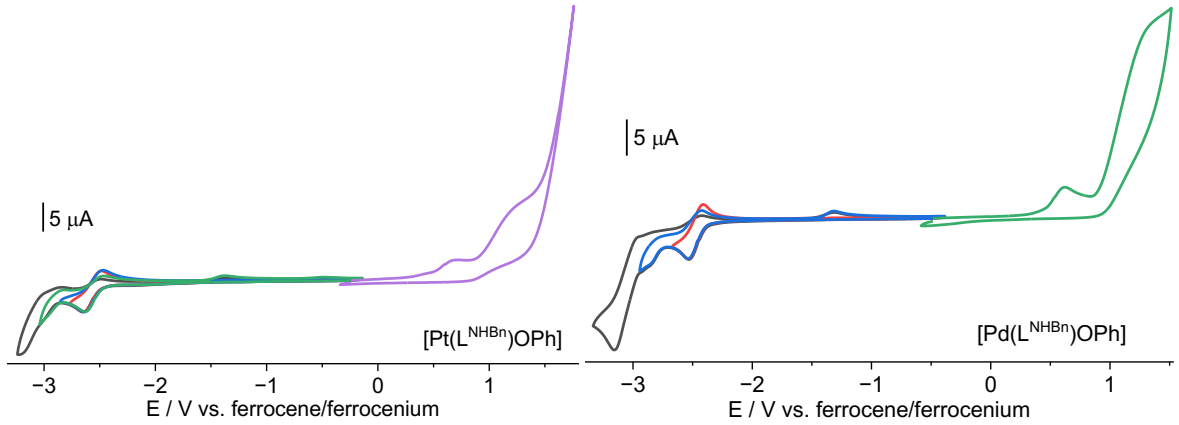
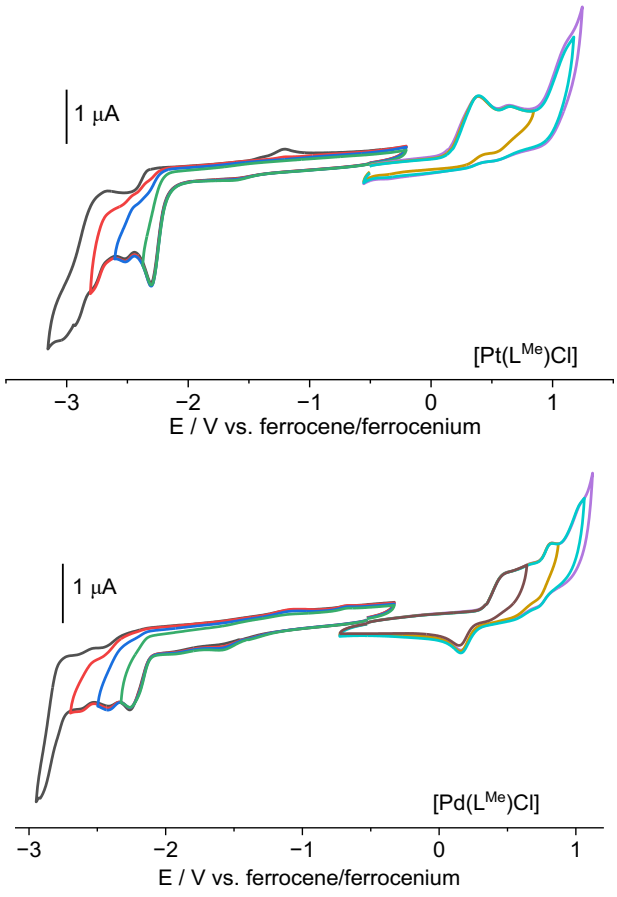


Figure A142. Cyclic voltammograms of the complexes [M(L^{NHBn})OPh] (M = Pt and Pd) in *n*-Bu$_4$NPF$_6$/THF.



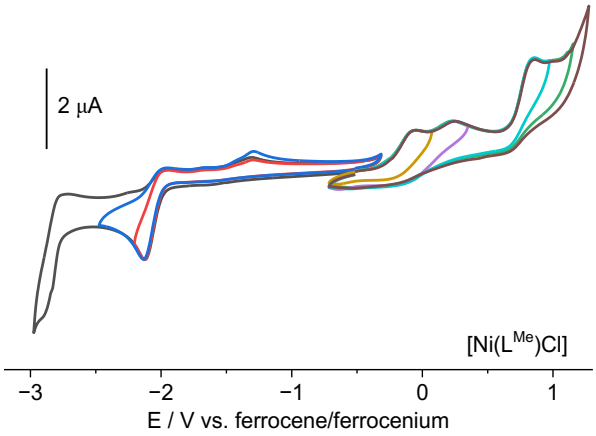


Figure A143. Cyclic voltammograms of the complexes [M(L^{Me})Cl] (M = Pt, Pd, and Ni) in *n*-Bu$_4$NPF$_6$/THF.

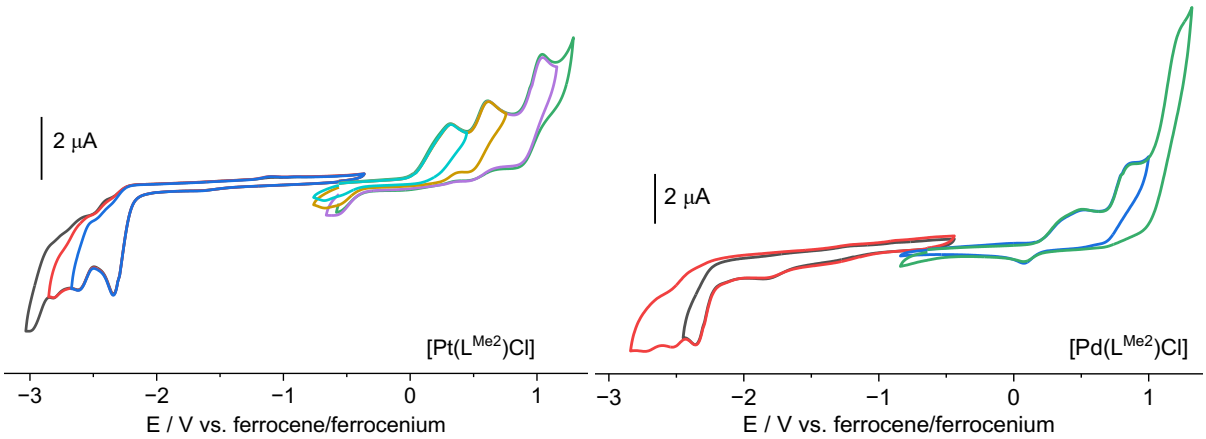
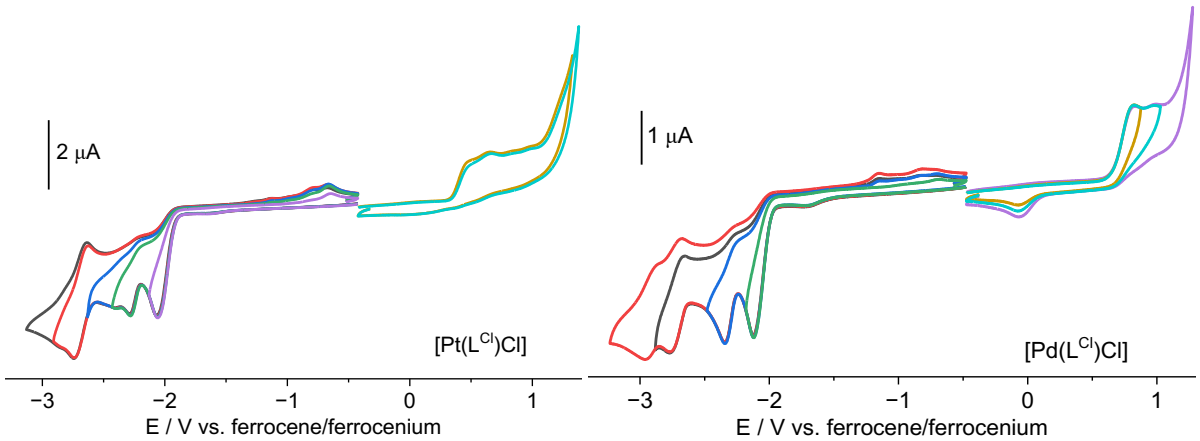


Figure A144. Cyclic voltammograms of the complexes [M(L^{Me2})Cl] (M = Pt, and Pd) in *n*-Bu$_4$NPF$_6$/THF.



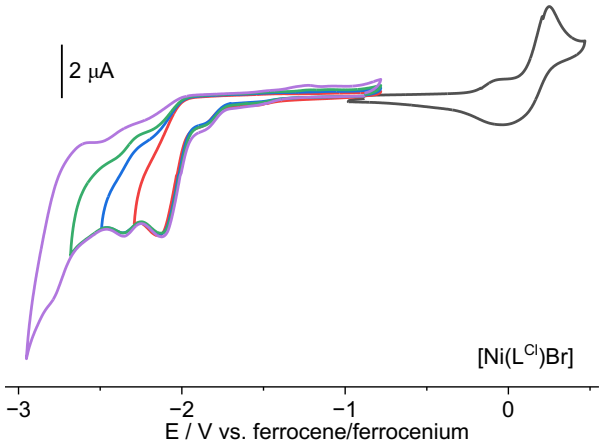


Figure A145. Cyclic voltammograms of the complexes [M(L^{Cl})X] (M = Pt, Pd, and Ni; X = Cl or Br) in *n*-Bu_4NPF_6/THF.

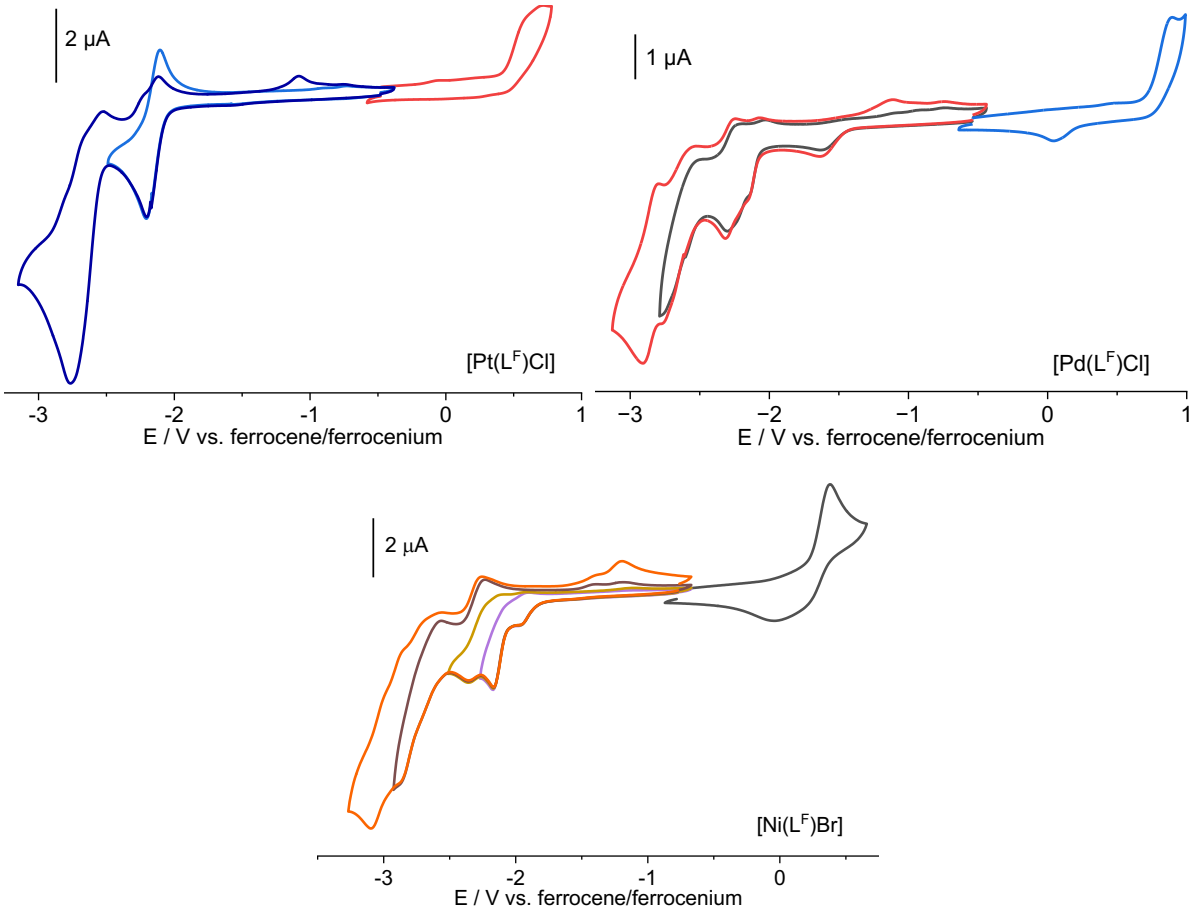


Figure A146. Cyclic voltammograms of the complexes [M(L^{F})X] (M = Pt, Pd, and Ni; X = Cl or Br) in *n*-Bu_4NPF_6/THF.

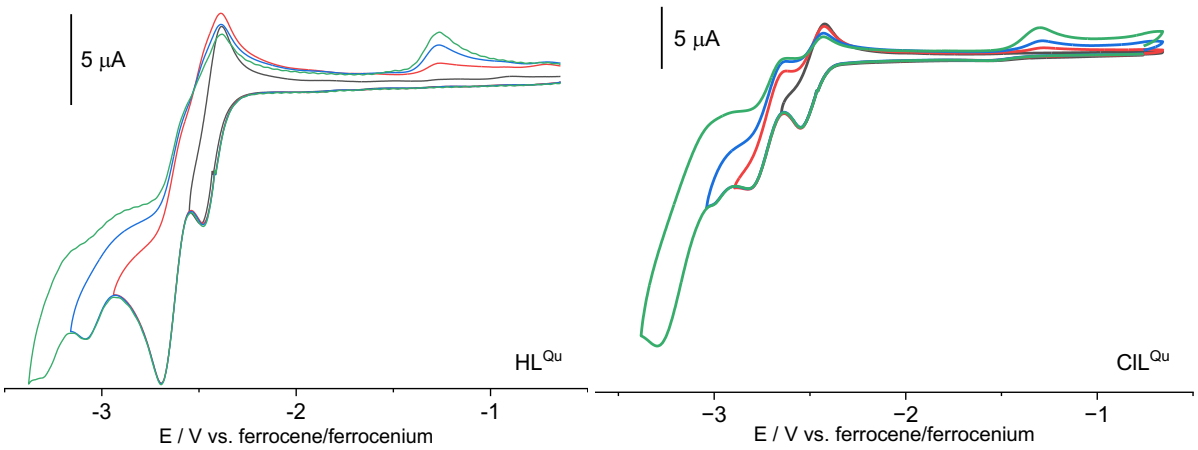


Figure A147. Cyclic voltammograms of HL^{Qu} and ClL^{Qu} in *n*-Bu_4NPF_6/THF.

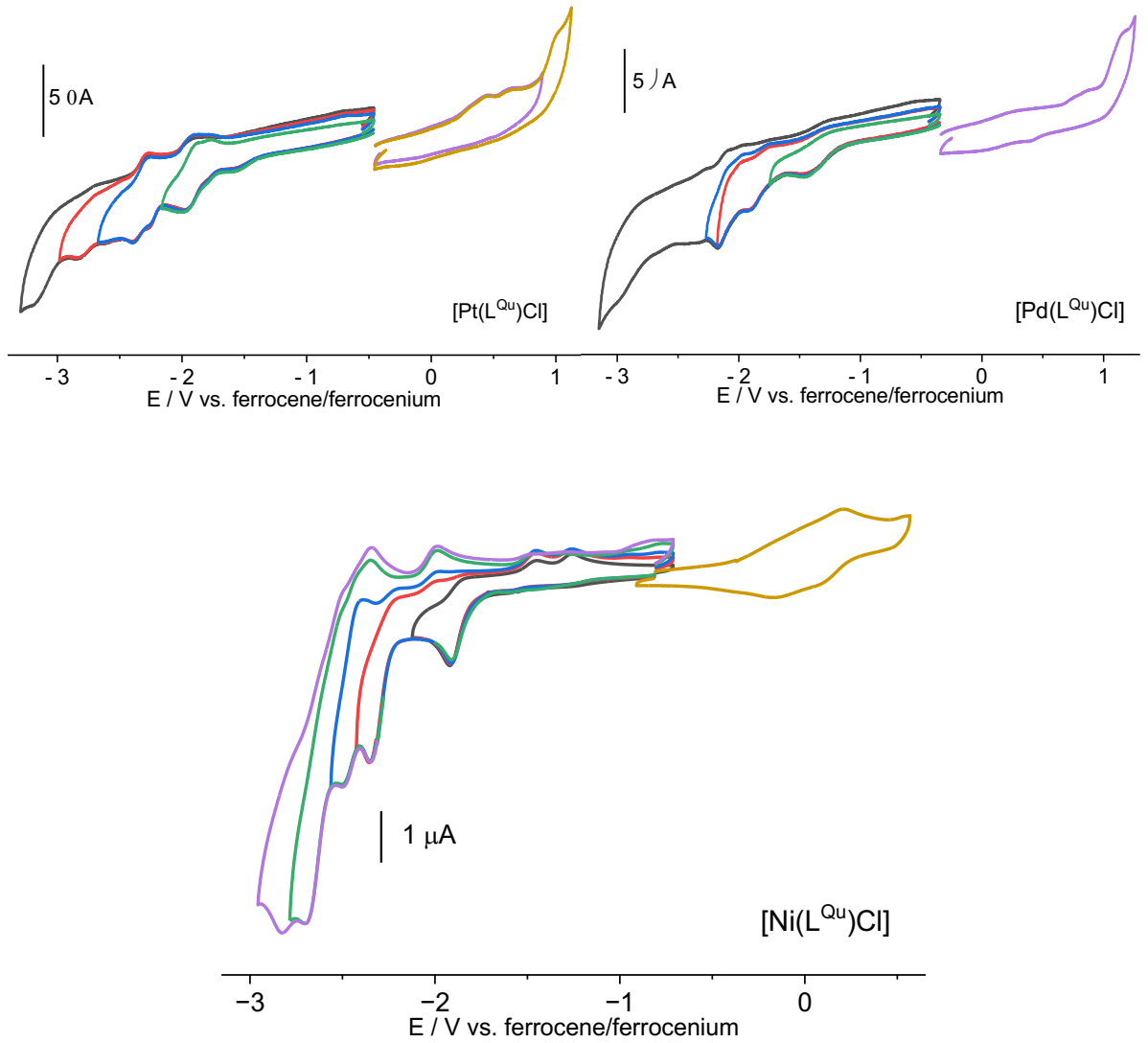


Figure A148. Cyclic voltammograms of the complexes [M(L^{Qu})Cl] (M = Pt, Pd, and Ni) in *n*-Bu_4NPF_6/THF.

Table A24. DFT-calculated calculated energies and compositions of frontier MOs in the S_0 ground state for [M(L^{NHPh})Cl] (M = Pt or Pd).[a]

complex	MO	energy (eV)	component %			
			M	N^C^N = L	NHPh = L′	Cl = X
[Pt(L^{NHPh})Cl]	LUMO+10	0.784	62	28	7	3
	LUMO+9	0.054	11	43	45	1
	LUMO+8	–0.118	5	78	17	0
	LUMO+7	–0.188	1	33	66	0
	LUMO+6	–0.480	0	6	94	0
	LUMO+5	–0.497	2	6	91	1
	LUMO+4	–0.890	29	54	14	3
	LUMO+3	–1.019	20	59	19	2
	LUMO+2	–1.111	2	70	28	0
	LUMO+1	–2.052	9	83	7	1
	LUMO	–2.082	2	96	2	0
	HOMO	–5.196	24	39	33	4
	HOMO-1	–5.264	8	36	55	1
	HOMO-2	–5.791	29	31	33	7
	HOMO-3	–5.913	88	8	1	3
	HOMO-4	–5.967	51	45	1	3
	HOMO-5	–6.451	17	32	37	14
	HOMO-6	–6.634	1	2	96	1
	HOMO-7	–6.635	9	4	84	3
	HOMO-8	–6.719	56	17	9	18
	HOMO-9	–6.909	19	41	28	12
	HOMO-10	–7.198	7	36	17	40
[Pd(L^{NHPh})Cl]	LUMO+10	0.751	73	19	6	2
	LUMO+9	0.095	8	44	47	1
	LUMO+8	–0.143	3	80	17	0
	LUMO+7	–0.181	0	33	67	0
	LUMO+6	–0.467	0	6	94	0
	LUMO+5	–0.483	3	6	91	0
	LUMO+4	–0.945	1	60	39	0
	LUMO+3	–1.103	1	72	27	0
	LUMO+2	–1.816	39	57	1	3

	LUMO+1	–2.008	10	83	6	1
	LUMO	–2.070	1	97	2	0
	HOMO	–5.270	3	38	58	1
	HOMO-1	–5.291	10	37	51	2
	HOMO-2	–5.928	36	35	19	10
	HOMO-3	–5.978	81	17	0	2
	HOMO-4	–6.155	38	53	6	3
	HOMO-5	–6.465	28	23	28	21
	HOMO-6	–6.618	1	2	96	1
	HOMO-7	–6.626	1	2	97	0
	HOMO-8	–6.869	56	15	5	24
	HOMO-9	–6.897	20	34	25	21
	HOMO-10	–7.135	3	30	16	51

[a] LUMO: Lowest Unoccupied Molecular Orbital, and HOMO: Highest Occupied Molecular Orbital. Major contributions (>30%) are marked in grey.

Table A25. DFT-calculated energies and compositions of frontier MOs in the T_1 excited state for [M(L^{NHPh})Cl] (M = Pt or Pd).[a]

complex	MO	energy (eV)	component %			
			M	N^C^N = L	NHPh = L′	Cl = X
[Pt(L^{NHPh})Cl]	HSOMO+3	–1.164	3	66	31	0
	HSOMO+2	–1.170	2	61	37	0
	HSOMO+1	–2.167	10	85	4	1
	HSOMO	–3.055	2	97	1	0
	LSOMO	–5.338	33	42	21	4
	LSOMO-1	–5.502	13	31	55	1
	LSOMO-2	–5.823	86	6	3	5
	LSOMO-3	–5.884	25	27	45	3
[Pd(L^{NHPh})Cl]	HSOMO+3	–1.247	1	60	39	0
	HSOMO+2	–1.696	39	57	1	3
	HSOMO+1	–1.973	6	89	5	0
	HSOMO	–3.162	4	94	2	0
	LSOMO	–5.228	7	38	55	0
	LSOMO-1	–5.742	24	44	27	5
	LSOMO-2	–5.918	83	0	15	2
	LSOMO-3	–6.000	18	31	46	5

[a] LSOMO: Lowest Singly Occupied Molecular Orbital, and HSOMO: Highest Singly Occupied Molecular Orbital. Major contributions (>30%) are marked in grey.

Table A26. DFT-calculated energies and compositions of frontier MOs in the T_1 excited state for [M(L^{NHBn})Cl] (M = Pt or Pd).[a]

complex	MO	energy (eV)	component %			
			M	N^C^N = L	NHBn = L′	Cl = X
[Pt(L^{NHBn})Cl]	HSOMO+3	–0.842	2	83	15	0
	HSOMO+2	–1.035	38	56	1	5
	HSOMO+1	–2.237	2	97	1	0
	HSOMO	–2.807	13	83	3	1
	LSOMO	–5.532	9	48	40	3
	LSOMO-1	–5.587	22	51	24	3

	LSOMO-2	–6.060	43	49	5	3
	LSOMO-3	–6.212	43	24	22	11
[Pd(L^{NHBn})Cl]	HSOMO+3	–0.859	1	84	15	0
	HSOMO+2	–1.660	39	56	1	4
	HSOMO+1	–1.906	6	91	3	0
	HSOMO	–3.164	4	95	1	0
	LSOMO	–5.389	11	52	35	2
	LSOMO-1	–5.841	31	51	11	7
	LSOMO-2	–5.901	84	14	0	1
	LSOMO-3	–6.095	48	8	40	4

[a] LSOMO: Lowest Singly Occupied Molecular Orbital, and HSOMO: Highest Singly Occupied Molecular Orbital. Major contributions (>30%) are marked in grey.

Table A27. DFT-calculated energies and compositions of frontier MOs in the S_0 ground state for [M(L^{NHBn})Cl] (M = Pt or Pd).[a]

complex	MO	energy (eV)	component %			
			M	N^C^N = L	NHBn = L′	Cl = X
[Pt(L^{NHBn})Cl]	LUMO+10	0.765	64	26	5	5
	LUMO+9	0.012	10	86	3	1
	LUMO+8	–0.373	1	38	60	0
	LUMO+7	–0.391	0	8	92	0
	LUMO+6	–0.416	2	15	83	0
	LUMO+5	–0.447	0	3	97	0
	LUMO+4	–0.509	1	39	60	0
	LUMO+3	–0.764	2	80	18	0
	LUMO+2	–0.878	40	54	2	4
	LUMO+1	–1.940	10	84	5	1
	LUMO	–1.992	2	97	1	0
	HOMO	–5.261	34	47	14	5
	HOMO-1	–5.360	13	46	38	3
	HOMO-2	–5.866	88	7	2	3
	HOMO-3	–5.892	49	46	2	3
	HOMO-4	–5.989	23	39	35	3
	HOMO-5	–6.392	4	2	93	1
	HOMO-6	–6.395	2	5	93	0
	HOMO-7	–6.523	20	6	65	9
	HOMO-8	–6.534	0	1	99	0
	HOMO-9	–6.574	46	13	18	23
	HOMO-10	–7.019	26	47	27	0
[Pd(L^{NHBn})Cl]	LUMO+10	0.703	69	19	10	3
	LUMO+9	0.009	6	90	4	0
	LUMO+8	–0.371	1	24	75	0
	LUMO+7	–0.390	1	14	85	0
	LUMO+6	–0.426	1	11	88	0
	LUMO+5	–0.432	2	5	93	0
	LUMO+4	–0.486	0	48	52	0
	LUMO+3	–0.769	1	82	17	0
	LUMO+2	–1.752	39	57	1	3

	LUMO+1	–1.910	12	83	4	1
	LUMO	–1.983	1	98	1	0
	HOMO	–5.395	5	53	40	2
	HOMO-1	–5.440	19	53	26	2
	HOMO-2	–5.940	83	14	0	3
	HOMO-3	–6.045	26	39	28	7
	HOMO-4	–6.099	44	42	9	5
	HOMO-5	–6.382	3	5	91	1
	HOMO-6	–6.393	5	4	87	4
	HOMO-7	–6.523	1	1	98	0
	HOMO-8	–6.535	0	1	99	0
	HOMO-9	–6.693	41	17	6	36
	HOMO-10	–6.982	16	31	4	49

[a] LUMO: Lowest Unoccupied Molecular Orbital, and HOMO: Highest Occupied Molecular Orbital. Major contributions (>30%) are marked in grey.

Table A28. DFT-calculated energies and compositions of frontier MOs in the S_0 ground state for [Ni(L^{NHPh})Cl].[a]

MO	energy (eV)	component %			
		Ni	N^C^N = L	NHPh = L′	Cl = X
LUMO+10	0.768	79	13	6	2
LUMO+9	0.086	7	48	44	1
LUMO+8	–0.114	3	78	19	0
LUMO+7	–0.174	0	32	68	0
LUMO+6	–0.479	0	6	94	0
LUMO+5	–0.493	2	6	92	0
LUMO+4	–0.915	1	60	39	0
LUMO+3	–1.126	1	73	26	0
LUMO+2	–1.928	26	67	4	3
LUMO+1	–2.029	1	97	2	0
LUMO	–2.111	35	60	3	2
HOMO	–5.170	38	29	27	6
HOMO-1	–5.246	14	31	54	1
HOMO-2	–5.383	84	10	4	2
HOMO-3	–5.699	38	24	36	2
HOMO-4	–5.722	70	25	2	3
HOMO-5	–6.332	9	53	35	3
HOMO-6	–6.591	20	41	32	7
HOMO-7	–6.630	46	7	27	20
HOMO-8	–6.643	31	5	51	13
HOMO-9	–6.654	9	19	69	3
HOMO-10	–7.072	4	42	35	19

[a] LUMO: Lowest Unoccupied Molecular Orbital, and HOMO: Highest Occupied Molecular Orbital. Major contributions (>30%) are marked in grey.

Table A29. DFT-calculated energies and compositions of frontier MOs in the T_1 excited state for [Ni(L^{NHPh})Cl].[a]

MO	energy (eV)	component %

		Ni	N^C^N = L	NHPh = L′	Cl = X
HSOMO+3	–1.047	0	73	27	0
HSOMO+2	–1.827	7	87	5	1
HSOMO+1	–1.872	0	98	2	0
HSOMO	–4.825	31	66	1	2
LSOMO	–5.241	1	39	60	0
LSOMO-1	–5.297	2	34	63	1
LSOMO-2	–6.061	9	75	15	1
LSOMO-3	–6.134	1	73	26	0

[a] LSOMO: Lowest Singly Occupied Molecular Orbital, and HSOMO: Highest Singly Occupied Molecular Orbital. Major contributions (>30%) are marked in grey.

Table A30 DFT-calculated energies and compositions of frontier MOs in the S_0 ground state for [Ni(L^{NHBn})Cl].[a]

MO	energy (eV)	component %			
		Ni	N^C^N = L	NHBn = L′	Cl = X
LUMO+10	0.711	72	14	13	1
LUMO+9	0.030	5	91	4	0
LUMO+8	–0.355	1	33	66	0
LUMO+7	–0.397	1	18	81	0
LUMO+6	–0.422	1	6	93	0
LUMO+5	–0.445	2	9	89	0
LUMO+4	–0.468	1	37	62	0
LUMO+3	–0.803	1	82	17	0
LUMO+2	–1.836	23	71	3	3
LUMO+1	–1.942	2	97	1	0
LUMO	–2.025	38	58	2	2
HOMO	–5.201	59	25	8	8
HOMO-1	–5.324	75	18	6	1
HOMO-2	–5.338	40	30	26	4
HOMO-3	–5.676	52	43	4	1
HOMO-4	–5.909	24	37	38	1
HOMO-5	–6.348	2	6	88	4
HOMO-6	–6.358	5	7	86	2
HOMO-7	–6.504	24	5	61	10
HOMO-8	–6.533	46	7	27	20
HOMO-9	–6.544	2	2	95	1
HOMO-10	–6.660	20	56	13	11

[a] LUMO: Lowest Unoccupied Molecular Orbital, and HOMO: Highest Occupied Molecular Orbital. Major contributions (>30%) are marked in grey.

Table A31. DFT-calculated energies and compositions of frontier MOs in the T_1 excited state for [Ni(L^{NHBn})Cl].[a]

MO	energy (eV)	component %

		Ni	N^C^N = L	NHBn = L′	Cl = X
HSOMO+3	–0.709	1	80	19	0
HSOMO+2	–1.727	8	87	4	1
HSOMO+1	–1.776	0	98	1	0
HSOMO	–4.783	31	66	1	2
LSOMO	–5.388	0	62	36	1
LSOMO-1	–5.511	3	58	38	2
LSOMO-2	–6.135	7	63	30	1
LSOMO-3	–6.258	3	36	60	1

[a] LSOMO: Lowest Singly Occupied Molecular Orbital, and HSOMO: Highest Singly Occupied Molecular Orbital. Major contributions (>30%) are marked in grey.

Table A32. DFT-calculated energies and compositions of frontier MOs in the S_0 ground state for [M(L^{Bn})Cl] (M = Pt, Pd, and Ni).[a]

complex	MO	energy (eV)	component %			
			M	NCN = L	Bn = L′	Cl = X
[Pt(L^{Bn})Cl]	LUMO+6	–0.736	18	51	29	2
	LUMO+5	–0.763	1	23	75	1
	LUMO+4	–0.827	6	25	69	0
	LUMO+3	–1.269	2	65	33	0
	LUMO+2	–1.561	1	87	12	0
	LUMO+1	–2.351	2	80	18	0
	LUMO	–2.377	3	87	10	0
	HOMO	–5.414	28	39	22	11
	HOMO-1	–5.841	49	37	10	4
	HOMO-2	–5.865	40	26	12	22
	HOMO-3	–6.235	6	65	17	12
	HOMO-4	–6.567	1	25	73	1
	HOMO-5	–6.588	28	20	42	10
	HOMO-6	–6.660	30	21	44	5
[Pd(L^{Bn})Cl]	LUMO+6	–0.743	1	12	87	0
	LUMO+5	–0.775	1	17	82	0
	LUMO+4	–1.247	2	67	31	0
	LUMO+3	–1.579	2	77	21	0
	LUMO+2	–1.677	24	64	10	2
	LUMO+1	–2.314	5	84	11	0
	LUMO	–2.354	1	82	17	0
	HOMO	–5.616	34	40	11	15
	HOMO-1	–5.899	61	31	6	2
	HOMO-2	–6.030	31	22	22	25
	HOMO-3	–6.264	1	75	17	7
	HOMO-4	–6.537	4	14	67	15
	HOMO-5	–6.594	2	23	70	5
	HOMO-6	–6.715	5	17	73	5
[Ni(L^{Bn})Cl]	LUMO+6	–0.743	0	8	92	0

	LUMO+5	–0.779	1	13	86	0
	LUMO+4	–1.158	0	56	44	0
	LUMO+3	–1.537	1	81	18	0
	LUMO+2	–1.867	24	47	25	4
	LUMO+1	–2.283	1	85	14	0
	LUMO	–2.296	6	74	20	0
	HOMO	–5.179	53	20	15	12
	HOMO-1	–5.481	51	44	3	2
	HOMO-2	–5.621	53	15	23	9
	HOMO-3	–6.232	0	77	18	5
	HOMO-4	–6.449	5	30	48	17
	HOMO-5	–6.495	39	13	26	22
	HOMO-6	–6.625	5	12	82	1

[a] LUMO: Lowest Unoccupied Molecular Orbital, and HOMO: Highest Occupied Molecular Orbital. Major contributions (>30%) are marked in grey.

Table A33. DFT-calculated energies and compositions of frontier MOs in the T_1 excited state for [M(L^{Bn})Cl] (M = Pt, Pd, and Ni).[a]

complex	MO	energy (eV)	component %			
[Pt(L^{Bn})Cl]			M	NCN = L	Bn = L′	Cl = X
	HSOMO+3	–1.479	1	88	11	0
	HSOMO+2	–1.578	22	65	9	4
	HSOMO+1	–2.349	2	85	13	0
	HSOMO	–3.132	9	82	9	0
	LSOMO	–5.714	29	44	10	17
	LSOMO-1	–6.182	8	86	6	0
	LSOMO-2	–6.195	35	33	21	11
	LSOMO-3	–6.464	27	25	23	25
[Pd(L^{Bn})Cl]	HSOMO+3	–1.420	1	76	23	0
	HSOMO+2	–1.988	5	79	15	1
	HSOMO+1	–2.112	0	89	11	0
	HSOMO	–3.968	32	64	3	1
	LSOMO	–5.747	36	36	6	22
	LSOMO-1	–6.120	36	45	5	14
	LSOMO-2	–6.145	5	87	6	2
	LSOMO-3	–6.282	33	20	11	36
[Ni(L^{Bn})Cl]	HSOMO+3	–1.432	0	72	28	0
	HSOMO+2	–2.018	3	78	18	1
	HSOMO+1	–2.096	0	81	19	0
	HSOMO	–4.666	18	78	2	2
	LSOMO	–6.007	17	73	4	6
	LSOMO-1	–6.100	0	92	7	1
	LSOMO-2	–6.428	15	17	41	27
	LSOMO-3	–6.534	10	27	49	14

[a] LSOMO: Lowest Singly Occupied Molecular Orbital, and HSOMO: Highest Singly Occupied Molecular Orbital. Major contributions (>30%) are marked in grey.

Table A34. DFT-calculated energies and compositions of frontier MOs in the S_0 ground state for [Pt(L^{NHPh})OPh] and [Pd(L^{NHPh})OPh] complexes.[a]

complex	MO	energy (eV)	component %			
			M	NCN = L	NHPh = L′	OPh = X
[Pt(L^{NHPh})OPh]	LUMO+10	–0.143	3	54	27	16
	LUMO+9	–0.282	2	56	28	14
	LUMO+8	–0.402	19	63	5	13
	LUMO+7	–0.420	5	35	20	40
	LUMO+6	–0.509	1	27	40	32
	LUMO+5	–0.790	1	6	79	14
	LUMO+4	–0.822	1	11	79	9
	LUMO+3	–1.112	1	44	43	12
	LUMO+2	–1.247	2	57	31	10
	LUMO+1	–2.148	7	72	8	13
	LUMO	–2.196	1	91	7	1
	HOMO	–5.292	13	23	22	42
	HOMO-1	–5.352	17	30	20	33
	HOMO-2	–5.400	10	41	43	6
	HOMO-3	–5.897	22	26	31	21
	HOMO-4	–5.966	65	26	3	6
	HOMO-5	–6.026	47	49	3	1
	HOMO-6	–6.498	1	9	8	82
	HOMO-7	–6.665	21	32	41	5
	HOMO-8	–6.785	30	24	14	32
	HOMO-9	–6.833	14	13	63	10
	HOMO-10	–6.877	2	7	81	10
[Pd(L^{NHPh})OPh]	LUMO+10	–0.125	1	55	34	10
	LUMO+9	–0.301	2	62	27	9
	LUMO+8	–0.399	1	23	28	48
	LUMO+7	–0.503	0	23	42	35
	LUMO+6	–0.778	1	7	76	16
	LUMO+5	–0.811	1	15	74	10
	LUMO+4	–1.099	1	50	44	5
	LUMO+3	–1.212	10	59	18	13

	LUMO+2	–1.329	22	64	9	5
	LUMO+1	–2.103	5	73	9	13
	LUMO	–2.188	1	92	6	1
	HOMO	–5.284	5	11	15	69
	HOMO-1	–5.398	5	42	51	2
	HOMO-2	–5.455	11	49	30	10
	HOMO-3	–5.949	57	25	7	11
	HOMO-4	–6.002	41	40	10	9
	HOMO-5	–6.191	42	49	7	2
	HOMO-6	–6.477	1	7	7	85
	HOMO-7	–6.673	22	36	23	19
	HOMO-8	–6.735	15	35	15	35
	HOMO-9	–6.841	3	6	85	6
	HOMO-10	–6.863	1	4	87	8

[a] LUMO: Lowest Unoccupied Molecular Orbital, and HOMO: Highest Occupied Molecular Orbital. Major contributions (>30%) are marked in grey.

Table A35. DFT-calculated energies and compositions of frontier MOs in the S_0 ground state for [Pt(L^{NHBn})OPh] and [Pd(L^{NHBn})OPh] complexes.[a]

complex	MO	energy (eV)	component %			
			M			
[Pt(L^{NHBn})OPh]	LUMO+10	–0.162	6	76	9	9
	LUMO+9	–0.328	20	65	8	7
	LUMO+8	–0.440	2	20	20	58
	LUMO+7	–0.546	2	68	23	7
	LUMO+6	–0.703	1	21	69	9
	LUMO+5	–0.730	1	13	75	11
	LUMO+4	–0.740	1	7	90	2
	LUMO+3	–0.760	1	23	60	16
	LUMO+2	–0.938	1	52	46	1
	LUMO+1	–2.073	7	65	18	10
	LUMO	–2.128	1	86	12	1
	HOMO	–5.268	10	16	9	65
	HOMO-1	–5.340	25	36	19	20
	HOMO-2	–5.469	11	41	47	1
	HOMO-3	–5.919	64	28	3	5
	HOMO-4	–5.963	47	50	2	1
	HOMO-5	–6.051	14	37	38	11
	HOMO-6	–6.487	2	7	10	81
	HOMO-7	–6.585	2	5	87	6
	HOMO-8	–6.602	4	4	88	4
	HOMO-9	–6.759	16	16	64	5
	HOMO-10	–6.784	22	17	54	7
[Pd(L^{NHBn})OPh]	LUMO+10	–0.174	3	86	8	3
	LUMO+9	–0.412	1	13	23	63
	LUMO+8	–0.530	1	68	27	4
	LUMO+7	–0.695	0	20	72	8
	LUMO+6	–0.719	1	16	75	8
	LUMO+5	–0.731	1	7	90	2
	LUMO+4	–0.756	1	20	66	13
	LUMO+3	–0.953	1	53	46	0
	LUMO+2	–1.214	26	63	5	6

	LUMO+1	–2.031	5	67	20	8
	LUMO	–2.117	1	87	12	0
	HOMO	–5.238	6	11	9	74
	HOMO-1	–5.491	14	48	31	7
	HOMO-2	–5.497	8	45	45	2
	HOMO-3	–5.909	65	30	2	3
	HOMO-4	–6.081	19	39	27	15
	HOMO-5	–6.136	50	44	5	1
	HOMO-6	–6.460	0	4	12	84
	HOMO-7	–6.576	3	8	81	8
	HOMO-8	–6.597	4	5	86	5
	HOMO-9	–6.714	7	46	8	39
	HOMO-10	–6.761	1	6	89	4

[a] LUMO: Lowest Unoccupied Molecular Orbital, and HOMO: Highest Occupied Molecular Orbital. Major contributions (>30%) are marked in grey.

Table A36. DFT-calculated energies and compositions of frontier MOs in the S_0 ground state for [M(L^{Me})Cl] (M = Pt, Pd, Ni).[a]

complex	MO	energy (eV)	component %			
			M	N^C^N = L	Me = L′	Cl = X
[Pt(L^{Me})Cl]	LUMO+6	0.424	0	92	8	0
	LUMO+5	–0.309	8	87	4	1
	LUMO+4	–0.694	26	70	2	2
	LUMO+3	–1.163	2	91	7	0
	LUMO+2	–1.469	2	94	4	0
	LUMO+1	–2.317	2	96	2	0
	LUMO	–2.333	3	94	2	1
	HOMO	–5.413	38	45	3	14
	HOMO-1	–5.797	40	23	6	30
	HOMO-2	–5.886	49	47	1	3
	HOMO-3	–6.163	13	73	3	11
	HOMO-4	–6.544	55	35	2	8
	HOMO-5	–6.826	15	40	2	43
	HOMO-6	–7.016	12	37	3	48
[Pd(L^{Me})Cl]	LUMO+6	0.419	0	97	3	0
	LUMO+5	–0.344	5	93	2	0
	LUMO+4	–1.144	2	93	5	0
	LUMO+3	–1.494	1	94	5	0
	LUMO+2	–1.597	27	70	1	2
	LUMO+1	–2.291	6	89	4	1
	LUMO	–2.317	1	97	2	0
	HOMO	–5.581	36	45	1	18
	HOMO-1	–5.893	63	35	1	1
	HOMO-2	–5.958	38	21	7	34
	HOMO-3	–6.239	4	86	3	7
	HOMO-4	–6.758	58	24	2	16
	HOMO-5	–6.762	5	36	4	55
	HOMO-6	–6.910	28	43	2	27

[Ni(L^{Me})Cl]	LUMO+6	0.494	0	96	4	0
	LUMO+5	–0.302	4	93	3	0
	LUMO+4	–1.081	1	93	6	0
	LUMO+3	–1.464	1	95	4	0
	LUMO+2	–1.769	33	61	1	5
	LUMO+1	–2.248	2	96	2	0
	LUMO	–2.279	8	83	8	1
	HOMO	–5.129	46	37	7	10
	HOMO-1	–5.428	72	26	1	1
	HOMO-2	–5.559	66	18	3	13
	HOMO-3	–6.210	5	78	4	13
	HOMO-4	–6.413	52	23	3	22
	HOMO-5	–6.607	15	60	4	21
	HOMO-6	–6.896	10	23	4	63

[a] LUMO: Lowest Unoccupied Molecular Orbital, and HOMO: Highest Occupied Molecular Orbital. Major contributions (>30%) are marked in grey.

Table A37. DFT-calculated energies and compositions of frontier MOs in the S_0 ground state for [M(L^{Me2})Cl] (M = Pt, Pd, Ni).[a]

complex	MO	energy (eV)	component %				
			M	N^C^N = L	Me^{P} = L′	Me^{B} = L′′	Cl = X
[Pt(L^{Me2})Cl]	LUMO+6	0.397	0	83	2	15	0
	LUMO+5	–0.237	10	81	6	3	0
	LUMO+4	–0.583	16	61	3	18	2
	LUMO+3	–1.159	2	91	5	2	0
	LUMO+2	–1.355	1	95	3	1	0
	LUMO+1	–2.206	2	89	3	6	0
	LUMO	–2.275	3	95	2	0	0
	HOMO	–5.293	31	52	5	0	12
	HOMO-1	–5.734	43	32	3	2	20
	HOMO-2	–5.763	35	61	1	1	2
	HOMO-3	–6.074	5	69	5	5	16
	HOMO-4	–6.587	57	26	2	1	14
	HOMO-5	–6.831	10	38	3	2	47
	HOMO-6	–6.932	24	38	2	1	35
[Pd(L^{Me2})Cl]	LUMO+6	0.374	0	82	1	17	0
	LUMO+5	–0.256	6	88	3	3	0
	LUMO+4	–1.130	3	90	4	3	0
	LUMO+3	–1.380	1	95	3	1	0
	LUMO+2	–1.481	16	74	1	8	1
	LUMO+1	–2.206	1	90	3	6	0
	LUMO	–2.223	5	89	4	1	1
	HOMO	–5.495	38	41	1	1	19
	HOMO-1	–5.793	48	49	0	1	2
	HOMO-2	–5.887	40	29	4	1	26
	HOMO-3	–6.099	2	73	5	5	15
	HOMO-4	–6.663	5	46	5	1	43
	HOMO-5	–6.742	54	22	2	0	22
	HOMO-6	–6.877	30	37	2	1	30

[Ni(L^{Me2})Cl]	LUMO+6	0.473	0	83	1	16	0
	LUMO+5	–0.199	3	92	2	3	0
	LUMO+4	–1.073	1	92	5	2	0
	LUMO+3	–1.356	1	95	4	0	0
	LUMO+2	–1.694	26	59	1	10	4
	LUMO+1	–2.145	2	89	2	7	0
	LUMO	–2.209	8	83	7	1	1
	HOMO	–5.063	43	41	5	0	11
	HOMO-1	–5.367	66	31	1	1	1
	HOMO-2	–5.489	66	21	1	0	12
	HOMO-3	–6.041	2	82	2	6	8
	HOMO-4	–6.402	52	19	2	1	26
	HOMO-5	–6.489	19	54	2	2	23
	HOMO-6	–6.864	10	27	6	1	56

[a] LUMO: Lowest Unoccupied Molecular Orbital, and HOMO: Highest Occupied Molecular Orbital. Major contributions (>30%) are marked in grey; Me^{P}: Me-substituents on the pyridine rings; Me^{B}: Me-substituents on the benzene ring.

Table A38. DFT-calculated energies and compositions of frontier MOs in the S_0 ground state for [M(L^{Cl})X] (M = Pt, Pd, Ni; X = Cl or Br).[a]

complex	MO	energy (eV)	component %			
			M	N^C^N = L	Cl^{P} = L′	Cl = X
[Pt(L^{Cl})Cl]	LUMO+6	0.044	0	93	7	0
	LUMO+5	–0.403	6	94	0	0
	LUMO+4	–0.712	4	94	2	0
	LUMO+3	–1.611	1	94	5	0
	LUMO+2	–1.811	3	92	5	0
	LUMO+1	–2.502	3	96	1	0
	LUMO	–2.620	9	90	0	1
	HOMO	–5.657	43	40	2	15
	HOMO-1	–6.155	49	51	0	0
	HOMO-2	–6.280	57	43	0	0
	HOMO-3	–6.319	37	24	0	39
	HOMO-4	–6.644	26	61	13	0
	HOMO-5	–6.943	6	34	5	55
	HOMO-6	–7.366	7	54	0	39
[Pd(L^{Cl})Cl]	LUMO+6	0.038	0	93	6	1
	LUMO+5	–0.437	3	97	0	0
	LUMO+4	–1.406	7	91	1	1
	LUMO+3	–1.605	0	94	5	1
	LUMO+2	–1.832	2	93	5	0
	LUMO+1	–2.498	2	97	1	0
	LUMO	–2.576	6	93	0	1
	HOMO	–5.873	40	40	2	18
	HOMO-1	–6.136	69	31	0	0
	HOMO-2	–6.417	29	23	0	48
	HOMO-3	–6.434	33	64	3	0
	HOMO-4	–6.721	51	39	10	0
	HOMO-5	–6.864	3	31	4	62
	HOMO-6	–7.188	10	68	0	22

[Ni(L^{Cl})Br]	LUMO+6	0.059	0	92	8	0
	LUMO+5	–0.412	2	98	0	0
	LUMO+4	–1.502	1	94	5	0
	LUMO+3	–1.818	2	93	5	0
	LUMO+2	–1.880	20	75	2	3
	LUMO+1	–2.457	2	97	1	0
	LUMO	–2.614	6	94	0	0
	HOMO	–5.605	56	26	2	16
	HOMO-1	–5.636	79	21	0	0
	HOMO-2	–5.947	84	16	0	0
	HOMO-3	–6.249	24	19	0	57
	HOMO-4	–6.500	6	83	11	0
	HOMO-5	–6.680	2	39	4	55
	HOMO-6	–7.087	27	26	13	34

[a] LUMO: Lowest Unoccupied Molecular Orbital, and HOMO: Highest Occupied Molecular Orbital. Major contributions (>30%) are marked in grey; Cl^{P}: Cl-substituents on the pyridine rings.

Table A39. DFT-calculated energies and compositions of frontier MOs in the S_0 ground state for [M(L^{F})X] (M = Pt, Pd, Ni; X = Cl or Br).[a]

complex	MO	energy (eV)	component %			
			M	N^C^N = L	F = L′	Cl = X
[Pt(L^{F})Cl]	LUMO+6	0.342	0	98	2	0
	LUMO+5	–0.567	4	93	2	1
	LUMO+4	–0.596	12	86	1	1
	LUMO+3	–1.416	1	99	0	0
	LUMO+2	–1.618	3	97	0	0
	LUMO+1	–2.340	2	93	5	0
	LUMO	–2.490	10	89	0	1
	HOMO	–5.762	45	37	0	18
	HOMO-1	–6.166	51	49	0	0
	HOMO-2	–6.179	43	51	6	0
	HOMO-3	–6.327	36	25	0	39
	HOMO-4	–6.642	43	53	4	0
	HOMO-5	–6.988	4	40	2	54
	HOMO-6	–7.478	9	36	2	53
[Pd(L^{F})Cl]	LUMO+6	0.321	0	98	2	0
	LUMO+5	–0.598	3	95	2	0
	LUMO+4	–1.406	1	99	0	0
	LUMO+3	–1.475	13	85	1	1
	LUMO+2	–1.633	2	98	0	0
	LUMO+1	–2.339	2	93	5	0
	LUMO	–2.453	7	92	0	1
	HOMO	–5.980	41	36	1	22
	HOMO-1	–6.169	69	31	0	0
	HOMO-2	–6.308	22	69	9	0
	HOMO-3	–6.431	27	25	0	48
	HOMO-4	–6.764	65	33	2	0
	HOMO-5	–6.911	2	38	2	58
	HOMO-6	–7.288	9	68	1	22

[Ni(L^F)Br]	LUMO+6	0.404	0	98	2	0
	LUMO+5	–0.571	2	97	1	0
	LUMO+4	–1.306	0	99	0	1
	LUMO+3	–1.622	1	98	1	0
	LUMO+2	–1.955	28	67	1	4
	LUMO+1	–2.296	2	93	5	0
	LUMO	–2.493	7	93	0	0
	HOMO	–5.660	87	13	0	0
	HOMO-1	–5.675	59	22	0	19
	HOMO-2	–5.935	76	22	2	0
	HOMO-3	–6.249	23	19	0	58
	HOMO-4	–6.420	16	75	9	0
	HOMO-5	–6.719	1	43	1	55
	HOMO-6	–7.178	34	29	0	37

[a] LUMO: Lowest Unoccupied Molecular Orbital, and HOMO: Highest Occupied Molecular Orbital. Major contributions (>30%) are marked in grey.

Table A40. DFT-calculated energies and compositions of frontier MOs in the S_0 ground state for [M(L^{Qu})Cl] (M = Pt, Pd, Ni).[a]

complex	MO	energy (eV)	component %		
			M	NCN = L	Cl = X
[Pt(L^{Qu})Cl]	LUMO+6	–0.500	1	99	0
	LUMO+5	–0.710	16	83	1
	LUMO+4	–0.930	15	84	1
	LUMO+3	–1.356	2	98	0
	LUMO+2	–1.774	0	100	0
	LUMO+1	–2.672	3	97	0
	LUMO	–2.734	4	96	0
	HOMO	–5.561	35	52	13
	HOMO-1	–5.716	34	48	18
	HOMO-2	–5.968	53	44	3
	HOMO-3	–6.388	19	58	23
	HOMO-4	–6.478	11	86	3
	HOMO-5	–6.536	28	62	10
	HOMO-6	–6.969	46	54	1
[Pd(L^{Qu})Cl]	LUMO+6	–0.494	1	99	0
	LUMO+5	–0.842	6	94	0
	LUMO+4	–1.368	2	98	0
	LUMO+3	–1.656	22	75	3
	LUMO+2	–1.792	0	100	0
	LUMO+1	–2.661	2	98	0
	LUMO	–2.703	4	96	0
	HOMO	–5.735	38	45	17
	HOMO-1	–5.849	32	43	25
	HOMO-2	–5.976	63	36	1
	HOMO-3	–6.405	8	70	22
	HOMO-4	–6.464	16	80	4
	HOMO-5	–6.599	21	61	18
	HOMO-6	–6.857	3	57	40

[Ni(L^{Qu})Cl]	LUMO+6	–0.476	0	100	0
	LUMO+5	–0.807	1	99	0
	LUMO+4	–1.303	1	99	0
	LUMO+3	–1.747	0	100	0
	LUMO+2	–1.885	20	78	2
	LUMO+1	–2.622	2	98	0
	LUMO	–2.672	5	94	1
	HOMO	–5.283	55	33	12
	HOMO-1	–5.534	63	35	2
	HOMO-2	–5.541	56	31	13
	HOMO-3	–6.333	11	85	4
	HOMO-4	–6.370	16	62	22
	HOMO-5	–6.403	40	47	13
	HOMO-6	–6.690	13	86	1

[a] LUMO: Lowest Unoccupied Molecular Orbital, and HOMO: Highest Occupied Molecular Orbital. Major contributions (>30%) are marked in grey.

Table A41. DFT-calculated energies and compositions of frontier MOs in the T_1 excited state for [M(L^{Qu})Cl] (M = Pt, Pd, Ni).[a]

complex	MO	energy (eV)	component %		
[Pt(L^{Qu})Cl]			M	NCN = L	Cl = X
	HSOMO+3	–1.685	0	100	0
	HSOMO+2	–1.730	25	72	3
	HSOMO+1	–2.832	3	97	0
	HSOMO	–3.274	8	91	1
	LSOMO	–5.857	39	36	25
	LSOMO-1	–6.046	18	76	6
	LSOMO-2	–6.231	25	63	12
	LSOMO-3	–6.445	3	95	2
[Pd(L^{Qu})Cl]	HSOMO+3	–1.701	0	100	0
	HSOMO+2	–2.477	3	96	1
	HSOMO+1	–2.481	1	99	0
	HSOMO	–4.016	34	65	2
	LSOMO	–5.765	33	45	22
	LSOMO-1	–6.094	27	61	12
	LSOMO-2	–6.113	18	69	13
	LSOMO-3	–6.316	25	44	32
[Ni(L^{Qu})Cl]	HSOMO+3	–1.679	0	100	0
	HSOMO+2	–2.484	0	100	0
	HSOMO+1	–2.499	2	97	1
	HSOMO	–4.736	20	78	2
	LSOMO	–6.017	14	82	5
	LSOMO-1	–6.127	5	91	4
	LSOMO-2	–6.389	18	47	35
	LSOMO-3	–6.403	16	62	22

[a] LSOMO: Lowest Singly Occupied Molecular Orbital, and HSOMO: Highest Singly Occupied Molecular Orbital. Major contributions (>30%) are marked in grey.

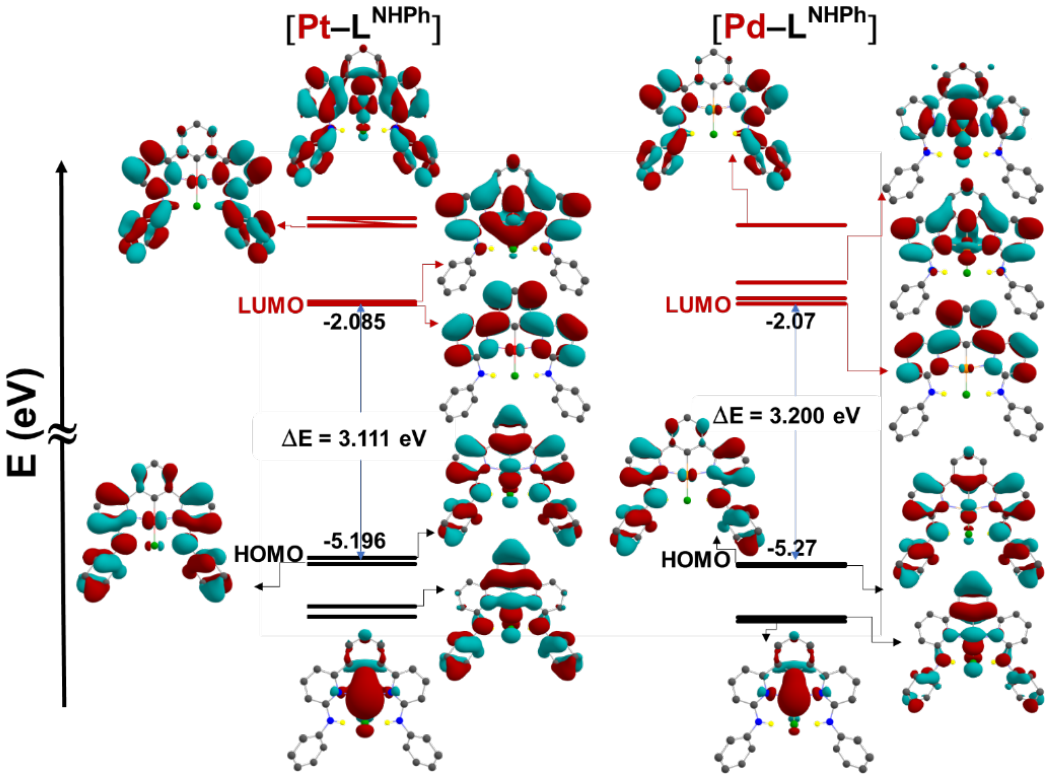


Figure A149. DFT-calculated energies of the highest occupied (HOMO, black) and lowest unoccupied (LUMO, red) molecular orbitals for [M(L^{NHPh})Cl] (M = Pt or Pd).

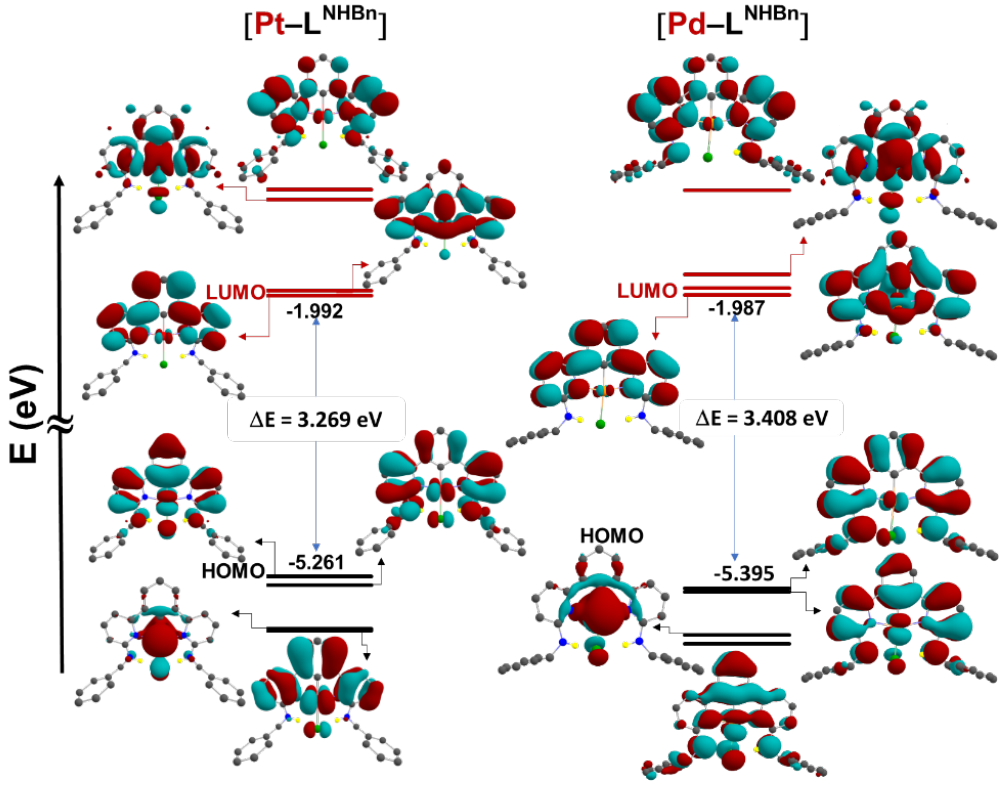


Figure A150. DFT-calculated energies of the highest occupied (HOMO, black) and lowest unoccupied (LUMO, red) molecular orbitals for [M(L^{NHBn})Cl] (M = Pt or Pd).

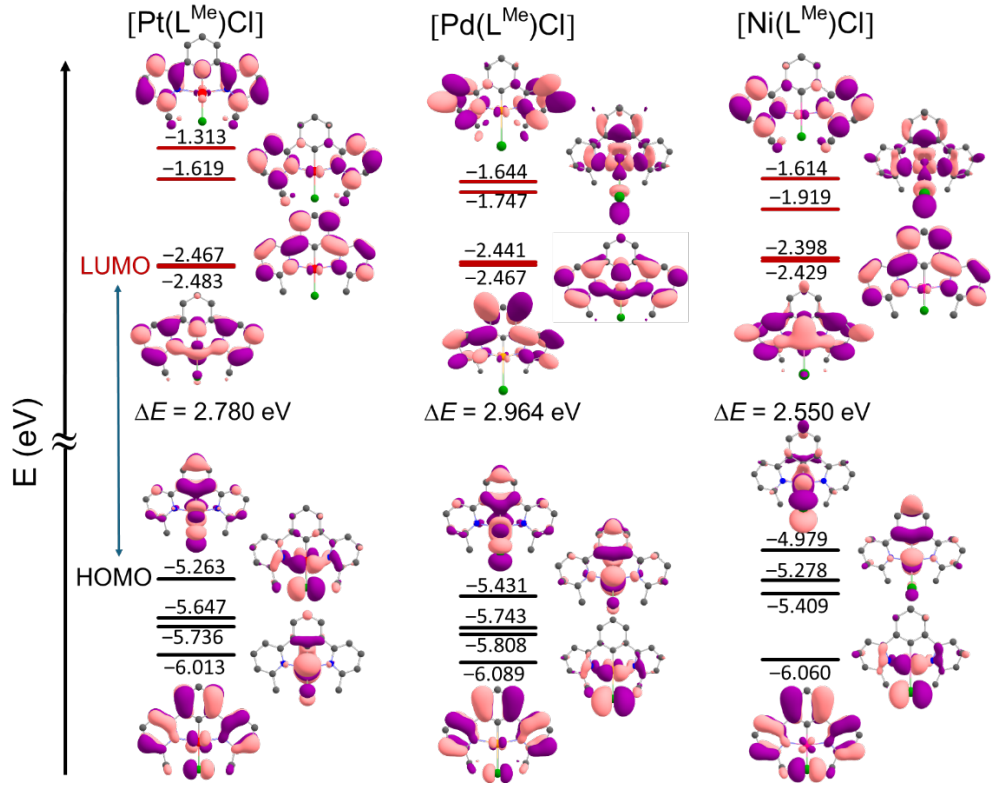


Figure A151. DFT-calculated energies of the highest occupied (HOMO, black) and lowest unoccupied (LUMO, red) molecular orbitals for [M(L^{Me})Cl] (M = Pt, Pd, and Ni).

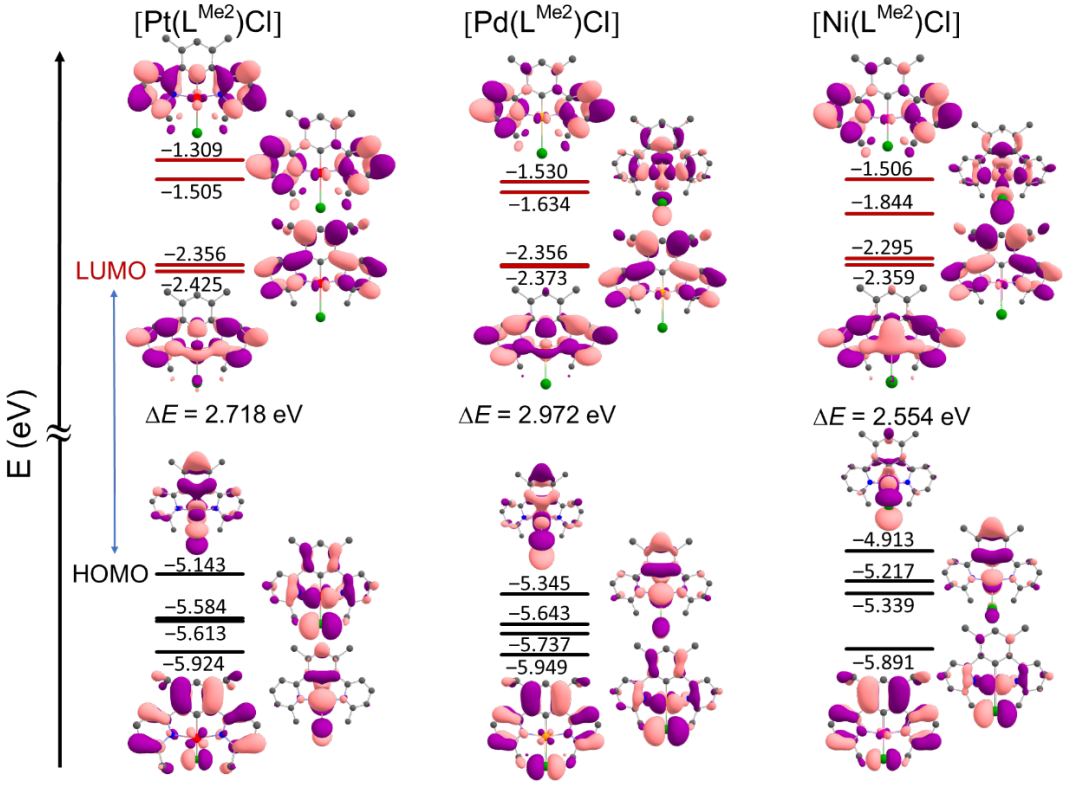


Figure A152. DFT-calculated energies of the highest occupied (HOMO, black) and lowest unoccupied (LUMO, red) molecular orbitals for [M(L^{Me2})Cl] (M = Pt, Pd, and Ni).

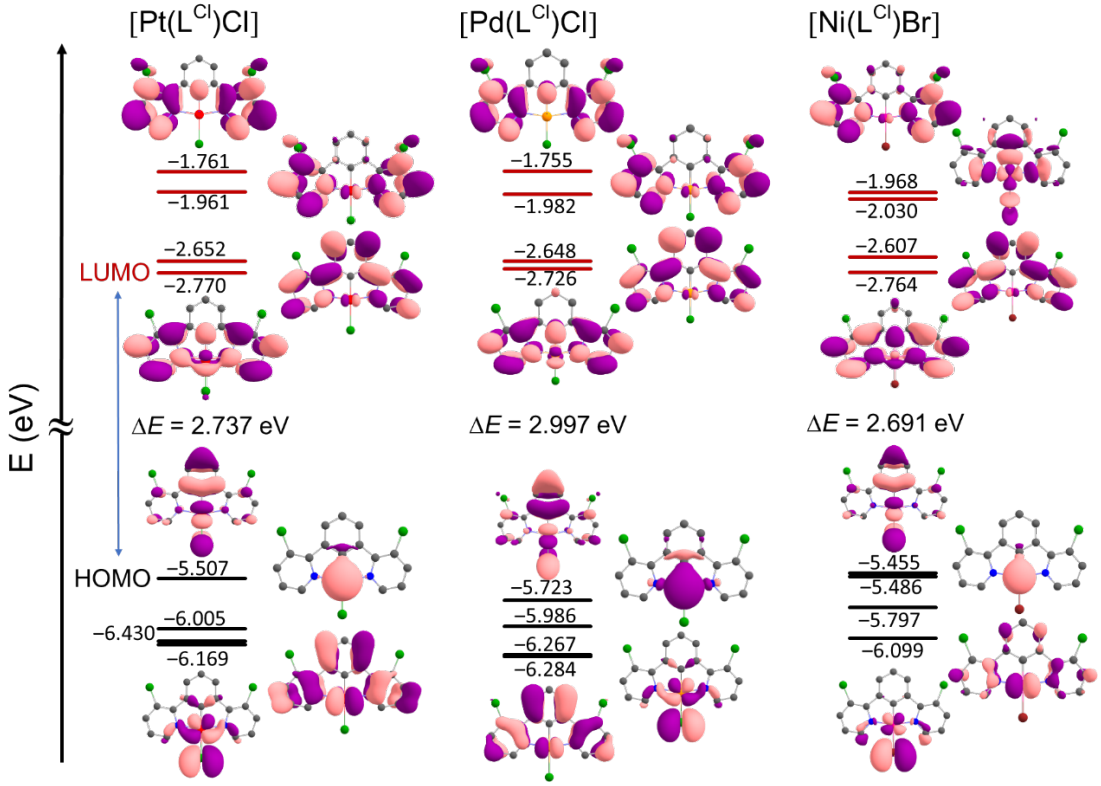


Figure A153. DFT-calculated energies of the highest occupied (HOMO, black) and lowest unoccupied (LUMO, red) molecular orbitals for [M(L^{Cl})X] (M = Pt, Pd, and Ni; X = Cl or Br).

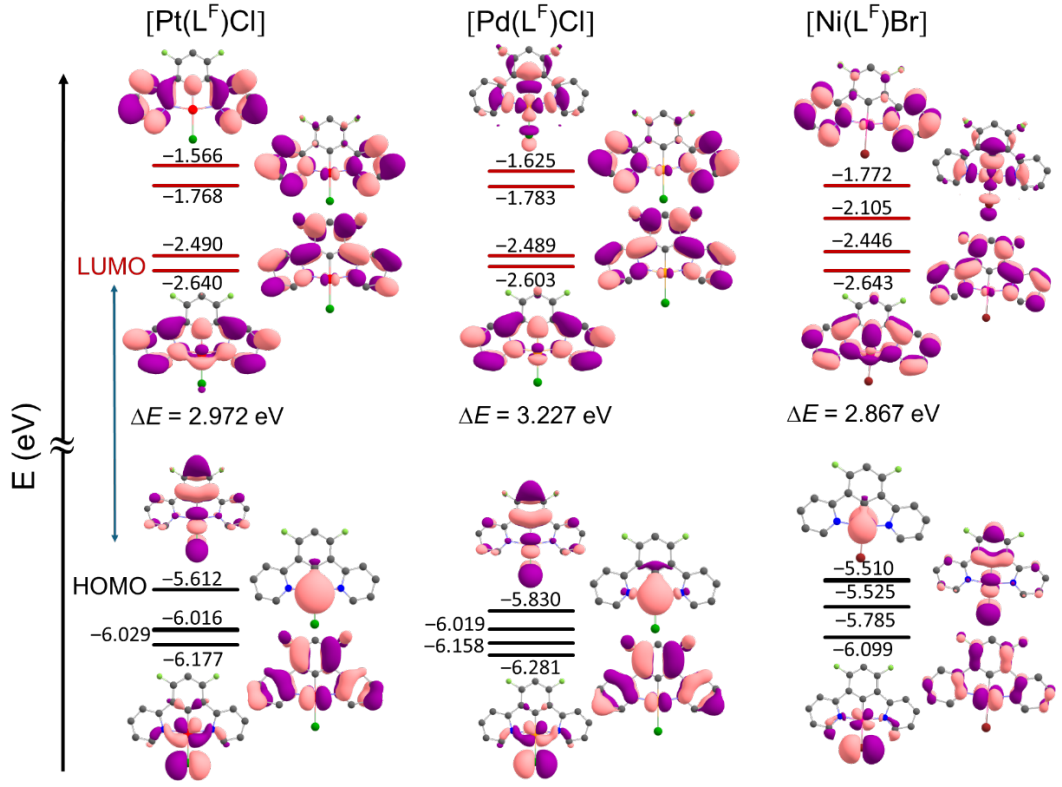


Figure A154. DFT-calculated energies of the highest occupied (HOMO, black) and lowest unoccupied (LUMO, red) molecular orbitals for [M(L^{F})Cl] (M = Pt, Pd, and Ni; X = Cl or Br).

7.5. UV-vis absorption spectra with TD-DFT-calculated electronic transitions

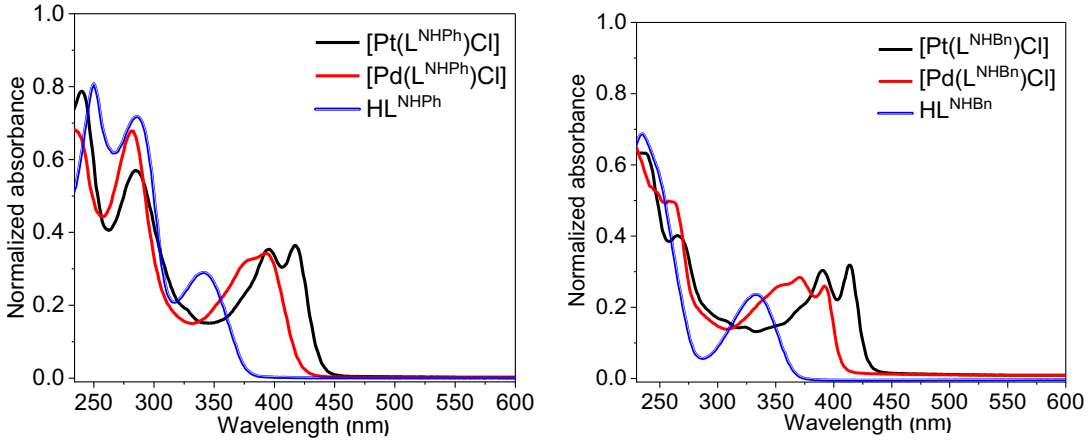


Figure A155. Experimental UV-vis absorption spectra of HL^{NHPh} (right) and HL^{NHBn} (left) and their Pd and Pt complexes measured in THF at 298 K.

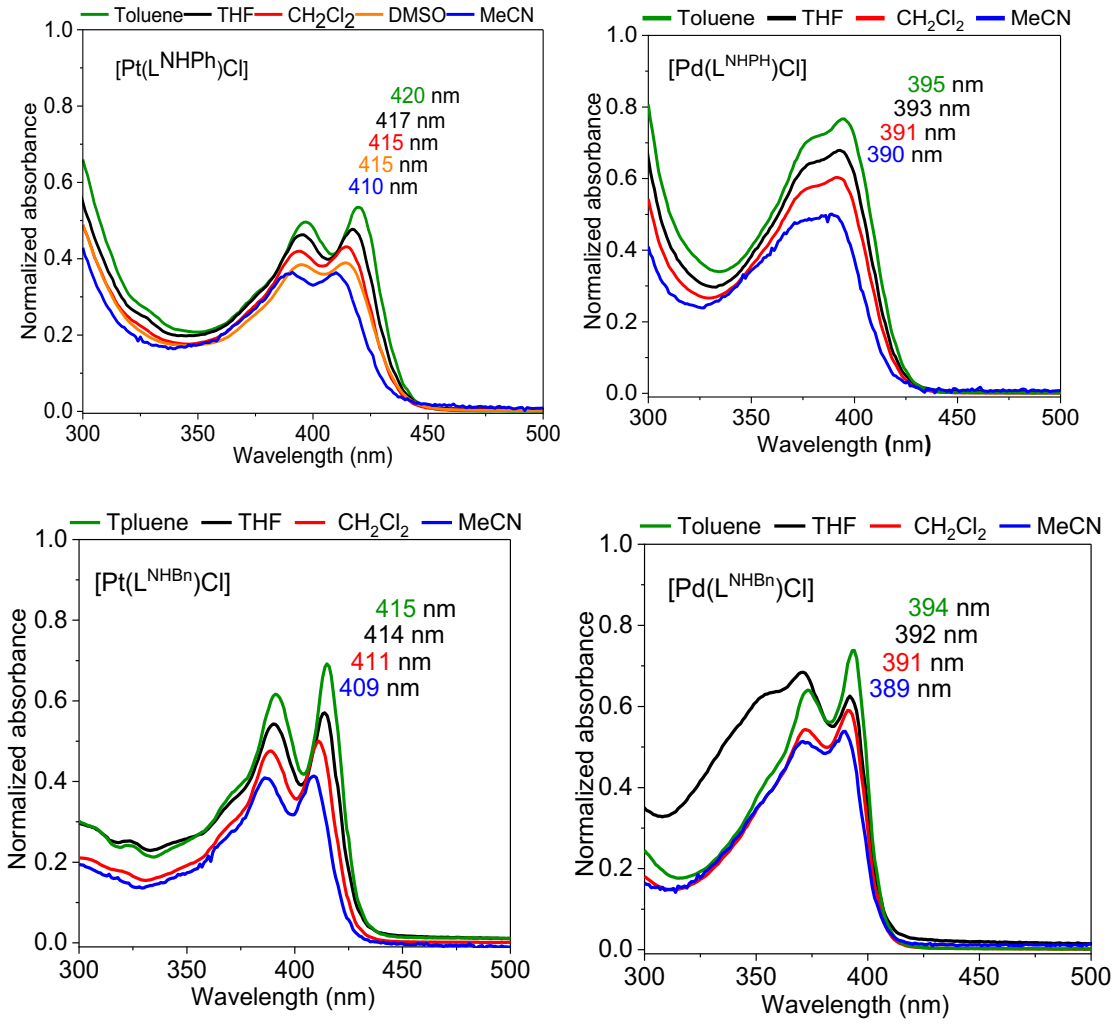


Figure A156. Experimental UV-vis absorption spectra of the complexes [M(N^C^N)Cl] (M = Pt and Pd) measured in toluene, THF, CH_2Cl_2, MeCN and DMSO (for [Pt-L^{NHPh}]) at 298 K.

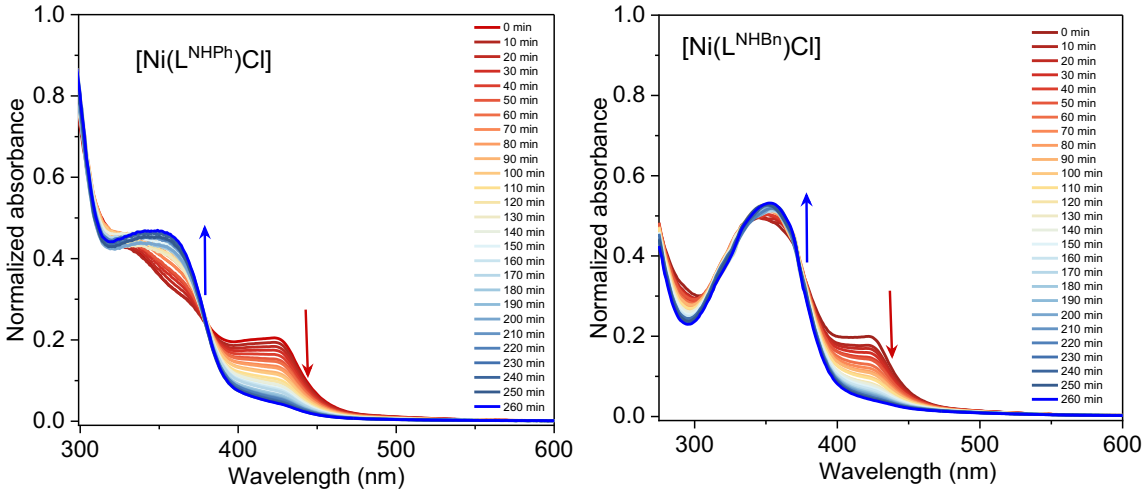


Figure A157. UV-vis absorption spectra of the [Ni(N^C^N)Cl] complexes over time in THF solution at 298 K.

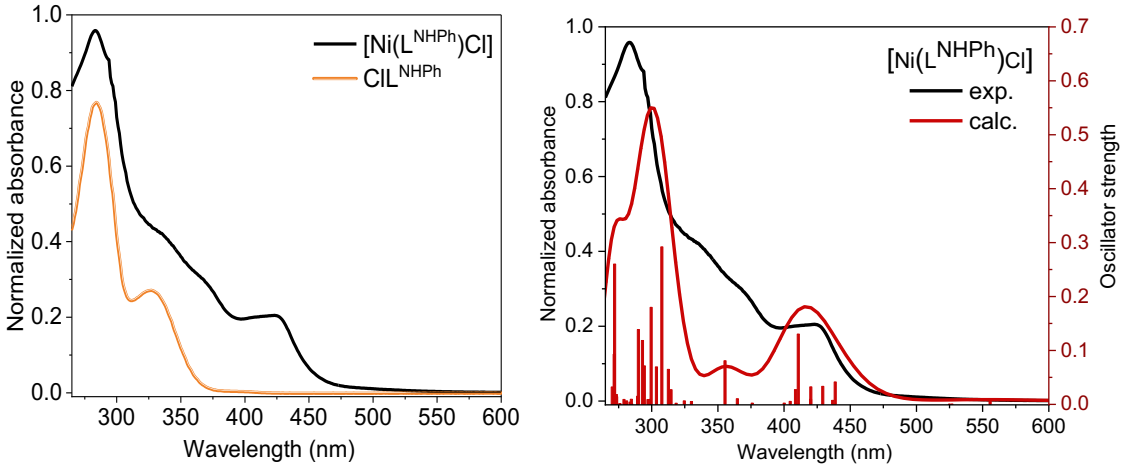


Figure A158. Experimental UV-vis absorption spectra of ClL^{NHPh}, and [Ni(L^{NHPh})Cl] measured in THF at 298 K with TD-DFT-calculated transitions (spectrum as line, individual transitions as sticks, in red).

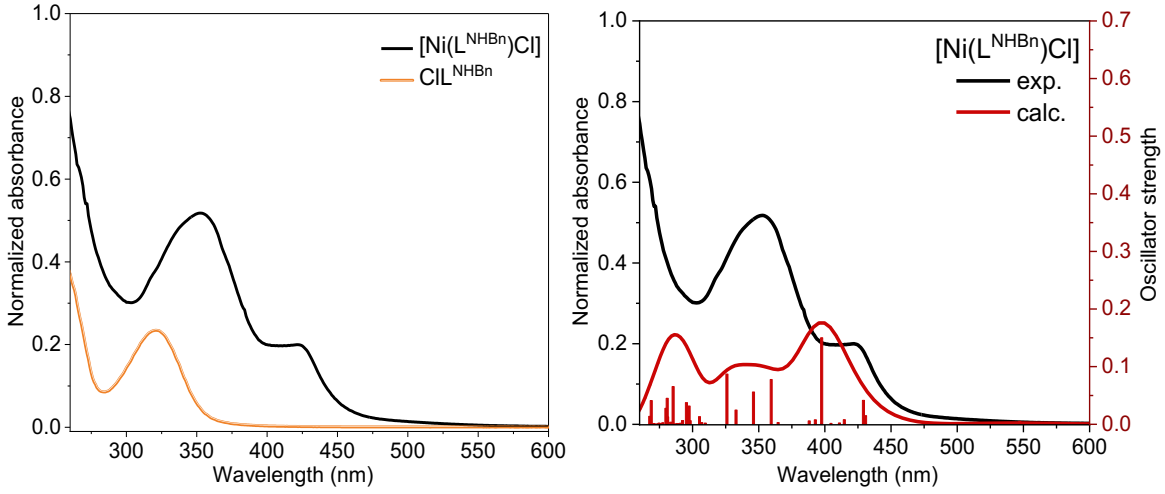


Figure A159. Experimental UV-vis absorption spectra of ClL^{NHBn}, and [Ni(L^{NHBn})Cl] measured in THF at 298 K with TD-DFT-calculated transitions (spectrum as line, individual transitions as sticks, in red).

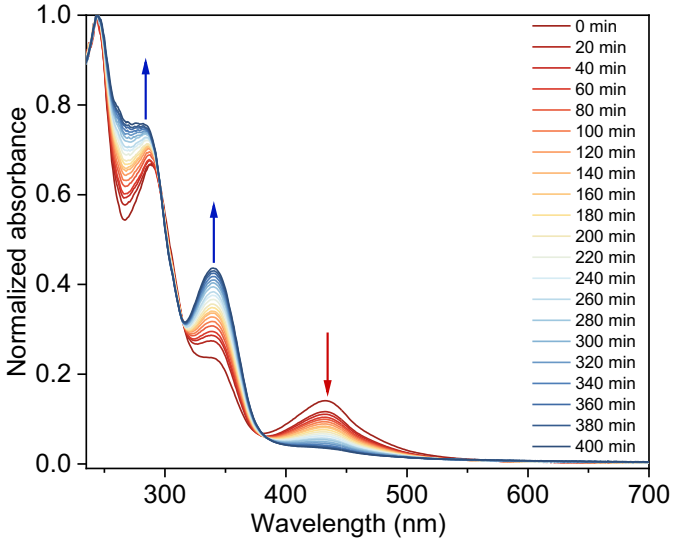


Figure A160. UV-vis absorption spectra of the complex [Ni(L^{Bn})Cl] over time in THF solution at 298 K.

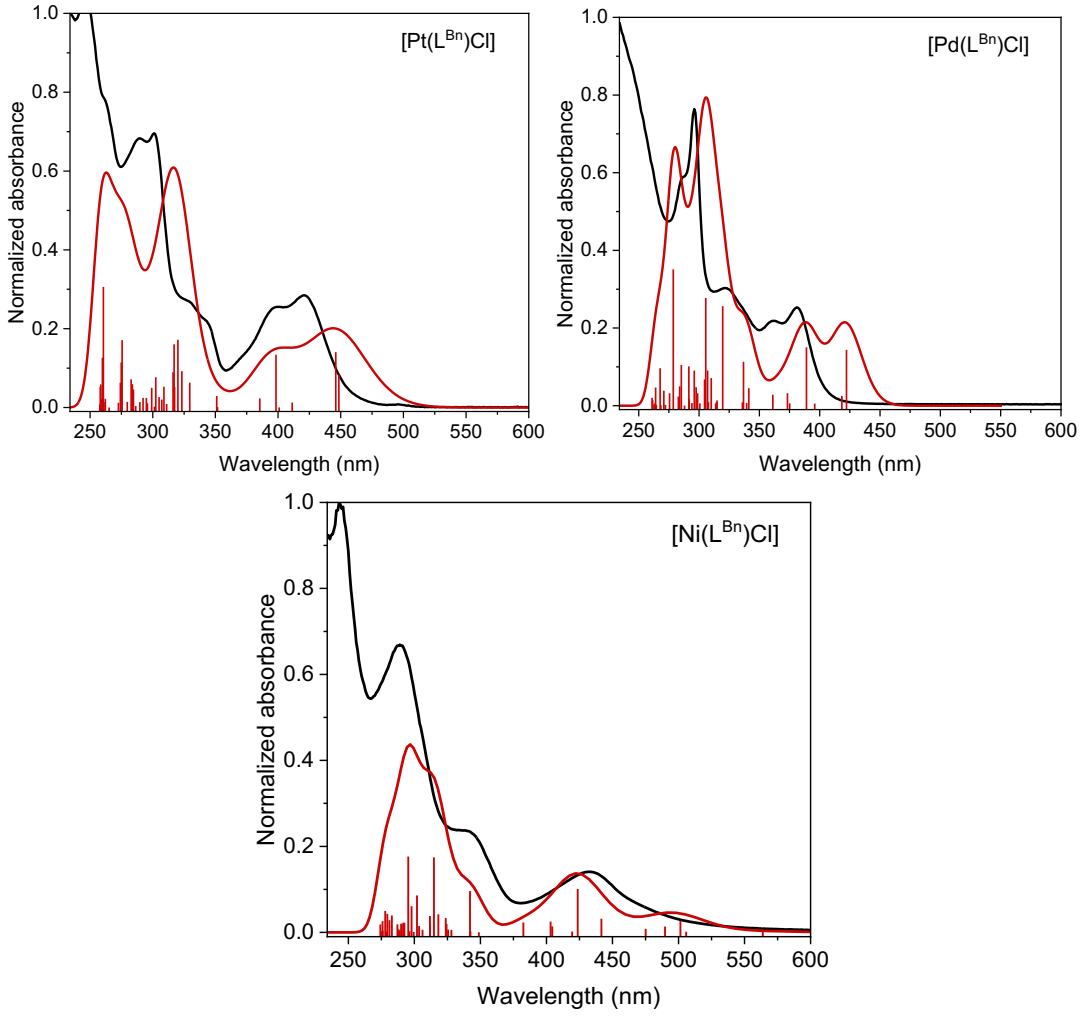


Figure A161. Experimental UV-vis absorption spectra the complexes [M(L^{Bn})Cl] (M = Pt, Pd, and Ni) measured in THF at 298 K with TD-DFT-calculated transitions on TPSSh/def2-TZVP/CPCM(THF) level of theory (sticks in red).

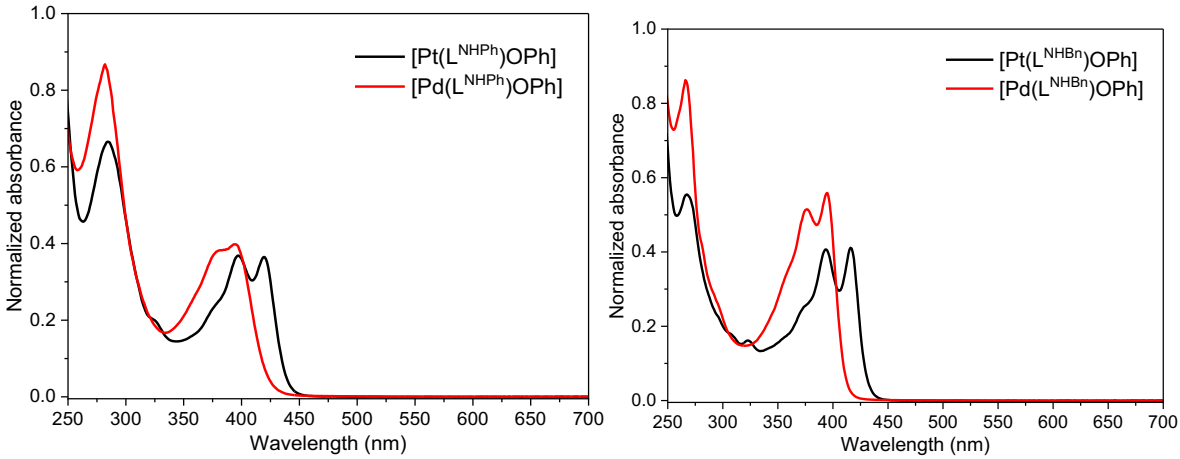


Figure A162. Experimental UV-vis absorption spectra the complexes [M(L^{NHPh})OPh] and [M(L^{NHBn})OPh] (M = Pt and Pd) measured in THF at 298 K.

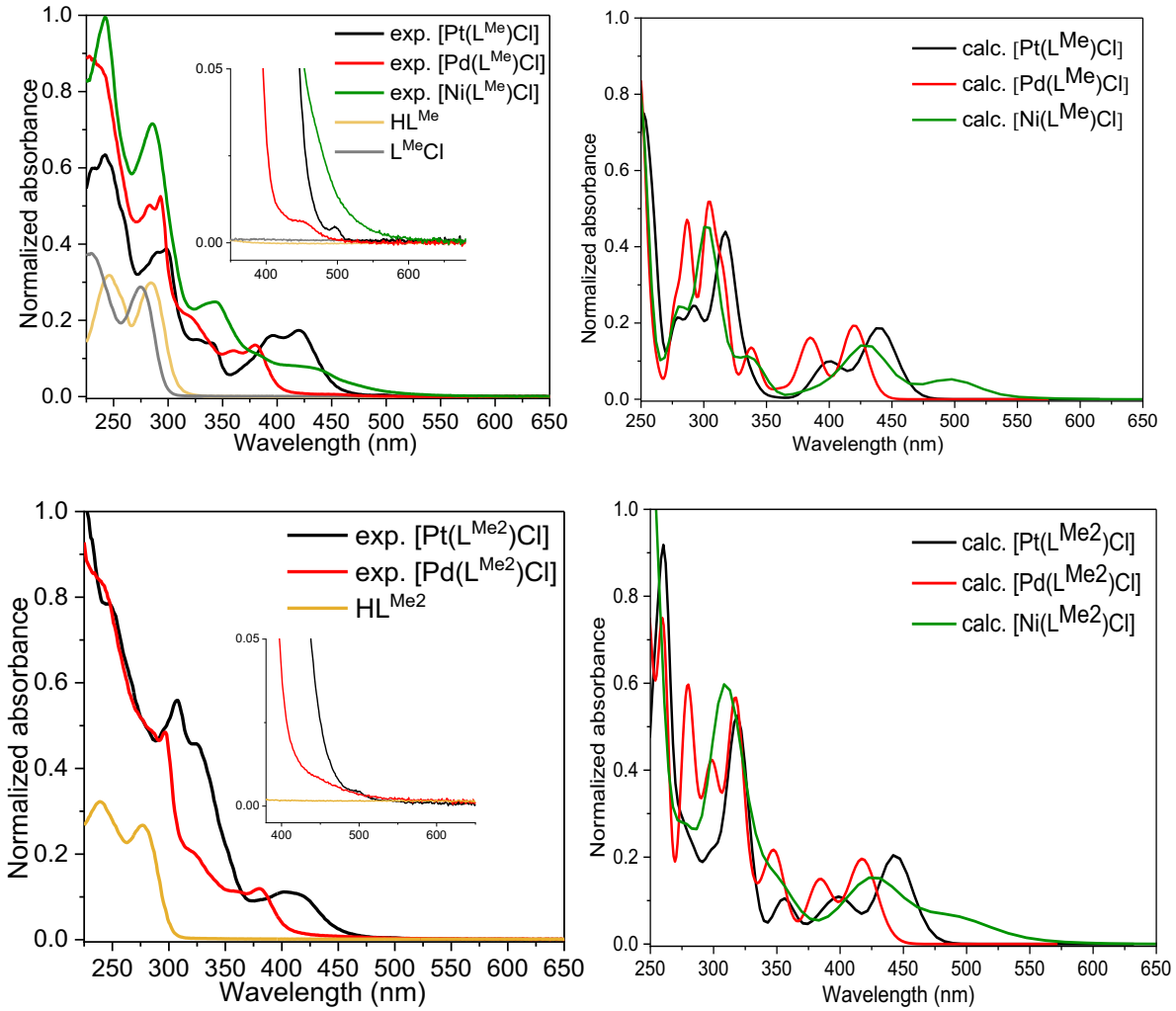


Figure A163. Experimental UV-vis absorption spectra of the complexes [M(L^{Me})Cl] and [M(L^{Me2})Cl] (M = Pt, Pd, and Ni) measured in THF at 298 K with TD-DFT-calculated transitions on TPSSh/def2-TZVP/CPCM(THF) level of theory.

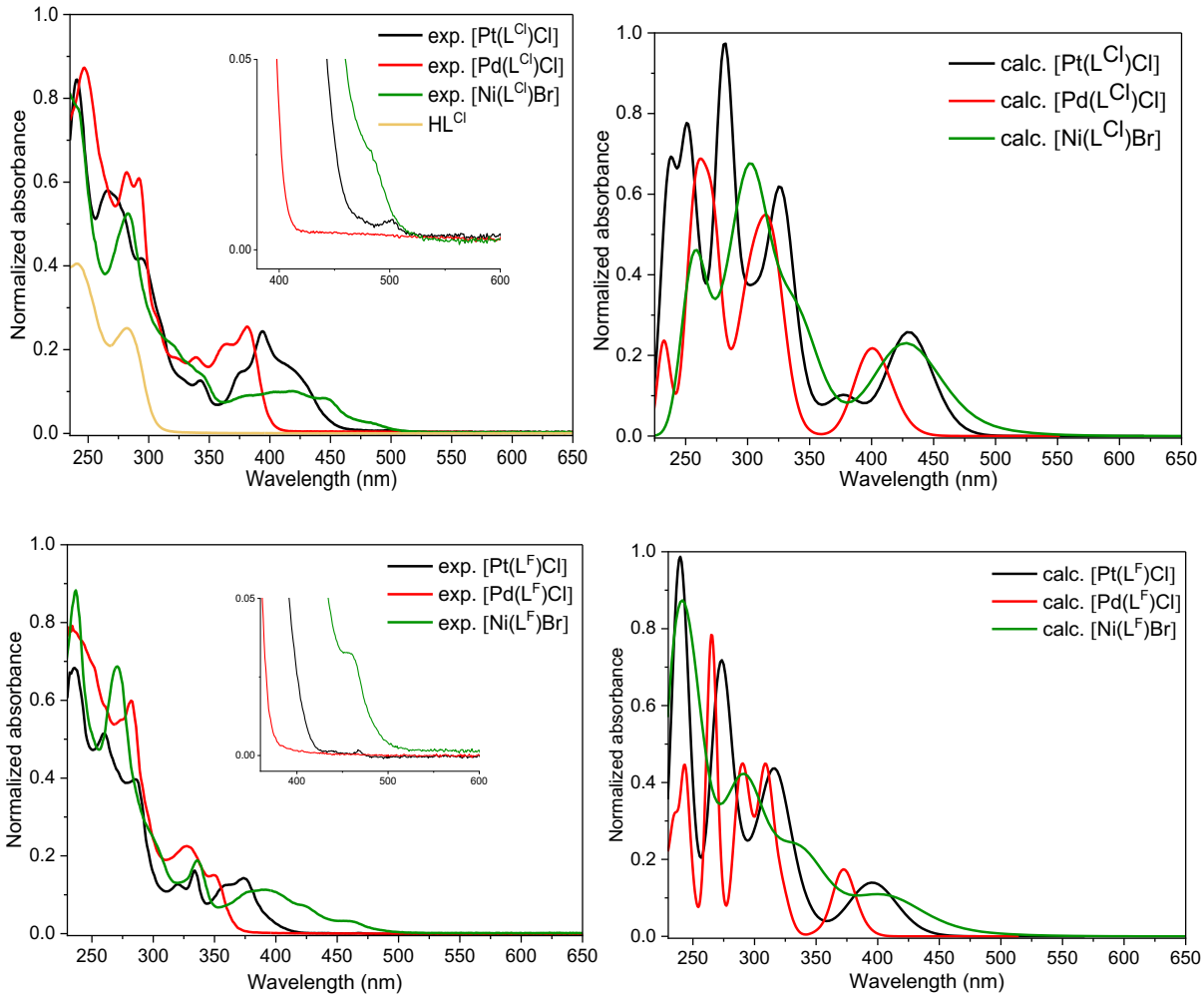


Figure A164. Experimental UV-vis absorption spectra of the complexes [M(L^{Cl})X] and [M(L^{F})X] (M = Pt, Pd, and Ni; X = Cl or Br) measured in THF at 298 K with TD-DFT-calculated transitions on TPSSh/def2-TZVP/CPCM(THF) level of theory.

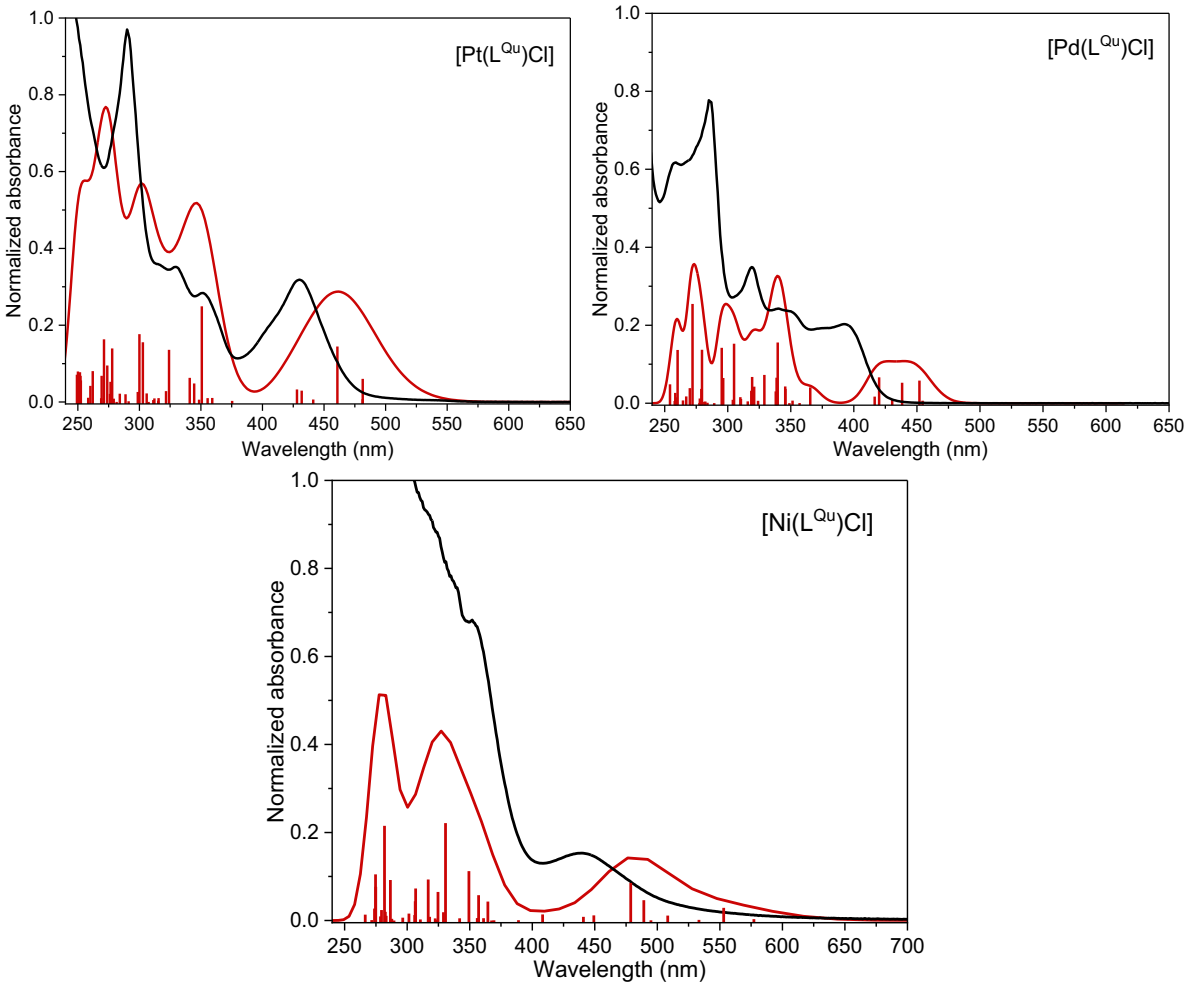


Figure A165. Experimental UV-vis absorption spectra the complexes [M(L^{Qu})Cl] (M = Pt, Pd, Ni) measured in THF at 298 K with TD-DFT-calculated transitions on TPSSh/def2-TZVP/CPCM(THF) level of theory (sticks in red).

Table A42. Selected TD-DFT-calculated vertical $S_0 \rightarrow S_n$ transitions for [M(L^{NHPh})Cl] (M = Pt or Pd).[a]

complex	S_n	oscillator strength f_{osc}	λ (nm)	transitions (major contribution)	assignment [b]
[Pt(L^{NHPh})Cl]	S_1	0.063	431.9	HOMO→LUMO (90%)	π–π* (L), L'LCT, MLCT
	S_2	0.012	425.6	HOMO→L+1 (90%)	π–π* (L), L'LCT, MLCT
	S_3	0.257	415.1	H-1→L+1 (90%)	L'LCT, π–π* (L)
	S_4	0.028	410.8	H-1→LUMO (87%)	L'LCT, π–π* (L)
	S_5	0.014	366.5	H-3→L+1 (93%)	MLCT
	S_7	0.039	357.2	H-2→LUMO (79%)	L'LCT, π–π* (L), MLCT
	S_{10}	0.028	334.9	H-4→LUMO (48%)	MLCT, π–π* (L)
	S_{11}	0.069	329.0	H-4→LUMO (34%)	MLCT, π–π* (L)
				HOMO→L+3 (34%)	π–π* (L), LMCT, L'LCT, L'MCT, MLCT
	S_{14}	0.051	310.3	H-1→L+2 (65%)	L'LCT, π–π* (L'), π–π* (L), LL'CT
	S_{15}	0.071	302.9	H-5→L+1 (65%)	L'LCT, π–π* (L)
				H-1→L+4 (17%)	L'LCT, L'MCT, π–π* (L), LMCT
	S_{16}	0.663	301.9	HOMO→L+4 (37%)	π–π* (L), LMCT, L'LCT, L'MCT, MLCT
				H-1→L+2 (27%)	L'LCT, π–π* (L'), π–π* (L), LL'CT
	S_{18}	0.044	296.1	H-5→LUMO (48)	L'LCT, π–π* (L)
				H-8→LUMO (17%)	MLCT
	S_{20}	0.080	290.5	H-8→L+1 (39%)	MLCT
				H-7→L+1 (19%)	L'LCT
				H-5→L+1 (18%)	L'LCT, π–π* (L)
	S_{27}	0.023	281.4	H-3→L+2 (42%)	MLCT, ML'CT
				H-4→L+3 (22%)	MLCT, d–d, π–π* (L), LMCT
	S_{36}	0.108	268.3	H-2→L+4 (42%)	L'LCT, L'MCT, π–π* (L), LMCT, MLCT
				H-2→L+3 (16%)	L'LCT, L'MCT, π–π* (L), LMCT, MLCT
	S_{37}	0.104	267.5	H-9→L+1 (56%)	π–π* (L), L'LCT
				H-4→L+2 (19%)	MLCT, ML'CT, π–π* (L), LL'CT
	S_{39}	0.226	259.7	H-4→L+4 (56%)	MLCT, d–d, π–π* (L), LMCT
				H-4→L+3 (17%)	MLCT, d–d, π–π* (L), LMCT
	S_{43}	0.055	253.1	H-1→L+7 (74%)	π–π* (L'), L'LCT, LL'CT, π–π* (L)
[Pd(L^{NHPh})Cl]	S_3	0.150	410.3	HOMO→L+1 (41%)	L'LCT, π–π* (L)
				H-1→LUMO (34%)	L'LCT, π–π* (L)
				HOMO→L+2 (25%)	L'LCT, L'MCT, π–π* (L), LMCT
	S_4	0.015	408.6	HOMO→LUMO (79%)	L'LCT, π–π* (L)
				H-1→L+2 (17%)	L'LCT, L'MCT, π–π* (L), LMCT
	S_5	0.098	402.0	HOMO→L+2 (72%)	L'LCT, L'MCT, π–π* (L), LMCT
				HOMO→L+1 (23%)	L'LCT, π–π* (L)
	S_6	0.038	399.2	H-1→L+1 (61%)	L'LCT, π–π* (L)
				H-1→L+2 (27%)	L'LCT, L'MCT, π–π* (L), LMCT
	S_7	0.015	362.5	H-3→L+1 (58%)	MLCT
				H-3→L+2 (34%)	MLCT, d–d
	S_{11}	0.079	345.5	H-2→LUMO (85%)	MLCT, π–π* (L)
	S_{15}	0.089	314.2	H-4→LUMO (65%)	π–π* (L), MLCT
				H-5→LUMO (27%)	MLCT, L'LCT, π–π* (L), XLCT
	S_{17}	0.149	307.6	HOMO→L+3 (85%)	L'LCT, π–π* (L'), π–π* (L), LL'CT
	S_{20}	0.623	294.9	H-1→L+4 (42%)	L'LCT, π–π* (L'), π–π* (L), LL'CT
				H-5→LUMO (35%)	MLCT, L'LCT, π–π* (L), XLCT
	S_{34}	0.089	272.3	H-2→L+3 (74%)	MLCT, ML'CT, π–π* (L), LL'CT

[a] For oscillator strength f > 0.01 except for the lowest-energy transition. M = Pt or Pd; L = N^C^N core; L' = NHPh; X = Cl. [b] Sorted from highest to lowest probability.

Table A43. Selected TD-DFT-calculated vertical $S_0 \rightarrow S_n$ transitions for [M(L^{NHBn})Cl] (M = Pt or Pd).[a]

complex	S_n	oscillator strength f_{osc}	λ (nm)	transitions (major contribution)	assignment [b]
[Pt(L^{NHBn})Cl]	S_1	0.066	412.6	HOMO→LUMO (85%)	π–π* (L), MLCT
	S_3	0.387	384.2	H-1→L+1 (85%)	π–π* (L), L'LCT
				HOMO→LUMO (13%)	π–π* (L), MLCT
	S_6	0.016	358.9	H-2→L+1 (98%)	MLCT
	S_{11}	0.143	319.4	H-4→L+1 (44%)	π–π* (L), L'LCT, MLCT
				H-3→LUMO (32%)	MLCT, π–π* (L)
				HOMO→L+2 (15%)	π–π* (L), LMCT, MLCT, d–d
	S_{15}	0.048	295.1	H-9→L+1 (63%)	MLCT, XLCT
				H-7→L+1 (17%)	L'LCT, MLCT
				H-6→LUMO (11%)	L'LCT
	S_{27}	0.042	272.9	HOMO→L+4 (54%)	LL'CT, π–π* (L), ML'CT, MLCT
				H-1→L+5 (14%)	LL'CT, π–π* (L')
				H-1→L+3 (13%)	π–π* (L), L'LCT
	S_{35}	0.071	262.9	HOMO→L+8 (50%)	LL'CT, π–π* (L), ML'CT, MLCT
				H-1→L+5 (26%)	LL'CT, π–π* (L')
	S_{43}	0.086	251.8	H-9→L+2 (50%)	MLCT, d–d, XLCT, XMCT
[Pd(L^{NHBn})Cl]	S_3	0.028	387.1	HOMO→L+2 (52%)	π–π* (L), LMCT, L'LCT, L'MCT
				H-1→LUMO (44%)	π–π* (L), L'LCT, MLCT
	S_4	0.011	380.2	HOMO→LUMO (65%)	π–π* (L), L'LCT
				H-1→L+1 (17%)	π–π* (L), L'LCT
	S_5	0.394	370.6	HOMO→L+1 (46%)	π–π* (L), L'LCT
				H-1→LUMO (26%)	π–π* (L), L'LCT
				HOMO→L+2 (22%)	π–π* (L), LMCT, L'LCT, L'MCT
	S_7	0.017	354.6	H-2→L+1 (48%)	MLCT
				H-2→L+2 (25%)	MLCT, d–d
				H-1→L+1 (16%)	π–π* (L), L'LCT
	S_{15}	0.147	308.7	H-4→LUMO (65%)	MLCT, π–π* (L)
				H-3→L+1 (14%)	π–π* (L), L'LCT, MLCT
	S_{30}	0.073	275.3	HOMO→L+3 (82%)	π–π* (L), L'LCT
	S_{42}	0.055	258.2	H-11→L+2 (18%)	MLCT, d–d, π–π* (L), LMCT, L'LCT
				H-11→L+1 (16%)	MLCT, π–π* (L), L'LCT
				HOMO→L+4 (14%)	LL'CT, π–π* (L), π–π* (L'), L'LCT
	S_{43}	0.034	257.4	H-1→L+4 (29%)	LL'CT, π–π* (L), π–π* (L'), L'LCT
				HOMO→L+6 (22%)	LL'CT, π–π* (L')
				H-1→L+6 (16%)	LL'CT, π–π* (L')

[a] For oscillator strength f > 0.01 except for the lowest-energy transition. M = Pt or Pd; L = N^C^N core; L' = NHBn; X = Cl. [b] Sorted from highest to lowest probability.

Table A44. Selected TD-DFT-calculated vertical $S_0 \rightarrow S_n$ transitions for [Ni(L^{NHPh})Cl].[a]

S_n	oscillator strength f_{osc}	λ (nm)	transitions (major contribution)	assignment [b]
S_1	0.004	555.6	H-2→LUMO (37%)	MLCT, d–d
			HOMO→LUMO (37%)	MLCT, d–d, π–π* (L), LMCT, L'LCT, L'MCT
			HOMO→L+2 (16%)	MLCT, d–d, π–π* (L), LMCT, L'LCT, L'MCT
S_3	0.000	524.9	H-4→LUMO (37%)	MLCT, d–d, π–π* (L), LMCT
			H-1→LUMO (32%)	L'LCT, L'MCT, LLCT, LMCT
S_4	0.042	438.7	HOMO→L+1 (77%)	MLCT, LLCT, L'LCT
			H-2→L+1 (18%)	MLCT
S_6	0.033	429.2	H-1→LUMO (61%)	L'LCT, L'MCT, π–π* (L), LMCT
			H-4→LUMO (13%)	MLCT, d–d, π–π* (L), LMCT
S_9	0.130	410.7	H-1→L+2 (63%)	L'LCT, L'MCT, π–π* (L), LMCT
			H-4→LUMO (18%)	MLCT, d–d, π–π* (L), LMCT
S_{16}	0.081	355.4	H-3→L+2 (44%)	MLCT, d–d, L'LCT, L'MCT, π–π* (L), LMCT
			H-4→L+1 (41%)	MLCT, π–π* (L)
S_{22}	0.292	307.7	HOMO→L+4 (44%)	MLCT, ML'CT, π–π* (L), LL'CT, L'LCT,
			H-1→L+3 (26%)	L'LCT, π–π* (L'), π–π* (L), LL'CT
			H-2→L+4 (23%)	MLCT, ML'CT
S_{23}	0.118	293.0	H-5→L+1 (35%)	π–π* (L), L'LCT
			H-8→L+1 (23%)	L'LCT, MLCT
			H-4→L+3 (22%)	MLCT, ML'CT, π–π* (L), LL'CT
S_{43}	0.260	272.0	H-3→L+4 (77%)	MLCT, ML'CT, L'LCT, π–π* (L'), π–π* (L), LL'CT

[a] For oscillator strength f > 0.01 except for the lowest-energy transition. M = Ni; L = N^C^N core; L' = NHPh; X = Cl. [b] Sorted from highest to lowest probability.

Table A45. Selected TD-DFT-calculated vertical $S_0 \rightarrow S_n$ transitions for [Ni(L^{NHBn})Cl].[a]

S_n	oscillator strength f_{osc}	λ (nm)	transitions (major contribution)	assignment [b]
S_1	0.003	547.3	HOMO→LUMO (50%)	MLCT, d–d, π–π* (L), LMCT
			H-1→LUMO (25%)	MLCT, d–d, π–π* (L), LMCT
			HOMO→L+2 (17%)	MLCT, d–d
S_2	0.001	523.8	H-2→LUMO (34%)	MLCT, d–d, π–π* (L), LMCT, L'LCT, L'MCT
			H-3→LUMO (25%)	MLCT, d–d, π–π* (L), LMCT
			H-2→L+2 (12%)	MLCT, d–d, π–π* (L), LMCT, L'LCT, L'MCT
S_4	0.015	430.7	HOMO→L+1 (44%)	MLCT, LLCT
			HOMO→L+2 (15%)	MLCT, d–d, π–π* (L), LMCT
			H-1→L+1 (11%)	MLCT
S_9	0.220	397.6	H-2→LUMO (22%)	MLCT, d–d, π–π* (L), LMCT, L'LCT, L'MCT
			H-2→L+2 (18%)	MLCT, d–d, π–π* (L), LMCT, L'LCT, L'MCT
S_{14}	0.056	346.0	H-3→L+1 (77%)	MLCT, π–π* (L)
S_{16}	0.087	326.0	H-4→L+2 (74%)	L'LCT, L'MCT, LLCT, LMCT, MLCT, d–d
S_{31}	0.065	285.3	H-2→L+3 (61%)	MLCT, π–π* (L), L'LCT
S_{44}	0.041	268.8	H-2→L+4 (39%)	ML'CT, MLCT, LL'CT, π–π* (L), π–π* (L'), L'LCT
			H-11→L+2 (20%)	π–π* (L), LMCT, L'LCT, L'MCT

[a] For oscillator strength f > 0.01 except for the lowest-energy transition. M = Ni; L = N^C^N core; L' = NHBn; X = Cl. [b] Sorted from highest to lowest probability.

Table A46. Selected TD-DFT-calculated vertical $S_0 \rightarrow S_n$ transitions for [M(L^{Bn})Cl] (M = Pt, Pd, and Ni).[a]

complex	S_n	oscillator strength f_{osc}	λ (nm)	transitions (major contribution)	Assignment [b]
[Pt(L^{Bn})Cl]	S_1	0.043	448.5	HOMO→LUMO (90%)	π–π* (L), MLCT
	S_2	0.072	446.0	HOMO→L+1 (90%)	π–π* (L), MLCT
	S_3	0.007	411.3	H-1→LUMO (90%)	MLCT, π–π* (L)
	S_5	0.069	398.3	H-2→LUMO (56%)	MLCT
				H-1→L+1 (27%)	MLCT, π–π* (L)
	S_9	0.032	329.6	H-3→L+1 (48%)	π–π* (L)
	S_{10}	0.047	323.3	HOMO→L+3 (63%)	π–π* (L), LL'CT, MLCT, ML'CT
	S_{11}	0.088	320.1	H-5→LUMO (41%)	L'LCT
				H-1→L+2 (30%)	MLCT, π–π* (L)
				H-6→LUMO (16%)	L'LCT, MLCT
	S_{13}	0.082	317.1	H-4→LUMO (52%)	L'LCT
	S_{14}	0.046	316.2	H-5→L+1 (37%)	L'LCT, MLCT
				H-2→L+2 (26%)	MLCT, π–π* (L)
	S_{19}	0.039	302.5	H-6→L+1 (41%)	L'LCT, MLCT
	S_{28}	0.023	284.6	H-10→LUMO (63%)	π–π* (L)
	S_{31}	0.037	282.8	HOMO→L+5 (61%)	LL'CT
	S_{33}	0.088	275.6	H-2→L+6 (44%)	MLCT, ML'CT, π–π* (L), LL'CT
	S_{45}	0.157	260.6	H-3→L+3 (44%)	π–π* (L), LL'CT
[Pd(L^{Bn})Cl]	S_1	0.060	422.2	HOMO→LUMO (93%)	π–π* (L), MLCT
	S_4	0.063	389.0	H-1→LUMO (87%)	MLCT, π–π* (L)
	S_7	0.012	361.0	H-2→LUMO (44%)	MLCT
				HOMO→L+2 (44%)	π–π* (L), MLCT
	S_8	0.019	341.3	H-3→L+1 (65%)	π–π* (L)
	S_{10}	0.047	336.8	H-2→L+2 (65%)	MLCT
	S_{12}	0.107	319.6	H-3→LUMO (61%)	π–π* (L)
	S_{16}	0.030	310.1	H-5→L+1 (50%)	L'LCT
	S_{24}	0.038	296.0	H-3→L+2 (74%)	π–π* (L)
	S_{30}	0.044	285.3	H-10→LUMO (50%)	π–π* (L)
	S_{33}	0.146	278.6	H-2→L+4 (72%)	MLCT, ML'CT
	S_{38}	0.040	267.7	H-5→L+2 (79%)	L'LCT
	S_{40}	0.020	264.0	H-4→L+3 (46%)	L'LCT
				H-11→L+1 (37%)	MLCT, π–π* (L)
[Ni(L^{Bn})Cl]	S_3	0.021	501.4	HOMO→ L+1 (58%)	MLCT
	S_4	0.078	423.7	H-2→LUMO (54%)	MLCT
				H-2→L+2 (26%)	MLCT
	S_{14}	0.074	342.1	H-3→LUMO (90%)	π–π* (L)
	S_{18}	0.026	323.8	H-4→LUMO (82%)	L'LCT, π–π* (L)
	S_{20}	0.134	314.8	H-3→L+1 (52%)	π–π* (L)
				H-1→L+4 (30%)	MLCT, ML'CT, π–π* (L), LL'CT
	S_{29}	0.136	295.3	H-7→L+1 (74%)	L'LCT, π–π* (L)
	S_{37}	0.030	282.9	H-10→LUMO (74%)	XLCT, L'LCT
	S_{43}	0.020	275.9	H-6→L+2 (56%)	L'LCT
				H-11→LUMO (37%)	MLCT, XLCT
	S_{45}	0.014	274.2	HOMO→L+9 (52%)	MLCT

[a] For oscillator strength f > 0.01 except for the lowest-energy transition. M = Pt, Pd, or Ni; L = NCN core; L' = Bn; X = Cl. [b] Sorted from highest to lowest probability.

Table A47. Selected TD-DFT-calculated vertical $S_0 \rightarrow S_n$ transitions for [M(L^{NHPh})OPh] (M = Pt and Pd).[a]

complex	S_n	oscillator strength f_{osc}	λ (nm)	transitions (major contribution)	Assignment [b]
[Pt(L^{NHPh})OPh]	S_1	0.027	436.1	HOMO→LUMO (87%)	XLCT
	S_5	0.141	411.8	H-2→LUMO (37%)	L'LCT, π–π* (L)
				H-2→L+1 (32%)	L'LCT, π–π* (L)
	S_6	0.171	406.8	H-2→L+1 (54%)	L'LCT, π–π* (L)
				H-2→LUMO (41%)	L'LCT, π–π* (L)
	S_8	0.012	370.0	H-4→L+1 (74%)	MLCT
	S_{12}	0.138	335.8	H-5→LUMO (82%)	π–π* (L), MLCT
	S_{17}	0.443	307.6	H-1→L+3 (42%)	XLCT, XL'CT, π–π* (L), LL'CT
				H-2→L+2 (29%)	L'LCT, π–π* (L'), π–π* (L), LL'CT
	S_{28}	0.083	287.5	H-7→LUMO (41%)	L'LCT, π–π* (L)
	S_{44}	0.180	271.9	H-3→L+3 (72%)	L'LCT, π–π* (L')
[Pd(L^{NHPh})OPh]	S_3	0.017	412.4	H-2→LUMO (41%)	π–π* (L), L'LCT
				H-1→LUMO (39%)	L'LCT, π–π* (L)
	S_5	0.237	402.7	H-1→L+1 (72%)	L'LCT, π–π* (L)
	S_6	0.076	394.5	H-2→L+1 (87%)	π–π* (L), L'LCT
	S_8	0.013	365.1	H-3→L+1 (74%)	MLCT
	S_9	0.019	352.5	H-4→LUMO (46%)	MLCT, π–π* (L)
	S_{10}	0.059	348.7	HOMO→L+2 (54%)	XLCT, XMCT
				H-4→LUMO (26%)	MLCT, π–π* (L)
	S_{19}	0.217	308.9	H-2→L+3 (42%)	π–π* (L), L'LCT
	S_{25}	0.369	296.6	H-2→L+4 (74%)	π–π* (L), LL'CT, L'LCT, π–π* (L')
	S_{35}	0.144	283.2	H-8→L+1 (37%)	π–π* (L), XLCT
[Pt(L^{NHBn})OPh]	S_3	0.075	421.8	H-1→ LUMO (90%)	π–π* (L)
	S_6	0.398	388.9	H-2→L+1 (87%)	L'LCT, π–π* (L)
	S_8	0.015	366.8	H-3→L+1 (98%)	MLCT, π–π* (L)
	S_{12}	0.189	326.9	H-5→L+1 (54%)	L'LCT, π–π* (L)
				H-4→LUMO (37%)	π–π* (L), MLCT
	S_{17}	0.033	292.7	H-8→LUMO (37%)	L'LCT
	S_{27}	0.024	285.1	H-1→L+3 (74%)	LL'CT
	S_{44}	0.012	272.3	H-2→L+6 (67%)	π–π* (L'), LL'CT
[Pd(L^{NHBn})OPh]	S_3	0.044	399.1	H-1→LUMO (67%)	π–π* (L), L'LCT
	S_5	0.399	378.7	H-2→L+1 (63%)	π–π* (L), L'LCT
	S_8	0.015	362.7	H-3→L+1 (95%)	MLCT, π–π* (L)
	S_{15}	0.147	319.1	H-5→LUMO (50%)	MLCT, π–π* (L)
				H-4→L+1 (35%)	π–π* (L)
	S_{17}	0.032	303.9	H-3→L+2 (77%)	MLCT, π–π* (L)
	S_{21}	0.028	292.5	HOMO→L+4 (37%)	XL'CT
	S_{31}	0.015	284.3	H-8→L+1 (37%)	L'LCT
	S_{33}	0.080	282.0	H-2→L+3 (61%)	π–π* (L), LL'CT, L'LCT, π–π* (L')

[a] For oscillator strength f > 0.01 except for the lowest-energy transition. M = Pt, Pd, or Ni; L = NCN core; L' = Bn; X = Cl. [b] Sorted from highest to lowest probability.

Table A48. Selected TD-DFT-calculated vertical $S_0 \rightarrow S_n$ transitions for [M(L^{Qu})Cl] (M = Pt, Pd, Ni).[a]

complex	S_n	oscillator strength f_{osc}	λ (nm)	transitions (major contribution)	Assignment [b]
[Pt(L^{Qu})Cl]	S_1	0.060	481	HOMO→ L+1 (77%)	π–π* (L), MLCT
	S_3	0.145	461	H-1→LUMO (79%)	π–π* (L), MLCT
	S_6	0.033	428	H-2→L+1 (98%)	MLCT, π–π* (L)
	S_{10}	0.249	351	H-5→LUMO (67%)	π–π* (L)
	S_{14}	0.136	324	H-5→L+1 (35%)	π–π* (L)
				H-1→L+2 (32%)	π–π* (L), MLCT
	S_{23}	0.177	300	H-1→L+3 (41%)	MLCT, π–π* (L)
				H-8→L+1 (27%)	π–π* (L), XLCT
	S_{30}	0.139	278	H-4→L+2 (41%)	π–π* (L)
				H-9→L+1 (41%)	π–π* (L)
	S_{37}	0.081	262	H-3→ L+3 (77%)	π–π* (L)
[Pd(L^{Qu})Cl]	S_2	0.058	452	HOMO→ L+1 (85%)	π–π* (L), MLCT
	S_5	0.067	420	H-2→ L+1 (92%)	MLCT, π–π* (L)
	S_7	0.041	365	H-3→LUMO (87%)	π–π* (L)
	S_{12}	0.043	346	H-5→ LUMO (46%)	π–π* (L)
				H-4→ L+1 (30%)	π–π* (L)
	S_{13}	0.156	340	HOMO→L+2 (52%)	π–π* (L), MLCT
				H-5→LUMO (29%)	π–π* (L)
	S_{18}	0.043	321	H-2→ L+2 (58%)	MLCT, π–π* (L)
	S_{28}	0.142	295	H-1→L+4 (79%)	π–π* (L), MLCT
	S_{36}	0.255	272	H-9→L+1 (44%)	π–π* (L)
				H-4→ L+2 (37%)	π–π* (L)
	S_{40}	0.137	260	H-3→ L+4 (39%)	π–π* (L)
				H-6→ L+2 (34%)	π–π* (L), XLCT
[Ni(L^{Qu})Cl]	S_2	0.029	553	HOMO→ L+1 (92%)	MLCT, π–π* (L)
	S_7	0.085	479	H-2→ L+2 (48%)	MLCT, π–π* (L)
	S_8	0.012	449	H-1→ L+2 (48%)	MLCT, π–π* (L)
	S_{16}	0.058	357	H-1→ L+3 (85%)	MLCT, π–π* (L)
	S_{20}	0.221	331	H-4→L+1 (41%)	π–π* (L)
				H-5→L+1 (30%)	π–π* (L), MLCT
	S_{26}	0.093	318	H-2→L+4 (42%)	MLCT, π–π* (L)
	S_{35}	0.092	287	H-2→ L+5 (48%)	MLCT, π–π* (L)
	S_{42}	0.105	275	H-10→L+1 (77%)	π–π* (L)

[a] For oscillator strength f > 0.01 except for the lowest-energy transition. M = Pt, Pd, or Ni; L = NCN; X = Cl. [b] Sorted from highest to lowest probability.

7.6. Photoluminescence data

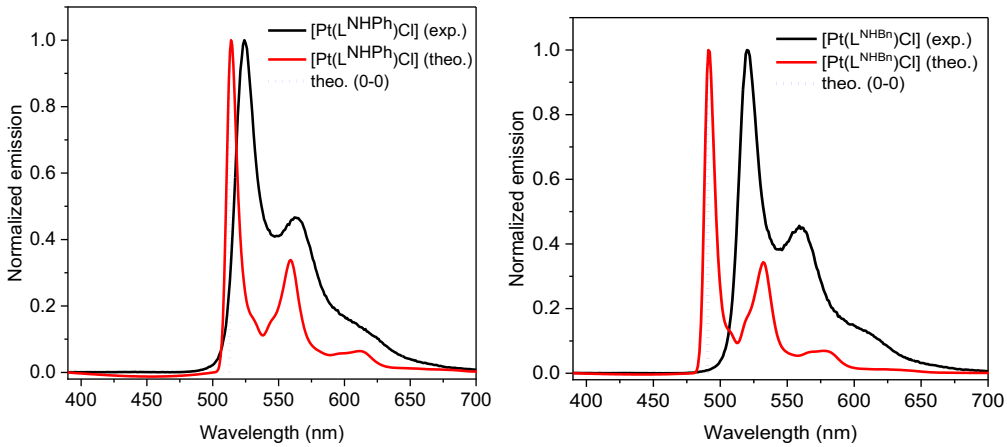


Figure A166. TD-DFT-calculated (theo.) vibrationally resolved luminescence spectra of the complexes [Pt(N^C^N)Cl] (N^C^N = L^{NHPh} or L^{NHBn}) in CH_2Cl_2 together with experimental (exp.) spectra in CH_2Cl_2 at room temperature. The calculated 0-0 transitions are shown as vertical blue dotted lines. concentration = 10^{-5} M for the experimental measurements.

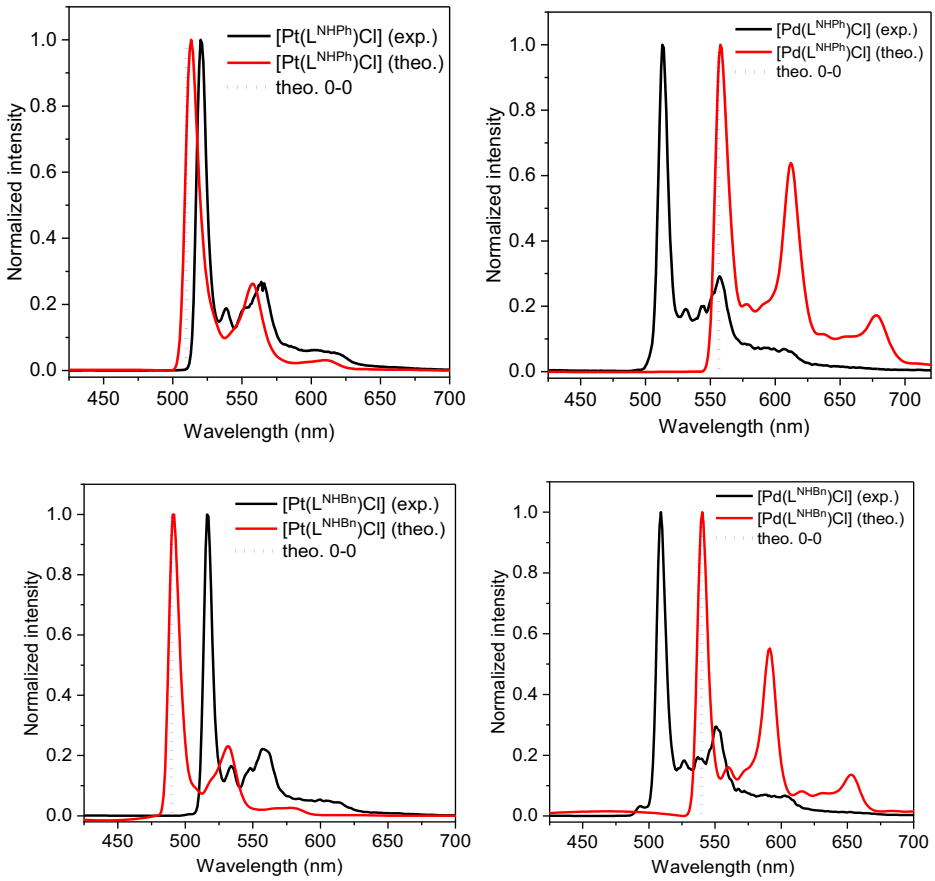
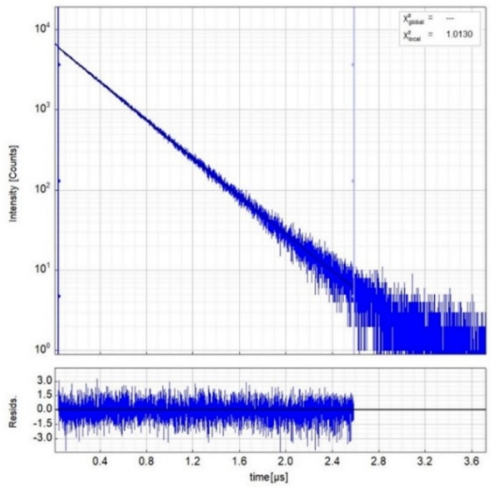
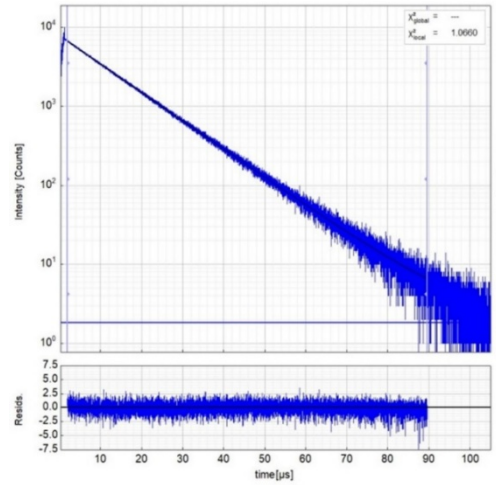


Figure A167. TD-DFT-calculated (theo.) vibrationally resolved luminescence spectra of the complexes [M(N^C^N)Cl] (M = Pt or Pd; N^C^N = L^{NHPh} or L^{NHBn}) together with experimental (exp.) spectra in 2-methyltetrahydrofuran (2-MeTHF) at 77 K (λ_{ex} = 350 nm). The calculated 0-0 transitions are shown as vertical blue dotted lines.



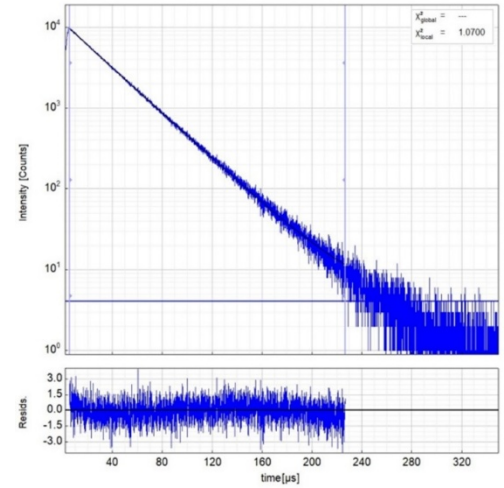
Parameter	Value	Δ	δ
A_1[kCnts/Chnl]	6.003	±0.014	0.2%
τ_1[ns]	364.28	±0.26	0.1%
I_1[kCnts]	4 270.9	±7.5	0.2%
A_{Ref1}[%]	100.0	---	---
I_{Ref1}[%]	100.0	---	---
$Bkgr_{Dec}$[kCnts]	0.0007	±0.0003	35%
τ_{AvInt}[ns]	364.28	±0.26	0.1%
τ_{AvAmp}[ns]	364.28	±0.26	0.1%

Figure A168. Left: Raw (experimental) time-resolved photoluminescence decay of [Pt(L^{NHPh})Cl] (c ≈ 10^{-5} M) in liquid CH_2Cl_2 at 298 K (air-equilibrated, λ_{ex} = 376 nm, λ_{em} = 500 nm) including the residuals. **Right**: Fitting parameters including pre-exponential factors and confidence limits.



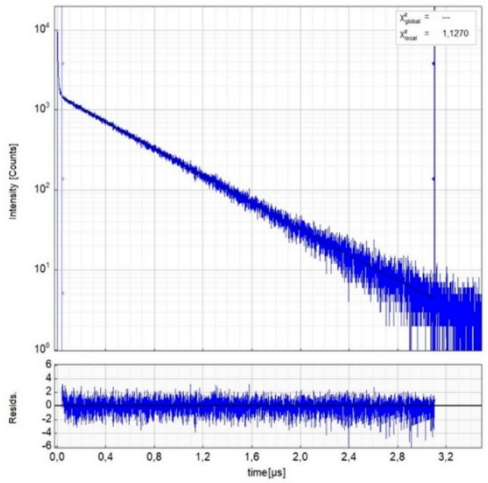
Parameter	Value	Δ	δ
A_1[kCnts/Chnl]	6.6844	±0.0062	0.1%
τ_1[ns]	12 110.2	±7.6	0.1%
I_1[kCnts]	10 118.6	±6.6	0.1%
A_{Ref1}[%]	100.0	---	---
I_{Ref1}[%]	100.0	---	---
$Bkgr_{Dec}$[kCnts]	0.0019	±0.0002	8.1%
τ_{AvInt}[ns]	12 110.2	±7.6	0.1%
τ_{AvAmp}[ns]	12 110.2	±7.6	0.1%

Figure A169. Left: Raw (experimental) time-resolved photoluminescence decay of [Pt(L^{NHPh})Cl] (c ≈ 10^{-5} M) in liquid CH_2Cl_2 at 298 K (Ar-purged, λ_{ex} = 376 nm, λ_{em} = 500 nm) including the residuals. **Right**: Fitting parameters including pre-exponential factors and confidence limits.



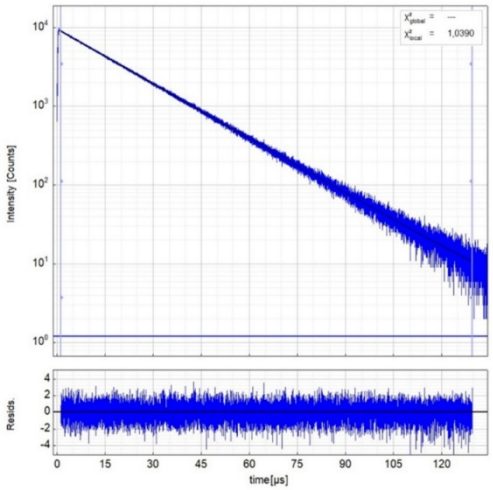
Parameter	Value	Δ	δ
A_1[kCnts/Chnl]	9.591	±0.017	0.2%
τ_1[ns]	30 896	±49	0.2%
I_1[kCnts]	4 629.7	±4.0	0.1%
A_{Ref1}[%]	100.0	---	---
I_{Ref1}[%]	100.0	---	---
$Bkgr_{Dec}$[kCnts]	0.0041	±0.0004	8.0%
τ_{AvInt}[ns]	30 896	±49	0.2%
τ_{AvAmp}[ns]	30 896	±49	0.2%

Figure A170. Left: Raw (experimental) time-resolved photoluminescence decay of [Pt(L^{NHPh})Cl] (c ≈ 10^{-5} M) in a frozen glassy matrix (2MeTHF) at 77 K (λ_{ex} = 376 nm, λ_{em} = 500 nm) including the residuals. **Right**: Fitting parameters including pre-exponential factors and confidence limits.



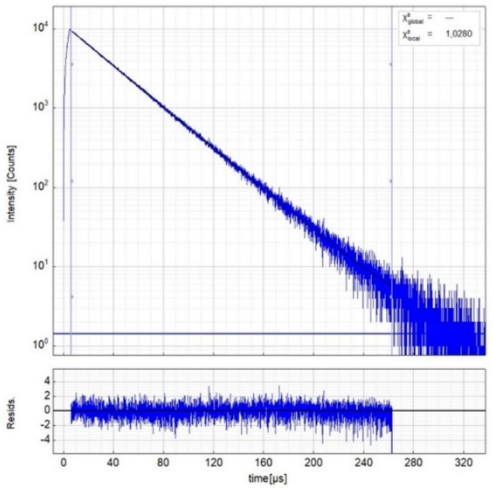
Parameter	Value	Δ	δ
A_1[kCnts/Chnl]	1,4246	±0,0027	0,2%
τ_1[ns]	514,7	±1,2	0,2%
I_1[kCnts]	1 432,0	±2,0	0,1%
A_{Rel1}[%]	100,0	---	---
I_{Rel1}[%]	100,0	---	---
$Bkgr_{Dec}$[kCnts]	0,0008	±0,0001	12%
τ_{AvInt}[ns]	514,7	±1,2	0,2%
τ_{AvAmp}[ns]	514,7	±1,2	0,2%

Figure A171. Left: Raw (experimental) time-resolved photoluminescence decay of [Pt(L^{NHBn})Cl] (c ≈ 10^{-5} M) in liquid CH_2Cl_2 at 298 K (air-equilibrated, λ_{ex} = 376 nm, λ_{em} = 500 nm) including the residuals. **Right**: Fitting parameters including pre-exponential factors and confidence limits.



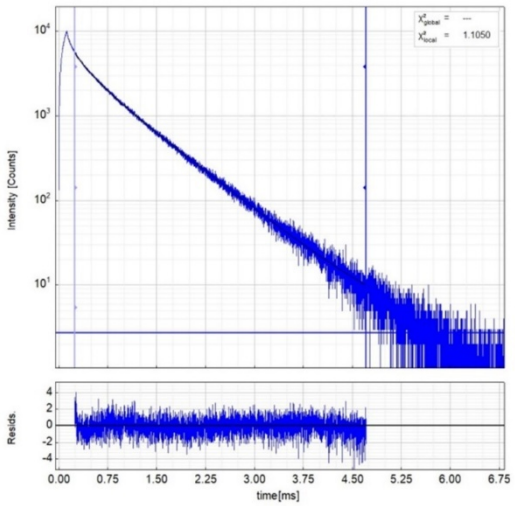
Parameter	Value	Δ	δ
A_1[kCnts/Chnl]	8,9791	±0,0065	0,1%
τ_1[ns]	18 728	±15	0,1%
I_1[kCnts]	21 019,3	±6,3	0,0%
A_{Rel1}[%]	100,0	---	---
I_{Rel1}[%]	100,0	---	---
$Bkgr_{Dec}$[kCnts]	0,0012	±0,0002	14%
τ_{AvInt}[ns]	18 728	±15	0,1%
τ_{AvAmp}[ns]	18 728	±15	0,1%

Figure A172. Left: Raw (experimental) time-resolved photoluminescence decay of [Pt(L^{NHBn})Cl] (c ≈ 10^{-5} M) in liquid CH_2Cl_2 at 298 K (Ar-purged, λ_{ex} = 376 nm, λ_{em} = 500 nm) including the residuals. **Right**: Fitting parameters including pre-exponential factors and confidence limits.



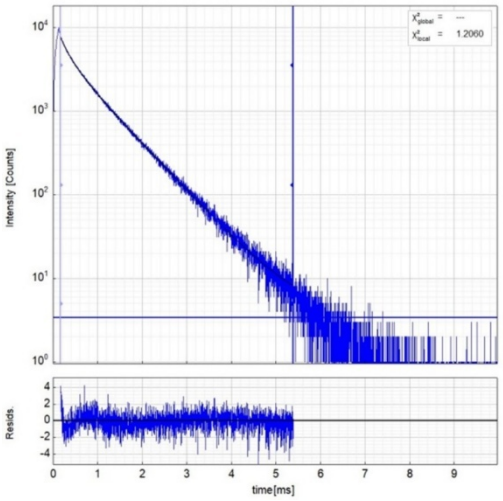
Parameter	Value	Δ	δ
A_1[kCnts/Chnl]	9,4569	±0,0090	0,1%
τ_1[ns]	33 306	±35	0,1%
I_1[kCnts]	4 921,4	±3,5	0,1%
A_{Rel1}[%]	100,0	---	---
I_{Rel1}[%]	100,0	---	---
$Bkgr_{Dec}$[kCnts]	0,0015	±0,0002	13%
τ_{AvInt}[ns]	33 306	±35	0,1%
τ_{AvAmp}[ns]	33 306	±35	0,1%

Figure A173. Left: Raw (experimental) time-resolved photoluminescence decay of [Pt(L^{NHBn})Cl] (c ≈ 10^{-5} M) in a frozen glassy matrix (2MeTHF) at 77 K (λ_{ex} = 376 nm, λ_{em} = 500 nm) including the residuals. **Right**: Fitting parameters including pre-exponential factors and confidence limits.



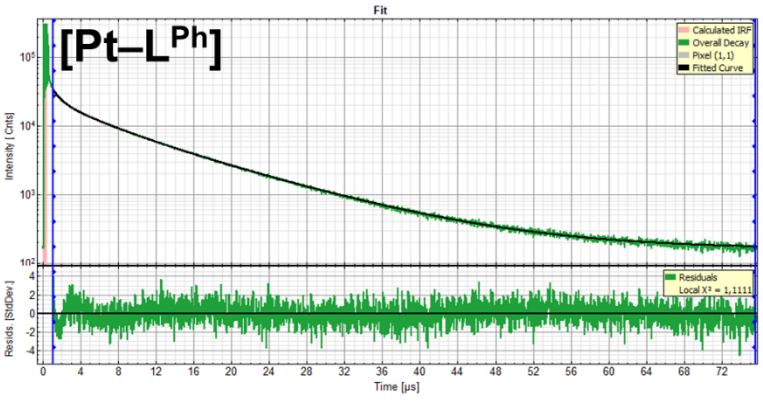
Parameter	Value	Δ	δ
A_1[kCnts/Chnl]	3.549	±0.054	1.5%
τ_1[ns]	721 200	±4 600	0.6%
I_1[kCnts]	2 500	±23	0.9%
A_{Ref1}[%]	64.7	±0.9	1.3%
I_{Ref1}[%]	85.1	±0.8	0.9%
A_2[kCnts/Chnl]	1.939	±0.043	2.2%
τ_2[ns]	231 400	±8 200	3.5%
I_2[kCnts]	438	±24	5.3%
A_{Ref2}[%]	35.4	±0.9	2.3%
I_{Ref2}[%]	15.0	±0.8	5.3%
$Bkgr_{Dec}$[kCnts]	0.0028	±0.0005	16%
τ_{AvIre}[ns]	648 200	±1 500	0.2%
τ_{AvAmp}[ns]	548 200	±2 500	0.4%

Figure A174. Left: Raw (experimental) time-resolved photoluminescence decay of [Pd(L^{NHPh})Cl] (c ≈ 10^{-5} M) in a frozen glassy matrix (2MeTHF) at 77 K (λ_{ex} = 376 nm, λ_{em} = 500 nm) including the residuals. **Right**: Fitting parameters including pre-exponential factors and confidence limits.



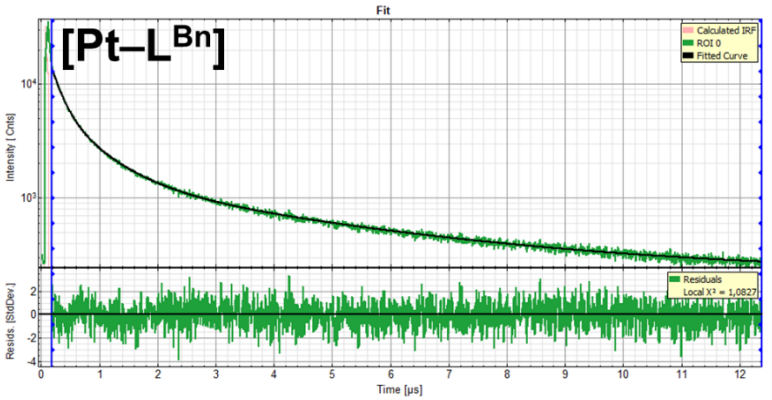
Parameter	Value	Δ	δ
A_1[kCnts/Chnl]	4.635	±0.058	1.3%
τ_1[ns]	758 200	±4 100	0.5%
I_1[kCnts]	1 716	±13	0.7%
A_{Ref1}[%]	61.0	±0.6	1.0%
I_{Ref1}[%]	85.4	±0.7	0.7%
A_2[kCnts/Chnl]	2.972	±0.051	1.7%
τ_2[ns]	203 200	±7 700	3.8%
I_2[kCnts]	295	±13	4.4%
A_{Ref2}[%]	39.1	±0.6	1.5%
I_{Ref2}[%]	14.7	±0.7	4.3%
$Bkgr_{Dec}$[kCnts]	0.0034	±0.0004	12%
τ_{AvIre}[ns]	676 800	±1 500	0.2%
τ_{AvAmp}[ns]	541 400	±4 000	0.7%

Figure A175. Left: Raw (experimental) time-resolved photoluminescence decay of [Pd(L^{NHBn})Cl] (c ≈ 10^{-5} M) in a frozen glassy matrix (2MeTHF) at 77 K (λ_{ex} = 376 nm, λ_{em} = 500 nm) including the residuals. **Right**: Fitting parameters including pre-exponential factors and confidence limits.



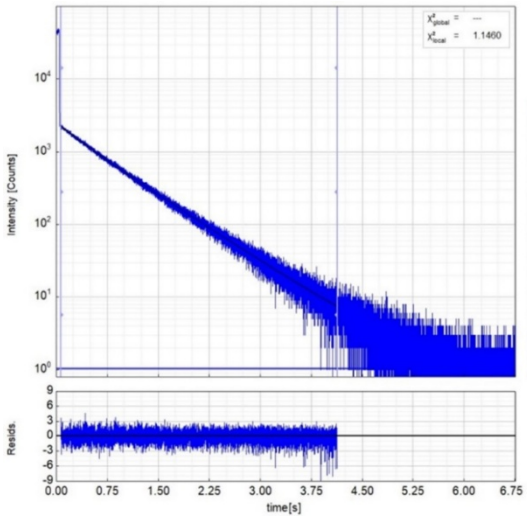
Parameter		Overall Decay
t_0[ns]		069,0000 ± ------
A_1[kCnts]	Limits	14,00 ± 0,33
A_2[kCnts]	Limits	9,440 ± 0,097
A_3[kCnts]	Limits	11,00 ± 0,17
τ_1[ns]	Limits	10842 ± 89
τ_2[ns]	Limits	4388 ± 197
τ_3[ns]	Limits	877 ± 40
$Bkgr_{Dec}$[Cnts]	Limits	160,0 ± 1,6
I_1[kCnts]		7154 ± 117
I_2[kCnts]		2023 ± 96
I_3[kCnts]		474 ± 32
I_{Sum}[kCnts]		9652,0 ± 8,9
A_{Sum}[kCnts]		34,00 ± 0,16
τ_{AvIre}[ns]		9000 ± 19
τ_{AvAmp}[ns]		5809 ± 26

Figure A176. Left: Time-resolved photoluminescence decay of crystalline [Pt(L^{NHPh})Cl] as crystal at 298 K, including the residuals (λ_{ex} = 376 nm). **Right**: Fitting parameters including pre-exponential factors and confidence limits.



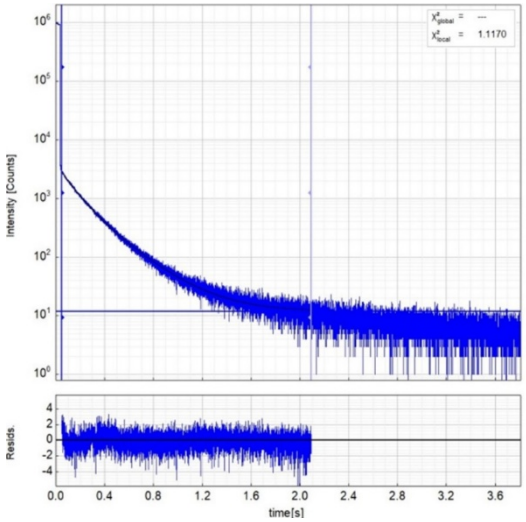
Parameter		Data Set (3)
t_0[ns]		185,6000 ± ------
A_1[kCnts]	Limits	1,290 ± 0,011
A_2[kCnts]	Limits	4,490 ± 0,033
A_3[kCnts]	Limits	7,790 ± 0,053
τ_1[ns]	Limits	3953 ± 43
τ_2[ns]	Limits	687,0 ± 4,4
τ_3[ns]	Limits	188,0 ± 1,7
$Bkgr_{Dec}$[Cnts]	Limits	215,0 ± 2,2
I_1[kCnts]		997,0 ± 5,7
I_2[kCnts]		602,0 ± 4,3
I_3[kCnts]		286 ± 3
I_{Sum}[kCnts]		1885,0 ± 5,4
A_{Sum}[kCnts]		14,00 ± 0,06
τ_{AvInt}[ns]		2338 ± 26
τ_{AvAmp}[ns]		711,0 ± 5,5

Figure A177. Left: Time-resolved photoluminescence decay of crystalline [Pt(L^{NHBn})Cl] as crystal at 298 K, including the residuals (λ_{ex} = 376 nm). **Right**: Fitting parameters including pre-exponential factors and confidence limits.



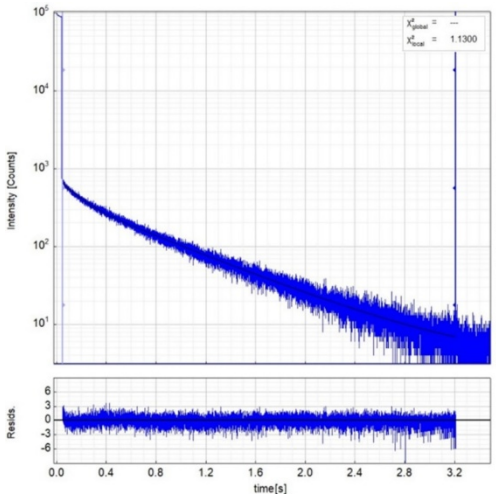
Parameter	Value	Δ	δ
A_1[kCnts/Chnl]	1.856	±0.084	4.5%
τ_1[ns]	718 000 000	±11 000 000	1.5%
I_1[kCnts]	5 080	±160	3.1%
A_{Rel1}[%]	82.2	±3.5	4.2%
I_{Rel1}[%]	91.1	±2.9	3.2%
A_2[kCnts/Chnl]	0.404	±0.077	19%
τ_2[ns]	326 000 000	±40 000 000	12%
I_2[kCnts]	510	±170	32%
A_{Rel2}[%]	17.9	±3.5	19%
I_{Rel2}[%]	9.0	±2.9	32%
$Bkgr_{Dec}$[kCnts]	0.0011	±0.0005	40%
τ_{AvInt}[ns]	682 500 000	±2 500 000	0.4%
τ_{AvAmp}[ns]	647 700 000	±2 700 000	0.4%

Figure A178. Left: Raw (experimental) time-resolved phosphorescence decay of [Ni(L^{NHPh})Cl] in a frozen glassy matrix of 2MeTHF at 77 K, including the residuals (λ_{ex} = 376 nm, λ_{em} = 525 nm, c = 10^{-5} M). **Right**: Fitting parameters including pre-exponential factors and confidence limits.



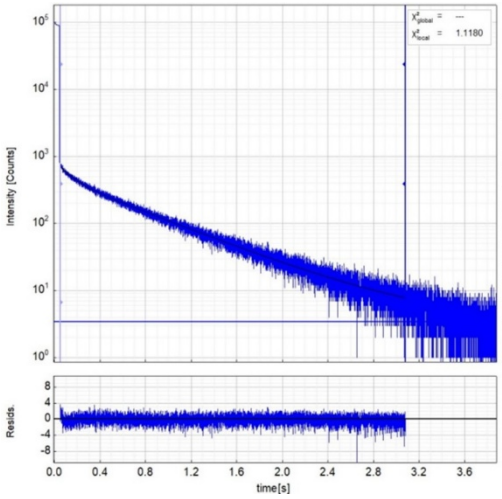
Parameter	Value	Δ	δ
A_1[kCnts/Chnl]	0.990	±0.082	8.2%
τ_1[ns]	281 000 000	±7 700 000	2.7%
I_1[kCnts]	1 061	±60	5.6%
A_{Rel1}[%]	35.0	±2.8	7.9%
I_{Rel1}[%]	55.4	±3.2	5.7%
A_2[kCnts/Chnl]	1.841	±0.072	3.9%
τ_2[ns]	122 000 000	±4 000 000	3.2%
I_2[kCnts]	857	±62	7.2%
A_{Rel2}[%]	65.1	±2.8	4.3%
I_{Rel2}[%]	44.7	±3.2	7.1%
$Bkgr_{Dec}$[kCnts]	0.0120	±0.0004	2.6%
τ_{AvInt}[ns]	210 000 000	±1 100 000	0.5%
τ_{AvAmp}[ns]	177 560 000	±930 000	0.5%

Figure A179. Left: Raw (experimental) time-resolved phosphorescence decay of [Ni(L^{NHBn})Cl] in a frozen glassy matrix of 2MeTHF at 77 K, including the residuals (λ_{ex} = 376 nm, λ_{em} = 525 nm, c = 10^{-5} M). **Right**: Fitting parameters including pre-exponential factors and confidence limits.



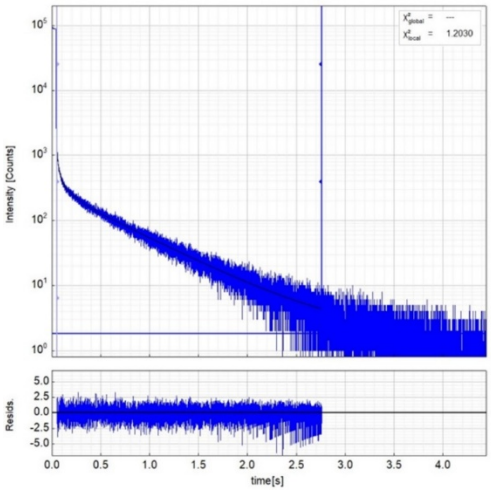
Parameter	Value	Δ	δ
A_1[kCnts/Chnl]	0.4051	±0.0076	1.9%
τ_1[ns]	676 500 000	±9 000 000	1.3%
I_1[kCnts]	1 045.4	±7.3	0.7%
A_{Rel1}[%]	62.7	±1.0	1.5%
I_{Rel1}[%]	89.0	±0.9	0.9%
A_2[kCnts/Chnl]	0.2420	±0.0060	2.5%
τ_2[ns]	140 100 000	±9 200 000	6.6%
I_2[kCnts]	129.4	±10.0	7.7%
A_{Rel2}[%]	37.4	±1.0	2.5%
I_{Rel2}[%]	11.1	±0.9	7.4%
$Bkgr_{Dec}$[kCnts]	0.0031	±0.0004	11%
τ_{AvInt}[ns]	617 500 000	±5 100 000	0.8%
τ_{AvAmp}[ns]	476 000 000	±5 500 000	1.1%

Figure A180. Left: Raw (experimental) time-resolved phosphorescence decay of [Ni(L^{NHPh})Cl] within a PMMA film at 6 K, including the residuals (λ_{ex} = 376 nm, λ_{em} = 525 nm). **Right**: Fitting parameters including pre-exponential factors and confidence limits.



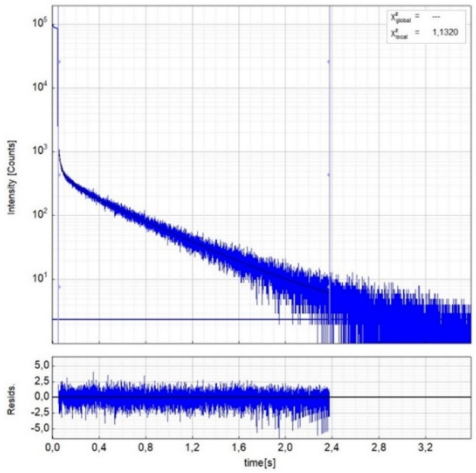
Parameter	Value	Δ	δ
A_1[kCnts/Chnl]	0.4545	±0.0063	1.4%
τ_1[ns]	652 600 000	±6 800 000	1.0%
I_1[kCnts]	1 131.3	±5.8	0.5%
A_{Rel1}[%]	64.8	±0.8	1.1%
I_{Rel1}[%]	91.1	±0.7	0.7%
A_2[kCnts/Chnl]	0.2473	±0.0061	2.5%
τ_2[ns]	117 400 000	±8 200 000	7.0%
I_2[kCnts]	110.7	±7.7	7.0%
A_{Rel2}[%]	35.3	±0.8	2.0%
I_{Rel2}[%]	9.0	±0.7	6.8%
$Bkgr_{Dec}$[kCnts]	0.0035	±0.0004	8.8%
τ_{AvInt}[ns]	604 900 000	±3 900 000	0.6%
τ_{AvAmp}[ns]	464 000 000	±5 600 000	1.2%

Figure A181. Left: Raw (experimental) time-resolved phosphorescence decay of [Ni(L^{NHPh})Cl] within a PMMA film at 100 K, including the residuals (λ_{ex} = 376 nm, λ_{em} = 525 nm). **Right**: Fitting parameters including pre-exponential factors and confidence limits.



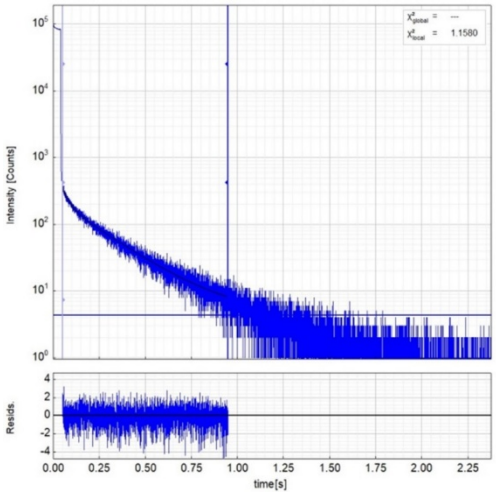
Parameter	Value	Δ	δ
A_1[kCnts/Chnl]	0.2662	±0.0088	3.3%
τ_1[ns]	583 000 000	±13 000 000	2.1%
I_1[kCnts]	591.7	±7.8	1.3%
A_{Rel1}[%]	22.9	±0.7	2.8%
I_{Rel1}[%]	82.5	±1.4	1.7%
A_2[kCnts/Chnl]	0.693	±0.027	3.8%
τ_2[ns]	16 700 000	±2 000 000	12%
I_2[kCnts]	44.0	±6.1	14%
A_{Rel2}[%]	59.5	±2.5	4.1%
I_{Rel2}[%]	6.2	±0.9	13%
A_3[kCnts/Chnl]	0.207	±0.030	14%
τ_3[ns]	104 000 000	±21 000 000	20%
I_3[kCnts]	81.8	±5.6	6.8%
A_{Rel3}[%]	17.8	±2.2	12%
I_{Rel3}[%]	11.4	±0.8	6.5%
$Bkgr_{Dec}$[kCnts]	0.0019	±0.0003	16%
τ_{AvInt}[ns]	493 500 000	±5 900 000	1.2%
τ_{AvAmp}[ns]	161 400 000	±5 300 000	3.2%

Figure A182. Left: Raw (experimental) time-resolved phosphorescence decay of [Ni(L^{NHPh})Cl] within a PMMA film at 200 K, including the residuals (λ_{ex} = 376 nm, λ_{em} = 525 nm). **Right**: Fitting parameters including pre-exponential factors and confidence limits.



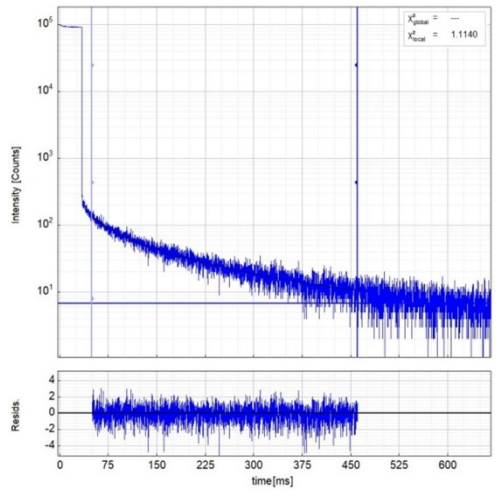
Parameter	Value	Δ	δ
A_1[kCnts/Chnl]	0,3325	±0,0096	2,9%
τ_1[ns]	523 000 000	±11 000 000	2,0%
I_1[kCnts]	662,2	±7,1	1,1%
A_{Rel1}[%]	26,8	±0,8	2,8%
I_{Rel1}[%]	85,8	±1,2	1,4%
A_2[kCnts/Chnl]	0,198	±0,017	8,5%
τ_2[ns]	101 000 000	±16 000 000	16%
I_2[kCnts]	76,3	±7,7	10,0%
A_{Rel2}[%]	16,0	±1,2	7,2%
I_{Rel2}[%]	9,9	±1,0	9,4%
A_3[kCnts/Chnl]	0,713	±0,026	3,5%
τ_3[ns]	12 500 000	±1 300 000	9,9%
I_3[kCnts]	33,8	±3,3	9,7%
A_{Rel3}[%]	57,4	±1,6	2,6%
I_{Rel3}[%]	4,4	±0,5	9,4%
$Bkgr_{Dec}$[kCnts]	0,0024	±0,0004	16%
τ_{AvInt}[ns]	458 300 000	±5 200 000	1,1%
τ_{AvAmp}[ns]	162 900 000	±4 500 000	2,7%

Figure A183. Left: Raw (experimental) time-resolved phosphorescence decay of [Ni(L^{NHPh})Cl] within a PMMA film at 250 K, including the residuals (λ_{ex} = 376 nm, λ_{em} = 525 nm). **Right**: Fitting parameters including pre-exponential factors and confidence limits.



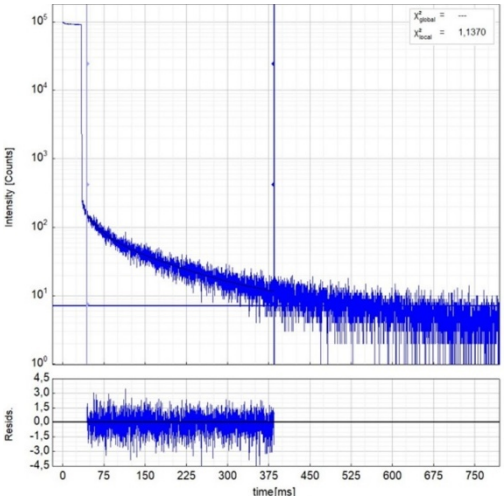
Parameter	Value	Δ	δ
A_1[kCnts/Chnl]	0.1894	±0.0069	3.6%
τ_1[ns]	230 200 000	±8 000 000	3.4%
I_1[kCnts]	166.3	±1.8	1.1%
A_{Rel1}[%]	55.5	±1.7	3.0%
I_{Rel1}[%]	89.1	±1.3	1.4%
A_2[kCnts/Chnl]	0.1520	±0.0071	4.7%
τ_2[ns]	35 300 000	±4 400 000	12%
I_2[kCnts]	20.5	±2.7	13%
A_{Rel2}[%]	44.6	±1.7	3.7%
I_{Rel2}[%]	11.0	±1.3	12%
$Bkgr_{Dec}$[kCnts]	0.0044	±0.0007	16%
τ_{AvInt}[ns]	208 900 000	±5 400 000	2.6%
τ_{AvAmp}[ns]	143 400 000	±4 700 000	3.2%

Figure A184. Left: Raw (experimental) time-resolved phosphorescence decay of [Ni(L^{NHPh})Cl] within a PMMA film at 300 K, including the residuals (λ_{ex} = 376 nm, λ_{em} = 525 nm). **Right**: Fitting parameters including pre-exponential factors and confidence limits.



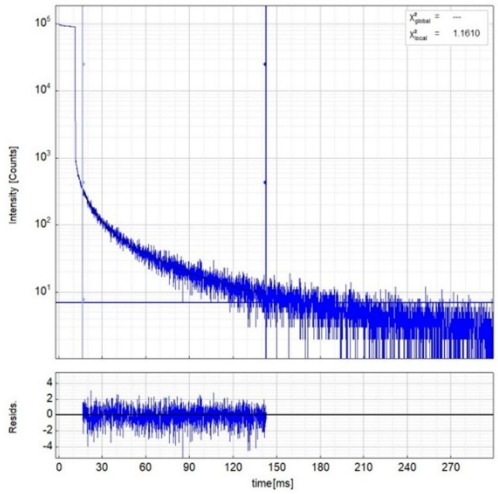
Parameter	Value	Δ	δ
A_1[kCnts/Chnl]	0.0716	±0.0036	4.9%
τ_1[ns]	140 500 000	±8 500 000	6.0%
I_1[kCnts]	76.8	±2.1	2.6%
A_{Rel1}[%]	57.0	±2.5	4.4%
I_{Rel1}[%]	85.8	±2.2	2.5%
A_2[kCnts/Chnl]	0.0542	±0.0030	5.4%
τ_2[ns]	30 800 000	±3 600 000	12%
I_2[kCnts]	12.8	±2.2	17%
A_{Rel2}[%]	43.1	±2.5	5.8%
I_{Rel2}[%]	14.3	±2.2	15%
$Bkgr_{Dec}$[kCnts]	0.0069	±0.0008	11%
τ_{AvInt}[ns]	124 900 000	±6 500 000	5.2%
τ_{AvAmp}[ns]	93 300 000	±3 100 000	3.3%

Figure A185. Left: Raw (experimental) time-resolved phosphorescence decay of [Ni(L^{NHBn})Cl] within a PMMA film at 6 K, including the residuals (λ_{ex} = 376 nm, λ_{em} = 525 nm). **Right**: Fitting parameters including pre-exponential factors and confidence limits.



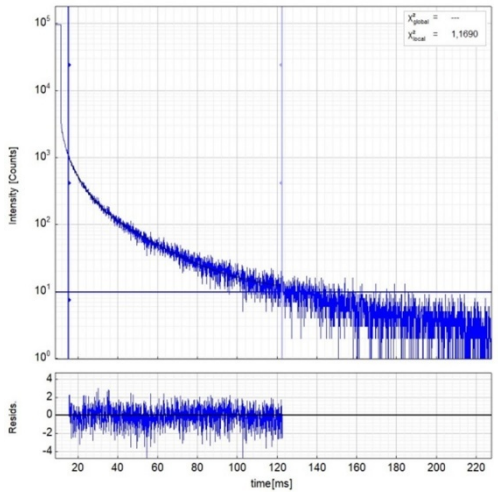
Parameter	Value	Δ	δ
A_1[kCnts/Chnl]	0,0749	±0,0044	5,8%
τ_1[ns]	121 900 000	±8 000 000	6,6%
I_1[kCnts]	69,7	±2,2	3,1%
A_{Rel1}[%]	51,9	±2,6	4,9%
I_{Rel1}[%]	85,1	±1,7	2,0%
A_2[kCnts/Chnl]	0,0696	±0,0043	6,2%
τ_2[ns]	23 200 000	±2 200 000	9,2%
I_2[kCnts]	12,3	±1,6	13%
A_{Rel2}[%]	48,2	±2,6	5,3%
I_{Rel2}[%]	15,0	±1,7	11%
$Bkgr_{Det}$[kCnts]	0,0071	±0,0011	14%
τ_{AvInt}[ns]	107 100 000	±6 600 000	6,1%
τ_{AvAmp}[ns]	74 400 000	±3 400 000	4,6%

Figure A186. Left: Raw (experimental) time-resolved phosphorescence decay of [Ni(L^{NHBn})Cl] within a PMMA film at 100 K, including the residuals (λ_{ex} = 376 nm, λ_{em} = 525 nm). **Right**: Fitting parameters including pre-exponential factors and confidence limits.



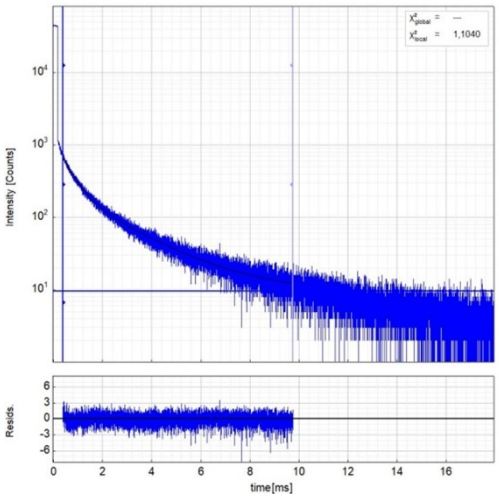
Parameter	Value	Δ	δ
A_1[kCnts/Chnl]	0.110	±0.012	11%
τ_1[ns]	33 800 000	±3 500 000	10%
I_1[kCnts]	56.4	±1.6	2.8%
A_{Rel1}[%]	34.8	±3.4	9.6%
I_{Rel1}[%]	72.0	±3.2	4.3%
A_2[kCnts/Chnl]	0.206	±0.011	5.1%
τ_2[ns]	7 000 000	±750 000	11%
I_2[kCnts]	22.0	±3.1	14%
A_{Rel2}[%]	65.3	±3.4	5.1%
I_{Rel2}[%]	28.1	±3.2	11%
$Bkgr_{Det}$[kCnts]	0.0070	±0.0012	16%
τ_{AvInt}[ns]	26 300 000	±2 000 000	7.4%
τ_{AvAmp}[ns]	16 300 000	±820 000	5.0%

Figure A187. Left: Raw (experimental), time-resolved phosphorescence decay of [Ni(L^{NHBn})Cl] within a PMMA film at 200 K, including the residuals (λ_{ex} = 376 nm, λ_{em} = 525 nm). **Right**: Fitting parameters including pre-exponential factors and confidence limits.



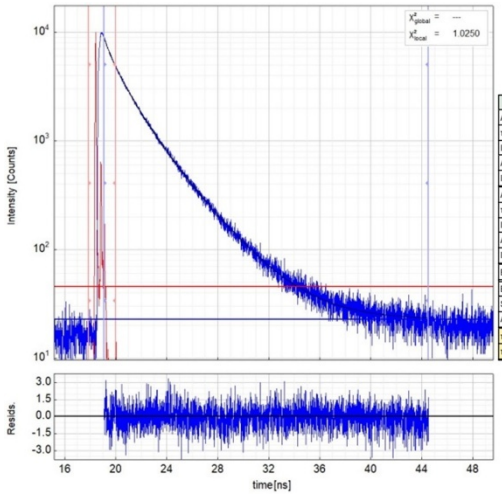
Parameter	Value	Δ	δ
A_1[kCnts/Chnl]	0,299	±0,019	6,2%
τ_1[ns]	22 260 000	±920 000	4,1%
I_1[kCnts]	101,5	±2,5	2,4%
A_{Rel1}[%]	30,8	±1,7	5,3%
I_{Rel1}[%]	66,1	±2,0	2,9%
A_2[kCnts/Chnl]	0,672	±0,016	2,3%
τ_2[ns]	5 100 000	±250 000	4,9%
I_2[kCnts]	52,3	±3,3	6,1%
A_{Rel2}[%]	69,3	±1,7	2,4%
I_{Rel2}[%]	34,0	±2,0	5,6%
$Bkgr_{Det}$[kCnts]	0,0098	±0,0008	7,2%
τ_{AvInt}[ns]	16 430 000	±400 000	2,4%
τ_{AvAmp}[ns]	10 380 000	±200 000	1,9%

Figure A188. Left: Raw (experimental) time-resolved phosphorescence decay of [Ni(L^{NHBn})Cl] within a PMMA film at 250 K, including the residuals (λ_{ex} = 376 nm, λ_{em} = 525 nm). **Right**: Fitting parameters including pre-exponential factors and confidence limits.



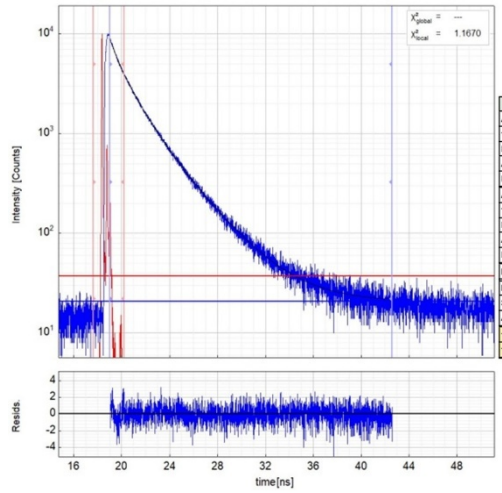
Parameter	Value	Δ	δ
A_1[kCnts/Chnl]	0,4426	±0,0059	1,3%
τ_1[ns]	498 000	±14 000	2,7%
I_1[kCnts]	215,2	±7,7	3,6%
A_{Rel1}[%]	66,7	±1,0	1,4%
I_{Rel1}[%]	31,6	±1,0	3,1%
A_2[kCnts/Chnl]	0,2212	±0,0072	3,2%
τ_2[ns]	2 160 000	±49 000	2,3%
I_2[kCnts]	466,4	±4,9	1,0%
A_{Rel2}[%]	33,4	±1,0	2,9%
I_{Rel2}[%]	68,5	±1,0	1,4%
$Bkgr_{Dec}$[kCnts]	0,0096	±0,0004	3,9%
τ_{Avint}[ns]	1 635 000	±23 000	1,4%
τ_{AvAmp}[ns]	1 052 000	±11 000	1,0%

Figure A189. Left: Raw (experimental) time-resolved phosphorescence decay of [Ni(L^{NHBn})Cl] within a PMMA film at 300 K, Including the residuals (λ_{ex} = 376 nm, λ_{em} = 525 nm). **Right**: Fitting parameters including pre-exponential factors and confidence limits.



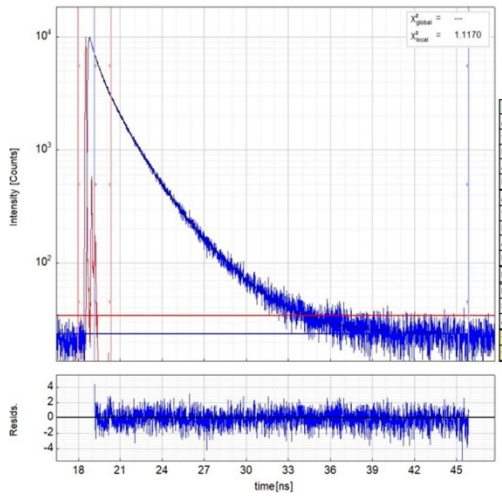
Parameter	Value	Δ	δ
A_1[kCnts/Chnl]	4.82	±0.27	5.5%
τ_1[ns]	3.024	±0.062	2.0%
I_1[kCnts]	1 818	±66	3.6%
A_{Rel1}[%]	36.1	±1.9	5.1%
I_{Rel1}[%]	57.1	±2.7	4.7%
A_2[kCnts/Chnl]	8.52	±0.27	3.1%
τ_2[ns]	1.287	±0.067	5.2%
I_2[kCnts]	1 370	±120	8.0%
A_{Rel2}[%]	64.0	±1.9	2.9%
I_{Rel2}[%]	43.0	±2.7	6.2%
$Bkgr_{Dec}$[kCnts]	0.0227	±0.0005	2.1%
$Bkgr_{Rel}$[Cnts/Chnl]	45.7	±8.2	18%
$Shift_{Rel}$[ps]	- 268	±12	4.4%
A_{Scat}[kCnts]	205	±70	34%
τ_{Avint}[ns]	2.278	±0.017	0.7%
τ_{AvAmp}[ns]	1.914	±0.035	1.8%

Figure A190. Left: Raw (experimental) fluorescence decay of [Ni(L^{NHPh})Cl] within a PMMA film at 6 K (blue) and the instrumental response function (IRF, red) Including the residuals (λ_{ex} = 376 nm, λ_{em} = 525 nm). **Right**: Fitting parameters including pre-exponential factors and confidence limits.



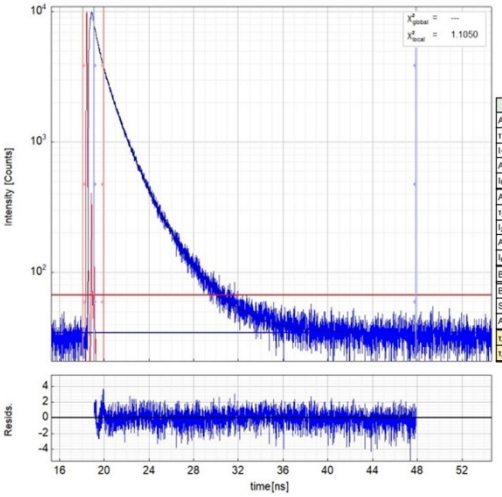
Parameter	Value	Δ	δ
A_1[kCnts/Chnl]	4.43	±0.35	7.8%
τ_1[ns]	2.948	±0.086	2.9%
I_1[kCnts]	1 629	±86	5.2%
A_{Rel1}[%]	32.3	±2.4	7.3%
I_{Rel1}[%]	52.7	±3.6	6.8%
A_2[kCnts/Chnl]	9.30	±0.38	4.1%
τ_2[ns]	1.258	±0.084	6.7%
I_2[kCnts]	1 470	±160	10%
A_{Rel2}[%]	67.8	±2.4	3.5%
I_{Rel2}[%]	47.4	±3.6	7.6%
$Bkgr_{Dec}$[kCnts]	0.0209	±0.0007	3.2%
$Bkgr_{Rel}$[Cnts/Chnl]	37.2	±8.1	22%
$Shift_{Rel}$[ps]	- 327	±26	7.8%
A_{Scat}[kCnts]	326	±70	21%
τ_{Avint}[ns]	2.149	±0.025	1.2%
τ_{AvAmp}[ns]	1.803	±0.049	2.7%

Figure A191. Left: Raw (experimental) fluorescence decay of [Ni(L^{NHPh})Cl] within a PMMA film at 100 K (blue) and the instrumental response function (IRF, red) Including the residuals (λ_{ex} = 376 nm, λ_{em} = 525 nm). **Right**: Fitting parameters including pre-exponential factors and confidence limits.



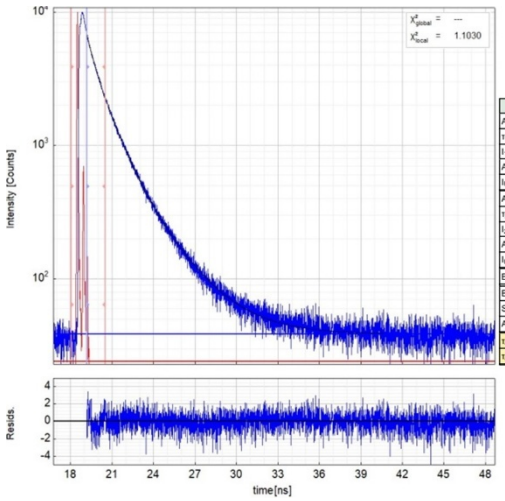
Parameter	Value	Δ	δ
A_1[kCnts/Chnl]	2.90	±0.31	11%
τ_1[ns]	2.86	±0.11	3.6%
I_1[kCnts]	1 035	±73	7.0%
A_{Ref1}[%]	27.3	±2.9	10%
I_{Ref1}[%]	46.2	±4.3	9.2%
A_2[kCnts/Chnl]	7.73	±0.34	4.4%
τ_2[ns]	1.250	±0.079	6.3%
I_2[kCnts]	1 210	±130	10%
A_{Ref2}[%]	72.8	±2.9	3.9%
I_{Ref2}[%]	53.9	±4.3	7.9%
$Bkgr_{Dec}$[kCnts]	0.0237	±0.0005	1.8%
$Bkgr_{IRF}$[Cnts/Chnl]	34.3	±8.2	24%
$Shift_{IRF}$[ps]	- 159	±24	15%
A_{Scatt}[kCnts]	286	±60	21%
τ_{AvInt}[ns]	1.993	±0.024	1.2%
τ_{AvAmp}[ns]	1.689	±0.043	2.5%

Figure A192. Left: Raw (experimental) fluorescence decay of [Ni(L^{NHPh})Cl] within a PMMA film at 200 K (blue) and the instrumental response function (IRF, red) Including the residuals (λ_{ex} = 376 nm, λ_{em} = 525 nm). **Right**: Fitting parameters including pre-exponential factors and confidence limits.



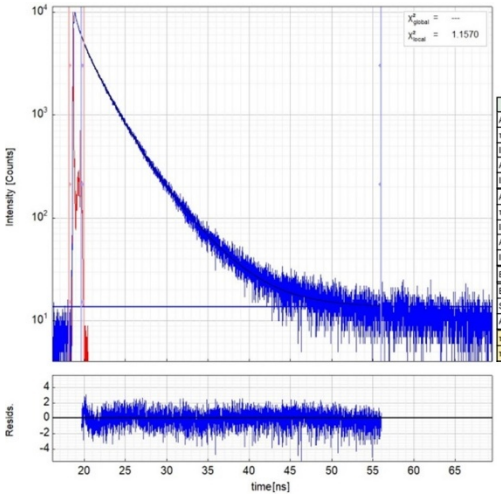
Parameter	Value	Δ	δ
A_1[kCnts/Chnl]	10.76	±0.29	2.6%
τ_1[ns]	1.172	±0.054	4.6%
I_1[kCnts]	1 580	±110	6.6%
A_{Ref1}[%]	79.7	±1.8	2.2%
I_{Ref1}[%]	62.1	±3.0	4.8%
A_2[kCnts/Chnl]	2.75	±0.25	9.0%
τ_2[ns]	2.815	±0.088	3.1%
I_2[kCnts]	966	±60	6.2%
A_{Ref2}[%]	20.4	±1.8	8.8%
I_{Ref2}[%]	38.0	±3.0	7.8%
$Bkgr_{Dec}$[kCnts]	0.0345	±0.0005	1.2%
$Bkgr_{IRF}$[Cnts/Chnl]	67.1	±8.6	13%
$Shift_{IRF}$[ps]	- 262	±12	4.6%
A_{Scatt}[kCnts]	168	±69	41%
τ_{AvInt}[ns]	1.796	±0.019	1.0%
τ_{AvAmp}[ns]	1.506	±0.033	2.1%

Figure A193. Left: Raw (experimental) fluorescence decay of [Ni(L^{NHPh})Cl] within a PMMA film at 250 K (blue) and the instrumental response function (IRF, red) Including the residuals (λ_{ex} = 376 nm, λ_{em} = 525 nm). **Right**: Fitting parameters including pre-exponential factors and confidence limits.



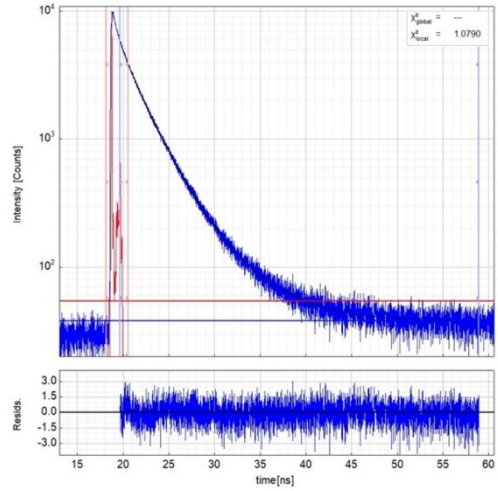
Parameter	Value	Δ	δ
A_1[kCnts/Chnl]	2.23	±0.34	15%
τ_1[ns]	2.65	±0.14	5.0%
I_1[kCnts]	736	±76	10%
A_{Ref1}[%]	20.3	±2.9	14%
I_{Ref1}[%]	38.0	±4.5	12%
A_2[kCnts/Chnl]	8.75	±0.24	2.7%
τ_2[ns]	1.101	±0.073	6.6%
I_2[kCnts]	1 210	±110	8.9%
A_{Ref2}[%]	79.8	±2.9	3.5%
I_{Ref2}[%]	62.1	±4.5	7.2%
$Bkgr_{Dec}$[kCnts]	0.0389	±0.0005	1.1%
$Bkgr_{IRF}$[Cnts/Chnl]	24.3	±6.9	28%
$Shift_{IRF}$[ps]	- 181	±12	6.5%
A_{Scatt}[kCnts]	432	±68	16%
τ_{AvInt}[ns]	1.686	±0.027	1.6%
τ_{AvAmp}[ns]	1.414	±0.043	3.0%

Figure A194. Left: Raw (experimental) fluorescence decay of [Ni(L^{NHPh})Cl] within a PMMA film at 300 K (blue) and the instrumental response function (IRF, red) Including the residuals (λ_{ex} = 376 nm, λ_{em} = 525 nm). **Right**: Fitting parameters including pre-exponential factors and confidence limits.



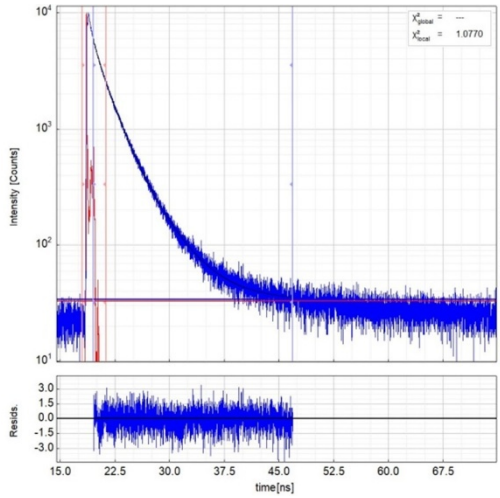
Parameter	Value	Δ	δ
A_1[kCnts/Chnl]	1.88	±0.25	13%
τ_1[ns]	4.29	±0.13	2.8%
I_1[kCnts]	1 010	±110	11%
A_{Ref1}[%]	29.9	±3.0	9.8%
I_{Ref1}[%]	47.0	±3.7	7.7%
A_2[kCnts/Chnl]	4.42	±0.30	6.8%
τ_2[ns]	2.067	±0.070	3.4%
I_2[kCnts]	1 140	±96	8.4%
A_{Red2}[%]	70.2	±3.0	4.2%
I_{Red2}[%]	53.1	±3.7	6.8%
$Bkgr_{Dec}$[kCnts]	0.0137	±0.0004	2.2%
$Bkgr_{IRF}$[Cnts/Chnl]	-95	±34	36%
$Shift_{IRF}$[ps]	-21.1	±10.0	47%
A_{Scat}[kCnts]	240	±30	12%
τ_{Avint}[ns]	3.110	±0.014	0.4%
τ_{AvAmp}[ns]	2.731	±0.022	0.8%

Figure A195. Left: Raw (experimental) fluorescence decay of [Ni(L^{NHBn})Cl] within a PMMA film at 6 K (blue) and the instrumental response function (IRF, red) Including the residuals (λ_{ex} = 376 nm, λ_{em} = 525 nm). **Right**: Fitting parameters including pre-exponential factors and confidence limits.



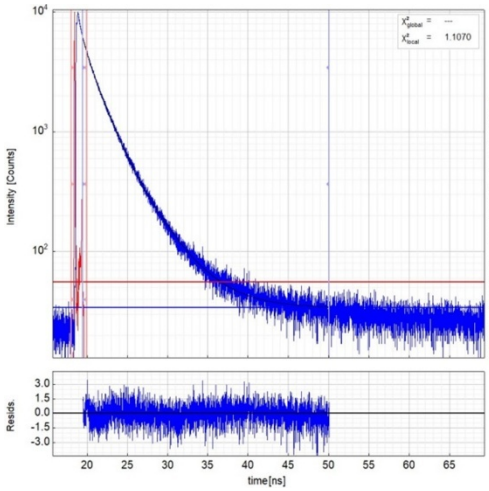
Parameter	Value	Δ	δ
A_1[kCnts/Chnl]	1.85	±0.33	18%
τ_1[ns]	4.54	±0.24	5.3%
I_1[kCnts]	1 050	±130	12%
A_{Ref1}[%]	21.6	±4.0	18%
I_{Ref1}[%]	36.5	±5.1	14%
A_2[kCnts/Chnl]	6.73	±0.43	6.3%
τ_2[ns]	2.176	±0.090	4.1%
I_2[kCnts]	1 830	±190	10%
A_{Red2}[%]	78.5	±4.0	5.0%
I_{Red2}[%]	63.6	±5.1	8.0%
$Bkgr_{Dec}$[kCnts]	0.0381	±0.0005	1.3%
$Bkgr_{IRF}$[Cnts/Chnl]	54.2	±8.9	16%
$Shift_{IRF}$[ps]	71	±22	31%
A_{Scat}[kCnts]	83	±23	27%
τ_{Avint}[ns]	3.037	±0.022	0.7%
τ_{AvAmp}[ns]	2.685	±0.029	1.1%

Figure A196. Left: Raw (experimental) fluorescence decay of [Ni(L^{NHBn})Cl] within a PMMA film at 100 K (blue) and the instrumental response function (IRF, red) Including the residuals (λ_{ex} = 376 nm, λ_{em} = 525 nm). **Right**: Fitting parameters including pre-exponential factors and confidence limits.



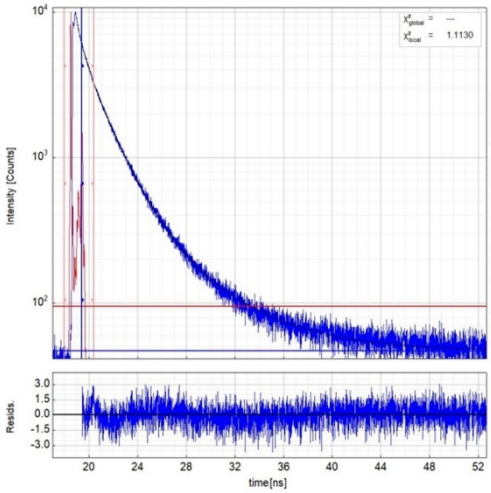
Parameter	Value	Δ	δ
A_1[kCnts/Chnl]	1.86	±0.41	22%
τ_1[ns]	4.12	±0.28	6.6%
I_1[kCnts]	960	±150	15%
A_{Ref1}[%]	23.7	±5.2	22%
I_{Ref1}[%]	39.6	±6.8	17%
A_2[kCnts/Chnl]	6.01	±0.40	6.5%
τ_2[ns]	1.96	±0.13	6.3%
I_2[kCnts]	1 470	±190	13%
A_{Red2}[%]	76.4	±5.2	6.7%
I_{Red2}[%]	60.5	±6.8	11%
$Bkgr_{Dec}$[kCnts]	0.0340	±0.0010	2.9%
$Bkgr_{IRF}$[Cnts/Chnl]	32.8	±6.4	19%
$Shift_{IRF}$[ps]	-90	±14	16%
A_{Scat}[kCnts]	149	±38	25%
τ_{Avint}[ns]	2.806	±0.037	1.3%
τ_{AvAmp}[ns]	2.462	±0.048	1.9%

Figure A197. Left: Raw (experimental) fluorescence decay of [Ni(L^{NHBn})Cl] within a PMMA film at 200 K (blue) and the instrumental response function (IRF, red) Including the residuals (λ_{ex} = 376 nm, λ_{em} = 525 nm). **Right**: Fitting parameters including pre-exponential factors and confidence limits.



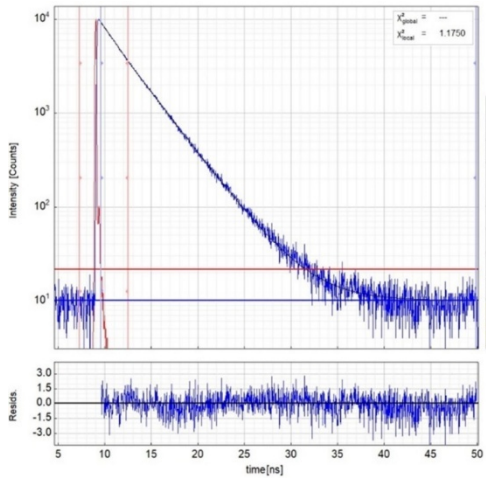
Parameter	Value	Δ	δ
A_1[kCnts/Chnl]	3.01	±0.31	10%
τ_1[ns]	3.80	±0.13	3.3%
I_1[kCnts]	1 425	±99	6.9%
A_{Ref1}[%]	27.3	±2.7	9.7%
I_{Ref1}[%]	46.2	±3.5	7.6%
A_2[kCnts/Chnl]	8.02	±0.40	4.9%
τ_2[ns]	1.660	±0.076	4.6%
I_2[kCnts]	1 670	±150	8.5%
A_{Ref2}[%]	72.8	±2.7	3.6%
I_{Ref2}[%]	53.9	±3.5	6.5%
$Bkgr_{Dec}$[kCnts]	0.0341	±0.0007	1.9%
$Bkgr_{IRF}$[Cnts/Chnl]	55.6	±9.1	16%
$Shift_{IRF}$[ps]	- 237	±34	14%
A_{Scat}[kCnts]	-79	±73	92%
τ_{AvInt}[ns]	2.646	±0.025	0.9%
τ_{AvAmp}[ns]	2.242	±0.037	1.6%

Figure A198. Left: Raw (experimental) fluorescence decay of [Ni(L^{NHBn})Cl] within a PMMA film at 250 K (blue) and the instrumental response function (IRF, red) Including the residuals (λ_{ex} = 376 nm, λ_{em} = 525 nm). **Right**: Fitting parameters including pre-exponential factors and confidence limits.



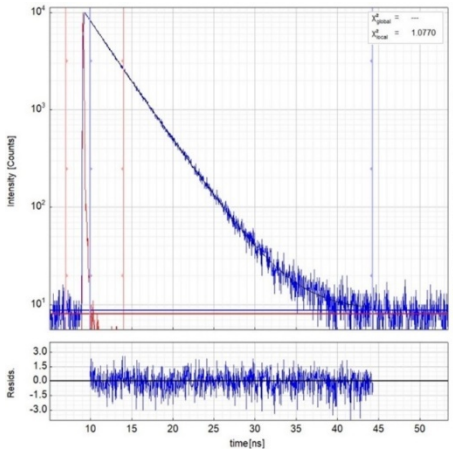
Parameter	Value	Δ	δ
A_1[kCnts/Chnl]	0.884	±0.099	11%
τ_1[ns]	5.30	±0.26	4.8%
I_1[kCnts]	585	±39	6.6%
A_{Ref1}[%]	10.0	±1.2	12%
I_{Ref1}[%]	24.1	±2.0	8.1%
A_2[kCnts/Chnl]	8.04	±0.22	2.7%
τ_2[ns]	1.841	±0.043	2.3%
I_2[kCnts]	1 850	±88	4.7%
A_{Ref2}[%]	90.1	±1.2	1.3%
I_{Ref2}[%]	76.0	±2.0	2.6%
$Bkgr_{Dec}$[kCnts]	0.0471	±0.0005	1.0%
$Bkgr_{IRF}$[Cnts/Chnl]	94.9	±8.4	8.8%
$Shift_{IRF}$[ps]	- 198	±24	12%
A_{Scat}[kCnts]	87	±14	16%
τ_{AvInt}[ns]	2.670	±0.027	1.0%
τ_{AvAmp}[ns]	2.183	±0.024	1.1%

Figure A199. Left: Raw (experimental) fluorescence decay of [Ni(L^{NHBn})Cl] within a PMMA film at 300 K (blue) and the instrumental response function (IRF, red) Including the residuals (λ_{ex} = 376 nm, λ_{em} = 525 nm). **Right**: Fitting parameters including pre-exponential factors and confidence limits.



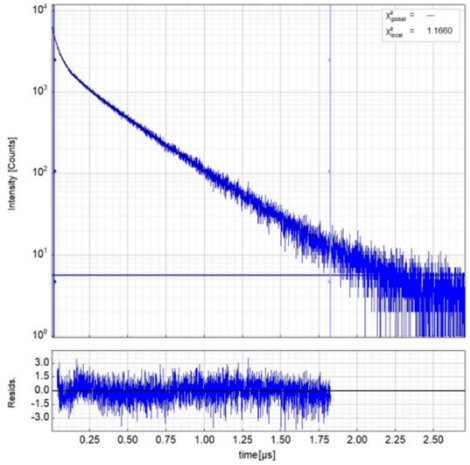
Parameter	Value	Δ	δ
A_1[kCnts/Chnl]	11.45	±0.88	7.6%
τ_1[ns]	3.338	±0.013	0.4%
I_1[kCnts]	1 194	±91	7.6%
A_{Ref1}[%]	100.0	---	---
I_{Ref1}[%]	100.0	---	---
$Bkgr_{Dec}$[kCnts]	0.0101	±0.0004	3.3%
$Bkgr_{IRF}$[Cnts/Chnl]	21.6	±1.5	6.7%
$Shift_{IRF}$[ps]	- 120	±240	185%
τ_{AvInt}[ns]	3.338	±0.013	0.4%
τ_{AvAmp}[ns]	3.338	±0.013	0.4%

Figure A200. Left: Raw (experimental) fluorescence decay of [Ni(L^{NHPh})Cl] within a glassy matrix (2MeTHF, c = 10^{-5} M) at 77 K (blue) and the instrumental response function (IRF, red) Including the residuals (λ_{ex} = 376 nm, λ_{em} = 525 nm). **Right**: Fitting parameters including pre-exponential factors and confidence limits.



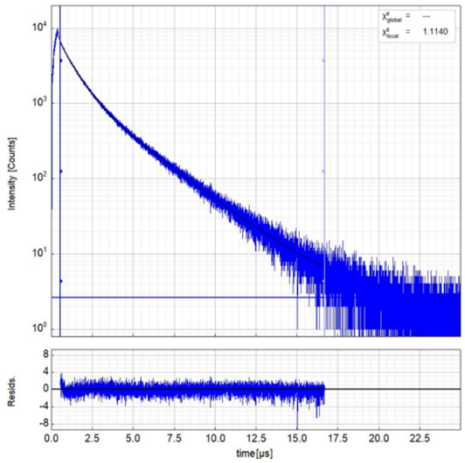
Parameter	Value	Δ	δ
A_1[kCnts/Chnl]	10.69	±0.17	1.5%
τ_1[ns]	3.634	±0.019	0.5%
I_1[kCnts]	1 214	±20	1.6%
A_{Rel1}[%]	100.0	---	---
I_{Rel1}[%]	100.0	---	---
$Bkgr_{Dec}$[kCnts]	0.0088	±0.0005	5.1%
$Bkgr_{IRF}$[Cnts/Chnl]	8.08	±0.92	11%
$Shift_{IRF}$[ps]	33	±50	153%
τ_{AvInt}[ns]	3.634	±0.019	0.5%
τ_{AvAmp}[ns]	3.634	±0.019	0.5%

Figure A201. Left: Raw (experimental) fluorescence photoluminescence decay of [Ni(L^{NHBn})Cl] within a glassy matrix (2MeTHF, c = 10^{-5} M) at 77 K (blue) and the instrumental response function (IRF, red) Including the residuals (λ_{ex} = 376 nm, λ_{em} = 525 nm). **Right**: Fitting parameters including pre-exponential factors and confidence limits.



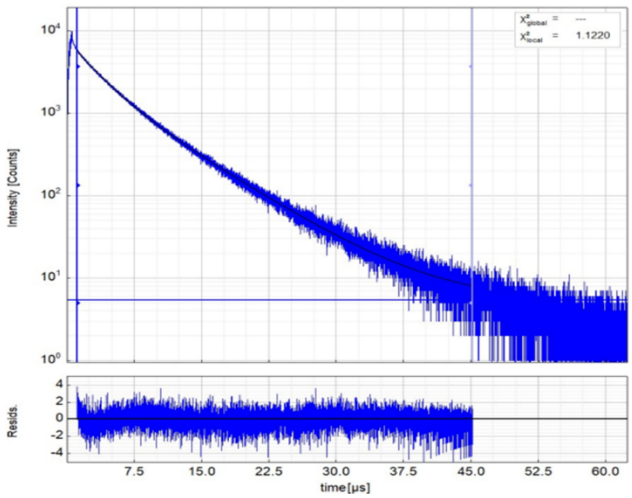
Parameter	Value	Δ	δ
A_1[kCnts/Chnl]	1.9959	±0.0067	0.3%
τ_1[ns]	324.25	±0.82	0.3%
I_1[kCnts]	1 264.0	±3.4	0.3%
A_{Rel1}[%]	55.0	±0.2	0.3%
I_{Rel1}[%]	89.0	±0.2	0.2%
A_2[kCnts/Chnl]	1.6334	±0.0091	0.6%
τ_2[ns]	49.0	±1.1	2.2%
I_2[kCnts]	156.3	±2.6	1.6%
A_{Rel2}[%]	45.1	±0.2	0.3%
I_{Rel2}[%]	11.1	±0.2	1.4%
$Bkgr_{Dec}$[kCnts]	0.0057	±0.0003	4.1%
τ_{AvInt}[ns]	293.97	±0.37	0.1%
τ_{AvAmp}[ns]	200.36	±0.88	0.4%

Figure A202. Left: Raw (experimental) time-resolved photoluminescence decay of [Pt(L^{Bn})Cl] in fluid CH_2Cl_2 at 298 K (air-equilibrated, λ_{ex} = 376 nm, λ_{em} = 580 nm) including the residuals. Right: Fitting parameters including pre-exponential factors and confidence limits.



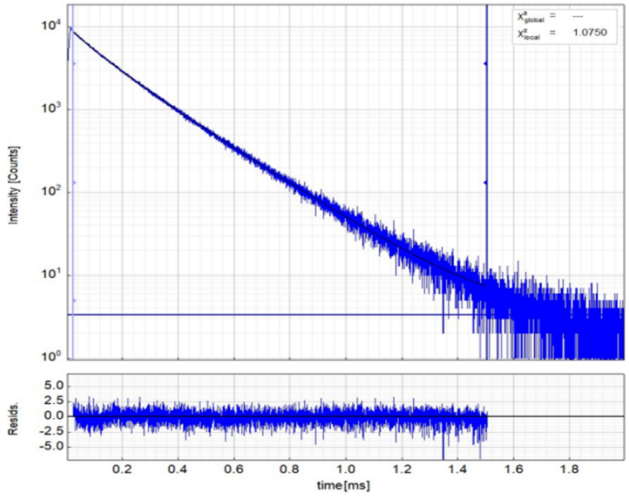
Parameter	Value	Δ	δ
A_1[kCnts/Chnl]	1.830	±0.030	1.6%
τ_1[ns]	2 650	±19	0.7%
I_1[kCnts]	2 425	±23	0.9%
A_{Rel1}[%]	28.9	±0.5	1.4%
I_{Rel1}[%]	56.0	±0.6	1.0%
A_2[kCnts/Chnl]	4.504	±0.024	0.5%
τ_2[ns]	846.5	±7.8	0.9%
I_2[kCnts]	1 907	±25	1.3%
A_{Rel2}[%]	71.2	±0.5	0.6%
I_{Rel2}[%]	44.1	±0.6	1.2%
$Bkgr_{Dec}$[kCnts]	0.0027	±0.0003	10%
τ_{AvInt}[ns]	1 855.8	±4.4	0.2%
τ_{AvAmp}[ns]	1 367.4	±4.1	0.3%

Figure A203. Left: Raw (experimental) time-resolved photoluminescence decay of [Pt(L^{Bn})Cl] in fluid CH_2Cl_2 at 298 K (Ar-purged, λ_{ex} = 376 nm, λ_{em} = 580 nm) including the residuals. Right: Fitting parameters including pre-exponential factors and confidence limits.



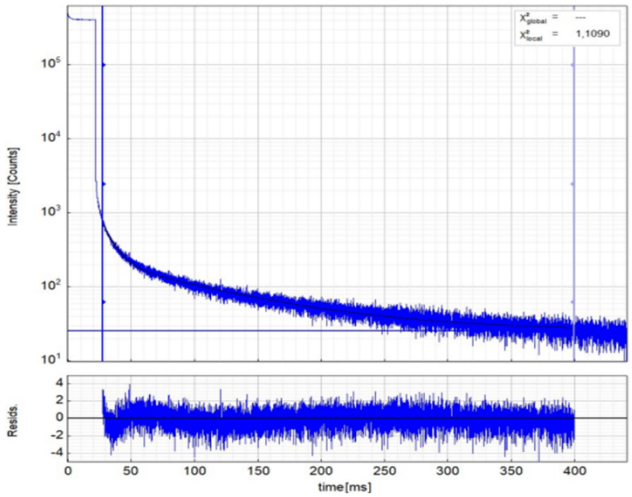
Parameter	Value	Δ	δ
A_1[kCnts/Chnl]	2.382	±0.069	2.9%
τ_1[ns]	6 496	±63	1.0%
I_1[kCnts]	3 869	±75	1.9%
A_{Rel1}[%]	41.8	±1.2	2.7%
I_{Rel1}[%]	63.3	±1.3	1.9%
A_2[kCnts/Chnl]	3.318	±0.060	1.8%
τ_2[ns]	2 706	±46	1.7%
I_2[kCnts]	2 244	±77	3.4%
A_{Rel2}[%]	58.3	±1.2	1.9%
I_{Rel2}[%]	36.8	±1.3	3.4%
$Bkgr_{Dec}$[kCnts]	0.0054	±0.0003	5.0%
τ_{AvInt}[ns]	5 105	±11	0.2%
τ_{AvAmp}[ns]	4 290	±12	0.3%

Figure A204. Left: Raw (experimental) time-resolved photoluminescence decay of [Pt(L^{Bn})Cl] in a frozen glassy CH_2Cl_2/MeOH matrix (V:V = 1:1) at 77 K, including the residuals (λ_{exc} = 376.7 nm, λ_{em} = 495 nm). **Right**: Fitting parameters including pre-exponential factors and confidence limits.



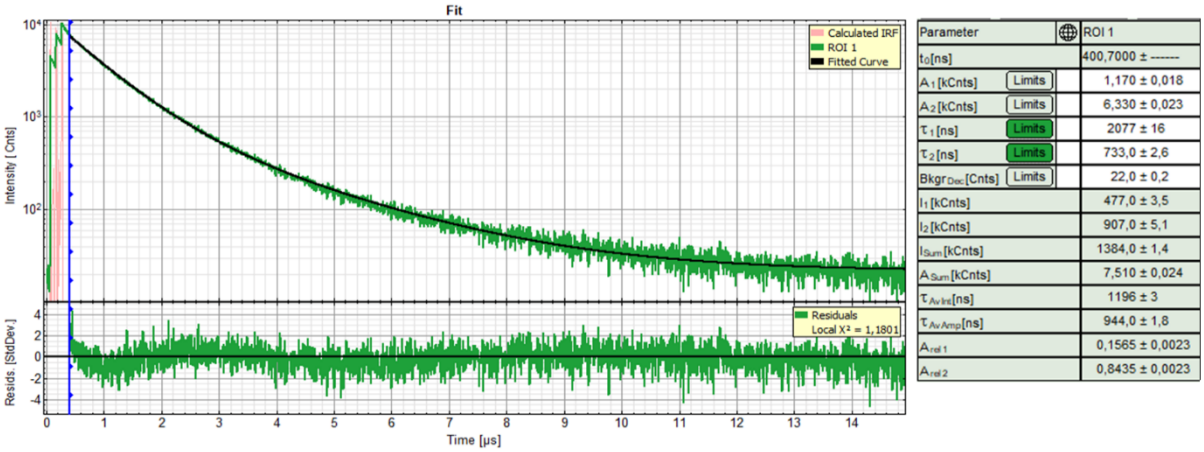
Parameter	Value	Δ	δ
A_1[kCnts/Chnl]	5.58	±0.20	3.6%
τ_1[ns]	204 700	±2 100	1.0%
I_1[kCnts]	4 470	±120	2.6%
A_{Rel1}[%]	64.4	±2.2	3.4%
I_{Rel1}[%]	78.7	±2.1	2.6%
A_2[kCnts/Chnl]	3.09	±0.19	6.0%
τ_2[ns]	100 300	±3 800	3.7%
I_2[kCnts]	1 210	±120	9.6%
A_{Rel2}[%]	35.7	±2.2	6.1%
I_{Rel2}[%]	21.4	±2.1	9.6%
$Bkgr_{Dec}$[kCnts]	0.0034	±0.0004	10%
τ_{AvInt}[ns]	182 410	±270	0.1%
τ_{AvAmp}[ns]	167 460	±410	0.2%

Figure A205. Left: Raw (experimental) time-resolved photoluminescence decay of [Pd(L^{Bn})Cl] in a frozen glassy CH_2Cl_2/MeOH matrix (V:V = 1:1) at 77 K, including the residuals (λ_{exc} = 376.7 nm, λ_{em} = 700 nm). **Right**: Fitting parameters including pre-exponential factors and confidence limits.



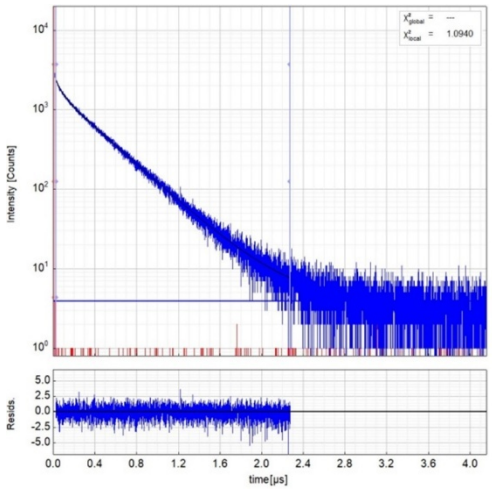
Parameter	Value	Δ	δ
A_1[kCnts/Chnl]	0,1872	±0,0028	1,5%
τ_1[ns]	87 200 000	±1 500 000	1,7%
I_1[kCnts]	497,9	±3,4	0,7%
A_{Rel1}[%]	26,6	±0,4	1,2%
I_{Rel1}[%]	77,3	±0,4	0,4%
A_2[kCnts/Chnl]	0,5168	±0,0072	1,4%
τ_2[ns]	9 320 000	±230 000	2,4%
I_2[kCnts]	147,0	±2,9	1,9%
A_{Rel2}[%]	73,5	±0,4	0,5%
I_{Rel2}[%]	22,8	±0,4	1,5%
$Bkgr_{Dec}$[kCnts]	0,0257	±0,0004	1,4%
τ_{AvInt}[ns]	69 500 000	±1 100 000	1,5%
τ_{AvAmp}[ns]	30 020 000	±450 000	1,5%

Figure A206. Left: Raw (experimental) time-resolved photoluminescence decay of [Ni(L^{Bn})Cl] in a frozen glassy CH_2Cl_2/MeOH matrix (V:V = 1:1) at 77 K, including the residuals (λ_{exc} = 376.7 nm, λ_{em} = 530 nm). Right: Fitting parameters including pre-exponential factors and confidence limits.



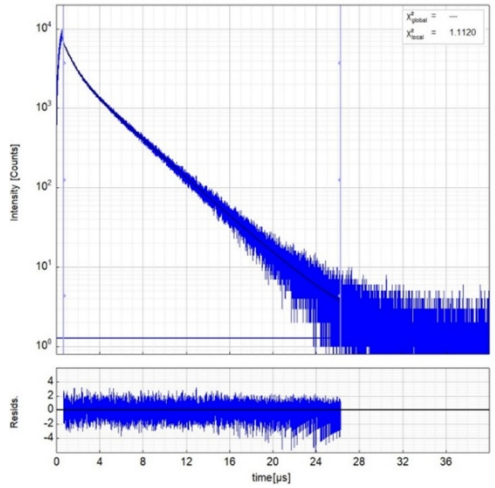
Parameter		ROI 1
t_0[ns]		400,7000 ± ------
A_1 [kCnts]	Limits	1,170 ± 0,018
A_2 [kCnts]	Limits	6,330 ± 0,023
τ_1 [ns]	Limits	2077 ± 16
τ_2 [ns]	Limits	733,0 ± 2,6
$Bkgr_{Dec}$ [Cnts]	Limits	22,0 ± 0,2
I_1 [kCnts]		477,0 ± 3,5
I_2 [kCnts]		907,0 ± 5,1
I_{Sum} [kCnts]		1384,0 ± 1,4
A_{Sum} [kCnts]		7,510 ± 0,024
$\tau_{Av Int}$ [ns]		1196 ± 3
$\tau_{Av Amp}$ [ns]		944,0 ± 1,8
$A_{rel 1}$		0,1565 ± 0,0023
$A_{rel 2}$		0,8435 ± 0,0023

Figure A207. Raw (experimental) time-resolved photoluminescence decay with the fitting parameters including pre-exponential factors and confidence limits of [Pt(L^{Bn})Cl] as a crystal at 298 K.



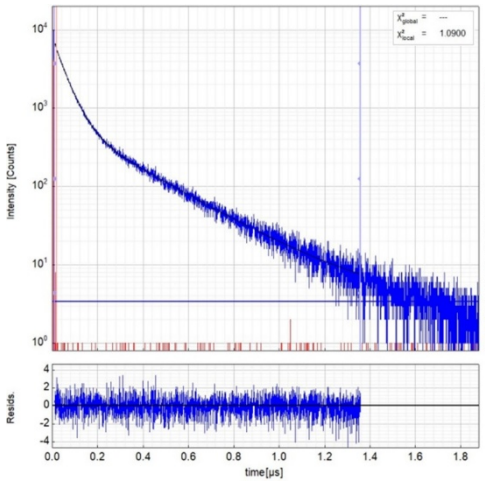
Parameter	Value	Δ	δ
A_1[kCnts/Chnl]	6.72	±0.11	1.6%
τ_1[ns]	369.1	±2.4	0.6%
I_1[kCnts]	4 840	±77	1.6%
A_{Ref1}[%]	65.8	±1.1	1.6%
I_{Ref1}[%]	92.3	±0.5	0.5%
A_2[kCnts/Chnl]	3.50	±0.17	4.6%
τ_2[ns]	59.8	±4.4	7.4%
I_2[kCnts]	408	±26	6.3%
A_{Ref2}[%]	34.3	±1.1	3.1%
I_{Ref2}[%]	7.8	±0.5	5.4%
$Bkgr_{Dec}$[kCnts]	0.0040	±0.0004	8.9%
$Bkgr_{IRF}$[Cnts/Chnl]	-11.8	±3.5	29%
$Shift_{IRF}$[ps]	-12.6	±2.7	21%
τ_{AvInt}[ns]	345.1	±1.5	0.4%
τ_{AvAmp}[ns]	263.2	±5.1	1.9%

Figure A208. Left: Raw (experimental) time-resolved photoluminescence decay of [Pt(L^{Me})Cl] in liquid air-equilibrated CH_2Cl_2 at 298 K (blue) and the instrument response function (red), including the residuals (λ_{ex} = 376 nm, λ_{em} = 500 nm). Right: Fitting parameters including pre-exponential factors and confidence limits.



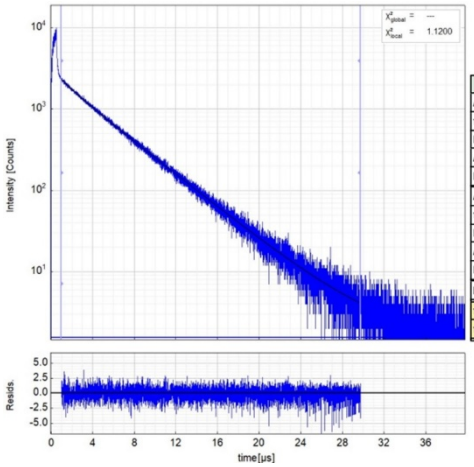
Parameter	Value	Δ	δ
A_1[kCnts/Chnl]	3.459	±0.022	0.6%
τ_1[ns]	899	±11	1.2%
I_1[kCnts]	1 554	±22	1.4%
A_{Ref1}[%]	52.2	±0.3	0.5%
I_{Ref1}[%]	21.6	±0.4	1.4%
A_2[kCnts/Chnl]	3.169	±0.022	0.7%
τ_2[ns]	3 579	±11	0.3%
I_2[kCnts]	5 669	±23	0.4%
A_{Ref2}[%]	47.9	±0.3	0.6%
I_{Ref2}[%]	78.5	±0.4	0.4%
$Bkgr_{Dec}$[kCnts]	0.0013	±0.0002	11%
τ_{AvInt}[ns]	3 002.0	±4.3	0.1%
τ_{AvAmp}[ns]	2 179.8	±6.7	0.3%

Figure A209. Left: Raw (experimental) time-resolved photoluminescence decay of [Pt(L^{Me})Cl] in liquid Ar-purged CH_2Cl_2 at 298 K, including the residuals (λ_{ex} = 376 nm, λ_{em} = 500 nm). Right: Fitting parameters including pre-exponential factors and confidence limits.



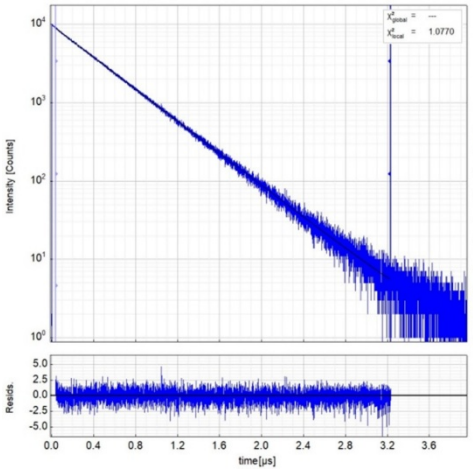
Parameter	Value	Δ	δ
A_1[kCnts/Chnl]	0.91	±0.27	29%
τ_1[ns]	263.8	±4.6	1.7%
I_1[kCnts]	470	±140	28%
A_{Rel1}[%]	9.7	±0.3	2.4%
I_{Rel1}[%]	36.5	±0.5	1.3%
A_2[kCnts/Chnl]	8.5	±2.4	28%
τ_2[ns]	49.32	±0.57	1.1%
I_2[kCnts]	810	±230	28%
A_{Rel2}[%]	90.4	±0.3	0.3%
I_{Rel2}[%]	63.6	±0.5	0.7%
$Bkgr_{Dec}$[kCnts]	0.0034	±0.0006	17%
$Bkgr_{IRF}$[Cnts/Chnl]	-3.9	±6.7	172%
$Shift_{IRF}$[ps]	130	±130	99%
A_{Scat}[kCnts]	430	±310	71%
τ_{AvInt}[ns]	127.6	±1.4	1.1%
τ_{AvAmp}[ns]	70.12	±0.63	0.9%

Figure A210. Left: Raw (experimental) time-resolved photoluminescence decay of [Pt(L^{Me2})Cl] in liquid air-equilibrated CH_2Cl_2 at 298 K (blue) and the instrument response function (red), including the residuals (λ_{ex} = 376 nm, λ_{em} = 500 nm). Right: Fitting parameters including pre-exponential factors and confidence limits.



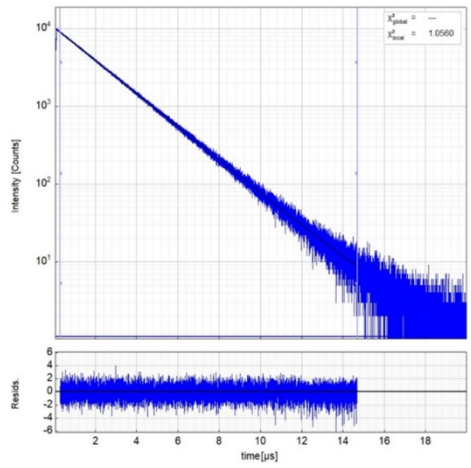
Parameter	Value	Δ	δ
A_1[kCnts/Chnl]	2.028	±0.057	2.8%
τ_1[ns]	4 306	±47	1.1%
I_1[kCnts]	2 183	±40	1.8%
A_{Rel1}[%]	87.6	±2.1	2.4%
I_{Rel1}[%]	95.4	±1.8	1.8%
A_2[kCnts/Chnl]	0.289	±0.047	16%
τ_2[ns]	1 470	±290	19%
I_2[kCnts]	106	±40	37%
A_{Rel2}[%]	12.5	±2.1	17%
I_{Rel2}[%]	4.7	±1.8	37%
$Bkgr_{Dec}$[kCnts]	0.0016	±0.0003	17%
τ_{AvInt}[ns]	4 175	±13	0.3%
τ_{AvAmp}[ns]	3 952	±26	0.6%

Figure A211. Left: Raw (experimental) time-resolved photoluminescence decay of [Pt(L^{Me2})Cl] in liquid Ar-purged CH_2Cl_2 at 298 K, including the residuals (λ_{ex} = 376 nm, λ_{em} = 500 nm). Right: Fitting parameters including pre-exponential factors and confidence limits.



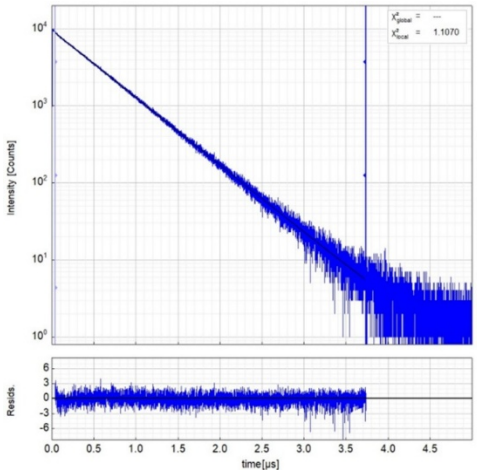
Parameter	Value	Δ	δ
A_1[kCnts/Chnl]	8.9489	±0.0084	0.1%
τ_1[ns]	424.45	±0.32	0.1%
I_1[kCnts]	7 418.5	±4.6	0.1%
A_{Rel1}[%]	100.0	---	---
I_{Rel1}[%]	100.0	---	---
$Bkgr_{Dec}$[kCnts]	0.0007	±0.0002	18%
τ_{AvInt}[ns]	424.45	±0.32	0.1%
τ_{AvAmp}[ns]	424.45	±0.32	0.1%

Figure A212. Left: Raw (experimental) time-resolved photoluminescence decay of [Pt(L^{Cl})Cl] in liquid air-equilibrated CH_2Cl_2 at 298 K, including the residuals (λ_{ex} = 376 nm, λ_{em} = 505 nm). Right: Fitting parameters including pre-exponential factors and confidence limits.



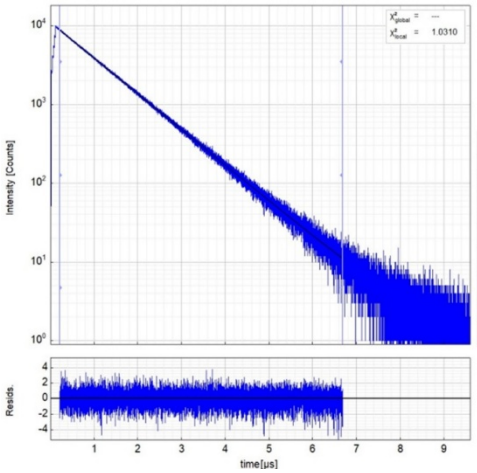
Parameter	Value	Δ	δ
A_1[kCnts/Chnl]	9.0788	±0.0052	0.1%
τ_1[ns]	2 034.1	±1.5	0.1%
I_1[kCnts]	18 468	±12	0.1%
A_{Rel1}[%]	100.0	---	---
I_{Rel1}[%]	100.0	---	---
$Bkgr_{Dec}$[kCnts]	0.0011	±0.0002	15%
τ_{AvInt}[ns]	2 034.1	±1.5	0.1%
τ_{AvAmp}[ns]	2 034.1	±1.5	0.1%

Figure A213. Left: Raw (experimental) time-resolved photoluminescence decay of [Pt(L^{Cl})Cl] in liquid Ar-purged CH_2Cl_2 at 298 K, including the residuals (λ_{ex} = 376 nm, λ_{em} = 505 nm). Right: Fitting parameters including pre-exponential factors and confidence limits.



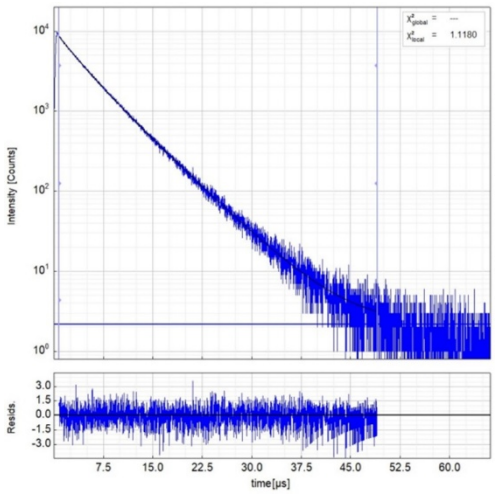
Parameter	Value	Δ	δ
A_1[kCnts/Chnl]	8.8942	±0.0040	0.0%
τ_1[ns]	496.10	±0.13	0.0%
I_1[kCnts]	8 617.9	±2.7	0.0%
A_{Rel1}[%]	100.0	---	---
I_{Rel1}[%]	100.0	---	---
$Bkgr_{Dec}$[kCnts]	0.0004	±0.0001	18%
τ_{AvInt}[ns]	496.10	±0.13	0.0%
τ_{AvAmp}[ns]	496.10	±0.13	0.0%

Figure A214. Left: Raw (experimental) time-resolved photoluminescence decay of [Pt(L^{F})Cl] in liquid air-equilibrated CH_2Cl_2 at 298 K, including the residuals (λ_{ex} = 376 nm, λ_{em} = 470 nm). Right: Fitting parameters including pre-exponential factors and confidence limits.



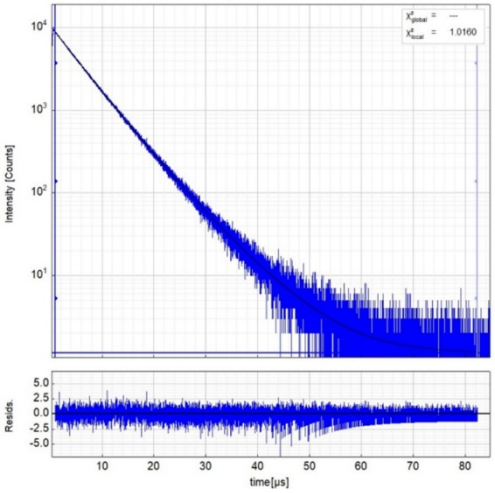
Parameter	Value	Δ	δ
A_1[kCnts/Chnl]	8.8387	±0.0053	0.1%
τ_1[ns]	956.57	±0.39	0.0%
I_1[kCnts]	16 909.5	±6.8	0.0%
A_{Rel1}[%]	100.0	---	---
I_{Rel1}[%]	100.0	---	---
$Bkgr_{Dec}$[kCnts]	0.0009	±0.0001	9.3%
τ_{AvInt}[ns]	956.57	±0.39	0.0%
τ_{AvAmp}[ns]	956.57	±0.39	0.0%

Figure A215. Left: Raw (experimental) time-resolved photoluminescence decay of [Pt(L^{F})Cl] in liquid Ar-purged CH_2Cl_2 at 298 K, including the residuals (λ_{ex} = 376 nm, λ_{em} = 475 nm). Right: Fitting parameters including pre-exponential factors and confidence limits.



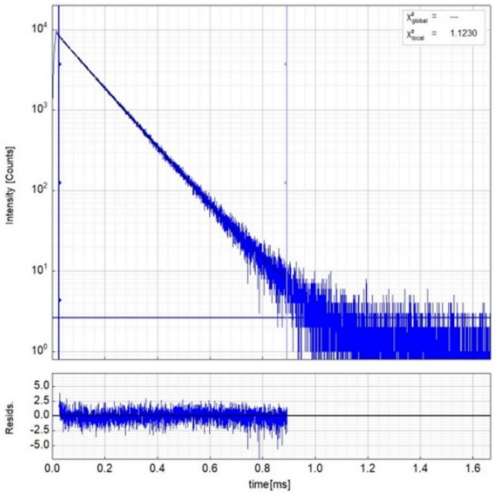
Parameter	Value	Δ	δ
A_1[kCnts/Chnl]	5.33	±0.33	6.1%
τ_1[ns]	5 607	±82	1.5%
I_1[kCnts]	1 867	±87	4.7%
A_{Rel1}[%]	62.2	±3.7	5.9%
I_{Rel1}[%]	75.4	±3.6	4.7%
A_2[kCnts/Chnl]	3.24	±0.32	9.6%
τ_2[ns]	3 020	±160	5.1%
I_2[kCnts]	611	±88	14%
A_{Rel2}[%]	37.9	±3.7	9.7%
I_{Rel2}[%]	24.7	±3.6	14%
$Bkgr_{Dec}$[kCnts]	0.0022	±0.0003	9.8%
τ_{AvInt}[ns]	4 968.5	±7.6	0.2%
τ_{AvAmp}[ns]	4 628	±15	0.3%

Figure A216. Left: Raw (experimental) time-resolved photoluminescence decay of [Pt(L^{Me})Cl] in a frozen glassy matrix of 2-MeTHF at 77 K, including the residuals (λ_{ex} = 376 nm, λ_{em} = 500 nm). Right: Fitting parameters including pre-exponential factors and confidence limits.



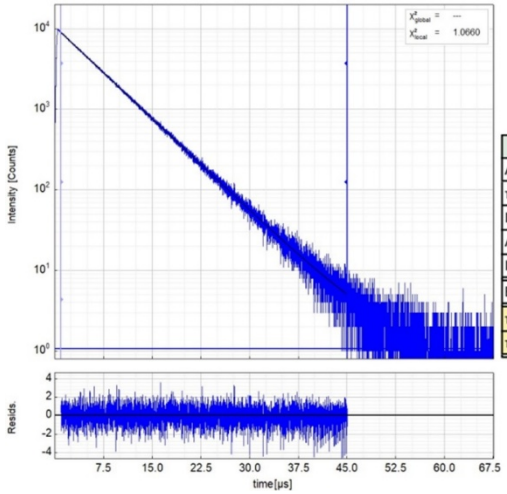
Parameter	Value	Δ	δ
A_1[kCnts/Chnl]	1.48	±0.30	20%
τ_1[ns]	7 810	±280	3.5%
I_1[kCnts]	1 440	±250	17%
A_{Rel1}[%]	16.7	±3.4	20%
I_{Rel1}[%]	23.7	±4.1	17%
A_2[kCnts/Chnl]	7.39	±0.29	3.9%
τ_2[ns]	5 020	±65	1.3%
I_2[kCnts]	4 640	±250	5.2%
A_{Rel2}[%]	83.4	±3.4	4.0%
I_{Rel2}[%]	76.4	±4.1	5.3%
$Bkgr_{Dec}$[kCnts]	0.0012	±0.0001	4.2%
τ_{AvInt}[ns]	5 680.3	±3.9	0.1%
τ_{AvAmp}[ns]	5 483.6	±6.0	0.1%

Figure A217. Left: Raw (experimental) time-resolved photoluminescence decay of [Pt(L^{Me2})Cl] in a frozen glassy matrix of 2-MeTHF at 77 K, including the residuals (λ_{ex} = 376 nm, λ_{em} = 500 nm). Right: Fitting parameters including pre-exponential factors and confidence limits.



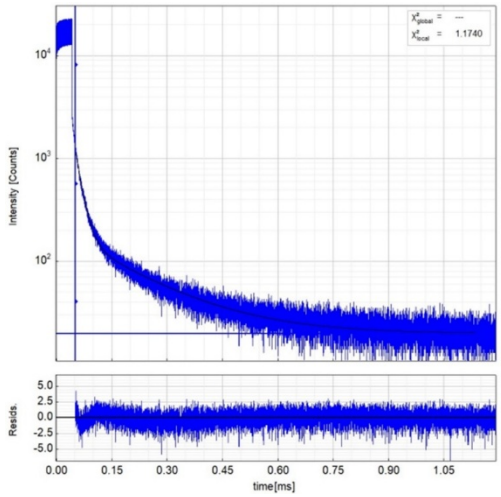
Parameter	Value	Δ	δ
A_1[kCnts/Chnl]	8.216	±0.017	0.2%
τ_1[ns]	118 120	±160	0.1%
I_1[kCnts]	3 790.7	±4.8	0.1%
A_{Rel1}[%]	100.0	---	---
I_{Rel1}[%]	100.0	---	---
$Bkgr_{Dec}$[kCnts]	0.0027	±0.0002	7.2%
τ_{AvInt}[ns]	118 120	±160	0.1%
τ_{AvAmp}[ns]	118 120	±160	0.1%

Figure A218. Left: Raw (experimental) time-resolved photoluminescence decay of [Pt(L^{Cl})Cl] in a frozen glassy matrix of 2-MeTHF at 77 K, including the residuals (λ_{ex} = 376 nm, λ_{em} = 500 nm). Right: Fitting parameters including pre-exponential factors and confidence limits.



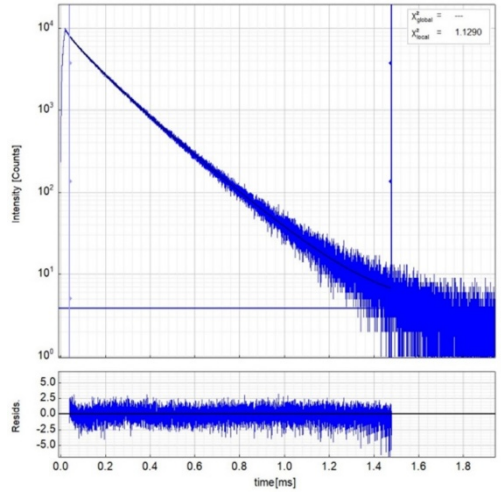
Parameter	Value	Δ	δ
A_1[kCnts/Chnl]	9.0121	±0.0078	0.1%
τ_1[ns]	5 702.9	±4.4	0.1%
I_1[kCnts]	6 424.4	±3.1	0.0%
A_{Rel1}[%]	100.0	---	---
I_{Rel1}[%]	100.0	---	---
$Bkgr_{Dec}$[kCnts]	0.0011	±0.0002	17%
τ_{AvInt}[ns]	5 702.9	±4.4	0.1%
τ_{AvAmp}[ns]	5 702.9	±4.4	0.1%

Figure A219. Left: Raw (experimental) time-resolved photoluminescence decay of [Pt(L^F)Cl] in a frozen glassy matrix of 2-MeTHF at 77 K, including the residuals (λ_{ex} = 376 nm, λ_{em} = 460 nm). Right: Fitting parameters including pre-exponential factors and confidence limits.



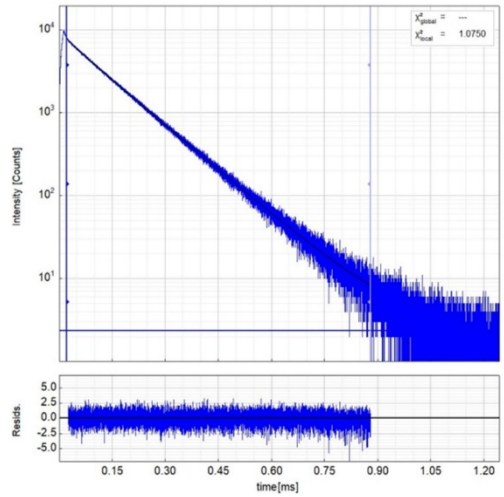
Parameter	Value	Δ	δ
A_1[kCnts/Chnl]	0.1443	±0.0023	1.6%
τ_1[ns]	182 800	±2 500	1.4%
I_1[kCnts]	412.1	±2.5	0.6%
A_{Rel1}[%]	12.5	±0.2	1.4%
I_{Rel1}[%]	59.6	±0.4	0.5%
A_2[kCnts/Chnl]	1.014	±0.011	1.0%
τ_2[ns]	17 700	±240	1.3%
I_2[kCnts]	280.3	±2.6	0.9%
A_{Rel2}[%]	87.6	±0.2	0.2%
I_{Rel2}[%]	40.5	±0.4	0.8%
$Bkgr_{Dec}$[kCnts]	0.0198	±0.0001	0.5%
τ_{AvInt}[ns]	116 000	±1 300	1.1%
τ_{AvAmp}[ns]	38 270	±370	1.0%

Figure A220. Left: Raw (experimental) time-resolved photoluminescence decay of [Pd(L^{Me})Cl] in a frozen glassy matrix of 2-MeTHF at 77 K, including the residuals (λ_{ex} = 376 nm, λ_{em} = 500 nm). Right: Fitting parameters including pre-exponential factors and confidence limits.



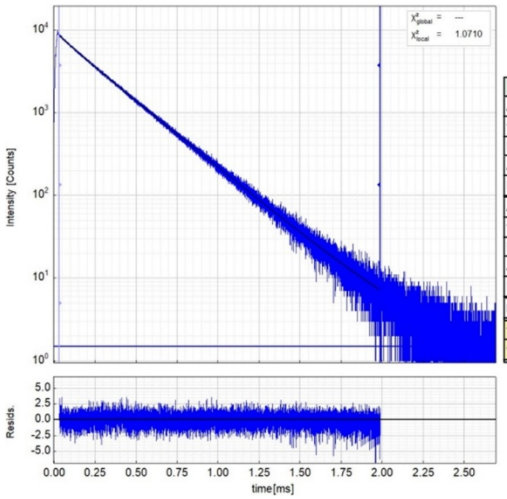
Parameter	Value	Δ	δ
A_1[kCnts/Chnl]	5.04	±0.17	3.3%
τ_1[ns]	192 900	±1 900	0.9%
I_1[kCnts]	7 580	±190	2.4%
A_{Rel1}[%]	63.6	±2.0	3.1%
I_{Rel1}[%]	78.2	±2.0	2.5%
A_2[kCnts/Chnl]	2.90	±0.16	5.3%
τ_2[ns]	93 700	±3 400	3.5%
I_2[kCnts]	2 120	±190	8.8%
A_{Rel2}[%]	36.5	±2.0	5.5%
I_{Rel2}[%]	21.9	±2.0	8.9%
$Bkgr_{Dec}$[kCnts]	0.0039	±0.0003	7.1%
τ_{AvInt}[ns]	171 190	±240	0.1%
τ_{AvAmp}[ns]	156 640	±390	0.2%

Figure A221. Left: Raw (experimental) time-resolved photoluminescence decay of [Pd(L^{Me2})Cl] in a frozen glassy matrix of 2-MeTHF at 77 K, including the residuals (λ_{ex} = 376 nm, λ_{em} = 640 nm). Right: Fitting parameters including pre-exponential factors and confidence limits.



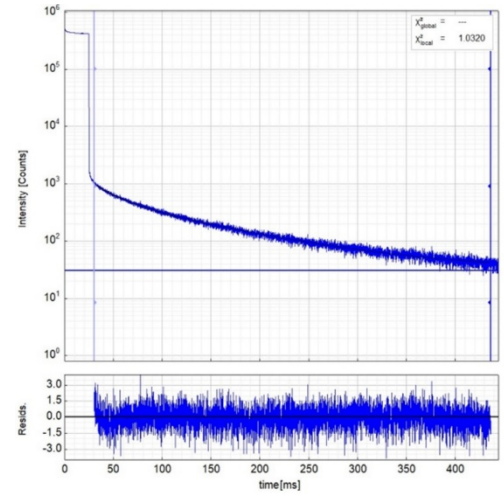
Parameter	Value	Δ	δ
A_1[kCnts/Chnl]	6.865	±0.082	1.2%
τ_1[ns]	120 970	±500	0.4%
I_1[kCnts]	12 980	±110	0.8%
A_{Rel1}[%]	92.1	±1.0	1.0%
I_{Rel1}[%]	96.9	±0.8	0.8%
A_2[kCnts/Chnl]	0.593	±0.072	12%
τ_2[ns]	45 100	±6 300	14%
I_2[kCnts]	420	±110	26%
A_{Rel2}[%]	8.0	±1.0	12%
I_{Rel2}[%]	3.2	±0.8	26%
$Bkgr_{Dec}$[kCnts]	0.0024	±0.0003	11%
τ_{AvInt}[ns]	118 610	±120	0.1%
τ_{AvAmp}[ns]	114 940	±290	0.2%

Figure A222. Left: Raw (experimental) time-resolved photoluminescence decay of [Pd(L^{Cl})Cl] in a frozen glassy matrix of 2-MeTHF at 77 K, including the residuals (λ_{ex} = 376 nm, λ_{em} = 475 nm). Right: Fitting parameters including pre-exponential factors and confidence limits.



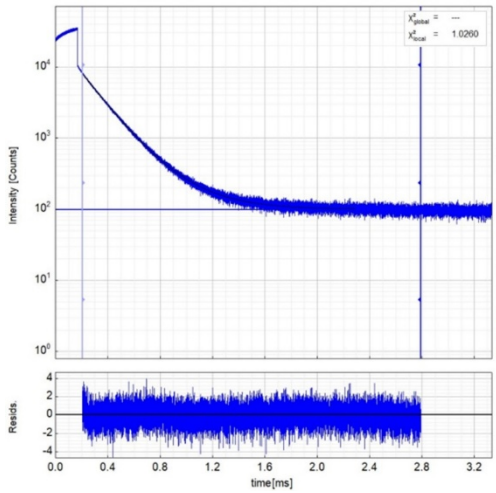
Parameter	Value	Δ	δ
A_1[kCnts/Chnl]	0.871	±0.093	11%
τ_1[ns]	111 000	±11 000	9.9%
I_1[kCnts]	750	±160	20%
A_{Rel1}[%]	10.2	±1.1	11%
I_{Rel1}[%]	4.4	±0.9	20%
A_2[kCnts/Chnl]	7.70	±0.11	1.3%
τ_2[ns]	271 500	±1 200	0.4%
I_2[kCnts]	16 330	±150	0.9%
A_{Rel2}[%]	89.9	±1.1	1.2%
I_{Rel2}[%]	95.7	±0.9	0.9%
$Bkgr_{Dec}$[kCnts]	0.0015	±0.0003	17%
τ_{AvInt}[ns]	264 350	±230	0.1%
τ_{AvAmp}[ns]	255 050	±580	0.2%

Figure A223. Left: Raw (experimental) time-resolved photoluminescence decay of [Pd(L^{F})Cl] in a frozen glassy matrix of 2-MeTHF at 77 K, including the residuals (λ_{ex} = 376 nm, λ_{em} = 450 nm). Right: Fitting parameters including pre-exponential factors and confidence limits.



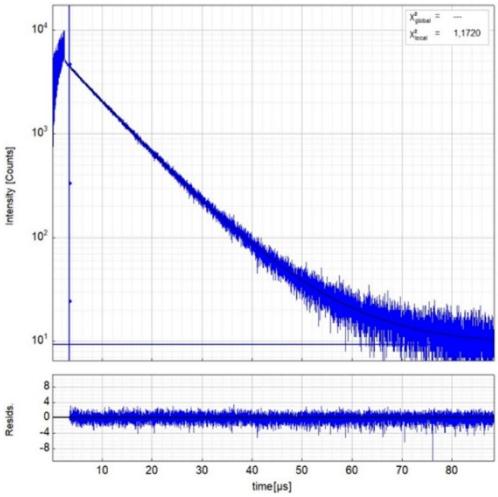
Parameter	Value	Δ	δ
A_1[kCnts/Chnl]	0.481	±0.019	3.9%
τ_1[ns]	109 800 000	±3 800 000	3.5%
I_1[kCnts]	804.3	±7.8	1.0%
A_{Rel1}[%]	50.8	±1.9	3.6%
I_{Rel1}[%]	81.8	±1.5	1.8%
A_2[kCnts/Chnl]	0.466	±0.016	3.4%
τ_2[ns]	25 200 000	±1 600 000	6.1%
I_2[kCnts]	179	±17	9.0%
A_{Rel2}[%]	49.3	±1.9	3.7%
I_{Rel2}[%]	18.3	±1.5	7.9%
$Bkgr_{Dec}$[kCnts]	0.0302	±0.0016	5.2%
τ_{AvInt}[ns]	94 400 000	±2 300 000	2.4%
τ_{AvAmp}[ns]	68 100 000	±1 200 000	1.8%

Figure A224. Left: Raw (experimental) time-resolved photoluminescence decay of [Ni(L^{Me})Cl] in a frozen glassy matrix of 2-MeTHF at 77 K, including the residuals (λ_{ex} = 376 nm, λ_{em} = 525 nm). Right: Fitting parameters including pre-exponential factors and confidence limits.



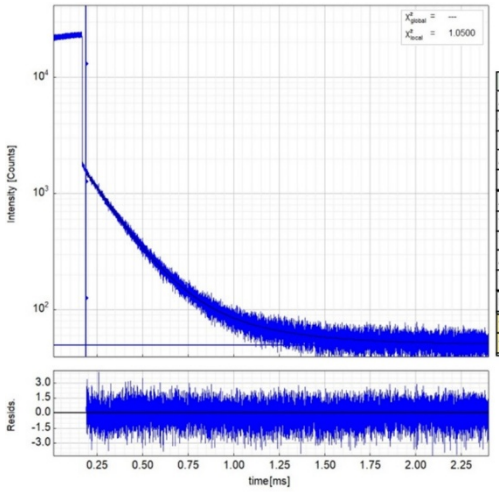
Parameter	Value	Δ	δ
A_1[kCnts/Chnl]	1.13	±0.20	18%
τ_1[ns]	328 000	±17 000	5.0%
I_1[kCnts]	2 880	±380	13%
A_{Rel1}[%]	14.2	±2.6	18%
I_{Rel1}[%]	24.0	±3.2	13%
A_2[kCnts/Chnl]	6.80	±0.20	2.8%
τ_2[ns]	172 200	±2 400	1.4%
I_2[kCnts]	9 150	±380	4.2%
A_{Rel2}[%]	85.9	±2.6	2.9%
I_{Rel2}[%]	76.1	±3.2	4.1%
$Bkgr_{Dec}$[kCnts]	0.0993	±0.0005	0.4%
τ_{AvInt}[ns]	209 260	±760	0.4%
τ_{AvAmp}[ns]	194 170	±380	0.2%

Figure A225. Left: Raw (experimental) time-resolved photoluminescence decay of [Ni(L^{Cl})Cl] in a frozen glassy matrix of 2-MeTHF at 77 K, including the residuals (λ_{ex} = 376 nm, λ_{em} = 475 nm). Right: Fitting parameters including pre-exponential factors and confidence limits.



Parameter	Value	Δ	δ
A_1[kCnts/Chnl]	0,61	±0,17	28%
τ_1[ns]	13 270	±920	6,9%
I_1[kCnts]	1 010	±230	22%
A_{Rel1}[%]	13,8	±3,9	28%
I_{Rel1}[%]	21,0	±4,7	22%
A_2[kCnts/Chnl]	3,81	±0,17	4,4%
τ_2[ns]	7 990	±130	1,6%
I_2[kCnts]	3 800	±230	6,0%
A_{Rel2}[%]	86,3	±3,9	4,4%
I_{Rel2}[%]	79,1	±4,7	5,9%
$Bkgr_{Dec}$[kCnts]	0,0093	±0,0002	1,4%
τ_{AvInt}[ns]	9 093	±23	0,2%
τ_{AvAmp}[ns]	8 713	±14	0,2%

Figure A226. Left: Raw (experimental) time-resolved photoluminescence decay of [Ni(L^{F})Cl] in a frozen glassy matrix of 2-MeTHF at 77 K, including the residuals (λ_{ex} = 376 nm, λ_{em} = 475 nm). Right: Fitting parameters including pre-exponential factors and confidence limits.



Parameter	Value	Δ	δ
A_1[kCnts/Chnl]	1.357	±0.026	1.9%
τ_1[ns]	175 600	±2 900	1.6%
I_1[kCnts]	1 860	±64	3.4%
A_{Rel1}[%]	92.1	±1.9	2.0%
I_{Rel1}[%]	81.0	±2.5	3.0%
A_2[kCnts/Chnl]	0.118	±0.028	24%
τ_2[ns]	480 000	±53 000	11%
I_2[kCnts]	440	±54	12%
A_{Rel2}[%]	8.0	±1.9	23%
I_{Rel2}[%]	19.1	±2.5	13%
$Bkgr_{Dec}$[kCnts]	0.0498	±0.0005	0.9%
τ_{AvInt}[ns]	233 600	±5 200	2.2%
τ_{AvAmp}[ns]	199 800	±1 400	0.7%

Figure A227. Left: Raw (experimental) time-resolved photoluminescence decay of [Ni(dpb)Cl] in a frozen glassy matrix of 2-MeTHF at 77 K, including the residuals (λ_{ex} = 376 nm, λ_{em} = 475 nm). Right: Fitting parameters including pre-exponential factors and confidence limits.

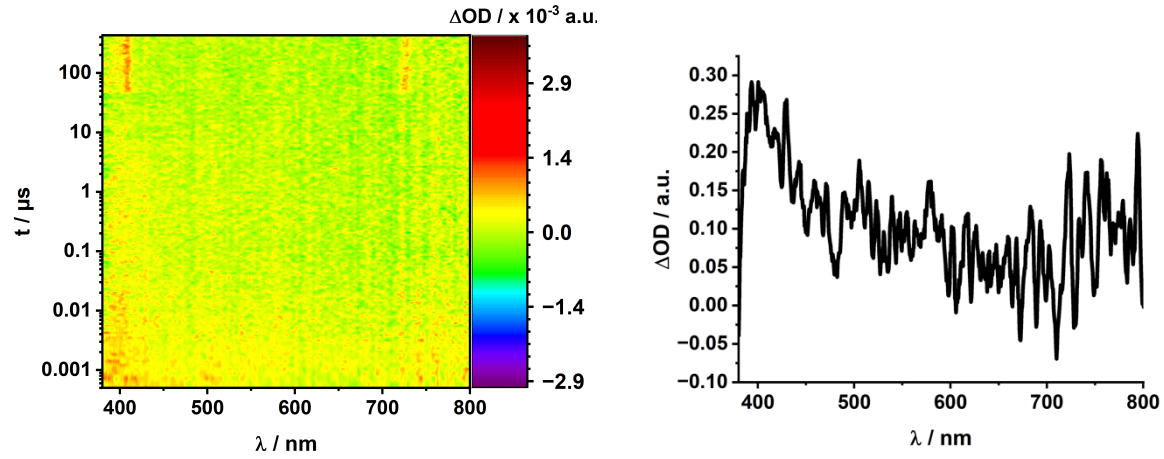


Figure A228. 3D heat map (left) of [Ni(L^{NHPh})Cl] at 298 K obtained by cryostat supported ns-TAS measurements in 2MeTHF. Evolution associated spectra (right) of the ns-TA data of [Ni(L^{NHPh})Cl] with a lifetime of 722 ps.

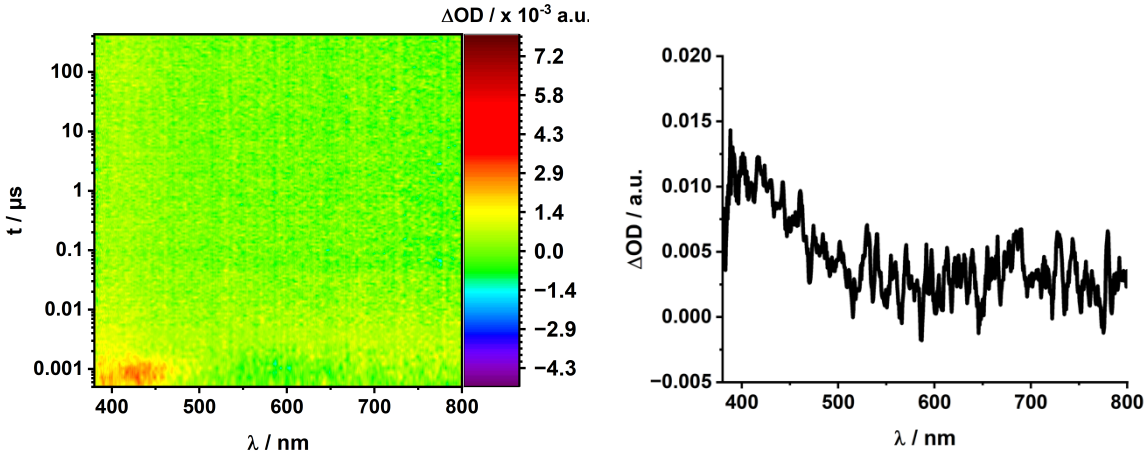


Figure A229. 3D heat map (left) of [Ni(L^{NHPh})Cl] at 150 K obtained by cryostat supported ns-TAS measurements in 2MeTHF. Evolution associated spectra (right) of the ns-TA data of [Ni(L^{NHPh})Cl] with a lifetime of 10.1 ns.

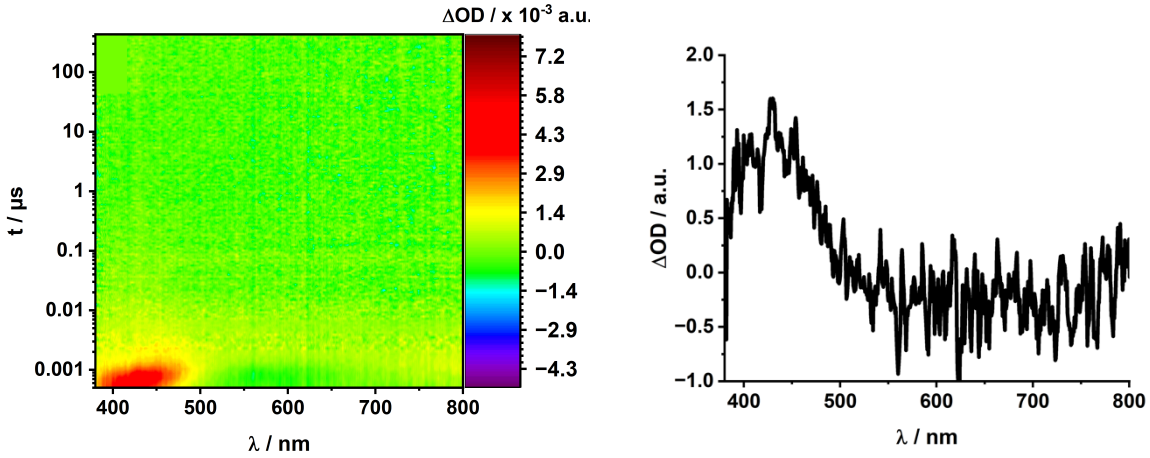


Figure A230. 3D heat map (left) of [Ni(L^{NHBn})Cl] at 298 K obtained by cryostat supported ns-TAS measurements in 2MeTHF. Evolution associated spectra (right) of the ns-TA data of [Ni(L^{NHBn})Cl] with a lifetime of 1.94 ns.

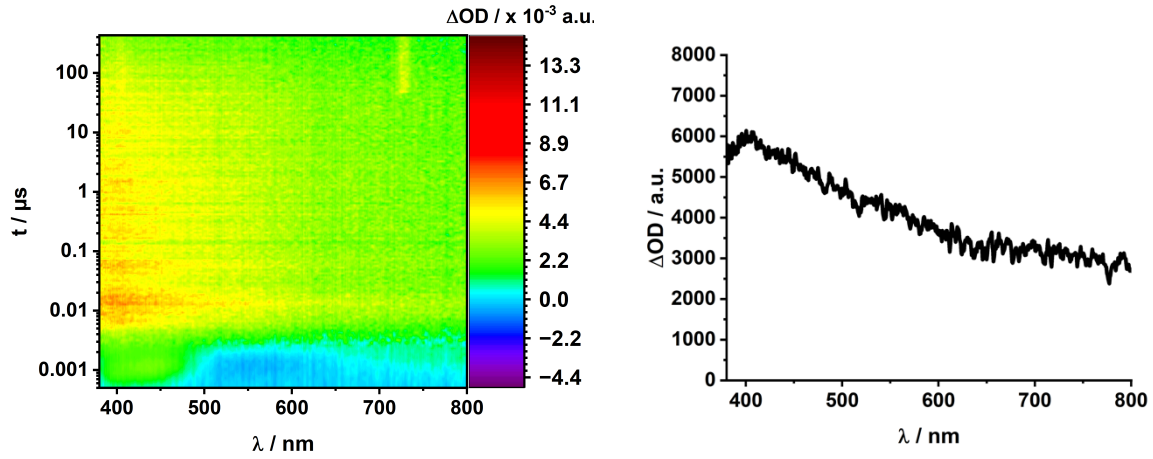


Figure A231. 3D heat map (left) of [Ni(L^{NHBn})Cl] at 180 K obtained by cryostat supported ns-TAS measurements in 2MeTHF. Evolution associated spectra (right) of the ns-TA data of [Ni(L^{NHBn})Cl] with a lifetime of 500 fs. The fit was not successful because of the high intensity of the instrument response function (IRF).

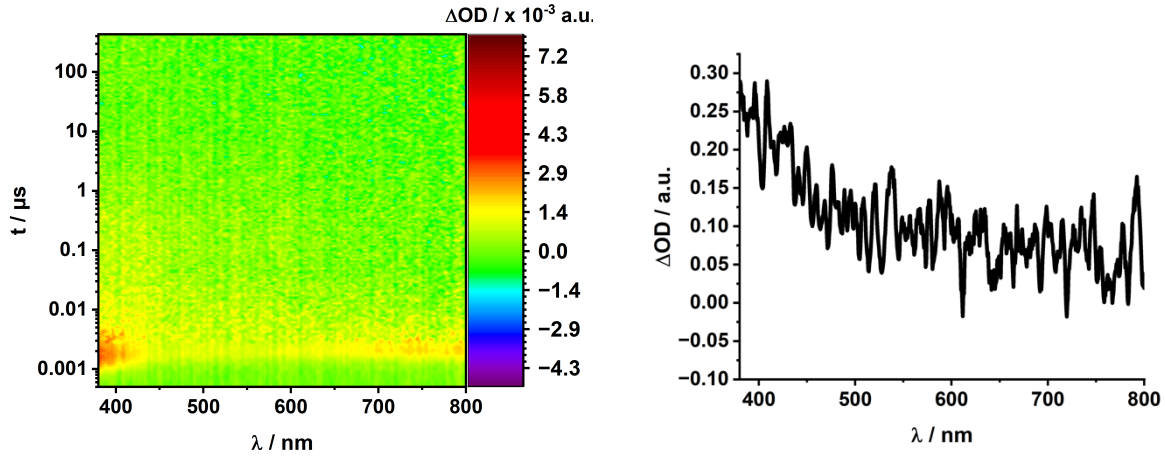


Figure A232. 3D heat map (left) of ClL^{NHPh} at 298 K obtained by ns-TAS measurements in 2MeTHF. Evolution associated spectra (right) of the ns-TA data of ClL^{NHPh} with a lifetime of 8.3 ns.

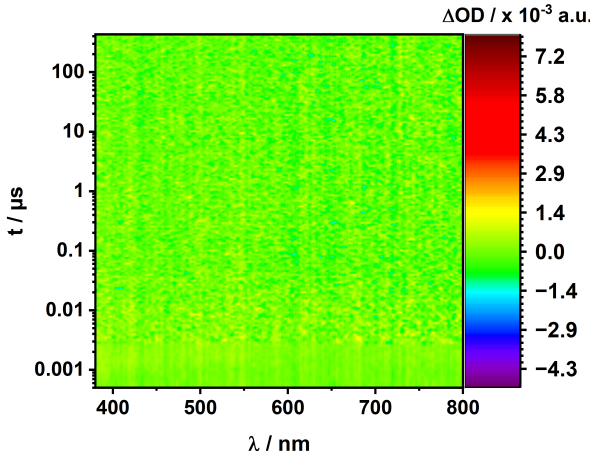


Figure A233. 3D heat map of ClL^{NHBn} at 298 K obtained by ns-TAS measurements in 2MeTHF. A fit was not possible due to the lack of signal.

7.7. Calculated coordinates of the optimized structures

Table A49. Calculated coordinates of the optimized singlet ground state structures for [M(L^{NHPh})Cl].[a]

[Pt(L^{NHPh})Cl]				[Pd(L^{NHPh})Cl]			
atom	coordinates (Å)			atom	coordinates (Å)		
	X	Y	Z		X	Y	Z
Pt	–0.00008	–0.71291	–0.24495	Pd	0.000000	–0.77137	–0.27731
Cl	0.000258	1.544590	–1.54130	Cl	–0.00001	1.485051	–1.51822
N	2.076205	–1.04679	–0.06880	C	–1.22820	–3.33631	0.112317
N	–2.07647	–1.04654	–0.06912	N	2.105515	–1.13079	–0.07674
N	2.735615	1.191844	–0.08826	C	0.000000	–2.66306	0.074751
H	1.809249	1.390982	–0.48193	N	2.771101	1.099761	–0.10274
C	–0.00023	–2.59526	0.137695	H	1.845195	1.295273	–0.50163
N	–2.73562	1.192191	–0.08907	N	–2.10551	–1.13079	–0.07674
H	–1.80929	1.391168	–0.48289	C	–2.40698	–2.46996	0.059037
C	3.085011	–0.12541	–0.02785	N	–2.77110	1.099760	–0.10274
C	–2.39232	–2.38788	0.090321	H	–1.84520	1.295273	–0.50163
C	–3.08516	–0.12502	–0.02827	C	–3.11761	–0.21924	–0.03087
C	1.227848	–3.27033	0.177489	C	1.228201	–3.33631	0.112317
C	3.706822	–2.82190	0.200750	C	3.117607	–0.21924	–0.03087
H	3.916710	–3.87726	0.325443	C	3.715823	–2.92195	0.177954
C	–1.22841	–3.27016	0.177412	H	3.918505	–3.98029	0.288995
C	4.437121	–0.53723	0.051275	C	2.406985	–2.46996	0.059037
H	5.215861	0.213354	0.005159	C	–5.11668	4.546231	0.565517
C	–3.56414	2.313005	0.142598	H	–5.70587	5.442363	0.736101
C	3.564470	2.312521	0.142902	C	–5.27638	3.428657	1.391207
C	4.740779	–1.88043	0.155015	H	–5.98337	3.456084	2.215756
H	5.777148	–2.19984	0.202790	C	1.218620	–4.73903	0.208504
C	–3.70732	–2.82138	0.200785	H	2.148004	–5.30073	0.239162
H	–3.91733	–3.87670	0.325644	C	–4.51657	2.275371	1.184200
C	2.391884	–2.38820	0.090456	H	–4.61791	1.429675	1.857340
C	1.220528	–4.67004	0.294623	C	4.516568	2.275371	1.184200
H	2.148381	–5.23426	0.328371	H	4.617911	1.429675	1.857340
C	–4.43731	–0.53664	0.051083	C	3.599102	2.221714	0.120363
H	–5.21594	0.214060	0.004935	C	–4.46778	–0.63905	0.060310
C	–5.07802	4.634659	0.609759	H	–5.25477	0.103698	0.026656
H	–5.66576	5.530030	0.789080	C	5.116667	4.546231	0.565516
C	4.478677	2.358499	1.209747	H	5.705873	5.442363	0.736100
H	4.578920	1.507473	1.876274	C	–3.71582	–2.92195	0.177954
C	–1.22128	–4.66988	0.294550	H	–3.91851	–3.98029	0.288995
H	–2.14921	–5.23399	0.328238	C	–4.75706	–1.98627	0.156518
C	5.237085	3.510630	1.427348	H	–5.79018	–2.31488	0.214047
H	5.941575	3.532613	2.254153	C	3.433085	3.346943	–0.70530
C	5.079010	4.633934	0.609077	H	2.716010	3.307564	–1.52043
H	5.667014	5.529211	0.788012	C	4.183664	4.501082	–0.47591
C	–4.47782	2.359048	1.209897	H	4.043617	5.363621	–1.12148
H	–4.57790	1.507965	1.876379	C	4.757058	–1.98627	0.156517
C	–5.23590	3.511297	1.427991	H	5.790177	–2.31488	0.214047
H	–5.93998	3.533328	2.255150	C	–1.21862	–4.73903	0.208504
C	–4.74115	–1.87977	0.155058	H	–2.14800	–5.30073	0.239162
H	–5.77756	–2.19903	0.203006	C	5.276383	3.428658	1.391206
C	3.400260	3.442849	–0.67566	H	5.983369	3.456085	2.215755
H	2.685975	3.408822	–1.49345	C	–3.43309	3.346943	–0.70530
C	–3.40013	3.443385	–0.67593	H	–2.71601	3.307564	–1.52044
H	–2.68628	3.409316	–1.49409	C	0.000000	–5.42430	0.257601
C	4.149608	4.595762	–0.43574	H	0.000000	–6.50755	0.329064
H	4.011258	5.462786	–1.07559	C	–3.59910	2.221714	0.120363
C	–4.14914	4.596414	–0.43552	C	4.467781	–0.63905	0.060309
H	–4.01095	5.463475	–1.07535	H	5.254765	0.103698	0.026655
C	–0.00042	–5.35314	0.357866	C	–4.18367	4.501082	–0.47591
H	–0.00050	–6.43510	0.446836	H	–4.04362	5.363621	–1.12148

[a] DFT calculations on TPSSh/6–31G(d)/LanL2DZ ecp/CPCM(THF) level of theory.

Table A50. Calculated coordinates of the optimized triplet excited state structures for [M(L^{NHPh})Cl].[a]

[Pt(L^{NHPh})Cl]				[Pd(L^{NHPh})Cl]			
atom	coordinates (Å)			atom	coordinates (Å)		
	X	Y	Z		X	Y	Z
Pt	–0.00001	–0.69510	–0.25853	Pd	–0.02326	–0.76591	–0.30277
Cl	0.000002	1.609434	–1.49910	Cl	0.036612	1.510047	–1.53084
N	2.075935	–1.02728	–0.09449	C	–1.38136	–3.27507	0.101998
N	–2.07595	–1.02728	–0.09449	N	2.066720	–1.19434	–0.05005
N	2.781573	1.186440	–0.16295	C	–0.09346	–2.65116	0.072732
H	1.842373	1.395833	–0.52711	N	2.818210	1.005109	–0.13455
C	–0.00000	–2.57757	0.141066	H	1.902307	1.222455	–0.54241
N	–2.78158	1.186444	–0.16296	N	–2.12361	–1.03636	–0.17687
H	–1.84238	1.395831	–0.52712	C	–2.46939	–2.40166	–0.04143
C	3.097941	–0.13689	–0.06940	N	–2.75379	1.185789	–0.20907
C	–2.36319	–2.38821	0.080122	H	–1.80542	1.361278	–0.58455
C	–3.09796	–0.13688	–0.06941	C	–3.10923	–0.12458	–0.11967
C	1.233064	–3.24088	0.201430	C	1.097895	–3.36067	0.170619
C	3.705898	–2.83494	0.166185	C	3.112762	–0.32467	–0.01329
H	3.902166	–3.89436	0.278835	C	3.597480	–3.03999	0.283374
C	–1.23306	–3.24089	0.201432	H	3.755536	–4.10214	0.425935
C	4.456218	–0.55898	0.001738	C	2.308742	–2.54121	0.125673
H	5.241100	0.181461	–0.07860	C	–4.90164	4.664341	0.771165
C	–3.59660	2.298169	0.121914	H	–5.44343	5.571794	1.019427
C	3.596599	2.298160	0.121922	C	–5.12331	3.491883	1.501843
C	4.744872	–1.91738	0.108433	H	–5.82690	3.489285	2.328883
H	5.777461	–2.24974	0.143454	C	1.043198	–4.76924	0.319059
C	–3.70590	–2.83494	0.166195	H	1.950026	–5.36196	0.388180
H	–3.90217	–3.89436	0.278858	C	–4.42365	2.324144	1.198537
C	2.363173	–2.38821	0.080118	H	–4.55513	1.432568	1.802729
C	1.225127	–4.68680	0.373369	C	4.585235	2.149445	1.152311
H	2.154154	–5.24431	0.434022	H	4.654161	1.313516	1.841435
C	–4.45623	–0.55897	0.001729	C	3.676860	2.104165	0.079940
H	–5.24111	0.181464	–0.07861	C	–4.50001	–0.47946	–0.04309
C	–5.09588	4.606510	0.677417	H	–5.24665	0.298714	–0.12882
H	–5.67792	5.497825	0.891262	C	5.261247	4.389911	0.500656
C	4.528329	2.298997	1.176721	H	5.876190	5.270410	0.661636
H	4.641014	1.419911	1.802925	C	–3.86636	–2.79563	0.006783
C	–1.22512	–4.68681	0.373372	H	–4.10286	–3.85345	0.044081
H	–2.15415	–5.24432	0.434029	C	–4.85808	–1.85220	0.004436
C	5.278256	3.446560	1.437806	H	–5.90456	–2.13659	0.022513
H	5.993793	3.436812	2.254965	C	3.554506	3.219829	–0.76670
C	5.095917	4.606482	0.677406	H	2.845266	3.188024	–1.58902
H	5.677963	5.497790	0.891243	C	4.337561	4.354468	–0.54949
C	–4.52833	2.299010	1.176707	H	4.230558	5.209111	–1.21176
H	–4.64104	1.419918	1.802900	C	4.675739	–2.14723	0.255828
C	–5.27824	3.446581	1.437803	H	5.693560	–2.51537	0.342323
H	–5.99378	3.436835	2.254958	C	–1.40508	–4.70148	0.271792
C	–4.74488	–1.91737	0.108435	H	–2.35119	–5.23321	0.318687
H	–5.77747	–2.24973	0.143460	C	5.377903	3.282577	1.347079
C	3.402022	3.468978	–0.63419	H	6.077073	3.302783	2.178531
H	2.672916	3.467805	–1.43921	C	–3.26477	3.506707	–0.59195
C	–3.40200	3.468994	–0.63419	H	–2.54379	3.499006	–1.40385
H	–2.67289	3.467820	–1.43920	C	–0.21463	–5.40673	0.370802
C	4.147218	4.612904	–0.35205	H	–0.24937	–6.48616	0.490697
H	3.990686	5.509668	–0.94450	C	–3.50687	2.321365	0.129355
C	–4.14718	4.612929	–0.35203	C	4.444194	–0.79257	0.114301
H	–3.99063	5.509696	–0.94447	H	5.261095	–0.08342	0.071201
C	0.000003	–5.35495	0.453338	C	–3.96283	4.667544	–0.26876
H	0.000004	–6.43421	0.581509	H	–3.77778	5.575990	–0.83390

[a] DFT calculations on TPSSh/6–31G(d)/LanL2DZ ecp/CPCM(THF) level of theory.

Table A51. Calculated coordinates of the optimized singlet ground state structures of the complexes [M(L^{NHBn})Cl] (M = Pt or Pd).[a]

[Pt(L^{NHBn})Cl]				[Pd(L^{NHBn})Cl]			
atom	coordinates (Å)			atom	coordinates (Å)		
	X	Y	Z		X	Y	Z
Pt	0.000000	0.739910	–0.25117	Pd	–0.04885	0.663556	–0.13816
Cl	0.000001	–1.83631	–0.26659	Cl	–0.26887	–1.76469	–0.94042
N	–2.08518	1.118970	–0.24250	N	–2.03719	1.019718	0.610678
N	2.795454	–0.89462	–1.19814	N	2.014660	1.077783	–0.60296
H	1.830523	–1.21180	–1.08789	N	–2.63035	–1.20130	1.012184
N	2.085177	1.118970	–0.24250	H	–1.77153	–1.44765	0.514084
N	–2.79545	–0.89462	–1.19814	N	2.770295	–1.12928	–0.69600
H	–1.83052	–1.21181	–1.08789	H	1.783189	–1.39493	–0.66067
C	1.226571	3.236039	0.473579	C	–0.02589	2.583038	0.028736
C	–1.21999	4.556717	0.952105	C	1.139591	3.276147	–0.32386
H	–2.14805	5.084146	1.154205	C	1.108836	4.681974	–0.32714
C	3.107108	0.304000	–0.65226	H	1.990531	5.256932	–0.59575
C	–2.39317	2.402831	0.183434	C	–0.07026	5.352935	0.012644
C	0.000001	2.603062	0.229122	H	–0.08775	6.438463	0.005963
C	4.748229	1.986849	–0.06515	C	–1.22841	4.648506	0.356834
H	5.780915	2.309796	0.024023	H	–2.13033	5.197976	0.611346
C	5.868314	–2.93464	–0.58658	C	–1.21538	3.242456	0.365877
H	6.375259	–2.72651	–1.52683	C	–2.33260	2.363104	0.713220
C	3.778823	–1.90078	–1.57912	C	–3.57361	2.818164	1.142163
H	3.219015	–2.66248	–2.13171	H	–3.77156	3.881154	1.206776
H	4.493803	–1.46571	–2.28755	C	–4.55175	1.880288	1.494514
C	–3.77882	–1.90078	–1.57912	H	–5.53411	2.209564	1.819403
H	–4.49380	–1.46571	–2.28755	C	–4.26186	0.532107	1.435648
H	–3.21901	–2.66248	–2.13171	H	–5.00467	–0.20918	1.700950
C	–5.91436	–3.84098	1.659457	C	–2.97507	0.109368	1.006771
H	–6.44932	–4.33534	2.465671	C	2.289063	2.428874	–0.64428
C	3.889505	–2.82236	0.796053	C	3.556882	2.919235	–0.93365
H	2.851235	–2.52944	0.933026	H	3.734442	3.987454	–0.96067
C	2.393166	2.402831	0.183435	C	4.596925	2.010330	–1.16297
C	–5.86831	–2.93464	–0.58658	H	5.597481	2.368249	–1.38602
H	–6.37526	–2.72652	–1.52684	C	4.350939	0.654208	–1.08791
C	–4.45868	0.723997	–0.53975	H	5.146676	–0.06615	–1.22975
H	–5.24916	0.040137	–0.82012	C	3.037687	0.194633	–0.80077
C	0.000001	5.204323	1.181285	C	–3.55979	–2.28815	1.293073
H	0.000001	6.224961	1.551516	H	–4.01922	–2.13346	2.276628
C	–3.70421	2.848950	0.287847	H	–2.94204	–3.18839	1.377735
H	–3.90416	3.856501	0.631549	C	–4.64530	–2.50810	0.243982
C	6.558098	–3.57711	0.446683	C	–4.37719	–2.33402	–1.12150
H	7.597013	–3.86321	0.306139	H	–3.38959	–2.00530	–1.43656
C	–3.10711	0.304001	–0.65226	C	–5.36959	–2.57942	–2.07458
C	3.704210	2.848949	0.287849	H	–5.14910	–2.43965	–3.12953
H	3.904166	3.856500	0.631552	C	–6.64153	–3.00438	–1.67489
C	5.914359	–3.84098	1.659457	H	–7.41266	–3.19285	–2.41680
H	6.449310	–4.33534	2.465671	C	–6.91587	–3.18078	–0.31531
C	4.578671	–3.46071	1.831021	H	–7.90240	–3.50479	0.005276
H	4.072129	–3.66174	2.771241	C	–5.92276	–2.93098	0.637420
C	4.528922	–2.55403	–0.42275	H	–6.14290	–3.06465	1.694812
C	–4.57868	–3.46070	1.831024	C	3.715856	–2.17827	–1.05308
H	–4.07214	–3.66172	2.771246	H	3.114965	–3.08337	–1.19145
C	–1.22657	3.236039	0.473578	H	4.186307	–1.96352	–2.02262
C	–6.55810	–3.57711	0.446680	C	4.792805	–2.44122	–0.00698
H	–7.59701	–3.86321	0.306134	C	4.537250	–2.26252	1.359434
C	–4.52892	–2.55403	–0.42275	H	3.567045	–1.88696	1.674298
C	–3.88951	–2.82236	0.796057	C	5.520711	–2.55489	2.308785
H	–2.85124	–2.52943	0.933032	H	5.309939	–2.40949	3.365004
C	4.458677	0.723996	–0.53975	C	6.771855	–3.03202	1.903263
H	5.249164	0.040136	–0.82012	H	7.536523	–3.25719	2.641613
C	1.219989	4.556717	0.952106	C	7.034425	–3.21190	0.541517
H	2.148051	5.084145	1.154206	H	8.005373	–3.57571	0.216111
C	–4.74823	1.986850	–0.06516	C	6.050605	–2.91497	–0.40684
H	–5.78091	2.309798	0.024020	H	6.262111	–3.05141	–1.46557

[a] DFT calculations on TPSSh/6–31G(d)/LanL2DZ ecp/CPCM(THF) level of theory.

Table A52. Calculated coordinates of the optimized triplet excited state structures of the complexes [M(L^{NHBn})Cl] (M = Pt or Pd).[a]

[Pt(L^{NHBn})Cl]				[Pd(L^{NHBn})Cl]			
atom	coordinates (Å)			atom	coordinates (Å)		
	X	Y	Z		X	Y	Z
Pt	0.000000	0.756526	–0.23798	Pd	–0.03198	0.676200	–0.16066
Cl	0.000001	–1.81331	–0.20559	Cl	–0.27821	–1.77613	–0.90487
N	–2.07733	1.129070	–0.24380	N	–2.01419	1.033896	0.532929
N	2.787149	–0.87752	–1.20888	N	2.044186	1.069774	–0.59916
H	1.822873	–1.19333	–1.09331	N	–2.68540	–1.14281	0.932110
N	2.077333	1.129071	–0.24380	H	–1.79663	–1.41177	0.489011
N	–2.78715	–0.87752	–1.20888	N	2.779478	–1.14150	–0.70317
H	–1.82287	–1.19333	–1.09331	H	1.790966	–1.39828	–0.66321
C	1.261822	3.242044	0.486477	C	0.012320	2.593373	0.006940
C	–1.23638	4.588966	0.848447	C	1.180589	3.273277	–0.31225
H	–2.15334	5.154620	0.986057	C	1.175201	4.691860	–0.29253
C	3.106322	0.311653	–0.64072	H	2.064242	5.259697	–0.54844
C	–2.40350	2.413264	0.213780	C	–0.01051	5.373174	0.059715
C	–0.00000	2.572004	0.323557	H	–0.00379	6.459606	0.077660
C	4.769850	1.974387	0.002459	C	–1.17817	4.700737	0.382108
H	5.805809	2.277144	0.111751	H	–2.06654	5.263703	0.653274
C	5.827130	–2.97933	–0.61866	C	–1.20727	3.261761	0.356470
H	6.335284	–2.78130	–1.56038	C	–2.28779	2.418488	0.632843
C	3.762940	–1.88699	–1.59958	C	–3.61000	2.880748	1.029217
H	3.200715	–2.63487	–2.16843	H	–3.80553	3.947291	1.025733
H	4.486897	–1.44571	–2.29462	C	–4.57730	1.987217	1.405703
C	–3.76294	–1.88700	–1.59958	H	–5.56469	2.319546	1.707143
H	–4.48689	–1.44571	–2.29462	C	–4.26709	0.606338	1.399276
H	–3.20071	–2.63488	–2.16843	H	–4.99800	–0.13307	1.696833
C	–5.86032	–3.89248	1.625053	C	–2.96541	0.171792	0.941734
H	–6.38634	–4.40205	2.427678	C	2.325846	2.419890	–0.62752
C	3.858053	–2.82043	0.773443	C	3.600496	2.902191	–0.90394
H	2.828368	–2.50169	0.916629	H	3.786125	3.969204	–0.92174
C	2.403497	2.413265	0.213784	C	4.635218	1.986803	–1.13418
C	–5.82713	–2.97934	–0.61866	H	5.639859	2.339293	–1.34805
H	–6.33528	–2.78131	–1.56038	C	4.379570	0.631639	–1.07289
C	–4.45644	0.712123	–0.50576	H	5.170520	–0.09368	–1.21655
H	–5.23973	0.025630	–0.80010	C	3.060148	0.181782	–0.79680
C	–0.00000	5.239727	1.030529	C	–3.59606	–2.22857	1.295581
H	–0.00000	6.290010	1.306144	H	–4.03419	–2.02648	2.277760
C	–3.73460	2.832564	0.352436	H	–2.95977	–3.11174	1.408350
H	–3.93734	3.829706	0.726472	C	–4.69157	–2.50147	0.272465
C	6.504807	–3.64200	0.409798	C	–4.41589	–2.48276	–1.10285
H	7.535446	–3.95407	0.263670	H	–3.41437	–2.23870	–1.44942
C	–3.10632	0.311651	–0.64072	C	–5.42224	–2.77433	–2.02699
C	3.734601	2.832565	0.352442	H	–5.19815	–2.75528	–3.09002
H	3.937332	3.829708	0.726479	C	–6.71277	–3.09168	–1.58793
C	5.860325	–3.89248	1.625052	H	–7.49411	–3.31674	–2.30844
H	6.386342	–4.40205	2.427676	C	–6.99228	–3.11455	–0.21870
C	4.535592	–3.47887	1.803560	H	–7.99230	–3.35560	0.131192
H	4.028330	–3.66891	2.745687	C	–5.98578	–2.81852	0.706609
C	4.498816	–2.56450	–0.44724	H	–6.20874	–2.83428	1.771397
C	–4.53559	–3.47887	1.803561	C	3.717269	–2.19756	–1.05713
H	–4.02833	–3.66891	2.745688	H	3.109600	–3.09673	–1.20464
C	–1.26183	3.242044	0.486474	H	4.197861	–1.98308	–2.02175
C	–6.50481	–3.64200	0.409799	C	4.783699	–2.47580	–0.00381
H	–7.53544	–3.95407	0.263670	C	4.521134	–2.29524	1.360998
C	–4.49881	–2.56450	–0.44724	H	3.553723	–1.90724	1.669319
C	–3.85805	–2.82043	0.773444	C	5.494154	–2.60101	2.316889
H	–2.82837	–2.50169	0.916630	H	5.277986	–2.45375	3.371782
C	4.456438	0.712125	–0.50576	C	6.741955	–3.09352	1.919574
H	5.239726	0.025633	–0.80009	H	7.498647	–3.32893	2.662951
C	1.236380	4.588966	0.848450	C	7.011606	–3.27532	0.559441
H	2.153335	5.154621	0.986061	H	7.980181	–3.65092	0.240374
C	–4.76985	1.974385	0.002452	C	6.038195	–2.96502	–0.39536
H	–5.80581	2.277141	0.111742	H	6.255415	–3.10286	–1.45277

[a] DFT calculations on TPSSh/6–31G(d)/LanL2DZ ecp/CPCM(THF) level of theory.

Table A53. Calculated coordinates of the optimized singlet ground state structures for [M(L^{NHPh})F].[a]

[Pt(L^{NHPh})F]				[Pd(L^{NHPh})F]			
atom	coordinates (Å)			atom	coordinates (Å)		
	X	Y	Z		X	Y	Z
Pt	0.007084	–0.69123	0.019581	Pd	0.000029	–0.76073	–0.00001
N	2.05869	–1.00869	0.152192	C	–1.22526	–3.34369	–0.11977
N	–2.03847	–1.04119	–0.13283	N	2.06678	–1.11551	0.139281
N	2.619596	1.242401	0.122029	C	0.000063	–2.6727	–0.00001
H	1.593314	1.40563	0.14659	N	2.634828	1.126278	0.083647
C	0.024718	–2.6008	–0.01546	H	1.60533	1.286867	0.083254
N	–2.63744	1.199054	–0.07049	N	–2.06672	–1.11557	–0.13928
H	–1.61387	1.378414	–0.05259	C	–2.38861	–2.45366	–0.22888
C	3.031986	–0.05244	0.220504	N	–2.63486	1.126193	–0.08362
C	–2.35556	–2.38841	–0.22832	H	–1.60537	1.286826	–0.08319
C	–3.02664	–0.09997	–0.1984	C	–3.04365	–0.16846	–0.2079
C	1.256357	–3.26444	0.096563	C	1.225405	–3.34366	0.119765
C	3.722384	–2.74819	0.367314	C	3.043675	–0.16836	0.2079
H	3.969805	–3.80233	0.406518	C	3.702514	–2.86908	0.409157
C	–1.19594	–3.28326	–0.133	H	3.93873	–3.92474	0.471979
C	4.38226	–0.4277	0.427642	C	2.388728	–2.45358	0.228864
H	5.133015	0.341721	0.553095	C	–4.87261	4.684296	0.330529
C	–3.4599	2.341766	0.043063	H	–5.43176	5.609433	0.434677
C	3.417343	2.39636	–0.03366	C	–5.33904	3.506416	0.922256
C	4.714606	–1.76771	0.497244	H	–6.25789	3.514508	1.502198
H	5.748086	–2.05711	0.661553	C	1.216819	–4.74929	0.120627
C	–3.66858	–2.80417	–0.40721	H	2.140187	–5.31537	0.210739
H	–3.89677	–3.86127	–0.47403	C	–4.62374	2.312646	0.798933
C	2.400293	–2.3519	0.211327	H	–4.97335	1.419129	1.305996
C	1.26095	–4.66879	0.087844	C	4.623638	2.312833	–0.79891
H	2.187751	–5.23019	0.172433	H	4.973308	1.419332	–1.30596
C	–4.36754	–0.49428	–0.43124	C	3.433502	2.280987	–0.05069
H	–5.13023	0.263963	–0.5519	C	–4.38902	–0.55215	–0.44026
C	–4.95078	4.716138	0.277694	H	–5.14848	0.208885	–0.56497
H	–5.53042	5.630407	0.364215	C	4.872363	4.684509	–0.33054
C	4.57948	2.426921	–0.82442	H	5.431449	5.609678	–0.43471
H	4.908202	1.533428	–1.34537	C	–3.70238	–2.86921	–0.40919
C	–1.17714	–4.68746	–0.14325	H	–3.93855	–3.92487	–0.47203
H	–2.09488	–5.26301	–0.23134	C	–4.70309	–1.89536	–0.53547
C	5.293231	3.619018	–0.96965	H	–5.73112	–2.19351	–0.71819
H	6.190342	3.626713	–1.58262	C	2.958839	3.469701	0.533006
C	4.851788	4.795997	–0.35721	H	2.031491	3.44648	1.098868
H	5.40918	5.720044	–0.47878	C	3.671521	4.66004	0.387488
C	–4.63891	2.36562	0.808174	H	3.290289	5.568481	0.845658
H	–4.95941	1.477295	1.343026	C	4.703183	–1.89519	0.535427
C	–5.38105	3.544979	0.909038	H	5.731226	–2.1933	0.718138
H	–6.29169	3.548071	1.501705	C	–1.21664	–4.74933	–0.1206
C	–4.6759	–1.83809	–0.52925	H	–2.13999	–5.31543	–0.21069
H	–5.70236	–2.14168	–0.7111	C	5.338871	3.506647	–0.92225
C	2.968019	3.583364	0.572258	H	6.257715	3.514787	–1.50219
H	2.062513	3.561106	1.172466	C	–2.95901	3.469594	–0.53301
C	–3.02164	3.523194	–0.58086	H	–2.03167	3.446422	–1.09888
H	–2.10354	3.505625	–1.16177	C	0.000101	–5.43354	0.000022
C	3.678435	4.77232	0.404734	H	0.000115	–6.51937	0.000039
H	3.31712	5.680099	0.879941	C	–3.4336	2.280861	0.050706
C	–3.76041	4.700369	–0.45747	C	4.389057	–0.552	0.440247
H	–3.40831	5.604228	–0.94683	H	5.148493	0.209064	0.564952
C	0.047651	–5.36169	–0.03289	C	–3.67177	4.659892	–0.38751
H	0.056622	–6.44747	–0.03952	H	–3.2906	5.568349	–0.84569
F	–0.0123	1.446734	0.095985	F	–0.00003	1.351912	0.000047

[a] DFT calculations on TPSSh/6–31G(d)/LanL2DZ ecp/CPCM(THF) level of theory.

Table A54. Calculated coordinates of the optimized singlet ground state structures for [M(L^{NHPh})H].[a]

[Pt(L^{NHPh})H]				[Pd(L^{NHPh})H]			
atom	coordinates (Å)			atom	coordinates (Å)		
	X	Y	Z		X	Y	Z
Pt	0.00000	–0.62106	–0.09519	Pd	0.000004	–0.68303	–0.10187
N	–2.05246	–0.99548	–0.06026	C	–1.22673	–3.31213	0.062656
N	2.052463	–0.99548	–0.06026	N	2.07255	–1.07968	–0.06685
N	–2.65566	1.240635	–0.18619	C	0.000015	–2.6372	0.038618
H	–1.63722	1.356431	–0.3022	N	2.661882	1.152911	–0.19052
C	0.00000	–2.57493	0.048087	H	1.638423	1.260152	–0.30114
N	2.65566	1.240636	–0.18619	N	–2.07254	–1.07971	–0.06682
H	1.637217	1.356432	–0.3022	C	–2.39468	–2.42159	–0.00216
C	–3.04974	–0.0624	–0.11765	N	–2.66189	1.152882	–0.19046
C	2.382696	–2.34362	0.010626	H	–1.63844	1.260133	–0.30109
C	3.049739	–0.0624	–0.11765	C	–3.06544	–0.14879	–0.12515
C	–1.22703	–3.24906	0.076935	C	1.226769	–3.31211	0.062638
C	–3.70907	–2.75821	0.014171	C	3.065442	–0.14876	–0.1252
H	–3.94136	–3.8146	0.078192	C	3.718942	–2.84656	–0.00375
C	1.227026	–3.24906	0.076934	H	3.950491	–3.90347	0.055564
C	–4.40784	–0.45818	–0.15458	C	2.394708	–2.42157	–0.00219
H	–5.17655	0.296414	–0.26159	C	–4.82992	4.747008	0.267076
C	3.434003	2.406672	–0.02568	H	–5.37383	5.68008	0.380368
C	–3.434	2.406671	–0.02569	C	–5.19494	3.621627	1.012555
C	–4.72643	–1.80134	–0.085	H	–6.0177	3.679513	1.719851
H	–5.76655	–2.11097	–0.11767	C	1.223475	–4.71681	0.132492
C	3.709073	–2.75821	0.014169	H	2.14987	–5.28529	0.155853
H	3.941357	–3.8146	0.078189	C	–4.49645	2.419358	0.878711
C	–2.3827	–2.34362	0.010628	H	–4.76081	1.567881	1.497595
C	–1.22553	–4.65242	0.152741	C	4.496404	2.419372	0.878733
H	–2.15033	–5.22337	0.179287	H	4.760758	1.567878	1.497596
C	4.407841	–0.45818	–0.15458	C	3.430652	2.324414	–0.03352
H	5.176546	0.296415	–0.26159	C	–4.42473	–0.54433	–0.1671
C	4.850149	4.817065	0.282752	H	–5.19688	0.20691	–0.27395
H	5.400706	5.745801	0.399359	C	4.829868	4.747042	0.267172
C	–4.48479	2.496915	0.903823	H	5.373762	5.680115	0.380503
H	–4.73063	1.646509	1.531788	C	–3.71891	–2.8466	–0.00371
C	1.225526	–4.65242	0.15274	H	–3.95045	–3.90351	0.05561
H	2.150329	–5.22337	0.179286	C	–4.73749	–1.8898	–0.10261
C	–5.19215	3.693457	1.04179	H	–5.77683	–2.20217	–0.13893
H	–6.0033	3.748562	1.762517	C	3.059479	3.458802	–0.7773
C	–4.85015	4.817064	0.282751	H	2.233214	3.386998	–1.47924
H	–5.40071	5.7458	0.399358	C	3.750859	4.660444	–0.61939
C	4.484786	2.496916	0.903824	H	3.450817	5.527669	–1.20101
H	4.730632	1.64651	1.531789	C	4.737509	–1.88975	–0.10266
C	5.192145	3.693458	1.041791	H	5.776856	–2.2021	–0.139
H	6.003296	3.748563	1.762518	C	–1.22342	–4.71682	0.13251
C	4.726426	–1.80134	–0.085	H	–2.14981	–5.28531	0.155884
H	5.766555	–2.11097	–0.11767	C	5.194879	3.621643	1.012628
C	–3.08595	3.538547	–0.78356	H	6.017618	3.679516	1.719945
H	–2.27137	3.469509	–1.49928	C	–3.0595	3.458752	–0.77732
C	3.085946	3.538548	–0.78356	H	–2.23321	3.386935	–1.47923
H	2.271372	3.469509	–1.49928	C	0.000031	–5.39956	0.170669
C	–3.78587	4.734821	–0.6217	H	0.000037	–6.48423	0.225872
H	–3.50417	5.600861	–1.21408	C	–3.43068	2.324382	–0.03352
C	3.785865	4.734822	–0.6217	C	4.42473	–0.54428	–0.16716
H	3.504165	5.600862	–1.21408	H	5.196878	0.206968	–0.27401
C	0.000001	–5.33384	0.193282	C	–3.75089	4.660394	–0.61946
H	0.000001	–6.41828	0.25304	H	–3.45084	5.527605	–1.2011
H	0.000001	1.104279	–0.27486	H	–0.00001	1.042881	–0.293

[a] DFT calculations on TPSSh/6–31G(d)/LanL2DZ ecp/CPCM(THF) level of theory.

Table A55. Calculated coordinates of the optimized singlet ground state structures for [M(L^{OMe})Cl].[a]

[Pt(L^{OMe})Cl]				[Pd(L^{OMe})Cl]			
atom	coordinates (Å)			atom	coordinates (Å)		
	X	Y	Z		X	Y	Z
Pt	0.00000	–0.31508	0.061436	Pd	–0.00000	–0.37791	0.088327
Cl	–0.00001	–2.65779	1.002307	Cl	0.000076	–2.57035	1.348659
N	2.064309	0.058093	–0.06136	C	–1.22769	2.222309	0.000143
N	–2.06431	0.058095	–0.06135	N	2.079045	0.012671	–0.09697
C	0.000001	1.607001	–0.0687	C	–0.00000	1.543507	–0.06984
C	3.06266	–0.84539	–0.21514	N	–2.07906	0.012656	–0.09695
C	–2.38711	1.402929	–0.02069	C	–2.40062	1.347897	–0.03779
C	–3.06266	–0.84539	–0.21515	C	–3.06164	–0.89527	–0.26885
C	1.226563	2.290781	–0.01181	C	1.227679	2.222315	0.000178
C	3.715779	1.825477	–0.01427	C	3.061623	–0.89525	–0.26891
H	3.941564	2.883988	0.033691	C	3.72915	1.772124	–0.04587
C	–1.22656	2.290782	–0.01179	H	3.963371	2.828328	0.013815
C	4.416143	–0.47025	–0.19784	C	2.400605	1.347908	–0.03774
H	5.190843	–1.21977	–0.29322	C	1.219135	3.624529	0.095841
C	4.735191	0.877536	–0.08258	H	2.148812	4.184706	0.147402
H	5.775301	1.187513	–0.07139	C	–4.41907	–0.52948	–0.27159
C	–3.71578	1.825477	–0.01423	H	–5.19196	–1.27848	–0.38576
H	–3.94156	2.883987	0.033746	C	–3.72916	1.772118	–0.04599
C	2.387107	1.402928	–0.0207	H	–3.96338	2.828327	0.013629
C	1.220706	3.69375	0.048715	C	–4.74174	0.817232	–0.14574
H	2.148818	4.257689	0.087108	H	–5.78324	1.123078	–0.14859
C	–4.41614	–0.47025	–0.19783	C	4.741726	0.817237	–0.14562
H	–5.19084	–1.21977	–0.29322	H	5.783227	1.123079	–0.14842
C	–1.2207	3.693751	0.048728	C	–1.21916	3.624524	0.095803
H	–2.14881	4.25769	0.08713	H	–2.14884	4.184696	0.147337
C	–4.73519	0.877536	–0.08255	C	–0.00001	4.310907	0.134995
H	–5.7753	1.187511	–0.07134	H	–0.00002	5.393955	0.208667
C	0.000002	4.380655	0.067589	C	4.419055	–0.52946	–0.27157
H	0.000003	5.465406	0.110347	H	5.191946	–1.27846	–0.38576
O	2.636081	–2.09368	–0.40688	O	–2.61442	–2.14114	–0.45722
O	–2.63608	–2.09367	–0.40692	O	2.614397	–2.1411	–0.4574
C	3.600848	–3.15629	–0.44926	C	–3.57236	–3.20731	–0.55196
H	4.255058	–3.05122	–1.32031	H	–4.18662	–3.25557	0.352291
H	4.191822	–3.17768	0.471424	H	–4.20477	–3.08245	–1.4365
H	3.008365	–4.0655	–0.53294	H	–2.97468	–4.11226	–0.64462
C	–3.60084	–3.15628	–0.44933	C	3.572333	–3.20727	–0.55215
H	–4.1918	–3.1777	0.471365	H	4.204806	–3.08236	–1.43664
H	–4.25507	–3.05118	–1.32037	H	4.186529	–3.25561	0.352144
H	–3.00836	–4.06549	–0.53306	H	2.974647	–4.11222	–0.64491

[a] DFT calculations on TPSSh/6–31G(d)/LanL2DZ ecp/CPCM(THF) level of theory.

Table A56. Calculated coordinates of the optimized singlet ground state structures of the complexes.[a]

[Ni(L^{NHPh})Cl]				[Ni(L^{NHBn})Cl]			
atom	coordinates (Å)			atom	coordinates (Å)		
	X	Y	Z		X	Y	Z
Cl	0.000041	0.712197	1.998640	Cl	–0.45660	–0.96514	–1.65564
C	1.224141	–3.43538	–0.14768	N	–1.85940	1.096781	0.576145
N	–1.95889	–1.20829	0.072724	N	1.892379	1.157801	–0.59799
C	–0.00021	–2.76326	–0.11329	N	–2.28181	–1.18276	0.872175
N	–2.44217	1.069396	0.082245	H	–1.52474	–1.33093	0.202593
H	–1.56419	1.171992	0.601774	N	2.475371	–1.10496	–0.59938
N	1.958713	–1.20856	0.072656	H	1.473272	–1.26718	–0.71294
C	2.361450	–2.51826	–0.08997	C	0.024880	2.686894	0.091704
N	2.442335	1.069051	0.082307	C	1.179787	3.380893	–0.27823
H	1.564416	1.171746	0.601917	C	1.164878	4.785776	–0.24930
C	2.896165	–0.22240	–0.00142	H	2.042551	5.362907	–0.52885
C	–1.22465	–3.43522	–0.14759	C	–0.00528	5.451608	0.139735
C	–2.89620	–0.22199	–0.00135	H	–0.01674	6.537298	0.160303
C	–3.69619	–2.87160	–0.24277	C	–1.16334	4.747134	0.495557
H	–3.97212	–3.91182	–0.36959	H	–2.05723	5.294783	0.782970
C	–2.36183	–2.51794	–0.08983	C	–1.15066	3.342236	0.466060
C	4.522571	4.691836	–0.52737	C	–2.22400	2.408421	0.802663
H	5.043290	5.632019	–0.6828	C	–3.45188	2.760615	1.347240
C	4.737142	3.614196	–1.39288	H	–3.6982	3.804381	1.503208
H	5.418387	3.716771	–2.23301	C	–4.33938	1.740578	1.711657
C	–1.22329	–4.83685	–0.24862	H	–5.30981	1.982712	2.134413
H	–2.15299	–5.39911	–0.28027	C	–3.97263	0.418833	1.543466
C	4.065430	2.404276	–1.20547	H	–4.64621	–0.38260	1.818300
H	4.207390	1.588883	–1.90803	C	–2.70715	0.106092	0.981626
C	–4.06519	2.404753	–1.20549	C	2.277608	2.482256	–0.63098
H	–4.20737	1.58931	–1.90794	C	3.580154	2.874181	–0.91204
C	–3.18262	2.253322	–0.12166	H	3.838113	3.926480	–0.93644
C	4.269379	–0.53552	–0.14025	C	4.546455	1.883312	–1.12374
H	4.997352	0.265821	–0.13215	H	5.574266	2.157512	–1.34165
C	–4.52186	4.692465	–0.52758	C	4.194779	0.549464	–1.02985
H	–5.04244	5.632718	–0.68305	H	4.935568	–0.23092	–1.15044
C	3.695757	–2.87211	–0.24303	C	2.848824	0.197014	–0.75386
H	3.971524	–3.91236	–0.36992	C	–3.12644	–2.33582	1.162431
C	4.660817	–1.8576	–0.24758	H	–3.48422	–2.26918	2.196473
H	5.714531	–2.10301	–0.33813	H	–2.46163	–3.20527	1.122061
C	–2.96017	3.338686	0.743456	C	–4.30783	–2.55096	0.220891
H	–2.27159	3.224366	1.576352	C	-4.22686	–2.21504	–1.13802
C	–3.62210	4.549408	0.533994	H	–3.31876	–1.75902	–1.52566
H	–3.43947	5.379281	1.210983	C	–5.3057	–2.46097	–1.99263
C	–4.66111	–1.85695	–0.24728	H	–5.23077	–2.19429	–3.04354
H	–5.71487	–2.10221	–0.33773	C	–6.47672	–3.04743	–1.50066
C	1.222591	–4.83701	–0.24871	H	–7.3148	–3.23597	–2.16600
H	2.152208	–5.3994	–0.28042	C	–6.56415	–3.38519	–0.14649
C	–4.73672	3.614766	–1.39295	H	–7.47174	–3.83552	0.246634
H	–5.41805	3.717364	–2.23301	C	–5.48606	–3.13495	0.708222
C	2.960807	3.338182	0.743708	H	–5.56138	–3.39451	1.762466
H	2.272301	3.223886	1.576675	C	3.336976	–2.22135	–0.97867
C	–0.00040	–5.51961	–0.30106	H	2.671498	–3.08319	–1.09550
H	–0.00048	–6.60279	–0.37707	H	3.799861	–2.04646	–1.96051
C	3.182966	2.252876	–0.12155	C	4.415174	–2.55353	0.044314
C	–4.26947	–0.53493	–0.14005	C	4.198478	–2.36728	1.416527
H	–4.99733	0.266524	–0.13193	H	3.259750	–1.93416	1.751750
C	3.622912	4.548815	0.534300	C	5.181136	–2.72461	2.344207
H	3.440507	5.378644	1.211402	H	5.001102	–2.57232	3.405141
Ni	–0.00008	–0.99603	0.317123	C	6.392385	–3.27512	1.911250
				H	7.156510	–3.55068	2.632880
				C	6.616045	–3.46312	0.543735
				H	7.556054	–3.88388	0.196904
				C	5.633433	–3.10111	–0.38302
				H	5.814861	–3.24411	–1.44645
				Ni	–0.04815	0.897169	–0.23221

[a] DFT calculations on TPSSh/6-31G(d)/LanL2DZ ecp/CPCM(THF) level of theory.

Table A57. Calculated coordinates of the optimized triplet excited state structures of the complexes.[a]

[Ni(L^{NHPh})Cl]				[Ni(L^{NHBn})Cl]			
atom	coordinates (Å)			atom	coordinates (Å)		
	X	Y	Z		X	Y	Z
Cl	0.000006	0.695938	1.923391	Cl	–0.42725	–1.07456	–1.54068
C	1.221909	–3.36993	–0.04951	N	–2.05665	0.980844	0.729041
N	–2.13773	–1.14957	–0.04047	N	2.055289	1.125918	–0.50779
C	0.000000	–2.69978	0.029811	N	–2.56938	–1.25279	1.051118
N	–2.74755	1.069715	0.053192	H	–1.77997	–1.42252	0.428387
H	–1.86453	1.191835	0.554037	N	2.788690	–1.06630	–0.60306
N	2.137733	–1.14957	–0.04048	H	1.799263	–1.27844	–0.73153
C	2.415894	–2.48871	–0.07264	C	–0.09966	2.590165	–0.04169
N	2.74755	1.069713	0.053194	C	1.058817	3.305897	–0.35089
H	1.864536	1.191828	0.554045	C	1.016997	4.712717	–0.33107
C	3.145003	–0.24801	–0.05387	H	1.890796	5.315707	–0.56636
C	–1.22191	–3.36993	–0.04950	C	–0.17960	5.355210	0.014893
C	–3.14500	–0.24801	–0.05386	H	–0.21362	6.441137	0.028477
C	–3.73038	–2.94810	–0.15446	C	–1.32555	4.630593	0.369832
H	–3.94112	–4.01058	–0.19004	H	–2.22182	5.171705	0.663782
C	–2.41589	–2.48871	–0.07263	C	–1.28068	3.223772	0.349788
C	4.977457	4.618338	–0.44921	C	–2.37468	2.311062	0.766566
H	5.538538	5.539244	–0.57690	C	–3.62798	2.743551	1.198764
C	5.212507	3.524748	–1.28875	H	–3.86823	3.799999	1.223455
H	5.951347	3.595622	–2.08229	C	-4.56769	1.787457	1.603846
C	–1.22392	–4.77397	–0.14893	H	–5.55006	2.101997	1.944408
H	–2.14814	–5.34369	–0.21071	C	–4.25683	0.437999	1.561408
C	4.490244	2.339076	–1.13722	H	-4.98364	–0.31137	1.849876
H	4.651791	1.513784	–1.82368	C	–2.97219	0.056066	1.104120
C	–4.49025	2.339067	–1.13723	C	2.257886	2.473475	–0.62040
H	–4.65181	1.513769	–1.82368	C	3.514500	2.992116	–0.93385
C	–3.53190	2.226671	–0.11414	H	3.662677	4.062008	–1.02253
C	4.495206	–0.65416	–0.13328	C	4.582944	2.105746	–1.11622
H	5.290366	0.080631	–0.11406	H	5.572549	2.488974	–1.34816
C	–4.97746	4.618335	–0.44923	C	4.385495	0.738122	–1.00656
H	–5.53854	5.539241	–0.57693	H	5.204410	0.041062	–1.13694
C	3.730375	–2.94810	–0.15449	C	3.082407	0.268479	–0.71514
H	3.941123	–4.01058	–0.19008	C	–3.47595	–2.37477	1.264743
C	4.77099	–2.01207	–0.18648	H	–3.92284	–2.28801	2.261925
H	5.802689	–2.34820	–0.23326	H	–2.84450	–3.26951	1.287476
C	–3.29065	3.328815	0.725604	C	–4.57670	–2.55002	0.222021
H	–2.54628	3.246910	1.513516	C	–4.35380	–2.24864	–1.12926
C	–4.00479	4.514723	0.551125	H	–3.39160	–1.84829	–1.44047
H	–3.80526	5.356466	1.208494	C	–5.36108	–2.45541	–2.07640
C	–4.77099	–2.01207	–0.18645	H	–5.17535	–2.2156	–3.12003
H	–5.80269	–2.34821	–0.23322	C	–6.60273	–2.96831	–1.68567
C	1.223922	–4.77398	–0.14894	H	–7.38531	–3.12627	–2.42272
H	2.148140	–5.34369	–0.21072	C	–6.83227	–3.27154	–0.34008
C	–5.21252	3.524738	–1.28876	H	–7.79546	–3.66432	–0.02531
H	–5.95136	3.595605	–2.08229	C	–5.82486	–3.06045	0.606678
C	3.290654	3.328807	0.725623	H	–6.01103	–3.29260	1.653558
H	2.546294	3.246895	1.513540	C	3.718693	–2.10947	–1.02283
C	–0.000001	–5.45663	–0.18318	H	3.113362	–3.00961	–1.17334
H	–0.000001	–6.54050	–0.25805	H	4.170926	–1.86803	–1.99601
C	3.531898	2.226671	–0.11413	C	4.816846	–2.40662	–0.01012
C	–4.49521	–0.65416	–0.13326	C	4.587499	–2.28469	1.367274
H	–5.29037	0.080631	–0.11404	H	3.621940	–1.92595	1.713963
C	4.004788	4.514716	0.551150	C	5.590094	–2.61091	2.285012
H	3.805263	5.356453	1.208529	H	5.399340	–2.50946	3.350185
Ni	0.000002	–0.77025	0.084035	C	6.834947	–3.06585	1.836674
				H	7.614475	–3.31763	2.550503
				C	7.071828	–3.18880	0.463945
				H	8.037603	–3.53486	0.105440
				C	6.068800	–2.85767	–0.45248
				H	6.260268	–2.94988	–1.51977
				Ni	–0.02570	0.660280	–0.00533

[a] DFT calculations on TPSSh/6-31G(d)/LanL2DZ ecp/CPCM(THF) level of theory.

Table A58. Calculated coordinates of the optimized singlet ground state structures of the complexes [M(L^{Bn})Cl] (M = Pt, Pd, and Ni).[a]

[Pt(L^{Bn})Cl]				[Pd(L^{Bn})Cl]				[Ni(L^{Bn})Cl]			
atom	coordinates (Å)			atom	coordinates (Å)			atom	coordinates (Å)		
	X	Y	Z		X	Y	Z		X	Y	Z
Pt	0.641753	–0.393854	0.520904	Pd	–0.599232	0.398201	0.461362	Ni	–0.000083	0.933972	0.116271
Cl	–0.245551	0.638134	2.624257	Cl	0.488508	–0.707751	2.449453	Cl	–0.000361	-0.580246	1.880743
N	2.523934	0.501729	0.416204	N	–2.578636	–0.315682	0.641999	N	–1.926947	1.155627	–0.130294
C	2.87833	1.770324	0.736663	N	1.007765	1.542548	–0.298837	N	1.926761	1.155806	–0.130164
N	–0.947993	–1.668476	0.061979	C	–1.555125	1.870147	–0.274658	C	–0.00016	2.719339	–0.152528
C	0.899527	–2.906447	–0.80153	C	–0.83005	2.994361	–0.678073	C	1.219681	3.390378	–0.076093
C	4.214137	2.16486	0.709651	C	–1.52977	4.163467	–0.998828	C	1.218344	4.78674	0.010712
H	4.459844	3.17788	1.000619	H	–1.004419	5.054957	–1.323104	H	2.145577	5.347293	0.064736
C	1.577302	–1.727085	–0.473187	C	–2.919536	4.190085	–0.890211	C	–0.000292	5.468417	0.041815
C	1.812224	2.781661	1.05277	H	–3.455568	5.097472	–1.14086	H	–0.000344	6.549919	0.108049
H	1.098711	2.358022	1.759789	C	–3.6296	3.076031	–0.444911	C	–1.218862	4.786623	0.010727
H	2.296709	3.637224	1.532174	H	–4.70777	3.13674	–0.346436	H	–2.146148	5.347089	0.064749
C	–1.039032	3.860827	1.238275	C	–2.943721	1.899788	–0.120312	C	–1.220066	3.390259	–0.076072
H	–2.119187	3.943779	–1.18756	C	–3.511028	0.655281	0.38347	C	–2.342736	2.46273	–0.096084
C	3.485526	–0.352628	–0.080936	C	–4.870371	0.42127	0.568666	C	–3.690744	2.796742	–0.124879
C	1.059867	3.26092	–0.180425	H	–5.581068	1.213547	0.375139	H	–3.98792	3.835925	–0.07188
C	2.969002	–1.621369	–0.5753	C	–5.293083	–0.827878	0.991167	C	–4.631893	1.785024	–0.241789
C	4.826535	0.017372	–0.120246	H	–6.345483	–1.0283	1.152444	H	–5.68974	2.018171	–0.265746
H	5.558554	-0.686813	–0.492407	C	–4.347696	–1.826699	1.174414	C	–4.199448	0.471914	–0.363789
C	–2.277069	–1.447799	0.210047	H	–4.642919	–2.826407	1.465912	H	–4.905199	–0.336286	–0.500488
C	5.202741	1.278502	0.305783	C	–2.993905	–1.556511	0.975949	C	–2.837808	0.176849	–0.318724
H	6.243654	1.578174	0.295316	C	0.613085	2.791001	–0.707751	C	2.342435	2.462952	–0.096121
C	1.629619	–3.976143	–1.329283	C	1.537157	3.736196	–1.139265	C	3.690409	2.797084	–0.125108
H	1.142566	–4.904593	–1.606285	H	1.198934	4.720287	–1.435025	H	3.987494	3.836302	–0.072276
C	–4.13543	0.286388	0.242289	C	2.878634	3.395157	–1.196383	C	4.631638	1.785441	–0.242023
C	1.728686	3.6365	–1.348976	H	3.616435	4.117106	–1.525536	H	5.68946	2.018685	–0.266145
H	2.809293	3.552914	–1.402909	C	3.258407	2.105291	–0.857642	C	4.199303	0.472274	–0.363801
C	–3.201261	–2.445785	–0.088638	H	4.290734	1.790907	–0.930164	H	4.905113	–0.335879	–0.50047
H	–4.252702	–2.236708	0.054111	C	2.304382	1.185601	–0.424147	C	2.837696	0.177091	–0.318531
C	–0.363249	4.232924	–2.397086	C	–1.983031	–2.666848	1.070159	C	–2.318874	–1.220721	–0.566763
H	–0.911989	4.60805	–3.253574	H	–1.121923	–2.32464	1.647031	H	–1.435182	–1.363098	0.060677
C	–0.331629	3.37609	–0.140311	H	–2.444796	–3.499435	1.607972	H	–1.979175	–1.254638	–1.60846
H	–0.859804	3.07975	0.759255	C	–1.508159	–3.147893	–0.293328	C	–3.311553	–2.331999	–0.325623
C	–1.428563	–3.865551	–0.812721	C	–2.412562	–3.540716	–1.28457	C	–3.919249	–2.997502	–1.392211
H	–1.06333	–4.787924	–1.244089	H	–3.479592	–3.481956	–1.095364	H	–3.676313	–2.707337	–2.409605
C	3.011202	–3.856216	–1.489501	C	–1.960829	–4.007538	–2.515199	C	–4.828176	–4.029395	–1.166319
H	3.571662	–4.686794	–1.901283	H	–2.676752	–4.308495	–3.272131	H	–5.288568	–4.535682	–2.007493
C	–5.65588	1.082572	–1.471919	C	–0.594111	–4.089758	–2.775035	C	–5.141211	–4.410335	0.135114
H	–5.823178	1.419674	–2.488903	H	–0.242055	–4.453092	–3.733942	H	–5.846391	–5.214149	0.3139
C	–4.376037	0.717875	–1.066289	C	0.314375	–3.701782	–1.794738	C	–4.53809	–3.75535	1.207563
H	–3.552258	0.774018	–1.770814	H	1.380235	–3.762059	–1.985999	H	–4.771152	–4.050665	2.224594
C	1.024263	4.117778	–2.44877	C	–0.141064	–3.232543	–0.564071	C	–3.631134	–2.725659	0.978168
H	1.560257	4.404613	–3.346834	H	0.56762	–2.927387	0.197876	H	–3.159777	–2.224573	1.817272
C	3.688475	–2.698902	–1.102677	C	2.66723	–0.257201	–0.165409	C	2.318847	–1.220593	–0.566091
H	4.767006	–2.655799	–1.207105	H	2.36644	–0.823293	–1.05462	H	1.435415	–1.362932	0.061741
C	–2.778237	–3.673525	–0.575279	H	2.04944	–0.618021	0.661411	H	1.978682	–1.254741	–1.607627
H	–3.494837	–4.455388	–0.795994	C	4.125912	–0.514156	0.124988	C	3.311836	–2.331666	–0.325245
C	–0.527246	–2.850077	–0.512956	C	4.964237	–1.078457	–0.838841	C	3.919486	–2.996877	–1.392047
C	–2.739894	–0.089484	0.684318	H	4.560455	–1.330794	–1.814342	H	3.676243	–2.706673	–2.409357
H	–2.025063	0.653377	0.32478	C	6.30792	–1.323976	–0.562627	C	4.828759	–4.028534	–1.166484
H	–2.671764	–0.059515	1.77363	H	6.942647	–1.764549	–1.323487	H	5.289101	–4.534591	–2.007824
C	–6.491371	0.596966	0.732876	C	6.832221	–1.007024	0.686989	C	5.142202	–4.409539	0.134834
H	–7.310886	0.552174	1.441517	H	7.876739	–1.198531	0.905319	H	5.847652	–5.213172	0.313365
C	–5.207652	0.233593	1.135469	C	6.004164	–0.447049	1.658332	C	4.539139	–3.754848	1.207491
H	–5.034989	–0.090394	2.156822	H	6.402692	–0.204066	2.637122	H	4.772516	–4.050207	2.224437
C	–6.719216	1.021724	–0.572754	C	4.663142	–0.204017	1.378948	C	3.631835	–2.725385	0.978424
H	–7.716232	1.308664	–0.887285	H	4.022739	0.224702	2.142801	H	3.16053	–2.224544	1.817701

[a] DFT calculations on TPSSh/def2-TZVP/CPCM(THF) level of theory.

Table A59. Calculated coordinates of the optimized triplet excited state structures of the complexes [M(L^{Bn})Cl] (M = Pt, Pd, and Ni).[a]

[Pt(L^{Bn})Cl]				[Pd(L^{Bn})Cl]				[Ni(L^{Bn})Cl]			
atom	coordinates (Å)			atom	coordinates (Å)			atom	coordinates (Å)		
	X	Y	Z		X	Y	Z		X	Y	Z
Pt	0.619226	–0.290175	0.3077	Pd	–0.538465	0.182863	0.292773	Ni	–0.000002	0.675309	–0.043261
Cl	–0.036826	0.175082	2.618083	Cl	–0.033697	–0.014027	2.644958	Cl	–0.000017	–0.585202	1.848201
N	2.507565	0.580724	0.380826	N	–2.819653	–0.196751	0.445992	N	–2.129201	1.063273	–0.240154
C	2.844533	1.835855	0.79275	N	1.313881	1.459998	–0.311208	N	2.129198	1.063278	–0.240131
N	–0.922459	–1.617154	–0.132008	C	–1.351603	1.975822	–0.255845	C	–0.000005	2.590087	0.026221
C	0.981794	–2.958003	–0.662546	C	–0.504386	3.001425	–0.671296	C	1.214448	3.266461	0.003128
C	4.172109	2.208968	0.923759	C	–1.073044	4.206136	–1.10967	C	1.218658	4.668041	0.014949
H	4.396677	3.216439	1.250718	H	–0.457599	5.031774	–1.450993	H	2.141544	5.238871	–0.004082
C	1.682518	–1.852834	–0.159068	C	–2.45994	4.348814	–1.123182	C	–0.000008	5.349937	0.032322
C	1.744492	2.826159	1.065794	H	–2.895273	5.280267	–1.466254	H	–0.00001	6.434043	0.038482
H	1.035926	2.393149	1.775751	C	–3.297629	3.312365	–0.713905	C	–1.218673	4.668038	0.014936
H	2.196728	3.696606	1.550459	H	–4.371707	3.45954	–0.754139	H	–2.14156	5.238866	–0.004106
C	–1.102308	3.931348	–1.219655	C	–2.739381	2.103461	–0.273078	C	–1.214459	3.266458	0.003115
H	–2.177418	4.059043	–1.156935	C	–3.524445	0.929043	0.171045	C	–2.400938	2.387675	–0.081704
C	3.52021	–0.321425	0.065707	C	–4.913499	0.945561	0.318392	C	–3.717407	2.841715	–0.01868
C	0.987894	3.283133	–0.171326	H	–5.472139	1.847048	0.10525	H	–3.920828	3.895494	0.119921
C	3.051354	–1.6277	–0.367284	C	–5.567736	–0.196804	0.751893	C	–4.755973	1.928928	–0.127352
C	4.857342	0.043906	0.175203	H	–6.644304	–0.195388	0.876859	H	–5.785605	2.264086	–0.078005
H	5.620241	–0.682343	–0.075284	C	–4.828474	–1.339675	1.030733	C	–4.465424	0.582092	–0.300658
C	–2.261114	–1.40371	–0.004138	H	–5.308226	–2.246678	1.376761	H	–5.253882	–0.152891	–0.393282
C	5.199404	1.311084	0.616135	C	–3.445113	–1.307194	0.864094	C	–3.132598	0.178155	–0.355108
H	6.237546	1.60095	0.719716	C	0.950267	2.726328	–0.631326	C	2.40093	2.387681	–0.08168
C	1.730513	–3.960158	–1.285639	C	1.922067	3.692208	–0.901538	C	3.717398	2.841725	–0.018643
H	1.255277	–4.85082	–1.68247	H	1.630372	4.704369	–1.147896	H	3.920814	3.895504	0.119959
C	–4.157454	0.292001	0.207554	C	3.261896	3.342896	–0.842712	C	4.755967	1.928941	–0.127306
C	1.652978	3.59242	–1.360837	H	4.027664	4.082487	–1.046303	H	5.785597	2.264101	–0.077951
H	2.728641	3.462835	–1.423287	C	3.616191	2.038605	–0.519306	C	4.465422	0.582103	–0.300615
C	–3.165932	–2.430155	–0.219035	H	4.653753	1.736536	–0.469044	H	5.253884	–0.152877	–0.393233
H	–4.222689	–2.222781	–0.116932	C	2.609024	1.113215	–0.257216	C	3.132598	0.178163	–0.355077
C	–0.429826	4.235278	–2.400239	C	–2.58789	–2.515924	1.151447	C	–2.724369	–1.263852	–0.58152
H	–0.976364	4.602612	–3.261449	H	–1.770128	–2.205089	1.807784	H	–1.861422	–1.45672	0.063516
C	–0.397226	3.456691	–0.116121	H	–3.19198	–3.246967	1.696629	H	–2.371336	–1.348672	–1.615375
H	–0.926061	3.219997	0.801299	C	–2.004742	–3.167073	–0.090588	C	–3.800517	–2.291085	–0.328543
C	–1.356373	–3.909711	–0.745475	C	–2.819595	–3.533046	–1.166476	C	–4.523082	–2.852523	–1.383647
H	–0.972278	–4.877106	–1.043089	H	–3.884656	–3.327796	–1.128681	H	–4.303494	–2.548184	–2.402221
C	3.114112	–3.800864	–1.426391	C	–2.280715	–4.156485	–2.28744	C	–5.51672	–3.799688	–1.145058
H	3.684645	–4.580175	–1.917807	H	–2.928159	–4.433565	–3.112079	H	–6.065316	–4.226537	–1.977333
C	–6.054942	0.930021	–1.1629	C	–0.914478	–4.425017	–2.352322	C	–5.800803	–4.199922	0.157515
H	–6.455021	1.215644	–2.129458	H	–0.494781	–4.910006	–3.226349	H	–6.571527	–4.938799	0.345609
C	–4.696856	0.655424	–1.029923	C	–0.094007	–4.065393	–1.287577	C	–5.083818	–3.649361	1.218104
H	–4.045759	0.728497	–1.895329	H	0.970392	–4.269263	–1.326882	H	–5.293665	–3.960675	2.235399
C	0.951113	4.062993	–2.466906	C	–0.63724	–3.441023	–0.165991	C	–4.09235	–2.703706	0.975565
H	1.484111	4.29788	–3.381687	H	0.006434	–3.164008	0.662579	H	–3.533487	–2.284086	1.805861
C	3.774803	–2.644598	–0.999463	C	2.885188	–0.335024	0.099187	C	2.724371	–1.263844	–0.58149
H	4.838764	–2.543158	–1.184906	H	2.372	–0.955332	–0.643467	H	1.861437	–1.456718	0.063562
C	–2.71766	–3.701144	–0.586458	H	2.387442	–0.528762	1.05528	H	2.371316	–1.348659	–1.615338
H	–3.42256	–4.506666	–0.750932	C	4.33953	–0.725967	0.177262	C	3.800527	–2.291076	–0.328541
C	–0.463864	–2.870456	–0.515844	C	5.010076	–1.2155	–0.946891	C	4.523092	–2.852484	–1.383662
C	–2.684044	0.000632	0.350835	H	4.472789	–1.323013	–1.883977	H	4.303497	–2.548123	–2.402228
H	–2.103647	0.680663	–0.285579	C	6.354661	–1.57072	–0.877776	C	5.516739	–3.799647	–1.145098
H	–2.359754	0.203162	1.375834	H	6.857404	–1.952183	–1.759582	H	6.065335	–4.226472	–1.977386
C	–6.371004	0.485672	1.181904	C	7.050328	–1.441527	0.321803	C	5.800831	–4.199908	0.157464
H	–7.017792	0.421758	2.049871	H	8.096459	–1.720324	0.378389	H	6.571561	–4.938783	0.345538
C	–5.010813	0.214229	1.310906	C	6.391751	–0.958515	1.450062	C	5.083846	–3.649377	1.218069
H	–4.605286	–0.057931	2.280144	H	6.92358	–0.861289	2.390004	H	5.293699	–3.960713	2.235356
C	–6.897178	0.843955	–0.056373	C	5.047089	–0.604939	1.376532	C	4.092369	–2.703724	0.975555
H	–7.954708	1.059962	–0.157939	H	4.538394	–0.234653	2.260897	H	3.533506	–2.284128	1.805864

[a] DFT calculations on TPSSh/def2-TZVP/CPCM(THF) level of theory.

Table A60. Calculated coordinates of the optimized singlet ground state structures of the complexes [M(L^{NHPh})OPh] (M = Pt and Pd).[a]

[Pt(L^{NHPh})OPh]				[Pd(L^{NHBh})OPh]			
atom	coordinates (Å)			atom	coordinates (Å)		
	X	Y	Z		X	Y	Z
Pt	-0.18711	0.966427	-0.07016	O	0.130875	-1.09223	0.062001
O	0.187254	-1.18322	0.045394	N	-2.27109	1.123017	0.019456
N	-2.26104	0.960062	0.070175	N	1.806098	1.702694	-0.33874
N	1.758685	1.65665	-0.33319	N	-2.59309	-1.14201	-0.32036
N	-2.52923	-1.31262	-0.29719	H	-1.56492	-1.21156	-0.2149
H	-1.49886	-1.35909	-0.21487	N	2.699212	-0.40575	-0.65395
N	2.721904	-0.42567	-0.65269	H	1.721366	-0.72624	-0.55478
H	1.75563	-0.78154	-0.56822	C	-0.4419	2.938933	-0.04358
C	-0.50939	2.849043	-0.02898	C	0.672098	3.776933	-0.10671
C	0.579682	3.720543	-0.10055	C	0.481328	5.157309	0.027214
C	0.350035	5.093786	0.034497	H	1.319538	5.844066	-0.01595
H	1.16469	5.80802	-0.01531	C	-0.8049	5.658865	0.226429
C	-0.95085	5.554977	0.246276	H	-0.94744	6.727782	0.332153
H	-1.12462	6.619225	0.352403	C	-1.9108	4.81157	0.296767
C	-2.03171	4.675096	0.332939	H	-2.89619	5.23504	0.457261
H	-3.02588	5.071556	0.508029	C	-1.73273	3.42979	0.161153
C	-1.81273	3.300375	0.195733	C	-2.76477	2.394812	0.190653
C	-2.79853	2.222391	0.242191	C	-4.11942	2.634869	0.338584
C	-4.15903	2.411686	0.403414	H	-4.48002	3.645549	0.470211
H	-4.5496	3.410898	0.537006	C	-4.99913	1.551864	0.318348
C	-5.0041	1.302233	0.391867	H	-6.06086	1.708605	0.468829
H	-6.06854	1.423949	0.554308	C	-4.52051	0.280218	0.103902
C	-4.48541	0.048685	0.166255	H	-5.1833	-0.57259	0.093152
H	-5.11875	-0.82616	0.155574	C	-3.13434	0.080414	-0.07749
C	-3.0971	-0.10865	-0.0316	C	1.934712	3.071967	-0.3198
C	1.853354	3.036614	-0.31306	C	3.155042	3.691854	-0.52055
C	3.060703	3.681778	-0.50729	H	3.226531	4.770178	-0.4907
H	3.102687	4.761571	-0.47492	C	4.271644	2.902395	-0.79792
C	4.199803	2.923692	-0.7772	H	5.232307	3.365253	-0.99132
H	5.149514	3.411378	-0.96289	C	4.151228	1.533549	-0.84984
C	4.113072	1.55282	-0.83146	H	4.995599	0.908301	-1.09929
H	4.973621	0.947492	-1.07464	C	2.895817	0.935765	-0.59998
C	2.87413	0.919907	-0.59189	C	0.365369	-1.69335	1.241267
C	0.435179	-1.81925	1.208291	C	0.710112	-3.05871	1.265642
C	0.825816	-3.17082	1.174599	H	0.788287	-3.59153	0.324006
H	0.927887	-3.65866	0.211258	C	0.951405	-3.71286	2.468435
C	1.080265	-3.86836	2.34987	H	1.216648	-4.76521	2.456059
H	1.381557	-4.90945	2.294341	C	0.858164	-3.03271	3.682603
C	0.953653	-3.24484	3.5911	H	1.047305	-3.54573	4.618391
H	1.152761	-3.79126	4.505665	C	0.518405	-1.68144	3.670453
C	0.567233	-1.90714	3.634166	H	0.441035	-1.13376	4.604275
H	0.462986	-1.40375	4.589966	C	0.274957	-1.01737	2.471427
C	0.310703	-1.1991	2.463002	H	0.011528	0.036397	2.470759
H	0.01108	-0.15665	2.503156	C	3.684781	-1.41043	-0.7545
C	3.746047	-1.39433	-0.73444	C	3.431438	-2.50384	-1.58965
C	3.559503	-2.48423	-1.59069	C	4.863597	-1.3846	-0.00154
C	4.896869	-1.33596	0.058567	C	4.345891	-3.54741	-1.67623
C	4.512441	-3.49452	-1.65728	H	2.514678	-2.52763	-2.16767
H	2.664477	-2.53199	-2.20037	C	5.781463	-2.42404	-0.10834
C	5.85355	-2.34164	-0.02774	H	5.050602	-0.56667	0.683307
H	5.031628	-0.51889	0.75676	C	5.530389	-3.5093	-0.9445
C	5.668612	-3.42468	-0.88397	H	4.134285	-4.38842	-2.32679
H	4.353009	-4.33425	-2.32413	H	6.690452	-2.39117	0.481668
H	6.740268	-2.28488	0.593489	H	6.246483	-4.31917	-1.01911
H	6.414376	-4.2087	-0.94225	C	-3.27894	-2.31553	-0.68972
C	-3.194	-2.49332	-0.68644	C	-2.8267	-3.53918	-0.18249
C	-2.7229	-3.71638	-0.19645	C	-4.34358	-2.30683	-1.59896
C	-4.25473	-2.48729	-1.59991	C	-3.43599	-4.7274	-0.56904
C	-3.30984	-4.90852	-0.60548	H	-1.99733	-3.55015	0.51554
H	-1.89635	-3.72434	0.504887	C	-4.95744	-3.49936	-1.96619
C	-4.8462	-3.68384	-1.98979	H	-4.67583	-1.37291	-2.03524
H	-4.60135	-1.55154	-2.02092	C	-4.51087	-4.71558	-1.45478
C	-4.38048	-4.90032	-1.49622	H	-3.07246	-5.66615	-0.16635
H	-2.93209	-5.84744	-0.2166	H	-5.78057	-3.4755	-2.67155
H	-5.6664	-3.66273	-2.69859	H	-4.98976	-5.64212	-1.74872
H	-4.8417	-5.83004	-1.80786	Pd	-0.17604	1.05153	-0.07784

[a] DFT calculations on TPSSh/def2-TZVP/CPCM(THF) level of theory.

Table A61. Calculated coordinates of the optimized singlet ground state structures of the complexes [M(L^{NHBn})OPh] (M = Pt and Pd).[a]

[Pt(L^{NHBn})OPh]				[Pd(L^{NHBn})OPh]			
atom	coordinates (Å)			atom	coordinates (Å)		
	X	Y	Z		X	Y	Z
Pt	0.146023	0.945939	-0.01145	O	-0.08662	-1.14388	-0.00527
O	-0.10343	-1.22667	-0.03301	N	-1.74385	1.601563	-0.68344
N	-1.74442	1.519424	-0.66374	N	2.170769	1.165048	0.565888
N	2.139683	1.070851	0.574366	N	-2.46422	-0.52174	-1.25922
N	-2.47914	-0.60025	-1.25259	H	-1.55988	-0.84567	-0.88955
H	-1.56972	-0.93158	-0.90477	N	2.653921	-1.08488	0.331993
N	2.622203	-1.1828	0.335348	H	1.657904	-1.19118	0.097738
H	1.632066	-1.28755	0.080983	C	0.327743	2.910651	0.120781
C	0.324028	2.843678	0.123227	C	1.525411	3.447012	0.598232
C	1.524583	3.374854	0.603035	C	1.610298	4.830342	0.794574
C	1.616167	4.75678	0.799046	H	2.521279	5.286689	1.166193
H	2.527335	5.212452	1.171223	C	0.506334	5.635381	0.513496
C	0.513324	5.565575	0.517082	H	0.576052	6.705593	0.668468
H	0.587815	6.635601	0.671054	C	-0.68723	5.089188	0.041398
C	-0.68624	5.025086	0.049245	H	-1.52839	5.742991	-0.16141
H	-1.52419	5.684693	-0.14829	C	-0.78482	3.707006	-0.15729
C	-0.78863	3.644196	-0.14871	C	-1.94356	2.960324	-0.64482
C	-1.94492	2.885866	-0.62254	C	-3.1295	3.536455	-1.06632
C	-3.13737	3.456743	-1.03035	H	-3.25692	4.609164	-1.02174
H	-3.26262	4.529486	-0.98137	C	-4.14056	2.709702	-1.55841
C	-4.15484	2.633096	-1.51176	H	-5.07978	3.136787	-1.89056
H	-5.09821	3.060676	-1.8308	C	-3.94556	1.350009	-1.62888
C	-3.95812	1.274353	-1.58902	H	-4.71989	0.69523	-2.00175
H	-4.73526	0.619252	-1.95485	C	-2.71809	0.798959	-1.18869
C	-2.72724	0.71955	-1.1669	C	2.572169	2.452369	0.827619
C	2.553069	2.36258	0.835205	C	3.860702	2.74464	1.240405
C	3.842649	2.639287	1.25333	H	4.146157	3.767528	1.44313
H	4.133439	3.660771	1.455435	C	4.778282	1.700705	1.368661
C	4.752276	1.590409	1.388191	H	5.793563	1.904724	1.688694
H	5.767142	1.787056	1.713679	C	4.402162	0.411473	1.070749
C	4.367281	0.304815	1.087019	H	5.108692	-0.40348	1.135918
H	5.066909	-0.51572	1.153641	C	3.073637	0.153018	0.656933
C	3.041067	0.052807	0.665837	C	-3.36972	-1.4901	-1.84494
C	-3.39534	-1.55927	-1.83859	H	-2.78056	-2.39598	-2.00804
H	-2.81123	-2.46576	-2.0154	H	-3.69589	-1.15113	-2.83434
H	-3.72968	-1.20955	-2.82142	C	-4.59312	-1.83732	-1.00956
C	-4.61126	-1.90844	-0.99348	C	-5.75435	-2.28087	-1.6462
C	-5.78792	-2.3209	-1.62244	H	-5.7844	-2.3328	-2.73052
H	-5.83484	-2.34714	-2.70708	C	-6.87353	-2.65217	-0.90628
C	-6.90114	-2.6938	-0.87422	H	-7.76827	-2.99217	-1.41593
H	-7.80817	-3.00934	-1.37783	C	-6.84607	-2.57842	0.484418
C	-6.8518	-2.65274	0.51713	H	-7.71782	-2.86223	1.063085
H	-7.71875	-2.93774	1.102386	C	-5.69339	-2.13182	1.125783
C	-5.68333	-2.23739	1.151021	H	-5.66403	-2.06886	2.207989
H	-5.63691	-2.20021	2.233819	C	-4.57365	-1.76466	0.383399
C	-4.5697	-1.86865	0.40043	H	-3.67906	-1.41719	0.888095
H	-3.66283	-1.54583	0.899608	C	3.471681	-2.27541	0.450494
C	3.437689	-2.37506	0.457319	H	2.7817	-3.12235	0.424107
H	2.746042	-3.22036	0.425007	H	3.961576	-2.30693	1.429923
H	3.919943	-2.40814	1.44027	C	4.517673	-2.45359	-0.63958
C	4.490735	-2.55359	-0.62573	C	4.340687	-1.91966	-1.91604
C	4.320276	-2.02344	-1.90466	H	3.457865	-1.32654	-2.12777
H	3.437758	-1.43249	-2.12368	C	5.289948	-2.13631	-2.91184
C	5.275711	-2.24141	-2.89418	H	5.13967	-1.71288	-3.89882
H	5.13057	-1.82105	-3.88322	C	6.428551	-2.89187	-2.64337
C	6.41385	-2.99452	-2.61688	H	7.168517	-3.05836	-3.41798
H	7.158547	-3.1621	-3.3867	C	6.613513	-3.4267	-1.37053
C	6.592212	-3.52552	-1.34154	H	7.50001	-4.01066	-1.14921
H	7.478262	-4.10751	-1.11339	C	5.664609	-3.20566	-0.37626
C	5.637147	-3.30319	-0.35346	H	5.818183	-3.61913	0.616059
H	5.785449	-3.71371	0.640877	C	-0.47321	-1.84485	1.070067
C	-0.48966	-1.96268	1.023909	C	-0.61655	-3.24331	0.966522
C	-0.61428	-3.35714	0.868659	H	-0.40852	-3.7157	0.011846
H	-0.39482	-3.79222	-0.10095	C	-1.01722	-4.00396	2.058478
C	-1.01142	-4.16088	1.930434	H	-1.12053	-5.07876	1.947624
H	-1.10045	-5.23219	1.78121	C	-1.28675	-3.40204	3.288121
C	-1.29519	-3.60523	3.178417	H	-1.59923	-3.99807	4.137705
H	-1.60472	-4.23428	4.00494	C	-1.14595	-2.02052	3.403533
C	-1.17304	-2.22722	3.342522	H	-1.34947	-1.53304	4.351758
H	-1.38853	-1.77569	4.305701	C	-0.74574	-1.24909	2.315779
C	-0.77655	-1.41206	2.28526	H	-0.63887	-0.17299	2.415767
H	-0.68557	-0.33954	2.422546	Pd	0.157129	1.015759	-0.00899

[a] DFT calculations on TPSSh/def2-TZVP/CPCM(THF) level of theory.

Table A62. Calculated coordinates of the optimized singlet ground state structures of the complexes [M(L^{Me})Cl] (M = Pt, Pd, Ni).[a]

[Pt(L^{Me})Cl]				[Pd(L^{Me})Cl]				[Ni(L^{Me})Cl]			
atom	coordinates (Å)			atom	coordinates (Å)			atom	coordinates (Å)		
	X	Y	Z		X	Y	Z		X	Y	Z
Pt	0	-0.524816	0.02976	Pd	0	-0.620196	0.027559	Ni	0.000002	-0.582612	0.053835
Cl	0	-2.813596	0.974103	Cl	0	-2.755075	1.340699	Cl	0.000038	-2.252526	1.647495
C	0	1.384273	-0.066497	C	0	1.28198	-0.064786	N	-1.926146	-0.345025	-0.177099
N	2.0629	-0.172791	-0.10244	C	-1.222333	1.950528	0.044482	N	1.926141	-0.345011	-0.177101
C	2.764785	-2.498852	-0.579311	N	-2.070517	-0.25405	-0.160891	C	-0.000004	1.21569	-0.109016
H	2.53693	-3.032026	0.344026	C	1.222333	1.950528	0.044482	C	1.219581	1.882533	0.004809
H	1.893017	-2.601245	-1.2253	C	-2.385371	1.074513	-0.035271	C	1.218629	3.271494	0.171891
H	3.629638	-2.962206	-1.055407	C	2.385371	1.074513	-0.035271	H	2.145819	3.82819	0.257971
N	-2.0629	-0.172791	-0.10244	N	2.070517	-0.25405	-0.16089	C	-0.000012	3.950353	0.242829
C	-1.2213	2.059356	0.023681	C	3.053776	-1.149044	-0.3966	H	-0.000016	5.02623	0.371688
C	0	4.137105	0.174287	C	3.707156	1.507403	-0.033561	C	-1.218648	3.271485	0.171897
H	0	5.217484	0.254491	H	3.926249	2.560213	0.084682	H	-2.145841	3.828175	0.257981
C	3.067715	-1.059329	-0.308668	C	-3.707156	1.507403	-0.033561	C	-1.219592	1.882524	0.004815
C	4.722188	0.692404	-0.120459	H	-3.92625	2.560213	0.084682	C	-2.34276	0.957586	-0.070863
H	5.756127	1.015472	-0.107028	C	-3.053775	-1.149044	-0.396601	C	-3.690709	1.293965	-0.091211
C	-2.373692	1.16974	-0.009971	C	4.723785	0.581418	-0.203503	H	-3.987835	2.328969	0.016239
C	-2.764785	-2.498852	-0.579311	H	5.760615	0.895876	-0.202301	C	-4.631212	0.291871	-0.276354
H	-1.893017	-2.601245	-1.2253	C	2.687661	-2.569374	-0.688148	H	-5.688719	0.526792	-0.297911
H	-2.53693	-3.032026	0.344026	H	2.152224	-3.013914	0.152247	C	-4.195674	-1.011285	-0.471503
H	-3.629638	-2.962206	-1.055407	H	2.016556	-2.611556	-1.550707	H	-4.900251	-1.809485	-0.666624
C	-1.21615	3.453712	0.134126	H	3.583275	-3.149051	-0.91049	C	-2.833883	-1.312655	-0.426621
H	-2.141817	4.015322	0.195926	C	-2.68766	-2.569373	-0.688149	C	2.342754	0.957601	-0.07087
C	-3.067715	-1.059329	-0.308668	H	-2.01655	-2.611555	-1.550703	C	3.690702	1.293979	-0.091224
C	3.692567	1.608594	0.005556	H	-2.152227	-3.013915	0.152249	H	3.987831	2.328983	0.016221
H	3.895773	2.666925	0.098931	H	-3.583273	-3.14905	-0.910496	C	4.631204	0.291883	-0.276369
C	1.2213	2.059356	0.023681	C	-1.214545	3.340067	0.212572	H	5.688711	0.526804	-0.297935
C	2.373692	1.16974	-0.009971	H	-2.142024	3.89577	0.295887	C	4.195666	-1.011274	-0.471513
C	-4.39906	-0.641866	-0.30568	C	-4.723785	0.581418	-0.203503	H	4.900241	-1.809474	-0.666638
H	-5.17057	-1.384758	-0.460858	H	-5.760615	0.895875	-0.202301	C	2.833875	-1.312642	-0.426622
C	4.39906	-0.641866	-0.30568	C	0	4.021026	0.28575	C	-2.355138	-2.706691	-0.693669
H	5.17057	-1.384758	-0.460858	H	0	5.096538	0.415617	H	-1.573062	-2.699817	-1.45733
C	-3.692567	1.608594	0.005556	C	4.390674	-0.748922	-0.409062	H	-1.922696	-3.144799	0.206949
H	-3.895773	2.666925	0.098931	H	5.155533	-1.493167	-0.58904	H	-3.182748	-3.324042	-1.043087
C	-4.722188	0.692404	-0.120459	C	1.214545	3.340067	0.212572	C	2.355124	-2.706678	-0.693659
H	-5.756126	1.015472	-0.107028	H	2.142024	3.895769	0.295887	H	1.572821	-2.699777	-1.45708
C	1.21615	3.453712	0.134126	C	-4.390674	-0.748922	-0.409062	H	1.922978	-3.144895	0.207049
H	2.141817	4.015322	0.195926	H	-5.155533	-1.493168	-0.589041	H	3.18267	-3.323954	-1.043367

[a] DFT calculations on TPSSh/def2-TZVP/CPCM(THF) level of theory.

Table A63. Calculated coordinates of the optimized singlet ground state structures of the complexes [M(L^{Me2})Cl] (M = Pt, Pd, Ni).[a]

[Pt(L^{Me2})Cl]				[Pd(L^{Me2})Cl]				[Ni(L^{Me2})Cl]			
atom	coordinates (Å)			atom	coordinates (Å)			atom	coordinates (Å)		
	X	Y	Z		X	Y	Z		X	Y	Z
Cl	-0.000017	-2.847825	1.453112	Pd	-0.000002	-0.902404	0.047948	Cl	0.000057	-2.417847	1.821595
C	0.000002	1.125766	-0.14349	Cl	0.000007	-2.883921	1.612561	C	-0.000037	0.900662	-0.160189
C	-1.242102	1.780677	-0.041804	C	-0.000001	0.999651	-0.128052	C	-1.234061	1.554725	-0.06638
N	-2.032972	-0.474605	-0.152588	C	-1.241073	1.651611	-0.032711	N	-1.90196	-0.692753	-0.191316
C	1.242107	1.780674	-0.04181	N	-2.03816	-0.583243	-0.183056	C	1.233975	1.554744	-0.066372
C	-2.3809	0.861606	-0.094975	C	1.241069	1.651612	-0.03271	C	-2.344854	0.60629	-0.135304
C	2.380902	0.861601	-0.094982	C	-2.388682	0.743344	-0.12011	C	2.344796	0.606336	-0.135301
N	2.032972	-0.474611	-0.152579	C	2.388679	0.743346	-0.120108	N	1.901971	-0.692726	-0.191396
C	2.981528	-1.411542	-0.390654	N	2.038158	-0.583241	-0.183063	C	2.770896	-1.696876	-0.428986
C	3.726407	1.226826	-0.141303	C	2.970264	-1.526667	-0.428297	C	3.708074	0.88754	-0.198758
H	4.004886	2.264412	-0.078818	C	3.733011	1.107986	-0.196133	H	4.057816	1.905049	-0.134066
C	-3.726406	1.226829	-0.141281	H	4.021	2.143359	-0.137016	C	-3.708142	0.887405	-0.198853
H	-4.004887	2.264414	-0.078779	C	-3.733014	1.107981	-0.196146	H	-4.057953	1.904897	-0.134244
C	-2.981525	-1.411535	-0.390677	H	-4.021005	2.143354	-0.137039	C	-2.770794	-1.696962	-0.42889
C	4.70677	0.261172	-0.295544	C	-2.970261	-1.526673	-0.428287	C	4.612244	-0.150058	-0.373466
H	5.751712	0.545523	-0.328589	C	4.704007	0.134535	-0.375049	H	5.674589	0.056862	-0.426163
C	2.574666	-2.830129	-0.640475	H	5.749151	0.414723	-0.432555	C	2.234759	-3.079819	-0.639662
H	2.14666	-3.281721	0.254829	C	2.52641	-2.93782	-0.651479	H	1.721377	-3.4345	0.255492
H	1.806205	-2.871532	-1.416594	H	1.995268	-3.321353	0.221341	H	1.505967	-3.080315	-1.455477
H	3.440484	-3.405702	-0.967551	H	1.830712	-2.980146	-1.494762	H	3.045698	-3.761253	-0.896442
C	-2.574649	-2.830114	-0.640525	H	3.38566	-3.570139	-0.874338	C	-2.23452	-3.079869	-0.639453
H	-1.8062	-2.871493	-1.416657	C	-2.5264	-2.937829	-0.65144	H	-1.504803	-3.08016	-1.454419
H	-2.146624	-3.281706	0.25477	H	-1.830604	-2.980154	-1.494642	H	-1.722254	-3.434956	0.256178
H	-3.440463	-3.405696	-0.967599	H	-1.995361	-3.321377	0.221437	H	-3.04525	-3.761138	-0.897364
C	-1.240484	3.184383	0.1096	H	-3.385632	-3.570134	-0.8744	C	-1.239978	2.95756	0.080186
C	-4.706768	0.261175	-0.29553	C	-1.238899	3.054314	0.136691	C	-4.612238	-0.150266	-0.37357
H	-5.751711	0.545524	-0.328563	C	-4.704007	0.134527	-0.375065	H	-5.67459	0.056592	-0.426355
C	0.000005	3.825907	0.16357	H	-5.749151	0.414713	-0.432582	C	-0.000066	3.602742	0.137636
H	0.000006	4.904624	0.282702	C	-0.000003	3.694885	0.205845	H	-0.000076	4.682185	0.253814
C	4.328223	-1.061691	-0.449352	H	-0.000003	4.771398	0.343582	C	4.13952	-1.445276	-0.515673
H	5.060629	-1.838351	-0.626354	C	4.319946	-1.188247	-0.514641	H	4.814622	-2.271177	-0.698826
C	1.240492	3.184381	0.109594	H	5.046799	-1.968437	-0.699449	C	1.239859	2.957583	0.080196
C	-4.328221	-1.061686	-0.449363	C	1.238894	3.054315	0.136692	C	-4.139432	-1.445461	-0.51568
H	-5.060627	-1.838343	-0.626374	C	-4.319943	-1.188256	-0.514645	H	-4.81447	-2.271414	-0.698838
C	2.466347	4.049884	0.242724	H	-5.046794	-1.968448	-0.699455	C	2.484219	3.797401	0.197461
C	-2.466338	4.049889	0.242735	C	2.467834	3.914757	0.273934	C	-2.484367	3.797336	0.197438
H	2.169325	5.086021	0.40824	C	-2.46784	3.914754	0.273934	H	2.216496	4.842321	0.358772
H	3.092478	3.742574	1.08513	H	2.174364	4.945479	0.475588	H	3.110168	3.477099	1.035354
H	3.084776	4.022099	-0.659471	H	3.108798	3.5815	1.094728	H	3.094172	3.744987	-0.709515
H	-2.169313	5.086026	0.408242	H	3.069118	3.914279	-0.640206	H	-2.216685	4.842259	0.358799
H	-3.084774	4.022098	-0.659454	H	-2.174372	4.945475	0.475596	H	-3.094283	3.744937	-0.709564
H	-3.092461	3.742584	1.085149	H	-3.069121	3.914281	-0.640208	H	-3.110338	3.476978	1.035292
Pt	-0.000002	-0.779721	0.027054	H	-3.108808	3.58149	1.094724	Ni	-0.000013	-0.893997	0.067899

[a] DFT calculations on TPSSh/def2-TZVP/CPCM(THF) level of theory.

Table A64. Calculated coordinates of the optimized singlet ground state structures of the complexes [M(L^{Cl})X] (M = Pt, Pd, Ni; X = Cl or Br).[a]

[Pt(L^{Cl})Cl]				[Pd(L^{Cl})Cl]				[Ni(L^{Cl})Br]			
atom	coordinates (Å)			atom	coordinates (Å)			atom	coordinates (Å)		
	X	Y	Z		X	Y	Z		X	Y	Z
Pt	0	1.02242	0.000062	Pd	0	-1.184642	-0.00003	Br	0	3.332658	-0.000327
Cl	0	3.470445	-0.000042	Cl	0	-3.623374	0.000145	Ni	0	0.906967	0.000113
Cl	4.378796	-2.523309	-0.00006	Cl	-4.384039	2.382251	0.000039	Cl	4.378585	-2.523659	-0.00012
Cl	-4.378796	-2.52331	-0.000121	Cl	4.384039	2.382251	0.000039	Cl	-4.378585	-2.523658	-0.000199
C	4.277312	1.434547	0.000205	N	2.020981	-0.848746	-0.000031	N	-1.925011	0.648614	0.000214
H	4.984434	2.252688	0.000289	N	-2.020981	-0.848746	-0.000031	N	1.925011	0.648614	0.000244
N	2.009629	0.705069	0.000072	C	0	0.720113	-0.000018	C	0	-3.673213	-0.000706
N	-2.009629	0.705069	0.000047	C	1.235407	1.389912	-0.000004	H	0	-4.75667	-0.000965
C	-2.379572	-0.627156	-0.000038	C	-2.387248	0.476344	-0.000012	C	1.224055	-1.594067	-0.00021
C	2.379572	-0.627156	-0.000008	C	2.387248	0.476344	-0.000012	C	0	-0.914322	-0.00007
C	-1.238896	-1.553342	-0.000115	C	-2.925047	-1.831608	-0.000053	C	-2.349697	-0.6601	-0.000002
C	1.238896	-1.553342	-0.000099	H	-2.516691	-2.834316	-0.000064	C	-1.224055	-1.594067	-0.00023
C	0	-3.62777	-0.000338	C	-1.235407	1.389912	-0.000004	C	2.349697	-0.6601	0.000037
H	0	-4.711131	-0.000465	C	4.286948	-1.577029	-0.000055	C	-1.2165	-2.99629	-0.000556
C	0	-0.884439	-0.000034	H	4.996036	-2.393594	-0.000074	H	-2.133187	-3.565652	-0.000701
C	-4.277312	1.434547	0.000147	C	0	3.46691	0.000017	C	4.648908	0.126833	0.000488
H	-4.984434	2.252688	0.000222	H	0	4.550263	0.000027	H	5.707693	-0.097359	0.000571
C	2.917595	1.689036	0.000174	C	1.217921	2.792691	0.000012	C	4.185074	1.429034	0.000735
H	2.509164	2.691201	0.000228	H	2.131416	3.366675	0.000018	H	4.86591	2.269414	0.001022
C	-2.917595	1.689036	0.000137	C	-1.217921	2.792691	0.000012	C	2.816432	1.647123	0.000598
H	-2.509164	2.6912	0.000197	H	-2.131416	3.366675	0.000018	H	2.398334	2.643496	0.00075
C	3.75544	-0.903196	0.00002	C	-4.286948	-1.577029	-0.000055	C	1.216499	-2.99629	-0.000536
C	-1.220554	-2.955419	-0.000271	H	-4.996036	-2.393594	-0.000074	H	2.133186	-3.565652	-0.000666
H	-2.131416	-3.533499	-0.00035	C	-3.761208	0.761413	-0.000004	C	3.727452	-0.913555	0.000141
C	4.700024	0.116494	0.000126	C	-4.706707	-0.258736	-0.000027	C	-2.816432	1.647124	0.000554
H	5.752211	-0.136374	0.000147	H	-5.758689	-0.004489	-0.000023	H	-2.398334	2.643496	0.000714
C	-4.700024	0.116494	0.000061	C	2.925047	-1.831608	-0.000054	C	-4.185074	1.429034	0.000665
H	-5.752211	-0.136374	0.000067	H	2.516691	-2.834316	-0.000064	H	-4.86591	2.269415	0.00094
C	-3.75544	-0.903196	-0.000031	C	3.761208	0.761413	-0.000004	C	-3.727452	-0.913555	0.000077
C	1.220555	-2.955419	-0.000256	C	4.706707	-0.258736	-0.000027	C	-4.648908	0.126833	0.000408
H	2.131416	-3.533499	-0.000323	H	5.758689	-0.004489	-0.000022	H	-5.707693	-0.097359	0.000471

[a] DFT calculations on TPSSh/def2-TZVP/CPCM(THF) level of theory.

Table A65. Calculated coordinates of the optimized singlet ground state structures of the complexes [M(L^F)X] (M = Pt, Pd, Ni; X = Cl or Br).[a]

[Pt(L^F)Cl]				[Pd(L^F)Cl]				[Ni(L^F)Br]			
atom	coordinates (Å)			atom	coordinates (Å)			atom	coordinates (Å)		
	X	Y	Z		X	Y	Z		X	Y	Z
Pt	0	0.940804	0.000037	Pd	0	1.09957	0.000008	Ni	0	0.813264	0.000002
Cl	0	3.378026	0.000087	Cl	0	3.525175	0.000614	N	-1.930205	0.554187	0.000002
C	4.314725	1.268518	0.000034	N	2.028094	0.761486	-0.000048	N	1.930205	0.554187	0.000005
H	5.040421	2.070728	0.000063	N	-2.028094	0.761486	-0.000031	C	0	-3.779875	-0.000009
N	2.016618	0.619286	0.000017	C	0	-0.810206	-0.000119	H	0	-4.861196	-0.000012
N	-2.016618	0.619286	0.000042	C	1.238078	-1.463999	-0.000097	C	1.227375	-1.676193	-0.000002
C	-2.379992	-0.709649	-0.000006	C	-2.387556	-0.56182	-0.000074	C	0	-1.012982	-0.000001
C	2.379992	-0.709649	-0.000038	C	2.387556	-0.56182	-0.000096	C	-2.35058	-0.751727	-0.000002
C	-1.241241	-1.623635	-0.000054	C	-2.971936	1.710206	-0.000048	C	-1.227375	-1.676193	-0.000004
C	1.241241	-1.623635	-0.00007	H	-2.604275	2.728705	-0.000009	C	2.35058	-0.751727	0.000002
C	0	-3.722926	-0.00015	C	-1.238078	-1.463999	-0.000086	C	-1.192603	-3.070255	-0.000008
H	0	-4.804147	-0.000196	C	4.325615	1.407278	-0.000142	C	4.64928	-0.053851	0.000009
C	0	-0.969841	-0.000035	H	5.053688	2.207428	-0.000166	H	5.706208	-0.291518	0.00001
C	-4.314725	1.268518	0.000095	C	0	-3.565689	-0.000023	C	4.217601	1.265594	0.000012
H	-5.040421	2.070728	0.000135	H	0	-4.646968	0.000021	H	4.915412	2.092415	0.000016
C	2.96275	1.570259	0.000051	C	1.194134	-2.859261	-0.000051	C	2.854652	1.525861	0.00001
H	2.593524	2.587729	0.000092	C	-1.194134	-2.859261	-0.00004	H	2.46771	2.53552	0.000012
C	-2.96275	1.570259	0.00009	C	-4.325615	1.407278	-0.0001	C	1.192603	-3.070255	-0.000006
H	-2.593524	2.587729	0.000125	H	-5.053688	2.207428	-0.000116	C	3.705236	-1.071969	0.000004
C	3.729194	-1.057985	-0.000058	C	-3.73453	-0.919159	-0.000113	C	-2.854652	1.525861	0.000005
C	-1.196352	-3.017369	-0.000112	C	-4.707999	0.071724	-0.000127	H	-2.467711	2.53552	0.000008
C	4.700984	-0.066618	-0.000021	H	-5.756347	-0.201128	-0.000163	C	-4.217601	1.265594	0.000005
H	5.749771	-0.337296	-0.000036	C	2.971936	1.710206	-0.000075	H	-4.915412	2.092415	0.000008
C	-4.700984	-0.066618	0.000047	H	2.604275	2.728705	-0.000031	C	-3.705235	-1.071969	-0.000002
H	-5.749771	-0.337297	0.000049	C	3.73453	-0.919159	-0.000151	C	-4.64928	-0.053851	0.000001
C	-3.729194	-1.057985	-0.000004	C	4.707999	0.071724	-0.000175	H	-5.706208	-0.291518	0.000001
C	1.196352	-3.017369	-0.000129	H	5.756347	-0.201128	-0.000223	H	-4.006362	-2.109367	-0.000005
H	4.006121	-2.101904	-0.000101	H	4.010471	-1.96322	-0.000181	H	4.006362	-2.109367	0.000001
H	-4.006121	-2.101904	-0.000042	H	-4.010471	-1.96322	-0.000139	F	2.340844	-3.784022	-0.000007
F	-2.338224	-3.739953	-0.000135	F	-2.337045	-3.579437	0.000004	F	-2.340844	-3.784022	-0.000011
F	2.338224	-3.739953	-0.000167	F	2.337045	-3.579437	-0.000018	Br	0	3.221061	-0.000002

[a] DFT calculations on TPSSh/def2-TZVP/CPCM(THF) level of theory.

Table A66. Calculated coordinates of the optimized singlet ground state structures of the complexes [M(L^{Qu})Cl] (M = Pt, Pd, Ni).[a]

[Pt(L^{Qu})Cl]				[Pd(L^{Qu})Cl]				[Ni(L^{Qu})Cl]			
atom	coordinates (Å)			atom	coordinates (Å)			atom	coordinates (Å)		
	X	Y	Z		X	Y	Z		X	Y	Z
Pt	0.00001	-0.149542	0.118167	Pd	-0.000011	-0.181951	0.183218	Ni	-0.000037	-0.056854	0.200037
Cl	-0.000444	-2.303967	1.344726	Cl	-0.000071	-2.286091	1.489796	Cl	-0.000633	-1.694435	1.784486
N	-2.053929	0.196039	-0.033585	N	-2.073194	0.180917	-0.026151	N	1.933823	0.173932	-0.034278
N	2.054011	0.195995	-0.033401	N	2.0732	0.180909	-0.02618	N	-1.93376	0.173966	-0.034144
C	0.000055	1.741746	-0.12597	C	-0.000015	1.704953	-0.069899	C	1.218378	2.395955	-0.078087
C	1.223943	2.418447	-0.065424	C	1.221845	2.381492	-0.024204	C	2.335244	1.464699	-0.057745
C	1.217552	3.817163	-0.023921	C	1.214847	3.781136	0.01762	C	3.424267	-3.15498	-0.47202
H	2.141999	4.382425	0.017206	H	2.141599	4.343031	0.049734	H	3.103122	-4.184484	-0.581125
C	0.000083	4.500213	-0.019834	C	-0.00002	4.465561	0.029649	C	2.480513	-2.168202	-0.307564
H	0.000096	5.58303	0.010021	H	-0.000018	5.548278	0.062507	H	1.428363	-2.410016	-0.270209
C	-1.2174	3.817188	-0.023808	C	-1.214887	3.781136	0.017661	C	3.696199	1.827901	-0.092999
H	-2.141834	4.382469	0.017381	H	-2.141645	4.343022	0.049786	H	3.962733	2.876557	-0.076716
C	-1.223821	2.418472	-0.065311	C	-1.221874	2.381493	-0.024149	C	-1.218484	2.395971	-0.07752
C	-2.365288	1.518728	-0.03499	C	-2.378045	1.496562	-0.028179	C	-0.000067	1.7202	-0.125138
C	-3.702978	1.965283	-0.030099	C	-3.71297	1.95235	-0.067133	C	1.21859	3.795324	-0.052063
H	-3.896286	3.029007	0.002911	H	-3.907159	3.016129	-0.038853	H	2.145299	4.358397	-0.023457
C	-4.727574	1.064089	-0.070508	C	-4.737284	1.051688	-0.149232	C	4.266554	-0.502969	-0.230317
H	-5.76075	1.392221	-0.05607	H	-5.76929	1.38316	-0.17593	C	2.874141	-0.818538	-0.174077
C	-4.437225	-0.314189	-0.173941	C	-4.448417	-0.327966	-0.234458	C	-2.873957	-0.818555	-0.174269
C	-3.069987	-0.727322	-0.173327	C	-3.081628	-0.739777	-0.179097	C	-2.335304	1.464695	-0.057098
C	2.365387	1.518683	-0.03518	C	2.378024	1.496563	-0.02828	C	4.653627	0.853973	-0.158354
C	3.703076	1.965245	-0.030785	C	3.712935	1.952381	-0.067335	H	5.707321	1.108539	-0.183959
H	3.896381	3.028982	0.001866	H	3.907107	3.016172	-0.039158	C	4.800729	-2.849798	-0.498956
C	4.727667	1.064057	-0.071327	C	4.737268	1.051742	-0.149415	H	5.527714	-3.643962	-0.620879
H	5.760844	1.392205	-0.057365	H	5.76926	1.383241	-0.17619	C	-4.266411	-0.503133	-0.230209
C	4.437294	-0.314256	-0.174207	C	4.448437	-0.327925	-0.234504	C	-1.218676	3.795337	-0.051444
C	3.070059	-0.727407	-0.172993	C	3.081658	-0.739773	-0.179074	H	-2.145404	4.358419	-0.022229
C	-2.779389	-2.094089	-0.362583	C	-2.779892	-2.110611	-0.323098	C	-4.653614	0.853742	-0.157594
H	-1.747345	-2.411324	-0.378485	H	-1.745124	-2.420486	-0.27743	H	-5.707357	1.108201	-0.182916
C	-3.796959	-3.00817	-0.514165	C	-3.789098	-3.028591	-0.497636	C	-3.6963	1.827761	-0.091981
H	-3.551377	-4.05287	-0.666305	H	-3.539329	-4.077018	-0.613013	H	-3.962947	2.876384	-0.07532
C	-5.147645	-2.609839	-0.475547	C	-5.141141	-2.629229	-0.52709	C	-2.480101	-2.168092	-0.308447
H	-5.933397	-3.347418	-0.587139	H	-5.920465	-3.370412	-0.658555	H	-1.427852	-2.409705	-0.270776
C	-5.45808	-1.282423	-0.310578	C	-5.461904	-1.300363	-0.397641	C	-0.000051	4.477849	-0.050473
H	-6.489721	-0.948533	-0.297918	H	-6.494461	-0.970619	-0.430601	H	-0.000047	5.561188	-0.031711
C	2.779431	-2.09428	-0.361418	C	2.779972	-2.110639	-0.322915	C	5.210967	-1.544943	-0.380441
H	1.747407	-2.411545	-0.376635	H	1.745281	-2.420578	-0.277166	H	6.263782	-1.287031	-0.413294
C	3.796969	-3.008412	-0.512932	C	3.789214	-3.028594	-0.497382	C	-5.210681	-1.545179	-0.380764
H	3.551356	-4.053197	-0.664424	H	3.539484	-4.077039	-0.612639	H	-6.263545	-1.287434	-0.413261
C	5.147656	-2.610025	-0.47506	C	5.141243	-2.629195	-0.526907	C	-3.423709	-3.154904	-0.473452
H	5.933388	-3.347636	-0.586607	H	5.920588	-3.370363	-0.658306	H	-3.102437	-4.184291	-0.583201
C	5.45812	-1.282525	-0.310798	C	5.461958	-1.300303	-0.397603	C	-4.800232	-2.84989	-0.500128
H	6.489756	-0.948608	-0.29864	H	6.494495	-0.970525	-0.4306	H	-5.52711	-3.644106	-0.622422

[a] DFT calculations on TPSSh/def2-TZVP/CPCM(THF) level of theory.

Table A67. Calculated coordinates of the optimized triplet excited state structures of the complexes [M(L^{Qu})Cl] (M = Pt, Pd, Ni).[a]

[Pt(L^{Qu})Cl]				[Pd(L^{Qu})Cl]				[Ni(L^{Qu})Cl]			
atom	coordinates (Å)			atom	coordinates (Å)			atom	coordinates (Å)		
	X	Y	Z		X	Y	Z		X	Y	Z
Pt	-0.000029	-0.166678	-0.085018	Pd	-0.000181	-0.461406	-0.093662	Ni	0.000008	-0.308917	0.042747
Cl	0.000306	-1.480385	1.971392	Cl	-0.000598	-1.446548	2.100391	Cl	-0.000098	-1.576096	1.913311
N	-2.039419	0.152827	-0.121563	N	-2.257907	0.089149	-0.176745	N	2.135681	0.090453	-0.160255
N	2.039404	0.152862	-0.121755	N	2.258056	0.08902	-0.176708	N	-2.135659	0.090467	-0.160338
C	-0.00002	1.753771	0.010085	C	0.000073	1.57667	-0.057371	C	1.213605	2.284703	-0.000998
C	1.241892	2.389523	-0.010944	C	1.221133	2.248154	-0.034244	C	2.396803	1.401642	-0.061994
C	1.224342	3.789609	-0.014637	C	1.215182	3.650197	0.022832	C	3.909494	-3.092657	-0.451361
H	2.146383	4.359866	-0.024962	H	2.13649	4.222208	0.041022	H	3.682177	-4.149265	-0.533656
C	-0.000048	4.464429	-0.00856	C	0.000149	4.333202	0.053283	C	2.884438	-2.182079	-0.355603
H	-0.000064	5.54791	-0.008271	H	0.000186	5.415982	0.098792	H	1.850684	-2.504165	-0.345571
C	-1.224435	3.789592	-0.014416	C	-1.214928	3.650283	0.022681	C	3.725807	1.888013	-0.035781
H	-2.146485	4.359841	-0.024655	H	-2.136206	4.222348	0.040752	H	3.901485	2.951932	0.053065
C	-1.241967	2.389502	-0.010712	C	-1.220951	2.248245	-0.03438	C	-1.213588	2.28471	-0.001008
C	-2.37869	1.487041	-0.045699	C	-2.439725	1.410577	-0.084451	C	0.000004	1.608109	0.052311
C	-3.716683	1.893535	-0.017342	C	-3.744272	1.964621	-0.044545	C	1.218121	3.686221	-0.0436
H	-3.936696	2.951537	0.046568	H	-3.86855	3.035974	0.035645	H	2.140438	4.25631	-0.085524
C	-4.730215	0.965657	-0.06133	C	-4.838554	1.146214	-0.106885	C	4.526831	-0.373428	-0.230046
H	-5.769017	1.271911	-0.026944	H	-5.840795	1.559844	-0.077468	C	3.165541	-0.800909	-0.244116
C	-4.411297	-0.413655	-0.162025	C	-4.667312	-0.252815	-0.21222	C	-3.165523	-0.800891	-0.244201
C	-3.035919	-0.799397	-0.199968	C	-3.330402	-0.749257	-0.242246	C	-2.396784	1.401651	-0.061997
C	2.378642	1.487074	-0.045994	C	2.439877	1.410435	-0.084242	C	4.774822	1.013303	-0.117897
C	3.716638	1.893597	-0.017663	C	3.744413	1.964499	-0.044116	H	5.798309	1.371849	-0.098375
H	3.936637	2.9516	0.046213	H	3.868665	3.035842	0.036232	C	5.257179	-2.671186	-0.439069
C	4.730186	0.965722	-0.061605	C	4.838717	1.146127	-0.106431	H	6.049996	-3.40597	-0.514191
H	5.768986	1.271987	-0.027244	H	5.840949	1.559765	-0.076828	C	-4.526814	-0.373419	-0.229997
C	4.411289	-0.413586	-0.162184	C	4.667499	-0.252884	-0.212006	C	-1.218096	3.686228	-0.043614
C	3.035918	-0.799332	-0.200091	C	3.330595	-0.749341	-0.24226	H	-2.140407	4.256323	-0.085563
C	-2.719014	-2.16294	-0.33362	C	-3.120678	-2.143801	-0.346409	C	-4.774805	1.013304	-0.117755
H	-1.682022	-2.467718	-0.368328	H	-2.10347	-2.517814	-0.35836	H	-5.798292	1.371844	-0.098135
C	-3.71638	-3.117182	-0.408441	C	-4.19187	-3.001792	-0.421817	C	-3.725788	1.888016	-0.03568
H	-3.446088	-4.161654	-0.511548	H	-4.019991	-4.06898	-0.501196	H	-3.901465	2.95193	0.053227
C	-5.068338	-2.745888	-0.356328	C	-5.515875	-2.511562	-0.393892	C	-2.884424	-2.182051	-0.355837
H	-5.842203	-3.501999	-0.415952	H	-6.346025	-3.205388	-0.453428	H	-1.850671	-2.50414	-0.345953
C	-5.40433	-1.413099	-0.23734	C	-5.748109	-1.161396	-0.289563	C	0.000015	4.368866	-0.051717
H	-6.444581	-1.10734	-0.20348	H	-6.760334	-0.772412	-0.265672	H	0.000018	5.452248	-0.087029
C	2.718998	-2.162888	-0.333477	C	3.120951	-2.143877	-0.346746	C	5.5589	-1.335529	-0.328916
H	1.681987	-2.467623	-0.368058	H	2.103778	-2.517956	-0.35895	H	6.589763	-0.998357	-0.316335
C	3.716364	-3.117152	-0.408092	C	4.192178	-3.001821	-0.422205	C	-5.558888	-1.335517	-0.328848
H	3.446067	-4.161648	-0.510944	H	4.020332	-4.068995	-0.501846	H	-6.589751	-0.99835	-0.316154
C	5.068324	-2.745849	-0.356044	C	5.516166	-2.511568	-0.39401	C	-3.909484	-3.092626	-0.451583
H	5.84219	-3.501973	-0.415497	H	6.346345	-3.205356	-0.453586	H	-3.682169	-4.149225	-0.533997
C	5.404323	-1.413052	-0.237313	C	5.748335	-1.161414	-0.289391	C	-5.25717	-2.671165	-0.439129
H	6.444573	-1.107293	-0.20347	H	6.760543	-0.772395	-0.26531	H	-6.04999	-3.405946	-0.514237

[a] DFT calculations on TPSSh/def2-TZVP/CPCM(THF) level of theory.

8. Declaration regarding the dissertation

Erklärung zur Dissertation

gemäß der Promotionsordnung vom 12. März 2020

„Hiermit versichere ich an Eides statt, dass ich die vorliegende Dissertation selbstständig und ohne die Benutzung anderer als der angegebenen Hilfsmittel und Literatur angefertigt habe. Alle Stellen, die wörtlich oder sinngemäß aus veröffentlichten und nicht veröffentlichten Werken dem Wortlaut oder dem Sinn nach entnommen wurden, sind als solche kenntlich gemacht. Ich versichere an Eides statt, dass diese Dissertation noch keiner anderen Fakultät oder Universität zur Prüfung vorgelegen hat; dass sie - abgesehen von unten angegebenen Teilpublikationen und eingebundenen Artikeln und Manuskripten - noch nicht veröffentlicht worden ist sowie, dass ich eine Veröffentlichung der Dissertation vor Abschluss der Promotion nicht ohne Genehmigung des Promotionsausschusses vornehmen werde. Die Bestimmungen dieser Ordnung sind mir bekannt. Darüber hinaus erkläre ich hiermit, dass ich die Ordnung zur Sicherung guter wissenschaftlicher Praxis und zum Umgang mit wissenschaftlichem Fehlverhalten der Universität zu Köln gelesen und sie bei der Durchführung der Dissertation zugrundeliegenden Arbeiten und der schriftlich verfassten Dissertation beachtet habe und verpflichte mich hiermit, die dort genannten Vorgaben bei allen wissenschaftlichen Tätigkeiten zu beachten und umzusetzen. Ich versichere, dass die eingereichte elektronische Fassung der eingereichten Druckfassung vollständig entspricht."

Teilpublikationen:

1. “Molecular Rigidification of Cyclometalated N^C^N Pt(II)- and Pd(II)-Based Triplet Emitters”. M. Niazi, I. Maisuls, C. A. Strassert, and A. Klein. *Organometallics* **2024**, *43* (14), 1547−1556.
2. “Conformational Locking of the Geometry in Photoluminescent Cyclometalated N^C^N Ni(II) Complexes”. M. Niazi, I. Maisuls, L. A. Mai, S. A. Schäfer, A. Oster, L. S. Diaz, D. M. Guldi, N. Doltsinis, C. A. Strassert, A. Klein. *Molecules* **2025**, *30*(9), 1901.

Köln 22.02.2025, Maryam Niazi